A Theory of Jamming and Elastic Instability in Low Temperature Amorphous Solids

Doctoral thesis for obtaining
the academic degree
Doctor of Natural Sciences (Dr. rer. nat.)

submitted by

Florian Vogel

at the

Mathematisch-Naturwissenschaftliche Sektion
Fachbereich Physik

Konstanz, 2025

Oral Examination Date:	29.07.2025
First Referee:	Prof. Dr. Matthias Fuchs
Second Referee:	Prof. Dr. Wolfgang Belzig
Head of the Oral Examination Committee:	Prof. Dr. Peter Baum

Abstract

Despite intense research, no first-principles theory has yet rationalized the rich phenomena and vibrational anomalies in amorphous solids. This monograph presents an analytical study, which in takes the first steps towards an exhaustive microscopic theory. The derived microscopic theory successfully describes the jammed and unjammed phase of disordered systems at zero temperature. Employing the Zwanzig-Mori projection operator formalism, we expand the Mode-Coupling Theory to coherently describe the jammed state. We identify a symmetry constraint in the sequence of local scattering events, compelling us to go beyond the standard self-consistent Born approximation: A planar theory does not recover the characteristic Rayleigh-sound attenuation in amorphous solids. Thus, we include non-planar contributions in the theoretical model.

The universal vibrational properties of amorphous solids at low temperatures are recovered in the jammed phase. We identify a diffusive regime of modes, characterized by a plateau in the vibrational Density of States. Here, the energy suffices to resolve the local disorder. Below the disorder-dominated regime, modes can propagate, and the system can be approximated as an elastic medium. The vanishing of the transverse speed of sound heralds the unjamming instability. The diffusive regime extends down to zero frequency directly at the critical point. In the unjammed phase, the theory predicts no viscous flow but the presence of modes with zero restoring forces. As a consequence, injected momentum causes plastic rearrangements of stable sub-clusters whose size diverges at the jamming transition. Utilizing the Euclidean Random Matrix model, we support our theory by deriving an equivalent theory in the harmonic approximation of the potential energy. The quantitative predictions of the theory are in good agreement with Philipp Baumgärtel's numerical solution of the scalar Euclidean Random Matrix model published in (Vogel *et al.*, 2025).

Deutsche Zusammenfassung

Trotz langer Forschung gibt es noch keine Theorie, welche die zahlreichen Phänomene und Anomalien in amorphen Festkörpern mit fundamentalen Prinzipien erklärt. In dieser Arbeit stellen wir eine mikroskopische Theorie ungeordneter Systeme bei verschwindender Temperatur vor, die sowohl deren stabile als auch instabile Phase beschreiben kann. Mit dem Zwanzig-Mori-Projektionsoperator-Formalismus erweitern wir die Modenkopplungs-Theorie, die für unterkühlte Flüssigkeiten und den Glasübergang gut etabliert ist, um auch die stabile athermische Phase beschreiben zu können. Hierbei identifizieren wir eine Symmetriebeschränkung in der Sequenz lokaler Streuereignisse. Diese macht es erforderlich, über die selbstkonsistente Born-Näherung hinauszugehen. Eine planare Theorie kann die charakteristische Rayleigh-Dämpfung nicht vorhersagen. Deshalb müssen nicht-planare Beiträge berücksichtigt werden müssen. Die Theorie charakterisiert die instabile Phase durch Moden ohne Rückstellkraft. Diese machen das System unter anderem anfällig für Scherung. Da keine viskose Strömung vorausgesagt wird, kann die Theorie zukünftig auf endliche Temperaturen und die allgemeine Glasphase verallgemeinert werden. Im stabilen Zustand werden die vibrationalen Eigenschaften von amorphen Festkörpern bei niedrigen Temperaturen korrekt vorhergesagt. Zwei unterschiedliche vibrationale Regime werden identifiziert: Falls die Moden ausreichend Energie haben, können sie die lokale Unordnung auflösen und haben einen diffusiven Charakter. Diese Moden führen zu einem Plateau in der vibrationalen Zustandsdichte. Für geringere Energien kann das System als elastischen Medium genähert werden. Das Verschwinden der transversalen Schallgeschwindigkeit markiert die Instabilität. Hier erstreckt sich das diffusive Regime bis zu verschwindender Frequenz. Unsere Theorie ist in Übereinstimmung mit einer ebenfalls abgeleiteten Verallgemeinerung des Euklidischen Zufallsmatrizen Models. Die quantitativen Vorhersagen der Theorie passen gut zu Philipp Baumgärtel's numerischer Analyse des skalaren Euklidischen Zufallsmatrizen Models (Vogel *et al.*, 2025).

Aknowledgment

My time as a PhD student in the group of Matthias Fuchs will be memorized as a special period of my life. The joy and success would not have been possible without the help of numberless people. I want to take this opportunity to thank in particular:

- Professor Matthias Fuchs for providing a position in his group and for our countless fruitful discussions. Matthias always had an open door for questions and always made time for me.
- Ann-Kathrin, for a wonderful time together, the support, and the effort of proofreading my thesis.
- My family for always being there for me and the most needed support at the beginning of my PhD.
- Philipp Baumgärtel for complementing my research with his investigations.
- My colleagues Niklas Grimm, Elias Kohler, Nikolas Ditz, Manuel Maier, Thomas Bissinger and Luca Horray for their support, feedback and the shared activities outside of the university.
- The people from P9 and the physics department in general for creating a great working atmosphere.
- Professor Grzegorz Szamel, Professor Matthias Krüger, and Valentin Wilhelm for the collaborations and discussions.

I am also grateful for the teaching opportunities at the Fachbereich Physik. Special thanks to Professor Alexandra Blessing and Professor Matthias Fuchs, with whom I have organized my first seminar about *Random Matrices*. Overall, I am grateful that I had the opportunity to do research in science.

Contents

1 | Introduction

From biological tissues, cell materials via foams all the way to window glass, many materials encountered in everyday life are disordered many-body systems. In general, we refer to them as *amorphous solids*. In principle, they exhibit elastic properties and they can sustain some external stresses. This is remarkable, as the microscopic topological disorder suggests that an amorphous solid is generally not in equilibrium but in a metastable state. The last century witnessed tremendous success in statistical physics describing crystalline solids with symmetry-related phonons (Ashcroft and Mermin, 1976). However, no unified description of amorphous solids yet exists. Consequently, some of the properties of disordered solids remain poorly understood even after decades. For example, Zeller and Pohl's experiments established already in 1971 that the heat capacity varies with the temperature T as T^γ with $\gamma \in [1, 2]$ (Zeller and Pohl, 1971). This observation opposes the Debye Theory valid in crystals: Here, phonon-dominated thermal transport implies that the heat capacity varies with T^3 (Gross and Marx, 2014, Chapter 6). The most prominent explanation of this phenomenon involves Tunneling-Two-Level system: Atoms that can tunnel through the energy barriers of two adjacent local minima in the energy landscape. However, this concept remains highly controversial even after half a century of research (Phillips, 1972; Yu and Carruzzo, 2022). Furthermore, the absence of a long-ranged spatial order of the constituents implies that the excitations in amorphous solids differ systematically from the vibrational modes in ordered states of the same chemical substances. Nevertheless, quite universal vibrational anomalies are documented: Sound waves are damped even without thermal fluctuation and nonlinearities. Furthermore, the vibrational Density of States deviates from Debye's law for intermediate frequencies (Baldi *et al.*, 2010; Richard *et al.*, 2020; Wuttke *et al.*, 1995). The Allen-Feldmann Theory credits the structural disorder for the distinctive vibrational features in amorphous solids, which also partly explain the anomalous thermal transport properties (Allen *et al.*, 1999; Tanguy, 2023): First of all, modes with insufficient energy to resolve the disorder resemble attenuated but propagating sound modes, as continuous elasticity

theory is valid for small frequencies. Secondly, excitations with sufficient energy to resolve the local structure perform a random walk through the medium, causing diffusive modes. Lastly, a mobility edge exists for very high energies, which implies the presence of localized modes. However, although this narrative is widely accepted, it remains a phenomenological interpretation and is not based on a first-principles investigation. Nevertheless, much work has been put into explaining the anomalous properties of amorphous solids in terms of the different vibrational modes. Indeed, the unstability transition can also be studied by characterizing the system's vibrational modes: As the speed of sound vanishes at the critical point, elasticity, *i.e.* the ability to support sound modes, becomes a synonym of stability for sufficiently soft perturbations.

In this monograph, we develop a theory for the vibrational modes in amorphous solids. We will discuss the nature of the excitations in the stable and unstable phase and how the nature of the modes changes at the stability transition. Generally, stability in amorphous solids can emerge from collective motion, as in glasses. Here, the particles get stuck in so-called *cages* when the system is cooled down, which causes the emergence of stability. These cages are microscopic structures and are part of the collective dynamics (Charbonneau *et al.*, 2017; Debenedetti and Stillinger, 2001; Li *et al.*, 2020). In this case, elasticity is of *entropic* origin, and the resilience against deformations is set by the thermal energy k_BT (Ikeda *et al.*, 2012). Alternatively, stability can emerge from mechanical reasons. This is the so-called *jamming scenario*. Here, the particles are held in position by their neighbours, and any displacement comes with an energy cost quantified by the interaction potential. Notable,

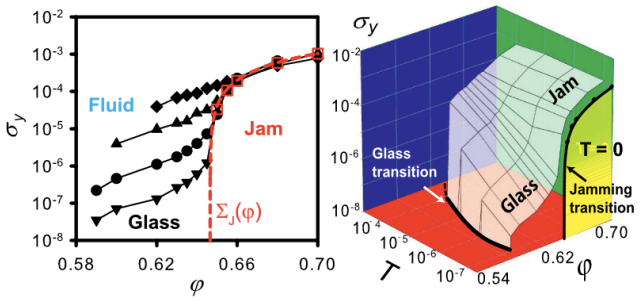

Figure 1.1: a) Dependence of yield stress σ_Y on the packing fraction φ for different temperatures T. b) The glass-jamming phase diagram. Same data as in a). Reprinted from *Unified study of glass and jamming rheology in soft particle systems*, by A. Ikeda, L. Berthier & P. Sollich, 2012, Phys. Rev. Lett., vol. 109, page 018301. Copyright [2025] by the American Physical Society. Reprinted with permission Doi:10.1103/PhysRevLett.109.018301 .

jamming is, therefore, a temperature-independent cause of stability. Here, elasticity is of *enthalpic* nature. For finite temperatures and general potential, there is usually an interplay between the entropic and the enthalpic contribution to stability. Nevertheless, the entropic contribution vanishes with the temperature, and the jamming transition as a mechanical instability in disordered systems can be isolatedly studied at $T = 0$ (Ikeda *et al.*, 2012). The cooperative dynamics ceases at zero temperature, implying that the entropic elasticity also vanishes. This can be recorded by measuring the temperature dependence of the yield stress σ_Y, quantifying the amount of stress a system can sustain before it flows (Voigtmann, 2011). Panel a) of Figure 1.1 visualizes that σ_Y approaches zero for $T \to 0$ below the jamming threshold at the critical volume fraction φ_c. Mechanical stability emerges at the jamming transition, and the yield stress σ_Y becomes independent of the temperature. In general, simulations have provided detailed insight into the low-temperature disordered stability transition and the properties of the respective phases (Gelin *et al.*, 2016; Giannini *et al.*, 2024; Horbach *et al.*, 2001; Hu and Tanaka, 2022; Kapteijns *et al.*, 2021; Mizuno and Ikeda, 2018; Mizuno *et al.*, 2017; Moriel *et al.*, 2019; Shimada *et al.*, 2018; Wang *et al.*, 2019a,b). However, no comprehensive and exhaustive theoretical explanation of the phase diagram in Figure 1.1 exists. Several mesoscopic theories have been proposed that rationalize the peculiarities of the spectrum of the jammed state. Furthermore, these theories also accomplish to partly explain the anomalous thermal transport properties of amorphous solids (DeGiuli *et al.*, 2014; Marruzzo *et al.*, 2013b; Schirmacher, 2006; Schirmacher and Ruocco, 2022). However, most theories predict a negative vibrational Density of States below the jamming transition, indicating the system loss of stability (Mossa *et al.*, 2023). While this is true at the glass transition, the Density of States is non-negative in the unjammed glass state reported in Figure 1.1. Here, viscous flow is absent as the system remains stable. Similarly, Euclidean Random matrix models (ERMs) also capture several features of disordered solids (Ciliberti *et al.*, 2003; Ganter and Schirmacher, 2010; Goetschy and Skipetrov, 2013; Grigera *et al.*, 2011; Vogel and Fuchs, 2023). Furthermore, ERMs have been used successfully to describe the distribution of local non-negative elastic constants (Szamel, 2025; Szamel and Flenner, 2022; Vogel *et al.*, 2025). However, their assumption of an existing reference frame breaks down at the glass transition. Mean-field theories succeed in describing the unjammed glass state (Benetti *et al.*, 2018; Feng *et al.*, 1985; Franz *et al.*, 2015; Zaccone and Scossa-Romano, 2011). Nevertheless, these models generally apply in

infinite dimension $d \to \infty$, and therefore often miss universal features of the spectrum of low-dimension amorphous solids like the Debye Density of States $D_D(\omega) \propto \omega^{(d-1)}$, valid for small frequencies $\omega \to 0$. The Debye Density of States is a direct consequence of elasticity and is well documented in amorphous solids (Baldi *et al.*, 2014, 2013; Kaya *et al.*, 2010; Mizuno and Ikeda, 2018; Ruffle *et al.*, 2010; Wang *et al.*, 2019b). However, a term $\propto \omega^{d-1}$ necessarily becomes marginal for $d \to \infty$. Furthermore, mean-field theories only consider interaction events, such as scattering processes, on the two-particle level. Thus, they miss multiple correlated events, which are heavily discussed in the current research (Lerner and Bouchbinder, 2021; Schirmacher *et al.*, 2024; Schober, 2011; Schober and Ruocco, 2004). To summarize, besides tremendous efforts, no exhaustive general theory exists that captures the salient features of both the jammed and the unjammed state. Such a theory could pave the way to study amorphous solids at finite temperatures and develop realistic models for quantitative comparisons with experiments. This monograph aims to construct such a first-principles theory.

This thesis contains an analytic study of athermal, disordered solids, *i.e.* topological disordered systems at $T = 0$. Aiming to understand the vibrational properties of the system, we construct a Self-Consistent Current Response Theory, which describes how the system reacts to perturbations and captures the loss of elasticity at the unjamming transition. The proposed theory is derived with the Zwanzig-Mori operator formalism and aspects from the Mode-Coupling Theory. Both have been frequently exploited to investigate supercooled liquids and the liquid–glass transition (Franosch *et al.*, 1997; Götze, 1998, 2009; Hansen and McDonald, 2009; Janssen, 2018; Janssen and Reichman, 2015; Szamel, 2003; Zwanzig, 2001). Moreover, MCT has also been used to study the glass phase, amorphous solids and their vibrational properties (Franosch and Götze, 1994; Götze and Mayr, 2000; Leutheusser, 1983). In this thesis, we also start our considerations in the fluid phase as it allows us to identify solidification as non-decaying restoring forces and the long-time presence of internal stresses. We express the forces acting on the particle velocities self consistently with the momentum current. The resulting theory is valid above and below the jamming threshold. The theory's prediction for the two states and the transition are elaborated on and qualitatively compared to simulations, *e.g.* (Mizuno and Ikeda, 2018; O'Hern *et al.*, 2003). The theory is developed for an underlying Langevin dynamics of the particles to investigate if details of the dynamics, such as

damping, change the stability transition. Furthermore, and left for future work, the theory can systematically be generalized to finite temperature to potentially rationalize the whole phase diagram in Figure 1.1. Nonetheless, this work restricts itself to the athermal limit $T = 0$. Here, the system is completely arrested in both the jammed and the unjammed state. Thus, our theory can be quantitatively compared to Euclidean Random Matrix models (Baumgärtel *et al.*, 2024; Grigera *et al.*, 2011; Szamel, 2025). The resulting agreement of the theory's and the numerical solutions is remarkable. As Euclidean Random Matrix models consider a quenched disorder and the Self-consistent Current Response Theory assumes perfect annealing, the accordance of the two descriptions is not trivial and emphasizes the universality of the jamming transition.

This monograph is structured as follows: Chapter 2 defines the investigated systems and gives an overview of the salient features of amorphous solids, their stability, and the jamming transition. The chapter discusses a selection of influential works on the topic to provide some qualitative insight into disordered solids, which will be helpful for the discussion in the subsequent chapters. Concretely, Section 2.5 discusses how the first part of Chapter 2 motivates the ensuing analytical investigation and clarifies the aim and the scope of the original work presented in this monograph. Chapter 3 introduces and discusses the analytical tools used, while Chapter 4 systematically introduces Euclidean Random Matrix models as a powerful instrument to investigate the jammed state. The concept arises from the idea that a harmonic energy expansion is a reasonable approximation for athermal systems as the particles stay close to their reference positions. Expressing the dynamic structure factor with the Hessian of this expansion leads to the Euclidean Random Matrix model proposed 25 years ago by Mézard and co-workers, which has since then been frequently exploited to analyze amorphous solids (Ciliberti *et al.*, 2003; Ganter and Schirmacher, 2011; Mézard *et al.*, 1999). Chapter 5 contains the main part of this monograph as it develops and discusses the Self-Consistent Current Response Theory. To test its predictions, we map it onto the scalar Euclidean Random Matrix model, where the vector character of the displacements is neglected. Here, we compare the analytical solution with the numerical investigations of Philipp Baumgärtel published in (Baumgärtel *et al.*, 2024; Vogel *et al.*, 2025). In general, many aspects of Chapter 5 have been published in (Vogel *et al.*, 2025). However, the chapter still contains unpublished content and generally provides additional details regarding the published calculations and considerations. Chapter 6 is dedicated to the stability

transition in the scalar Euclidean Random Matrix model. This simplified model allows detailed and instructive results on the change in the nature of modes at the transition. An overview of the numerical methods used to solve the self-consistent model is provided in Appendix C. Lastly, Appendix A generalizes Szamel's discussion of the scalar Euclidean Random Matrix model to vector displacements, to non-trivial distribution functions of the particles in the quenched disorder, and furthermore shows how initial stresses can be correctly taken into account.

2 | Stability in athermal disordered solids and their vibrational modes

This thesis develops a theory for the vibrational modes in amorphous solids and investigates the consequences of the disorder and instabilities. Throughout this work, we say a system is stable if a sufficiently small applied force only causes elastic but not plastic deformations. As elasticity requires the presence of restoring forces, stability is connected to the persistence of stresses: If stresses can decay over time, the system eventually yields to the perturbations and starts flowing. Conversely, the system can sustain external forces if the stresses do not decay. The main goal of this thesis is to develop a self-consistent theory that expresses the evolution of displacement via the internal stresses, which themselves are a function of the displacements. Hereby, this thesis focuses on sufficiently small perturbations. While any solid can break if subjected to strong enough forces, this work asks the question: Can the system sustain some degree of strain?

In crystals, Bloch's theorem implies that plane wave-like excitations, or phonons, are the exact eigenstates of the Hamiltonian (William Jones, 1973, page 13). Hence, a small perturbation travels as a wave-package through the system. The situation is more complicated in a disordered system. Here, plane waves are never exact eigenstates. This leads to sound attenuation even in the absence of thermal motion. Moreover, the assumption of continuous elasticity breaks down if a mode has enough energy to resolve the local structure. Thus, the nature of the eigenmodes highly depends on their frequency, which causes significant differences between crystals and amorphous solids in their macroscopic properties. Prominent examples are the heat conductivity and the specific heat. This first chapter discusses these and other well-established phenomena in disordered systems. It is an introductory part, which provides an overview of the

stability of disordered systems at zero temperature and the vibrational modes within them. Here, we discuss a selection of theoretical, empirical, and computational results to draw a qualitative, stringent picture of athermal disordered solids and the unjamming transition. Since this task involves reviewing the last 50 years of research, we had to make a selection. This has been done following the general aim of making the original research presented in Chapter 4, Chapter 5 and Chapter 6 understandable. We begin by defining our system. Afterward, we briefly review the theory of elasticity in Section 2.2, where we also define the strain and stress tensors. They lead us to the definition of the elastic constants, which serve as the fundamental parameters of elastic materials since they quantify the response to long-wavelength perturbations. The vanishing of an elastic constant indicates an instability and the absence of restoring forces. In Section 2.3, we discuss a geometric criterion for stability known as the Maxwell criterion. Based on this stability criterion, we provide a discussion of the dominant vibrational modes in disordered materials and how their characteristics depend on the disorder and their energy. In Section 2.4, we lay out the impact of the different modes on the thermal properties of amorphous solids. Lastly, Section 2.5 clarifies the aim and scope of this monograph.

2.1 The system

This monograph considers N identical spherical particles with mass m placed in a d-dimensional volume V in the thermodynamic limit $N, V \to \infty$ with constant number density $n = \frac{N}{V}$. We consider disordered systems at zero temperature $T = 0$ where the particles' positions $\{\boldsymbol{r}_i\}_{i=1}^N$ are drawn from a probability distribution $P(\{\boldsymbol{r}\})$, which is assumed to be invariant under a global translation and a global rotation of the system. In this thesis, we additionally restrict ourselves to frictionless d-dimensional spheres. Experimentally, foam is a good realization (Drenckhan and Hutzler, 2015). Known facts about ellipsoidal or rough particles are summarized in the review (van Hecke, 2009). Throughout this work, we assume that the pair interactions are quantified by a potential $U(r)$, which only depends on the absolute value of the binary distance between particles. Due to Newtons third law, the total force $\boldsymbol{F}_i$ acting on the i^{th} particle equals the sum over all pair interactions:

$$\boldsymbol{F}_i = \sum_{j=1}^{N} \boldsymbol{F}_{ij} = -\sum_{j=1} \nabla \cdot U(|\boldsymbol{r}_i - \boldsymbol{r}_j|) \ . \tag{2.1}$$

We can always think of a system constituted of soft, granular particles for visualization purposes. Here, the pair interaction has finite support $U(r > \sigma) = 0$ for an atomic length scale σ and the system can be pictured as a network where bonds result from contacts between the particles. However, our considerations are generally not limited to short-ranged interactions. We will always make it clear when we assume a concrete form of the interaction potential $U(r)$. We will discuss in Section 2.3.2 that the scaling of some observables close to the transition depends on the interaction details. However, different interaction laws only cause quantitative differences deep in the jammed state and on large length scales where the system can be treated as an *continuous medium*. We discuss this case in the next section.

2.2 Theory of elasticity

Throughout this monograph, we use the notion *elasticity* to refer to a solid's property to regain its original shape and volume after a deforming force is removed. At zero temperature the initial and final configurations coincide after the injected momentum has dissipated. Thus, the initial configuration defines a reference frame $\{\boldsymbol{R}_i\}_{i=1}^N$, where $\boldsymbol{R}_i$ denotes the position of the i^{th} particle before a perturbation. In general, the reference frame is in mechanical equilibrium and the total forces acting on each particle balance each other $\boldsymbol{F}_i = 0$. However, there can still be tension in a force-free system. We call the force acting on a specified area the *stress*. When an external force is applied, the particles are displaced away from their reference positions. We call the deformation relative to the reference frame *strain*. This section introduces the concepts of stress and strain and discusses their relation in a disordered system: While an applied strain always leads to additional stresses in the stable phase, no stress is built up by deformations along modes that feel no restoring forces in the unjammed phase. Thus, the stress-strain relation can be used to determine the stiffness of a material. Subsection 2.2.1 defines the stress and the strain tensor, while Subsection 2.2.2 discusses a microscopic expansion of the potential energy, which we use in Subsection 2.2.3 to define the coupling parameters in the strain-stress relation. Lastly, we discuss in Subsection 2.2.4 that a linear relation between stress and strain gives rise to a wave equation for the displacement field.

2.2.1 The strain- and the stress tensor

We restrict ourselves to stable systems to introduce the concepts of stress and strain. Hereinafter, we inquire how the system reacts to an atomic displacement of the particles $\boldsymbol{R}_i \longrightarrow \boldsymbol{r}_i$. While we label the set of the references position as $\{\boldsymbol{R}_i\}_{i=1}^N$ the actual positions are contained in $\{\boldsymbol{r}_i\}_{i=1}^N$. The difference between the two positions defines the atomic displacement vector

$$\boldsymbol{u}_i = \boldsymbol{r}_i - \boldsymbol{R}_i \ , \tag{2.2}$$

which leads to the introduction of the strain tensor.

The strain tensor: When applying a force to a many-body system, the body deforms. The i^{th} particle originally positioned at $\boldsymbol{R}_i$ in reference frame is displaced to the new position $\boldsymbol{r}_i$. A deformation leads to a change in the distance between two points $\boldsymbol{r}_i$ and $\boldsymbol{r}_j$. We denote the radius vector joining the centres of two particles in the reference frame with $\boldsymbol{R}_{ij}$. Conversely, $\boldsymbol{r}_{ij}$ denotes their actual distance vector. The associated euclidean distances read R_{ij} and r_{ij} respectively. In the following, we assume that there are only small differences in the displacements of adjacent particles. This suggests that we can construct a smooth displacement field $\boldsymbol{u}(\boldsymbol{r})$, which reasonably accounts for all $\boldsymbol{u}_i$. Assuming that the atomic displacements $\{\boldsymbol{u}_i\}_{i=1}^N$ are small, we can perform a gradient expansion (Landau *et al.*, 1970, Chapter 1):

$$r_{ij}^2 = R_{ij}^2 + \left(\frac{\partial u_\beta}{\partial r_\alpha} + \frac{\partial u_\alpha}{\partial r_\beta} + \frac{\partial u_\gamma}{\partial r_\alpha} \frac{\partial u_\gamma}{\partial r_\beta} \right) \Big|_{\boldsymbol{r}=\boldsymbol{R}_i} R_{ij}^\alpha R_{ij}^\beta \ . \tag{2.3}$$

Here, Greek letters denote spatial indices, $\alpha, \beta \in \{1, ..., d\}$, while Latin indices label the particles. Throughout this thesis, we use Einstein's sum convention for the spatial indices as we did in the previous equation. Equation (2.3) defines the strain tensor

$$\epsilon_{\alpha\beta}(\boldsymbol{R}_i) \equiv \underbrace{\frac{1}{2}\Big(\frac{\partial \boldsymbol{u}_\beta}{\partial \boldsymbol{r}_\alpha} + \frac{\partial \boldsymbol{u}_\alpha}{\partial \boldsymbol{r}_\beta} \Big) \Big|_{\boldsymbol{r}=\boldsymbol{R}_i}}_{\equiv \epsilon_{\alpha\beta}^{(1)}} + \underbrace{\frac{1}{2} \frac{\partial \boldsymbol{u}_\gamma}{\partial \boldsymbol{r}_\alpha} \frac{\partial \boldsymbol{u}_\gamma}{\partial \boldsymbol{r}_\beta} \Big|_{\boldsymbol{r}=\boldsymbol{R}_i}}_{\equiv \epsilon_{\alpha\beta}^{(2)}} \ . \tag{2.4}$$

The strain tensor quantifies the change in the Euclidean distances when the system is deformed. The strain tensor is a symmetric tensor of rank two $\epsilon_{\alpha\beta} = \epsilon_{\beta\alpha}$. In this work, we denote a tensor with an underbar $\epsilon_{\alpha\beta} \equiv (\underline{\boldsymbol{\epsilon}})_{\alpha\beta}$. Importantly, the non-linear

part of the strain tensor is often neglected $\epsilon_{\alpha\beta} \approx \epsilon_{\alpha\beta}^{(1)}$ (Landau *et al.*, 1970, Chapter 1). However, we will discuss in Section (2.2.2) that we can not neglect $\underline{\boldsymbol{\epsilon}}^{(2)}$ as this part still appears in a harmonic expansion of the potential energy. In any case, changing the interparticle distance generally causes the buildup of force and stresses. We define the associated stress tensor in the next paragraph.

The stress tensor: As the pair interaction potential $U(r)$ depends on the distances between particles, deformations generally lead to new interparticle forces. In the following, we assume that the system was in mechanical equilibrium before a perturbation distorted the system

$$\boldsymbol{F}_i = 0 \ , \quad \forall i \in \{1, ..., N\} \tag{2.5}$$

However, tension and stress can still be present even if all the interparticle forces are balanced. To derive an expression for the stress tensor $\underline{\boldsymbol{\sigma}}$, we follow Landau, Lifschitz, and consider a small part $\overline{V}$ of the system (Landau *et al.*, 1970, Chapter 1). The total force $\tilde{\boldsymbol{F}}$ acting on this subvolume equals the sum of all the forces acting on its parts $\tilde{\boldsymbol{F}} = \int \boldsymbol{f} dV_i$. Here, $\boldsymbol{f}$ denotes the force per unit volume and $\boldsymbol{f} dV_i$ represents the force in the volume element dV_i. Newton's third law and the requirement of mechanic equilibrium imply that forces acting between these subvolumes V_i add up to zero. Thus, the total force acting on $\overline{V}$ are the forces exerted by its surroundings. Using the Gauß-integral theorem for surface integrals, the force can be written as the divergence of a second-rank tensor (Landau *et al.*, 1970, Chapter 1):

$$\begin{aligned} \tilde{F}_\alpha &= \frac{\partial \sigma_{\alpha\beta}}{\partial r_\beta} \ . \\ \int F_\alpha dV &= \int \frac{\partial \sigma_{\alpha\beta}}{\partial r_\beta} dV = \oint \sigma_{\alpha\beta} dA_\beta \ . \end{aligned} \tag{2.6}$$

Here, A_β is the surface element with its normal vector pointing outwards and $\underline{\boldsymbol{\sigma}}$ defines the stress tensor. Notably, $\sigma_{\alpha\beta} = \sigma_{\beta\alpha}$ is symmetric. The entries of $\sigma_{\alpha\beta}$ can be interpreted as force times unit area (Landau *et al.*, 1970, Chapter 1). The first index specifies the direction of the force and the second denotes the normal vector of the area the force acts on. As we deal with a disordered medium, the stresses are generally not uniformly distributed and the stress tensor depends on the position inside the system $\underline{\boldsymbol{\sigma}} = \underline{\boldsymbol{\sigma}}(\boldsymbol{r})$.

Irving and Kirkwood derived a microscopic expression for the stress at point $\boldsymbol{r}$ inside the medium (Irving and Kirkwood, 1950; Schofield *et al.*, 1982; Shi *et al.*, 2023)

$$\sigma_{\alpha\beta}(\boldsymbol{r}) = \frac{1}{2}\sum_{ij} F_{ij}^{\alpha} r_{ij}^{\beta} \int_0^1 \delta(\boldsymbol{r} - \boldsymbol{r}_i + \lambda \boldsymbol{r}_{ij}) d\lambda \ . \tag{2.7}$$

We will frequently encounter this expression in Chapter 5.

After we have introduced the stress tensor $\underline{\boldsymbol{\sigma}}$, we can ask for its relation to the strain tensor $\underline{\boldsymbol{\epsilon}}$. Generally, an applied strain deforms the system and induces additional stress. When the deformation is small, we can assume that the internal stress increases linearly with the strain:

$$\sigma_{\alpha\beta}(\boldsymbol{r}) = \sigma_{\alpha\beta}^{(0)}(\boldsymbol{r}) + D_{\alpha\beta\gamma\delta}(\boldsymbol{r}) \epsilon_{\beta\delta}^{(1)}(\boldsymbol{r}) \ . \tag{2.8}$$

This is Hooke's law with the additional inclusion of initial stresses $\sigma_{\alpha\beta}^{(0)}$ (Alexander, 1998; Landau *et al.*, 1970). Here, the $\underline{\boldsymbol{D}}$ is a fourth-rank tensor. Its components $D_{\alpha\beta\gamma\delta}$ are the so-called elastic constants or elastic moduli (Gross and Marx, 2014, Chapter 4). They quantify the buildup of restoring forces due to a deformation. Thus, the elastic constant specifies the system's stiffness. Their vanishing indicates the unjamming transition as a deformation no longer leads to restoring forces. The system can yield to an arbitrarily small strain. The following paragraph paraphrases Alexander's microscopic derivation of the elastic constant $\underline{\boldsymbol{D}}$ (Alexander, 1998).

2.2.2 Microscopic expansion of the energy

A microscopic expansion of the energy does not only provide a microscopic expression for the elastic constants introduced in Equation (2.8). It is also the basis for the variational arguments by Matthieu Wyart and co-workers, used to derive the scaling behaviour of some observables close to the unjamming transition (Silbert *et al.*, 2002; Wyart, 2005). Their work is introduced in Section 2.3 and Section 2.3.2. Moreover, we will encounter the microscopic expansion of the energy again when we consider the eigenmodes of the system. As we consider a system at zero temperature, the kinetic part of the energy is neglected in the following.

To get to the linearized equations of motion for a deformation $\{\boldsymbol{u}_i\}_{i=1}^N$, we want to expand the potential energy $E_{\mathrm{Pot}} = \frac{1}{2}\sum_{i,j=1}^N U(|\boldsymbol{r}_i - \boldsymbol{r}_j|)$ around the reference state $\{\boldsymbol{R}_i\}_{i=1}^N$ (Landau and Lifshitz, 1987). Such expansion requires that the system is sufficiently stable and that the amplitude of fluctuations is small enough:

$$\frac{\langle r_{ij}^2 - R_{ij}^2 \rangle}{R_{ij}^2} \ll 1 \ , \tag{2.9}$$

The brackets $\langle \cdot \rangle$ denote the average. Generally, anharmonic effects have to be taken into account if the consistency criterion in Equation (2.9) does not apply. In 3d solids, the empirical Lindemann criterion

$$\frac{\langle \boldsymbol{u}_i^2 \rangle}{\sigma^2} < 0.1 \tag{2.10}$$

has turned out to be a good phenomenological benchmark for stability (Alexander, 1998; Lindemann, 1910). Here, σ is the diameter of the smallest particles. If this inequality holds, the consistency requirement in Equation (2.9) is generally satisfied as well. As the potential energy depends by construction only on the absolute value of binary distances $|\boldsymbol{r}_i - \boldsymbol{r}_j|$, the system is invariant under a global translation and a global rotation. These three properties must be conserved in the expansion of the potential energy E_{Pot} (Alexander, 1998). Thus, we follow Alexander and expand E_{Pot} in terms of the distances' changes $\Delta r_{ij} = r_{ij} - R_{ij}$. This automatically conserves the global symmetries and ensures that the resulting expression depends only on the binary distances r_{ij}. The resulting scalar harmonic expansion around the reference frame reads

$$E_{\mathrm{Pot}}(\{\boldsymbol{r}\}) \approx E_{\mathrm{Pot}}(\{\boldsymbol{R}\}) + \sum_{i,j=1}^{N} \left.\frac{\partial E_{\mathrm{Pot}}}{\partial r_{ij}}\right|_{\{\boldsymbol{R}\}} \Delta r_{ij} + \frac{1}{2}\sum_{i,j,k,l} \left.\frac{\partial^2 E_{\mathrm{Pot}}}{\partial r_{ij}\partial r_{kl}}\right|_{\{\boldsymbol{R}\}} \Delta r_{ij}\Delta r_{kl}. \tag{2.11}$$

Here, the underscored $\{\boldsymbol{R}\}$ indicates that the quantities have to be evaluated in the reference frame. We strive for an expression of E_{Pot} in terms of the displacements $\{\boldsymbol{u}_i\}$. This will enable us to write the potential energy with the stress and the strain tensor.

Expanding Δr_{ij} for small relative displacements $\boldsymbol{u}_{ij} = \boldsymbol{u}_i - \boldsymbol{u}_j$ gives (Alexander, 1998):

$$\begin{aligned} \Delta r_{ij} = r_{ij} - R_{ij} = \sqrt{|\boldsymbol{u}_{ij} + \boldsymbol{R}_{ij}|^2} - R_{ij} \approx u_{ij}^{\parallel} + \frac{(u_{ij}^{\perp})^2}{2R_{ij}} \ , \\ u_{ij}^{\parallel} = \boldsymbol{u}_{ij} \cdot \hat{\boldsymbol{R}}_{ij} \ , \qquad (u_{ij}^{\perp})^2 = u_{ij}^2 - (u_{ij}^{\parallel})^2 \end{aligned} \tag{2.12}$$

Here, the unit vector $\hat{\boldsymbol{R}}_{ij} = \boldsymbol{R}_{ij}/R_{ij}$ points from the center of the i^{th} particle to the center of the j^{th} particle. The deviations parallel to $\hat{\boldsymbol{R}}_{ij}$ is denoted $u_{ij}^{\parallel}$, while $u_{ij}^{\perp}$ denotes the changes perpendicular to $\hat{\boldsymbol{R}}_{ij}$. Importantly, the linear order in the relative displacements $\boldsymbol{u}_{ij}$ have to vanish due to the assumed mechanical equilibrium condition:

$$\boldsymbol{F}_i = 0 = -\sum_{j=1}^{N} \left.\frac{\partial E_{\mathrm{Pot}}}{\partial \boldsymbol{r}_{ij}}\right|_{\{\boldsymbol{R}\}} = -\sum_{j=1}^{N} \mathcal{T}_{ij} \hat{\boldsymbol{R}}_{ij} = -\sum_{j=1}^{N} \left.\frac{\partial E_{\mathrm{Pot}}}{\partial u_{ij}^{\parallel}}\right|_{\boldsymbol{u}=0} \hat{\boldsymbol{R}}_{ij} = -\sum_{j=1}^{N} \left.\frac{\partial E_{\mathrm{Pot}}}{\partial \boldsymbol{u}_{ij}}\right|_{\boldsymbol{u}=0} , \tag{2.13}$$

Here, the bond tension $\mathcal{T} \equiv \left.\frac{\partial E_{\mathrm{Pot}}}{\partial r_{ij}}\right|_{\{\boldsymbol{R}\}}$ quantifies the stress contribution from the interaction of the i^{th} and j^{th} particle. We say a bond exists if $U(\boldsymbol{R}_i - \boldsymbol{R}_j) \neq 0$ holds. However, even though the system is assumed to be in mechanical equilibrium, the harmonic extension of the energy in Equation (2.11) still depends on the bond tension because of the perpendicular relative deviations $(u_{ij}^{\perp})^2$. Perpendicular deviations do not give rise to restoring interparticle forces in the lowest order. However, they contribute to the potential energy. As said before, we disregard many-body interactions. Thus, the second term in Equation (2.11) characterizes the curvature at the bottom of the potential energy landscape. We define the spring constant $\mathcal{K}_{ij}$ of the bond $[ij]$ as

$$\sum_{k,l} \left.\frac{\partial^2 E_{\mathrm{Pot}}}{\partial r_{ij} \partial r_{kl}}\right|_{\{\boldsymbol{R}\}} = \left.\frac{\partial^2 E_{\mathrm{Pot}}}{\partial r_{ij}^2}\right|_{\{\boldsymbol{R}\}} \equiv \mathcal{K}_{ij} \ . \tag{2.14}$$

Thinking of a spring network, $\mathcal{K}$ describes the strength of the relaxed springs, while $\mathcal{T}$ quantifies the initial elongation of these springs and the resulting prestress. Putting it all together, we arrive at the following expression for the harmonic expansion (Alexander, 1998)

$$E_{\mathrm{Pot}}(\{\boldsymbol{r}\}) - E_{\mathrm{Pot}}(\{\boldsymbol{R}\}) = \frac{1}{2} \sum_{i,j=1}^{N} \mathcal{T}_{ij} \frac{(u_{ij}^{\perp})^2}{R_{ij}} + \frac{1}{2} \sum_{i,j=1}^{N} \mathcal{K}_{ij} (u_{ij}^{\parallel})^2 + \mathcal{O}(\boldsymbol{u}^3) \ . \tag{2.15}$$

This expression in itself is quite remarkable, especially the occurrence of the term depending on the bond tension. Euclidean Random Matrix models generally neglect this term altogether (Ciliberti *et al.*, 2003; Ganter and Schirmacher, 2010; Mézard *et al.*, 1999; Vogel and Fuchs, 2023). However, this is quite a restrictive assumption, at least in disordered materials: Neglecting the term depending on the bond tension is equivalent to assuming that all binary pair potentials are in a local minimum. Such an assumption or approximation might be reasonable when dealing with crystals but not for amorphous materials (Alexander, 1998). Ikeda and Mizuno investigated the differences arising due to the initial stresses (Mizuno and Ikeda, 2018). They found that the sound attenuation is about two orders of magnitude stronger in a stressed reference frame than in an unstressed one. We will qualitatively explain this at the end of this section. Moreover, the authors found that stresses in purely repulsive systems with $U'(r) \leq 0 \ \forall r > 0$ destabilize the system. We will further look into the impact of stresses on the system's stability in Section 2.3.

Naturally, the bond tension appears in the expression of initial stresses. One obtains from the Irving-Kirkwood Stress tensor in Equation: (2.7) an expression for the global stress (van Hecke, 2009)

$$\sigma^{\mathrm{gl}}_{\alpha\beta} = \int d^d\boldsymbol{r}\sigma_{\alpha\beta}(\boldsymbol{r}) = \frac{1}{2}\sum_{ij} r^\alpha_{ij}F^\beta_{ij} = -\frac{1}{2}\sum_{ij}\frac{r^\alpha_{ij}r^\beta_{ij}}{r_{ij}}\frac{\partial E_{\mathrm{Pot}}}{\partial r_{ij}} \ . \tag{2.16}$$

The initial stresses read

$$\sigma^{(0)}_{\alpha\beta}(\boldsymbol{r}) = -\frac{1}{2}\sum_{ij}\frac{R^\alpha_{ij}R^\beta_{ij}}{R_{ij}}\mathcal{T}_{ij}\int_0^1 \delta(\boldsymbol{r}-\boldsymbol{R}_i+\lambda\boldsymbol{R}_{ij})d\lambda \tag{2.17a}$$

$$\sigma^{\mathrm{gl},(0)}_{\alpha\beta} = -\frac{1}{2}\sum_{ij}\frac{R^\alpha_{ij}R^\beta_{ij}}{R_{ij}}\mathcal{T}_{ij} \tag{2.17b}$$

Landau and Lifschitz considered the work ΔW done by a small change in the perturbation $\boldsymbol{u}_i \to \boldsymbol{u}_i + \Delta\boldsymbol{u}_i$ (Landau *et al.*, 1970, Chapter 1). They found $\Delta W = -\sigma_{\alpha\beta}\Delta\epsilon^{(1)}_{\alpha\beta}$. This leads to the generalized first law of thermodynamics

$$dE = TdS + \sigma_{\alpha\beta}d\epsilon^{(1)}_{\alpha\beta} \ . \tag{2.18}$$

With the temperature T and the entropy S. When considering a compression, $\sigma_{\alpha\beta} \propto \delta_{\alpha\beta}$ leading to a volume change dV, one recovers the usual first law of thermodynamics and finds that the global pressure p in the system is given by (Landau *et al.*, 1970, Section 3)

$$p = -\frac{\sigma^{\mathrm{gl}}_{\alpha\alpha}}{d} \ . \tag{2.19}$$

This leads to the idea that the term in the harmonic expansion coupled to the transverse displacements varies linearly with the global pressure(van Hecke, 2009; Wyart, 2005):

$$\frac{1}{2}\sum_{i,j=1}^{N} \mathcal{T}_{ij}\frac{(u^{\perp}_{ij})^2}{R_{ij}} \propto p \ . \tag{2.20}$$

We will come back to this point when we discuss the stability of amorphous solids in Section 2.3. We will see that the pressure vanishes when approaching the unjamming transition in a soft sphere system at $T = 0$. However, we first discuss the continuity approximation for the microscopic expansion of the energy in Equation (2.11). This approximation applies in the hydrodynamic limit or on small energy scales. As we will see, the modes populating this small frequency regime can be approximated by longitudinal and transverse plane waves. The vanishing of the associated speed of sound is a good indicator of the point of phase transition.

2.2.3 The elastic constants

To express the potential energy expansion in Equation (2.11) with the strain and the stress tensor, we need to perform the continuous medium approximation. This section follows again (Alexander, 1998) To perform the continuous medium approximation, we replace the particle displacements $\boldsymbol{u}_i$ by a continuous field $\boldsymbol{u}(r)$ with $\boldsymbol{u}_i = \boldsymbol{u}(\boldsymbol{R}_i)$. Implicitly, such a continuity approximation abstracts from particles and considers adjacent and touching volume elements. Assuming that the field varies sufficiently slowly, the relative displacement can be written as

$$\boldsymbol{u}_{ij} = \boldsymbol{u}_i - \boldsymbol{u}_j \longrightarrow \boldsymbol{u}(\boldsymbol{R}_i) - \boldsymbol{u}(\boldsymbol{R}_i - \boldsymbol{R}_{ij}) \approx (\boldsymbol{R}_{ij} \cdot \nabla)\boldsymbol{u}(\boldsymbol{R}_i) \ . \tag{2.21}$$

Thus, the parallel and the transverse components become

$$\begin{aligned} u_{ij}^{\parallel} &\approx \frac{R_{ij}^{\alpha} R_{ij}^{\beta}}{R_{ij}} \partial_{\beta} u_{ij}^{\alpha} = \frac{R_{ij}^{\alpha} R_{ij}^{\beta}}{R_{ij}} e_{\alpha\beta}^{(1)} \\ (u_{ij}^{\perp})^2 = u_{ij}^2 - (u_{ij}^{\parallel})^2 &\approx R_{ij}^{\alpha} R_{ij}^{\beta} \partial_{\alpha} u_{\gamma} \partial_{\beta} u_{\gamma} - (u_{ij}^{\parallel})^2 \ . \end{aligned} \tag{2.22}$$

The strain tensor $\underline{\boldsymbol{e}}^{(1)}$ was defined in Equation (2.4). Inserting the previous expression in equation (2.15), the microscopic expansion of the energy becomes

$$\Delta E_{\mathrm{Pot}} \approx -\int d^d \boldsymbol{r} \sigma_{\alpha\beta}^{(0)}(\boldsymbol{r}) \epsilon_{\alpha\beta}^{(2)}(\boldsymbol{r}) + \frac{1}{2} \int d^d \boldsymbol{r} \tilde{D}_{\alpha\beta\gamma\delta}(\boldsymbol{r}) \epsilon_{\alpha\beta}^{(1)}(\boldsymbol{r}) \epsilon_{\gamma\delta}^{(1)}(\boldsymbol{r}) \ . \tag{2.23}$$

where we relied on the equations (2.8) and (2.18). The coupling coefficients read

$$\tilde{D}_j^{\alpha\beta,\gamma\delta} = \frac{1}{\mathcal{V}_{j,C}} \sum_i \Big(\mathcal{K}_{ij} - \frac{\mathcal{T}_{ij}}{R_{ij}} \Big) \frac{R_{ij}^{\alpha} \cdot R_{ij}^{\beta} \cdot R_{ij}^{\gamma} \cdot R_{ij}^{\delta}}{R_{ij}^2} \ , \tag{2.24}$$

where $\mathcal{V}_{i,C}$ denotes the volume of the Voronoi cell around $\boldsymbol{R}_i$. Looking at Hook's law in Equation (2.8), we see that only the first component of the strain $\underline{\boldsymbol{e}}^{(1)}$ leads to an increase of the stresses in the lowest order. The second contribution of the strain just couples to the initial stresses in the harmonic extension. We write

$$\partial_{\alpha} u_{\gamma} = \epsilon_{\alpha\gamma}^{(1)} + d_{\alpha\gamma} \ , \tag{2.25}$$

where the anti-symmetric tensor $d_{\alpha\gamma} = \frac{1}{2}\Big(\partial_{\alpha} u_{\gamma} - \partial_{\gamma} u_{\alpha} \Big)$ encodes rotations in the strain field (Alexander, 1998). Inserting this in the expression for the potential energy gives

$$\begin{aligned} \Delta E_{\mathrm{Pot}} \approx & \int d^d \boldsymbol{r} \sigma_{\alpha\beta}^{(0)}(\boldsymbol{r}) d_{\alpha\gamma}(\boldsymbol{r}) d_{\beta\gamma}(\boldsymbol{r}) \\ & + \frac{1}{2} \int d^d \boldsymbol{r} \underbrace{\Big(\tilde{D}_{\alpha\beta\gamma\tau}(\boldsymbol{r}) + \sigma_{\alpha\gamma}^{(0)}(\boldsymbol{r}) \delta_{\beta\tau} \Big)}_{D_{\alpha\beta\gamma\tau}} \epsilon_{\alpha\beta}^{(1)}(\boldsymbol{r}) \epsilon_{\gamma\tau}^{(1)}(\boldsymbol{r}) \ . \end{aligned} \tag{2.26}$$

Here, we used the fact that the trace of a symmetric matrix times an antisymmetric matrix vanishes. The coefficients $D_{\alpha\beta\gamma\tau}$ define the elastic constants. The appearance of the antisymmetric tensor $d_{\beta\gamma}(\boldsymbol{r})$ has a peculiar effect. As we will discuss in the next section, neglecting this term leads to a linear equation of motion where the rotation and the divergence-free components decouple. As a result, the excitations in an unstressed

elastic medium can be expressed as the superposition of independent longitudinal and transverse plane waves. Interactions between *monochromatic* waves in unstressed media are encoded in higher order terms in the expansion of the energy and give rise to *anharmonic effects* (Landau *et al.*, 1970, Section 26). This is qualitatively different in disordered, prestressed systems. Here, interactions already enter in the lowest order of the expansion. Consequentially, sound modes are damped even when considering an athermal disordered system in the harmonic approximation. We will return to this point in Section 2.3.2, where we discuss the nature of the vibrational modes in disordered systems in more detail. In the next section, we will review the equation of motion in an unstressed system. Neglecting the coupling between plane-wave-like excitations is equivalent to considering only displacements on the atomic level, which are dictated by the associated wavevector of the perturbation. Such displacements are called *affine*.

2.2.4 The wave equation in unstressed elastic systems

Renowned textbooks like Landau and Lifschitz (Landau *et al.*, 1970, Chapter 1) or Gross and Marx (Gross and Marx, 2014, Chapter 4) only discuss the influence of the linear term of the strain tensor $\underline{\boldsymbol{\epsilon}}^{(1)}$. They neglect the influence of initial stresses altogether. This leads to a simple expression for the elastic constants and allows the definition of the so-called *Lamè coefficients* λ and μ in a coherent way. The idea is that any sufficiently small perturbation in an isotropic and homogeneous medium without initial stresses can be decomposed into two independent parts: Compression and Shear. Strictly speaking, this is not correct in disordered media, but the concept has still proven adequate since the coupling between wave-like excitation is sufficiently small (Mizuno and Ikeda, 2018; Schirmacher and Ruocco, 2022; Wyart *et al.*, 2005). Thus, it can be treated as sound attenuation. Hence, we also set $\mathcal{T}_{ij} = 0$ in this subsection, where we review the wave equation in a continuous elastic medium. In the following, we strive to express the speed of sound with the elastic constants. This subsection follows (Landau *et al.*, 1970, Chapter 1& 3)

When ignoring the initial stresses, the elastic constants simplify to

$$D_j^{\alpha\beta,\gamma\delta} = \frac{1}{\mathcal{V}_{j,C}} \sum_i \mathcal{K}_{ij} \frac{R_{ij}^{\alpha} \cdot R_{ij}^{\beta} \cdot R_{ij}^{\gamma} \cdot R_{ij}^{\delta}}{R_{ij}^2} \,. \tag{2.27}$$

The continuum's approximation is only valid on length scales much larger than any scale intrinsic to the system. Here, the local disorder does not matter and the system can be assumed to be rotationally and translationally invariant. The assumed homogeneity of the system implies that the elastic moduli are the same for all positions inside the elastic medium, at least after sufficient coarse-graining. Thus, we can set $\underline{\boldsymbol{D}}_i \approx \underline{\boldsymbol{D}}$. Secondly, the energy can only depend on powers of the trace of the strain tensor $\mathrm{Tr}(\underline{\boldsymbol{\epsilon}}^n)$ due to rotational invariance valid on large scales. This implies that the elastic moduli in a continuous elastic medium must be proportional to all possible combinations of two Kronecker-deltas compatible with the symmetry constraints of the strain- and the stress tensor (Landau *et al.*, 1970, Chapter 1):

$$D^{\alpha\beta\gamma\tau} = \lambda\delta_{\alpha\beta}\delta_{\gamma\tau} + \mu\Big(\delta_{\alpha\tau}\delta_{\gamma\beta} + \delta_{\alpha\gamma}\delta_{\tau\beta}\Big)\,. \tag{2.28}$$

Hence, the change of the energy due to an applied perturbation reads

$$E_{\mathrm{Pot}}(\boldsymbol{r}) - E_{\mathrm{Pot}}(\{\boldsymbol{R}\}) \approx \int d^d\boldsymbol{r}\left[\frac{\lambda}{2}\mathrm{Tr}(\underline{\boldsymbol{\epsilon}})^2 + \mu\mathrm{Tr}(\underline{\boldsymbol{\epsilon}}^2)\right] = \int d^d\boldsymbol{r}\left[\frac{\lambda}{2}\epsilon_{\alpha\alpha}^2 + \mu\epsilon_{\alpha\beta}^2\right]\,. \tag{2.29}$$

Here, λ and μ are the so-called *Lamé-coefficients.* The volume change due to deformation is determined by the diagonal elements of the strain tensor $\epsilon_{\alpha\alpha}$. The vanishing of the sum $\epsilon_{\alpha\alpha}^2$ means that the volume stays constant. Such a deformation is called *pure shear*. In the other case, a deformation is called a *pure compression*. Due to neglecting initial stresses, any deformation can be written as the sum of a pure shear and a pure compression. This leads to

$$E_{\mathrm{Pot}}(\{\boldsymbol{r}\}) - E_{\mathrm{Pot}}(\{\boldsymbol{R}\}) \approx nm\int d^d\boldsymbol{r}\left[B(\mathrm{Tr}\{\underline{\boldsymbol{\epsilon}}\})^2 + G\ \mathrm{Tr}\Big\{\Big(\underline{\boldsymbol{\epsilon}} - \underline{\mathbf{1}}\frac{1}{d}\mathrm{Tr}\{\underline{\boldsymbol{\epsilon}}\}\Big)^2\Big\}\right]\,. \tag{2.30}$$

Here, $B = \frac{\lambda+\frac{2}{d}\mu}{nm}$ is the longitudinal modulus, $G = \mu/(nm)$ is the shear modulus and $\underline{\mathbf{1}}$ denotes the unit matrix. We divided the conventional moduli by the mass density (nm). This ensures coherence and notational uniformity with the latter chapters and the publication (Vogel *et al.*, 2025). When considering systems in mechanical equilibrium, both moduli are non-negative: $\lambda, \mu \geq 0$. Generally, the longitudinal modulus is thus larger than the shear modulus and is even finite in liquids and gases due to the ideal gas

contribution $B_{idealGas} \propto T$ (Landau and Lifshitz, 1980). However, this contribution is zero in athermal systems. Bulk and shear modulus simultaneously vanish at the unjamming transition in soft-sphere systems (van Hecke, 2009). We will discuss this further in Section 2.3.1.

From equation (2.30) follows that the stress tensor is given by (Landau *et al.*, 1970, Equation 4.6)

$$\frac{\sigma_{\alpha\beta}(\boldsymbol{r})}{nm} = B\epsilon_{\gamma\gamma}(\boldsymbol{r})\delta_{\alpha\beta} + 2\mu\left(\epsilon_{\alpha\beta}(\boldsymbol{r}) - \frac{1}{d}\epsilon_{\gamma\gamma}(\boldsymbol{r})\delta_{\alpha\beta}\right) . \tag{2.31}$$

When the medium is distorted, the stresses give rise to the restoring forces. Thus, the displacement field $\boldsymbol{u}$ feels the restoring force (Landau *et al.*, 1970, Chapter 3)

$$nm\ddot{\boldsymbol{u}}(\boldsymbol{r}) = \boldsymbol{F}(\boldsymbol{r}) = \frac{\partial}{\partial \boldsymbol{r}} \cdot \underline{\boldsymbol{\sigma}}(\boldsymbol{r}) = \underline{\boldsymbol{D}} \cdot \frac{\partial}{\partial \boldsymbol{r}} \cdot \underline{\boldsymbol{\epsilon}} = (\lambda + \mu)\nabla(\nabla \cdot \boldsymbol{u}(\boldsymbol{r})) + \mu\Delta\boldsymbol{u}(\boldsymbol{r}) . \tag{2.32}$$

The prefactor n results from considering volume elements, which is a consequence of the continuity approximation. Considering an infinitely large elastic medium, a deformation can be regarded as a plane wave. Thus, we can assume that $\boldsymbol{u}$ depends only on time and on just one spatial direction, which we arbitrarily call the $\hat{z}$ direction. One arrives at the two decoupled wave equations (Landau *et al.*, 1970, Section 22)

$$(v^{\parallel})^2\frac{\partial^2 u_z}{\partial z^2} - \frac{\partial^2 u_z}{\partial t^2} = 0 , \tag{2.33a}$$

$$(v^{\perp})^2\frac{\partial^2 u_x}{\partial z^2} - \frac{\partial^2 u_x}{\partial t^2} = 0 , \tag{2.33b}$$

with the longitudinal and transverse speed of sound $v^{\parallel}$ and $v^{\perp}$, respectively given by

$$v^{\parallel} = \sqrt{B} , \quad v^{\perp} = \sqrt{G} . \tag{2.34}$$

Hence, one finds the general solution

$$\boldsymbol{u}(\boldsymbol{r}, t) = A_1\boldsymbol{e}(\boldsymbol{q})e^{-i(qz+\omega t)} + A_2\boldsymbol{e}(\boldsymbol{q})e^{i(qz-\omega t)} . \tag{2.35}$$

Here, $\boldsymbol{e}(\boldsymbol{q})$ is a polarisation vector, ω is the frequency of the plane wave, $q = \frac{\omega}{v^{\parallel/\perp}}$ is the wavenumber and $\boldsymbol{q} = q\hat{\boldsymbol{e}}_z$ is the wavevector. $A_{1/2}$ are two constants depending on

the initial conditions. The plane wave excitations are the eigenmodes of an unstressed elastic system possessing rotational and translational symmetry. The energy of such a displacement field is given by the square of the frequency $\frac{\Delta E_{\mathrm{Pot}}}{m} = \omega^2 = q^2\left(v^{\parallel/\perp}\right)^2$ and the relation between wavenumber and frequency is called the dispersion relation. The Density of States $D(\omega)d\omega$ gives the number of states per particle in the frequency band $d\omega$. For plane-waves holds the Debye Density of States (Ashcroft and Mermin, 1976, Chapter 23)

$$D_D(\omega) \propto \omega^{d-1}\left(\frac{d-1}{(v^{\perp})^d} + \frac{1}{(v^{\parallel})^d}\right) . \tag{2.36}$$

Since the local disorder of an amorphous solid can not be resolved when the frequency of a mode is too small, plane waves are reasonable approximations for the low-energy modes of the system $(\omega, q \to 0)$. However, plane waves are no exact eigenmodes in disordered systems due to the initial stresses[1]. The additional term $\propto \sigma^{(0)}_{\alpha\beta}$ prevents the decoupling of the longitudinal and transverse components of the displacement field. Looking at low-frequency excitations (as shown in the first row of Figure 2.8), one sees swirls and vortices, implying the coupling of the transverse and longitudinal components. This coupling is also present in crystals, but due to anharmonic effects, *i.e.* higher order terms in the expansion of the energy. However, the Nambu-Goldstone theorem suggests that the deviation of the eigenmodes from plane waves has to be small for small frequencies and even vanishes completely for $\boldsymbol{q} \to 0$ (Chaikin and Lubensky, 1995, Section 8.5). Hence, it has been proven a useful concept to subsume the influence of the disorder and the initial stresses in an effective damping $\Gamma_q^{\parallel/\perp}$, which vanishes for $\boldsymbol{q} \to 0$. The sound attenuation $\Gamma_q^{\parallel/\perp}$ quantifies how quickly the energy stored in a plane wave excitation dissipates into the continuum of modes, effectively heating the system. Thus, one adds a damping coefficient to the plane wave solution $\propto e^{-\frac{\Gamma_q^{\parallel/\perp}}{2}t}$. The sound attenuation coefficient $\Gamma_q^{\parallel/\perp}$ is also called *linewidth*. It defines the lifetime of a plane wave-like excitation (Srednicki, 2007, Chapter 25).

[1] Additionally, the Bloch theorem (Ashcroft and Mermin, 1976, Chapter 8), stating that phonons or quantized periodic lattice vibrations are the eigenmodes in crystals, is not valid in amorphous systems. Again, this suggests that plane wave excitations are no exact eigenmodes for finite wavelengths. However, when removing the initial stresses, Ikeda and Mizuno measured a drop in the sound attenuation by two orders of magnitude (Mizuno and Ikeda, 2018). This is compatible with the idea that the deviation of a low-frequency eigenmode from a plane wave mainly results from the initial stresses.

We saw in this section that a transverse and longitudinal speed of sound can be defined on sufficiently large length scales in disordered but stable systems. When the energy of the plane wave-like excitations is sufficiently small. In this case, the mode can not resolve the disorder and the system can be approximated as a continuous elastic medium. The initial stresses lead to an effective damping of wave-like excitations. Conversely, if the energy of the modes suffices to resolve the local disorder, the continuous medium approximation breaks down, causing a transition in the nature of the modes. This suggests defining a characteristic frequency ω_*, which marks this transition. In the next section, we look at the modes with a frequency $\omega > \omega_*$. As the continuous medium approximation completely fails at the instability, one expects $\omega_* \to 0$ when approaching the critical point. This suggests that we have to study the stability in amorphous systems first before we can look at the disorder-dominated modes. Hence, we start the next section by reviewing a microscopic stability criterion for athermal $T = 0$. This criterion was already introduced and discussed by Maxwell 150 years ago by simply counting the constraints on each particle necessary for the system to be stable (Maxwell, 1867). Afterward, we use the microscopic expansion of the energy presented in Equation (2.15) for a general discussion of the eigenmodes in amorphous solids.

2.3 Stability, diffusive motion and non-affine displacements

In the previous section, we looked at the harmonic expansion of the microscopic energy in terms of the displacement field. Coarse-graning leads to the appearance of the stress tensor. Assuming rotational and translational invariance, we discussed that the potential energy can be written in terms of the two Lame coefficients λ and μ. We only showed this when neglecting initial stresses. Within these approximations, deformations only lead to affine displacements: local particle displacements follow the global deformation like an applied external flow field (van Hecke, 2009). However, non-affine displacements are crucial for understanding the amorphous solids, especially when they lose their stability (Flenner and Szamel, 2025; Szamel and Flenner, 2022; van Hecke, 2009). For example, more than 90% percent of the vibrational modes in disordered solids do not have a plane wave but a disorder-dominated character (Allen *et al.*, 1999): If the energy of the mode traveling through the system is sufficiently high

to resolve the disorder, the coherence of its wavefront is immediately lost due to strong scattering. Here, no polarisation can be defined. This has been used to explain parts of the thermal properties of amorphous solids, which show universal features that differ characteristically from their crystalline counterpart. This section presents a qualitative picture of amorphous solids in terms of the dominating vibrational modes.

We start this section by discussing Maxwell's geometric isostaticity criterion (Maxwell, 1867). After that, we briefly recall Wyarts variational arguments, which are more or less a generalization of Maxwell's and Alexander's discussion of stability (Alexander, 1998; Liu *et al.*, 2011; Wyart, 2005; Wyart *et al.*, 2005). This enables us to quickly go through the salient properties of disordered materials and to draw a qualitative unified picture of the vibrational modes in amorphous solids.

2.3.1 Macroscopic stability and floppiness

Assuming that the pair potential $U(r)$ is sufficiently short-ranged, we can regard the disordered system at $T = 0$ as a bonded network. We have discussed in Section 2.2 that the stress in an elastic stabile system increases due to an applied strain. Accordingly, any global deformation of a stable network comes with an energy cost. The only exception is if the transformation coincides with one of the global symmetries. This condition can be formulated in terms of the Hessian $\underline{\boldsymbol{\mathcal{H}}}$ constituting the harmonic expansion of the energy:

$$E_{\mathrm{Pot}}(\{\boldsymbol{r}\}) - E_{\mathrm{Pot}}(\{\boldsymbol{R}\}) \equiv \Delta E_{\mathrm{Pot}} \approx \frac{m}{2} \sum_{i,j=1}^{N} u_{i\alpha} \mathcal{H}_{i\alpha,j\beta} u_{j\beta} \ . \tag{2.37}$$

Here, we have pulled out the mass m so that the entries and thus the eigenvalues of $\underline{\boldsymbol{\mathcal{H}}}$ have the dimension of frequency square $[\mathcal{H}_{i\alpha,j\beta}] = [\omega^2]$. The idea that the elastic constants in Equation (2.27) do not vanish in a stable solid translates into the criterion that the eigenvalues of the Hessian corresponding to eigenvectors with an extensive number of non-vanishing entries are positive $\omega^2 > 0$. All the *Nullmodes*, *i.e.* eigenvectors, where the corresponding eigenvalue is zero, have to correspond to global symmetries or so-called *rattlers*. The latter are particles or groups of particles that are so weakly connected to the network that they trivially do not contribute to its stability. In the literature, rattlers are defined as particles with less than d contacts as they can be

moved around without any energy cost while the other particles can kept still (Mizuno and Ikeda, 2018; van Hecke, 2009).

The dynamical matrix $\underline{\boldsymbol{\mathcal{H}}}$ can be expressed via the spring matrix $\underline{\boldsymbol{\mathcal{K}}}$ and the bond tension matrix $\underline{\boldsymbol{\mathcal{T}}}$. The result reads (Maloney, 2006)

$$\begin{aligned}\mathcal{H}_{i\alpha,j\beta} &= \delta_{ij}\sum_k M_{i\alpha,k\beta} - M_{i\alpha,j\beta}\ ,\\ M_{i\alpha,j\beta} &= \frac{1}{m}\hat{R}^{\alpha}_{ij}\Big(\mathcal{K}_{ij} - \frac{\mathcal{T}_{ij}}{R_{ij}}\Big)\hat{R}^{\beta}_{ij} + \frac{\mathcal{T}_{ij}}{mR_{ij}}\delta_{\alpha\beta}\end{aligned} \tag{2.38}$$

The Hessian $\underline{\boldsymbol{\mathcal{H}}}$ is symmetric, which implies that all eigenvalues are real. Furthermore, $\underline{\boldsymbol{\mathcal{H}}}$ has no negative eigenvalues for purely repulsive interactions and for arbitrary reference positions $\{\boldsymbol{R}_i\}_{i=1}^N$ if the initial stresses are neglected ($\underline{\boldsymbol{\mathcal{T}}} = 0$). In such a case,

$$\sum_{ij}\underbrace{K_{ij}}_{\geq 0}(u_{ij}^{\parallel})^2 \geq 0 \tag{2.39}$$

holds for any displacement field. The square root of the eigenvalues gives the frequencies of the normal modes $\omega = \sqrt{\lambda}$. Because of global translational invariance, the uniform displacement of all particles is an eigenvector of the Hessian with eigenvalue 0 even for nonzero initial stress. The vector $\boldsymbol{e}_{i,\alpha=1,2,..,d} = \frac{1}{\sqrt{N}}(1,1,1,...,1)^T$ is therefore always a nullmode of the system. We have already discussed this fact in Section 2.2.4 under the notion of the Nabu-Goldstone theorem, where we argued that the damping has to vanish in the hydrodynamic limit $\Gamma^{\parallel/\perp}_{q\to 0} \to 0$. Hereinafter, we focus on the nature of the modes when the local disorder is resolvable. As we will see, the associated modes have a diffusive character and resemble those populating the system at the critical point. Thus, we first consider Maxwell's *isostatic criterion*.

Stability of disordered materials with no initial stresses: Following Alexander and Wyart, we first discuss eigenvectors of the Hessian with eigenvalue zero in an unstressed system $\underline{\boldsymbol{\mathcal{T}}} = 0$ (Alexander, 1998; Wyart *et al.*, 2005). Let us consider a set of displacements $\{\boldsymbol{u}_i\}_{i=1}^N$ for which $\Delta E_{\rm Pot} = 0$ holds and where the first order strain $\underline{\boldsymbol{e}}^{(1)}$ stays finite. We call $\{\boldsymbol{u}_i\}_{i=1}^N$ a *floppy mode*. The underlying displacement field $\{\boldsymbol{u}_i\}_{i=1}^N$ can only change the pair-distances $(\boldsymbol{u}_i - \boldsymbol{u}_j)\cdot\boldsymbol{R}_{ij} = u_{ij}^{\parallel} \neq 0$ if the spring constants vanish $\mathcal{K}_{ij} = 0$. Since we have the guiding picture of soft particles in mind, we say that the

spring constants vanish, $K_{ij} = 0$, if the associated particles are not in contact. Each non-vanishing spring constant results in one constraint on the atomic displacements of a floppy mode. Let us denote the number of total constraints due to contacts with N_c. Because of global symmetry constraints, there are

$$\#F = Nd - \frac{d(d+1)}{2} \tag{2.40}$$

degrees of freedom of how particles can be moved. Since the constraints are generally independent, floppy modes can only exist if $\#F > N_c$ holds. Such networks are called *hypostatic*. Here, the shear and longitudinal modules vanish, and a perturbation leads to a plastic instead of an elastic response if it overlaps with a floppy mode. Thus, a floppy mode represents a direction of fragility (Wyart, 2005). Hence, a hypostatic system is unstable. If $Nd = N_c$ holds, the network is called *marginally stable* or *isostatic*. Over-constrained networks are called *hyperstatic*. Such systems can be treated as a continuous elastic medium above a certain length scale. All in all, these considerations lead to the global stability condition $Nd \leq N_c$. It can be translated in a condition for the average number of bonds or contacts z per particle: Let b_i be the number of bonds of the i^{th} particle. One finds

$$zN = \sum_{i}^{N} b_i = 2N_c \ , \tag{2.41}$$

since each bond is counted twice. Equation (2.41) leads to Maxwell's stability criterion, which states that $z \geq 2d$ has to hold for stability (Alexander, 1998; Maxwell, 1867; Wyart, 2005). While d bonds are necessary to fix the position of a single particle, $2d$ bonds are, on average, necessary to fix the positions of all particles simultaneously. This is a global criterion. Consequentially, a floppy mode in the unstable phase ($z < 2d$) is generally extended. There can be unstable regions even in isostatic or hyperstatic systems. However, they generally correspond to particles or groups of particles having less than d contacts with the largest cluster. Close to the instability, approximately 5% of all particles are such *rattles* (van Hecke, 2009). They trivially do not contribute to the stability of the largest cluster. (O'Hern *et al.*, 2003). Equation (2.41) suggests a unique instability transition, which is a direct consequence of the assumption that the individual constraints are independent. The validity of the unique transition point has

been confirmed numerically. O'Hern and Silbert have analyzed the dependency of the critical point on the system size in computer simulations with monodisperse particles. They found that the critical point becomes unique after removing the rattlers for large N and that the critical density is in accordance with Maxwell's isostatic criterion (Benetti *et al.*, 2018; Mizuno and Ikeda, 2018). As rattlers have to be removed for its validity, Maxwell's isostatic criterion is only applicable in analytical investigations or computer works. Rattlers can not be identified in large-scale experiments. The volume fraction ϕ or the density n is already better, but the notion of a critical density is always ambiguous due to the rattlers. Later in this section, we will discuss that a vanishing global pressure ($p = 0$) in soft sphere systems is an unambiguous accessible criterion for the critical point. However, we first discuss the general effect of pressure on the stability before turning to the critical point.

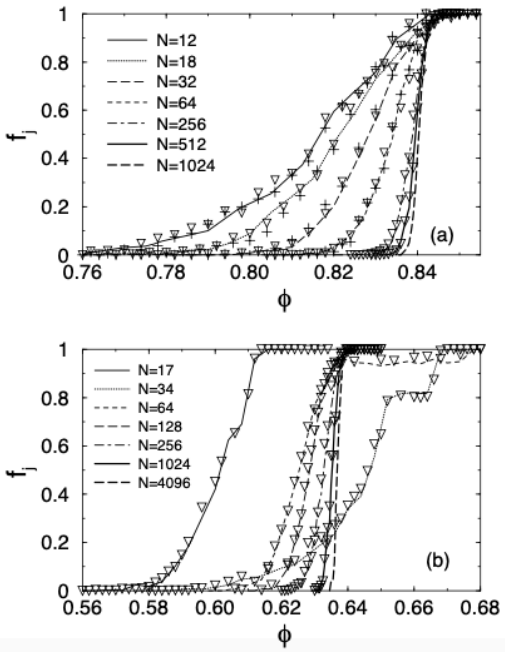

Figure 2.1: Fraction f_j of jammed states as a function of ϕ. Panel a) 2d bidisperse 50:50 mixture with a size ration 1:1.4. Panel b) 3d monodisperse systems. The lines, downward triangles, and plus symbols represent the data for different interaction potentials. Reprinted from *Jamming at zero temperature and zero applied stress: The epitome of disorder*, by C. O'Hern , *et al.*, Phys. Rev. E. 2003, vol. 68, page 011306, Copyright [2025] by the American Physical Society. Reprinted with permission. Doi:10.1103/physreve.68.011306

The (de-) stabilising effect of pressure in networks: Initial stresses $\underline{\boldsymbol{\mathcal{T}}} \neq 0$ can have both a stabilising and a destabilising effect. For illustration, we present Alexander's discussion of the finite 2D square lattice, where the bonds are modeled by relaxed springs of arbitrary strength (Alexander, 1998). The system is visualized in Figure 2.2. Each particle inside the network has four neighbors. However, the particles at the edges have

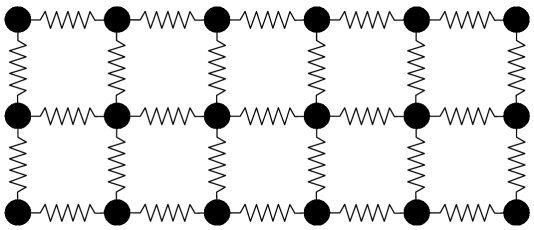

Figure 2.2: Schematic illustration of a 2d square lattice. The particles are connected by identical relaxed springs

only three, and at the corners only two contacts. Therefore, the system is marginally stable and its stability depends on the boundary conditions. The network yields to applied shear if the position at the edges are not fixed. This can also be seen by looking at the microscopic elastic moduli in Equation (2.27). The geometry implies

$$D^{xxxx} = D^{yyyy} > 0 \qquad D^{xxyy} = D^{xyxy} = 0 \,, \tag{2.42}$$

independent of the interaction strength. Here, x and y denote the horizontal and vertical spatial axis of the 2D system. Notably, we dropped the particle index j due to the symmetry properties of the network. A shear deformation $\partial_y u_x$ comes without an energy cost since the elastic constants D^{xxyy} vanish. Conversely, one has to perform work on the system for a volume-changing deformation $\partial_x u_x$ since the bulk modulus does not vanish. Now, let us apply a uniform decompression of the system. The resulting stretch of the springs leads to $\mathcal{T}_{ij} = \mathcal{T} < 0$ and according to Equation (2.19) to a negative pressure $p < 0$. The uniform stress distribution ensures that the system's geometry remains unchanged. However, the Equations (2.23) and (2.17a) report an additional term $\propto (\partial_x u_y)^2 + (\partial_y u_x)^2$ in the expansion of the energy. Thus, the network has developed some stability against an applied shear stress due to the nonzero pressure. Generally, Alexander has argued that negative pressure $p < 0$ resulting from stretched bonds can stabilize disordered systems even if the average contact number is well below $z < 2d$ (Alexander, 1998). This corresponds to the example discussed above. However, more connections are needed to stabilize the system when the bonds are loaded, and when the pressure is positive $p > 0$. Using variational arguments and in a later work when developing an effective medium theory, Wyart and co-workers showed that the additional number of contacts Δz grows with the square root of the pressure (DeGiuli *et al.*, 2014;

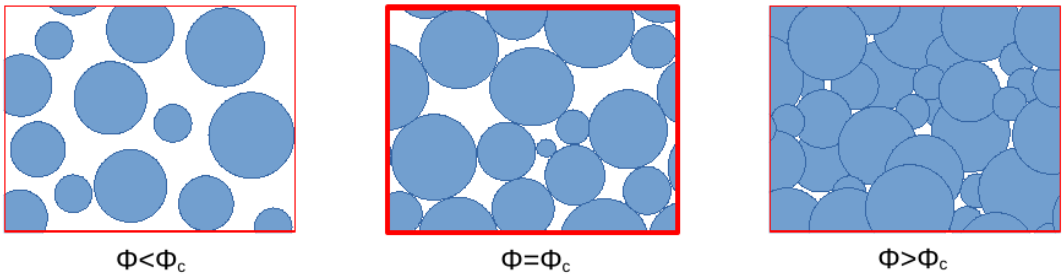

Figure 2.3: Schematic illustration of soft disk system a) below and c) above jamming and b) directly at the critical density $\phi = \phi_c$ where $z = 2d = 4$ holds. the global pressure is nonzero only in the hyperstatic configuration c).

Wyart *et al.*, 2005)

$$z - z_c \equiv \Delta z \propto \sqrt{p}. \tag{2.43}$$

In soft sphere systems and above the jamming transition, particles overlap or deform each other due to geometrical frustration. This leads to a positive pressure. Hence, the pressure is a function of the excess coordination Δz or equivalently on excess packing fraction $\Delta\phi = \phi - \phi_c$. We must analyze the corresponding structure to understand the interdependence of $\Delta z, \Delta\phi$, and p close to the instability. This is the topic of the following paragraph.

Structure of soft sphere systems at the jamming transition: Hereinafter, we consider a monodisperse system with a general soft sphere potential (O'Hern *et al.*, 2003; van Hecke, 2009):

$$U(r_{ij}) = \begin{cases} \epsilon\delta_{ij}^{\alpha} & \text{for } \delta_{ij} \geq 0 \\ 0 & \text{else} \end{cases} \tag{2.44}$$

Here, $\delta_{ij} = 1 - \frac{r_{ij}}{\sigma}$ is the dimensionless overlap and σ is the particle diameter. The parameter ϵ quantifies the potential. We restrict ourselves to repulsive potentials $\alpha > 0$. Due to the repulsive interaction, particles' overlaps are unstable at $T = 0$ and below jamming. The particles push each other apart, and there is no kinetic energy or stress to compete with the repulsive forces. Thus, no particles overlap for sufficient low densities in mechanical equilibrium $\boldsymbol{F}_i = 0 \quad \forall \quad i \in \{1, ..., N\}$. As a consequence, the mean

dimensionless overlap $\langle\delta\rangle$ and the average[2] coordination number are zero $\langle\delta\rangle = z = 0$. From Equation (2.15) follows that the pressure p, as well as the longitudinal and shear modules B, G are all zero. Due to geometric frustration, the particles cannot push each other away for sufficiently high densities. The critical packing fraction ϕ_c marks the point where particles start touching each other and marks jamming transition (Mizuno and Ikeda, 2018; O'Hern *et al.*, 2003; van Hecke, 2009). We have already discussed in the context of Figure 2.1 that the transition at ϕ_c is in accordance with Maxwell isostatic criterion if the rattlers with less than d contacts are removed. Hence, the average coordination number jumps at the critical point. This jump is reported in (Makse *et al.*, 1999). Figure 2.3 shows three snapshots of configurations for different packing fractions ϕ. The particles overlap for $\phi > \phi_c$, leading to a nonzero pressure and non-vanishing elastic constants. Equation (2.19) suggest the scaling $p \propto \left\langle \frac{\partial U(r)}{\partial r} \right\rangle \propto \langle\delta\rangle^{\alpha-1}$. The mean overlap scales as $\langle\delta\rangle \propto \Delta\phi = \phi - \phi_c$. Thus, we expect $p \propto (\phi - \phi_c)^{\alpha-1}$ for the scaling of the pressure. This was confirmed in simulations (O'Hern *et al.*, 2003). There, the authors prepared the system by randomly placing particles in a box and letting them relax until the energy was minimized. Their results are shown in Figure 2.5a. The pressure vanishes at the transition. Noticeably, this characteristic of the instability does not require removing rattlers. Thus, the vanishing of the pressure p unambiguously marks the transition [3] making p a good quantity for sim-

[2]Throughout this work, the pointy brackets $\langle\cdot\rangle$ indicate the ensemble average. We will give an exhaustive introduction to the stochastic description in Section 3. There, we also define the average. In this introductory chapter, it suffices to think of $\langle\cdot\rangle$ as the mean.

[3] To convince ourselves that $\langle\delta\rangle \propto \Delta\phi$ holds in $d = 3$, we consider a rectangular solid with the measures $\sigma \times \sigma \times (N-1)\sigma$ in the thermodynamic limit $N \to \infty$. This cuboid is filled with N soft spheres of diameter σ. The spheres uniformly overlap with $\langle\delta\rangle = \delta = 1/N$. The spherical spherical cap V_δ with height $\delta\sigma/2$ of two overlapping spheres is given by

$$V_g = \frac{2\pi}{3}\left(\frac{\sigma}{2}\right)^3 \int_0^{\cos^{-1}(1-\delta)} \sin(\theta) d\theta = \frac{2\pi}{3}\left(\frac{\sigma}{2}\right)^3 \frac{\delta}{2} \,. \quad (2.45)$$

Figure 2.4 illustrates two overlapping disks. In $d = 3$ equals the grey shaded volume $2V_g$. The packing fraction for $\delta = 1/N$ reads

$$\phi = \frac{\text{covered volume}}{\text{total volume}} = \frac{2\pi}{3}\frac{1}{8}\frac{2N-1}{N-1} \xrightarrow[N\to\infty]{} \phi_c + \frac{2\pi}{3}\frac{1}{8}\delta \,. \quad (2.46)$$

Thus, we indeed find $\Delta\phi \propto \langle\delta\rangle$.

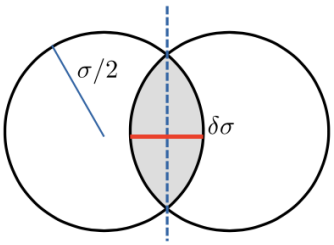

Figure 2.4: Illustration of two overlapping disks

ulation and experiments studying jamming in granular media (Mizuno and Ikeda, 2018).

The jamming transition corresponds to a configuration where the particles are just touching but not overlapping, as illustrated in Figure 2.3. This structural effect of the unjamming transition in soft sphere systems can also be observed in the pair correlation function

$$g(r) = \frac{1}{n} \left\langle \frac{1}{N} \sum_{i \neq j}^{N} \delta(\boldsymbol{r} - \boldsymbol{r}_j + \boldsymbol{r}_i) \right\rangle \ . \tag{2.47}$$

In $d = 3$, $g(r)$ gives the average number of particles within a shell of diameter r and thickness dr as $4\pi n g(r) dr$ (Hansen and McDonald, 2009, Chapter 2). Notably, in a homogeneous and isotropic system, $g(r)$ depends only on the absolute value of the interparticle distance $r = |\boldsymbol{r}|$. In this case, $g(r)$ is often called the radial distribution function. Particles losing contact at ϕ_c implies a divergence of $g(r)$. Simulations of monodisperse soft spheres established that the first peak in the radial pair distribution diverges and narrows when approaching the critical point (O'Hern *et al.*, 2003; Silbert *et al.*, 2006). This is shown in Figure 2.5b. From the small r-side, the peak approaches the form of a delta spike, while on the large r- or the right- side, a power law decay manifests

$$g(r \to \sigma^+) \propto \frac{1}{\sqrt{\frac{r}{\sigma} - 1}} \ . \tag{2.48}$$

Wyart has explained this power law decay as a *vestige* of the large number of particles on the verge of touching or overlapping (Wyart, 2005). The area under the peak, corresponding to the average number of neighbors at the transition, is in agreement with Maxwell's isostaticity criterion[4] (Silbert *et al.*, 2006; van Hecke, 2009). When the system is compressed, particles come simultaneously into contact. Again, this causes the coordination number's jump at the transition. Compressing the system further, more

[4]Actually, the authors of (Silbert *et al.*, 2006) found that the area under the peak corresponds to a critical coordination number below $z_c = 2d = 6$ in three dimensions. The authors found $\tilde{z}_c = 5.88$. However, they did not remove the weakly connected particles or rattlers. According to the results in (O'Hern *et al.*, 2003), up to 5% percent of all particles can be regarded as rattlers and do not contribute to stability. Thus, the findings in (Silbert *et al.*, 2006) are in accordance with Maxwell's criterion of isostaticity.

particles come into contact and start to overlap or deform each other. For example, this causes the typical polygon shape of foam bubbles (Drenckhan and Hutzler, 2015).

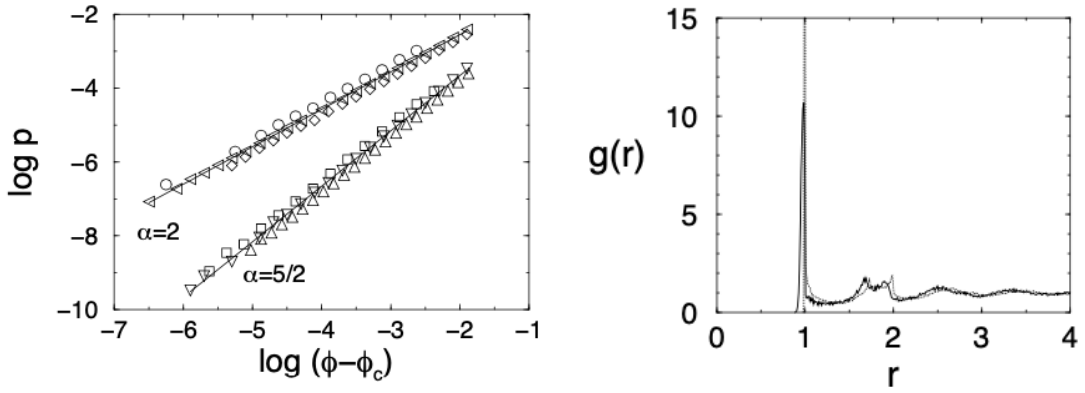

(a) Global pressure over $\Delta\phi$. The upper line $\propto \Delta\phi^1$ displays the pressure for a harmonic interaction $\alpha = 2$. The circles show the results for 3D monodisperse systems, the diamonds for 3D bidisperse, and leftward triangles for 2D bidisperse. The lower curve $\propto \Delta\phi^{1.5}$ displays the results for Hertzian interaction $\alpha = 2.5$. The squares display the result for monodisperse 3D systems, upward triangles 3D, and downward triangles 2D bidisperse systems. Reprinted from *Jamming at zero temperature and zero applied stress: The epitome of disorder*, by C. O'Hern , *et al.*, Phys. Rev. E. 2003, vol. 68, page 011306, Copyright [2025] by the American Physical Society Reprinted with permission. Doi:10.1103/physreve.68.011306

(b) The pair correlation function $g(r)$ over r in dimensionless units $r \to r/\sigma$. The solid line depicts the data for $\Delta\phi = 10^{-1}$ and the dotted line for $\Delta\phi = 10^{-6}$. In the latter case lies the maximum of the first peak approximately at 10^{-6}, far beyond the scale of the graph. The first peak's height, position, and width are purely geometric quantities at $T = 0$. It does not depend on the interaction potential. Reprinted from *Structural signatures of the unjamming transition at zero temperature*, by L. Silbert, A. Liu & S.Nagel, 2006, Phys. Rev. E., vol. 73, page 041304. Copyright [2025] by the American Physical Society. Reprinted with Permission. Doi:10.1103/physreve.73.041304

Figure 2.5: Panel (a): The pressure over $\Delta\phi$. Panel (b) Examples of the pair correlation function.

It was found in simulations that the excess coordination number $\Delta z = z - z_c$, with $z_c = 2d$ increases with the square root of the excess volume fraction $\Delta\phi = \phi - \phi_c$ (Makse *et al.*, 1999; O'Hern *et al.*, 2003; van Hecke, 2009):

$$\Delta z \propto \sqrt{\Delta\phi} \tag{2.49}$$

This result is independent of spatial dimension, interaction potential, or polydispersity. However, it only applies if the rattlers are ignored when calculating the coordination number but included in the density (van Hecke, 2009). The scaling (2.49) can be understood from the divergence of the radial distribution function in Equation (2.48) (van Hecke, 2009): To see this, let us compress a marginal stable system such that the average overlap increases from 0 to δ. Assuming that all the displacements due to the compression are affine, one closes all the gaps between particles that were initially smaller than $\delta\sigma$ causing

$$\Delta z \propto \int_{\sigma}^{\sigma(1+\delta)} dr \frac{1}{\sqrt{\frac{r}{\sigma}-1}} \propto \sqrt{\delta} \propto \sqrt{\Delta\phi}\,. \tag{2.50}$$

Actually, $z = 0$ in the unjammed state only holds if the system has fully relaxed. A finite contact number can be due to an applied perturbation (Ikeda *et al.*, 2020; Saitoh *et al.*, 2020). The relaxation time diverges when the jamming transition is approached from below. Furthermore, the contact number does not jump in emulsions or if the system is damped due to the energy transfer (Ikeda *et al.*, 2020). Nevertheless, we continue our discussion by focusing on frictionless spheres in mechanical equilibrium. Here, the coordination number z indeed jumps. As a consequence, both the longitudinal and the shear modulus must vanish with the excess coordination. However, B and G scale differently with Δz due to non-affine displacements. We analyze the vibrational modes and their properties in the next section.

2.3.2 Disorder dominated modes

In this section, we discuss the modes populating the intermediate energy range of the spectrum of disordered solids. Here, the energy of the modes suffices to resolve the local disorder, which implies that an elastic medium approximation would be qualitatively inaccurate. As we will see, the nature of these modes can be understood by the physics dominating at the critical point of isostaticity. A characteristic frequency ω_* marks the crossover of the validity of the elastic medium approximation to the range of disorder-dominated modes. The crossover frequency ω_* vanishes at the transition. We discuss the associated scaling relation and the Boson peak, which is a prominent feature of the crossover from wave-like excitations to disorder-dominated modes. We start this section

by paraphrasing the works[5] of Matthieu Wyart following (Liu *et al.*, 2011; Wyart *et al.*, 2005; Yan *et al.*, 2016): We introduce the modes present at the isostatic point. Later, we will see that these modes have a diffusive character and generally occur above a characteristic length scale that marks the crossover to the elastic medium regime. This length scale vanishes at the transition.

The vibrational modes of isostaticity : Following Wyart, we consider an infinite network at the isostatic point ($z = z_c = 2d$) where we model all edges as relaxed springs (Wyart *et al.*, 2005). By construction, there are no initial stresses. Additionally, we dismiss rattlers and groups of particles with less than d contacts to the largest cluster. Hereinafter, we discuss that the modes in such an isostatic system are characterized by a constant Density of States.

Cutting out a subsystem of volume l^d, with box length l, creates floppy modes with no restoring forces. Since $\propto l^{d-1}$ bonds were cut, $\propto l^{d-1}$ floppy modes were created. The resulting floppy modes are generally extended[6] because all rattlers are ignored. The conceptual idea is to use these modes with no restoring forces to model the low-energy modes in the isostatic system. Mimicking the procedure to identify low-frequency modes of ordinary solids, Wyart constructs trial modes by distorting floppy modes. The idea is to modulate a sine function on top of the floppy mode, such that the new distorted mode vanishes at the boundary of the subvolume l^d. By construction, only the distortion, but not the original floppy mode, contributes to the potential energy. Due to the sine-function differ nearby particles' displacements associated with a trial mode by an order $\mathcal{O}(1/l^2)$ from the displacement of the floppy mode. Thus, the considered displacement fields $\{\boldsymbol{u}_i\}_{i=1}^N$ of the constructed trial mode give $\Delta E_{\mathrm{Pot}} \propto \frac{1}{l^2}$ and the mode has a frequency $\omega_l \propto \frac{1}{l}$. Seeing that the dynamic matrix is positive definite, there must be an eigenvalue $\lambda_0 \leq \omega_l^2$. If there are m trial modes with energy $\leq \omega_l^2$, there are at least $\frac{m}{2}$ eigenmodes with associated eigenvalues $\lambda \leq 4\omega_l^2$ (Horn, 1954; Wyart *et al.*, 2005).

[5] A rigorous mathematical treatment can be found in (Wyart, 2005; Yan *et al.*, 2016)

[6] Note that Wyart and co-workers have published a work in 2016 (Yan *et al.*, 2016) where they state that floppy modes arisen due to cut bonds can actually be localized. They constructed a more general variational argument by adding and not cutting bonds. It leads to the same results. However, this introductory chapter discusses the older work since it is more instructive.

As we will see shortly, this implies that the averaged Density of States

$$D(\omega) = \lim_{N\to\infty} \frac{2\omega}{N} \sum_{i=1}^{N} \overline{\delta(\omega^2 - \lambda_i)} \tag{2.51}$$

stays constant for $\omega \to 0$ and for $z = z_c$. Here λ_i is an eigenvalue of the dynamical matrix (2.38). The bar denotes the average of the disorder, and the factor 2ω results from the transformation of the variable $D(\lambda) = 2\omega D(\omega)$, where $D(\lambda)$ is the density of eigenvalues and $\omega^2 = \lambda$ holds by definition. In order to show that $D(\omega \to 0)$ stays constant, we consider a frequency $\omega_l \propto \frac{1}{l}$ for $l \to \infty$. As $\propto l^{d-1}$ eigenmodes with smaller frequency exist, one finds $\propto l^{d-1}$ modes in a volume $\propto l^d$ (Liu *et al.*, 2011; Wyart *et al.*, 2005). This gives for the Density of States

$$\int_0^{\omega_l} d\omega D(\omega) \propto \frac{l^{d-1}}{l^d} = \frac{1}{l} \,, \tag{2.52}$$

Assuming that the Density of States follows a power law for $\omega \to 0$, *i.e.*meaning $D(\omega) \propto \omega^\alpha$, the assumption $\omega_l \propto \frac{1}{l}$ implies $\alpha = 0$ and $D(\omega) = const.$ Thus, a marginal stable solid can not be regarded as an elastic solid, where the Debye-law $D \propto \omega^{d-1}$ holds. This was also claimed by Tkachenko and Witten already in 1999 (Tkachenko and Witten, 1999). They analyzed the force propagation in a disordered solid at $z = z_c$ and argued that forces propagate *undirected* in a marginal stable solid. This is in opposition to elastic media, where forces propagate in a directed fashion. Again looking at a subvolume l^d, the idea is, that half of the exterior forces on the resulting network fully determine the interior forces and the second half of the exterior forces. This is in opposition to an elastic medium, where the second half of exterior forces is undetermined as long as the total net force and the total torque on the subvolume vanish. Here, we briefly recall the microscopic argument presented in (Tkachenko and Witten, 1999): Consider a subvolume $\overline{V}$ containing N' particles with $\overline{V}$ sufficiently large so that the average coordination number is again given by $z' = 2d$. Let b_{int} be the number of contacts inside the subvolume and b_{ext} the number of bonds crossing the boundary of the subsystem. Then, one has $z' = \frac{2b_{int}+b_{ext}}{N'}$. The factor 2 appears due to double counting. There are $b_{int} + b_{ext} = N'd$ force balance equations. Since these equations are coupled, the internal forces can not be determined without knowing the external forces if the external

contact forces are independent. The number of required forces is

$$N'd - b_{int} = N'\left[d - \frac{z'}{2}\right] + \frac{b_{ext}}{2} = \frac{b_{ext}}{2} \ . \tag{2.53}$$

As the authors call it, this results in *undirected* force propagation in isostatic systems. Only half of the forces applied on bonds crossing the boundary are needed to determine the loads on all external contacts. This contrasts elastic media, where Equation (2.33) implies a directed force propagation.

In direct contrast to wave-like excitations, Wyart and co-workers have called the modes constituting the constant density of state *anomalous modes* (Liu *et al.*, 2011; Wyart, 2005; Wyart *et al.*, 2005). Later on, we will discuss that they have a diffusive character. While these *anomalous modes* dominate the low-energy modes in the isostatic case, sound modes are present in a hyperstatic system if their energy is sufficiently low. Higher energy modes can again resolve the disorder and one finds again the physics discussed in this section. We look at this transition in the next paragraph.

Sound modes in disordered solids: As discussed in Section 2.2, sound modes dominate low energy excitations in elastic media due to global translational invariance. The extended eigenmodes for small energies can be labeled with the wavenumber q. The speed of sound $v^{\parallel/\perp}$ determines the linear dispersion relation

$$\omega = qv^{\parallel/\perp} \ . \tag{2.54}$$

However, we have discussed in the previous paragraph that no sound modes exist in marginal stable solids, where other modes dominate due to the strong disorder. Here, we look at a hyperstatic system with $z > z_0$ and strive to characterize its vibrational modes. Again following Wyart and co-workers, we cut out a subvolume l^d (Liu *et al.*, 2011). The total number of excess bonds in a subvolume l^d scales with $\Delta z l^d$. By removing the contacts at the boundary of the subvolume $\propto l^{d-1}$ bonds are cut. The removal of the boundary bonds only leads to the emergence of floppy modes if the number of cut bonds exceeds the number of excess bonds. This introduces a crossover length-scale l_*,

where the numbers of excess bonds and cut contacts are just equal to each other:

$$(l_*)^{d-1} \simeq \Delta z (l_*)^d \Longrightarrow l_* \simeq \frac{1}{\Delta z} \,. \tag{2.55}$$

The disorder dominates below l_*. The arguments for the constant Density of States also apply for $l < l_*$. This introduces a characteristic frequency or crossover frequency ω_* (Liu *et al.*, 2011):

$$\omega_* \simeq \frac{1}{l_*} \simeq \Delta z, \tag{2.56}$$

which vanishes at the transition. Modes with a frequency smaller than ω_* can not resolve the disorder. Here, the continuous elastic medium approximation applies. The Density of States follows Debye's law $\propto \omega^{d-1}$, and one recovers the linear relation $\omega = v^{\parallel/\perp} q$ for wave-like excitation. Figure 2.6 depicts the Density of States for different packing fractions. The Debye regime and the flat part are clearly visible. As suggested by the graphic, the plateau in the Density of States extends down to $\omega = 0$ at the critical point (Ellenbroek *et al.*, 2009a; Makse *et al.*, 1999). The predicted length l_* scale has been observed in response measurements in simulations (Ellenbroek *et al.*, 2006, 2009a). The restriction that Equation (2.54) is only valid for $\omega < \omega_*$ raises the question of the scaling of the speed of sound $v^{\parallel,\perp}$ when approaching the instability. The jump in the average coordination number z already suggests that $G = B = 0$ holds below jamming. We refer back to Equation (2.14) for the

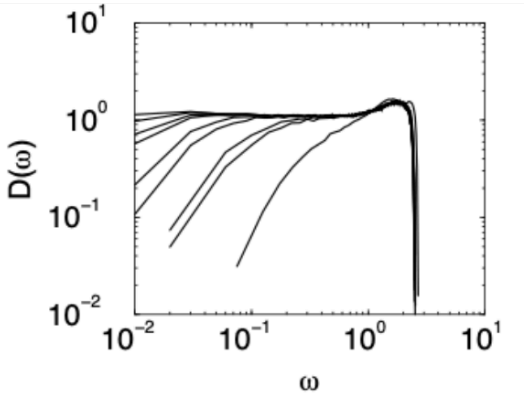

Figure 2.6: Vibrational Density of States $D(\omega)$ over the the dimensionless frequency ω. The graphic depicts simulation data with monodisperse $N = 1024$ soft particles with $\alpha = 2$. The lines display different excess packing fractions. One has from right to left $\Delta\phi = 10^{-1}\,,\ 10^{-2}\,,\ 5 \cdot 10^{-3}\,,\ 10^{-3}\,,\ 5 \cdot 10^{-4}\,,\ 10^{-4}\,,\ 5 \cdot 10^{-5}\,,\ 10^{-6}\,,\ 10^{-8}$. Reprinted from *Vibrations and Diverging Length Scales Near the Unjamming Transition.*, by L. Silbert, A. Liu & S.Nagel, 2006, Phys. Rev. Lett., vol. 95, page 098301. Copyright [2025] by the American Physical Society. Reprinted with Permission.Doi:10.1103/PhysRevLett.95.098301

spring constants $\mathcal{K}_{ij}$ to determine how the moduli B and G vanish with Δz or $\Delta\phi$: The scaling $\langle\delta\rangle \propto \Delta\phi$ implies $\langle\mathcal{K}_{ij}\rangle \propto \langle\delta\rangle^{\alpha-2} \propto (\Delta\phi)^{\alpha-2}$. Here, α characterizes the soft sphere potential in Equation (2.44). However, this is only observed for the longitudinal modulus $B \propto \frac{p}{\langle\delta\rangle} \propto (\Delta\phi)^{\alpha-2}$. The shear modulus vanishes faster with the distance to the critical point. Simulations have established the scaling relation $G \propto \frac{p}{\sqrt{\langle\delta\rangle}} \propto (\Delta\phi)^{\alpha-3/2}$ (Ellenbroek *et al.*, 2009a; Liu *et al.*, 2011; Makse *et al.*, 1999; Mizuno and Ikeda, 2018; Mizuno *et al.*, 2016b; O'Hern *et al.*, 2003; van Hecke, 2009). This qualitative difference in the scaling of the moduli is ascribed to non-affine displacements. While a non-affine response leads to a decrease of both moduli, the shear modulus is much more affected. The affine and non-affine contributions were isolated by Mizuno *et. al* and by O'Hern *et. al* (Mizuno *et al.*, 2016b; O'Hern *et al.*, 2003). The latter results are shown in Figures 2.7a and 2.7b. The qualitative influence of non-affine displacements is clearly visible. The vanishing of the elastic constants together with the vanishing of ω_* and the divergence of l_* suggests that the majority of vibrational modes, corresponding to the normal modes or eigenvectors of the Hessian (2.38), do not have the character of propagating sound modes close to the transition. Before we continue discussing the nature and characteristics of the vibrational modes in disordered materials, we first focus on a phenomenon related to the breakdown of the elastic medium approximation, namely the *Boson peak*.

The Boson peak: Experiments and simulations alike observe an excess over the Debye level $D_D(\omega)$ in the reduced Density of States $\frac{D(\omega)}{D_D(\omega)}$ (Mizuno and Ikeda, 2018; Monaco and Mossa, 2009; Wuttke *et al.*, 1995). This excess is called the Boson peak. It has been documented that the peak position[7] ω_{BP} is close ω_* (Mizuno and Ikeda, 2018). Not only vanishes ω_{BP} at the transition, also the height of the peak has been found to diverge for $\Delta\phi \to 0$ in simulations (Shintani and Tanaka, 2008):

$$\frac{D(\omega_{BP})}{\omega_{BP}} \propto \frac{1}{B} + \frac{1}{G} \approx \frac{1}{G} \tag{2.57}$$

[7]The name *Boson Peak* arose since the first evidence for this peak comes from Raman scattering experiments (Flubacher *et al.*, 1959; Leadbetter, 1969). There, a maximum was also observed at ω_{BP} in the scattering intensity. The peak obeyed the temperature dependency of the Bose-statistics $n(T,\omega) = \left(e^{\frac{\hbar\omega}{k_B T}} - 1\right)^{-1}$ (Schirmacher and Ruocco, 2022). However, the intensity is proportional to $(n(T,\omega) + 1)D(\omega)$, indicating the harmonic origin of this excess (Caponi *et al.*, 2009).

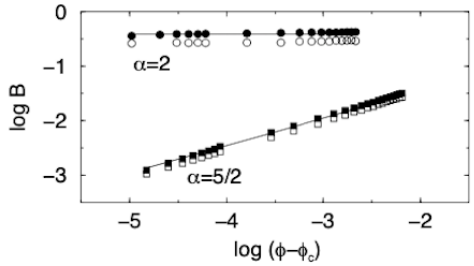

(a) Bulk modulus in monodisperse 3D systems for harmonic ($\alpha = 2$) and Hertzian ($\alpha = 2.5$) interactions. The closed symbols display the bulk modulus solely due to affine displacements. The data depicted by the open symbols was recorded after relaxation processes following the affine displacements took place. Hence, the open symbols include non-affine displacements. The results look similar for 2D and bidisperse systems.

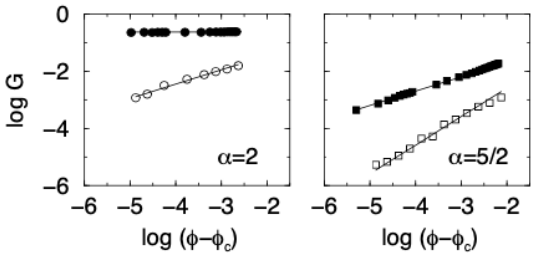

(b) Shear modulus in monodisperse 3D systems for harmonic ($\alpha = 2$) and hertzian ($\alpha = 2.5$) interactions. The meaning of open and closed symbols is the same as in Figure 2.7a. As one can see, non-affine displacements have a qualitative effect on the scaling of the modulus. The results look similar for 2D and bidisperse systems.

Figure 2.7: Scaling of the bulk and shear modulus with the distance to the critical point. Reprinted from *Jamming at zero temperature and zero applied stress: The epitome of disorder*, by C. O'Hern , *et al.*, Phys. Rev. E., vol. 68, page 011306, Copyright [2025] by the American Physical Society. Reprinted with permission. Doi:10.1103/physreve.68.011306

The discussion so far has established that a crossover in the nature of the vibrational modes occurs around ω_*, where the elastic medium approximation breaks down. In the following section, we will take a closer look at this crossover and the normal modes in amorphous solids.

2.3.3 The vibrational modes in glasses

This section studies the vibrational modes in stable glasses with $z > z_c$ at zero temperature $T = 0$. Here, the atomic displacements are generally quite small, which makes the harmonic approximation of the potential energy reasonable:

$$\Delta E_{\mathrm{Pot}} \approx \frac{m}{2} \sum_{i,j=1}^{N} u_{i,\alpha} \mathcal{H}_{i\alpha,j\beta} u_{j,\beta} \tag{2.58}$$

The Hessian $\underline{\boldsymbol{\mathcal{H}}}$ was defined Equation (2.38). The eigenmodes $\boldsymbol{e}_k$ of the system equal the eigenvectors of $\underline{\boldsymbol{\mathcal{H}}}$. As the Hessian is a symmetric matrix, the eigenvectors with nonzero eigenvalues are generally orthogonal (Tanguy, 2023). The eigenvectors are often referred to as *normal modes*, and the square root of their associated eigenvalues gives the eigenfrequencies ω_k. As we saw when discussing ω_* in Section 2.3.2, the characteristic properties of a mode highly depend on its frequency. This section discusses some of the salient features of the normal modes in jammed glasses. A frequently used quantity for the characterization of the modes is the participation ratio (Hu and Tanaka, 2022; Lerner and Bouchbinder, 2021; Mizuno *et al.*, 2017; Shimada *et al.*, 2018; Wang *et al.*, 2019b)

$$P^k = \frac{1}{N} \frac{1}{\sum_i (e_i^k \, e_i^k)^2} \, . \tag{2.59}$$

P^k quantifies how uniformly the particles participate in an eigenmode. For an extended mode holds $P^k = \mathcal{O}(1)$ while $P^k = \mathcal{O}(1/N)$ is valid for localised modes.

Sufficiently below ω_*, the eigenmodes are close to plane waves. An example is depicted in the first row of Graphic 2.8. The participation ratio is approximately $P^k = 2/3$ (Wang *et al.*, 2019b). However, as discussed in Section 2.2, plain waves are not exact eigenvectors of the Hessian, even for very low frequencies. Sound modes are damped due to initial stresses and the disorder. One could say that the mode loses some of its energy to the disorder by exciting other modes. Szamel and Flenner have argued that the attenuation is mainly caused by non-affine displacements (Szamel and Flenner, 2022). Again, this fits into the picture provided in Section 2.2. There, we discussed that initial stresses enhance the coupling the longitudinal and the transverse components degrees of freedom, which can also be seen in the first row of Graphic

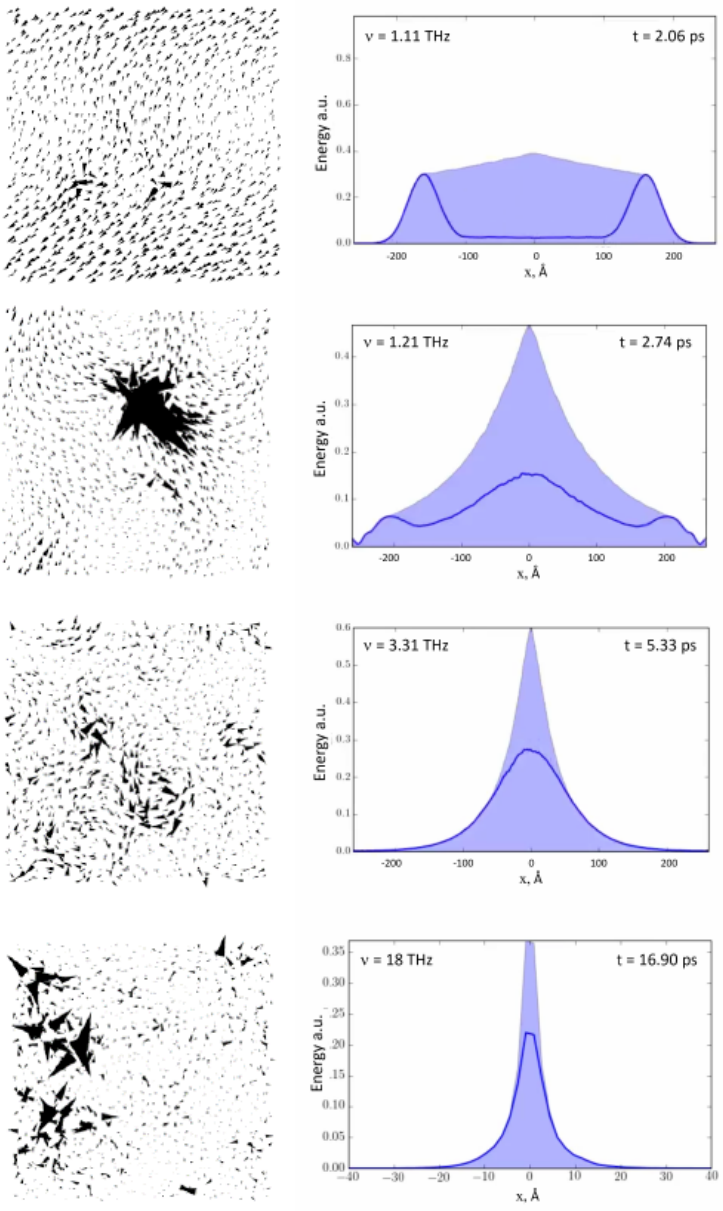

Figure 2.8: Left column: Illustration of the eigenmodes in a numerical model. The arrows display the instantaneous displacement of the particle due to the mode specified in the right panel. Right column: Wave-packed propagation envelope for different excitation frequencies. The blue curve is the energy distribution at the given time. The blue-colored region displays the kinetic energy distribution from previous times. From top to bottom: Plane-wave-like excitations, Floppy mode, Diffuson, Locon. Floppy modes were discussed in Section 2.3.2. Reprinted from *Vibrations and Heat Transfer in Glasses: The Role Played by Disorder*, by Anne Tanguy, Comptes Rendus. Physique, vol. 24, 73-97, open-source. Reprinted with permission. Doi:10.5802/crphys.162

2.8. It has been observed both in simulations and experiments that the sound damping is Rayleigh-like $\Gamma_q^{\parallel/\perp} \propto q^{d+1}$ (Mizuno and Ikeda, 2018; Monaco and Giordano, 2009; Monaco and Mossa, 2009; Wang *et al.*, 2019a). Here $\Gamma_q^{\parallel/\perp}$ is the sound attenuation coefficient. Actually, it had been a long debate in the scientific community until it became a consensus that the damping in the hydrodynamic limit (neglecting thermal effects) results from Rayleigh scattering and consequentially has a q^{d+1} dependence on the mode's wavenumber, where d is the spatial dimension (Benassi *et al.*, 1996; Ciliberti *et al.*, 2003; Ganter and Schirmacher, 2010; Mizuno and Ikeda, 2018; Monaco *et al.*, 1998). This is reasonable from a physicist's point of view, as the scattering of sound modes in topological disorder is analogous to the inelastic scattering of phonons at inhomogeneities in a crystal or to the scattering of electromagnetic waves from particles in the air [8] (Gross and Marx, 2014, Chapter 5). Rayleigh scattering is why the cloudless sky appears to be blue and why the sunset includes warmer colors. Together with the speed of sound, it is possible to define a mean free path

$$l_{MFP}^{\parallel/\perp} \equiv 2\pi \frac{v^{\parallel/\perp}}{\Gamma_q^{\parallel/\perp}} \ , \tag{2.60}$$

which quantifies the average path length a wave travels before scattering inelastically with the disorder. When the mean free-path length becomes equal to the wavelength $\lambda = \frac{2\pi}{q}$, the concept of a plane-wave excitation breaks down. If the mean free-path length is too short, the coherence of a wavefront is destroyed so quickly that the notion of wavenumber q or wavelength $\lambda = \frac{2\pi}{q}$ loses its meaning. Hence, the so-called Ioffe-Regel limit $\frac{l_{MFP}^{\parallel/\perp}}{\lambda_{IR}} = \frac{\Gamma(\Omega_{IR})^{\parallel/\perp}}{\Omega_{IR}^{\parallel/\perp}} = 1$ marks a crossover[9] in the nature of the modes. Here, we introduced the propagating frequency $\Omega^{\parallel/\perp} \equiv (qv)^{\parallel/\perp}$ to keep the notations concise. While plane-wave like excitation dominate for lower frequencies than $\omega_{IR}^{\parallel/\perp} = \Omega_{IR}^{\parallel/\perp}$, no propagating sound modes are observed above ω_{IR} in random matrix models for disordered system (Beltukov *et al.*, 2013). Ikeda *et al.* found that the Ioffe-Regel frequency ω_{IR}, the frequency of the Boson peak ω_{BP} and the characteristic frequency ω_*, specify-

[8] It has been argued that long-range correlations between the local elastic moduli can lead to logarithmic corrections in the sound attenuation coefficient $\Gamma_q^{\parallel/\perp} \propto q^{d+1}\log(q)$ (Caroli and Lemaître, 2019; Gelin *et al.*, 2016). However, this is debated as some simulation studies like (Mizuno and Ikeda, 2018; Wang *et al.*, 2019a,b) do not pick up this enhancement. This debate is just mentioned for the sake of completeness. In this work, we neglect such long-range correlation.

[9] Originally, the Ioffe-Regel criterion was proposed in the context of semiconductors (Ioffe and Regel, 1960). Notably, the vibrational modes in disordered solids are not localized but rather of diffusive nature (Allen *et al.*, 1999).

ing the onset of the plateau in the DOS, are related and close to each other in harmonic soft-sphere systems (Mizuno and Ikeda, 2018). It was found that the Boson peak frequency corresponds to the transverse Ioffe-Regel limit in hard-sphere systems (Shintani and Tanaka, 2008). This suggests that the ability to resolve the local disorder and, consequentially, the disorder itself is behind some of the universal vibrational properties of amorphous solids. Let us look at a concrete example to convince ourselves that our discussions in Section 2.3.2 2.3.3 provide a coherent picture of the vibrational modes in amorphous systems: We look at the soft spheres in three dimension with the interaction potential given in Equation (2.44). We look at harmonic interactions with $\alpha = 2$. In Section 2.3.2, we arrived at the scaling for the elastic moduli $B \propto (\Delta\phi)^{\alpha-2}$, $G \propto (\Delta\phi)^{\alpha-1.5}$ and $\omega_* \propto \Delta z \propto \sqrt{\Delta\phi}$. The scaling of the Ioffe-Regel limit with ω_* suggests for $\alpha = 2$:

$$B \propto \omega_*^0;, \qquad G \propto \omega_* \,, \qquad \Gamma_q^\perp \propto \frac{q^4}{\omega_*} \,. \tag{2.61}$$

Notably, the longitudinal modulus jumps at the instability. These predictions were confirmed in simulations (Mizuno and Ikeda, 2018).

After discussing the low-frequency regime, we now look at modes with intermediated frequencies $\omega > \omega_{IR}$. The change in the nature of the modes at the Ioffe-Regel limit ω_{IR} is well documented. For example, a change in the attenuation is observed in experiments and simulations (Mizuno and Ikeda, 2018; Monaco and Giordano, 2009; Monaco and Mossa, 2009; Taraskin and Elliott, 2000; Wang *et al.*, 2019a). The damping's dependence on the mode index crosses over from $\propto q^{d+1}$ to q^2. Additionally, this change is discussed in theoretical works as well (Marruzzo *et al.*, 2013b; Schirmacher *et al.*, 2007). As mentioned in the last paragraph, the concept of a propagating wave no longer applies for $\omega > \omega_{IR}$. Hence, q is no longer the wavenumber. Instead, q quantifies the spatial exponential decay of a mode: Preparing again an initially well-localized wave package, one observes that the center of this peak hardly moves (Allen *et al.*, 1999; Tanguy, 2023). This is illustrated in the third row of Figure 2.8. No group velocity can be ascribed. However, the radius of the peak grows linearly with time $\langle r^2 \rangle \approx 6Dt$, where D is the diffusion coefficient. Hence, the normal modes in this frequency interval have a diffusive character. No polarisation can be assigned to the modes either since any coherence is lost due to the strong scattering (Allen *et al.*, 1999). The susceptibility

to an external perturbation $\chi_q(t)$ varies according to

$$\chi_q(t) = \frac{1}{D}\left(1 - e^{-q^2 D t}\right) . \tag{2.62}$$

An example of the spatial structure of such a mode is provided in the left picture in the second row of Graphic 2.8. Even though the diffusive modes are still extended, the participation ratio $P^k \approx 0.3$ (Beltukov and Parshin, 2011) is well below the participation ratio of propagating waves. Allen, Feldman *et al.* (Allen *et al.*, 1999) reported that only a few percent of the vibrational modes in an amorphous solid can usually be regarded as propagating waves while the vast majority, more than 90%, have this diffusive character.

The nature of the normal modes changes again at the upper end of the spectrum. Here, the participation ratio quickly drops and becomes of order $P^k \approx \mathcal{O}(1/N)$. The modes get localized. The associated eigenvectors $\boldsymbol{e}_k$ of the hessian decay exponentially with the distance from their center $\boldsymbol{r}_0$

$$|\boldsymbol{e}_k(\boldsymbol{R}_n)| \propto e^{-\frac{|\boldsymbol{r}_n - \boldsymbol{r}_0|}{\xi_k}} . \tag{2.63}$$

Here, ξ_k is the localization length. Localized modes do not contribute to any transport due to this rapid decay (Tanguy, 2023). Additionally, they usually appear in especially dense regions of the solid and hardly interact with each other. Consequently, the eigenvalues of localized modes can lie arbitrarily close together and are generally independent. This is different for the propagating and diffusive modes due to their extended character. Here, level repulsion is observed, causing characteristic differences in the average distance between the eigenvalues[10] (Baumgärtel *et al.*, 2024; Schirmacher *et al.*, 1998; van Hecke, 2009). According to Allen, Feldman *et al.* only a few percent ($\approx 4\%$) of the vibrational mode are localized (Allen *et al.*, 1999). A snapshot of a localized mode is shown in the last row of Figure 2.8. As visible in the left picture, the spatial extent of the modes is much smaller than for the diffusive modes in the second row of Figure 2.8. Furthermore, the energy dis-

[10] A way of quantifying the underlying statistics is to look at the distribution of the level spacing: Let $r = (\omega_{k+1})^2 - (\omega_k)^2$ be the distance between two eigenvalues of the Hessian $\underline{\boldsymbol{\mathcal{H}}}$. One finds in the case of the independent localized modes that the distribution of the normalized distance $P\left(\frac{r}{\langle r \rangle}\right)$ follows a Poisson distribution. At the same time, the level spacing statistics of the Gaussian orthogonal random matrix ensemble are obtained for the diffusive modes (Baumgärtel *et al.*, 2024; Beltukov and Parshin, 2011; Mehta, 2014; Schirmacher *et al.*, 1998).

tribution displayed in the right picture is also quite narrow and hardly evolves with time.

Allen and Feldmann coined the terms *Propagons, Diffusons and Locons* for the vibrational modes discussed in the last three paragraphs[11] (Allen *et al.*, 1999). The authors claimed that this rather simple model for the vibrational modes can explain some of the anomalous thermal properties of amorphous solids, which are quite different from those of crystals. We will review them in the next section and discuss how the nature of the vibrational modes can partly explain the observation.

2.4 Thermal properties of amorphous solids

The low-temperature properties of glasses differ characteristically from those of crystals Zeller and Pohl prominently reported qualitative differences in the specific heat capacity $C_V(T)$ and the heat conductivity $\kappa(T)$ already back in 1971 (Zeller and Pohl, 1971). These differences are universal as they even appear between amorphous and ordered systems of the same chemical substance (Zeller and Pohl, 1971). Furthermore, there are only minor quantitative differences between glasses of different substrates. The vibrational modes are the only potential heat carriers because there is no heat transport due to convection or radiation at zero temperature. Additionally, the specific heat C_V results from the ability of exciting modes. Hence, the transport properties trace back to the vibrational properties. Moreover, Allen and Feldman and later Schirmacher argued that the heat transport properties can mainly be explained within a harmonic theory (Allen and Feldman, 1993; Allen *et al.*, 1999; Schirmacher, 2006). Again, this is

[11] The simple picture of vibrational modes in disordered solids, whose properties mainly depend on their frequency is complemented by the concept of quasi-localised modes (Kumar *et al.*, 2021; Lerner and Bouchbinder, 2021; Schober, 2011; Wang *et al.*, 2019a). That is the established name for a second kind of low-frequency excitation. Their displacement field resembles the well-known Eshellby-pattern, and the amplitude of the mode decays algebraically $\propto |\boldsymbol{r} - \boldsymbol{r}_0|^{d-1}$ (Eshelby and Peierls, 1957; Lerner and Bouchbinder, 2023). This clearly distinguishes them from the localized modes discussed in this section. Additionally, they interact and hybridize with the propagating mode, enhancing the sound attenuation (Schober, 2011; Wang *et al.*, 2019a). Lastly, their Density of States supposedly follows a ω^4 dependency independent of the spatial dimension (Lerner and Bouchbinder, 2021; Richard *et al.*, 2020). However, this has recently been questioned in (Schirmacher *et al.*, 2024). Quasi-localized modes and their importance for the properties of disordered solids have gained much interest, and much work has been assigned to understanding their properties. For example, their influence on the sound attenuation coefficient and on the thermal properties are topics of ongoing research (Xiang *et al.*, 2023). Besides the amount of work and their currently investigated importance, quasi-localized modes will not play a major role in this monograph.

different to crystals, where anharmonic umklapp-processes have to be included to explain the decrease of the heat capacity C_V with the temperature for high T (Gross and Marx, 2014, Chapter 6.2). In crystals, the Debye theory predicts $C_V \propto T^3$ for the low-temperature limit $T \to 0$ if the (Gross and Marx, 2014, Eq. 6.151) in three dimensional solids (Gross and Marx, 2014, Chapter 6) . Conversely, a maximum appears in C_V/T^3 around $10K$ in amorphous solids. This maximum was related to the Boson peak in the reduced Density of States $\frac{D(\omega)}{D_D(\omega)}$ (Wuttke *et al.*, 1995). Generally, the specific heat C_V and Density of States $D(\omega)$ are closely related. This follows from the definition of C_V via the thermal energy $C_V = \frac{\partial U(T)}{\partial T}$ with (Gross and Marx, 2014, Chapter 6)

$$U(T) \propto \int d\omega \frac{D(\omega)\omega}{e^{\frac{\hbar\omega}{k_B T}} - 1} \,. \quad (2.64)$$

Here, $n(T,\omega) = \left(e^{\frac{\hbar\omega}{k_B T}} - 1\right)^{-1}$ denotes the Bose-Einstein statistic and $\hbar$ represents the Planck-constant. Since they have the same origin, the peak in C_V is also called the Boson peak. Figure 2.9 shows the thermal conductivity for different materials depending on the temperature. We notice the formation of a plateau in the temperature regime of the Boson peak. Allen and Feldman, and later Schirmacher, have explained this saturation with the vibrational modes entering a strong scattering regime (Allen *et al.*, 1999; Schirmacher, 2006). This conjecture emphasizes the relation of ω_{BP} with the Ioffe-Regel limit. This fits nicely with the narrative of the transition from plane-wave-like modes to Diffusons. Indeed, Schirmacher derived

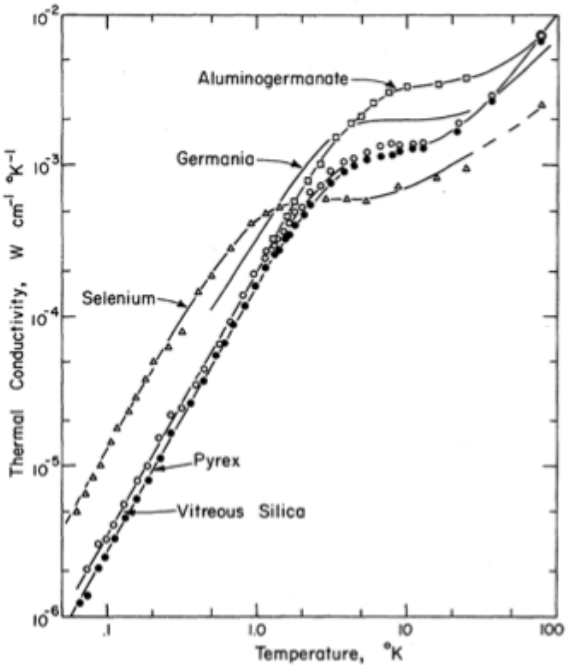

Figure 2.9: Thermal conductivity of different amorphous solids over the temperature. All materials show the same universal qualitative aspects. Reprinted from *Thermal Conductivity and Specific Heat of Noncrystalline Solids*, by R. Zeller, & R.Pohl, 1971, Phys. Rev. B., vol. 4, pages 2029–2041. Copyright [2025] by the American Physical Society. Doi:10.1103/PhysRevB.4.2029

a concise equation for the heat conductivity starting from a general Green-Kubo relation (Schirmacher, 2006):

$$\kappa(T) \propto \int d\omega D_i(\omega)\omega \frac{\partial}{\partial T} \frac{1}{e^{\frac{\hbar\omega}{k_B T}} - 1} \,. \tag{2.65}$$

Allen and Feldman derived a similar but less instructive equation (Allen and Feldman, 1993). $D_i(\omega)$ is a mode's characteristic (energy) diffusivity. Generally, $D_i(\omega) = 0$ holds for localized modes as these modes do not contribute to the heat transport. In $d = 3$, Schirmacher derived for the Propagons and the Diffusons $d = 3$ (Schirmacher, 2006):

$$D_i(\omega) \propto \frac{l_{MFP}\omega^2}{D(\omega)} \,. \tag{2.66}$$

A constant diffusivity $D_i(\omega)$ above the Ioffe-Regel limit explains the increase of the heat conductivity and the plateau both qualitatively and quantitatively (Allen and Feldman, 1993; Schirmacher, 2006). However, this concept can not explain the anomalous small temperature scaling of the heat conductivity $\kappa(T \to 0) \propto T^2$. Rayleigh damping and consequentially $l_{MFP} \propto \frac{1}{\omega^4}$ would lead to a stronger temperature dependency. Similarly, the close to linear temperature dependence of the specific heat $C_V(T)$ can not be rationalized with the vibrational modes characterized in section 2.3.3. Allen, Feldmann *et al.* argued that $D_i(\omega) \propto \frac{1}{\omega^2}$ leads to good agreement with the experiments (Allen *et al.*, 1999). Hence, one needs stronger scattering to explain this behavior. Usually, one invokes the concept of bistable structural arrangements. The tunneling between the two positions can explain the low-temperature anomalies (Anderson *et al.*, 1972; Yu and Carruzzo, 2022). However, this topic is beyond the scope of this monograph, which only discusses a classical theory of athermal stability. Quantum effects like tunneling-two-level-states are neglected. We finish this chapter by giving a more detailed statement about the goal and scope of the thesis.

2.5 The aim of this monograph

As we have seen in this introductory chapter, simulations, experiments, and analytical investigations have provided deep insight into the physics of low-temperature amorphous solids. From the theory side, the works by Matthieu Wyart and co-workers and

Walter Schirmacher and co-workers stand out (DeGiuli *et al.*, 2014; Marruzzo *et al.*, 2013a,b; Schirmacher *et al.*, 1998, 2024; Schirmacher and Ruocco, 2022; Schirmacher *et al.*, 2007; Wyart, 2005, 2010; Wyart *et al.*, 2005; Yan *et al.*, 2016). However, a first-principles theory that can be systematically generalized to finite temperatures has not yet been proposed. Many works by Matthieu Wyart and co-authors are based on a network analysis at $T = 0$, where the potential has only finite support. A limitation of their work is that it is unclear how to systematically generalize the theory to include long-range interactions (Xu *et al.*, 2007). Also, network models cannot consider kinetic effects due to finite temperature. On the other hand, the *Heterogeneous Elasticity Theory* of Schirmacher and co-authors is a mesoscopic and not a microscopic theory (Schirmacher and Ruocco, 2022). Additionally, the Heterogeneous Elasticity Theory predicts negative eigenvalues of the Hessian $\underline{\boldsymbol{\mathcal{H}}}$ below the jamming instability, which implies that the theory can not be generalized to the unjammed glass state. The same applies for the effective medium theory by Wyart and DeGiuli (DeGiuli *et al.*, 2014). In this sense, a general first-principles theory of stability, which correctly captures the athermal $T = 0$ case and which can be generalized to finite temperatures to potentially even analyze the unjammed-glass state and glass transition, is still lacking.

This monograph presents the first steps towards a theory explaining the phase diagram in Figure 1.1. Since a displacement field $\boldsymbol{u}(\boldsymbol{r})$ can only be defined with respect to a reference point, $\boldsymbol{u}$ is not a good quantity for the unstable state. Thus, we will look at the autocorrelation function $\underline{\mathbf{K}}(\boldsymbol{q}, t)$ of the velocity field $\boldsymbol{v}(\boldsymbol{q}, t) = \partial_t \boldsymbol{u}(\boldsymbol{q}, t)$. As we will discuss in Section 5, $\underline{\mathbf{K}}(\boldsymbol{q}, t)$ is a good quantity for determining the value of the elastic constants since the behavior of $\underline{\mathbf{K}}(\boldsymbol{q}, t)$ depends qualitatively on the (non-)decay of restoring forces. Since the correlation function can be defined for arbitrary interactions and arbitrary temperatures, a theory of $\underline{\mathbf{K}}(\boldsymbol{q}, t)$ has good changes to become a general theory of stability in amorphous solids.

However, this thesis only aims to take the first steps towards this general goal. First of all, we restrict ourselves to the transverse velocity field $\boldsymbol{v}^{\perp}(\boldsymbol{q}, t)$. This is not a good approximation, as we saw multiple times in this chapter. Nevertheless, it greatly simplifies the theory as it allows the neglect of structural rearrangements. We rely on the Mode-Coupling theory (MCT) to express the velocity autocorrelation function $\underline{\mathbf{K}}(\boldsymbol{q}, t)$ in terms of a generalized viscosity $\underline{\mathbf{G}}(\boldsymbol{q}, t)$ appearing as a memory kernel in the

associated generalized Langevin equation. We will self-consistently express $\underline{\mathbf{G}}(\boldsymbol{q}, t)$ in terms of $\underline{\mathbf{K}}(\boldsymbol{q}, t)$, leading to a closed set of equations. Here, it will be crucial to include the correct topology of the microscopic inelastic scattering events of a mode with the disorder. Only the inclusion of non-mean-field or non-planar terms reproduces the physics discussed in this chapter. Neglecting correlated local events causes an erroneous prediction of the sound attenuation in the stable phase. The presentation of this novel approximation scheme is the main task of Chapter 5 and the primary goal of this thesis. The derivation of a generalized theory incorporating longitudinal fields and finite temperature will be a systematic task. This is left for future work.

To test the Self-Consistent Current theory for $\underline{\mathbf{K}}(\boldsymbol{q}, t)$, we interpret the Hessian $\underline{\boldsymbol{\mathcal{H}}}$ as a random matrix and we extend the known theory on the Euclidean Random Matrix model, which has become an established model for disordered solids (Amir *et al.*, 2008; Ciliberti *et al.*, 2003; Goetschy and Skipetrov, 2013; Mézard *et al.*, 1999). Here, we compare our predictions to numerical results obtained by Philipp Baumgärtel. Before we derive and discuss the theory for the current in Chapter 5, we first introduce the analytical tools in Chapter 3. Secondly, we motivate and discuss the Euclidean Random Matrix model in Chapter 4.

3 | Stochastic description

This monograph aims to develop a theory for amorphous solids, which captures all the salient features discussed in Chapter 2. While we restrict ourselves to athermal systems, we strive for a model that can straightforwardly be generalized to incorporate the effects of finite temperatures. Generally, we look at a d-dimensional box with volume V containing N identical spherical particles with positions $\{\boldsymbol{r}\}_i^N$ and mass m. We consider the thermodynamic limit $N, V \to \infty$ such that the density $n = N/V$ stays constant. On the one hand, in the unjammed phase, the particles can explore the whole volume V as they can move freely on reasonable time scales. Conversely, in the jammed state, here the particles can only move around their reference positions $\{\boldsymbol{R}\}_{i=1}^N$. As the interaction potential generally depends on the coordinates of all N particles, we have dN partial and coupled differential equations, determining the trajectories of the particles. Such a large number of equations can not be solved even numerically for $N \to \infty$. Thus, we have to rely on a statistical description of the system and ask for its averaged properties. This chapter introduces the relevant notions of averages, correlations, and related concepts used in this work.

Nevertheless, the emergence of a reference frame in the solidified phase urges us to discuss a subtle detail. Let us assume that the particles possess a vanishing amount of kinetic energy. Then, in the unjammed phase, the particle positions' evolution is governed by the principle of *free energy minimization*. One could say: *all random variables (the positions $\boldsymbol{r}_i$) evolve with time*. However, the positions $\boldsymbol{R}_i$ in the reference frame are also random variables since we deal with a topological disordered system. Importantly, they neither evolve with time nor are they in accordance with a minimization principle. The system falls out of equilibrium at the jamming transition. We say that the disorder is *quenched* in the jammed state and *annealed* in the unjammed state. Consequently, we have to introduce different averages in this chapter. First, we discuss the *annealed* average in Section 3.1. To simplify the problem, we assume that the system is in thermal equilibrium and that the particles' equations of motion are Langevin equations where

the strength of the noise is proportional to the temperature T. Thus, the *annealed* average becomes the *thermal* average. In principle, we assume thermal equilibrium in the remaining part of this work, and as we discuss the athermal limit, we take $T \to 0$ at the end of our calculations. In Section 3.2, we introduce the Zwanzig-Mori projection operator formalism as our primary tool in Chapter 5 to investigate the equilibrium correlation functions. However, we will also apply the projection operator formalism to quenched disorder in Appendix A. Lastly, in Section 3.3, we discuss quenched disorder and the concept of *self-averaging*.

3.1 Annealed disorder and thermal averages

In this section, we primarily discuss the stochastic description of a many-body system subject to Langevin dynamics. The interparticle forces derive from pair potentials $E_{\mathrm{Pot}}(\{\boldsymbol{r}\}_i^N) = \sum_{i,j>i} U(|\boldsymbol{r}_i - \boldsymbol{r}_j|)$ and the equations of motion read (Vogel *et al.*, 2025)

$$\frac{d}{dt}\boldsymbol{p}_i(t) = -\nabla_{\boldsymbol{r}_i} E_{\mathrm{Pot}}(\{\boldsymbol{r}\}_i^N) - \zeta_0 \boldsymbol{v}_i(t) + \sqrt{2\zeta_0 k_B T}\, \boldsymbol{\mu}_i(t)\ . \tag{3.1}$$

Here, $\boldsymbol{p}_i$ is the momentum of the ith particle and ζ_0 is the Langevin friction coefficient, while $\boldsymbol{\mu}_i(t)$ denotes uncorrelated Gaussian white noise with zero mean $\langle \boldsymbol{\mu}_i(t) \rangle_\mu = 0$ and unit variance $\langle \boldsymbol{\mu}_i(t)\boldsymbol{\mu}_j(t') \rangle_\mu = \underline{\mathbf{1}}\delta_{ij}\delta(t-t')$. Here, i, j are particle indices and the index μ of the pointy brackets indicates that the average is taken over the noise realization. For example, the noise can result from the N-particles of interest being emerged in a bath constituted by much smaller particles. Due to their small size, the bath particles equilibrate very fast, and their influence on the dynamics of the larger particles can hence be treated as noise (Hansen and McDonald, 2009, Chapter 7). Aiming for a stochastic description of the system, we need the N–particle distribution function $\Psi(\Gamma, t) = \Psi(\{\boldsymbol{r}_i\}_{i=1}^N, \{\boldsymbol{p}_i\}_{i=1}^N, t)$. It specifies the likelihood of the system to be in a specific region in the $2dN$-dimensional microscopic phase space $\Gamma = (\{\boldsymbol{r}_i\}_{i=1}^N, \{\boldsymbol{p}_i\}_{i=1}^N, t)$. First, we discuss the time evolution of $\Psi(\Gamma, t)$, which is governed by the Klein-Kramers equation. Then, we discuss how this can be used to describe the system via functions of the phase space $A(\Gamma, t) = A(\{\boldsymbol{r}_i\}_{i=1}^N, \{\boldsymbol{p}_i\}_{i=1}^N, t)$. This leads us to the concepts of *thermal* averages and correlation functions. Lastly, we discuss the consequences of the assumed symmetry relations of the probability distribution function.

The Klein-Kramers Equation: Due to the noise term, the Langevin equation is a stochastic differential equation. Ultimately, the N particles perform random walks in a potential. However, some of the resulting trajectories are more likely than others. Based on the weights of each trajectory, one can derive a partial differential equation for the probability distribution:

$$\partial_t \Psi(\Gamma) = \Omega(\Gamma)\Psi(\Gamma)\,. \tag{3.2}$$

This is the so-called Fokker-Planck equation for underdamped Brownian motion, or alternatively, also known as the Klein-Kramers equation. Details are provided in (Kamenev, 2011, Chapter 4) and (van Kampen, 1992, Chapter 8). The Klein-Kramers Operator reads (Risken, 1996, Chapter 10)

$$\Omega(\Gamma) = \sum_i \left(\frac{\partial H}{\partial \boldsymbol{r}_i} \cdot \frac{\partial}{\partial \boldsymbol{p}_i} - \frac{\partial H}{\partial \boldsymbol{p}_i} \cdot \frac{\partial}{\partial \boldsymbol{r}_i} \right) + \zeta_0 \sum_i \frac{\partial}{\partial \boldsymbol{p}_i} \cdot \left(k_B T \frac{\partial}{\partial \boldsymbol{p}_i} + \frac{\partial H}{\partial \boldsymbol{p}_i} \right) \,. \tag{3.3}$$

Here, $H(\Gamma) = \sum_{i=1}^{N} \frac{\boldsymbol{p}_i^2}{2m} + \sum_{i,j>i} U(|\boldsymbol{r}_i - \boldsymbol{r}_j|)$ is the Hamilton function. Notably, equation (3.3) only depends on the phase space variables. Here, we have ignored hydrodynamic interactions via the solvent. If hydrodynamic interactions are considered, the friction coefficient becomes a matrix $\zeta_0 \to \zeta_{ij}$ (Hess and Klein., 1983, Chapter 2 & 3). Additionally, we assumed that the friction coefficient ζ_0 does not depend on the atomic positions $\{\boldsymbol{r}_i\}_{i=1}^N$. Ultimately Ω is a generalised Liouville's operator, as it includes dissipation and random forces. Thermal energy $k_B T$ sets the noise scale. The only stationary, normalized solution of the Klein-Kramers equation is the well-known Boltzmann distribution:

$$\Psi_{\mathrm{eq}} \propto e^{-\beta H} \,. \tag{3.4}$$

This is an equilibrium distribution, as detailed balance holds (Risken, 1996, Chapter 6). Having specified the time evolution of the probability density, we can ask how functions of the phase space variables evolve with time.

Dynamic variables and correlation functions: Since there are too many microscopic degrees of freedom, we are interested in evaluating characterizing functions of the phase space Γ, which can be used to describe the state of the system. Quite

often, a small set of variables suffices. For example, the ideal gas in equilibrium can be characterized by relying solely on temperature T, global pressure p, and density n. In other settings, frequently used state variables are the (free-)energy and the entropy. Each variable defines a hyperplane in the phase space. This drastically reduces the problem's dimension. Hereinafter, we assume that all those characteristic functions are continuous, arbitrarily often differentiable, and vanish for $|\boldsymbol{p}_i|, |\boldsymbol{r}_i| \to \infty$ at least if they are weighted with the Boltzmann distribution. The set of dynamical variables constitutes a vector space $\mathcal{W}$ (Götze, 2009, Chapter2). We start our consideration by discussing the functions of the phase space in general. We first introduce their averages and the notion of correlation functions before we again turn to the question of what the *relevant variables* Section 3.2 in the context of the Zwanzig-Mori formalism. The remainder of this section follows (Götze, 2009, Chapter 2).

The time evolution of a function $A(\Gamma)$ generally fluctuates due to the underlying stochastic process. Thus, we are interested in its ensemble average. It is given by integrating over all possible states weighted with the probability distribution $\Psi(\Gamma, t)$:

$$\langle A(t) \rangle = \int d\Gamma A(\Gamma) \Psi(\Gamma, t) \ . \tag{3.5}$$

The probability distribution $\Psi(\Gamma, t)$ is the solution of the Fokker-Planck Equation (3.2) with the initial condition $\Psi_0(\Gamma)$. The formal solution can be written as

$$\Psi(\Gamma, t) = e^{\Omega t} \Psi_0(\Gamma) \ , \tag{3.6}$$

where the operator-exponential is defined via its Taylor series. Successive partial integrations lead to

$$\langle A(t) \rangle = \int d\Gamma \Psi_0(\Gamma) e^{\Omega^\dagger t} A(\Gamma) \ . \tag{3.7}$$

Here, we introduced the adjoined Klein-Kramers Operator:

$$\Omega^\dagger(\Gamma) = -\sum_i \left(\frac{\boldsymbol{p}_i}{m} \frac{\partial}{\partial \boldsymbol{r}_i} + \boldsymbol{F}_i \frac{\partial}{\partial \boldsymbol{p}_i} \right) + \zeta_0 \sum_i \left(k_B T \frac{\partial}{\partial \boldsymbol{p}_i} - \frac{\boldsymbol{p}_i}{m} \right) \frac{\partial}{\partial \boldsymbol{p}_i} \tag{3.8}$$

While Ω determines the evolution of the probability density $\Psi(\Gamma, t)$, the adjoint operator $\Omega^\dagger$ specifies how a subvolume of the phase space $d\Gamma(t)$ evolves with time.

Thus, $\Omega^\dagger$ can also be regarded as the time-differential operator for functions $A(\Gamma)$ of the phase space: $\partial_t A(\Gamma) = \Omega^\dagger A(\Gamma)$. In the following, we are not interested in transient regimes or initial dynamics. Thus, we assume the initial condition is given by the equilibrium distribution[1] $\Psi_0 = \Psi_{eq} \propto \exp[-\beta H]$. Because of this, we restrict ourselves to equilibrium where averages are time independent: $\partial_t \langle A(t) \rangle_{\mathrm{eq}} = 0$.

However, we are still interested in the dynamic properties of the systems, which are in quiescent systems given by their response properties to external stimuli. Therefore, we define the correlation function of two dynamic variables A, B for $t_2 > t_1$:

$$\langle A(t_2)B(t_1)\rangle = \int d\Gamma_2 d\Gamma_1 A(\Gamma_1)B(\Gamma_2)^* \Psi_2(\Gamma_2, t_2; \Gamma_1, t_1) \tag{3.9}$$

The asterisk denotes complex conjugation[2] and $\Psi_2(\Gamma_2, t_2; \Gamma_1, t_1)$ is the joint probability distribution. It specifies the distribution of the pairs (Γ_2, t_2) and (Γ_1, t_1). For $t_2 > t_1$, $\Psi_2(\Gamma_2, t_2; \Gamma_1, t_1)$ can be expressed with the solution of the Fokker-Planck Equation and the conditional probability $p(\Gamma_2, t_2|\Gamma_1, t_1)$ (Hess and Klein., 1983, Chapter 2). The conditional probability specifies the likelihood that the system is at time t_2 in a small volume around the state Γ_2 provided it was at t_1 in a small volume around the state Γ_1. One has

$$\Psi_2(\Gamma_2, t_2; \Gamma_1, t_1) = p(\Gamma_2, t_2|\Gamma_1, t_1)\Psi(\Gamma_1, t_1) \; . \tag{3.10}$$

Again, we assume $\Psi(\Gamma_1, t_1) = \Psi_{\mathrm{eq}}(\Gamma_1)$. As we saw earlier, the phase space volume element evolves according to $d\Gamma_2 = e^{\Omega^\dagger (t_2 - t_1)} d\Gamma_1$. This leads to

$$\langle A(t_2)B(t_1)\rangle = \int d\Gamma \left(e^{\Omega^\dagger (t_2 - t_1)} A(\Gamma) \right) B^*(\Gamma) \Psi_{eq}(\Gamma) \; . \tag{3.11}$$

Note that this result implies that the correlation function only depends on the time difference $|t_2 - t_1|$. This is a direct consequence of the time-independent Hamiltonian and the

[1] According to the H-theorem, fully-connected or ergodic systems converge to a stationary distribution maximizing the entropy (Chapman, 1937) and (Pitaevskii and Lifshitz, 1981, Chapter 1). Since the dynamic is generated by the Klein-Kramer operator Ω, the stationary distribution is the equilibrium Boltzmann distribution.

[2] The complex conjugation ensures that the imaginary part of the Fourier-transformed correlation function is positive (Risken, 1996; Wilhelm *et al.*, 2024). In this sense, correlation functions have a positive spectrum.

assumed initial equilibrium distribution. Equation (3.11) expresses time-translational invariance. As a consequence, one has

$$\langle A(t+t_0)B(t_0)\rangle = \langle A(t)B(t=0)\rangle \equiv C_{AB}(t)\ . \tag{3.12}$$

Equation (3.11) defines a sesquilinear mapping $\langle\cdot\rangle : \mathcal{W}\times\mathcal{W}\to\mathbb{C}$, which is positive definite for equal time autocorrelation functions $\langle A(t)A(t)\rangle$. Thus, Equation (3.11) defines an inner-product, and the vector space of $\mathcal{W}$ becomes a Hilbert space. We call the elements of this vector space *dynamic variables*. Without further consideration, we assume that our observables of interest are such dynamic variables. Besides the local displacement field, defined and discussed in Section 2.2, our dynamical variables of main interest are the local density

$$\langle\rho(\boldsymbol{r})| = \langle\sum_{i=1}^{N}\delta(\boldsymbol{r}-\boldsymbol{r}_i)| \tag{3.13}$$

and the local current

$$\langle\boldsymbol{v}(\boldsymbol{r})| = \langle\sum_{i=1}^{N}\boldsymbol{v}_i\delta(\boldsymbol{r}-\boldsymbol{r}_i)|\ , \tag{3.14}$$

where $\boldsymbol{v}_i = \frac{\boldsymbol{p}_i}{m}$ denotes the velocity of the i^{th} particle. The two observables are connected via the continuity equation

$$\frac{d}{dt}\langle\rho(\boldsymbol{r},t)| = \nabla\cdot\langle\boldsymbol{v}(\boldsymbol{r})|\,. \tag{3.15}$$

In the following chapters, we will mainly discuss the special case of the correlation of a dynamic variable with itself. We call

$$C_A(t) \equiv C_{AA}(t) = \langle A(t)A(0)\rangle \tag{3.16}$$

an autocorrelation function. It can be shown, that $C_A(t)$ is bounded by its initial value (Götze, 2009, Chapter 2)

$$|C_A(t)| < |C_A(0)|\ . \tag{3.17}$$

Additionally, the spectrum, given by the temporal Fourier-transformation[3] spectrum, given by the temporal Fourier-transformation[4]

$$\tilde{C}_A(\omega) = \int_{-\infty}^{\infty} C_A(t) e^{i\omega t} dt \ , \tag{3.18}$$

is positive $\tilde{C}(\omega) \geq 0$ (Götze, 2009; Risken, 1996; Wilhelm *et al.*, 2024). Hereinafter, the (time-) Fourier transformation is indicated by a superscripted Tilde $\tilde{\cdot}$. A more detailed discussion of correlation functions, their properties, and dynamical variables in general is given in (Götze, 2009, Chapter 2).

In Chapter 5, we will use the framework of correlation functions to describe the athermal limit of the many-body state. The implicit assumption is that the system is perfectly annealed. The limit $T \to 0$ can be pictured as cooling the system so slowly that all the particle positions remain in equilibrium. Thus, the thermal average, *e.g.* in Equation (3.11), is basically an average over an *annealed* disorder. Strictly speaking, this procedure is only valid in the unjammed phase. In the jammed phase, the system can not relax due to geometric frustration, and the system falls out of equilibrium. Here, the disorder is not of *annealed* but of *quenched* nature. Nevertheless, we also extend the validity of the thermal average to the jammed phase. We will comment more on this in Section 3.3 and Section 5.1. Next, we discuss how correlation functions simplify due to global symmetry constraints.

Symmetry relations: By assumption, the pair-interaction potential $U(|\boldsymbol{r}_i - \boldsymbol{r}_j|)$ depends only on the scalar distance between two particles. Thus, the Hamiltonian

$$H(\Gamma) = \sum_{i=1}^{N} \frac{\boldsymbol{p}_i^2}{2m} + \sum_{i,j>i} U(|\boldsymbol{r}_i - \boldsymbol{r}_j|) \tag{3.19}$$

is invariant under

(I) A global spatial translation: $\boldsymbol{r}_i \to \boldsymbol{r}_i + \boldsymbol{y}$ for $i \in \{1, .., N\}$ and $y \in \mathbf{R}^d$.

[3]The Fourier Transformation is discussed in more details in Appendix F. Noticable, we defined the temporal Fourier transformation with an additional minus sign in the exponent. This ensures consistency with ()

[4]The Fourier Transformation is discussed in more details in Appendix F. Noticable, we defined the temporal Fourier transformation with an additional minus sign in the exponent. This ensures consistency with (Vogel *et al.*, 2025)

(II) A global rotation: $\boldsymbol{r}_i \to \underline{\boldsymbol{O}}\boldsymbol{r}_i\,,\ \boldsymbol{p}_i \to \underline{\boldsymbol{O}}\boldsymbol{p}_i$ for $i \in \{1,..,N\}$ and for any orthogonal matrix $\underline{\boldsymbol{O}}$ with determinat 1.

(III) Inversion of the phase space: $\Gamma \to -\Gamma$.

(IV) Time reversal, *i.e.* the inversion of all momenta: $\boldsymbol{p}_i \to -\boldsymbol{p}_i$ for $\forall i \in \{1,..,N\}$

Due to these invariants, the system is homogeneous, isotropic, and non-chiral. Additionally, it is invariant under time reversal. The correlation functions of field variables simplify because of the spatial symmetries. Here, we call a variable a field if it depends on a single point in spacetime $(\boldsymbol{r}, t)$. Consequentially, all Fouriertransformed components of a field variable depend on the same Fourier mode. The simplifications due to the symmetry constraints become more apparent in the reciprocal space. We thus consider the spatial Fourier transformation:

$$\mathrm{FT}[f(\boldsymbol{r})](\boldsymbol{q}) = \int_V d^d\boldsymbol{r} e^{-i\boldsymbol{q}\cdot\boldsymbol{r}} f(\boldsymbol{r}) \tag{3.20}$$

of a continuous, absolute integrable function $f(\boldsymbol{r})$. Hereinafter, a Fourier transformed dynamical variable is indicated by a Fourier mode: $\mathrm{FT}[A(\boldsymbol{r})](\boldsymbol{q}) \equiv A(\boldsymbol{q})$. The correlator

$$\langle A(\boldsymbol{q},t)B(-\boldsymbol{k})\rangle = \langle A(\boldsymbol{q},t)B(-\boldsymbol{q})\rangle\,\delta_{\boldsymbol{q},\boldsymbol{k}} \tag{3.21}$$

vanishes unless the two Fourier modes add up to zero. This is a direct consequence of the homogeneity of the system. Due to isotropy, the correlation of two scalar dynamical variables (*e.g.* the local density $\rho(\boldsymbol{q})$ defined in Equation (3.13)) depends only on the absolute value $q = |\boldsymbol{q}|$:

$$C_{AB}(q,t) = \langle A(\boldsymbol{q},t)B(-\boldsymbol{q})\rangle\ . \tag{3.22}$$

On the other hand, the correlation functions of two vector-valued dynamical variables (*e.g.* the local current $\boldsymbol{v}(\boldsymbol{q})$ defined in Equation (5.1)) can be split up into a component parallel $g^{\parallel}$ and perpendicular $g^{\perp}$ to the wavevector $\boldsymbol{q}$:

$$\langle \boldsymbol{A}(\boldsymbol{q},t)\boldsymbol{B}(-\boldsymbol{q})\rangle = g^{\parallel}(q,t)\hat{\boldsymbol{q}}\hat{\boldsymbol{q}} + g^{\perp}(q,t)(\underline{\mathbf{1}} - \hat{\boldsymbol{q}}\hat{\boldsymbol{q}})\ , \tag{3.23}$$

where the coefficients $g^{\parallel,\perp}(q,t)$ again depend only on the absolute value of the Fourier mode. Here, $\hat{\boldsymbol{q}} = \frac{\boldsymbol{q}}{q}$ is the normalised Fourier mode. Equation (3.23) is also a

consequence of the non-chirality. A derivation of these and other consequences of the spatial symmetries can be found in (Götze, 2009, Chapter 3 & Appendix C), which is the main source for this paragraph. The symmetry relations simplify the structure of the correlation functions drastically. That is why we will mainly work in the reciprocal space in this monograph. However, in Appendix B, we derive the theory in real space, which has the advantage of another symmetry constraint becoming apparent, which stays hidden in the Fourier space.

In addition to the translational and rotational symmetry, the time-reversal symmetry implies that the overlap between two dynamical variables $\langle AB \rangle$ vanishes unless they behave similarly under inversion of all the momenta. More concretely, we say a dynamical variable has even time-inversion parity if $A(\{\boldsymbol{p}_i\}_{i=1}^N, \{\boldsymbol{r}_i\}_{i=1}^N) = A(\{-\boldsymbol{p}_i\}_{i=1}^N, \{\boldsymbol{r}_i\}_{i=1}^N)$ holds. Similarly, a dynamical variable has odd time-inversion parity if $B(\{\boldsymbol{p}_i\}_{i=1}^N, \{\boldsymbol{r}_i\}_{i=1}^N) = -B(\{-\boldsymbol{p}_i\}_{i=1}^N, \{\boldsymbol{r}_i\}_{i=1}^N)$ is true. The overlap of two dynamical variables with different time-inversion parity is zero (Götze, 2009, Chapter 3). Lastly, we discuss how the system's dynamics can be described with a few distinguished variables. This is the core idea of the Zwanzig-Mori projection operator formalism.

3.2 The Zwanzig-Mori formalism

Quite often in statistical mechanics, one observes *concentration phenomena*. For example, the difference between the canonical and microcanonical ensemble becomes marginal for large particle numbers. The concrete microscopic dynamic is of secondary importance as a few state variables are often sufficient to describe the macroscopic properties of the system. The idea behind the Zwanzig-Mori formalism is to rely on this insight and to describe the dynamics with a small set of *relevant* variables. Utilizing the Hilbert space structure of the vector space of dynamical variables $\mathcal{W}$, we can project the observables of interest on the subspace spanned by those *relevant variables* to derive new exact equations of motion depending on fewer variables. This section provides a short introduction mainly following the textbooks (Zwanzig, 2001, Chapter 8), (Hansen and McDonald, 2009, Chapter 9) and (Götze, 2009, Chapter 2). However, statistical mechanics itself does not determine the set of *distinguished variables*, and additional arguments must be invoked to develop them. Ultimately, one must choose depending on the setting and the problem. We keep this section on a formal basis and

discuss our choice of distinguished variables in Section 5.1.

Let $\boldsymbol{A} = (A_1, ..., A_n)$ denote an arrangement of our set of distinguished and linearly independent dynamical variables. They span a subspace of the whole Hilbert space. The operator

$$P = \sum_{i,k=1}^{n} |A_i\rangle \left(\langle \boldsymbol{A}\boldsymbol{A}\rangle\right)^{-1}_{ik} \langle A_k| \tag{3.24}$$

projects onto this subspace. The required normalization is given by the inverse of the overlap matrix $(\langle \boldsymbol{A}\boldsymbol{A}\rangle)_{ik} = \langle A_i A_k\rangle$. The operator $Q = \underline{\mathbf{1}} - P$ conversely projects on the orthogonal complement containing all the *irrelevant variables.* The following operator identities hold: (Reichman and Charbonneau, 2005)

$$\Omega = P\Omega + Q\Omega \ , \tag{3.25a}$$

$$e^{\Omega t} = e^{Q\Omega t} + \int_0^t ds\ e^{(t-s)\Omega} P\Omega e^{Q\Omega s} \tag{3.25b}$$

Here, the second equality can be proven by simply differentiating. Using Equation (3.25b) one arrives at a formally exact equation of motion (Zwanzig, 2001, Equation 8.29)

$$\Omega^\dagger \boldsymbol{A}(t) = \underline{\boldsymbol{\Theta}} \cdot \boldsymbol{A}(t) + \int_0^t ds \underline{\boldsymbol{M}}(t-s)\boldsymbol{A}(s) + \boldsymbol{f}(t) \ . \tag{3.26}$$

This equation is a generalized Langevin equation with memory. Here, $\boldsymbol{f}(t) \equiv e^{Q\Omega t}\Omega^\dagger \boldsymbol{A}(t)$ is called the fluctuating force and serves as an effective noise. By construction, the relevant variables are constants during the evolution of the fluctuating forces, making them *fast* variables. On the other hand, the relevant variables are often called *slow.* In Equation (3.26), $\Theta_{ij} = \sum_k \langle \Omega^\dagger A_i A_k\rangle \left(\langle \boldsymbol{A}\boldsymbol{A}\rangle\right)^{-1}_{kj}$ is the frequency-matrix. It describes the coupling between the distinguished variables. The memory kernel $\underline{\boldsymbol{M}}(t) = \langle \boldsymbol{f}(t)\boldsymbol{f}(0)\rangle \cdot \left(\langle \boldsymbol{A}\boldsymbol{A}\rangle\right)^{-1}$ describes the coupling between fast and slow variables. The Zwanzig-Mori equation of motion (3.26) for slow variables is exact without any free-fitting parameters. However, the memory kernel depends on fast variables and is generally non-accessible. Thus, one has to rely on approximation schemes. Physical insight can motivate such approximations. For example, when investigating the slowing down of the dynamics close to the glass transition, a generalized Maxwell model is

a reasonable approximation (Maier *et al.*, 2018; Vogel and Fuchs, 2020; Vogel *et al.*, 2019). Alternatively, Mode-Coupling Theory (MCT) expresses the memory kernel through correlations between distinguished variables (Janssen, 2018). We will come back to the MCT approximation when we derive our self-consistent model.

In the following, we will mainly work not in the time but in the Laplace domain. Working in the Laplace domain circumvents– or delays at least– the challenge of dealing with integro-differential equations. For a sufficiently well-behaving function $g(t)$, the Laplace transform is defined as:

$$\mathrm{LT}[g(t)](s) = \int_0^\infty dt e^{-st} g(t) \equiv \hat{g}(s) \ , \quad \mathrm{Re}\{s\} > 0 \ , \tag{3.27}$$

where $\mathrm{Re}\{\cdot\}$ denotes the real part of a quantity. On the contrary, $\mathrm{Im}\{\cdot\}$ is the imaginary part. Hereinafter, a hat indicates the Laplace transform. Importantly, the Fourier transformation can be obtained from the Laplace transformation. One has for $\mathrm{Re}[s] \longrightarrow 0^+$:

$$\hat{g}(s) = \tilde{g}(\omega = is) \tag{3.28}$$

Appendix G comments further on the properties of the Laplace transformation and its mathematical requirements. A Laplace-transformed correlation function reads

$$\mathrm{LT}[C_{AB}(t)](s) \equiv \hat{C}_{AB}(s) = \langle A \hat{R}(s) B \rangle \ , \tag{3.29}$$

where $\hat{R}(s) = [s - \Omega]^{-1}$ is the resolvent of the Klein-Kramers Operator. As the derivation of the theory unfolds, $\hat{R}_Q(s) = [s - Q\Omega Q]^{-1}$ denotes the resolvent of the reduced dynamics describing the evolution projected on the Q-subspace. Note that $\langle A \hat{R}_Q(s) B \rangle$ again defines a correlation function with all the associated properties. The operator identity (3.25b) has its analogy in the Laplace domain. After some manipulations, one finds (Götze, 2009, Equation 2.59)

$$\Big[s - P\Omega P - P\Omega \hat{R}_Q(s) \Omega P \Big] P \hat{R}(s) P = P \ . \tag{3.30}$$

We will repeatedly exploit this relation when deriving the theory in Chapter 5. We will use the thermal average in the zero temperature limit $T \to 0$ for the annealed average throughout the derivation. However, we have already discussed that this is reasonable

in the unjammed but not in the jammed state. There, we deal with a quenched disorder, which we introduce in the next section.

3.3 Quenched disorder and self-averaging

The system can not relax in the jammed state due to geometric frustration. The reference frame positions $\boldsymbol{R}_i$ are random but fixed. Hence, we deal with *quenched disorder*[5] (Dotsenko, 2000; Mezard *et al.*, 1986, Chapter 1). The emergence of a reference frame generally breaks a system's translational and rotational invariance. However, these properties are restored after averaging over all possible realizations of the disorder. We call

$$\overline{\cdots} = \int \prod_{m=1}^{N} d^d \boldsymbol{R}_m (\cdots) \Psi_Q(\{\boldsymbol{R}\}_{i=1}^N) = \int d\Gamma' (\cdots) \Psi_Q(\Gamma') \ , \tag{3.31}$$

the disorder average. Here, we set $\Gamma' = \{\boldsymbol{R}\}_{i=1}^N$. Ψ_Q specifies the probability of a specific configuration. Each configuration or each sample is a specific realization of the randomness described by Ψ_Q. Again, we assume that Ψ_Q is invariant under global translation and rotation. Thus, the properties of the correlation function arising from symmetry constraints- as discussed in Section 3.1- still apply. Naturally, the question arises of whether all of these samples are expected to show distinct and unique behaviour or if the differences are just marginal. The discussion in Chapter 2 suggests that the properties of a jammed system do not depend on concrete preparation, provided that the system is sufficiently large. For example, the transition becomes unique in the thermodynamic limit, and even the divergence of the pair correlation function is universal for $N \to \infty$. Thus, we say our system is *self-averaging* as it suffices to consider a large sample instead of considering multiple smaller samples to determine the disorder average. To make the considerations more precise, let us denote the distribution of a dynamic variable A in the quenched disorder of the jammed state as $\psi(A)$. As A generally depends on the reference frame, one has

$$\psi(A) = \int d\Gamma' \Psi_Q(\Gamma') \delta(A - A(\Gamma')) \ . \tag{3.32}$$

[5]This section mainly follows the lecture notes in (Cugliandolo, 2022). However, the two cited books also provide a good introduction into the topic of quenched disorder and self-averaging.

With increasing system size, the self-averaging property implies that the distribution $\psi(A)$ becomes increasingly narrow and concentrates around a single value. This typical value A_{typ} is the only one which is observable for $N, V \to \infty$. The fluctuations from sample to sample become negligible.

The central assumption in Chapter 5 is that our system is indeed self-averaging in the jammed state and that the statistic of the fluctuations around the reference frame is sufficiently well described by the thermal average discussed in Section 3.1. As a consequence of these assumptions, we will not pay attention to the probability distribution $\Psi(\Gamma)$ and that the system actually falls out of equilibrium at the transition. We continue considering thermal averages. We discuss the reasoning behind this equilibrium approach to non-equilibrium further in Section 5.1. However, we first introduce the Euclidean Random Matrix model in the next Chapter. Here, we explicitly calculate the average over the quenched disorder.

4 | The Euclidean Random Matrix model

In Chapter 2, we have discussed some of the structural and vibrational aspects of disordered amorphous solids. We looked at the influence of the disorder and the initial stresses on the propagation of sound modes and how the nature of the mode highly depends on its energy, which quantifies its capability to resolve the local disorder. We have seen that numerical studies and general considerations of the scaling laws have greatly advanced our understanding of disordered systems and the jamming transition. However, a consistent and exhaustive first-principles theory is not available yet. In 1999, Mezard, Parisi and Zee introduced the Euclidean Random Matrices (ERM) model as a simple but instructive model for studying the properties of amorphous solids in detail (Mézard *et al.*, 1999). The idea is to start from the harmonic expansion of the energy in Equation (2.37) and to interpret the Hessian $\underline{\underline{\mathcal{H}}}$ as a random matrix since its entries depend on the principally unknown particle positions. Thus, one assumes that the particle positions are drawn from a probability distribution. As we consider only pair interactions, the Euclidean distance of the particles then determines the spring constants $\mathcal{K}_{ij}$ in Equation (2.14) and the bond tension $\mathcal{T}_{ij}$ defined in Equation (2.14) and Equation (2.13) respectively:

$$\mathcal{K}_{ij} = \mathcal{K}(|\boldsymbol{R}_i - \boldsymbol{R}_j|) \ , \qquad \mathcal{T}_{ij} = \mathcal{T}(|\boldsymbol{R}_i - \boldsymbol{R}_j|) \tag{4.1}$$

Interpreting $\underline{\underline{\mathcal{H}}}$ as a random matrix allows studying the averaged vibrational properties of the system. In general, random matrix theory has become a well-established tool in statistical and theoretical physics (Goetschy and Skipetrov, 2013; Mehta, 2014). However, ERMs, in particular, have been widely discussed for the last 25 years by Grigera and colleagues (Ciliberti *et al.*, 2003; Grigera *et al.*, 2011, 2001; Martin-Mayor *et al.*, 2001), by Schirmacher and colleagues (Folli *et al.*, 2017; Ganter and Schirmacher, 2010, 2011; Schirmacher *et al.*, 2019) and others (Amir *et al.*, 2013; Beltukov *et al.*, 2013).

This chapter introduces the Euclidean Random Matrix model for amorphous solids. In Section 4.1, we provide a systematic derivation of the vectorial ERM-model starting from analysing the dynamic structure factor (Martin-Mayor *et al.*, 2001). Then, in Section 4.2, we consider the standard scalar ERM approximation. Within this approximation, we will show in Section 4.3 that the eigenmodes with eigenvalue zero correspond to the uniform shift of disconnected clusters of particles. Next, we discuss how our derivation of the ERM model connects to the approaches discussed in the literature (Baumgärtel *et al.*, 2024; Szamel, 2025). There, the authors looked at the incoherent correlation function of the time derivatives with specific initial conditions. However, the analysis in Section 4.1 suggests that the ERM model is motivated by a coherent response function of the displacements. We resolve this apparent incommensurability in Section 4.4. Lastly, in Section 4.5, we discuss that analyzing the current correlation function is more reasonable for investigating the jamming transition as it does not require the existence of a reference frame $\{\boldsymbol{R}_i\}_{i=1}^N$.

4.1 Scattering, the dynamic structure factor and the resolvent

This section motivates the Euclidean Random Matrix as a tool to investigate the structure of the system. The presented discussion is inspired by (Martin-Mayor *et al.*, 2001)[1]. We have discussed in Section 2.3.1 that the jamming transition is ultimately of a geometric nature– at least in soft sphere systems. Moreover, as the transition becomes unique, different configurations characterized by the same parameters like particle size σ and density n are supposed to exhibit the same features and properties. Thus, the structure of the disordered system is of primary concern when investigating disordered materials and the unjamming instability. The structure of a many-body system can be experimentally investigated with scattering events (Chaikin and Lubensky, 1995, Chapter 2) and (Simon, 2013, Chapter 14). As we look at systems constituted by uncharged particles,

[1] In their works, the authors of (Grigera *et al.*, 2001; Martin-Mayor *et al.*, 2001; Martín-Mayor *et al.*, 2000) also motivated the Euclidean Random Matrix Model via the one-phonon approximation of the dynamic structure factor, as we will do hereinafter. However, the following discussion is solely based on (Ashcroft and Mermin, 1976, Appendix N). Although the derivation in this section is not included in the works (Grigera *et al.*, 2001; Martin-Mayor *et al.*, 2001; Martín-Mayor *et al.*, 2000), the wording and concepts therein motivated the investigation of the relation between the dynamic structure factor and the Euclidean Random Matrix Model presented below.

neutron spectroscopy comes to mind. Hereinafter, we look at an incident neutron beam described by a plane wave with wavevector $\boldsymbol{p}$ scattered by the system and emerging with the new wavevector $\boldsymbol{p}'$. The probability per unit time for the associated scattering process $\boldsymbol{p} \to \boldsymbol{p}'$ is connected to the double differential cross-section $\frac{d^2\sigma}{d\Omega dE}$, which counts the scattered neutrons per time in the angle window $d\Omega$ and the energy interval dE. The double differential cross-section provides insight into the structure of the solid due to the relation (Ashcroft and Mermin, 1976, Appendix N)

$$\frac{d^2\sigma}{d\Omega dE} \propto \int dt e^{-i\omega t} \frac{1}{N} \langle \sum_{ij} e^{-i\boldsymbol{q}\cdot\boldsymbol{r}_i(t)} e^{-i\boldsymbol{q}\cdot\boldsymbol{r}_j} \rangle \ . \tag{4.2}$$

Here, ω is the frequency associated with the energy transfer due to the inelastic scattering event $\boldsymbol{p} \to \boldsymbol{p}'$ and $\boldsymbol{q} = \boldsymbol{p} - \boldsymbol{p}'$ is the wavevector difference. The brackets $\langle \cdot \rangle$ indicate the annealed average introduced in Section 3.1. The right-hand side of Equation (4.2) is connected to the dynamic structure factor

$$S_{\boldsymbol{q}}(t) \equiv \frac{1}{N} \langle \delta\rho(\boldsymbol{q}, t) \delta\rho(-\boldsymbol{q}, 0) \rangle \ . \tag{4.3}$$

Here, $\delta\rho(\boldsymbol{q}, t) = \rho(\boldsymbol{q}, t) - \langle \rho(\boldsymbol{q}, t) \rangle$ denotes the local density fluctuation and

$$\rho(\boldsymbol{q}, t) = \sum_i e^{-i\boldsymbol{q}\cdot\boldsymbol{r}_i(t)} = \int d^d\boldsymbol{r} e^{-i\boldsymbol{q}\cdot\boldsymbol{r}} \sum_i \delta(\boldsymbol{r} - \boldsymbol{r}_i(t)), \tag{4.4}$$

denotes the Fourier-transformed local density. Throughout this chapter, we assume the existence of a reference frame $\{\boldsymbol{R}_i\}_{i=1}^N$. Thus, the average of the local density is given by $\langle \rho(\boldsymbol{q}, t) \rangle = \sum_{i=1}^N e^{-i\boldsymbol{q}\cdot\boldsymbol{R}_i}$. As the name suggests, $S_{\boldsymbol{q}}(t)$ gives information about the structure's evolution. The remaining part of this section is dedicated to expressing $S_{\boldsymbol{q}}(t)$ in terms of the Hessian $\underline{\boldsymbol{\mathcal{H}}}$ defined in Equation (2.38).

We start our analysis by assuming that the harmonic expansion of the elastic energy is valid:

$$\mathcal{E}(\{\boldsymbol{r}\}) - \mathcal{E}(\{\boldsymbol{R}\}) \equiv \Delta\mathcal{E} \approx \frac{m}{2} \sum_{ij} u_{i\alpha} \mathcal{H}_{i\alpha,j\beta} u_{j\beta} \ , \tag{4.5}$$

Rewriting the equation for the structure factor in terms of the displacements $\{\boldsymbol{u}_i\}_{i=1}^N$ around the reference positions $\{\boldsymbol{R}_i\}_{i=1}^N$ gives

$$NS_{\boldsymbol{q}}(t) = \sum_{i,j}^{N} e^{i\boldsymbol{q}\cdot(\boldsymbol{R}_i-\boldsymbol{R}_j)} \Big(\langle e^{i\boldsymbol{q}\cdot(\boldsymbol{u}_i(t)-\boldsymbol{u}_j(0))}\rangle - \langle e^{-i\boldsymbol{q}\cdot\boldsymbol{u}_i(t)}\rangle \langle e^{i\boldsymbol{q}\cdot\boldsymbol{u}_j(0)}\rangle \Big) \tag{4.6}$$

as the reference frame, by definition, is time-independent. The harmonic expansion of the energy (Equation (4.5)) suggests a Gaussian action, which in turn implies that the averages can easily be calculated using Wick's Theorem (Hertz *et al.*, 2016). The expectation $\langle e^{-i\boldsymbol{q}\cdot\boldsymbol{u}_i(t)}\rangle$ reads in the Gaussian approximation (Ashcroft and Mermin, 1976, Appendix N):

$$\langle e^{i\boldsymbol{q}\cdot\boldsymbol{u}_i(t)}\rangle \approx \sum_{m=0}^{\infty} \frac{(2m-1)!!}{2m!} (-\langle(\boldsymbol{q}\cdot\boldsymbol{u}_i(t))^2\rangle)^m = e^{-\frac{1}{2}\langle(\boldsymbol{q}\cdot\boldsymbol{u}_i(t))^2\rangle} = e^{-W} \tag{4.7}$$

Here, $e^{-2W} = e^{-\langle(\boldsymbol{q}\cdot\boldsymbol{u}_i(t))^2\rangle}$ is the Debye-Waller Factor, which describes the attenuation of the scattering intensity due to thermal motion (Gross and Marx, 2014, Chapter 2.2.7). At zero temperature holds $e^{-2W} = 1$. Similarly, we find

$$\begin{aligned}\langle e^{i\boldsymbol{q}\cdot(\boldsymbol{u}_i(t)-\boldsymbol{u}_j(0))}\rangle &= \sum_{m=0}^{\infty} \frac{(2m-1)!!}{2m!} \Big[-\langle \Big[\boldsymbol{q}\cdot(\boldsymbol{u}_i(t)-\boldsymbol{u}_j(0))\Big]^2\rangle \Big]^m \\ &= e^{-\frac{1}{2}\langle \left[\boldsymbol{q}\cdot(\boldsymbol{u}_i(t)-\boldsymbol{u}_j(0))\right]^2\rangle} = e^{-2W} e^{\langle[\boldsymbol{q}\cdot\boldsymbol{u}_i(t)][\boldsymbol{q}\cdot\boldsymbol{u}_j(0)]\rangle} \,. \end{aligned} \tag{4.8}$$

We used the linearity of the average in the last line. Thus, we get for the dynamic structure factor:

$$N\big(S_{\boldsymbol{q}}(t) + S_{\boldsymbol{q}}\big) = \sum_{i,j}^{N} e^{-i\boldsymbol{q}\cdot(\boldsymbol{R}_i-\boldsymbol{R}_j)} \sum_{m=0}^{N} \frac{\langle[\boldsymbol{q}\cdot\boldsymbol{u}_i(t)][\boldsymbol{q}\cdot\boldsymbol{u}_j(0)]\rangle^m}{m!} \tag{4.9}$$

Here, $S_{\boldsymbol{q}} = S_{\boldsymbol{q}}(t=0)$ is the static structure factor. Notably, the dynamic structure factor depends on the Fourier mode $\boldsymbol{q}$ and not only on its absolute value $|\boldsymbol{q}|$. This stems from the reference frame breaking translational invariance. Each term in the sum on the right-hand side of the previous equation has a physical interpretation. The m^{th} summand accounts for the case where the incident beam undergoes m inelastic scattering events. Thus, in solid state physics, the notion was coined that the m^{th} term corresponds to the $m-$phonon process (Ashcroft and Mermin, 1976, Appendix N). The term $m = 0$ cor-

responds to zero inelastic scattering events and, therefore, accounts for Bragg reflection and the Bragg peaks in the scattering pattern. It becomes apparent that the zero phonon contribution equals the static structure factor $S_{\boldsymbol{q}}$, which contains all the information on the frozen-in arrangements of the particles. The static structure factor $S_{\boldsymbol{q}}$ is equivalent to the pair correlation function $g(\boldsymbol{r})$ defined in Equation (2.47) (Hansen and McDonald, 2009, Equation 4.1.3):

$$S_{\boldsymbol{q}} = 1 + n \int d\boldsymbol{r} e^{-i\boldsymbol{q}\cdot\boldsymbol{r}} \Big(g(\boldsymbol{r}) - \frac{1}{N} \langle \rho(\boldsymbol{r}) \rangle \Big) \, . \tag{4.10}$$

On the other hand, the one-phonon contribution gives rise to a two-point correlation function (Martin-Mayor *et al.*, 2001):

$$\underline{\boldsymbol{C}}(\boldsymbol{q}, t) = \frac{1}{N} \sum_{i,j}^{N} e^{-i\boldsymbol{q}\cdot(\boldsymbol{R}_i - \boldsymbol{R}_j)} \langle \boldsymbol{u}_i(t) \boldsymbol{u}_j(0) \rangle \tag{4.11}$$

The next step is to express the right-hand side of the previous equation in terms of the Hessian $\underline{\boldsymbol{\mathcal{H}}}$. To achieve this, we look for a differential equation determining $\underline{\boldsymbol{C}}(\boldsymbol{q}, t)$: The time evolution of a displacement in the zero temperature limit is governed by the Newtonian equation of motion

$$\ddot{\boldsymbol{u}}_i(t) = -\frac{1}{m} \frac{\partial E[\{\boldsymbol{u}_l\}_{l=1}^N]}{\partial \boldsymbol{u}_i} = -\sum_{j=1}^{N} \underline{\boldsymbol{\mathcal{H}}}_{ij} \cdot \boldsymbol{u}_j(t) \, . \tag{4.12}$$

Hence, the perturbation spreads deterministically. This in turn suggests that the response function $\underline{\boldsymbol{C}}(\boldsymbol{q}, t)$ is fully determined by the reference position $\{\boldsymbol{R}_i\}$ and by the pair potential $U(r)$. Using Equation (4.12) and the properties of Laplace transformation, we get for the second time derivative of the correlation function $\underline{\boldsymbol{F}}_{ij}(t) = \langle \boldsymbol{u}_i(t) \boldsymbol{u}_j(0) \rangle$

$$\mathrm{LT}[\ddot{\underline{\boldsymbol{F}}}_{ij}(t)](s) = s^2 \hat{\underline{\boldsymbol{F}}}_{ij}(s) - \dot{\underline{\boldsymbol{F}}}_{ij}(t=0) - s \underline{\boldsymbol{F}}_{ij}(t=0) = -\sum_{k=1}^{N} \underline{\boldsymbol{\mathcal{H}}}_{ik} \hat{\underline{\boldsymbol{F}}}_{kj}(s) \, . \tag{4.13}$$

The inital conditions $\dot{\underline{\boldsymbol{F}}}_{ij}(t=0) = 0$ and $\underline{\boldsymbol{F}}_{ij}(t=0) = \underline{\boldsymbol{F}}^0_{ij}$ lead to

$$\hat{\underline{\boldsymbol{F}}}_{i\alpha,j\beta}(s) = s \sum_{k=1}^{N} \big[s^2 + \underline{\boldsymbol{\mathcal{H}}} \big]^{-1}_{i\alpha,k\gamma} \cdot F^{(0)}_{k\gamma,j\beta} \, . \tag{4.14}$$

The inital value $\underline{\boldsymbol{F}}^0_{ij} \in \mathbb{R}^{N\times d\times N\times d}$ generally depends on the perturbation. It has the dimension of length square $[\underline{\boldsymbol{F}}^0_{ij}] = [\sigma^2]$. Furthermore, we have to emphasize the notational inconsistency that $\underline{\boldsymbol{\mathcal{H}}}_{ij}$ denotes a $d \times d$ matrix while $\underline{\boldsymbol{\mathcal{H}}}$ represents a $dN \times dN$ matrix with block structure. Hereinafter, we only look at the one-phonon contribution. This approximation is equivalent to the Born approximation in standard scattering theory (Sakurai and Napolitano, 2011, Chapter 6). All in all, we can express the dynamic structure factor in the one phonon approximation in terms of the resolvent of the Hessian (Martin-Mayor *et al.*, 2001):

$$\hat{S}_{\boldsymbol{q}}(s) = \frac{s q_\alpha q_\beta}{N} \sum_{i,j,k=1}^{N} e^{-i\boldsymbol{q}\cdot(\boldsymbol{R}_i - \boldsymbol{R}_j)} \left[s^2 + \underline{\boldsymbol{\mathcal{H}}}\right]^{-1}_{i\alpha,k\gamma} \cdot F^{(0)}_{k\gamma,j\beta} \tag{4.15}$$

We note that the dynamic structure factor equals a response quantity times an initial condition, which generally depends on the perturbation. In the next section, we look at the associated susceptibility as it becomes the main quantity of interest.

4.2 Quenched disorder and the scalar ERM-model

The analysis in the last section suggests that the susceptibility

$$\hat{\chi}_{\alpha\beta}(\boldsymbol{q}, s) = \frac{1}{N} \sum_{i,j}^{N} e^{-i\boldsymbol{q}\cdot(\boldsymbol{R}_i - \boldsymbol{R}_j)} \left[s^2 + \underline{\boldsymbol{\mathcal{H}}}\right]^{-1}_{i\alpha,j\beta} \tag{4.16}$$

is a crucial quantity when analyzing disordered athermal systems. Remarkably, $\underline{\hat{\boldsymbol{\chi}}}_{\boldsymbol{q}}(s)$ depends only on the interaction details via the pair potential and the reference frame. However, the positions $\{\boldsymbol{R}_{i=1}\}_{i=1}^N$ are generally unknown due to the disorder. Nevertheless, we discussed in Chapter 2 that many observables become universal in the thermodynamic limit as they do not depend on the concrete configuration of the reference frame. This suggests averaging over the quenched disorder as this supposedly preserves the important physics but dispenses with the dependence on the specific reference frame,

i.e. the concrete configuration:

$$\begin{aligned}\hat{\chi}_{\alpha\beta}(\boldsymbol{q},s) \to \frac{1}{N}\int \prod_{m=1}^{N} d^d\boldsymbol{R}_m \sum_{i,j}^{N} e^{-i\boldsymbol{q}\cdot(\boldsymbol{R}_i-\boldsymbol{R}_j)} \left[s^2+\underline{\boldsymbol{\mathcal{H}}}^{\mathrm{ERM}}\right]^{-1}_{i\alpha,j\beta} \Psi_Q(\{\boldsymbol{R}_l\}_{l=1}^N) \\ \equiv \frac{1}{N}\overline{\sum_{i,j}^{N} e^{-i\boldsymbol{q}\cdot(\boldsymbol{R}_i-\boldsymbol{R}_j)} \left[s^2+\underline{\boldsymbol{\mathcal{H}}}^{\mathrm{ERM}}\right]^{-1}_{i\alpha,j\beta}} \\ \equiv \hat{\chi}^{\mathrm{ERM}}_{\alpha\beta}(\boldsymbol{q},s)\ .\end{aligned} \tag{4.17}$$

Here, $\Psi_Q(\{\boldsymbol{R}\}_{i=1}^N)$ specifies the distribution function for the reference frame $\{\boldsymbol{R}_i\}_{i=1}^N$. Throughout this thesis, we assume that $\Psi_Q(\{\boldsymbol{R}_i\}_{i=1}^N)$ is rotational and translation invariant. The approach in Equation (4.17) renders the reference positions as random variables. Thus, the Hessian

$$\begin{aligned}\mathcal{H}^{\mathrm{ERM}}_{i\alpha,j\beta} &= \delta_{ij}\sum_k M_{i\alpha,k\beta} - M_{i\alpha,j\beta}\ , \\ M_{i\alpha,j\beta} &= \frac{1}{m}\hat{R}^{\alpha}_{ij}\Big(\mathcal{K}(R_{ij}) - \frac{\mathcal{T}(R_{ij})}{R_{ij}}\Big)\hat{R}^{\beta}_{ij} + \frac{\mathcal{T}(R_{ij})}{mR_{ij}}\delta_{\alpha\beta}\end{aligned} \tag{4.18}$$

becomes a random matrix or rather a random tensor as it depends on random positions in the Nd-dimensional energy landscape. Mèzard *et al.* coined the term *Euclidean Random Matrix* (ERM) (Mézard *et al.*, 1999). In this thesis, a superscripted label, ERM, refers to a Euclidean Random Matrix or to a quantity evaluated with $\underline{\boldsymbol{\mathcal{H}}}^{\mathrm{ERM}}$ like $\underline{\hat{\boldsymbol{\chi}}}^{\mathrm{ERM}}(\boldsymbol{q},s)$ in Equation (4.17).

Thus, the task of calculating the susceptibility now translates into calculating the spectral properties of a random matrix. However, calculating the spectral properties of $\mathcal{H}_{i\alpha,j\beta}$ is hardly feasible due to the tensor structure and the dependence on both the first and second derivatives of the potential energy. Thus, Mèzard *et al.* proposed to drastically simplify the model by neglecting the bond tension ($\mathcal{T}_{ij}=0$) and by additionally neglecting the vector character of displacements $\boldsymbol{u}_i(t) \longrightarrow u_i(t)$ (Mézard *et al.*, 1999). This heavily simplifies the problem at hand as the Hessian $\mathcal{H}^{\mathrm{SERM}}_{ij}$ now reads:

$$\mathcal{H}^{\mathrm{SERM}}_{ij} = -\frac{1}{m}\mathcal{K}(|\boldsymbol{R}_i-\boldsymbol{R}_j|) + \frac{\delta_{ij}}{m}\sum_k \mathcal{K}(|\boldsymbol{R}_i-\boldsymbol{R}_k|)\ , \tag{4.19}$$

where $\mathcal{K}(|\boldsymbol{R}_i - \boldsymbol{R}_k|)$ is a function of the Euclidean distance between the particles. Equation (4.19) together with the distribution function Ψ_Q defines the scalar Euclidean Random Matrix (SERM) model[2]:

$$\hat{\chi}_q^{\text{SERM}}(s) = \frac{1}{N}\overline{\sum_{i,j=1}^{N} e^{-i\boldsymbol{q}\cdot(\boldsymbol{R}_i-\boldsymbol{R}_j)}\left[s^2 + \underline{\boldsymbol{\mathcal{H}}}^{\text{SERM}}\right]^{-1}_{ij}} \tag{4.20}$$

Notably, the susceptibility of the scalar ERM model depends only on the absolute value of the Fourier mode. This stems from assuming that the distribution function Ψ_Q is rotational and translational invariant. The energy in this model consequentially reads

$$E^{\text{SERM}} = \frac{m}{2}\sum_{ij=1}^{N}\mathcal{H}_{ij}^{\text{SERM}}u_i u_j = \frac{1}{4}\sum_{ij=1}^{N}\mathcal{K}(|\boldsymbol{R}_i - \boldsymbol{R}_j|)(u_i - u_j)^2 \ . \tag{4.21}$$

For the analytical investigations, it is generally assumed that $\mathcal{K}(r)$ is Fourier transformable (Grigera *et al.*, 2011). Furthermore, theoretical and numerical investigations generally assume a uniform distribution of the particles

$$\Psi_Q(\{\boldsymbol{R}\}_{i=1}^N) = P(\boldsymbol{R}_1)\cdot ... \cdot P(\boldsymbol{R}_N) = \frac{1}{V^N} \ . \tag{4.22}$$

However, in Appendix A, we solve the SERM model for arbitrary distribution functions with the projection-operator formalism introduced in Section 3.2. This analysis follows (Szamel, 2025). Additionally, we generalize Szamel's approach to vector displacements and also include initial stresses.

All the figures and numerical solutions discussed later in this monograph are based on the scalar ERM model with a uniform distribution function Ψ_Q. We look at three different spring functions. The Gaussian spring function, $\mathcal{K}^G(r) = m\omega_0^2\exp[-r^2/(2\sigma^2)]$, has been discussed most in the literature (Baumgärtel *et al.*, 2024; Ciliberti *et al.*, 2003; Ganter and Schirmacher, 2010; Vogel and Fuchs, 2023)). Here, ω_0 is a material-specific frequency scale and σ denotes a length scale. However, having a spring function with

[2]Notably, (Mézard *et al.*, 1999) introduced the scalar ERM-model. Furthermore, when the ERM model is discussed in the literature, generally a uniform distribution of the particles is assumed, *e.g.* (Ciliberti *et al.*, 2003). In this monograph, we use the term ERM model in a broader sense, as it refers to every quantity calculated with an Euclidean Random matrix. In contrast, we use the label SERM to specifically refer to the scalar ERM-model.

infinite support always leads to a fully connected system with infinite coordination number. Hence, the Gaussian spring function can only describe the jammed phase. However, we also look at the Θ-spring function $\mathcal{K}^{\Theta}(r) = m\omega_0^2\Theta(1-r/\sigma)$ and a linear spring function $\mathcal{K}^{L}(r) = m\omega_0^2(1-r/\sigma)\Theta(1-r/\sigma)$, where $\Theta(\cdot)$ denotes the Theta-function. Both have finite support, leading to a transition for sufficiently small densities where the system disintegrates into disconnected clusters. Here, the unjamming transition eventually occurs if the system is sufficiently dilute. The parameter σ can be interpreted as the diameter of the spheres, and the dimensionless density $n^* = N\sigma^d/V$ becomes the single control parameter. In the next subsection, we are going to show that the zero eigenvalues of the random matrix $\underline{\boldsymbol{\mathcal{H}}}^{\text{SERM}}$ correspond to the uniform shift of a disconnected cluster of particles. This suggests that more and more eigenvalues become zero for sufficiently low densities, which implies the presence of floppy modes in the low-density regime.

4.3 Geometric multiplicity of the eigenvalue zero

The diagonal elements of the Hessian defined in Equation (2.38) and Equation (4.19) are just the negative sum of the associated row or column. This ensures that the unit vector $\boldsymbol{e} = \frac{1}{\sqrt{N}}(1,...,1)^T$ is an eigenvector of the system to eigenvalue zero. As this corresponds to a uniform shift of the system, this eigenvector directly corresponds to the global translational invariance and to the system's symmetry. In this section, we analyze the other eigenvectors with eigenvalue 0 in the scalar ERM model. We conclude that they also have a geometric interpretation as they correspond to the uniform shift of single clusters disconnected from the bulk. This interpretation holds if the interaction is purely repulsive $\mathcal{K}(r) \geq 0$. This leads to the interpretation of $\underline{\boldsymbol{\mathcal{H}}}^{\text{SERM}}$ being a diagonal block matrix, with each block corresponding to one cluster[3].

The idea is to show that every eigenvector with eigenvalue zero corresponds to a uniform shift of one or multiple disconnected clusters. For this purpose, let $\boldsymbol{e} \in \mathbb{R}^N$ denote a normalized eigenvector of $\underline{\boldsymbol{\mathcal{H}}}^{\text{SERM}}$ with associated eigenvalue λ. Furthermore, let $\mathcal{A}$ be a partition of the set of particle labels $\{1,....,N\}$. The sets $A_n \in \mathcal{A}$ for $1 \leq n \leq M$ are defined in the following way: Two different indices $1 \leq i \neq j \leq N$ belong to the same set, $i,j \in A_n$, if and only if $e_i = e_j$ holds. The eigenvalue λ

[3]The following proof has been taken from (Vogel *et al.*, 2025). Only the notation has been changed, but the wording is similar. It was the present author who came up with the proof.

corresponding to $\boldsymbol{e}$ directly relates to the energy as

$$\boldsymbol{e}^T \underline{\boldsymbol{\mathcal{H}}}^{\text{SERM}} \boldsymbol{e} = \lambda = \frac{2}{m} E^{\text{SERM}} \tag{4.23}$$

holds. Thus, the energy associated with the atomic displacements encoded in the entries of $\boldsymbol{e}$ is zero if the eigenvalue of the eigenmode is zero. The partition $\mathcal{A}$ provides a convenient criterion for the eigenvalue to be zero. Setting $\boldsymbol{u} = \boldsymbol{e}$, Equation (4.21) gives

$$\begin{aligned} 4E^{\text{SERM}} = 0 &\overset{!}{=} \sum_{i,j}^{N} \mathcal{K}(\boldsymbol{r}_i - \boldsymbol{r}_j) \underset{\geq 0}{(e_i - e_j)^2} \underset{\geq 0}{} \\ &= \sum_{m,l=1}^{M} \sum_{i \in A_m} \sum_{j \in A_l} \mathcal{K}(\boldsymbol{r}_i - \boldsymbol{r}_j)(e_i - e_j)^2 \\ &= \sum_{m,l \neq m}^{M} \sum_{i \in A_m} \sum_{j \in A_l} \mathcal{K}(\boldsymbol{r}_i - \boldsymbol{r}_j) \underset{>0}{(e_i - e_j)^2} \, . \end{aligned} \tag{4.24}$$

Thus, we conclude that $\mathcal{K}(\boldsymbol{r}_i - \boldsymbol{r}_j) = 0$ has to hold $i \in A_m$ and $j \in A_l$ with $m \neq l$. Otherwise, the eigenvalue could not be zero. This draws the following picture: If $\boldsymbol{e}$ corresponds to a floppy mode with eigenvalue 0, a set A_n has to contain the particles belonging to the same connected cluster, which has to be disconnected from all the other particles. The number $M = \#\mathcal{A}$ equals the number of disconnected clusters, and as the proof shows, M also equals the number of linearly independent eigenvectors with eigenvalue zero. The geometric interpretation is straightforward: The eigenvectors with eigenvalue zero correspond to the uniform shift of one disconnected cluster. As translational invariance is encoded in the Hessian, $M \geq 1$ has to hold.

Importantly, this proof does not apply when considering vector displacements. Here, floppy modes can also exist in a fully connected system in accordance with the Maxwell criterion (Section 2.3.1). In the next section, we relate our consideration of the dynamic structure factor modeled by an ERM to a frequently studied incoherent correlation function (Szamel, 2025).

4.4 Connection to approaches via the incoherent correlation function

This section aims to resolve an apparent contradiction in the theoretical and numerical treatment of the SERM model. In (Szamel, 2025) and (Baumgärtel *et al.*, 2024), the authors assumed the specific initial conditions $u_i = 0$ and $\dot{u}_i = \exp[-i\boldsymbol{q}\cdot\boldsymbol{R}_i]\omega_0\sigma$. Here, σ is a characteristic length scale of the system, for example, the particle diameter, and ω_0 is a characteristic frequency scale. This approach follows (Gelin *et al.*, 2016). It somehow simplifies the numerical investigation and will later enable us to interpret our equations diagrammatically. We will come back to this in Section 5.2.5. The incoherent autocorrelation function of the displacement derivatives

$$\begin{aligned}\hat{\tilde{F}}^{\mathrm{SERM}}_{ii}(s) = \overline{\mathrm{LT}\{\dot{u}_i(t)\dot{u}_i(0)\}} &= \frac{s}{N}\sum_{i,j=1}^{N}\overline{\dot{u}_j(0)\dot{u}_i^*(0)\left[s^2+\underline{\boldsymbol{\mathcal{H}}}^{\mathrm{SERM}}\right]^{-1}_{ji}} \\ &= \frac{s\sigma^2\omega_0^2}{N}\sum_{i,j=1}^{N}\overline{e^{-i\boldsymbol{q}\cdot(\boldsymbol{R}_j-\boldsymbol{R}_i)}\left[s^2+\underline{\boldsymbol{\mathcal{H}}}^{\mathrm{SERM}}\right]^{-1}_{ji}}\end{aligned} \tag{4.25}$$

is already similar to the response function defined in Equation (4.20) up to a factor $s\sigma^2\omega_0^2$. When comparing with experiments, the scales σ and ω_0 are free fit parameters. Notably, no ensemble average is necessary due to the deterministic motion. The complex conjugate in the previous equation results from the sesquilinear property of correlation functions. After dividing by the initial condition $\ddot{\tilde{F}}^{\mathrm{SERM}}_{ii}(t=0) = \sigma^2\omega_0^2$, we can identify the incoherent correlation function of the displacements time derivative in Equation (4.25) with the one-phonon response function in Equation (4.20). However, we have to resolve an additional apparent incommensurability. In Equation (4.15), we assumed that the initial displacements are non-zero. However, (Szamel, 2025) and (Baumgärtel *et al.*, 2024) assumed that an initial momentum has been injected into the system. Both approaches are equivalent up to the correct scales. This is a consequence of dealing with a harmonic theory, as velocities $\dot{u}_i$ and the displacement u_i fulfill the same differential equation

$$\ddot{\dot{u}}_i(t) = -\mathcal{H}^{\mathrm{SERM}}_{ij}\dot{u}_j(t)\ . \tag{4.26}$$

The last apparent incommensurability is that the normalized coherent correlation function for arbitrary initial conditions equals unity as shown by Philipp Baumgärtel[4]:

$$\frac{\sum_{i,j=1}^{N} \dot{u}_i(t)\dot{u}_j(0)}{\sum_{i,j=1}^{N} \dot{u}_i(0)\dot{u}_j(0)} = 1 \ . \tag{4.27}$$

Hereinafter, we will first discuss the proof of Equation (4.27) and then elaborate on why this statement does not imply that the one phonon-approximation in Equation (4.9) predicts a constant averaged dynamic structure factor $\overline{S}_{\boldsymbol{q}}(t)$.

As $\underline{\boldsymbol{\mathcal{H}}}^{\text{SERM}}$ is a real and symmetric matrix, there exists an orthonormal basis $\{\boldsymbol{e}_k\}_{k=1}^{N}$ of $\mathbb{R}^N$ of eigenvectors of $\underline{\boldsymbol{\mathcal{H}}}^{\text{SERM}}$. We label the associated eigenvalues as λ^k. They fulfill the relation $\underline{\boldsymbol{\mathcal{H}}}^{\text{SERM}} \cdot \boldsymbol{e}^k = \lambda^k \boldsymbol{e}^k$. Orthonormality implies that $\boldsymbol{e}^k \cdot \boldsymbol{e}^{k'} = \delta_{k,k'}$ holds. Using that N is large but finite so that different sums commute, Philipp Baumgärtel has shown the following property of the eigenvectors:

$$\sum_{i \neq j} e_i^k = -e_j^k \tag{4.28}$$

for arbitrary $j \in \{1, .., N\}$ provided that the associated eigenvector is non-zero $\lambda^k \neq 0$. This follows immediately from the sum rule $\sum_{i=1}^{N} \mathcal{H}_{ij}^{\text{SERM}} = \sum_{j=1}^{N} \mathcal{H}_{ij}^{\text{SERM}} = 0$:

$$\sum_{i=1}^{N}\sum_{j=1}^{N} \mathcal{H}_{ij}^{\text{SERM}} e_j^k = \sum_{j=1}^{N}\sum_{i=1}^{N} \mathcal{H}_{ij}^{\text{SERM}} e_j^k = 0 = \lambda^k \sum_{i=1}^{N} e_j^k \ , \tag{4.29}$$

which proofs Equation (4.28) for $\lambda^k \neq 0$. The Newtonian equation of motion in Equation (4.26) can easily be solved on a formal level. The solution reads

$$\begin{aligned} \dot{u}_i(t) &= \sum_{k=1}^{N} \dot{u}_k(t) e_i^k \\ \dot{u}_k(t) &= (\boldsymbol{e}^k \cdot \boldsymbol{u}(0)) \cos(\sqrt{\lambda^k} t) \ . \end{aligned} \tag{4.30}$$

[4]Here, Philipp's proof is displayed for the sake of completeness, which is in accordance with the requests of the supervisor of this monograph, Matthias Fuchs. Philipp's calculation is unpublished, but the following derivation is entirely his intellectual property. The original contribution of the present author is just the inclusion of eigenvectors with eigenvalue 0, which is straightforward.

Inserting these last two results in $\sum_{i,j=1}^{N} \dot{u}_i(t)\dot{u}_j(0)$ gives for the coherent correlation function:

$$\begin{aligned}\sum_{i,j=1}^{N} \dot{u}_i(t)\dot{u}_j(0) &= \sum_{i=1}^{N} \dot{u}_i(t)\dot{u}_i(0) + \sum_{i}\sum_{j\neq i} \dot{u}_i(t)\dot{u}_j(0) \\ &= \sum_{k=1}^{N} \dot{u}_k(t)\dot{u}_k(0) + \sum_{i,k=1}^{N} \dot{u}_k(t) e_i^k \sum_{k',j\neq i} \dot{u}_{k'}(0) e_j^{k'} = ...\end{aligned} \tag{4.31}$$

In the second line, we inserted the solutions from Equation (4.30) and used the orthonormality of the eigenvectors. In order to apply Equation (4.28), we distinguish between eigenvectors with finite eigenvalues and eigenvectors with eigenvalue zero:

$$\begin{aligned}... &= \sum_{k\in\{\lambda^k\neq 0\}} \dot{u}_k(t)\dot{u}_k(0) + \sum_{k'}\sum_{k\in\{\lambda^k\neq 0\}}\sum_{i=1}^{N} \dot{u}_k(t) e_i^k \sum_{j\neq i} \dot{u}_k(0) e_j^{k'} \\ &\quad + \sum_{k'}\sum_{k\in\{\lambda^k=0\}}\sum_{i,j=1}^{N} \dot{u}_k(t)\dot{u}_{k'}(0) e_i^k e_j^{k'} \\ &\overset{\text{Eq.(4.28)}}{=} \sum_{k'}\sum_{k\in\{\lambda^k=0\}}\sum_{i,j=1}^{N} \dot{u}_k(0)\dot{u}_{k'}(0) e_i^k e_j^{k'} \ .\end{aligned} \tag{4.32}$$

As the cancellation of the first and second term in the first line holds for arbitrary times, one similarly finds

$$\sum_{i,j=1}^{N} \dot{u}_i(0)\dot{u}_j(0) = \sum_{k'}\sum_{k\in\{\lambda^k=0\}}\sum_{i,j=1}^{N} \dot{u}_k(0)\dot{u}_{k'}(0) e_i^k e_j^{k'} \ . \tag{4.33}$$

This result leads to the conclusion[5] that the normalized coherent correlation function just equals unity

$$\frac{\sum_{i,j=1}^{N} \dot{u}_i(t)\dot{u}_j(0)}{\sum_{i,j=1}^{N} \dot{u}_i(0)\dot{u}_j(0)} = 1 \ . \tag{4.34}$$

This result is a direct consequence of the translational invariance of the system and, hence, of the conservation of the total momentum. The momentum a single mode

[5] Philipp's crucial insight was the cancellation of the two terms. The contribution of the present author was just the realization that this cancellation does not extend to the eigenvectors with eigenvalue zero.

transfers to the continuum constituted by the other modes is simultaneously restored. Notably, this does not contradict the definition of the dynamic structure factor in Equation (4.3), which is a coherent quantity. The coincidence of the Equations (4.20) and (4.25) follows from the fact that the reference frame has been included in the initial conditions. In the remaining part of this thesis, we mainly adopt the interpretation that the ERM model deals with the time evolution of an incoherent correlation function. In Section 5.2.5, this point of view will allow us to diagrammatically interpret the Self-Consistent Current Response Theory developed in Chapter 5.

Up to this point, the discussion has heavily relied on the assumption of an existing reference frame $\{\boldsymbol{R}_i\}_{i=1}^N$. However, we are generally interested in the unjamming transition where the system becomes soft. Below jamming, even a small perturbation leads to unquantifiable displacements in the absence of friction, and even a small temperature T makes the assumption of a reference frame invalid. Thus, we have to go beyond the assumption of an existing reference frame $\{\boldsymbol{R}_i\}_{i=1}^N$ to develop a theory valid in both phases and which can even be generalized to finite temperatures $T > 0$.

4.5 Going beyond the reference frame

Especially in its scalar version, the ERM model provides a simplistic model for amorphous systems. It only depends on the distribution function $\Psi_Q(\{\boldsymbol{R}_i\}_{i=1}^N)$ and the pair interaction potential or rather its derivatives $\mathcal{T}(r)$ and $\mathcal{K}(r)$. However, similarly to the discussion in Chapter 2, the ERM model assumes the existence of a reference frame $\{\boldsymbol{R}_i\}_{i=1}^N$. This assumption is valid in the solidified state and also at $T = 0$. However, it loses its justification below the instability as soon as we turn on the temperature T. Thus, we aim for a description of the problem that does not require a reference frame but becomes equivalent to Equation (4.17) for the susceptibility $\underline{\boldsymbol{\chi}}(\boldsymbol{q}, t)$ in the rigid phase, where a harmonic expansion around a reference frame becomes possible. To avoid the dependence on the reference frame, we focus on the time derivatives of the displacements $\boldsymbol{v}_i = \dot{\boldsymbol{u}}_i$ hereinafter. This suggests that the current autocorrelation function

$$\underline{\mathbf{K}}(\boldsymbol{r}_1, \boldsymbol{r}_2, t_1, t_2) \propto \langle \boldsymbol{v}(\boldsymbol{r}_1, t_1) \boldsymbol{v}(\boldsymbol{r}_2, t_2) \rangle \ , \tag{4.35}$$

can serve as a good observable to follow the system through the transition and which sufficiently well describes both phases, potentially even for finite temperatures. Here,

$$\boldsymbol{v}(\boldsymbol{r},t)=\sum_i \boldsymbol{v}_i\delta(\boldsymbol{r}-\boldsymbol{r}_i(t)) \tag{4.36}$$

defines the local current as $\boldsymbol{v}_i$ is the i^{th}-particle velocity. Furthermore, $\delta(\boldsymbol{r})$ denotes the vectorial delta-distribution. We introduced the correlation function together with the concrete stochastic description of our system in a rigorous way in Section 3. Here, we just intend to motivate Chapter 5 by showing that Equation (4.35) becomes equivalent to the response function of the displacements defined in Equation (4.11) when a harmonic expansion around a reference frame is valid.

As we discussed in Section 3, the generally assumed translational invariance implies that the current autocorrelation function depends only on the spatial difference $\boldsymbol{r}_1-\boldsymbol{r}_2$. Additionally, the correlation function only depends on the time difference $t=t_1-t_2$. Thus, the spatial Fourier transformation reads

$$\underline{\mathbf{K}}(\boldsymbol{q},t)\propto\langle\sum_{ij}e^{-i\boldsymbol{q}\cdot(\boldsymbol{r}_i(t)-\boldsymbol{r}_j(0))}\boldsymbol{v}_i(t)\boldsymbol{v}_j(0)\rangle\ . \tag{4.37}$$

In the solidified phase, a reference frame $\{\boldsymbol{R}_i\}_{i=1}^N$ emerges, and the harmonic expansion of the energy in Equation (2.37) becomes reasonable. Here, expressing the current autocorrelation function $\underline{\mathbf{K}}_{\boldsymbol{q}}(t)$ in terms of the displacement field leads to

$$\underline{\mathbf{K}}(\boldsymbol{q},t)\propto\sum_{ij}e^{-i\boldsymbol{q}\cdot(\boldsymbol{R}_i-\boldsymbol{R}_j)}\left\langle\dot{\boldsymbol{u}}_i(t)\dot{\boldsymbol{u}}_j(0)\sum_{m=0}^{N}\frac{\left([\boldsymbol{q}\cdot\boldsymbol{u}_i(t)][\boldsymbol{q}\cdot\boldsymbol{u}_j(0)]\right)^m}{m!}\right\rangle\ . \tag{4.38}$$

The one-phonon approximation only considers the $m=0$ contribution. In the harmonic approximation, the equation of motion for the time derivatives of the displacement field reads

$$\ddot{\boldsymbol{u}}_i(t)=-\sum_{j=1}^{N}\underline{\boldsymbol{\mathcal{H}}}_{ij}\cdot\dot{\boldsymbol{u}}_j(t)\ . \tag{4.39}$$

Redoing the same calculation as at the end of Section 4.1, we end up with

$$\hat{\mathrm{K}}_{\alpha\beta}(\boldsymbol{q}, s) \propto \frac{s}{N} \sum_{i,j,k=1}^{N} e^{-i\boldsymbol{q}\cdot(\boldsymbol{R}_i - \boldsymbol{R}_j)} \left[s^2 + \underline{\boldsymbol{\mathcal{H}}}\right]^{-1}_{i\alpha,k\gamma} \cdot \ddot{F}^{(0)}_{k\gamma,j\beta} \,. \tag{4.40}$$

Now, we assume that the initial displacements are uniform. For example, we can assume that they arise from thermal fluctuations for small but finite temperature T. We define the current autocorrelation as normalized by the initial conditions and subsequently take the limit $T \to 0$. This leads to

$$\underline{\hat{\mathbf{K}}}(\boldsymbol{q}, s) \equiv \frac{s}{N} \sum_{i,j=1}^{N} e^{-i\boldsymbol{q}\cdot(\boldsymbol{R}_i - \boldsymbol{R}_j)} \left[s^2 + \underline{\boldsymbol{\mathcal{H}}}\right]^{-1}_{ij} \,. \tag{4.41}$$

Lastly, we assume that the system is self-averaging. As discussed in Section 3.3, this assumption basically implies that averaging over the quenched disorder equals considering the ensemble average of a sufficiently large system. Thus, we can identify in the jammed state

$$\frac{\underline{\hat{\mathbf{K}}}_{\boldsymbol{q}}(s)}{s} = \underline{\hat{\boldsymbol{\chi}}}^{\mathrm{ERM}}(\boldsymbol{q}, s) \,, \tag{4.42}$$

where $\underline{\hat{\boldsymbol{\chi}}}^{\mathrm{ERM}}(\boldsymbol{q}, s)$ equals the susceptibility defined in Equation (4.17). We will argue that the self-averaging assumption is indeed justified by calculating the left-hand side of Equation (4.42) in Chapter 5 and the right-hand side in Appendix A. As we will see, minor differences arise only due to the initial stresses. Generally, the identification in Equation (4.42) might be surprising at first glance. In the previous part of this Chapter, we analyzed the right-hand side of Equation (4.42) under the explicit assumption of an existing reference frame, while its left-hand side can be defined without this assumption. Nevertheless, the question arises *how can the current-correlation function be sensitive to stability and the emergence of a solid structure, i.e. a reference frame*. The answer is that the evolution of the current depends on the presence of restoring forces and whether they decay with time. If they decay, plastic events generally occur, and the system is not in the rigid phase, provided that the perturbation is sufficiently weak. Thus, we can use non-decaying forces or non-decaying stresses in the system as a hallmark of stability. Apparently, the current autocorrelation is sensitive to this shift in the nature of the stresses from decaying to non-decaying. Moreover, a theory for $\underline{\mathbf{K}}(\boldsymbol{q}, t)$ in the

athermal limit $T \to 0$ can straightforwardly be generalized to finite temperatures T. All of this suggests that $\underline{\mathbf{K}}(\boldsymbol{q}, t)$ is suitable for following the system through the jamming transition. Developing a theory for $\underline{\mathbf{K}}(\boldsymbol{q}, t)$ is precisely the content of Chapter 5. We will rely on the scalar ERM model to test our Equations as we can compare to data obtained from exact numerical diagonalization of the SERM defined in Equation (4.19).

5 | The Self-Consistent Transverse Current Response Theory

This chapter presents the detailed derivation and discussion of the Self-Consistent Current Response Theory. Interested in the system's stability, we inquire how it reacts to a perturbation: *Does the system support transverse sound modes or does it yield along floppy modes?* As the system yields if restoring forces decay, we are interested in the persistence of stresses. To follow the time-dependence of stresses or forces, we consider the evolution of the atomic particle displacement field $\boldsymbol{u}(\boldsymbol{r}, t)$. However, we mainly investigate its derivative, the local current $\boldsymbol{v}(\boldsymbol{r}, t) = \dot{\boldsymbol{u}}(\boldsymbol{r}, t)$ to avoid assuming the existence of a reference frame $\{\boldsymbol{R}_i\}_{i=1}^N$. The local current is defined as

$$\boldsymbol{v}(\boldsymbol{r}, t) = \sum_i \boldsymbol{v}_i(t)\delta(\boldsymbol{r} - \boldsymbol{r}_i(t)) \ . \tag{5.1}$$

Here, $\delta(\boldsymbol{r})$ denotes the vectorial delta-distribution and $\boldsymbol{v}_i$ and $\boldsymbol{r}_i$ denote the velocity and the position of the i^{th} particle. The stress-strain relation discussed in Section 2.2 implies that $\boldsymbol{v}(\boldsymbol{r}, t)$ quantifies the temporal changes of the stresses. However, stresses in turn give rise to forces, which again affect the velocity field $\boldsymbol{v}$. This conceptual picture will guide us through the ensuing derivation of the theory and eventually lead to a self-consistent model. Interested in whether the system can sustain stress, we inquire about the system's response properties. Thus, we look at the current autocorrelation function:

$$\underline{\mathbf{K}}(\boldsymbol{r}_1, \boldsymbol{r}_2, t_1, t_2) = \frac{\int d\Gamma \ \boldsymbol{v}(\boldsymbol{r}_1, t_1)\boldsymbol{v}^*(\boldsymbol{r}_2, t_2) \ \Psi(\Gamma)}{\frac{1}{d}\langle|\boldsymbol{v}(\boldsymbol{r})|^2\rangle} = \frac{\langle \boldsymbol{v}(\boldsymbol{r}_1, t_1)\boldsymbol{v}(\boldsymbol{r}_2, t_2)\rangle}{\frac{1}{d}\langle|\boldsymbol{v}(\boldsymbol{r})|^2\rangle} \tag{5.2}$$

Generally, $\underline{\mathbf{K}}$ describes how the current $\boldsymbol{v}$ at one point in spacetime $(\boldsymbol{r}_1, t_1)$ affects the current at $(\boldsymbol{r}_2, t_2)$ with $t_2 \geq t_1$. We discussed in Section 4.5 that $\underline{\mathbf{K}}$ is related to the response function of the one-phonon approximation in the stable phase. Equation (5.2) averages over the phase space with volume element $d\Gamma$ and $\Gamma = \{\boldsymbol{p}_i, \boldsymbol{r}_i\}_{i=1}^N$ according to a distribution function $\Psi(\Gamma)$. Here, $\boldsymbol{p}_i = m\boldsymbol{v}_i$ is the momentum of the i^{th} particle. Even

though an amorphous solid is in a metastable state and out of equilibrium, we use an equilibrium distribution function $\Psi = \Psi_{\mathrm{eq}}$. This allows us to systematically investigate the temperature dependence of the single contributions to the stresses. We employ a stochastic framework where the temperature governs the strength of the noise. We take the small noise or zero temperature limit at the end of our derivations. Furthermore, the equilibrium distribution Ψ_{eq} gives rise to several symmetry relations. This is one of the main reasons, why we work with the Fourier transformed correlation function $\underline{\mathbf{K}}(\boldsymbol{q}, t)$ in this chapter. Hereinafter, we utilize the Zwanzig-Mori projection operator formalism to develop a self-consistent theory for $\underline{\mathbf{K}}$ (Hansen and McDonald, 2009, Chapter 9). The applications of the Zwanzig-Mori formalism in the context of the Mode-Coupling Theory suggest that the projection operator formalism is capable of correctly capturing the transition from decaying to persistent stresses (Götze, 2009, Chapter 4). Thus, the formalism is supposedly well attuned to correctly describe the (un-)jamming transition. However, we will see that special care is needed to predict the correct sound attenuation in the stable phase. We must go beyond the standard self-consistent Born theory. The statistical equivalence of the positions in the medium necessitates that the sequence of microscopic scattering events must be symmetric under permutation up to second order. This constraint was coined *Leutheusser-symmetry* (Vogel *et al.*, 2025). Leutheusser discussed this symmetry constraint first in 1983 when proposing a kinetic theory for the Lorentz-gas (Leutheusser, 1983).

This chapter is organized as follows: Section 5.1 provides more information on the approach and the underlying idea. Section 5.2 presents the derivation of the self-consistent model. The resulting equations describe two phases: The stable jammed phase, where restoring forces do not decay, and the unjammed state, where they vanish. Both states are analyzed in Section 5.3 and Section 5.4, respectively. Section 5.5 is dedicated to the transition, which we investigate using the β-scaling analysis from the Mode-Coupling Theory. Substantial parts of this chapter's content are already published (Vogel *et al.*, 2025). While the prose text has been rewritten for this monograph, the equations appearing in both publications were generally not altered. This is supposed to ensure continuity. Among the three authors of the publication, the present author and Professor Matthias Fuchs derived and developed the theory. The original idea of developing a Self-Consistent Current-Response Theory to investigate jamming stems from Matthias Fuchs in cooperation with Annette Zippelius. However, the first attempt

failed since the resulting theory did not predict the correct sound attenuation. It was the present author's contribution to first develop and work out the full theoretical framework presented in (Vogel *et al.*, 2025). This work presents a detailed derivation of the model. Calculations done by Matthias Fuchs are carefully pointed out. The model's predictions are compared to the numerical solution of the scalar ERM model by Philipp Baumgärtel. All data resulting from numerical diagonalization of an Euclidean random matrix was created by Philipp Baumgärtel and is shown here with permission.

5.1 The idea behind the Transverse Current Response Theory

This section strives to motivate our approach. It provides arguments why the current autocorrelation is a good quantity for studying the response properties of an amorphous solid. Furthermore, we comment on using the Boltzmann distribution to model an out-of-equilibrium phase. Lastly, we motivate why we primarily focus on the transverse current.

The current autocorrelation as a response function As outlined in Chapter 4, we are interested in the susceptibility $\hat{\underline{\boldsymbol{\chi}}}(\boldsymbol{q}, s) = \hat{\underline{\mathbf{K}}}(\boldsymbol{q}, s)/s$. With this quantity, we can answer the question *if particle displacements $\boldsymbol{u}_i = \boldsymbol{r}_i(t) - \boldsymbol{R}_i$ due to a deformation lead to a plastic or an elastic response:* We have discussed in Section 4.5, that $\underline{\boldsymbol{\chi}}(\boldsymbol{q}, t)$ equals the time derivative of the displacement correlation function $\underline{\boldsymbol{C}}(\boldsymbol{q}, t)$ defined in Equation (4.11). This applies if the system is in the jammed state and if the harmonic expansion of the energy is justified. Thus, knowing $\underline{\mathbf{K}}(\boldsymbol{q}, t)$ gives access to the susceptibility in the stable arrested state. However, $\underline{\mathbf{K}}(\boldsymbol{q}, t)$ itself is a response function for a suitable perturbation[1]: To see this, let us consider an externally imposed velocity field $\boldsymbol{v}^{\mathrm{ex}}(t)$ coupled to the particles' momenta. We assume the external field is modeled by a plane wave with wavevector $\boldsymbol{q}$. The external perturbation shifts the energy $H \to H + \delta H$ with

$$\delta H = -\frac{m}{N}\boldsymbol{v}(-\boldsymbol{q}) \cdot \boldsymbol{v}^{\mathrm{ex}}(t) \; . \tag{5.3}$$

[1]The consideration in this paragraph were already contained in the early unpublished work of Matthias Fuchs and Annette Zippelius.

The system develops a non-zero expectation value $\langle \boldsymbol{v}(\boldsymbol{q},t)\rangle^{\mathrm{lr}}$ due to the driving. We assume that the perturbation has been turned on adiabatically in the infinite past $\boldsymbol{v}^{\mathrm{ex}}(t) = \boldsymbol{v}_0^{\mathrm{ex}} e^{\epsilon t}$ with $\epsilon = 0^+$ being an infinitesimal constant. The perturbation is then turned off at $t = 0$ leading to $\boldsymbol{v}^{\mathrm{ex}}(t > 0) = 0$. According to linear response theory, the shifted average couples linearly to the external perturbation (Risken, 1996, Chapter 7):

$$\langle \boldsymbol{v}(\boldsymbol{q},t)\rangle^{\mathrm{lr}} = \int_{-\infty}^{t} \langle \boldsymbol{v}(\boldsymbol{q},t-\tau)\delta\Omega(\tau)\ln(\Psi_{\mathrm{eq}})]\rangle_{\mathrm{eq}} d\tau \ . \tag{5.4}$$

The subscripted eq emphasizes that the correlation function is calculated with the unperturbed distribution function Ψ_{eq}. Notably, the differential operator $\delta\Omega$ in the previous equation does not act on the dsitrbution function. This is indicated by the square brackets. According to Equation (3.3) the perturbation encodes the shifted Fokker Planck operator $\delta\Omega(\tau)$:

$$\begin{aligned}
\delta\Omega(t)\Psi_{\mathrm{eq}} &= \frac{1}{N}\sum_{j=1}^{N} e^{i\boldsymbol{q}\cdot\boldsymbol{r}_j}\Big(\frac{\partial}{\partial \boldsymbol{r}_j}\cdot\boldsymbol{v}^{\mathrm{ex}}(t) - i\boldsymbol{p}_j\cdot\boldsymbol{v}^{\mathrm{ex}}(t)\ \boldsymbol{q}\cdot\frac{\partial}{\partial \boldsymbol{p}_j} - \zeta_0\frac{\partial}{\partial \boldsymbol{p}_j}\cdot\boldsymbol{v}^{\mathrm{ex}}(t)\Big)\Psi_{\mathrm{eq}} \\
&= \frac{1}{Nk_BT}\sum_{j=1}^{N} e^{i\boldsymbol{q}\cdot\boldsymbol{r}_j}\Big(\boldsymbol{F}_j + (i\boldsymbol{q}\cdot\boldsymbol{p}_j + \zeta_0)\frac{\boldsymbol{p}_j}{m}\Big)\cdot\boldsymbol{v}^{\mathrm{ex}}(t)\Psi_{\mathrm{eq}} \\
&= -\frac{m}{Nk_BT}\big[\Omega\boldsymbol{v}(-\boldsymbol{q})\Psi_{\mathrm{eq}}\big]\cdot\boldsymbol{v}^{\mathrm{ex}}(t)
\end{aligned} \tag{5.5}$$

Inserting this result in Equation (5.4) gives the linear response of the velocity field:

$$\langle \boldsymbol{v}(\boldsymbol{q},t)\rangle^{\mathrm{lr}} = \frac{m}{Nk_BT}\int_{-\infty}^{t}\boldsymbol{v}^{\mathrm{ex}}(\tau)\cdot\frac{d}{d\tau}\langle \boldsymbol{v}(\boldsymbol{q})e^{\Omega(t-\tau)}\boldsymbol{v}(-\boldsymbol{q})\rangle_{\mathrm{eq}} \underset{t>0}{=} \frac{\langle \boldsymbol{v}(\boldsymbol{q},t)\boldsymbol{v}(-\boldsymbol{q})\rangle_{\mathrm{eq}}}{N\frac{k_BT}{m}}\cdot\boldsymbol{v}^{\mathrm{ex}} \tag{5.6}$$

For the last equality, we relied on partial integration. Thus, the normalized equilibrium current autocorrelation function quantifies the evolution of the perturbation for $t > 0$:

$$\underline{\mathbf{K}}(\boldsymbol{r}_1,\boldsymbol{r}_2,t) = \frac{\int d\Gamma\ \boldsymbol{v}(\boldsymbol{r}_1)e^{\Omega t}\ \boldsymbol{v}(\boldsymbol{r}_2)\ \Psi_{\mathrm{eq}}}{N\frac{k_BT}{m}} = \frac{\langle \boldsymbol{v}(\boldsymbol{r}_1,t)\boldsymbol{v}(\boldsymbol{r}_2)\rangle}{N\frac{k_BT}{m}} \ . \tag{5.7}$$

This calculation and the considerations in Section 4.5 suggest that $\underline{\mathbf{K}}(\boldsymbol{r}_1, \boldsymbol{r}_2, t)$ is a good response function in the both phases. Hereinafter, the current autocorrelation function $\underline{\mathbf{K}}(\boldsymbol{r}_1, \boldsymbol{r}_2, t)$ is the main object of interest.

An equilibrium approach to non-equilibrium: It must be mentioned that the system falls out of equilibrium at the jamming transition. This contrasts our assumption of an equilibrium distribution function Ψ_{eq}. As we saw in Section 2.3.1, the jamming transition originates from geometric frustration. The configuration can not relax due to the high packing fraction. Thus, the system is stuck in a metastable state, and relaxation to the ground state and towards equilibrium is impossible. Nevertheless, relying on equilibrium relations is still a fruitful idea due to the following reasons:

(I) It is convenient! Including contributions arising from the non-equilibrium state highly complicates the problem. For example, the stationary distribution function is generally unknown. Hence, it is unclear which terms survive in the $T \to 0$ limit. Furthermore, an additional term appears in the fluctuation-dissipation theorem quantifying the change in the activity of the system *i.e.* how the energy landscape changes due to the perturbation (Baiesi *et al.*, 2009; Basu *et al.*, 2015; Maes, 2020). Those effects generally depend on the concrete dynamics of the system.

(II) As we saw in Section 2, the jammed state, as well as the critical dynamics, exhibit several universal properties independent of the concrete non-equilibrium state.

(III) Lastly, our theory requires the structure and the pair-correlation function $g(r)$ as an input. Since the pair distribution function is not unique out of equilibrium, this re-introduces the dependence on the preparation protocol and the explicit state of the system.

These three reasons are taken as justification for investigating non-equilibrium phenomena with an equilibrium approach and an equilibrium distribution function Ψ_{eq}.

Focusing on the transverse current: To simplify the derivation from the start, we consider a purely transverse perturbation $\boldsymbol{q} \cdot \boldsymbol{v}^{ex}(t) = 0$. According to Equation (5.6), it suffices to focus on the transverse velocity field:

$$\boldsymbol{v}^{\perp}(\boldsymbol{q}) = \hat{\boldsymbol{q}} \times (\boldsymbol{v}(\boldsymbol{q}) \times \hat{\boldsymbol{q}}) \, . \tag{5.8}$$

The longitudinal component of the velocity $\boldsymbol{v}^{\parallel}(\boldsymbol{q}) = (\boldsymbol{v}(\boldsymbol{q}) \cdot \hat{\boldsymbol{q}})\ \hat{\boldsymbol{q}}$ is neglected entirely in the following. However, the changes in the local density profile are caused by the longitudinal current $\Omega^{\dagger}\delta\rho(\boldsymbol{q}, t) = -i\boldsymbol{q} \cdot \boldsymbol{v}(\boldsymbol{q}, t)$. Thus, neglecting $\boldsymbol{v}^{\parallel}$ amounts to assuming a time-independent structure factor $S_q(t) = S_q$. However, only looking at the transverse field might appear as a rather unjustifiable simplification. Nonetheless, we can indeed argue for a primary role of the transverse modes at solidification: We have discussed in Section 2.3.2 that the transverse modes perpendicular to the wavevector are more sensitive to the distance to the critical point. Moreover, even though the bulk modulus B also vanishes at the instability, B acquires a finite value as soon as the temperature is turned on due to the ideal gas contribution. One could say that only the transverse modes change their character at the transition in any realistic system with $T \neq 0$. Furthermore, the Boson-peak has been related to the Ioffe-Regel limit of the transverse modes. Lastly, it was found in computer simulation that the transverse modes dominate relaxation processes (Horbach *et al.*, 2001). All of this suggests that the transverse modes are of primary concern when investigating the jamming transition.

Besides the arguments above, neglecting the longitudinal current $\boldsymbol{v}^{\parallel} = \frac{\boldsymbol{q}}{q^2}\boldsymbol{q} \cdot \boldsymbol{v}(\boldsymbol{q}, t)$ is ultimately too strong an assumption. The continuity equation

$$\frac{\partial}{\partial t}\rho(\boldsymbol{q}, t) = -i\boldsymbol{q} \cdot v(\boldsymbol{q}, t) = -iqv^{\parallel}(\boldsymbol{q}, t) \tag{5.9}$$

suggests that neglecting the influence of the longitudinal current ($v^{\parallel} = 0$) equals neglecting structural changes and ultimately translates to assuming an incompressible system, invalid in soft sphere systems. Furthermore, longitudinal modes should be included to capture some of the salient features of disordered systems at the jamming transition. For example, we discussed in Section 2.2.4 that stresses generally couple transverse and longitudinal modes, giving rise to non-affine displacements and enhancing the effective sound attenuation. Moreover, Section 2.3.1 discussed that non-affine responses are considered necessary for the critical dynamics as they supposedly explain the different scaling of the bulk and the shear modulus. Lastly, the athermal unjamming transition is ultimately nothing else than the system falling apart. This causes a characteristic undirected force propagation and, therefore, again, the coupling of longitudinal and transverse displacements. Besides such concerns, a purely transverse theory still has its merits, and may it only be because longitudinal modes can systematically be included.

The rest of this chapter discusses a purely transverse theory. The following section presents the derivation of the theory. A more general theory, including longitudinal displacements, is outlined in Appendix B. Discussing the critical dynamics of the entire model and comparing its prediction with experimental data is left for future work.

5.2 The construction of the theory

Generally speaking, the difference between the fluid and stable phase transpires in the distinctive behaviour of the stresses $\underline{\boldsymbol{\sigma}}$ for small perturbation $\boldsymbol{v}^{\mathrm{ex}}(\boldsymbol{q},t) \to 0$. While the system can relax in the fluid phase $\underline{\boldsymbol{\sigma}}(t \to \infty) = 0$, stresses stay finite in the jammed or stable phase $\underline{\boldsymbol{\sigma}}(t \to \infty) > 0$. Thus the system develops a finite yield stress σ^Y, which quantifies the minimal stress needed to plastically deform the system. Here, the system's response is elastic for sufficiently small perturbations. This transition from dissipative to elastic stresses can be captured by the Zwanzig-Mori formalism (Voigtmann, 2011). Furthermore, a Mode-Coupling Theory (MCT) approximation applied to the Zwanzig-Mori equations of motion is capable of predicting several aspects of the dynamics in the solidified state, *e.g.* the Boson-Peak (Götze and Mayr, 2000). Inspired by these successes, we employ the Zwanzig-Mori formalism in this section to construct a theory for the transverse current autocorrelation

$$\underline{\mathbf{K}}^{\perp}(\boldsymbol{q},t) = \frac{\int d\Gamma\ \boldsymbol{v}^{\perp}(\boldsymbol{q})\ e^{\Omega t}\ \boldsymbol{v}^{\perp}(-\boldsymbol{q})\ \Psi_{\mathrm{eq}}}{\frac{1}{(d-1)}\langle|\boldsymbol{v}^{\perp}(\boldsymbol{q})|^2\rangle}\ . \tag{5.10}$$

Equation (3.23) simplifies the matrix structure: $\underline{\mathbf{K}}^{\perp}(\boldsymbol{q},t) = \mathrm{K}_q^{\perp}(t)(\underline{\mathbf{1}} - \hat{\boldsymbol{q}}\hat{\boldsymbol{q}})$. Here, $\mathrm{K}_q^{\perp}(t) = \frac{1}{d-1}\mathrm{Tr}\{\underline{\mathbf{K}}^{\perp}(\boldsymbol{q},t)\}$ only depends on $q = |\boldsymbol{q}|$ and $\mathrm{Tr}[\cdot]$ denotes the trace of a matrix. Notably, Equation (5.10) corresponds to Equation (4.40) where the initial momenta are due to thermal motion and hence uniform, *i.e* $\ddot{F}^{(0)}_{k\gamma,j\beta} = \frac{k_BT}{m}\delta_{kj}\delta_{\gamma\beta}$. We exploit the Zwanzig-Mori formalism in the following to construct a closed theory for $\mathrm{K}_q^{\perp}$. As we will see, we will need several successive projections. We first express $\mathrm{K}_q^{\perp}$ in terms of a memory-kernel, which we can relate to the shear modulus.

5.2.1 The generalised shear modulus

As discussed in Section 5.1, our subspace of time-dependent distinguished variables is spanned only by the transverse current $\boldsymbol{v}^{\perp}$, since longitudinal modes and consequentially structural changes are generally neglected. Thus, we start with a single projection operator

$$P_1 = |\boldsymbol{v}^{\perp}(-\boldsymbol{q})\rangle \cdot \langle \boldsymbol{v}^{\perp}(\boldsymbol{q})| \, \frac{m}{Nk_BT} \, . \tag{5.11}$$

Here, the normalization is given by

$$\begin{aligned} &\langle v_{\alpha}(\boldsymbol{q}) v_{\beta}(-\boldsymbol{q})\rangle = \frac{Nk_BT}{m}\delta_{\alpha\beta} \\ &\Longrightarrow \langle |\boldsymbol{v}^{\perp}(\boldsymbol{q})|^2\rangle = (d-1)\frac{Nk_BT}{m} \, . \end{aligned} \tag{5.12}$$

This result is known as the equipartition theorem. Multiplying the operator-identity (3.30), from left and right with $\frac{m}{Nk_BT}\langle \boldsymbol{v}^{\perp}(\boldsymbol{q})|$ and $|\boldsymbol{v}^{\perp}(-\boldsymbol{q})\rangle$ respectively leads to

$$\left[\underline{\mathbf{1}}s - \frac{m}{Nk_BT}\langle \boldsymbol{v}^{\perp}(\boldsymbol{q})\Omega \boldsymbol{v}^{\perp}(-\boldsymbol{q})\rangle - \frac{m}{Nk_BT}\langle \boldsymbol{v}^{\perp}(\boldsymbol{q})\Omega \hat{R}_1(s)\Omega \boldsymbol{v}^{\perp}(-\boldsymbol{q})\rangle\right] \cdot \hat{\underline{\mathbf{K}}}^{\perp}(\boldsymbol{q},s) = \underline{\mathbf{1}} \, . \tag{5.13}$$

Here, the reduced resolvent, $\hat{R}_1(s) = Q_1[s-\Omega_1]^{-1}Q_1$ is defined by the reduced Klein-Kramers Operator $Q_1\Omega Q_1 \equiv \Omega_1$ with $Q_1 = 1 - P_1$. Rotational symmetry implies that the Equation $\hat{\mathrm{K}}_q^{\perp}(s)$ reduces to a simple scalar expression:

$$\hat{\mathrm{K}}_q^{\perp}(s) = \frac{1}{s + \xi + q^2\hat{\mathrm{G}}_q^{\perp}(s)} \, . \tag{5.14}$$

We are going to discuss the single occurring terms one by one. Essentially, all of the quantities have their origin in Netwon's second law:

$$m\dot{\boldsymbol{v}}(\boldsymbol{q}) = m\Omega^{\dagger}\boldsymbol{v} = \sum_{j=1}^{N}\left[\frac{-i\boldsymbol{q}\cdot\boldsymbol{p}_j}{m}\boldsymbol{p}_j - \boldsymbol{F}_j + \frac{\zeta_0}{m}\boldsymbol{p}_j\right]e^{-i\boldsymbol{q}\cdot\boldsymbol{r}_j} \, . \tag{5.15}$$

The right-hand side introduces the force fluctuations: The first two terms result from the kinetic and potential part of the stress tensor or rather its divergence $\boldsymbol{F}(\boldsymbol{q}) = -i\boldsymbol{q}\cdot\underline{\boldsymbol{\sigma}}(\boldsymbol{q})$

(Hansen and McDonald, 2009; Wajnryb *et al.*, 1995). Here, the stress tensor is the same as in Section 2.2.1 and Equation (2.7) but with the inclusion of the kinetic contribution. However, this inclusion is just formal as the kinetic part of the stress becomes neglectible for $T \to 0$. The third term $-\zeta_0 \boldsymbol{v}(\boldsymbol{q})$ results directly from the considered Langevin dynamics and the local friction. This term breaks momentum conservation and gives raise to the Langevin damping rate $\xi = \zeta_0/m$ in Equation (5.14). This term originates from the frequency matrix $\frac{m}{(d-1)Nk_BT} \langle [\Omega^\dagger v_\alpha^\perp(\boldsymbol{q})] v_\alpha^\perp(-\boldsymbol{q})| \rangle = -\xi$. Moreover, the force-force autocorrelation

$$\hat{\underline{\mathbf{G}}}^\perp(\boldsymbol{q}, s) = \hat{\mathrm{G}}_q^\perp(s)\ (\mathbf{1} - \hat{\boldsymbol{q}}\hat{\boldsymbol{q}}) = \frac{1}{Nmk_BTq^2} \langle \boldsymbol{F}^\perp(\boldsymbol{q}) \hat{R}_1(s)\ \boldsymbol{F}^\perp(-\boldsymbol{q}) \rangle\ . \tag{5.16}$$

defines the memory kernel. It is a generalized shear modulus that depends on time or frequency. Here, the dynamics of $\hat{\mathrm{G}}_q^\perp(t)$ is generated by the reduced resolvent $\hat{R}_1(s) = Q_1[s + Q_1 \Omega Q_1]^{-1} Q_1$. Writing down Equation (5.16), we used $\zeta_0 Q_1 \boldsymbol{v}^\perp(\boldsymbol{q}) = 0$ and $Q_1 \boldsymbol{F}^\perp = \boldsymbol{F}^\perp$. The first equality holds by construction and the second due to time-reversal symmetry. The generalized shear modulus[2] has concrete physical interpretations depending on the phases, jammed or unjammed.

Relation to the shear viscosity and the shear modulus: In order to substantiate the quantity $\hat{\mathrm{G}}_q^\perp(s)$ with physical meaning, we are going to discuss Equation (5.14) for spatially and timely slowly varying modes in the long time limit. This case corresponds to the *hydrodynamic limit* $q, s \to 0$. The fluid phase is defined by decaying stresses $\underline{\boldsymbol{\sigma}}(t \to \infty) = 0$. This implies the vanishing of the generalized shear modulus for long times $\mathrm{G}_q^\perp(t = \infty) = \lim_{s \to 0} s \hat{\mathrm{G}}_q^\perp(s)$. We will show in Section 5.4 that the hydrody-

[2]Noteable $\hat{\underline{\mathbf{G}}}^\perp(\boldsymbol{q}, s)$ becomes equal to the force autocorrelation function with the fully dynamic $\hat{R}(s)$ for $\boldsymbol{q} \to 0$ and finite s:

$$\hat{\underline{\boldsymbol{G}}}^\perp(\boldsymbol{q}, s) \underset{\boldsymbol{q} \to 0}{\longrightarrow} \frac{1}{Nmk_BTq^2} \langle \boldsymbol{F}^\perp(\boldsymbol{q}) \hat{R}(s)\ \boldsymbol{F}^\perp(-\boldsymbol{q}) \rangle$$

This follows from a second operator identity for the resolvent (Götze, 2009, Equation 2.59b)

$$\hat{R}(s) = \hat{R}_1(s) + [P_1 - \hat{R}_1(s)\Omega] P_1 \hat{R}(s) P_1 [P_1 - \Omega \hat{R}_1(s)]\ .$$

Multiplying with $\frac{1}{Nk_BTmq^2} \langle \boldsymbol{F}^\perp(\boldsymbol{q})|$ from the left and $|\boldsymbol{F}^\perp(-\boldsymbol{q})\rangle$ from the right gives

$$\frac{1}{Nmk_BTq^2} \langle \boldsymbol{F}^\perp(\boldsymbol{q}) \hat{R}(s)\ \boldsymbol{F}^\perp(-\boldsymbol{q}) \rangle = \hat{\underline{\mathbf{G}}}^\perp(\boldsymbol{q}, s) + q^2 \hat{\underline{\mathbf{G}}}^\perp(\boldsymbol{q}, s) \cdot \hat{\underline{\mathbf{K}}}^\perp(\boldsymbol{q}, s) \cdot \hat{\underline{\mathbf{G}}}^\perp(\boldsymbol{q}, s)\ .$$

The second term on the right hand side vanishes for $\boldsymbol{q} \to 0$ but finite s, which proofs the claim.

namic limit of the shear modulus stays finite

$$\lim_{\boldsymbol{q},s\to 0} \hat{\mathrm{G}}_q^{\perp}(s) \equiv \frac{\eta^{\perp}}{nm}\xi \; . \tag{5.17}$$

Here, $\eta^{\perp}$ defines the kinematic shear viscosity. To understand this interpretation, we transform $\hat{\mathrm{K}}_q^{\perp}(s)$ back to the time domain: Relying on the properties of the Laplace transform[3] and the initial condition $\mathrm{K}_q^{\perp}(t=0)=1$, we get for $t\to\infty$ the following linear differential equation for $\boldsymbol{q}\to 0$:

$$\lim_{t\to\infty} \dot{\mathrm{K}}_{q\to 0}^{\perp}(t) = -\lim_{t\to\infty} \xi\left(1+q^2\frac{\eta^{\perp}}{nm}\right)\mathrm{K}_{q\to 0}^{\perp}(t) \; , \tag{5.18}$$

which gives rise to a linearised and spatially Fourier-transformed Navier-Stokes Equation for an incompressible fluid with zero pressure (Hansen and McDonald, 2009, Chapter 8.3):

$$\lim_{t\to\infty} \dot{\boldsymbol{v}}^{\perp}(\boldsymbol{q}\to 0,t) = -\xi \lim_{t\to\infty}\left(1+q^2\frac{\eta^{\perp}}{nm}\right)\boldsymbol{v}^{\perp}(\boldsymbol{q}\to 0,t) \; . \tag{5.19}$$

Thus, our equations predict a laminar flow in the response to a sufficiently weak perturbation in the unjammed phase. This result also shows that $\eta^{\perp}$ is indeed the kinematic shear viscosity.

However, stresses do not decay in the jammed phase. Here, the generalised shear modulus develops a longtime limit $\lim_{s,q\to 0} s\hat{\mathrm{G}}_q^{\perp}(s) = (v_0^{\perp})^2$. The inverse Laplace transformation of $\hat{\mathrm{K}}_q^{\perp}(s)/s$ gives with the inital conditions $\mathrm{K}_q^{\perp}(t=0)=1$ and $\dot{\mathrm{K}}_q^{\perp}(t=0)=-\xi$:

$$\lim_{t\to\infty} \ddot{\mathrm{K}}_{q\to 0}^{\perp}(t) = -\lim_{t\to\infty}\left((qv_0^{\perp})^2\mathrm{K}_{q\to 0}^{\perp}(t) - \xi\dot{\mathrm{K}}_{q\to 0}^{\perp}\right) \; . \tag{5.20}$$

This results gives rise to the interpretation of $(v_0^{\perp})^2$ as the shear modulus and the idea that the system can be regarded as a stable elastic medium in the hydrodynamic limit $\boldsymbol{q}, s\to 0$. We show in Section 5.3 that our equations predict such non-decaying elastic response in the jammed phase. The considerations above suggest, that the shear modulus G introduced in Section 2.2.4 equals the hydrodynamic limit of the

[3]The properties of the Laplace transform are enlisted in Appendix G

generlaized shear modulus $\lim_{q,s\to 0} sG_q^{\perp}(s)$. Similarly, the hydrodynamic bulk modulus B can be obtained from the autocorrelation function of the longitudinal velocities.

While the long time behaviour of $\mathrm{K}_q(t)$ highly depends on the phase, our equations always predict elastic responses in the short time limit. They are quantified by an instantaneous modulus $(c_q^{\perp})^2$, which we will discuss in the next paragraph.

The instantaneous modulus: The short time or zero frequency limit $\mathrm{G}_q^{\perp}(t=0) = \lim_{s\to\infty} s\hat{\mathrm{G}}_q^{\perp}(s)$ of the generalized shear modulus defines the instantaneous modulus. This already hints at short-time oscillations with $(qc_q^{\perp})^2 \equiv q^2\mathrm{G}_q^{\perp}(t=0)$ being the associated dispersion relation. This follows from an equivalent consideration to Equation (5.20) but only for the short time limit $t \to 0$ instead of the long time limit.

Hereinafter, we derive an expression for $(c_q^{\perp})^2$ in the athermal limit $T \to 0$. We rely on a useful property of the Boltzmann distribution $\Psi_{\mathrm{eq}} \propto \exp[-\beta H]$: For any dynamical variable A holds $\int d\Gamma \boldsymbol{F}_j A\Psi_{\mathrm{eq}} = -k_BT \int d\Gamma \Psi_{\mathrm{eq}} \nabla_j A$. With this, we find

$$
\begin{aligned}
(d-1)Nmk_BTq^2(c_q^{\perp})^2 \overset{T\to 0}{\longrightarrow} \mathrm{Tr}\left[\langle \sum_{j,l} \boldsymbol{F}_j e^{-i\boldsymbol{q}\cdot\boldsymbol{r}_j} \cdot [\underline{\mathbf{1}} - \hat{\boldsymbol{q}}\hat{\boldsymbol{q}}][\underline{\mathbf{1}} - \hat{\boldsymbol{q}}\hat{\boldsymbol{q}}] \cdot \boldsymbol{F}_l e^{i\boldsymbol{q}\cdot\boldsymbol{r}_l}\rangle\right] \\
= -k_BT \langle \sum_{j,l} \frac{\partial}{\partial \boldsymbol{r}_j} e^{-i\boldsymbol{q}\cdot\boldsymbol{r}_j} \cdot [\underline{\mathbf{1}} - \hat{\boldsymbol{q}}\hat{\boldsymbol{q}}] \cdot \boldsymbol{F}_l e^{i\boldsymbol{q}\cdot\boldsymbol{r}_l}\rangle \\
= -k_BT \langle \sum_{j,l} e^{-i\boldsymbol{q}\cdot\boldsymbol{r}_j} e^{i\boldsymbol{q}\cdot\boldsymbol{r}_l} \Big(\frac{\partial}{\partial \boldsymbol{r}_j} \cdot [\underline{\mathbf{1}} - \hat{\boldsymbol{q}}\hat{\boldsymbol{q}}] \cdot \boldsymbol{F}_l \Big)\rangle \\
= k_BT \langle \sum_{j,l} e^{-i\boldsymbol{q}\cdot(\boldsymbol{r}_j - \boldsymbol{r}_l)} \Big(\frac{\partial}{\partial \boldsymbol{r}_j} \cdot [\underline{\mathbf{1}} - \hat{\boldsymbol{q}}\hat{\boldsymbol{q}}] \cdot \sum_{m\neq l} \frac{\partial}{\partial \boldsymbol{r}_l} U(\boldsymbol{r}_l - \boldsymbol{r}_m) \Big)\rangle \ .
\end{aligned}
\tag{5.21}
$$

We have neglected any kinetic contributions as they all vanish for $T \to 0$. For any pair potential or- even more general- for any function f holds

$$
f(\boldsymbol{r}_i - \boldsymbol{r}_j) = \frac{1}{V} \sum_{\boldsymbol{\kappa}} \int d^d\boldsymbol{r} f(\boldsymbol{r}) e^{i\boldsymbol{\kappa}\cdot[\boldsymbol{r} - (\boldsymbol{r}_i - \boldsymbol{r}_j)]} \ , \tag{5.22}
$$

where the sum over all Fouriermodes is to be understood as the discretized Riemann Integral $\int \frac{d^d\kappa}{(2\pi)^d} \to \frac{1}{V}\sum_{\kappa}$. This notation results from the idea that we ultimately deal with

a finite but large volume $V = L^d$. The trick (5.22) allows expressing the instantaneous modulus as a functional of the structure and the pair-interaction potential alone:

$$\begin{aligned}(c_q^{\perp})^2 &= \frac{1}{V}\sum_{\kappa}\langle\sum_{j,l\neq j}\frac{1-e^{-i\boldsymbol{q}\cdot(\boldsymbol{r}_j-\boldsymbol{r}_l)}}{(d-1)Nmq^2}\frac{\partial}{\partial\boldsymbol{r}_l}\cdot[\underline{\mathbf{1}}-\hat{\boldsymbol{q}}\hat{\boldsymbol{q}}]\cdot\int d^d\boldsymbol{r}\frac{\partial}{\partial\boldsymbol{r}_l}U(r)e^{i\boldsymbol{\kappa}\cdot[\boldsymbol{r}-(\boldsymbol{r}_l-\boldsymbol{r}_j)|}\rangle \\ &= \frac{1}{V}\sum_{\boldsymbol{\kappa}}\int\frac{d^d\boldsymbol{r}e^{i\boldsymbol{\kappa}\cdot\boldsymbol{r}}}{q^2(d-1)Nm}\langle\sum_{j,l\neq j}e^{-i\boldsymbol{\kappa}\cdot(\boldsymbol{r}_j-\boldsymbol{r}_l)}-e^{-i(\boldsymbol{q}-\boldsymbol{\kappa})\cdot(\boldsymbol{r}_j-\boldsymbol{r}_l)}\Big)\rangle\,\nabla^{\perp,\boldsymbol{q}}\cdot\nabla U(r) \\ &= \frac{1}{V}\sum_{\boldsymbol{\kappa}}\int d^d\boldsymbol{r}e^{i\boldsymbol{\kappa}\cdot\boldsymbol{r}}\frac{S_\kappa+\langle\rho(\boldsymbol{\kappa})\rangle^2}{(d-1)m}\frac{1-e^{-i\boldsymbol{q}\cdot\boldsymbol{r}}}{q^2}\nabla\cdot[\underline{\mathbf{1}}-\hat{\boldsymbol{q}}\hat{\boldsymbol{q}}]\cdot\nabla U(r)\,.\end{aligned} \tag{5.23}$$

Here, we have used the abbreviation $\nabla^{\perp,\boldsymbol{q}}\equiv\nabla\cdot[\underline{\mathbf{1}}-\hat{\boldsymbol{q}}\hat{\boldsymbol{q}}]$ The structure factor S_κ was defined in Equation (4.3) as $t\to 0$ limit of the dynamic structure factor. Notably, the sum in Equation (5.23) can safely be extended to include the contribution $j=l$ as the two contributions in the average cancel each other in this particular case. Importantly, the contribution of the average $\langle\rho(\boldsymbol{k})\rangle$ is non-trivial as its value sensitively depends on the phases. In the unstable phase, translational invariance implies $\langle\rho(\boldsymbol{\kappa})\rangle = N\delta_{\boldsymbol{\kappa},0}$. Nevertheless, this term does not contribute to the instantaneous modulus due to the additional rotational invariance. This becomes apparent, if the integral over the Fourier-mode is performed in spherical coordinates. However, in the stable phase, the system develops a reference frame $\{\boldsymbol{R}\}_{i=1}^N$, which suggest $\langle\rho(\boldsymbol{\kappa})\rangle = \sum_{i=1}^N e^{-i\boldsymbol{\kappa}\cdot\boldsymbol{R}_i}$. However, this reference frame is not unique as it depends on the preparation protocol. This dependence on the phase suggests that it is more convenient to express the instantaneous modulus via the pair-correlation function $g(r) = \frac{1}{nN}\langle\sum_{j,l\neq j}\delta(\boldsymbol{r}-(\boldsymbol{r}_l-\boldsymbol{r}_j)\rangle$ as the resulting expression is valid in both phases, eventhough the pair-correlation function again becomes non-unique in the jammed state. More concretely, instead of Equation (5.22), we can also use

$$f(\boldsymbol{r}_i-\boldsymbol{r}_j) = \int d^d\boldsymbol{r}f(\boldsymbol{r})\delta\Big(\boldsymbol{r}-(\boldsymbol{r}_i-\boldsymbol{r}_j)\Big)\,, \tag{5.24}$$

which leads to

$$
\begin{aligned}
(c_q^{\perp})^2 &= \frac{1}{(d-1)Nm}\int d^d\boldsymbol{r}\left\langle\sum_{l\neq m}\delta\Big(\boldsymbol{r}-(\boldsymbol{r}_l-\boldsymbol{r}_m)\Big)\right\rangle\frac{1-e^{i\boldsymbol{q}\cdot\boldsymbol{r}}}{q^2}\nabla\cdot[\underline{\mathbf{1}}-\hat{\boldsymbol{q}}\hat{\boldsymbol{q}}]\cdot\nabla\, U(r)\\
&= \frac{n}{(d-1)m}\int d^d\boldsymbol{r}\, g(r)\frac{1-e^{i\boldsymbol{q}\cdot\boldsymbol{r}}}{q^2}\nabla\cdot[\underline{\mathbf{1}}-\hat{\boldsymbol{q}}\hat{\boldsymbol{q}}]\cdot\nabla\, U(r)\ .
\end{aligned}
\tag{5.25}
$$

This last expression indicate that $(c_q^{\perp})^2$ scales with n. This could have been anticipated as the forces arise from pair interactions. Additionally note, that $c_q^{\perp}$ has a finite value for $T \to 0$. Later on, we will see that $(qc_q^{\perp})^2$ characterizes high-frequency modes and the dispersion relation in an infinitely dense system $n \to \infty$. Here, the elastic, continuous medium approximation becomes exact. Interactions with the disorder or scattering events renormalized the instantaneous modulus. That is why we call $(qc_q^{\perp})^2$ the *bare dispersion relation*. After considering the long- and short time limits of Equation (5.14), we now proceed to discussing potential approximations of $\hat{\mathrm{G}}_q^{\perp}(s)$.

Approximating the generalized viscosity: We have shifted the task from developing a theory for $\hat{\mathrm{K}}_q^{\perp}$ to finding an expression for the generalized shear modulus $\hat{\mathrm{G}}_q^{\perp}$. In the past, a generalized Maxwell model

$$
\hat{\mathrm{G}}_q^{\perp}(s) \approx \hat{\mathrm{G}}^{gM}(s) = \frac{G_\infty}{s+\frac{1}{\tau}},
\tag{5.26}
$$

has been used to describe the slowing down of the dynamics when approaching the glass transition (Maier *et al.*, 2018; Vogel *et al.*, 2019). Here, the phenomenology of increasing viscosity and the approach to solidification is modeled by a single relaxation time τ. In the solid-state holds $\tau = \infty$. However, such an approximation is not available for us as we strive to express $\hat{\mathrm{G}}_q^{\perp}(s)$ again in terms of $\hat{\mathrm{K}}_q^{\perp}(s)$ to get closure. Furthermore, we discussed in Section 2.3.1 the emergence of a diverging length scale when approaching the unjamming transition. This indicates spatially varying stresses in the system. Hence, we can not ignore the wavevector dependence of $\hat{\mathrm{G}}_q^{\perp}(s)$. In the context of computer simulations of plastic flow in a driven glassy dispersion in confinement and under shear,a spatially varying fluidity $\hat{\mathrm{W}}_q$ has been introduced (Goyon *et al.*, 2008). The idea was to quantify the response of the local stresses to the external velocity field $\hat{\mathrm{W}}_q = \frac{v^{\mathrm{ex}}}{\sigma_q}$. Here, the long-wavelength limit of the fluidity is given by the inverse vis-

cosity, hence specifying the fluidity of the bulk. The idea of a spatially varying fluidity was also tested experimentally (Jop *et al.*, 2012). Looking at the generalized Maxwell model in Equation (5.26), this corresponds to generalizing $1/\tau$ to a response kernel. In the next section. we will again use the Zwanzig-Mori formalism to write down the equation of motion for $\hat{\mathrm{G}}_q^{\perp}(s)$, and by doing so, we find an expression for $\hat{\mathrm{W}}_q(s)$.

5.2.2 The fluidity

To elaborate on the Zwanzig-Mori equation for the generalized shear modulus, we first introduce a second projector

$$P_2 = \frac{|\boldsymbol{F}^{\perp}(-\boldsymbol{q})\rangle \cdot \langle \boldsymbol{F}^{\perp}(\boldsymbol{q})|}{\frac{1}{d-1}\langle |\boldsymbol{F}^{\perp}(\boldsymbol{q})|^2\rangle} \ . \tag{5.27}$$

The normalization is given by the instantaneous modulus

$$\frac{1}{d-1}\mathrm{Tr}\Big[\ \langle \boldsymbol{F}^{\perp}(\boldsymbol{q})\ \boldsymbol{F}^{\perp}(-\boldsymbol{q})\rangle\ \Big] = (Nmk_BT)\ (qc_q^{\perp})^2 \ . \tag{5.28}$$

Note again that the fluctuating force $\boldsymbol{F}(\boldsymbol{q})$ has zero overlap with the current $\boldsymbol{v}(\boldsymbol{q})$ due to different time-inversion parity[4]. This leads to the orthogonality of the two projection operators $P_2P_1 = 0$. The adjusted operator identity (3.30) reads:

$$\Big[s - P_2\Omega_1P_2 - P_2\Omega_1\hat{R}_2(s)\Omega_1P_2\Big]P_2\hat{R}_1(s)P_2 = P_2 \tag{5.29}$$

Here, the velocity and the fluctuating forces are both constants of motion as the second reduced dynamics is given by $\hat{R}_2(s) = Q_2\frac{1}{s-\Omega_2}Q_2$, with $\Omega_2 = Q_2\,\Omega\,Q_2$ and the orthogonal projection $Q_2 = 1 - P_1 - P_2$. Multiplying Equation (5.29) with $\frac{1}{Nmk_BTq^2}\ \langle \boldsymbol{F}^{\perp}(\boldsymbol{q})|$ from the left and $|\boldsymbol{F}^{\perp}(-\boldsymbol{q})\rangle$ from the right, leads to the Zwanzig-Mori Equation for the generalised shear modulus. It expresses $\hat{\underline{\mathbf{G}}}^{\perp}(\boldsymbol{q},s) = \hat{\mathrm{G}}_q^{\perp}(s)[\underline{\mathbf{1}} - \hat{\boldsymbol{q}}\hat{\boldsymbol{q}}]$ by its instantaneous

[4]At this point, we could have additionally projected out states linearly in local density fluctuation $\delta\rho(\boldsymbol{r})$. However, the overlap $\langle \boldsymbol{F}^{\perp}(\boldsymbol{q})\delta\rho(-\boldsymbol{q})\rangle$ vanishes with the temperature. Nevertheless, this becomes a more complex question at finite temperatures, where $\delta\rho(\boldsymbol{q},t)$ has to be included in the set of distinguished variables as it is generally a slow variable as well.

value $(c_q^\perp)^2$ and the time-derivatives of the stresses:

$$\hat{\mathrm{G}}_q^\perp(s) = \frac{(c_q^\perp)^2}{s + \gamma_q^\perp + (c_q^\perp)^2\,\hat{\mathrm{W}}_q^\perp(s)}\,, \tag{5.30}$$

$$\begin{aligned}\underline{\hat{\mathbf{W}}}^\perp(\boldsymbol{q},s) &= \hat{\mathrm{W}}_q^\perp(s)\;(\mathbf{1}-\hat{\boldsymbol{q}}\hat{\boldsymbol{q}}) \\ &= \frac{-1}{Nmk_BTq^2(c_q^\perp)^4}\,\langle \boldsymbol{F}^\perp(\boldsymbol{q})\Omega_1\,\hat{R}_2(s)\,\Omega_1\boldsymbol{F}^\perp(-\boldsymbol{q})\rangle\;. \end{aligned}\tag{5.31}$$

The second Zwanzig-Mori step also introduces an instantaneous damping rate via the frequency matrix. In the next paragraph, we analyze $\gamma_q^\perp$ and show that it vanishes in the athermal limit $T \to 0$.

The instantaneous damping coefficient $\gamma^\perp$: To make the matrix multiplications more transparent, we use the index notation and the sum convention in this paragraph. Additionally using $P_2Q_1 = P_2$ leads to an exact expression for the instantaneous damping:

$$\begin{aligned}\gamma_q^\perp &= -\frac{(\delta_{\tau\beta}-\hat{q}_\tau\hat{q}_\beta)(\delta_{\rho\beta}-\hat{q}_\rho\hat{q}_\beta)}{(d-1)Nmk_BT(qc_q^\perp)^2}\,\langle q_\alpha[\Omega^\dagger\sigma_{\alpha\tau}(\boldsymbol{q})]q_\eta\sigma_{\eta\rho}(-\boldsymbol{q})\rangle \\ &= -2\frac{\zeta_0(\delta_{\tau\rho}-\hat{q}_\tau\hat{q}_\rho)}{(d-1)Nmk_BT(qc_q^\perp)^2}\left\langle q_\alpha\sum_j\Big[\frac{k_BT}{m}\delta_{\alpha\tau}-\frac{p_j^\alpha p_j^\tau}{m^2}\Big]e^{-i\boldsymbol{q}\cdot\boldsymbol{r}_j}q_\eta\sigma_{\eta\rho}(-\boldsymbol{q})\right\rangle = \ldots\end{aligned}\tag{5.32}$$

Here, we have relied on the invariance under time inversion. Thus, we only had to consider the part of Ω which conserves the time inversion partiy. The potential part of the second stress term $q_\eta\sigma_{\eta\rho}$ does not contribute due to the transverse spatial projection $(\delta_{\tau\rho}-\hat{q}_\tau\hat{q}_\rho)$. This follows from the identity $\int d\Gamma F_iA\Psi_{\mathrm{eq}} = -k_BT\int d\Gamma\Psi_{\mathrm{eq}}\nabla_iA$. The

remaining part of the calculation involves more basic maniplulations:

$$\begin{aligned}
... &= -2\frac{\zeta_0\hat{q}_\alpha\hat{q}_\eta(\delta_{\tau\rho}-\hat{q}_\tau\hat{q}_\rho)}{(d-1)Nmk_BT(c_q^\perp)^2}\left\langle\sum_{ij}\left[\frac{k_BT}{m}\frac{p_i^\eta p_i^\rho}{m}\delta_{\alpha\tau}-\frac{p_j^\alpha p_j^\tau p_i^\eta p_i^\rho}{m^3}\right]e^{-i\boldsymbol{q}\cdot(\boldsymbol{r}_j-\boldsymbol{r}_i)}\right\rangle \\
&= 2\frac{\zeta_0\hat{q}_\alpha\hat{q}_\eta(\delta_{\tau\rho}-\hat{q}_\tau\hat{q}_\rho)}{(d-1)Nmk_BT(c_q^\perp)^2}\left(\left\langle\sum_i\frac{p_i^\alpha p_i^\tau p_i^\eta p_i^\rho}{m^3}\right\rangle - N\frac{(k_BT)^2}{m}\delta_{\alpha\tau}\delta_{\eta\rho}\right) \\
&= 2\frac{\zeta_0\hat{q}_\alpha\hat{q}_\eta(\delta_{\tau\rho}-\hat{q}_\tau\hat{q}_\rho)}{(d-1)Nm(c_q^\perp)^2}\left\langle\sum_i\frac{p_i^\eta p_i^\tau\delta_{\alpha\rho}+p_i^\eta p_i^\rho\delta_{\alpha\tau}+p_i^\tau p_i^\rho\delta_{\eta\alpha}}{m^2}\right\rangle \\
&= 2k_BT\frac{\xi\hat{q}_\alpha\hat{q}_\eta(\delta_{\tau\rho}-\hat{q}_\tau\hat{q}_\rho)}{(d-1)m(c_q^\perp)^2}\Big(\delta_{\eta\tau}\delta_{\alpha\rho}+\delta_{\alpha\tau}\delta_{\eta\rho}+\delta_{\rho\tau}\delta_{\eta\alpha}\Big) \\
&= 2\frac{k_BT\xi}{m(d-1)(c_q^\perp)^2}(\delta_{\tau\rho}-\hat{q}_\tau\hat{q}_\rho)\Big(2\hat{q}_\tau\hat{q}_\rho+\delta_{\rho\tau}\Big) \\
&= 2\frac{k_BT\xi}{m(d-1)(c_q^\perp)^2}(2+d-2-1) = 2\frac{k_BT\xi}{m(c_q^\perp)^2}\ .
\end{aligned} \tag{5.33}$$

Since this damping rate vanishes with the temperature, we will not include $\gamma_q^\perp$ in the following equations.

At $T=0$, the generalized viscosity is a function of the fluidity alone, as $\hat{\mathrm{W}}_q^\perp$ indeed has a finite zero-temperature limit. As we can see from Equation (5.30), the fluidity vanishes for high frequencies $s\to\infty$. Together with Equation (5.14), this already hints at the presence and possibility of vibration, as $\hat{\chi}_q^\perp(s) = -\frac{1}{s}\hat{\mathrm{K}}_q^\perp(s)$ features a sound pole for high frequencies, even in the fluid phase. These vibrations are characterized by the bare dispersion relation $q^2(c_q^\perp)^2$. However, in the unstable phase, these modes will decay over time as the restoring forces vanish. But they persist in the jammed or solid phase. We have already discussed this in the context of Equation (5.19) and Equation (5.20). Next, we look for closure. The idea is to search for an approximation, which allows writing the fluidity as a functional of the current $\hat{\mathrm{W}}^\perp = \hat{\mathrm{W}}^\perp[\hat{\mathrm{K}}^\perp]$.

The first steps to closure: First of all, we write the fluctuating forces again as the divergence of the stress $\boldsymbol{F}(\boldsymbol{q}) = -i\boldsymbol{q} \cdot \underline{\boldsymbol{\sigma}}(\boldsymbol{q})$. Kinetic contributions to the stresses are neglected as they only lead to contributions vanishing with the temperature. As discussed in Section (2.2.1), only the potential part of the stresses remains:

$$|\underline{\boldsymbol{\sigma}}(\boldsymbol{q})\rangle \approx |\underline{\boldsymbol{\sigma}}(\boldsymbol{q})^{(p)}\rangle = \left| \frac{1}{2} \sum_{j,k} \frac{\boldsymbol{r}_{jk}\boldsymbol{r}_{jk}}{r_{jk}} \left(\frac{\partial}{\partial r_{jk}} U(\{\boldsymbol{r}\}_{i=1}^{N}) \right) \frac{1 - e^{-\boldsymbol{q}\cdot\boldsymbol{r}_{jk}}}{i\boldsymbol{q} \cdot \boldsymbol{r}_{jk}} e^{i\boldsymbol{q}\cdot\boldsymbol{r}_j} \right\rangle \ . \tag{5.34}$$

This is the Fourier transformed Irving-Kirkwood tensor introduced in Equation (2.7) (Maier, 2018). Our proceeding is motivated by the observation that for sufficiently smooth potential, the potential part of the stress tensor $\underline{\boldsymbol{\sigma}}^{(p)}$ and hence its time derivative can be expressed via a pair of density fields $|\rho\rho\rangle$ or a pair density and current $|\rho\boldsymbol{v}\rangle$ respectively (Schmid, 2011):

$$\begin{aligned} |\sigma_{\alpha\beta}^{(p)}(\boldsymbol{q})\rangle &= \frac{1}{V} \sum_{\boldsymbol{\kappa}} X_{\alpha\beta}(\boldsymbol{\kappa}, \boldsymbol{q}) \, |\rho(\boldsymbol{q} - \boldsymbol{\kappa})\rho(\boldsymbol{\kappa})\rangle \ , \\ |\dot{\sigma}_{\alpha\beta}^{(p)}(\boldsymbol{q})\rangle &= \frac{-2i}{V} \sum_{\boldsymbol{\kappa}} \mathrm{Re}\{X_{\alpha\beta}(\boldsymbol{\kappa}, \boldsymbol{q})\} \, |\rho(\boldsymbol{q} - \boldsymbol{\kappa})(\kappa_\eta v_\eta(\boldsymbol{\kappa}))\rangle \end{aligned} \tag{5.35}$$

This relation is obtained by applying the identity $f(\boldsymbol{r}_j - \boldsymbol{r}_k) = \int d^d\boldsymbol{r} f(\boldsymbol{r})\delta(\boldsymbol{r} - \boldsymbol{r}_{jk})$ to Equation (5.34) and then by expressing the δ– distribution via its Fourier transformation. The weights $X_{\alpha\beta}(\boldsymbol{\kappa}, \boldsymbol{q}) = \frac{1}{2} \int d^d\boldsymbol{r} e^{i\boldsymbol{\kappa}\cdot\boldsymbol{r}} \frac{r_\alpha r_\beta}{r} U'(r) \frac{1 - e^{-i\boldsymbol{q}\cdot\boldsymbol{r}}}{i\boldsymbol{q}\cdot\boldsymbol{r}}$ stay finite at the origin $X_{\alpha\beta}(0, 0) = \frac{1}{2} \int d\boldsymbol{r} \frac{r_\alpha r_\beta}{r} U'(r) \propto \delta_{\alpha\beta}$. The second term in Equation (5.35) follows from $\underline{\boldsymbol{X}}(\boldsymbol{\kappa}, \boldsymbol{q}) = \underline{\boldsymbol{X}}^*(\boldsymbol{q} - \boldsymbol{\kappa}, \boldsymbol{q})$. As the notation in Equation (5.35) suggests, the weights do not depend on any phase space variable, which is why we can pull them out of the state vector. Here, we introduced the abbreviation $U'(r) = \partial_r U(r)$. The relation (5.35), even though not valid, for example, for hard spheres, suggests projecting the time derivative of the stress on $|\delta\rho\boldsymbol{v}\rangle$. Importantly, $\langle\dot{\sigma}_{\alpha\beta}^{(p)}(\boldsymbol{q})|$ has a finite overlap with both the longitudinal and the transverse current and hence also with the product state of current and density. We can calculate the overlap explicitly using the relation (5.35). We again

employ Einstein's sum notation, to make the matrix multiplications transparent:

$$\begin{aligned}
&\langle \dot{\sigma}^{(p)}_{\alpha\beta}(\boldsymbol{q})\delta\rho(\boldsymbol{k}-\boldsymbol{q})v_\gamma(-\boldsymbol{k})\rangle \\
&= -\frac{2i}{V}\sum_{\boldsymbol{\kappa}} \kappa_\eta \,\mathrm{Re}\{X_{\alpha\beta}(\boldsymbol{\kappa},\boldsymbol{q})\}\Big(\langle \rho(\boldsymbol{q}-\boldsymbol{\kappa})v_\eta(\boldsymbol{\kappa})v^\perp_\gamma(-\boldsymbol{k})\delta\rho(\boldsymbol{k}-\boldsymbol{q})\rangle \\
&\quad + \langle \rho(\boldsymbol{q}-\boldsymbol{\kappa})v_\eta(\boldsymbol{\kappa})v^\parallel_\gamma(-\boldsymbol{k})\delta\rho(\boldsymbol{k}-\boldsymbol{q})\rangle \Big) \\
&= -2i\frac{k_BT}{m}\sum_{\boldsymbol{\kappa}} \kappa_\zeta \,\mathrm{Re}\{X_{\alpha\beta}(\boldsymbol{\kappa},\boldsymbol{q})\}\Big[(\delta_{\gamma\zeta}-\hat{k}_\gamma\hat{k}_\zeta)\,\langle \rho(\boldsymbol{\kappa}-\boldsymbol{k})\rho(\boldsymbol{q}-\boldsymbol{\kappa})\delta\rho(\boldsymbol{k}-\boldsymbol{q})\rangle \\
&\quad + \hat{k}_\gamma\hat{k}_\zeta\,\langle \rho(\boldsymbol{\kappa}-\boldsymbol{k})\rho(\boldsymbol{q}-\boldsymbol{\kappa})\delta\rho(\boldsymbol{k}-\boldsymbol{q})\rangle\Big]\,.
\end{aligned} \tag{5.36}$$

Since their is no vectorial dependency on $\boldsymbol{q}$, both the overlaps of $\langle\dot{\sigma}^{(p)}(\boldsymbol{q})|\cdot(\underline{\mathbf{1}}-\hat{\boldsymbol{q}}\hat{\boldsymbol{q}})$ with $|\delta\rho(\boldsymbol{k}-\boldsymbol{q})\boldsymbol{v}^\parallel(\boldsymbol{k})\rangle$ and $|\delta\rho(\boldsymbol{k}-\boldsymbol{q})\boldsymbol{v}^\perp(\boldsymbol{k})\rangle$ are non-zero. Thus, the transverse part of the stress has a finite overlap with the longitudinal current. Remembering our discussion of Section 2.2.4, this stems from the fact that stresses couple longitudinal and transverse modes. Since the mediation through density fluctuation leads to a coupling of transverse and longitudinal velocities, our theory so far and the Zwanzig-Mori formalism in general, are therefore well attuned to pick up on the consequential non-affine displacements. However, hereinafter, we neglect the coupling to the longitudinal modes and discard the second term in the brackets in (5.36). This simplification is in accordance with our assumption that the transverse modes alone are sufficient to capture the salient features of amorphous solids. However, we saw in Chapter 2 that this assumption is not valid close to unjamming and that non-affine displacements are actually of qualitative importance. The only honest reason to neglect the overlap $|\delta\rho\boldsymbol{v}^\parallel\rangle$ is the consequential simplification of the theory as it leaves us with just one field, namely the transverse current. All of this leads to the next projector:

$$P_3 = \sum_{\boldsymbol{k}} \frac{|\boldsymbol{v}^\perp(-\boldsymbol{k})\delta\varrho(\boldsymbol{k}-\boldsymbol{q})\rangle\cdot\langle\boldsymbol{v}^\perp(\boldsymbol{k})\delta\varrho(\boldsymbol{q}-\boldsymbol{k})|}{N^2 S_{|\boldsymbol{q}-\boldsymbol{k}|}\frac{k_BT}{m}}\,. \tag{5.37}$$

and the consequential approximation

$$\begin{aligned}\underline{\hat{\mathbf{W}}}^{\perp}(\boldsymbol{q},s) &= -\frac{\langle \boldsymbol{F}^{\perp}(\boldsymbol{q})\Omega_1\,\hat{R}_2(s)\,\Omega_1\boldsymbol{F}^{\perp}(-\boldsymbol{q})\rangle}{Nmk_BTq^2(c_q^{\perp})^4} \\ &\approx -\frac{\langle \boldsymbol{F}^{\perp}(\boldsymbol{q})\Omega_1\,Q_2\,P_3\,\hat{R}_2(s)\,P_3\,Q_2\,\Omega_1\boldsymbol{F}^{\perp}(-\boldsymbol{q})\rangle}{Nmk_BTq^2(c_q^{\perp})^4}\ .\end{aligned} \tag{5.38}$$

The projection P_3 introduces the vertex

$$\underline{\boldsymbol{V}}_{\boldsymbol{q},\boldsymbol{k}} = -\frac{1}{Nk_BTq(c_q^{\perp})^2\,S_{|\boldsymbol{q}-\boldsymbol{k}|}}\ \langle \boldsymbol{F}^{\perp}(\boldsymbol{q})\Omega_1 Q_2\delta\rho(\boldsymbol{k}-\boldsymbol{q})\boldsymbol{v}^{\perp}(-\boldsymbol{k})\rangle\ , \tag{5.39}$$

and motivates expressing the fluidity with a frequency-dependent retarded renormalized vertex

$$\hat{\mathrm{W}}_q^{\perp}(s) = \frac{1}{(d-1)}\,\mathrm{Tr}\left\{\ \frac{1}{N}\sum_{\boldsymbol{k}}\ \underline{\boldsymbol{V}}_{\boldsymbol{q},\boldsymbol{k}}\cdot\underline{\hat{\boldsymbol{\mathcal{V}}}}_{\boldsymbol{q},\boldsymbol{k}}(s)\ \right\} = \frac{1}{N}\sum_{\boldsymbol{k}}\ \underline{\boldsymbol{V}}_{\boldsymbol{q},\boldsymbol{k}}\ :\ \underline{\hat{\boldsymbol{\mathcal{V}}}}_{\boldsymbol{k},\boldsymbol{q}}(s) \tag{5.40}$$

with

$$\underline{\hat{\boldsymbol{\mathcal{V}}}}_{\boldsymbol{k},\boldsymbol{q}}(s) = \sum_{\boldsymbol{p}}\frac{m}{N^2k_BT}\,\langle \boldsymbol{v}^{\perp}(\boldsymbol{k})\delta\rho(\boldsymbol{q}-\boldsymbol{k})\hat{R}_2(s)\,\delta\rho(\boldsymbol{p}-\boldsymbol{q})\boldsymbol{v}^{\perp}(-\boldsymbol{p})\rangle\cdot\underline{\boldsymbol{V}}^{\dagger}_{\boldsymbol{p},\boldsymbol{q}}\ . \tag{5.41}$$

Here, we have introduced the operation " : ", which connects two second rang tensors and renders a scalar via the formula $\underline{\boldsymbol{A}} : \underline{\boldsymbol{B}} = \frac{1}{d-1}\mathrm{Tr}\big\{\underline{\boldsymbol{A}}\cdot\underline{\boldsymbol{B}}\big\}$.

Performing the calculation in real space as done in Appendix B reveals that the fluidity $\mathrm{W}_q^{\perp}(t)$ is constituted by the scattering events of the transverse momentum excitations with the frozen-in amorphous structure. This allows a diagrammatic interpretation of the fluidity, presented in Section 5.2.5 and in Section B.5. While the topology of the scattering events is encoded in the renormalized vertex $\underline{\hat{\boldsymbol{\mathcal{V}}}}_{\boldsymbol{q},\boldsymbol{k}}(s)$, the so-called *bare vertex* $\underline{\boldsymbol{V}}_{\boldsymbol{q},\boldsymbol{k}}$ determines the amplitude of a single scattering event. Importantly all quantities above, including the vertex $\underline{\boldsymbol{V}}_{\boldsymbol{q},\boldsymbol{k}}$ stay finite for $N,V\to\infty$ and $T\to 0$. A detailed evaluation of the vertex and its properties is given in Appendix D. Here, we mention a few of its properties:

$$\underline{\boldsymbol{V}}^{\dagger}_{\boldsymbol{k},\boldsymbol{q}} = (\underline{\boldsymbol{V}}_{-\boldsymbol{q},-\boldsymbol{k}})^T = (\underline{\boldsymbol{V}}_{\boldsymbol{q},\boldsymbol{k}})^T\ ,\qquad \underline{\boldsymbol{V}}_{\boldsymbol{q},0} = \underline{\boldsymbol{V}}_{-\boldsymbol{q},0}\ ,\qquad \underline{\boldsymbol{V}}_{0,\boldsymbol{k}} = -\underline{\boldsymbol{V}}_{0,-\boldsymbol{k}} \tag{5.42}$$

Here, $(\underline{\boldsymbol{V}}_{\boldsymbol{q},\boldsymbol{k}})^T$ denotes the matrix transposed of the vertex interpreted as a $\mathbb{C}^{d\times d}$ matrix. Importantly, the vertex stays finite for $\boldsymbol{q}\to 0$ or $\boldsymbol{k}\to 0$. However, $\underline{\boldsymbol{V}}_{0,0}=0$ holds.

The standard MCT-Approximation consists of a diagonalization and a subsequential factorization and dressing[5] approximation (Götze, 2009; Janssen, 2018; Pihlajamaa *et al.*, 2023; Reichman and Charbonneau, 2005):

$$\frac{m}{N^2k_BT}\left\langle \boldsymbol{v}^{\perp}(\boldsymbol{k})\delta\rho(\boldsymbol{q}-\boldsymbol{k})\hat{R}_2(s)\,\delta\rho(\boldsymbol{p}-\boldsymbol{q})\boldsymbol{v}^{\perp}(-\boldsymbol{p})\right\rangle \longrightarrow \hat{\underline{\mathbf{K}}}^{\perp}(\boldsymbol{k},s)S_{|\boldsymbol{q}-\boldsymbol{k}|}\delta_{\boldsymbol{p},\boldsymbol{k}}\,. \quad (5.43)$$

However, such an approximation has the topology of a self-consistent ring theory (Leutheusser, 1983) or a self-consistent Born approximation (Altland and Simons, 2010; Kamenev, 2011). It has been pointed out in several works that such a theory leads to qualitatively wrong predictions as the resulting theory features an erroneous divergence (Ganter and Schirmacher, 2010; Grigera *et al.*, 2011; Leutheusser, 1983; Vogel and Fuchs, 2023). We show in Appendix B that Equation (5.43) disregards the statisitcal equivalence of the position in the system and hence violates a symmetry constraint. As a consequence and as we will see in Section 5.3.2 and in Section 5.5, the sound attenuation deviates from Rayleigh's law and the predicted scaling close to the transition does not coincide with observations (Ciliberti *et al.*, 2003). Thus, we continue the sequence of consequential Zwanzig-Mori steps and look at the equation of motion for the renormalized vertex.[6]

5.2.3 The renormalised vertex and non-planar MCT

This section aims to derive a constituting equation for the renormalized vertex, which solves the problems faced by the self-consisted Born-theory. As it turns our, we have to perform two more Zwanzig-Mori projections steps before we can close our equations without making a qualitative mistake.

[5]The notion *dressing* refers to replacing the reduced resolvent $\hat{R}_Q(s)$ by the $\hat{R}(s)=\left[s+\Omega\right]^{-1}$

[6]In the original approach, Matthias Fuchs also arrived at Equation (5.38) for the fluidity $\hat{\mathrm{W}}_q^{\perp}(s)$ including the expression for the vertex derived in Appendix D. However, the first attempt was to look at a self-consistent Born theory for $\hat{\mathrm{W}}_q^{\perp}(s)$, which did not capture the correct physics. The original contribution of the present author was to understand the origin of the shortcomings and to correct them. Without the mentioned exceptions, the remainder of this chapter contains original work by Florian Vogel. Nevertheless, there were always helpful discussions with Matthias Fuchs, especially on how to present the results.

The third Zwanzig-Mori step and the memory function $\underline{\mathbf{\Pi}}$: The projection operator P_3 defines the third reduced resolvent $\hat{R}_3(s) = Q_3[s + \Omega_3]^{-1}Q_3$ via $Q_3 = 1 - P_3$ and $\Omega_3 = Q_3\Omega_2 Q_3$. The associated operator identity adjusted from Equation (3.30) reads

$$\Big[s - P_3\Omega_2 P_3 - P_3\Omega_2\hat{R}_3(s)\Omega_2 P_3\Big] P_3\hat{R}_2(s)P_3 = P_3 \; . \tag{5.44}$$

Multiplying from the left with $\frac{m}{N^2 k_B T}\langle \boldsymbol{v}^{\perp}(\boldsymbol{k})\delta\rho(\boldsymbol{q}-\boldsymbol{k})|$ and from the right with $|\delta\rho(\boldsymbol{p}-\boldsymbol{q})\boldsymbol{v}^{\perp}(-\boldsymbol{p})\rangle$ gives the Zwanzig-Mori Equation for the four-point correlation function in Equation (5.41). Additionally multiplying with the adjoint bare vertex $\underline{\boldsymbol{V}}^{\dagger}_{\boldsymbol{k},\boldsymbol{q}}$ from the right and summing over the Fourier mode $\boldsymbol{p}$ leads to the constituting generalized Langevin-equation for the renormalized vertex reads:

$$(s+\xi)\,\underline{\hat{\boldsymbol{\mathcal{V}}}}_{\boldsymbol{k},\boldsymbol{q}}(s) + \sum_{\boldsymbol{p}} \underline{\hat{\mathbf{\Pi}}}^{\perp}(\boldsymbol{q},\boldsymbol{k},\boldsymbol{p},s)\cdot\underline{\hat{\boldsymbol{\mathcal{V}}}}_{\boldsymbol{p},\boldsymbol{q}}(s) = S_{|\boldsymbol{q}-\boldsymbol{k}|}\cdot\underline{\boldsymbol{V}}^{\dagger}_{\boldsymbol{k},\boldsymbol{q}} \; . \tag{5.45}$$

From here on, we discuss the different terms and their origin starting with the Langevin damping rate ξ: When writing down Equation (5.45), we relied on the identity

$$\begin{aligned}\frac{m}{N^2 k_B T S_{|\boldsymbol{q}-\boldsymbol{k}|}}&\langle \boldsymbol{v}^{\perp}(\boldsymbol{k})\delta\rho(\boldsymbol{q}-\boldsymbol{k})Q_2\Omega Q_2\boldsymbol{v}^{\perp}(-\boldsymbol{p})\delta\rho(\boldsymbol{p}-\boldsymbol{q})\rangle \\ &= \frac{m}{N^2 k_B T S_{|\boldsymbol{q}-\boldsymbol{k}|}}\langle \boldsymbol{v}^{\perp}(\boldsymbol{k})\delta\rho(\boldsymbol{q}-\boldsymbol{k})Q_1\Omega Q_1\boldsymbol{v}^{\perp}(-\boldsymbol{p})\delta\rho(\boldsymbol{p}-\boldsymbol{q})\rangle\end{aligned} \tag{5.46}$$

and on the following simplification valid for $N \to \infty$

$$\begin{aligned}&\langle \boldsymbol{v}^{\perp}(\boldsymbol{k})\delta\rho(\boldsymbol{q}-\boldsymbol{k})Q_1\Omega Q_1\boldsymbol{v}^{\perp}(-\boldsymbol{p})\delta\rho(\boldsymbol{p}-\boldsymbol{q})\rangle \\ &\qquad \underset{N\to\infty}{\longrightarrow} -\xi\frac{k_B T}{m}\langle\rho(\boldsymbol{k}-\boldsymbol{p})\delta\rho(\boldsymbol{q}-\boldsymbol{k})\delta\rho(\boldsymbol{p}-\boldsymbol{q})\rangle\,[\underline{\mathbf{1}} - \hat{\boldsymbol{q}}\hat{\boldsymbol{q}}] \\ &\qquad = -\xi\frac{N^2 k_B T}{m}S_{\boldsymbol{q}-\boldsymbol{k}}\delta_{\boldsymbol{p},\boldsymbol{k}}[\underline{\mathbf{1}} - \hat{\boldsymbol{q}}\hat{\boldsymbol{q}}] \; .\end{aligned} \tag{5.47}$$

The last line holds due to global translational invariance and $\langle\rho(\boldsymbol{q}=0)\rangle = N$. Ultimately, this leads to

$$\frac{m}{N^2 k_B T S_{|\boldsymbol{q}-\boldsymbol{k}|}}\langle \boldsymbol{v}^{\perp}(\boldsymbol{k})\delta\rho(\boldsymbol{q}-\boldsymbol{k})Q_2\Omega Q_2\boldsymbol{v}^{\perp}(-\boldsymbol{p})\delta\rho(\boldsymbol{p}-\boldsymbol{q})\rangle \underset{N\to\infty}{\longrightarrow} -\xi[\underline{\mathbf{1}} - \hat{\boldsymbol{q}}\hat{\boldsymbol{q}}]\delta_{\boldsymbol{k},\boldsymbol{p}} \; . \tag{5.48}$$

Next, we turn to the new memory kernel $\underline{\hat{\mathbf{\Pi}}}^{\perp}(\boldsymbol{q},\boldsymbol{k},\boldsymbol{p},s)$. As Equation (5.45) is a Langevin-equation for a matrix-valued quantity, the new memory function is a $d \times d$ matrix as well. Its expression follows directly from the Zwanzig-Mori formalism:

$$\begin{aligned}\underline{\hat{\mathbf{\Pi}}}^{\perp}(\boldsymbol{q},\boldsymbol{k},\boldsymbol{p},s) &= -m\frac{\langle \boldsymbol{v}^{\perp}(\boldsymbol{k})\delta\rho(\boldsymbol{q}-\boldsymbol{k})\Omega_2\,\hat{R}_3(s)\,\Omega_2\delta\rho(\boldsymbol{p}-\boldsymbol{q})\boldsymbol{v}^{\perp}(-\boldsymbol{p})\rangle}{N^2k_BTS_{|\boldsymbol{q}-\boldsymbol{p}|}} \\ &\approx \frac{\langle \boldsymbol{F}^{\perp}(\boldsymbol{k})\delta\rho(\boldsymbol{q}-\boldsymbol{k})\,\hat{R}_3(s)\,\delta\rho(\boldsymbol{p}-\boldsymbol{q})\boldsymbol{F}^{\perp}(-\boldsymbol{p})\rangle}{N^2mk_BTS_{|\boldsymbol{q}-\boldsymbol{p}|}}\,.\end{aligned} \tag{5.49}$$

We have again neglected longitudinal current contributions when proceeding from the first to the second line. Furthermore, we used that the contribution arising from $m\,\langle \boldsymbol{v}^{\perp}(\boldsymbol{k})\delta\rho(\boldsymbol{q}-\boldsymbol{k})|\,P_1\Omega Q_2 \approx S_{|\boldsymbol{q}-\boldsymbol{k}|}\,\langle \boldsymbol{F}^{\perp}(\boldsymbol{q})|\,Q_2 = 0$ vanishes for $N \to \infty$.

As discussed in the context of Equation (5.36) the fluctuating force $|\boldsymbol{F}(-\boldsymbol{q})\rangle$ can be thought of as a sum over pair states of density fluctuations with appropriated weights. This is the idea behind the third projection operator P_3 defined in Equation (5.37). This holds, at least as long as only potential stresses are considered. This renders $\underline{\hat{\mathbf{\Pi}}}^{\perp}(\boldsymbol{q},\boldsymbol{k},\boldsymbol{p},s)$ a complicated functional of a six-point density correlation function. However, the structure factor is assumed to be static, $S_q(t) \approx S_q(t=0)$, since we neglect longitudinal current contributions. Because of this, performing a factorization and dressing approximation in the spirit of the Mode-Coupling Theory at this point, can not lead to a time or frequency-dependent variable. Hence, we need to go to the next Zwanzig-Mori level. There, the occurring memory kernel again depends on the current, our basic time-dependent variable.

The fourth Zwanzig-mori step and the memory function $\underline{\Xi}^{\perp}$: The definition of the latest memory function dictates the new projection operator

$$P_4 = \sum_{\boldsymbol{k}} \frac{|\boldsymbol{F}^{\perp}(-\boldsymbol{k})\delta\rho(\boldsymbol{k}-\boldsymbol{q})\rangle \cdot \langle \delta\rho(\boldsymbol{q}-\boldsymbol{k})\boldsymbol{F}^{\perp}(\boldsymbol{k})|}{N^2mk_BT(kc_k^{\perp})^2S_{|\boldsymbol{q}-\boldsymbol{k}|}}\,. \tag{5.50}$$

Here, we approximated the overlap by its diagonal contribution

$$\frac{1}{d-1}\,\langle |\boldsymbol{F}^{\perp}(\boldsymbol{k})\delta\rho(\boldsymbol{q}-\boldsymbol{k})|^2\rangle \approx N^2mk_BT(kc_k^{\perp})^2S_{|\boldsymbol{q}-\boldsymbol{k}|}\,. \tag{5.51}$$

It was pointed out in (Szamel, 2025) that the diagonal approximation in the previous equation is ultimately not justified as non-diagonal contributions are neglected. In Appendix A.1.2, we comment further on this approximation's validity and explicitly calculate the overlap. As one might anticipate, this approximation is solely driven by the wish for convenience as it greatly simplifies the forthcoming derivation and interpretation. The new projection operator P_4 also defines a reduced resolvent $\hat{R}_4(s) = Q_4[s + \Omega_4]^{-1}Q_4$ via $Q_4 = 1 - P_4$ and $\Omega_4 = Q_4\Omega_3 Q_4$. The new operator identity consequentially reads

$$\Big[s - P_4\Omega_3 P_4 - P_4\Omega_3\hat{R}_4(s)\Omega_3 P_4\Big] P_4\hat{R}_3(s)P_4 = P_4 \; . \tag{5.52}$$

After multiplying with $\frac{1}{N^2 m k_B T S_{|\boldsymbol{q}-\boldsymbol{p}|}} \langle \boldsymbol{F}^\perp(\boldsymbol{k})\delta\rho(\boldsymbol{q}-\boldsymbol{k})|$ from the left and $|\boldsymbol{F}^\perp(-\boldsymbol{k})\delta\rho(\boldsymbol{k}-\boldsymbol{q})\rangle$ from the right leads to the Zwanzig-Mori Equation for the memory function $\hat{\underline{\boldsymbol{\Pi}}}^\perp$:

$$[s + \underline{\tilde{\boldsymbol{\gamma}}}(\boldsymbol{q},\boldsymbol{k},\boldsymbol{p})] \cdot \hat{\underline{\boldsymbol{\Pi}}}^\perp(\boldsymbol{q},\boldsymbol{k},\boldsymbol{p},s) + \sum_{\boldsymbol{b}} \hat{\underline{\boldsymbol{\Xi}}}^\perp(\boldsymbol{q},\boldsymbol{k},\boldsymbol{b},s) \cdot \hat{\underline{\boldsymbol{\Pi}}}^\perp(\boldsymbol{q},\boldsymbol{b},\boldsymbol{p},s) = (kc_k^\perp)^2(\underline{\mathbf{1}} - \hat{\boldsymbol{k}}\hat{\boldsymbol{k}})\delta_{\boldsymbol{k},\boldsymbol{p}} \tag{5.53}$$

Here, $\underline{\tilde{\boldsymbol{\gamma}}}(\boldsymbol{q},\boldsymbol{k},\boldsymbol{p})$ denotes a second instantaneous attenuation rate

$$\underline{\tilde{\boldsymbol{\gamma}}}(\boldsymbol{q},\boldsymbol{k},\boldsymbol{p}) = -\frac{\langle \boldsymbol{F}^\perp(\boldsymbol{k})\delta\rho(\boldsymbol{q}-\boldsymbol{k})\Omega_3\delta\rho(\boldsymbol{p}-\boldsymbol{q})\boldsymbol{F}^\perp(-\boldsymbol{p})\rangle}{N^2 m k_B T (kc_k^\perp)^2 S_{|\boldsymbol{q}-\boldsymbol{k}|}} \; . \tag{5.54}$$

The final memory kernel reads

$$\hat{\underline{\boldsymbol{\Xi}}}^\perp(\boldsymbol{q},\boldsymbol{k},\boldsymbol{p},s) = -\frac{\langle \boldsymbol{F}^\perp(\boldsymbol{k})\delta\rho(\boldsymbol{q}-\boldsymbol{k})\Omega_3\,\hat{R}_4(s)\,\Omega_3\delta\rho(\boldsymbol{p}-\boldsymbol{q})\boldsymbol{F}^\perp(-\boldsymbol{p})\rangle}{N^2 m k_B T (pc_p^\perp)^2 S_{|\boldsymbol{q}-\boldsymbol{p}|}} \; . \tag{5.55}$$

In Appendix E, we analyse the matrix-valued attenuation rate $\underline{\tilde{\boldsymbol{\gamma}}}$. In a diagonal approximation, we find

$$\underline{\tilde{\boldsymbol{\gamma}}}(\boldsymbol{q},\boldsymbol{k},\boldsymbol{p}) \approx 2\frac{\xi k_B T}{m(c_k^\perp)^2}\delta_{\boldsymbol{k},\boldsymbol{p}}[\underline{\mathbf{1}} - \hat{\boldsymbol{k}}\hat{\boldsymbol{k}}] \; , \tag{5.56}$$

which is in direct analogue to the attenuation rate $\gamma_q^\perp$ in Equation (5.32). Again, this damping vanishes with the temperature T.

Keeping in mind that the potential part of the fluctuating forces can be expressed with a pair state of densities for smooth enough potential, the $\hat{\underline{\underline{\Xi}}}$-memory function can be thought of as being expressible as sums or integrals over a six-point correlation function with two velocities and four density fluctuation as suggested by Equation (5.35). Equation (5.53) is our last result solely based on the projection operator formalism and the guiding ideas of a frozen-in structure and the discardability of longitudinal modes. Now, the aim is to express the last memory function via the bare vertex, the static structure factor, and the transverse velocity autocorrelation function. This requires factorizing the six-point correlation function constituting the previous memory function $\hat{\underline{\underline{\Xi}}}$. This essential approximation is reminiscent of the standard approximation in the Mode-Coupling Theory (Götze, 2009; Janssen, 2018; Pihlajamaa *et al.*, 2023; Reichman and Charbonneau, 2005). Hereinafter, two approximation schemes are presented to get closure. The first one, labeled (A), was invented by the present author and is also printed in the publication (Vogel *et al.*, 2025). The second one, labelled (B), is entirely due to Matthias Fuchs and is still unpublished. It is included here upon Professor Fuchs's explicit wish.

(A) Gaussian-fluctuation approximation: The conceptual starting point is to consider only the potential part of the stress tensor. Equation (5.35) and the findings that the derivation of the potential stresses is expressible via the current and the density provide the guiding idea. However, this is strictly speaking only valid for smooth enough potentials. Furthermore, we approximate $Q_3 Q_2 \left|\Omega F_\alpha\right\rangle \approx 0$, which appears to be justified again because of Equation (5.35). Neglecting the longitudinal part of the current leads to simplification

$$Q_3 Q_2 \Omega Q_2 \left|\delta\rho(\boldsymbol{p}-\boldsymbol{q})\boldsymbol{F}^\perp(-\boldsymbol{p})\right\rangle \approx Q_3 \left|\delta\rho(\boldsymbol{p}-\boldsymbol{q})(\Omega\boldsymbol{F}^\perp(-\boldsymbol{p}))\right\rangle \ . \tag{5.57}$$

We assume that the pair state of force derivative and density fluctuation can be written as a direct product of two single states, indicated by the sign $\otimes$. Here, a pair state $|AB\rangle$ is called a product state $|A\rangle \otimes |B\rangle$ if and only if $\langle AB, (AB)^*\rangle = \langle A, A^*\rangle \langle B, B^*\rangle$ holds. This assumption amounts to taking the two field fluctuations as independent, which is why we call the approximation scheme *Gaussian-fluctuation approximation*. With this

and utelizing the bra-ket notation, we find

$$\begin{aligned}
\hat{\underline{\Xi}}^{\perp}(\boldsymbol{q},\boldsymbol{k},\boldsymbol{p},s) &\approx \frac{-\langle \delta\rho(\boldsymbol{q}-\boldsymbol{k})[\Omega^{\dagger}\boldsymbol{F}^{\perp}(\boldsymbol{k})|\, Q_3\hat{R}_4(s)Q_3\,|\delta\rho(\boldsymbol{p}-\boldsymbol{q})[\Omega\boldsymbol{F}^{\perp}(-\boldsymbol{p})]\rangle}{N^2 m k_B T (pc_p^{\perp})^2 S_{|\boldsymbol{q}-\boldsymbol{p}|}} \\
&\approx -\frac{\langle (\Omega^{\dagger}\boldsymbol{F}^{\perp}(\boldsymbol{k}))|\otimes\langle \delta\rho(\boldsymbol{q}-\boldsymbol{k})|\, Q_3\hat{R}_4(s)Q_3\,|\delta\rho(\boldsymbol{p}-\boldsymbol{q})\rangle\otimes|(\Omega\boldsymbol{F}^{\perp}(-\boldsymbol{p}))\rangle}{N^2 m k_B T (pc_p^{\perp})^2 S_{|\boldsymbol{q}-\boldsymbol{p}|}} \\
&\approx -\frac{\langle (\Omega^{\dagger}\boldsymbol{F}^{\perp}(\boldsymbol{k}))|\, P_3\otimes\langle \delta\rho(\boldsymbol{q}-\boldsymbol{k})|\, Q_3\hat{R}_4(s)Q_3\,|\delta\rho(\boldsymbol{p}-\boldsymbol{q})\rangle\otimes P_3\,|(\Omega\boldsymbol{F}^{\perp}(-\boldsymbol{p}))\rangle}{N^2 m k_B T (pc_p^{\perp})^2 S_{|\boldsymbol{q}-\boldsymbol{p}|}} \\
&\underset{\underline{\boldsymbol{\sigma}}=\underline{\boldsymbol{\sigma}}^{(p)}}{=} \frac{mk(c_k^{\perp})^2}{N^2 k_B T p S_{|\boldsymbol{q}-\boldsymbol{p}|}}\sum_{\boldsymbol{k}',\boldsymbol{p}'}\underline{\boldsymbol{V}}_{\boldsymbol{k},\boldsymbol{k}'} \\
&\quad\times\langle \boldsymbol{v}^{\perp}(\boldsymbol{k}')\delta\rho(\boldsymbol{k}-\boldsymbol{k}')\delta\rho(\boldsymbol{q}-\boldsymbol{k})Q_3\hat{R}_4(s)Q_3\delta\rho(\boldsymbol{p}-\boldsymbol{q})\delta\rho(\boldsymbol{p}'-\boldsymbol{p})\boldsymbol{v}^{\perp}(-\boldsymbol{p}')\rangle\cdot\underline{\boldsymbol{V}}^{\dagger}_{\boldsymbol{p}',\boldsymbol{p}} \\
&\approx \frac{(c_k^{\perp})^2}{N}\sum_{\boldsymbol{p}'}\underline{\boldsymbol{V}}_{\boldsymbol{k},\boldsymbol{p}'}\cdot\underline{\hat{\mathbf{K}}}^{\perp}(\boldsymbol{p}',s)\Big[S_{|\boldsymbol{k}-\boldsymbol{p}'|}\delta_{\boldsymbol{k},\boldsymbol{p}}+\frac{k}{p}S_{|\boldsymbol{q}-\boldsymbol{k}|}\delta_{\boldsymbol{k}-\boldsymbol{p}',\boldsymbol{q}-\boldsymbol{p}}\Big]\cdot\underline{\boldsymbol{V}}^{\dagger}_{\boldsymbol{p}',\boldsymbol{p}}
\end{aligned} \tag{5.58}$$

As announced beforehand, the pair state was assumed to be a product state in the second line. In the third line, we inserted unity, which recovered the bare vertex. In the last line, the six-point correlation function of currents and local densities was decomposed into the product of pair-correlators, and they were dressed. This last approximation is reminiscent of the Mode-Coupling approximation scheme. Furthermore, in the last line, we also relied on translation invariance, which leads to the disappearance of one integral as $\langle \boldsymbol{v}^{\perp}(\boldsymbol{k}')|R(s)|\boldsymbol{v}^{\perp}(-\boldsymbol{p}')\rangle \propto \delta_{\boldsymbol{k}',\boldsymbol{p}'}$ holds. This also gives the additional Kronecker deltas in the square brackets.

If we neglect the second term in the square bracket in (5.58), we would perform the diagonalization step in the standard mode-coupling procedure (Götze, 2009; Pihlajamaa *et al.*, 2023) and reproduce the qualitatively wrong approximation (Leutheusser, 1983). Such an approximation is equivalent to setting $\hat{\underline{\Sigma}}^{\perp}(\boldsymbol{q},\boldsymbol{k},\boldsymbol{p},s) \approx \delta_{\boldsymbol{k},\boldsymbol{p}}k^2\hat{\underline{\mathbf{G}}}^{\perp}(\boldsymbol{q},s)$ and $\hat{\underline{\Xi}}^{\perp}(\boldsymbol{q},\boldsymbol{k},\boldsymbol{p},s) \approx \hat{\underline{\mathbf{W}}}^{\perp}(\boldsymbol{q},s)\delta_{\boldsymbol{k},\boldsymbol{p}}$. This resembles a self-consistent Born approximation. Here, only planar terms are considered, where density fluctuations do not overlap. Such a model is qualitatively wrong (Ciliberti *et al.*, 2003; Grigera *et al.*, 2011; Vogel and Fuchs, 2023).

(B) Mode-coupling factorisation: As an alternative to the previous paragraph, we can also exploit the Mode-Coupling approxmation scheme to get closure: We recall that the transverse velocity field $\boldsymbol{v}^{\perp}(\boldsymbol{q})$ and the density fluctuation $\delta\rho(\boldsymbol{q})$ are our two main fields. Thus, the *simplest term* in the subspace, spanned by the previous projections P_1, P_2, P_3 and P_4, which has a finite overlap with the states appearing in Equation (5.55) is the triple state of two density fluctuations and one velocity field. Two or more velocity fields lead to higher temperature corrections. This suggest the fifth projection (Götze, 2009; Janssen, 2018):

$$P_5 = \sum_{\boldsymbol{b},\boldsymbol{b}'} \frac{|\boldsymbol{v}^{\perp}(-\boldsymbol{b})\delta\rho(\boldsymbol{b}-\boldsymbol{b}')\delta\rho(\boldsymbol{b}'-\boldsymbol{q})\rangle \langle\delta\rho(\boldsymbol{q}-\boldsymbol{b}')\delta\rho(\boldsymbol{b}'-\boldsymbol{b})\boldsymbol{v}^{\perp}(\boldsymbol{b})|}{N^3(k_BT/m)S_{|\boldsymbol{q}-\boldsymbol{b}'|}S_{|\boldsymbol{b}-\boldsymbol{b}'|}} \tag{5.59}$$

Here, we assumed an ordering of the wavevectors $\boldsymbol{b}$ and $\boldsymbol{b}'$, such that $\langle\delta\rho(\boldsymbol{q}-\boldsymbol{b}')\delta\rho(\boldsymbol{b}-\boldsymbol{b}')\rangle = 0$ holds. This ordering is in the spirit of the Mode-Coupling Theory, as it suggests that we can approximate the overlap by its diagonal contribution. This leads to the normalisation in Equation (5.59). Furthermore, the ordering also implies that non-diagonal contributions can be neglected when factorizing the six-point correlation function:

$$\begin{aligned}\langle\delta\rho(\boldsymbol{q}-\boldsymbol{b}')\delta\rho(\boldsymbol{b}'-\boldsymbol{b})\boldsymbol{v}^{\perp}(\boldsymbol{b})\hat{R}_3(s)\boldsymbol{v}^{\perp}(-\bar{\boldsymbol{b}})\delta\rho(\bar{\boldsymbol{b}}-\bar{\boldsymbol{b}}')\delta\rho(\bar{\boldsymbol{b}}'-\boldsymbol{q})\rangle \\ \approx N^3\frac{k_BT}{m}S_{|\boldsymbol{q}-\boldsymbol{b}'|}S_{|\boldsymbol{b}-\boldsymbol{b}'|}\underline{\hat{\mathbf{K}}}^{\perp}(\boldsymbol{b},s)(\underline{\mathbf{1}}-\hat{\boldsymbol{b}}\hat{\boldsymbol{b}})\;\delta_{\boldsymbol{b},\bar{\boldsymbol{b}}}\;\delta_{\boldsymbol{b}',\bar{\boldsymbol{b}}'}\end{aligned} \tag{5.60}$$

As in the last step of Equation (5.58), we performed the MCT inherent breaking and dressing of the multiple field correlation function. No off-diagonal terms appear due to the ordering in Equation (5.59). Again, the structure was taken as time-independent. Inserting the projector P_5 to the left and to the right of $\hat{R}_4(s)$ in Equation (5.55) gives after inserting Equation (5.60):

$$\begin{aligned}\hat{\underline{\underline{\Xi}}}^{\perp}(\boldsymbol{q},\boldsymbol{k},\boldsymbol{p},s) \approx -\frac{1}{2N^2mk_BT(pc_p^{\perp})^2S_{|\boldsymbol{q}-\boldsymbol{p}|}}\sum_{\boldsymbol{b},\boldsymbol{b}'} N^3\frac{k_BT}{m}S_{|\boldsymbol{q}-\boldsymbol{b}'|}S_{|\boldsymbol{b}'-\boldsymbol{b}|}\times \\ \frac{\langle\boldsymbol{F}^{\perp}(\boldsymbol{k})\delta\rho(\boldsymbol{q}-\boldsymbol{k})\Omega_2Q_3\,\boldsymbol{v}^{\perp}(-\boldsymbol{b})\delta\rho(\boldsymbol{b}-\boldsymbol{b}')\delta\rho(\boldsymbol{b}'-\boldsymbol{q})\rangle}{N^3(k_BT/m)S_{|\boldsymbol{q}-\boldsymbol{b}'|}S_{|\boldsymbol{b}'-\boldsymbol{b}|}}\cdot\underline{\hat{\mathbf{K}}}_b^{\perp}(s)\cdot \\ \frac{\langle\boldsymbol{v}^{\perp}(\boldsymbol{b})\delta\rho(\boldsymbol{b}'-\boldsymbol{b})\delta\rho(\boldsymbol{q}-\boldsymbol{b}')Q_3\Omega_2\,\delta\rho(\boldsymbol{p}-\boldsymbol{q})\boldsymbol{F}^{\perp}(-\boldsymbol{p})\rangle}{N^3(k_BT/m)S_{|\boldsymbol{q}-\boldsymbol{b}'|}S_{|\boldsymbol{b}'-\boldsymbol{b}|}}\end{aligned} \tag{5.61}$$

Here, we added a factor $1/2$ to approximately account for the ordering of $\boldsymbol{b}$ and $\boldsymbol{b}'$. Thus, we now sum over all wavevectors. To recover the vertex $\underline{\boldsymbol{V}}_{\boldsymbol{q},\boldsymbol{k}}$, we approximate

$$\begin{aligned}
&\langle \boldsymbol{F}^{\perp}(\boldsymbol{k})\delta\rho(\boldsymbol{q}-\boldsymbol{k})\Omega_2 Q_3\, \boldsymbol{v}^{\perp}(-\boldsymbol{b})\delta\rho(\boldsymbol{b}-\boldsymbol{b}')\delta\rho(\boldsymbol{b}'-\boldsymbol{q})\rangle \\
&\quad\approx \langle \delta\rho(\boldsymbol{q}-\boldsymbol{k})\delta\rho(\boldsymbol{b}'-\boldsymbol{q})\rangle \langle \boldsymbol{F}^{\perp}(\boldsymbol{k})\Omega_1 Q_2\, \boldsymbol{v}^{\perp}(-\boldsymbol{b})\delta\rho(\boldsymbol{b}-\boldsymbol{b}')\rangle \\
&\qquad+ \langle \delta\rho(\boldsymbol{q}-\boldsymbol{k})\delta\rho(\boldsymbol{b}-\boldsymbol{b}')\rangle \langle \boldsymbol{F}^{\perp}(\boldsymbol{k})\Omega_1 Q_2\, \boldsymbol{v}^{\perp}(-\boldsymbol{b})\delta\rho(\boldsymbol{b}'-\boldsymbol{q})\rangle \\
&\quad= -N^2 k_B T k (c_k^{\perp})^2 S_{|\boldsymbol{k}-\boldsymbol{b}|} S_{|\boldsymbol{q}-\boldsymbol{k}|} \underline{\boldsymbol{V}}_{\boldsymbol{k},\boldsymbol{b}} \left(\delta_{\boldsymbol{k},\boldsymbol{b}'} + \delta_{\boldsymbol{q}+\boldsymbol{b},\boldsymbol{k}+\boldsymbol{b}'}\right) .
\end{aligned} \tag{5.62}$$

In the last line, we used the definition for $\underline{\boldsymbol{V}}_{\boldsymbol{q},\boldsymbol{k}}$ from Equation (5.39). Inserting all of this back in Equation (5.60) leads to

$$\begin{aligned}
\hat{\underline{\Xi}}^{\perp}(\boldsymbol{q},\boldsymbol{k},\boldsymbol{p},s) = \sum_{\boldsymbol{b},\boldsymbol{b}'} \underline{\boldsymbol{V}}_{\boldsymbol{k},\boldsymbol{b}} \cdot \hat{\underline{\mathbf{K}}}^{\perp}(\boldsymbol{b},s) \cdot \underline{\boldsymbol{V}}^{\dagger}_{\boldsymbol{b},\boldsymbol{p}} \frac{S_{|\boldsymbol{q}-\boldsymbol{b}'|} S_{|\boldsymbol{b}'-\boldsymbol{b}|} S_{|\boldsymbol{k}-\boldsymbol{b}|} S_{|\boldsymbol{q}-\boldsymbol{k}|} S_{|\boldsymbol{p}-\boldsymbol{b}|} S_{|\boldsymbol{q}-\boldsymbol{p}|}}{S_{|\boldsymbol{q}-\boldsymbol{p}|} S^2_{|\boldsymbol{q}-\boldsymbol{b}'|} S^2_{|\boldsymbol{b}'-\boldsymbol{b}|}} \\
\times \frac{k(c_k^{\perp})^2}{2Np} \Big(\delta_{\boldsymbol{k},\boldsymbol{b}'} + \delta_{\boldsymbol{q}+\boldsymbol{b},\boldsymbol{k}+\boldsymbol{b}'}\Big)\Big(\delta_{\boldsymbol{p},\boldsymbol{b}'} + \delta_{\boldsymbol{q}+\boldsymbol{b},\boldsymbol{p}+\boldsymbol{b}'}\Big)
\end{aligned} \tag{5.63}$$

After summing over $\boldsymbol{b}'$, we re-obtain the result from Equation (5.58). All in all, we expressed the memory terms as a functional of the current autocorrelation function. Thus, we have constructed a self-consistent theory. The next section summarizes our model.

The self-consistent model: Both approximation schemes lead to the same expression for the memory kernel

$$\hat{\underline{\Xi}}^{\perp}(\boldsymbol{q},\boldsymbol{k},\boldsymbol{p},s) \approx (c_k^{\perp})^2 \left\{ \hat{\mathrm{M}}_k^{\perp}(s) \underline{\boldsymbol{\delta}}^{\perp}_{\boldsymbol{k},\boldsymbol{p}} + \frac{1}{N} \tilde{\underline{\boldsymbol{V}}}(\boldsymbol{q},\boldsymbol{k},\boldsymbol{p}) \hat{\mathrm{K}}^{\perp}_{|\boldsymbol{q}-\boldsymbol{k}-\boldsymbol{p}|}(s) \right\} , \tag{5.64}$$

with

$$\begin{aligned}
\hat{\mathrm{M}}_k^{\perp}(s) &= \frac{1}{N} \sum_{\boldsymbol{b}} \underline{\boldsymbol{V}}_{\boldsymbol{k},\boldsymbol{b}} : \underline{\boldsymbol{V}}^{\dagger}_{\boldsymbol{b},\boldsymbol{k}}\, S_{|\boldsymbol{k}-\boldsymbol{b}|}\, \hat{\mathrm{K}}_b^{\perp}(s) , \\
\tilde{\underline{\boldsymbol{V}}}(\boldsymbol{q},\boldsymbol{k},\boldsymbol{p}) &= \frac{k}{p} \underline{\boldsymbol{V}}_{\boldsymbol{k},\boldsymbol{p}+\boldsymbol{k}-\boldsymbol{q}} \cdot \underline{\boldsymbol{V}}^{\dagger}_{\boldsymbol{p}+\boldsymbol{k}-\boldsymbol{q},\boldsymbol{p}} S_{|\boldsymbol{q}-\boldsymbol{k}|}
\end{aligned} \tag{5.65}$$

and the abbreviation $\underline{\boldsymbol{\delta}}^{\perp}_{\boldsymbol{q},\boldsymbol{k}} = \delta_{\boldsymbol{k},\boldsymbol{q}}[\underline{\mathbf{1}} - \hat{\boldsymbol{q}}\hat{\boldsymbol{q}}]$. Here, we made use of the tensor structure of the vertex $\underline{\boldsymbol{V}}_{\boldsymbol{k},\boldsymbol{b}}$ and of the identity $\hat{\underline{\mathbf{K}}}^{\perp}(\boldsymbol{b},s) = \hat{\mathrm{K}}_b^{\perp}(s)[\underline{\mathbf{1}} - \hat{\boldsymbol{b}}\hat{\boldsymbol{b}}]$. The first term in Equation (5.64) results from a factorization of a six-point memory kernel diagonal in

the contained density fluctuations indicated by the Kronecker-delta $\delta_{\boldsymbol{k},\boldsymbol{p}}$. According to (Pihlajamaa *et al.*, 2023), factorizing and diagonalizing the memory function along with the subsequential dressing is at the heart of standard MCT. Nevertheless, the second term in Equation (5.64) contains the off-diagonal correlations. Looking at the last line of Equation (5.58), it becomes apparent that there is no good reason why either of them could be neglected. Indeed, it was argued in (Leutheusser, 1983) that both have to be kept even in a simple model of a solid, namely the Lorentz gas, in order to prevent unintended divergences. We call this imperative *Leutheusser symmetry* and show in Appendix B that the two terms in Equation (5.64) arise from different topologies of microscopic scattering events, again as in the simplistic Lorentz-gas model. In Section 5.2.5 and Appendix B, we show that off-diagonal contribution correspond to local events with a non-planar topology. Hence, we call the second contribution in Equation (5.64) the *non-planar* term. After having obtained closure, we can state our self-consistent model. All in all, we end up with the following set of self-consistent equations:

$$\hat{\mathrm{K}}_q^{\perp}(s) = \frac{1}{s + \xi + q^2 \hat{\mathrm{G}}_q^{\perp}(s)} \tag{5.66a}$$

$$\hat{\mathrm{G}}_q^{\perp}(s) = \frac{(c_q^{\perp})^2}{s + (c_q^{\perp})^2 \, \hat{\mathrm{W}}_q^{\perp}(s)} \tag{5.66b}$$

$$\hat{\mathrm{W}}_q^{\perp}(s) = \frac{1}{N} \sum_{\boldsymbol{k}} \underline{\boldsymbol{V}}_{\boldsymbol{q},\boldsymbol{k}} \, : \, \hat{\underline{\boldsymbol{\mathcal{V}}}}_{\boldsymbol{k},\boldsymbol{q}}(s) \tag{5.66c}$$

$$\begin{aligned} \sum_{\boldsymbol{p}} \Big[\Big(s(s+\xi) + (p c_p^{\perp})^2 \Big) \underline{\boldsymbol{\delta}}_{\boldsymbol{k},\boldsymbol{p}}^{\perp} + (s+\xi) \underline{\hat{\boldsymbol{\Xi}}}^{\perp}(\boldsymbol{q},\boldsymbol{k},\boldsymbol{p},s) \Big] \cdot \hat{\underline{\boldsymbol{\mathcal{V}}}}_{\boldsymbol{p},\boldsymbol{q}}(s) \\ = \sum_{\boldsymbol{p}} \Big[s \underline{\boldsymbol{\delta}}_{\boldsymbol{k},\boldsymbol{p}}^{\perp} + \underline{\hat{\boldsymbol{\Xi}}}^{\perp}(\boldsymbol{q},\boldsymbol{k},\boldsymbol{p},s) \Big] \cdot \underline{\boldsymbol{V}}_{\boldsymbol{p},\boldsymbol{q}}^{\dagger} S_{|\boldsymbol{q}-\boldsymbol{p}|} \, , \end{aligned} \tag{5.66d}$$

complemented by the memory kernel $\underline{\hat{\boldsymbol{\Xi}}}$ specified in Equation (5.64). The set of equations (5.66) display our self-consistent model. As this non-planar MCT model is unprecedented, some explanatory comments are appropriate (Vogel *et al.*, 2025):

(I) The derived model goes beyond standard MCT by explicitly not diagonalizing the matrix elements occurring in the first equation for the fluidity (5.40). We label our approach a *Non-planar Self-Consistent Current Response Theory*, where the notion *non-planar* originates from a diagrammatic interpretation of the equations, which we will present in Section 5.2.5.

(II) The sequence of Zwanzig-Mori steps was stopped when it became clear where the standard MCT went wrong. *I.e.* the correct level is indicated by where the standard MCT-approximation scheme becomes equivalent to neglecting a (crucial) term. Also, finding the bare propagator $[s(s+\xi)+q^2(c_q^\perp)^2]^{-1}$ on this level suggests that we can stop the sequence of projections here.

(III) Diagonalising in Equation (5.40) is equivalent to the approximation

$$\underline{\hat{\boldsymbol{\Xi}}}^\perp(\boldsymbol{q},\boldsymbol{k},\boldsymbol{p},s) \approx (c_k^\perp)^2 \hat{\mathrm{M}}_k^\perp(s)\underline{\boldsymbol{\delta}}_{\boldsymbol{k},\boldsymbol{p}}^\perp \,. \tag{5.67}$$

This renders the model a self-consistent Born-approximation, and, since no density fluctuations cross, to a planar theory. The fluidity acquires a simple form as it can be written as

$$\hat{\mathrm{W}}_q^\perp(s) = \frac{1}{N}\sum_{\boldsymbol{k}} \underline{\boldsymbol{V}}_{\boldsymbol{q},\boldsymbol{k}} S_{|\boldsymbol{q}-\boldsymbol{k}|} \hat{\mathrm{K}}_k^\perp(s) : \underline{\boldsymbol{V}}_{\boldsymbol{k},\boldsymbol{q}}^\dagger \,. \tag{5.68}$$

In the high-density limit, this model becomes topologically equivalent to the planar ERM model discussed in (Ciliberti *et al.*, 2003). As discussed in the literature, this leads to an erroneous sound attenuation (Ganter and Schirmacher, 2010; Grigera *et al.*, 2011). It was shown that the attenuation could be be fixed by taking the off-diagonal elements in Equation (5.64) into account (Ganter and Schirmacher, 2010; Grigera *et al.*, 2011; Vogel and Fuchs, 2023). Hereinafter, we call them *non-planar* contributions.

(IV) Including the essential non-planar correction terms has the downside that the weights– occurring when expressing the fluidity $\hat{\mathrm{W}}_q^\perp(s)$ as a functional of the velocity autocorrelation function– are not necessarily positive anymore (Götze, 2009, Equation 4.56c). This might violate the positivity of the spectra of the correlation function $\hat{\mathrm{K}}_q^\perp(s=-i\omega+0^+)$. Here, 0^+ denotes an infitesimal real part. We comment on the positivity of the spectrum further in Section C.

e) The symmetry of the bare vertex: $\underline{\boldsymbol{V}}_{-\boldsymbol{q},-\boldsymbol{k}} = \underline{\boldsymbol{V}}_{\boldsymbol{q},\boldsymbol{k}}$ implies the symmetry of the last memory kernel $\lim\limits_{\boldsymbol{q}\to 0} \underline{\hat{\boldsymbol{\Xi}}}^\perp(\boldsymbol{q},-\boldsymbol{k},-\boldsymbol{p},s) = \lim\limits_{\boldsymbol{q}\to 0} \underline{\hat{\boldsymbol{\Xi}}}^\perp(\boldsymbol{q},\boldsymbol{k},\boldsymbol{p},s)$. Together with the vertex's property $\underline{\boldsymbol{V}}_{\boldsymbol{0},-\boldsymbol{k}} = -\underline{\boldsymbol{V}}_{\boldsymbol{0},\boldsymbol{k}}$, this leads to the following property of the renormalized vertex $\lim\limits_{\boldsymbol{q}\to 0} \underline{\hat{\boldsymbol{\mathcal{V}}}}_{\boldsymbol{q},-\boldsymbol{k}}(s) = -\lim\limits_{\boldsymbol{q}\to 0} \underline{\hat{\boldsymbol{\mathcal{V}}}}_{\boldsymbol{q},\boldsymbol{k}}(s)$. This property has been

extensively discussed, as it ensures Rayleigh-damping in a high-density expansion of the shear modulus to arbitrary order (Vogel and Fuchs, 2023).

In principle the set of self-consistent Equations (5.66) allows two different phases. In the following sections, we will identify one of them as the jammed and one of them as the unjammed state. We will discuss their distinct properties and eventually investigate the scaling of the critical observables close the transition in Section 5.3, Section 5.4 and Section 5.5.

5.2.4 Phase transition

In general, our self-consistent model can describe two different phases as it allows two different solutions for the long time limit:

$$\lim_{t\to\infty} \mathrm{G}_q^{\perp}(t) = \lim_{s\to 0} s\hat{\mathrm{G}}_q^{\perp}(s) = \begin{cases} = 0 & \hat{=} \text{ unjammed} \\ > 0 & \hat{=} \text{ jammed} \end{cases} \tag{5.69}$$

On the one hand, forces and stresses can not completely decay in the jammed or stable state, even for $t \to \infty$. This leads to elastic responses for sufficiently small perturbations as the system can support low-frequency (transverse) vibrational modes. Hence, this phase is indicated by a long-time limit of the generalized shear modulus $\mathrm{G}_q^{\perp}(t \to \infty) > 0$. On the other hand, restoring forces decay in the unjammed phase, *i.e.* $\mathrm{G}_q^{\perp}(t \to \infty) = 0$. Their absence implies the presence of so-called *floppy modes* referring to displacements with no restoring forces. The system yields even to arbitrarily small deformations along these modes. Thus, the macroscopic shear elasticity is zero. This characterization is independent of the Langevin damping rate ξ. Later, we find that the equations of the order parameter of the jammed phase, *i.e.* the inverse compliance, are also independent of ξ. As it will turn out, the stability of the system is unaltered by the dynamical details. We discuss the two phases in the Sections 5.3 and 5.4. Afterward, we turn to the critical dynamics in Section 5.5.

In the jammed phase, restoring forces stay present even in the long time limit. Thus, an applied strain leads to an elastic response, allowing the propagation of sound modes even with small frequencies. Mathematically, this is represented by a small frequency divergence of the shear modulus $\hat{\mathrm{G}}_q(s) \propto 1/s$. It becomes apparent from Equation

(5.66) that a dependence as $\frac{1}{s}$ of the shear modulus implies that the transverse current autocorrelation vanishes with the frequency $\hat{\mathrm{K}}_q^{\perp}(s) \propto s$ for $s \to 0$. The response to the perturbation dies out with time. As no plastic events have taken place, the system returns to its initial configuration. The vanishing of $\hat{\mathrm{K}}_q^{\perp}(s)$ suggests that we can define a susceptibility $\hat{\chi}_q^{\perp}(s) = \frac{1}{s}\hat{\mathrm{K}}_q^{\perp}(s)$. As explained in Section 4.2, $\hat{\chi}_q^{\perp}(s)$ equals the transverse susceptibility in the one-phonon approximation. The two parameters s, q are the mode's frequency and wavenumber. The Equations (5.14) and (5.30) for the autocorrelation function and the shear modulus give:

$$\hat{\chi}_q^{\perp}(s) = \frac{1}{s(s+\xi) + q^2(\hat{v}_q^{\perp}(s))^2} \ . \tag{5.70}$$

Here, the complex dispersion relation reads

$$q^2(\hat{v}_q^{\perp}(s))^2 = (q\tilde{v}_q^{\perp}(s))^2 + s\Gamma_q^{\perp}(s) \ , \tag{5.71}$$

where $(q\tilde{v}_q^{\perp}(s))^2$ characterizes the propagation of a mode while $\Gamma_q^{\perp}(s)$ quantifies the attenuation. The introduction of the susceptibility $\hat{\chi}_q^{\perp}(s)$ allows us to connect our self-consistent model with the ERM Model, as already outlined in Chapter 4. We will discuss this connection in the next section. As we will see, this also leads to a diagrammatic interpretation of our equations.

5.2.5 Connection to the ERM model

Our set of self-consistent equations in Equation (5.66) has been derived rigorously. However, the model and the equations remain somehow elusive. This section provides the physical interpretation. We will discuss the picture, that the self-consistent model describes a single mode traveling through the system and suffering from inelastic scattering events with the disorder:

As already discussed in Section 4.5, the current autocorrelation function $\underline{\mathbf{K}}_q(t)$ becomes equivalent to the derivative of the one-phonon response function $\underline{\boldsymbol{\chi}}_q^{\mathrm{ERM}}(t)$ in the Euclidean Random Matrix (ERM) model under the assumption that the system is self-averaging. Appendix A shows that this assumption is valid, as solving the vector ERM model gives essentially the same self-consistent model with the same bare dispersion relation $(qc_q^{\perp})^2$ and the same bare vertex $\underline{\boldsymbol{V}}_{\boldsymbol{q},\boldsymbol{k}}$ when the initial stresses are

neglected. The only true difference is that the quantities describing the structure, like the pair-correlation function $g(r)$ or the static structure factor S_q, are replaced by their averaged quantity $g(r) \to \overline{g}(r)$ and $S_q \to \overline{S}_q$. Here, the line denotes the quenched disorder average. However, assuming self-averaging, $g(r) = \overline{g}(r)$ and $S_q = \overline{S}_q$ holds. Hereinafter, we show how the Self-Consistent Transverse Current Theory can be mapped to the ERM model, defined in Equation (4.20). This mapping directly allows the illustrative picture outlined above. Furthermore, the connection to the ERM model also suggests a diagrammatic expression of our equations. Lastly, we use the connection to the ERM model to derive a simplified version of our equations that can be solved numerically. We will introduce this simple model at the end of this section.

The ERM model $\hat{\underline{\chi}}^{\mathrm{ERM}}(\boldsymbol{q}, s)$ has been introduced in Chapter 4 as a simplified model for the spread of a perturbation in a stable system. The propagator $\hat{\underline{\boldsymbol{\chi}}}^{\mathrm{ERM}}(\boldsymbol{q}, s)$ was motivated by a one-phonon approximation, and it was discussed in Section 4.4 how the ERM model can be regarded as a model for the propagation of an initially imposed plane wave. As a reminder, the ERM model is defined as

$$\begin{aligned}
\hat{\underline{\boldsymbol{\chi}}}^{\mathrm{ERM}}(\boldsymbol{q}, s) &= \Big\langle \sum_{i,j} e^{-i\boldsymbol{q}\cdot(\boldsymbol{R}_i - \boldsymbol{R}_j)} \left[\frac{1}{s^2 + \underline{\boldsymbol{\mathcal{H}}}^{\mathrm{ERM}}} \right]_{ij} \Big\rangle \ , \\
\mathcal{H}^{\mathrm{ERM}}_{i\alpha,j\beta} &= \delta_{ij} \sum_k M_{i\alpha,k\beta} - M_{i\alpha,j\beta} \ , \\
M_{i\alpha,j\beta} &= \hat{R}^{\alpha}_{ij} \left(\mathcal{K}(R_{ij}) - \frac{\mathcal{T}(R_{ij})}{R_{ij}} \right) \hat{R}^{\beta}_{ij} + \frac{\mathcal{T}(R_{ij})}{R_{ij}} \delta_{\alpha\beta} \ ,
\end{aligned} \tag{5.72}$$

with the spring constant $\mathcal{K}(|\boldsymbol{R}_i - \boldsymbol{R}_j|)$ and the bond tension $\mathcal{T}(|\boldsymbol{R}_i - \boldsymbol{R}_j|)$ defined in Equation (2.14) and Equation (2.13). In this Section, we set $\xi = 0$ as the ERM model has been defined for Newtonian systems[7]. Szamel recently showed how the projection operator formalism can be applied to the scalar ERM model with a uniform distribution of the particles (Szamel, 2025). This calculation is redone in Appendix A. There, Szamel's original approach is also generalized to arbitrary distributions of the particles, to include vector displacements and even to systems with initial stresses.

[7] It has been attempted before to map the Self-Consistent Current Theory onto the ERM model (Vogel *et al.*, 2025): $\hat{\chi}^{\perp}_q(s) \longleftrightarrow \hat{\chi}^{\mathrm{SERM}}_q(s)$. However, this identification was flawed as the vector character of the displacements was ignored. Furthermore, the mapping in (Vogel *et al.*, 2025) was based on a high-density approximation ($n \to \infty$). Thus, no general and principled mapping has been published so far.

The elementary insight from this novel calculation is that the Self-Consistent Current Response Theory is equivalent to the unstressed vector ERM model after ignoring the longitudinal modes. In the following, we outline the single steps of the identification.

The mapping to the ERM relies on one assumption only: The annealed average for $T \to 0$ implicitly applied in Section 5.2 is supposed to be the same as the average over the quenched disorder at $T = 0$ introduced in Section 3.3. This supposed equivalence implies $S_q = \overline{S}_q$ and $g^{(n)} = \overline{g^{(n)}}$. The remaining mapping steps consist of simple identification or redefinition of quantities. First of all, we notice:

$$-q(c_q^{\perp})^2 \underline{\boldsymbol{V}}_{\boldsymbol{q},\boldsymbol{k}} = \underline{\boldsymbol{V}}_{\boldsymbol{q},\boldsymbol{k}}^{\perp,\perp} \tag{5.73}$$

The vertex of the Self-Consistent Current Response Theory is equivalent to the transverse vertex in the vector ERM model when the initial stresses are neglected, *i.e.* $\mathcal{T} = 0$. In this case, it becomes furthermore apparent from the explicit results, stated in Equation (5.25) and Equation (A.2), that the transverse bare dispersion relations $(qc_q^{\perp})^2$ and $(qc_q^{\mathrm{ERM},\perp})^2$ also coincides in both approaches. After neglecting the longitudinal modes, the transverse one-phonon propagator of the ERM model $\hat{\chi}_q^{\mathrm{ERM},\perp}(s)$ can be written as

$$\hat{\chi}_q^{\mathrm{ERM},\perp}(s) = \frac{1}{s^2 + \frac{(qc_q^{\mathrm{ERM},\perp})^2}{1+\frac{\Sigma_q^{\mathrm{ERM},\perp}(s)}{(qc_q^{\mathrm{ERM},\perp})^2}}} \tag{5.74a}$$

$$\hat{\Sigma}_q^{\mathrm{ERM},\perp}(s) = \frac{1}{N(d-1)} \mathrm{Tr}\Big\{ \sum_{\boldsymbol{k}} \underline{\boldsymbol{V}}_{\boldsymbol{q},\boldsymbol{k}}^{\perp,\perp} S_{|\boldsymbol{q}-\boldsymbol{k}|} \hat{\chi}_k^{(0),\perp}(s) \cdot \hat{\underline{\boldsymbol{\mathcal{V}}}}_{\boldsymbol{k},\boldsymbol{q}}^{\perp,\perp}(s) \Big\} \tag{5.74b}$$

$$\sum_{\boldsymbol{p}} \left[\underline{\boldsymbol{\delta}}_{\boldsymbol{k},\boldsymbol{p}}^{\perp} + s^2 \frac{\hat{\underline{\boldsymbol{\Sigma}}}^{\mathcal{V},\perp}(\boldsymbol{q},\boldsymbol{k},\boldsymbol{p},s)}{(pc_p^{\mathrm{ERM},\perp})^2} \hat{\chi}_p^{(0),\perp}(s) \right] \cdot \hat{\underline{\boldsymbol{\mathcal{V}}}}_{\boldsymbol{p},\boldsymbol{q}}^{\perp,\perp}(s) = \sum_{\boldsymbol{p}} \left[\underline{\boldsymbol{\delta}}_{\boldsymbol{k},\boldsymbol{p}}^{\perp} + \frac{\hat{\underline{\boldsymbol{\Sigma}}}^{\mathcal{V},\perp}(\boldsymbol{q},\boldsymbol{k},\boldsymbol{p},s)}{(pc_p^{\mathrm{ERM},\perp})^2} \right] \cdot \left(\underline{\boldsymbol{V}}_{\boldsymbol{q},\boldsymbol{p}}^{\perp,\perp} \right)^T \tag{5.74c}$$

$$\hat{\underline{\boldsymbol{\Sigma}}}^{\mathcal{V},\perp}(\boldsymbol{q},\boldsymbol{k},\boldsymbol{p},s) = \frac{1}{N} \sum_{\boldsymbol{b}} \underline{\boldsymbol{V}}_{\boldsymbol{q},\boldsymbol{b}}^{\perp,\perp} \hat{\chi}_b^{\mathrm{ERM},\perp}(s) \cdot \left(S_{|\boldsymbol{k}-\boldsymbol{b}|} \delta_{\boldsymbol{k},\boldsymbol{p}} + S_{|\boldsymbol{q}-\boldsymbol{p}|} \delta_{\boldsymbol{k}-\boldsymbol{b},\boldsymbol{q}-\boldsymbol{p}} \right) \left(\underline{\boldsymbol{V}}_{\boldsymbol{q},\boldsymbol{b}}^{\perp,\perp} \right)^T . \tag{5.74d}$$

Here, we used $\left(\underline{\boldsymbol{V}}^{\perp,\perp}\right)_{\boldsymbol{k},\boldsymbol{q}}^{\dagger} = \left(\underline{\boldsymbol{V}}_{\boldsymbol{q},\boldsymbol{k}}^{\perp,\perp} \right)^T$ for notational ease. $\chi_q^{(0),\perp}(s) \equiv [s^2 + q^2(c_q^{\perp})^2]^{-1}$ defines the bare propagator. To see the equivalence with Equation (5.66) it suffices to

insert Relation (5.73) in Equation (5.74) and to set

$$\hat{\underline{\boldsymbol{\mathcal{V}}}}^{\perp,\perp}_{\boldsymbol{k},\boldsymbol{q}}(s) \equiv -\chi_k^{(0),\perp}(s) S_{|\boldsymbol{q}-\boldsymbol{k}|} \underline{\boldsymbol{\mathcal{V}}}_{\boldsymbol{k},\boldsymbol{q}}(s) \; . \tag{5.75}$$

As the ERM model describes the propagation of an imposed mode in a disordered medium, this intuitive interpretation of the equations consequentially also extends to the self-consistent current theory. Nevertheless, redefining the vertices $\underline{\boldsymbol{V}}$ and $\hat{\underline{\boldsymbol{\mathcal{V}}}}$ as in the Equations (5.73) and (5.75) also led to replacing the fluidity $(c_q^{\perp})^2 \hat{\mathrm{W}}_q^{\perp}(s)$ with $\hat{\Sigma}_q^{\mathrm{ERM},\perp}(s)/(qc_q^{\perp})^2$. Here $\hat{\Sigma}_q^{\mathrm{ERM},\perp}(s)$ defines the self-energy, which is the energy a mode has due to the changes and interactions the mode causes in its environment (Coleman, 2015, Chapter 7). This replacement stems from a change in the associated physical interpretation. We briefly want to elucidate on this: In Equation (5.30), we introduced the fluidity $\hat{\mathrm{W}}_q^{\perp}(s)$ as a response function for the force autocorrelation function $\mathrm{G}_q^{\perp}(s)$. Motivated by the computer simulations discussed in (Goyon *et al.*, 2008) and the experiments presented in (Jop *et al.*, 2012), both studying a spatially varying fluidity, we introduced the fluidity such that $\lim_{q,s\to 0} \hat{\mathrm{W}}_q^{\perp}(s)$ has a finite limit identifiable with the inverse viscosity $\eta^{\perp}$. This approach was motivated by picturing a fluid and investigating where the system falls out of equilibrium and where stresses can not fully relax anymore. However, the ERM model was introduced in Section 4 starting from the one-phonon approximation in an arrested system. As it was argued, the propagator $\hat{\chi}_q^{\mathrm{ERM},\perp}(s)$ describes the evolution of an initially imposed plane wave. For $q \to 0$, the plane wave $e^{-i\boldsymbol{q}\cdot\boldsymbol{r}}$ becomes an exact eigenmode of the system as no energy cost has to be paid for a uniform shift of all the particles. Thus, one has $\hat{\Sigma}_{q\to 0}^{\mathrm{ERM},\perp}(s) \propto q^2$ in contrast to $\hat{\mathrm{W}}_0^{\perp}(s) \neq 0$. Even though both pictures are ultimately equivalent as they can be mapped onto each other by simply redefining the vertex, two different concepts underlie the formulation with the self-energy $\hat{\Sigma}_q^{\mathrm{ERM},\perp}(s)$ and with the fluidity $\hat{\mathrm{W}}_q^{\perp}(s)$.

Diagrammatic representation: Formulating the model with the self-energy $\hat{\Sigma}_q^{\mathrm{ERM},\perp}(s)$ additionally allows the interpretation of our equations as describing the evolution of a single mode initially imposed on the system. Adopting this narrative, we can

introduce a diagrammatic representation of our model:

$$\hat{\Sigma}_q^{\mathrm{ERM}\perp}(s) = \frac{1}{N(d-1)}\mathrm{Tr}\left\{\right\} \tag{5.76}$$

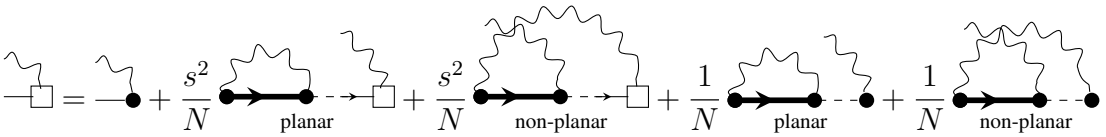

Here, a thin line denotes the bare propagator $\hat{\chi}_q^{(0),\perp}(s)$ and a thick line displays the dressed propagator $\hat{\chi}_q^{\perp}(s)$. Furthermore, a density fluctuation S_q is displayed by a curly line, while a circle depicts the bare vertex. To summarize, the Feynmann rules read:

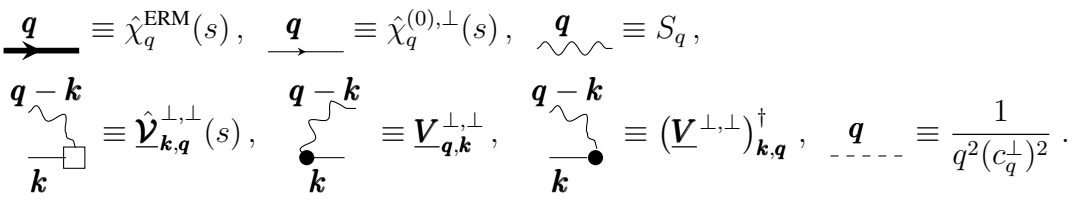

(5.77)

The subscripted wavenumber of $S_q, \chi_q^{\mathrm{ERM},\perp}, \chi_q^{(0),\perp}$ represents the different momenta carried by a line. The first wavenumber in a vertex defines the incoming and the second number the outgoing momentum. Importantly, the momentum is conserved at every vertex, and we have to integrate over the internal momenta according to the integration rule $\frac{1}{n}\int \frac{d^d\boldsymbol{k}}{(2\pi)^d}$. Here, $n = N/V$ denotes the particle density. We chose $\boldsymbol{q}$ to be the overall incoming wavevector. The occurrence of the prefactor s^2 in equation (5.76) already implies that the associated contributions become negligible in the small s limit in the jammed state. For small frequencies, the s-dependence of the dashed lines can be reintroduced: 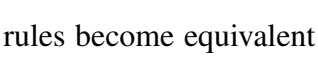 $\hat{=}\chi_k^{(0),\perp}(s)$. With the full s-dependence, the Feynmann rules become equivalent to the ones used in the field theoretical discussion[8] presented in (Grigera *et al.*, 2011). The diagrammatic representation suggests the following narrative. A (transverse) mode travels through the system. Its time evolution is described by the bare propagator $\chi_q^{(0),\perp}(s)$, which describes the evolution of a mode in an perfectly

[8]The authors of (Grigera *et al.*, 2011) assumed a uniform distribution of the particles which amounts to setting $S_q = g^{(n)} = 1$. Additionally, they only investigated the scalar ERM model. However these simplifying assumptions only affect the vertex: $\underline{\boldsymbol{V}}_{\boldsymbol{q},\boldsymbol{k}} \longrightarrow V_{\boldsymbol{q},\boldsymbol{k}}^{\mathrm{SERM}} = \frac{n}{m}\Big(\mathcal{K}(\boldsymbol{k}) - \mathcal{K}(\boldsymbol{q}-\boldsymbol{k})\Big)$. It was shown in (Vogel *et al.*, 2025) that the self-consistent current response theory can be compared to the scalar ERM models discussed in (Grigera *et al.*, 2011) and (Ciliberti *et al.*, 2003) for high densities.

elastic medium. Here, inelastic scattering events are neglected (Ciliberti *et al.*, 2003; Ganter and Schirmacher, 2010; Grigera *et al.*, 2011). However, for finite densities or in a medium where the continuum's approximation does not hold, the travelling mode eventually scatters inelastically with the disorder. This scattering process is quantified by the vertex $\underline{\boldsymbol{V}}^{\perp,\perp}_{\boldsymbol{q},\boldsymbol{k}}$ and causes a density fluctuation S_q. The mode with a new momentum travels on, experiences new scattering events, and eventually recombines with S_q. The key message from the diagrammatic representation is that the two terms in Equation (5.64) correspond to different topologies of scattering events: A planar sequence, where density fluctuations do not overlap, and a non-planar sequence, which gives rise to crossing terms. As we will see when discussing the attenuation in Section 5.3.2, both terms must be considered to capture the correct attenuation.

Numerical analysis: Before discussing the jammed and the unjammed state, we need to elaborate on the numerical implementation of the Self-Consistent Current Response Theory summarized in Equation (5.66). The numerical solution of the vector ERM model and the Self-Consistent Current Response Theory are quite costly due to the tensorial nature of the vertex. Thus, we restrict ourselves to the numerical analysis of the scalar ERM model introduced in Section 4.2 and discussed in Appendix A.1. Furthermore, we reduce the problem's complexity by assuming that the particles are uniformly distributed in the volume V. This amounts to setting $g^{(n)} = S_q = 1$. Here, $g^{(n)}$ denotes the n-particle correlation function. Furthermore, we assume that the spring-constants $\mathcal{K}(r)$ occurring in the harmonic expansion of the energy and defined in Equation (2.14) can be Fourier transformed. This leads to concise expressions for the bare dispersion relation $(qc_q^{\mathrm{SERM}})^2$ and the bare vertex $V^{\mathrm{SERM}}_{\boldsymbol{q},\boldsymbol{k}}$ commonly used in the literature (Ciliberti *et al.*, 2003; Ganter and Schirmacher, 2010; Grigera *et al.*, 2011; Martin-Mayor *et al.*, 2001; Mézard *et al.*, 1999; Szamel, 2025; Vogel and Fuchs, 2023):

$$(qc_q^{\mathrm{SERM}})^2 = \frac{n}{m}\Big(\mathcal{K}(0) - \mathcal{K}(q)\Big)\ , \quad V^{\mathrm{SERM}}_{\boldsymbol{q},\boldsymbol{k}} = \frac{n}{m}\Big(\mathcal{K}(k) - \mathcal{K}(|\boldsymbol{k}-\boldsymbol{q}|)\Big). \tag{5.78}$$

As a reminder, we indicate the spatial Fourier transformation by the argument being a Fourier mode. As already announced in Section 4.2, we investigate a Gaussian spring function $\mathcal{K}^G(r) = m\omega_0^2 \exp[-r^2/(2\sigma^2)]$, a step spring function $\mathcal{K}^\Theta(r) = m\omega_0^2\Theta(\sigma - r)$ and linear springfunction $\mathcal{K}^L(r) = m\omega_0^2(1 - r/\sigma)\Theta(\sigma - r)$. Here $\Theta(r)$ denotes the Theta-function. In all three cases, m denotes the mass of the particles, and ω_0 and σ denote the system's frequency- and microscopic length scale, respectively. Lastly,

for the full numerical solution of our model, we neglect the non-linear terms in Equation (5.76). This approximation is known in the literature as $F1$-approximation (Götze, 2009; Voigtmann, 2011). It becomes exact in the $s \to 0$ limit in the jammed phase. Within this approximation, the self-energy reads

$\hat{\Sigma}_q^{\mathrm{SERM}}(s) \approx$ 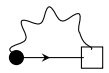 ,

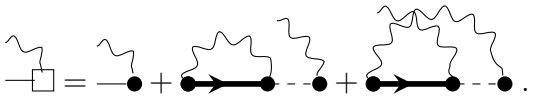 . (5.79)

Here, the black dots now represent the scalar vertex $V_{\boldsymbol{q},\boldsymbol{k}}^{\mathrm{SERM}}$, while the thin arrow and the dashed line are defined with the bare dispersion relation $(qc_q^{\mathrm{SERM}})^2$. Both quantities are defined in equation (5.78). Together with the simplification $S_q = 1$, this defines a set of equations for the scalar ERM model:

$$\hat{\chi}_q^{\mathrm{SERM}}(s) = \overline{\frac{1}{N}\sum_{i,j=1}^{N} e^{-i\boldsymbol{q}\cdot(\boldsymbol{R}_i-\boldsymbol{R}_j)}\left[s^2 + \underline{\boldsymbol{\mathcal{H}}}^{\mathrm{SERM}}\right]_{ij}^{-1}} = \frac{1}{s^2 + \frac{q^2(c_q^{\mathrm{SERM}})^2}{1+\frac{\hat{\Sigma}_q^{\mathrm{SERM}}(s)}{(qc_q^{\mathrm{SERM}})^2}}} \tag{5.80}$$

The explicit expression for $\hat{\Sigma}_q^{\mathrm{SERM}}(s)$ is given in Equation (A.70). All the figures we discuss in the remainder of this thesis originate from either solving the set of equations numerically or by analyzing the random Euclidean Matrix

$$\mathcal{H}_{ij}^{\mathrm{SERM}} = -\frac{1}{m}\mathcal{K}(|\boldsymbol{R}_i - \boldsymbol{R}_j|) + \frac{1}{m}\delta_{ij}\sum_k \mathcal{K}(|\boldsymbol{R}_i - \boldsymbol{R}_k|), \tag{5.81}$$

via exact numerical diagonalization done by Philipp Baumgärtel. For all data shown, a uniform distribution of the particles was assumed. His data is shown with his permission. To indicate that the presented quantities were obtained by solving the scalar ERM model, the superscripted $\perp$ is dropped in the figures and graphics hereinafter. More details on the numerical solutions of the self-consistent equations are provided in Appendix C.

After discussing the self-consistent models and introducing the model used for the numerical investigations, we now turn to the different phases our model predicts. In the next section, we start with the jammed phase.

5.3 The jammed phase

Up to rattlers[9], no floppy modes exist in the jammed phase, and an applied strain leads to an elastic response encoded in the generalized viscosity. As outlined in Section 2.3.3, sound modes are damped due to the topological disorder. Figure 5.1 displays an example of $\mathrm{K}_q(t)$ for different scaled wavenumbers σq. Damped oscillations are visible.

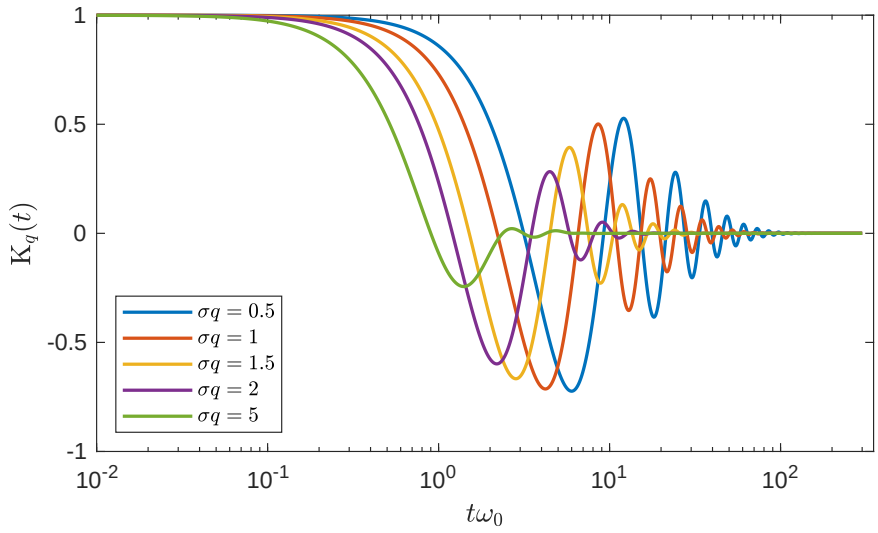

Figure 5.1: Numerical Solution of Equation (5.80) for five different wavenumbers with $\mathcal{K}(r) = m\omega_0^2\Theta(1 - r/\sigma)$. The spatial dimension has been set to $d = 3$, and the number density equals $n^* = \frac{N\sigma^3}{V} = 2$. This is well above the instability at $n^*_{c,T} = 0.830(1)$.

As discussed in Section 5.2.4, damped oscillations imply restoring forces even for $t \to \infty$. The non-decaying stresses allow the propagation of sound modes. Mathematically, this causes a small frequency divergence of the shear modulus $\hat{\mathrm{G}}^{\perp}_q(s) \propto 1/s$, which implies that the current autocorrelation $\hat{\mathrm{K}}^{\perp}_q(s)$ and the fluidity $\hat{\mathrm{W}}^{\perp}_q(s)$ vanish linearly with the frequency $\hat{\mathrm{K}}^{\perp}_q(s)$, $\hat{\mathrm{W}}^{\perp}_q(s) \propto s$ for $s \to 0$. However, this suggests that the susceptibility $\hat{\chi}^{\perp}_q(s) = \frac{1}{s}\hat{\mathrm{K}}^{\perp}_q(s)$ stays finite even for $s \to 0$. The defining equations

[9]The phenomenon of rattlers was discussed in Section 2.3. The notion *rattlers* refers to weakly connected particles.

read:

$$\hat{\chi}_q(s) = \frac{1}{s(s+\xi) + q^2(\hat{v}_q^\perp(s))^2} \,, \tag{5.82a}$$

$$q^2(\hat{v}_q^\perp(s))^2 = \frac{(qc_q^\perp)^2}{1 + (c_q^\perp)^2 \hat{\mathrm{w}}_q(s)} \,. \tag{5.82b}$$

Here, $(q\hat{v}_q^\perp(s))^2$ denotes the complex dispersion relation and $\hat{\mathrm{w}}_q(s) = \frac{1}{s}\hat{\mathrm{W}}_q^\perp(s)$ is the time integrated fluidity. To see that all of these quantities remain finite in the limit $s \to 0$, we write down the constituting equation for the time-integrated renormalized vertex $\hat{\underline{\boldsymbol{U}}}(\boldsymbol{q}, \boldsymbol{k}, s) = \frac{1}{s}\hat{\underline{\boldsymbol{V}}}_{\boldsymbol{q},\boldsymbol{k}}(s)$. Dividing Equation (5.67) by s leads to

$$\begin{aligned}
&\Big[\Big(s(s+\xi) + k^2(c_k^\perp)^2\Big) + s(s+\xi)\,(c_k^\perp)^2 \hat{\underline{\boldsymbol{m}}}_k(s)\Big] \cdot \hat{\underline{\boldsymbol{U}}}_{\boldsymbol{k},\boldsymbol{q}}(s) \\
&+ \frac{s(s+\xi)(c_k^\perp)^2}{N} \sum_{\boldsymbol{p}} \underline{\tilde{\boldsymbol{V}}}(\boldsymbol{q}, \boldsymbol{k}, \boldsymbol{p}) \cdot \hat{\underline{\boldsymbol{U}}}_{\boldsymbol{p},\boldsymbol{q}}(s)\; \hat{\chi}^\perp_{|\boldsymbol{q}-\boldsymbol{k}-\boldsymbol{p}|}(s) = ... \\
= \big[1 + (c_k^\perp)^2 \hat{\underline{\boldsymbol{m}}}_k(s)\big] \cdot \underline{\boldsymbol{V}}^\dagger_{\boldsymbol{k},\boldsymbol{q}} S_{|\boldsymbol{q}-\boldsymbol{k}|} &+ (c_k^\perp)^2 \frac{1}{N} \sum_{\boldsymbol{p}} \underline{\tilde{\boldsymbol{V}}}(\boldsymbol{q}, \boldsymbol{k}, \boldsymbol{p}) \cdot \underline{\boldsymbol{V}}^\dagger_{\boldsymbol{p},\boldsymbol{q}} \hat{\chi}^\perp_{|\boldsymbol{q}-\boldsymbol{k}-\boldsymbol{p}|}(s) S_{|\boldsymbol{q}-\boldsymbol{p}|} \,.
\end{aligned} \tag{5.83}$$

The vanishing of autocorrelation function $\hat{\mathrm{K}}_q(s) \propto s$ implies that $\underline{\boldsymbol{m}}_k(s) = \frac{\mathrm{M}_k(s)}{s}[\underline{\mathbf{1}} - \hat{\boldsymbol{k}}\hat{\boldsymbol{k}}]$ stays finite for $s \to 0$. Thus, it becomes clear that the right-hand side must converge to a finite limit for $s \to 0$, which implies that also the integrated renormalized vertex $\hat{\underline{\boldsymbol{U}}}_{\boldsymbol{p},\boldsymbol{q}}(s)$ has a finite small frequency limit. In turn, this leads to a finite value of $\hat{\mathrm{w}}_q(s)$ and also of $\hat{v}_q^\perp(s)$.

For sufficiently small frequencies $s = -i\omega + 0^+$, we can write the susceptibility as the Green's function of a damped oscillator:

$$\hat{\chi}_q(s = -i\omega + 0^+) \underset{\omega \to 0}{\longrightarrow} \frac{1}{-\omega(\omega + i\xi) + (qv_q^\perp)^2 - i\omega\,\Gamma_q^\perp} \,. \tag{5.84}$$

Here, $(qv_q^\perp)^2 \equiv (q\hat{v}_q^\perp(s))\big|_{s=0}$ defines the inverse compliance, which sufficiently well approximates the frequency-dependent dispersion relation $(q\tilde{v}_q^\perp(s))^2$ for small s. The zero wavenumber limit $v_0^\perp$ gives the speed of sound. The imaginary part of the shear modulus gives the other quantity, $\Gamma_q^\perp$, appearing in Equation (5.84). It quantifies the sound attenuation. In the next section, we will look at the compliance $\hat{\chi}_q(s = 0)$. It

quantifies the deformation of a time-independent strain and hence equals the inverse stiffness of the system. For small frequencies, $(qv_q^\perp)^2$ is a good estimate for the dispersion relation, which is generally frequency dependent. Section 5.3.2 is dedicated to the sound attenuation $\Gamma_q^\perp$. We will see that including the non-planar terms was crucial for the theory to predict Rayleigh sound attenuation. Lastly, Section 5.3.3 defines and analyzes the Density of States $D(\omega)$.

5.3.1 The dispersion relation

As discussed in Section 2.33, the speed of sound $v_0^\perp$ is directly related to the elastic constants of the system. Generally, the system can be regarded as a stable, disordered solid if the transverse speed of sound $v_0^\perp$ is finite. Thus, the vanishing of $v_0^\perp$ or equivalently the divergence of the compliance $\hat{\chi}_q^\perp(s=0)$ herald approaching the transition and signals that the system becomes soft. Consequently, $v_q^\perp$ is one of the main observables. In the first part of this section, we solve our equations for $s=0$ to find an expression for the compliance. In the second part, we discuss the numerical solutions and compare the inverse compliance $(qv_q^\perp)^2$ with the true dispersion relation $(q\tilde{v}_q^\perp(s))^2$ which is frequency dependent.

The compliance: Equation (5.83) for the time-integrated renormalised vertex $\hat{\underline{\boldsymbol{\mathcal{U}}}}_{\boldsymbol{k},\boldsymbol{q}}(s)$ simplifies for $s \to 0$. The exact solution reads

$$\begin{aligned} k^2\hat{\underline{\boldsymbol{\mathcal{U}}}}_{\boldsymbol{k},\boldsymbol{q}}(s=0) = \frac{1}{(c_k^\perp)^2}\underline{\boldsymbol{V}}^\dagger_{\boldsymbol{k},\boldsymbol{q}} S_{|\boldsymbol{q}-\boldsymbol{k}|} + \underline{\hat{\boldsymbol{m}}}_k(s=0)\cdot\underline{\boldsymbol{V}}^\dagger_{\boldsymbol{k},\boldsymbol{q}} S_{|\boldsymbol{q}-\boldsymbol{k}|} \\ +\frac{1}{N}\sum_{\boldsymbol{p}}\underline{\tilde{\boldsymbol{V}}}(\boldsymbol{q},\boldsymbol{k},\boldsymbol{p})\cdot\underline{\boldsymbol{V}}^\dagger_{\boldsymbol{p},\boldsymbol{q}}\hat{\chi}^\perp_{|\boldsymbol{q}-\boldsymbol{k}-\boldsymbol{p}|}(s=0)S_{|\boldsymbol{q}-\boldsymbol{p}|}\ . \end{aligned} \tag{5.85}$$

Consequentially, and by Equation (5.66c), the time-integrated fluidity at $s=0$ follows from an inhomogeneous but linear integral equation

$$\hat{\mathrm{w}}_q(s=0) = \frac{1}{d-1}\mathrm{Tr}\Big\{\sum_{\boldsymbol{k}}\underline{\boldsymbol{V}}_{\boldsymbol{q},\boldsymbol{k}}\frac{S_{|\boldsymbol{q}-\boldsymbol{k}|}}{(k^2c_k^\perp)^2}\hat{\underline{\boldsymbol{\mathcal{U}}}}_{\boldsymbol{k},\boldsymbol{q}}(s=0)\Big\} = \hat{\Delta}_q(0) + \sum_p p^{d-3}C_{q,p}\frac{1}{(v_p^\perp)^2}\ . \tag{5.86}$$

The first order contribution $\hat{\Delta}_q(s)$ gives the Born renormalisation. The expression reads

$$\hat{\Delta}_q(s) = \frac{1}{N(d-1)} \mathrm{Tr} \left\{ \sum_{\boldsymbol{k}} \underline{\boldsymbol{V}}_{\boldsymbol{q},\boldsymbol{k}} \frac{S_{|\boldsymbol{q}-\boldsymbol{k}|}}{s(s+\xi)+k^2(c_k^\perp)^2} \cdot \underline{\boldsymbol{V}}^\dagger_{\boldsymbol{k},\boldsymbol{q}} \right\} . \tag{5.87}$$

This one-loop correction term dominates the integrated fluidity $\hat{\mathrm{w}}_q(s)$ for $n \to \infty$. The reason is, that the stability matrix $p^{d-3}C_{q,p}$ varies with n^{-2} for large densities[10]. Its exact expression reads:

$$\begin{aligned} C_{q,p} = \frac{1}{N^2(d-1)} \int d^{d-1}\hat{p} \mathrm{Tr} \Bigg\{ \sum_{\boldsymbol{k}} \frac{1}{k^2} \underline{\boldsymbol{V}}_{\boldsymbol{q},\boldsymbol{k}} \cdot \underline{\boldsymbol{V}}_{\boldsymbol{k},\boldsymbol{p}} S_{|\boldsymbol{q}-\boldsymbol{k}|} \cdot \ldots \\ \cdot \left[\underline{\boldsymbol{V}}^\dagger_{\boldsymbol{p},\boldsymbol{k}} \cdot S_{|\boldsymbol{k}-\boldsymbol{p}|} \underline{\boldsymbol{V}}^\dagger_{\boldsymbol{k},\boldsymbol{q}} + \underline{\boldsymbol{V}}^\dagger_{\boldsymbol{p},\boldsymbol{q}+\boldsymbol{p}-\boldsymbol{k}} \cdot \frac{k}{|\boldsymbol{p}+\boldsymbol{q}-\boldsymbol{k}|} S_{|\boldsymbol{k}-\boldsymbol{p}|} \underline{\boldsymbol{V}}^\dagger_{\boldsymbol{p}+\boldsymbol{q}-\boldsymbol{k},\boldsymbol{q}} \right] \Bigg\} \end{aligned} \tag{5.88}$$

Inserting the integrated fluidity back into the Equation (5.84) for the susceptibility $\hat{\chi}_q^\perp(0)$ leads to a linear equation for the inverse compliance $(qv_q^\perp)^2$:

$$\begin{aligned} (v_q^\perp)^2 &= \frac{(c_q^\perp)^2}{1+(c_q^\perp)^2 \hat{\mathrm{w}}_q(0)} \\ \Longleftrightarrow \sum_p \Big(\delta_{q,p} - p^{d-3} C_{q,p} \Big) \frac{1}{(v_p^\perp)^2} &= \hat{\Delta}_q(s=0) + \frac{1}{(c_q^\perp)^2} \equiv \frac{1}{(\tilde{c}_q^\perp)^2} . \end{aligned} \tag{5.89}$$

Here, $(q\tilde{c}_q^\perp)^2$ denotes the first order renormalized inverse compliance. The linear Equation (5.89) is only guaranteed a unique and non-zero solution if the bracket on the left-hand side is invertible. This is the case if, and only if, the stability matrix's maximal eigenvalue is smaller than unity. This and the already discussed fact that the stability matrix $p^{d-3}C_{q,p}$ depends reciprocally on the density suggest that the small eigenvalue or high-density case corresponds to the jammed phase. The integrated fluidity $\hat{\mathrm{w}}_q(s)$ also vanishes with $1/n$ in the high-density limit. As the eigenvalues are only controlled by the number density, $n = \frac{N}{V}$ becomes the only control parameter of our model. Before proceeding to the numerical solution of Equation (5.89), two more comments are in order:

[10]The scaling $p^{d-3}C_{q,p} \propto n^{-2}$ becomes apparent from Equation (D.16). For $n \to \infty$ holds $g^{(3)}(\boldsymbol{r},\boldsymbol{r}') \approx g(r) \approx 1$. Thus, the bare vertex $\underline{\boldsymbol{V}}$ becomes independent of n in the large density limit. Taking the thermodynamic limit $\sum_{\boldsymbol{k}} \to \frac{V}{(2\pi)^d} \int d^d\boldsymbol{k}$ gives the scaling $p^{d-3}C_{q,p} \propto n^{-2}$ for $n \to \infty$.

(I) The compliance and the system's stiffness are independent of the Langevin damping rate. This mirrors the fact that stability is independent of the dynamical details. The solution close to the unjamming transition is discussed in Section 5.5.

(II) It is noteworthy that the equation for the fluidity in the jammed state reduces to the $F1$-model, which is extensively studied in the literature (Götze, 2009; Voigtmann, 2011). This suggests that the linear approximation

$$\hat{\mathrm{w}}_q(s) \approx \hat{\Delta}_q(s) + \sum_p p^{d-1} C_{q,p} \hat{\chi}_p^{\perp}(s) \tag{5.90}$$

becomes valid for small frequencies. We will return to this when discussing the numerical solutions of the model in Appendix C. The diagrammatic representation of this approximation has been discussed in the context of Equation (5.79).

Figure 5.2 displays the solution of Equation (5.89) in the scalar ERM approximation in $d = 3$ and compares the prediction for the compliance with the results of the direct numerical diagonalization of the ERM performed by Philipp Baumgärtel. Panel 5.2a and panel 5.2b display data of the Gaussian and the Theta spring function, respectively, already shown in (Vogel *et al.*, 2025). Panel 5.2c shows the result for the linear spring function. Generally, the data shows good qualitative and even good quantitative agreement for high densities. Notably, the y-axis has been rescaled by $1/(\omega_0\sqrt{n^*})$ to render a dimensionless scalar. Here, $n^* = n\sigma^d$ denotes the dimensionless number density. Additionally, the trivial scaling of the compliance with n^* has been removed by dividing the data for $(qv_q)^2$ by $\sqrt{n^*}$. Thus, the decrease of the inverse compliance $(v_q^{\perp})^2$ with the density indicates that the system becomes soft. As the Gaussian spring function has infinite support, the system is always fully connected, and the critical point is at $n^* = 0$. However, Equation (5.89) predicts a divergence of the compliance at $n^*_{c,G} = 0.0560(1)$ in $d = 3$. Generally, the inverse compliance calculated from Equation (5.89) vanishes faster than $(qv_q)^2$ obtained by numerical diagonalization. As we discussed in Chapter 2, the jamming transition is of a geometric nature and, therefore, independent of the interaction details. While the ERM model principally captures this fact, the transition predicted by the theory erroneously depends on the interaction potential. The theory predicts for the Theta springfucntion $n^*_{c,T} = 0.830(1)$ and for the linear spring function $n^*_{c,T} = 1.220(3)$ in three dimensions. The next paragraph compares the inverse compliance with the true dispersion relation.

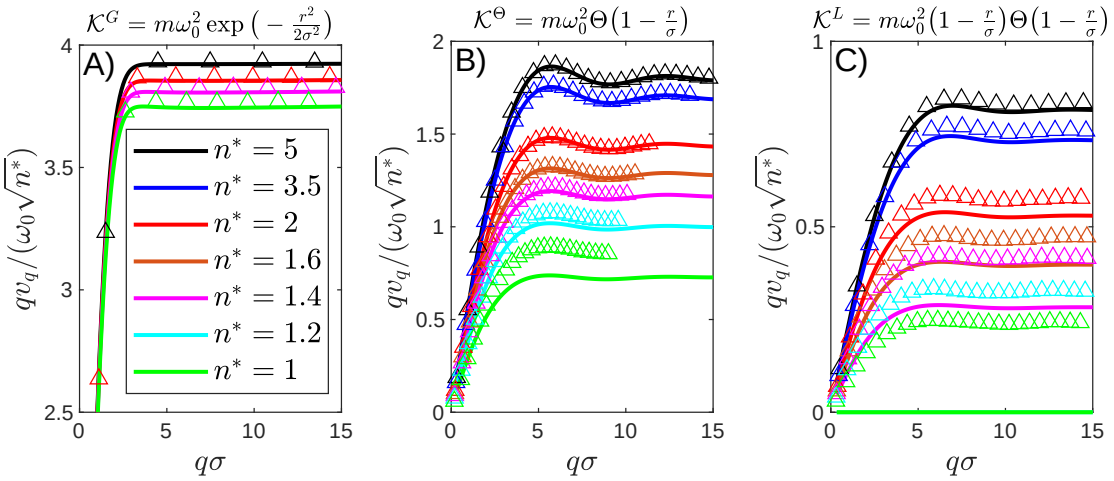

(a) Gaussian Spring function **(b)** Theta Spring function **(c)** Linear Spring function

Figure 5.2: The figure compares the square root of the inverse compliance calculated with Equation (5.89) (solid lines) with data obtained from numerical diagonalization by Philipp Baumgärtel (triangles). The figure displays the result for three different spring functions. The legend in Panel 5.2a includes the shown number densities $n^* = n\sigma^3$, and applies to all three panels. The calculations were performed in $d = 3$. The results for the Gaussian and the Theta spring function have been published in (Vogel *et al.*, 2025). There, the numerical methods were discussed in detail. The linear spring function was calculated in a system with 10.000 particles. As the analysis was performed in the scalar ERM model, the superscripted $\perp$ was omitted.

The dispersion relation: As an alternative to Equation (5.89), the inverse compliance $(v_q^\perp)^2$ is also extractable from the solution of the self-consistent model in the time domain, *e.g.* shown in Figure 5.1. Furthermore, this allows comparing the compliance, *i.e.* the $s \to 0$ limit of the susceptibility $\hat{\chi}_q^\perp(s)$ with the inverse of the true dispersion relation, *i.e.* the peak position in the real part of Laplace transformed autocorrelation function $\mathrm{Re}\{\hat{\mathrm{K}}_q^\perp(s)\}$. Figure 5.3 displays the results. It becomes apparent that the inverse compliance and the dispersion relation agree well for small wavevectors. Here, a linear relation holds $\omega = qv_q$ for $\omega \to 0$. The inverse compliance has been determined with two different methods: First of all, the static calculation via (5.89) and secondly, via the zero frequency limit of the full time-dependent solution $\mathrm{K}_q(t)$. The differences between the static and the dynamic calculation most likely arise from the approximations applied to the self-consistent model, which were necessary to stabilize the numeric. More details are provided in Section C. The two different ways of obtaining the dispersion

relation do also not fully agree. Here, the differences stem from neglecting the transient dynamics when fitting the data with a damped oscillator. Another source of error is the damped harmonic oscillator fit itself, which was not perfect.

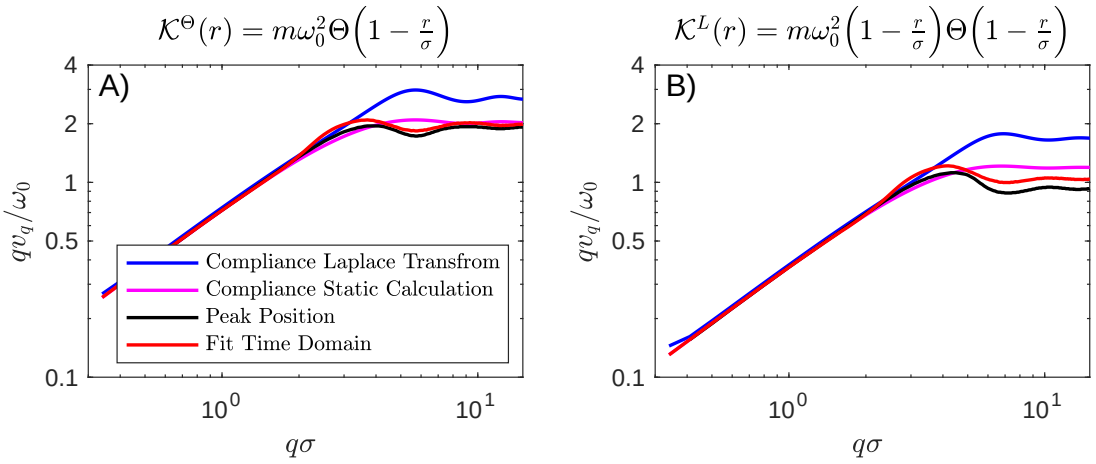

(a) Theta Spring function

(b) Linear Spring function

Figure 5.3: Comparison of the square root of the inverse compliance qv_q (purple and blue) with the true dispersion relation (black and red): Panel 5.3a depicts the solution for the Theta spring function, for $n^* = 2$. Panel 5.3b depicts the solution for the linear function for $n^* = 3$. The legend applies to both figures. The blue curve depicts the zero frequency limit of the Laplace transform of $\mathrm{K}_q(t)$, while the purple line has been obtained from Equation (5.89). The black curve was obtained from the Laplace transform of $\mathrm{K}_q(t)$ by determining the peak position of the spectrum. The red curve displays the parameters obtained by fitting the time-dependent solution of $\mathrm{K}_q(t)$ with a damped harmonic oscillator. To neglect the transient regime, we waited for four periods of oscillations for $q\sigma \leq 1.7$ and for one period for $1.7 < q\sigma < 4.8$ before fitting the data.

Experimental and Numerical investigations have reported a dip in the dispersion relation $\tilde{v}_q(s)$ in the frequency regime of the Boson peak (Baldi *et al.*, 2010; Mizuno and Ikeda, 2018). This phenomenon has been labelled *sound softening* (Schirmacher and Ruocco, 2022). Figure 5.4 depicts the dispersion relation results for the four methods described above. The two curves displaying $v_q = \hat{v}_q(s \to 0)$ exhibit no dip for either of the two analysed spring functions. This is expected as the compliance is not sensitive to sound softening, a finite frequency phenomenon. The numerical investigations of Philipp Baumgärtel have confirmed this. Only the curve displaying the harmonic oscillator fit exhibits a dip. Indeed, the decrease and subsequential increase appear just before

the saturation of qv_q depicted in Figure 5.3. The associated frequency $\omega = \max(qv_q)$ marks the position of a peak in the Density of States depicted in the figures 5.6a and 5.6b. Thus, the dip in the red curve could indeed be an indication of sound softening. However, the analysis is not conclusive. First of all, the data obtained from the Laplace transformation of the data does not feature the characteristic dip. This suggests that the recorded dip in the red curve might be due to the suboptimal dampened oscillator fit. Furthermore, the numerical solution's general shortcomings affect the finite frequency range as outlined in Appendix C. Thus, we conjecture that our numerical solutions for the dispersion relation do not allow any conclusive statements about the presence of sound softening. After having discussed the real part of the complex dispersion relation $(q\hat{v}_q^{\perp}(s))^2$ we now turn to the sound attenuation and derive an equation for Γ_q in the limit of vanishing frequency $s \to 0$.

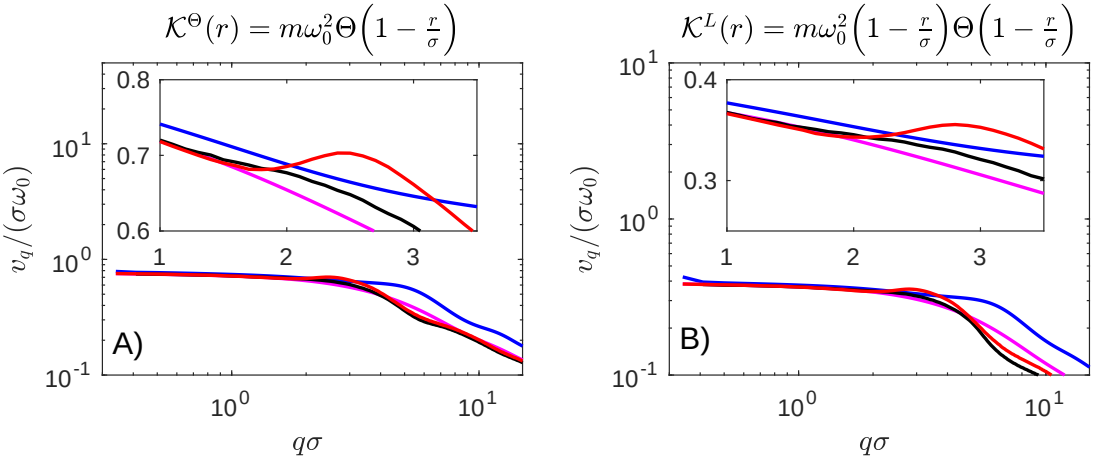

(a) Theta Spring function **(b)** Linear Spring function

Figure 5.4: Same data as in Figure 5.3 but divided by σq to show the wavenumber dependency of v_q. The insert also show v_q as a function of σq but focuses on a selected wavenumber interval. The colour coding is the same as in Figure 5.3.

5.3.2 Rayleigh-damping

We have already discussed in Section 2.2.4 that plane waves are no exact eigenmodes in amorphous solids due to the topological disorder and the initial stresses. Thus, sound modes are damped even in the absence of thermal fluctuations. To investigate the disorder-induced attenuation, we set $\xi = 0$ in the following. The imaginary contribution to the inverse of the susceptibility $\hat{\chi}_q^{\perp}(s = -i\omega + 0^+)$ causes an exponential decay of

the correlation function. Here, ω denotes the Fourier- frequency and 0^+ is an infitesimal real part. Thus, the attenuation is determined by the imaginary part of the complex dispersion relation $\mathrm{Im}(q\hat{v}_q^{\perp}(s=-i\omega+0^+)^2) \equiv -\omega\Gamma_q^{\perp}(\omega)$ evaluated on the imaginary axis, which specifies the damping or the *lifetime* of a mode (Srednicki, 2007, Chapter 25). As we will see in the following, $\Gamma_q^{\perp}(\omega)$ originates from a non-analyticity of the propagator at the sound pole $\omega = \hat{v}_q^{\perp}(\omega)q$ for $\omega \to 0$. Figure 5.3 shows that the dispersion relation $(qv_q^{\perp})^2$ becomes independent of the frequency ω for sufficiently small frequencies. Here, the attenuation is supposed to become Rayleigh-like *i.e* $\omega\Gamma_q^{\perp}(\omega = qv_q^{\perp}) \propto \omega q^{d+1}$ for small wavenumbers q. This was discussed in Section 2.3. Hereinafter, we will show that including the non-planar contributions in Equation (5.64) is crucial, as the theory would otherwise not predict Rayleigh-damping.

To investigate the imaginary part of the generalised shear modulus $\hat{\mathrm{G}}_q^{\perp}(-i\omega+0^+)$, we will frequently rely on the Sokhotski–Plemelj formula

$$\frac{1}{x \pm i0^+} = \mathcal{P}\frac{1}{x} \mp i\pi\delta(x) \,, \tag{5.91}$$

with $x \in \mathbb{R}$ and where $\mathcal{P}$ denotes the Cauchy principal value. Additionally, we will assume that we deal with small frequencies, *i.e.* $\omega\,, s \to 0$. By expanding $s\hat{G}_q^{\perp}(s)\big|_{s=-i\omega+0^+}$ in Equation (5.66b) for small imaginary parts $\mathrm{Im}\{\hat{\mathrm{w}}_q(s=-i\omega+0^+)\}$, we observe that the complex dispersion relation can be written as

$$(q\hat{v}_q^{\perp}(s=-i\omega+0^+))^2 \underset{\omega\to 0}{\longrightarrow} (qv_q^{\perp})^2 - q^2(v_q^{\perp})^4\,\mathrm{Im}\{\hat{\mathrm{w}}_q(s=-i\omega+0^+)\} \,. \tag{5.92}$$

The neglected terms vanish faster than sq^{d+1} for $s, q \to 0$. Equation (5.83) for the integrated renormalized vertex is non-linear, which makes a systematic discussion of the imaginary part arising from the renormalized vertex $\hat{\underline{\boldsymbol{\mathcal{V}}}}_{\boldsymbol{k},\boldsymbol{q}}(s)$ difficult. Thus, we isolate three different and independent terms and calculate their arising contributions to the imaginary part one by one. For that, we express the time-integrated fluidity as

$$\hat{\mathrm{w}}_q^{(i)}(s) = \frac{1}{N}\sum_{\boldsymbol{k}} \underline{\boldsymbol{V}}_{\boldsymbol{q},\boldsymbol{k}} : \hat{\underline{\boldsymbol{\mathcal{U}}}}_{\boldsymbol{k},\boldsymbol{q}}^{(i)}(s) \,. \tag{5.93}$$

The first two terms stem from the one and the two-loop corrections in Equation (5.76), respectively. The associated parts of the renormalized vertex read:

$$\hat{\underline{\boldsymbol{U}}}^{(1)}_{\boldsymbol{k},\boldsymbol{q}}(s) = \frac{1}{\left[(s(s+\xi)+k^2(c_k^{\perp})^2)\right]}\,\underline{\boldsymbol{V}}^{\dagger}_{\boldsymbol{k},\boldsymbol{q}} S_{|\boldsymbol{q}-\boldsymbol{k}|}\;, \tag{5.94}$$

$$\begin{aligned}\hat{\underline{\boldsymbol{U}}}^{(2)}_{\boldsymbol{k},\boldsymbol{q}}(s) = \frac{(c_k^{\perp})^2}{\left[(s(s+\xi)+k^2(c_k^{\perp})^2)\right]}\Big\{&\hat{\underline{\boldsymbol{m}}}_k(s)\cdot\underline{\boldsymbol{V}}^{\dagger}_{\boldsymbol{k},\boldsymbol{q}} S_{|\boldsymbol{q}-\boldsymbol{k}|} \\ &+\frac{1}{N}\sum_{\boldsymbol{p}}\underline{\tilde{\boldsymbol{V}}}(\boldsymbol{q},\boldsymbol{k},\boldsymbol{p})\cdot\underline{\boldsymbol{V}}^{\dagger}_{\boldsymbol{p},\boldsymbol{q}}\hat{\chi}^{\perp}_{|\boldsymbol{q}-\boldsymbol{k}-\boldsymbol{p}|}(s)S_{|\boldsymbol{q}-\boldsymbol{p}|}\Big\}\end{aligned} \tag{5.95}$$

The remainder contains all the non-linear contributions. The term is given by

$$\hat{\underline{\boldsymbol{U}}}^{(3)}_{\boldsymbol{k},\boldsymbol{q}}(s) = -\frac{s^2}{k^2}\underline{\boldsymbol{m}}_k(s)\cdot\hat{\underline{\boldsymbol{U}}}_{\boldsymbol{k},\boldsymbol{q}}(s) - \frac{s^2}{k^2 N}\sum_{\boldsymbol{p}}\underline{\tilde{\boldsymbol{V}}}(\boldsymbol{q},\boldsymbol{k},\boldsymbol{p})\cdot\hat{\underline{\boldsymbol{U}}}_{\boldsymbol{p},\boldsymbol{q}}(s)\hat{\chi}^{\perp}_{|\boldsymbol{q}-\boldsymbol{k}-\boldsymbol{p}|}(s)\;. \tag{5.96}$$

Hereinafter, we consider the three contributions $\mathrm{w}_q^{(i)}$ and their imaginary part separately. However, one more remark is in order. As said, the attenuation arises from interactions of the mode with the disorder and the initial stresses. Basically, a sound mode gradually loses its energy to the continuum of modes, effectively heating the systems. To correctly address this, we change the notation in this subsection and consider integrals over all wavevectors instead of sums:

$$\sum_{\boldsymbol{p}} \longrightarrow V\int\frac{d^d\boldsymbol{p}}{(2\pi)^d}\;. \tag{5.97}$$

Practically, this assumed continuity of the wavenumbers allows applying the Sokhotski–Plemelj theorem from Eqaution (5.91). Now, we look at the imaginary part of the three contributions $\hat{\mathrm{w}}_q^{(i)}(s=-i\omega+0^+)$ separately.

The Born term $\hat{\mathrm{w}}_q^{(1)}$: The first contribution arises from the Born term or the one-loop corrections term of the self-energy in Equation (5.76). This contribution dominates for high densities or deep in the jammed phase. Introducing the one-loop correction matrix

$$C^{(0)}_{q,p} = \frac{1}{n(d-1)}\mathrm{Tr}\Big\{\int\frac{d^{d-1}\hat{\boldsymbol{p}}}{(2\pi)^d}\underline{\boldsymbol{V}}_{\boldsymbol{q},\boldsymbol{p}}S_{|\boldsymbol{q}-\boldsymbol{p}|}\cdot\underline{\boldsymbol{V}}^{\dagger}_{\boldsymbol{p},\boldsymbol{q}}\Big\} \tag{5.98}$$

provides a convenient way of expressing the imaginary part of the Born term:

$$\begin{aligned}\operatorname{Im}\hat{\mathrm{w}}_q^{(1)}(s=-i\omega+0^+) &\underset{\omega\to 0}{\longrightarrow} = \operatorname{Im}\lim_{\omega\to 0}\int_0^\infty dpp^{d-1}C_{q,p}^{(0)}\frac{1}{-\omega^2-i0^+ + p^2(c_p^\perp)^2}\\ &= -\operatorname{Im}\lim_{\omega\to 0}\int_0^\infty dpp^{d-1}C_{q,p}^{(0)}\frac{1}{2\omega}\left[\frac{1}{\omega+i0^+ + pc_p^\perp}+\frac{1}{\omega+i0^+ - pc_p^\perp}\right]\\ &= \frac{\beta^{1,1}}{2(k_D c_0^\perp)^d}\omega^{d-2}q^2 + \frac{\beta^{1,2}}{2k_D^d(c_0^\perp)^{d+2}}\omega^d\,.\end{aligned} \tag{5.99}$$

We relied on Equation (5.91) in the third line. Furthermore, we utilized the properties of the vertex. As the vertex is an analytic function of the wavenumbers, rotational invariance and Equation (5.42) lead to $C_{q\to 0,0}^{(0)} = \frac{\beta_0^{(1,1)}}{k_D^d}q^2$ and $C_{0,p\to 0}^{(0)} = \frac{\beta_0^{(1,2)}}{k_D^d}p^2$, with the Debye-wavevector $k_D = 2\sqrt{\pi}\sqrt[d]{\overline{\Gamma}(1+d/2)n}$, which is only included to render the coefficients $\beta^{(i,j)}$ unit-less scalars and $\overline{\Gamma}(x)$ denotes the Gamma-function. Their numerical value is obtained from the small wavenumber expansion of the matrix $C_{\boldsymbol{q},\boldsymbol{p}}^{(0)}$:

$$\begin{aligned}\beta^{(1,1)} &= k_D^d\lim_{q,p\to 0}\frac{1}{q^2}C_{q,p}^{(0)}\,,\\ \beta^{(1,2)} &= k_D^d\lim_{q,p\to 0}\frac{1}{p^2}C_{q,p}^{(0)}\,.\end{aligned} \tag{5.100}$$

Thus, the attenuation arising from the one-loop term is indeed in accordance with Rayleigh-damping $\omega\Gamma_q^{\perp,(1)}(\omega\to 0)\propto q^4\omega^{d-2}$ around the sound pole $\omega = qv_0^\perp$. Here, $\Gamma_q^{\perp,(1)}(\omega\to 0)$ denotes the attenuation arising from the Born term. In the next paragraph, we look at the imaginary part of the self-consistent two-loop term $\hat{w}_q^{(2)}(s)$.

The self-consistent term $\hat{\mathrm{w}}_q^{(2)}$: The second contribution arises from the self-consistent term $\hat{\boldsymbol{\mathcal{U}}}_{\boldsymbol{k},\boldsymbol{q}}^{(2)}(s)$ or the two-loop correction in Equation (5.76). The constituting equation reads

$$\operatorname{Im}\hat{\mathrm{w}}_q^{(2)}(s=-i\omega+0^+)\underset{\omega\to 0}{\longrightarrow}\operatorname{Im}\lim_{\omega\to 0}\int_0^\infty dpp^{d-1}C_{q,p}\frac{1}{-\omega^2-i0^+ + p^2(v_p^\perp)^2}\,. \tag{5.101}$$

The matrix $C_{q,p}$ was defined in Equation (5.88). In principle, we can repeat the same calculation as for the Born term. However, before concluding that the imaginary part of the self-consistent term agrees with Rayleigh-damping, we have to note that the stability

matrix crucially vanishes at the origin:

$$C_{0,0} = \frac{V}{N^2(d-1)} \int d^{d-1}\hat{p}\, \mathrm{Tr}\Bigg\{ \sum_{\boldsymbol{k}} \frac{1}{k^2} \underline{\boldsymbol{V}}_{0,\boldsymbol{k}} \\ \times \underline{\boldsymbol{V}}_{\boldsymbol{k},0} S_k \cdot \Big[\underline{\boldsymbol{V}}_{\boldsymbol{k},0} \cdot S_k \underline{\boldsymbol{V}}_{0,\boldsymbol{k}} + \underline{\boldsymbol{V}}_{-\boldsymbol{k},0} \cdot S_k \underline{\boldsymbol{V}}_{0,-\boldsymbol{k}} \Big] \Bigg\} = 0 \tag{5.102}$$

To obtain this relation, we had to use the symmetry of the vertex $\underline{\boldsymbol{V}}^{\dagger}_{\boldsymbol{k},\boldsymbol{q}} = \underline{\boldsymbol{V}}_{\boldsymbol{q},\boldsymbol{k}}$ and the other properties of the bare vertex like $\lim_{q\to 0} \underline{\boldsymbol{V}}_{\boldsymbol{q},-\boldsymbol{k}} = -\lim_{q\to 0} \underline{\boldsymbol{V}}_{\boldsymbol{q},\boldsymbol{k}}$ and $\lim_{k\to 0} \underline{\boldsymbol{V}}_{-\boldsymbol{q},\boldsymbol{k}} = \lim_{k\to 0} \underline{\boldsymbol{V}}_{\boldsymbol{q},\boldsymbol{k}}$. See Equation (5.42) for details. Remarkably, Equation (5.102) only holds because of the inclusion of the non-planar terms in Equation (5.76) or Equation (5.64). They cancel the erroneous contribution of the planar terms exactly. This results from a symmetry of the underlying scattering events, which was coined *Leutheusser-Symmetry* (Vogel *et al.*, 2025). We elaborate further on this in Appendix B. There, we show, that Leutheusser symmetry traces back to the statistical equivalence of the positions in the medium. Equation (5.102) together with rotational invariance again implies that $C_{q\to 0,0} = \frac{\beta_0^{(2,1)}}{k_D^d} q^2$ and $C_{0,p\to 0} = \frac{\beta_0^{(2,2)}}{k_D^d} p^2$ hold in the hydrodynamic limit. All in all, this leads to

$$\mathrm{Im}\, \hat{\mathrm{w}}_q^{(2)}(s = -i\omega + 0^+) \underset{\omega\to 0}{\longrightarrow} \frac{\beta^{(2,1)}}{(2k_D v_0^{\perp})^d} \omega^{d-2} q^2 + \frac{\beta^{(2,2)}}{2k_D^d (v_0^{\perp})^{d+2}} \omega^d \,. \tag{5.103}$$

Again, the self-consisted term also predicts Rayleigh-damping $\omega\Gamma_q^{\perp,(2)}(\omega \to 0) \propto q^4\omega^{d-2}$ around the sound pole. Here, $\Gamma_q^{\perp,(2)}$ denotes the contribution arising from the self-consistent term. In analogy to the one-loop correction matrix $C_{q,p}^{(0)}$, the coefficient $\beta^{(2,j)}$ can be obtained by expanding $C_{q,p}$ for $q,\, p \to 0$. The defining equations read

$$\beta^{(2,1)} = k_D^d \lim_{q,p\to 0} \frac{1}{q^2} C_{q,p} \,, \\ \beta^{(2,2)} = k_D^d \lim_{q,p\to 0} \frac{1}{p^2} C_{q,p} \,. \tag{5.104}$$

Note, that the dimensionless coefficients $\beta^{(2,i)}$ vary with $\frac{1}{n^*}$. This is due to the additional k-integration in Equation (5.88). Lastly, we look at the non-linear term.

The non-linear term $\hat{\mathrm{w}}_q^{(3)}$: The last contribution to the integrated fluidity reads

$$\hat{\mathrm{w}}_q^{(3)}(s) = \frac{1}{N} \sum_{\boldsymbol{k}} \underline{\boldsymbol{V}}_{\boldsymbol{q},\boldsymbol{k}} : \hat{\underline{\boldsymbol{U}}}_{\boldsymbol{k},\boldsymbol{q}}^{(3)}(s) \; . \tag{5.105}$$

Here, the third part of the time-integrated renormalized vertex $\hat{\underline{\boldsymbol{U}}}_{\boldsymbol{k},\boldsymbol{q}}^{(3)}(s)$ is given in Equation (5.96). Its contribution $\Gamma_q^{\perp,(3)}(\omega)$ can be calculated iteratively by inserting Equation (5.85) again and again for finite frequencies $s = -i\omega + 0^+$. Subsequently, the steps of the previous two paragraphs can be repeated. However, this immediately leads to the conclusion, that $\operatorname{Im} \hat{\mathrm{w}}_q^{(3)}(s = -i\omega + 0^+)$ is at least of order $\mathcal{O}(q^2\omega^d)$. The resulting contribution is subdominant $\omega, q \to 0$ to the terms discussed in the previous paragraphs in any dimension.

To summarize the results, Equation (5.92) gives for the Rayleigh-sound attenuation for $\omega \to 0$:

$$\Gamma_q^{\perp} \equiv \Gamma_q^{\perp}(\omega)\big|_{\omega = v_0^{\perp} q} \underset{\omega \to 0}{\longrightarrow} \frac{(q v_0^{\perp})^{d+1}}{2 k_D^d} \left(\frac{\beta_0^{(1)}}{(c_0^{\perp})^d} + \frac{\beta_0^{(2)}}{(v_0^{\perp})^d} \right) \tag{5.106}$$

Here, we followed (Mizuno and Ikeda, 2018) as we evaluated the attenuation at the propagation frequency $\omega \overset{!}{=} q v_0^{\perp}$. As finite frequency contributions to the dispersion relation are neglected, this only holds for vanishing frequencies. The final coefficients are given by $\beta_0^{(1)} = \beta_0^{(1,1)} + \beta_0^{(1,2)} \frac{(v_0^{\perp})^2}{(c_0^{\perp})^2}$ and $\beta_0^{(2)} = \beta_0^{(2,1)} + \beta_0^{(2,2)}$, where $\beta_0^{(2)}$ includes an additional factor $1/n^*$ but $\beta_0^{(1)}$ is independent of the density. Thus, the scaling of the attenuation agrees with the findings in the stable Gaussian ERM model for large number densities n^* (Baumgärtel *et al.*, 2024). Here, the attenuation is dominated by the Born term and, therefore, by $\Gamma_q^{(1)}$. Importantly, the theory only predicts Rayleigh-damping due to the inclusion of the non-planar diagrams. This was already mentioned in the remarks after Equation (5.66). The importance of non-planar terms can be analytically verified from Equation (5.102): The crucial second term would be missing in a planar theory and damping would therefore be much stronger for $q \, , \omega \to 0$.

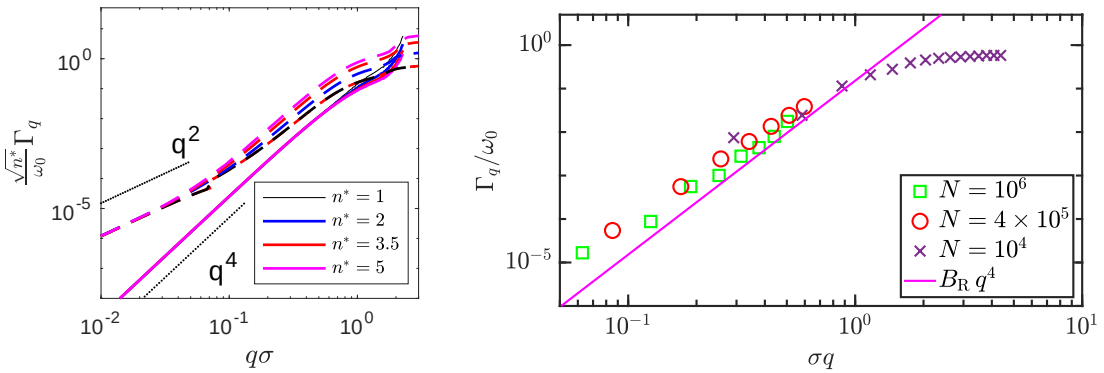

(a) Importance of the non-planar diagrams

(b) Comparison of theoretical and numerical investigation

Figure 5.5: Panel 5.5a displays the sound attenuation coefficient Γ_q calculated in a high density approximation in $d = 3$. The panel shows the data for different densities and for the Gaussian spring function $\mathcal{K}^G(r) = m\omega_0^2 \exp[-r^2/(2\sigma^2)]$. The high density approximation amounts to replacing the full propagator $\hat{\chi}_q^{\mathrm{SERM}}(s)$ in Equation (5.79) with the bare propagator $\hat{\chi}_q^{(0)}(s)$. Additionally $\hat{\chi}_q^{\mathrm{SERM}}(s) \approx \left[s^2 + (qc_q^{\mathrm{SERM}})^2 - \hat{\Sigma}_q^{\mathrm{SERM}}(s)\right]^{-1}$ was used. Both approximations are valid for $n^* \to \infty$. The dashed lines show the result for the second-order Born theory, where the non-planar diagrams were neglected. The full lines depict the data for the non-planar topology. The figure in Panel 5.5a is adapted from from *Vibrational Phenomena in Glasses at Low Temperatures Captured by Field Theory of Disordered Harmonic Oscillators*, by F. Vogel & M. Fuchs, Phys. Rev. Lett. 2023, vol. 130, page 236101, Copyright [2025] by the American Physical Society Reprinted with permission Doi:10.1103/PhysRevLett.130.236101. Panel 5.5b compares the theoretical prediction (solid purple line) with results from numerical investigations by Philipp Baumgärtel of the scalar ERM model (symbols). The different symbols represent different system sizes. The data was recorded for $n^* = \omega_0 = 1$. For numerical details, see (Baumgärtel *et al.*, 2024). The figure has been created by Philipp Baumgärtel and is reprinted from *Properties of stable ensembles of Euclidean random matrices.*, by P. Baumgärtel, F. Vogel & M. Fuchs, Phys. Rev. E. 2024, vol. 109, page 014120, Copyright [2025] by the American Physical Society Reprinted with permission Doi:10.1103/PhysRevE.109.014120

We have also investigated the influence of the non-planar diagrams numerically. Figure 5.5b shows the result of a high-density perturbation calculation valid deep in the jammed state. As one can see, the self-consistent Born theory erroneously predicts a q^2 scaling of Γ_q in the hydrodynamic limit in three dimensions. Noteably, the data

collapses after rescaling with $\sqrt{n^*}$, which is a consequence of being sufficiently deep in the stable phase. Figure 5.5b compares the theoretical prediction with the results from a numerical investigation of the Euclidean Random Matrix model (Baumgärtel *et al.*, 2024). The numeric and the theory show appreciable accordance. The visible quantitative discrepancies can arise from terminating the high-density approximation of the self-energy at order $\mathcal{O}(n^{-2})$. In the next section, we look at another frequency-dependent quantity: the Density of States $D(\omega)$.

5.3.3 Vibrational Density of States

This section discusses the (transverse) vibrational Density of States (vDOS) $D_\lambda(\lambda)$ in a disordered athermal system. Here, λ denotes an eigenvalue of one of the system's eigenmodes. The aim is to express $D_\lambda(\lambda)$ in terms of the susceptibility $\hat{\chi}_q^\perp(-i\omega + 0^+)$, where the frequency of the mode is the square root of the eigenvalue $\omega^2 = \lambda$. However, we face several difficulties in the derivation of a constituting equation for D_λ: First of all, the concept of a dispersion relation $\omega^2 = (q\tilde{v}_q^\perp(\omega))^2$ breaks down for higher energies where the modes have sufficient energy to resolve the disorder. We have discussed this in Section 5.3.1, and it is also visible in Figure 5.3b. Consequently, the wavenumber does not specify the eigenmodes alone, as it is true in crystals. Moreover, it is, in general, unclear if the requirements of the implicit function theorem are met (Krantz and Parks, 2002, Theorem 3.2.1). Thus, the relation

$$D_\lambda(\lambda) = \frac{1}{n} \int \frac{d^d\boldsymbol{k}}{(2\pi)^d} \delta(\lambda - \lambda(\boldsymbol{k})) \, , \tag{5.107}$$

is, in general, not valid (Ashcroft and Mermin, 1976, Equation 8.57). Here, $\lambda(\boldsymbol{k})$ represents an eigenvalue of a mode characterized by the wavevector $\boldsymbol{k}$. The second difficulty arises from the Self-Consistent Current Response Theory taking anharmonic effects into account. Hence, there is generally no Hamiltonian available, which we could diagonalize. In contrast, in the harmonic case, the vDOS is given by the eigenvalues of the associated dynamical matrix $\underline{\boldsymbol{\mathcal{H}}}$. Here, the eigenvalues can be obtained from the Green's function $\mathcal{G}_{ij}(\lambda) = -[\lambda + i0^+ - \underline{\boldsymbol{\mathcal{H}}}]^{-1}_{ij}$ (Altland and Simons, 2010, Equation 3.59).

This section is split into three parts. First of all, we argue how the vDOS can be obtained from the susceptibility $\hat{\chi}_q^{\perp}(-i\omega + 0^+)$ defined in Equation (5.70). Assuming that the one particle velocities together span the whole vector space of dynamic variables. We arrive at the result that the vDOS is given by the integral over $\mathrm{Im}\{\hat{\chi}_q^{\perp}(-i\omega + 0^+)\}$. In the second part, we discuss the vDOS in the one-phonon approximation of the ERM model and state that the averaged vDOS can be obtained from the high momentum limit $q \to \infty$ of the averaged susceptibility $\underline{\boldsymbol{\chi}}^{\mathrm{ERM}}(\boldsymbol{q}, -i\omega + 0^+)$. Lastly, we discuss numerical results for the scalar ERM model.

Density of States in the Mode-Coupling Approximation As stated in the introduction to this chapter, the eigenmodes of an amorphous system are generally not known. As discussed in Section 2, sound modes are no exact eigenmodes of the system due to the topological disorder and due to initial stresses, leading to the attenuation even in the absence of noise and temperature T and for $\omega, \boldsymbol{q} \to 0$. To circumvent the unknown true eigenmodes, we define the two-particle susceptibility:

$$\hat{\underline{\boldsymbol{\chi}}}_{ij}(s) \equiv \frac{1}{s} \frac{\langle \boldsymbol{v}_i \hat{R}(s) \boldsymbol{v}_j \rangle}{d\frac{k_B T}{m}} \ . \tag{5.108}$$

Here, $\boldsymbol{v}_i$ is the velocity of the i^{th}- particle. The conceptual idea is that any vibrational mode in accordance with the consistency criterion in Equation (2.9) can be expressed with the knowledge of the two-particle susceptibility $\hat{\chi}_{ij}(s)$. Thus, we define the vDOS as the imaginary part of the trace of the one-particle susceptibility:

$$D_\lambda(\lambda) \equiv \frac{\mathrm{Im}}{d^2\pi} \sum_i \frac{\mathrm{Tr}\{\langle \boldsymbol{v}_i \hat{R}(s) \boldsymbol{v}_i \rangle\}}{sN\frac{k_B T}{m}} \ . \tag{5.109}$$

This definition is motivated by Quantum Field Theory[11], where the DOS is related to the one particle propagator or Green's function (Altland and Simons, 2010, Section 3.3). The spectrum of the one-particle velocity auto-correlation has been computed for

[11] If the dynamics are generated by a Hamiltonian H, the DOS coincides with the spectrum of H, and it can be computed in a basis of the associated Hilbert space: Denoting the normalized eigenfunctions of H with $|\lambda_i\rangle$ and the associated eigenvalue as λ_i, one finds for an arbitrary normalized basis of the vector space $\{|\boldsymbol{x}\rangle\}_i$:

$$\sum_j \mathrm{Im}\, \langle \boldsymbol{x}_j | | \lambda + i0^+ - \mathrm{H}]^{-1} | \boldsymbol{x}_j \rangle = \sum_{j,i} \langle \boldsymbol{x}_j | \lambda_i \rangle \, \mathrm{Im} \frac{1}{\omega + i0^+ - \lambda_i} \, \langle \lambda_i | \boldsymbol{x}_j \rangle$$

the Newtonian case for finite temperature (Bosse *et al.*, 1978). In the following, we will derive the spectrum of the one-particle velocity autocorrelation function in the more general Langevin case following the footsteps of (Bosse *et al.*, 1978). We define

$$\hat{\mathrm{K}}^{(1)}(s) = \frac{m}{dk_BT} \left\langle v_1^\alpha \hat{R}(s) v_1^\alpha \right\rangle \ . \tag{5.110}$$

Here, the index 1 refers to one of the N particles, which are all statisitcally equivalent. As a reminder, Einsteins sum convention is used for the spatial indices. The initial condition reads $\mathrm{K}^{(1)}(t=0) = 1$. Using consecutively Equation (3.30) with the one-particle projection-operators $P_1^{(1)} = \frac{m}{k_BT} \left|v_1^\alpha\right\rangle \left\langle v_1^\alpha\right|$ and later with $P_2^{(1)} = \frac{m}{k_BT\omega_0^2} \left|\Omega^\dagger v_1^\alpha\right\rangle \left\langle [\Omega^\dagger v_1^\alpha]\right|$ expresses $\hat{\mathrm{K}}^{(1)}(s)$ in terms of the memory functions $\hat{\mathrm{G}}^{(1)}(s)$ and $\hat{\mathrm{W}}^{(1)}(s)$:

$$\hat{\mathrm{K}}^{(1)}(s) = \frac{1}{s + \xi + \hat{\mathrm{G}}^{(1)}(s)} \ , \tag{5.111a}$$

$$\hat{\mathrm{G}}^{(1)}(s) = \frac{m}{dk_BT} \left\langle v_1^\alpha \Omega \hat{R}_{Q_1^{(1)}}(s) \Omega v_1^\alpha \right\rangle = \frac{\omega_0^2}{s + \omega_0^2 \hat{\mathrm{W}}^{(1)}(s)} \ , \tag{5.111b}$$

$$\hat{\mathrm{W}}^{(1)}(s) = \frac{m}{k_BT\omega_0^4} \left\langle v_1^\alpha \Omega Q_1^{(1)} \Omega \hat{R}_{Q_2^{(1)}}(s) \Omega Q_1^{(1)} \Omega v_1^\alpha \right\rangle \ . \tag{5.111c}$$

Here, $\hat{\mathrm{G}}^{(1)}(s)$ denotes the one-particle fluctuation force autocorrelation in analogy to Equation (5.16). Similarly, $\hat{\mathrm{W}}^{(1)}(s)$ is defined in analogy to Equation (5.30). The two complementary projection operators read $Q_1^{(1)} = 1 - P_1^{(1)}$ and $Q_2^{(1)} = 1 - P_1^{(1)} - P_2^{(1)}$. They define the reduced resolvents

$$\begin{aligned} \hat{R}_{Q_1^{(1)}}(s) &= Q_1^{(1)} \left[s + Q_1^{(1)} \Omega Q_1^{(1)} \right]^{-1} Q_1^{(1)} \ , \\ \hat{R}_{Q_2^{(1)}}(s) &= Q_2^{(1)} \left[s + Q_2^{(1)} \Omega Q_2^{(1)} \right]^{-1} Q_2^{(1)} \ . \end{aligned} \tag{5.112}$$

$$= -\pi \sum_i \delta(\lambda - \lambda_i) \left\langle \lambda_i \right| \underbrace{\sum_j \left|\boldsymbol{x}_j\right\rangle \left\langle \boldsymbol{x}_j\right|}_{=1} \left|\lambda_i\right\rangle = -\pi \sum_i \delta(\lambda - \lambda_i) \ .$$

In the second line, we used the Sokhotski–Plemelj theorem from Equation (5.91). The driving idea is that a reference frame $\{\boldsymbol{R}\}_{i=1}^N$ exists in the stable phase. Excluding structural changes or equivalently assuming quenched disorder suggests that the phase space is spanned by the velocities $\Gamma \to \{\boldsymbol{v}\}_{i=1}^N$ alone. Additionally, we assume that any dynamic variable of interest can be expressed as a linear combination of the single velocities $\boldsymbol{v}_i$. This ultimately harmonic approximation reflects that elongations in a stable body from the reference position $\boldsymbol{R}_i$ must be small to avoid melting the structure. All of these assumptions amount to the assumed completeness relation $1 = \frac{m}{k_BT} \sum_{i=1}^N \left|\boldsymbol{v}_i\right\rangle \left\langle \boldsymbol{v}_i\right|$. Of course, this argument is only informal.

Furthermore $\omega_0 = \sqrt{G^{(1)}(t=0)}$ denotes the Einstein frequency. The derivation of Equation (5.111) is in complete analogy to the derivation of the self-consistent current theory in Section 5.2. Again, we have ignored all but the potential contributions of the stress in the contributions for $m(s)$. In general, the following derivation continues in complete analogy to the construction of the self-consistent model in Section 5.2. Using the explicit expression for the adjoint Klein-Kramers-Operator from Equation (3.8) but neglecting kinetic contributions leads to

$$Q_1^{(1)}\Omega^\dagger \boldsymbol{v}_1 \approx -\frac{1}{m}\sum_{j\neq 1}\frac{U(|\boldsymbol{r}_1-\boldsymbol{r}_j|)}{\partial \boldsymbol{r}_1} \approx \frac{i}{m}\int \frac{d^3\boldsymbol{k}}{(2\pi)^3}U(k)\boldsymbol{k}\varrho_1(-\boldsymbol{k})\varrho(\boldsymbol{k})\;. \tag{5.113}$$

with the density $\varrho(\boldsymbol{k}) = \sum_j e^{-i\boldsymbol{k}\cdot\boldsymbol{r}_j}$ and the one-particle density $\varrho_1(\boldsymbol{k}) = e^{-i\boldsymbol{k}\cdot\boldsymbol{r}_1}$. Note that the last step in Equation (5.113) only holds approximately. We made use of the approximation $\varrho(\boldsymbol{k}) - \varrho_1(\boldsymbol{k}) \approx \varrho(\boldsymbol{k})$, which holds for $N \to \infty$. To calculate the Einstein frequency, we again use the relation $\int d\Gamma \boldsymbol{F}_j A\Psi_{\mathrm{eq}} = -k_B T \int d\Gamma \Psi_{\mathrm{eq}} \nabla_j A$, valid for any variable A, if the distribution Ψ is given by the Gibbs-measure $\Psi_{\mathrm{eq}} \propto \exp[-\beta H]$. This immediately leads to

$$\begin{aligned}\omega_0^2 = G^{(1)}(t=0) &= \frac{1}{dm}\int d^d\boldsymbol{r}\,\langle\sum_{j\neq 1}\delta(\boldsymbol{r}-\boldsymbol{r}_1+\boldsymbol{r}_j)\rangle\,\frac{\partial^2}{\partial \boldsymbol{r}^2}U(r) \\ &= \frac{n}{dm}\int d^d\boldsymbol{r} g(r)\frac{\partial^2}{\partial r^2}U(r)\;,\end{aligned} \tag{5.114}$$

where $g(r)$ denotes the pair-correlation function $g(r) = \frac{1}{n}\langle\sum_{l\neq 1}\delta(\boldsymbol{r}-(\boldsymbol{r}_1-\boldsymbol{r}_l))\rangle$. The initial value ω_0^2 is labeled Einstein frequency since neglecting the second memory kernel $\hat{\mathrm{W}}^{(1)}(s)$ would imply that Equation (5.109) predicts a single delta-peak in the spectrum at $\lambda = \omega_0^2$. From Equation (5.113) follows that the second derivative of the one-particle velocity reads

$$\Omega^\dagger Q_1^{(1)}\Omega^\dagger v_0^\alpha = \frac{1}{m}\int \frac{d^d\boldsymbol{k}}{(2\pi)^d}U(k)k^\alpha k^\beta\Big[\varrho_1(-\boldsymbol{k})v^\beta(\boldsymbol{k}) - j_1^\beta(-\boldsymbol{k})\varrho(\boldsymbol{k})\Big]\;. \tag{5.115}$$

Here, we have defined the one-particle current $\boldsymbol{j}_1(\boldsymbol{k}) = \boldsymbol{v}_1 e^{-i\boldsymbol{k}\cdot\boldsymbol{r}_1}$. Following (Bosse *et al.*, 1978); we neglect the second term in the square bracket in Equation 5.115 and

then insert the third projection operator

$$P_3^{(1)} = \frac{|\rho_1(-\boldsymbol{k})\boldsymbol{v}(\boldsymbol{k})\rangle \cdot \langle \rho_1(\boldsymbol{k})\boldsymbol{v}(-\boldsymbol{k})|}{N\frac{k_BT}{m}} , \tag{5.116}$$

to the left and the right of the reduced resolvent $\hat{R}_{Q_2^{(1)}}$ in Equation 5.111c. Now, the proceeding is in complete analogy to expressing the fluidity $\underline{\hat{\mathbf{W}}}(\boldsymbol{q}, s)$ with the vertex $\underline{\boldsymbol{V}}_{\boldsymbol{q},\boldsymbol{k}}$ in Equation (5.40). Factorizing and dressing the resulting four-point correlation function gives

$$\frac{m}{Nk_BT} \langle \rho_1(-\boldsymbol{k})\boldsymbol{v}(\boldsymbol{k})\hat{R}_{Q_2^{(1)}}(s)\rho_1(\boldsymbol{k})\boldsymbol{v}(-\boldsymbol{k})\rangle = \hat{\phi}_k^{(1)}(s)\underline{\hat{\mathbf{K}}}(\boldsymbol{k}, s) . \tag{5.117}$$

This result connects the dynamics of a single particle with the coherent velocity field $\underline{\hat{\mathbf{K}}}(\boldsymbol{q}, s)$ generated by all particles. We approximate the one-point density correlation function $\phi_k^1(s) = \langle \rho_1(\boldsymbol{k})\hat{R}(s)\rho_1(-\boldsymbol{k})\rangle \approx 1$ to be time-independent since changes in the structure are neglected altogether. This leads to a concise expression for the memory kernel in terms of the velocity field:

$$\hat{\mathrm{W}}^{(1)}(s) = \int \frac{d^d\boldsymbol{k}}{(2\pi)^d} \mathrm{Tr}\Big\{ \underline{\boldsymbol{V}}_{\boldsymbol{k}}^{(1)} \cdot \underline{\hat{\mathbf{K}}}(\boldsymbol{k}, s) \cdot \Big(\underline{\boldsymbol{V}}_{\boldsymbol{k}}^{(1)}\Big)^\dagger \Big\} , \tag{5.118}$$

with the vertex (Bosse *et al.*, 1978)

$$\underline{\boldsymbol{V}}_{\boldsymbol{k}}^{(1)} = \frac{\langle \boldsymbol{F}_1 \Omega Q_2^{(1)} \rho_1(\boldsymbol{k})\boldsymbol{v}(-\boldsymbol{k})\rangle}{\omega_0^2 dk_BTm} = n\frac{\omega_0^2}{dm} \int d^d\boldsymbol{r} e^{-i\boldsymbol{k}\cdot\boldsymbol{r}} g(r) \frac{\partial}{\partial r^\alpha} \frac{\partial}{\partial r^\beta} U(r) . \tag{5.119}$$

The trace of the vertex becomes 1 for $\boldsymbol{k} \to 0$ according to Equation (5.114) and decays to zero for large wavevectors. Thus, we approximate the one particle vertex as $\underline{\boldsymbol{V}}_{\boldsymbol{k}} \approx \underline{\mathbf{1}}\Theta(k_{\max} - k)$. The vertex introduces an upper cut-off, leading to

$$\hat{\mathrm{W}}^{(1)}(s) = \int_{k \geq k_{\max}} \frac{d^d\boldsymbol{k}}{(2\pi)^d} \Big[\hat{\mathrm{K}}_k^{\parallel}(s) + (d-1)\hat{\mathrm{K}}_k^{\perp}(s) \Big] , \tag{5.120}$$

and the one-point velocity autocorrelation reads in the small frequency limit

$$\hat{\mathrm{K}}^{(1)}(s) = \frac{1}{s + \xi + \frac{\omega_0^2}{s + \omega_0^2 m(s)}} \underset{|s|\to 0}{\longrightarrow} \frac{m(s)}{\xi m(s) + 1} . \tag{5.121}$$

All in all, the small frequency part of the spectrum of the one-point velocity autocorrelation function is for $\xi = 0$ given by the integral over the coherent velocity correlation function:

$$\hat{\mathrm{K}}^{(1)}(s) \approx \int_{|\boldsymbol{k}|<k_{max}} \frac{d^d\boldsymbol{k}}{(2\pi)^d} \left[\hat{\mathrm{K}}_k^{\parallel}(s) + (d-1)\hat{\mathrm{K}}_k^{\perp}(s)\right] \tag{5.122}$$

We choose the Debye-wavevector $k_D = 2\sqrt{\pi}\sqrt[d]{\overline{\Gamma}(1+d/2)n}$ with the Gamma-function $\overline{\Gamma}$ as a cut-off, to be in accordance with other works (Mizuno and Ikeda, 2018; Vogel *et al.*, 2025). We arrive at the known approximation that the vibrational Density of States is related to the integral over the imaginary part of the susceptibility.

$$\begin{aligned} D(\omega) &= 2\omega D_\lambda(\lambda = \omega^2) \\ &\approx \frac{2\omega}{dn\pi} \int_{|\boldsymbol{q}|<k_D} \frac{d^d\boldsymbol{q}}{(2\pi)^d} \operatorname{Im}\left[\hat{\chi}_q^{\parallel}(s = -i\omega + 0^+) + (d-1)\hat{\chi}_q^{\perp}(s = -i\omega + 0^+)\right], \end{aligned} \tag{5.123}$$

Notably, the continuum limit $\sum_{\boldsymbol{q}} \to V \int \frac{d^d\boldsymbol{q}}{(2\pi)^d}$ implies that the normalisation must be proportional to n instead of N as in Equation (5.109). Throughout this work, we have neglected the longitudinal contribution, which amounts to setting the first term in the square bracket in the previous equation to zero. The result stated in Equation (5.123) is frequently used in theoretical investigations and simulation works, see for example (Mizuno and Ikeda, 2018; Schirmacher and Ruocco, 2022). Nevertheless, Equation (5.123) is, after all, an approximation. The validity of the different steps in the derivation of Equation (5.123) was tested by comparing with experimental data with decent agreement (Bosse *et al.*, 1978). However, the authors did not apply the small $\boldsymbol{k}$ approximation to the vertex $\underline{\boldsymbol{V}}_{\boldsymbol{k}}^{(1)} \approx \underline{\mathbf{1}}\Theta(k_{max} - k)$. Thus, Equation (5.123) is supposedly only a reasonable approximation in the small frequency regime, where one expects a Debye vDOS $D(\omega) \propto \omega^{d-1}$. However, here the dispersion relation $\omega = qv_q^{\perp}$ holds, and we could have started directly from Equation (5.107) with $\lambda = \omega^2$. Nevertheless, to approximate the spectrum for higher frequencies, we should calculate the full spectrum of the one particle propagator as suggested by Equation (5.109) and importantly not perform the small s and small $\boldsymbol{k}$ approximation in the Equations (5.120) and (5.121) respectively.

This paragraph has dealt with the difficulty of neither knowing the eigenfunctions of the dynamic in disordered system nor having a Hamiltonian that could be diagonalized

to find at least a formal expression for the vDOS D_λ. The situation changes when a harmonic approximation applies. Here, the dynamic is generated by the Hessian $\underline{\boldsymbol{\mathcal{H}}}$, defined in Equation (2.38). The entries of $\underline{\boldsymbol{\mathcal{H}}}$ are given by a function of the reference frame $\{\boldsymbol{R}\}_{i=1}^N$ and the equations of motions reduce to dN coupled but linear equations

$$\ddot{\boldsymbol{v}}_i = -\underline{\boldsymbol{\mathcal{H}}}_{ij} \cdot \boldsymbol{v}_j \ . \tag{5.124}$$

Here, the vDOS is given by the eigenvalues λ_i of $\underline{\boldsymbol{\mathcal{H}}}$:

$$D_\lambda(\lambda) = \frac{1}{dN} \sum_{i=1} \delta(\lambda - \lambda_i) \ . \tag{5.125}$$

In the ERM model, this leads to the vDOS being related to the high momentum limit of the resolvent

$$\begin{aligned} \mathrm{Tr}\{\underline{\hat{\boldsymbol{\chi}}}^{\mathrm{ERM}}(\boldsymbol{q} \to \infty, s = -i\omega + 0^+)\} &= \hat{\chi}^{\mathrm{ERM},\parallel}_{q\to\infty}(-i\omega + 0^+) + (d-1)\hat{\chi}^{\mathrm{ERM},\perp}_{q\to\infty}(-i\omega + 0^+) \\ &= -\pi D_\lambda(\lambda = \omega^2) \ . \end{aligned} \tag{5.126}$$

We will prove this relation in the following paragraph.

The vDOS in the Euclidean Random Matrix Model Equation (5.126) is a direct consequence of the *Riemann-Lebesgue Lemma* (Grafakos, 2024, Proposition 2.2.3):

Theorem 1 (Riemann-Lebesgue Lemma)**.** *If $f \in L^1(\mathbb{R}^d)$ is an absolute integrable function $f : \mathbb{R}^d \to \mathbb{C}$, i.e. the integral over $|f|$ is finite, then is its Fourier transformed function $\tilde{f}$ a C_0-function, i.e. a continuous function, that vanishes at infinity.*

We will proof Equation (5.126) by looking at the trace of the ERM susceptibility:

$$\begin{aligned} \mathrm{Tr}\{\underline{\boldsymbol{\chi}}^{\mathrm{ERM}}(\boldsymbol{q}, -i\omega + 0^+)\} &= \chi^{\mathrm{ERM}}_{\alpha\alpha}(\boldsymbol{q}, -i\omega + 0^+) \\ &= \frac{1}{N} \overline{\sum_{i,j=1}^{N} e^{-i\boldsymbol{q}\cdot(\boldsymbol{R}_i - \boldsymbol{R}_j)} \Big[-\omega^2 - i0^+ + \underline{\boldsymbol{\mathcal{H}}} \Big]^{-1}_{i\alpha, j\alpha}} \ . \end{aligned} \tag{5.127}$$

Here, we understand $\underline{\boldsymbol{\mathcal{H}}}$ as a $\mathbb{R}^{dN\times dN}$ block matrix. As $\underline{\boldsymbol{\mathcal{H}}}$ is a real and symmetric matrix, its eigenvalues are real, and $\underline{\boldsymbol{\mathcal{H}}}$ is orthogonal diagonalizable. We write $\underline{\boldsymbol{\mathcal{H}}} = \underline{\boldsymbol{U}}^T \cdot \underline{\boldsymbol{D}} \cdot \underline{\boldsymbol{U}}$, where $\boldsymbol{D}$ is a diagonal matrix with the eigenvalues of $\underline{\boldsymbol{\mathcal{H}}}$ as its entries and $\underline{\boldsymbol{U}}^T \cdot \underline{\boldsymbol{U}} = \underline{\mathbf{1}}$

holds. Since the eigenvalues of $\underline{\boldsymbol{\mathcal{H}}}$ are real, one has $\left|[-\omega^2 - i\epsilon + \underline{\boldsymbol{D}}]^{-1}_{k,l}\right| \leq \frac{1}{\epsilon}$ for some $\epsilon > 0$. Thus, one finds

$$\frac{1}{N}\int \prod_{m=1}^{N} d^d\boldsymbol{R}_m \Big| \big[-\omega^2 - i\epsilon + \underline{\boldsymbol{\mathcal{H}}}\big]^{-1}_{i\alpha,j\alpha}\Big| \Psi_Q(\{\boldsymbol{R}_j\}_{j=1}^N) \leq \frac{1}{N\epsilon} \, , \tag{5.128}$$

where $\Psi_Q(\{\boldsymbol{R}_j\}_{j=1}^N)$ denotes the distribution function of particles' positions in the quenched disorder $\{\boldsymbol{R}_j\}_{j=1}^N$. Thus, the function

$$f(\boldsymbol{R}_i, \boldsymbol{R}_j) = \frac{1}{N}\int \prod_{m=1, m\neq i,j}^{N} d^d\boldsymbol{R}_m \big[-\omega^2 - i\epsilon + \underline{\boldsymbol{\mathcal{H}}}\big]^{-1}_{i\alpha,j\alpha} \Psi_Q(\{\boldsymbol{R}_l\}_{l=1}^N) \tag{5.129}$$

is absolute integrable. After understanding

$$\int d^d\boldsymbol{R}_i d^d\boldsymbol{R}_j e^{-i\boldsymbol{q}\cdot(\boldsymbol{R}_i - \boldsymbol{R}_j)} f(\boldsymbol{R}_i, \boldsymbol{R}_j) = \int d^d\boldsymbol{x} e^{-i\boldsymbol{q}\cdot\boldsymbol{x}} \int d^d\boldsymbol{y} f(\boldsymbol{x}+\boldsymbol{y}, \boldsymbol{x}-\boldsymbol{y}) = \tilde{g}_{ij}(\boldsymbol{q}) \tag{5.130}$$

as a Fourier transfomation, the Riemann-Lebesgue Theorem 1 gives $\tilde{g}(\boldsymbol{q} \to \infty)_{ij} = 0$ for $j \neq i$. In Equation (5.130), we used the linear transformation $2\boldsymbol{x} = \boldsymbol{R}_i + \boldsymbol{R}_j$ and $2\boldsymbol{y} = \boldsymbol{R}_i - \boldsymbol{R}_j$. Altogether, we find with the sum convention

$$\begin{aligned} \mathrm{Tr}\big\{ \mathrm{Im}\{\underline{\boldsymbol{\chi}}^{\mathrm{ERM}}(\boldsymbol{q} \to \infty, -i\omega + 0^+)\}\big\} &= \frac{1}{N}\overline{\sum_{i=1}^{N} \mathrm{Im}\Big[-\omega^2 - i0^+ + \underline{\boldsymbol{\mathcal{H}}}\Big]^{-1}_{i\alpha,i\alpha}} \\ &= \frac{\pi}{N}\overline{\sum_{i=1}^{dN} \delta(\omega^2 - \lambda_i)} \, . \end{aligned} \tag{5.131}$$

Here, we used the Sokhotski–Plemelj Theorem from Equation (5.91) for the last equality. Equation (5.131) proves that the high momentum limit of the resolvent gives the vDOS in the ERM model, as it leads to the eigenvalues of the Hessian. Notably, this result also holds in the Self-Consistent Current Theory when the zero-phonon approximation, *i.e.* Equation (4.38), is applied. After deriving different methods of calculating the vDOS, we will discuss the numerical results in the following paragraph.

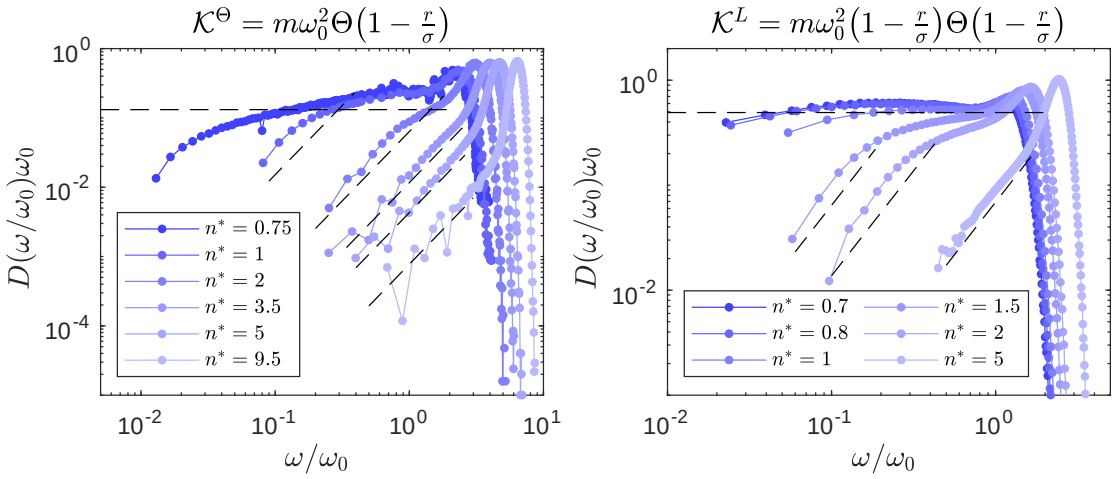

(a) Theta Spring function **(b)** Linear Spring function

Figure 5.6: Averaged Density of States in the scalar ERM model obtained by Philipp Baumgärtel via numerical diagonalization: Panel 5.6a depicts the data for the Theta spring function $\mathcal{K}^{\Theta}$ and panel 5.6b for $\mathcal{K}^{L}$ for different number densities n^*. Even though the Hessian $\underline{\boldsymbol{\mathcal{H}}}^{\mathrm{SERM}}$ can also be diagonalized in the unjammed state, only the results for the stable phase are displayed. The theories' predictions for the Debye-law and and for the plateau are indicated by dashed black lines. The frequency of the peak at the right end of the spectrum shifts with $\sqrt{n^*}$ as the pair interactions scale with the density. A uniform distribution of the particles was assumed. The data for the Theta-spring function has been shown in (Vogel *et al.*, 2025). There, the results for the unjammed phase were discussed as well.

Results for the Density of States: We have discussed in the Sections 5.3.1 and 5.3.2, that the attenuation $\omega\Gamma_q^{\perp}(\omega)$ vanishes for $\omega \to 0$ and that the dispersion relation becomes frequency independent $(q\tilde{v}_q^{\perp}(\omega))^2 \to (qv_q^{\perp})^2$. Thus, Equation (5.123) gives the Debye spectrum for $\omega \to 0$:

$$D(\omega) = \frac{\omega^{d-1}}{(k_D v_0^{\parallel})^d} + (d-1)\frac{\omega^{d-1}}{(k_D v_0^{\perp})^d} \ . \tag{5.132}$$

We again turn to the scalar ERM model for the numerical investigation. As there is no difference between longitudinal and transverse modes in the scalar ERM model, we find for the vDOS in $d = 3$

$$D^{\mathrm{SERM}}(\omega) = \frac{\omega^2}{2\pi^2 n v^3} \ . \tag{5.133}$$

Figure 5.6 displays the Density of States of the scalar ERM model for two different spring functions. The theory's prediction for the Debye law is depicted by dashed black lines with convincing agreement. Furthermore, the theory predicts that the DOS develops a plateau when approaching the unjamming transition. The value for this constant interval of the DOS is derived in Section 5.5 and is also depicted by a black dashed line. It is visible from the numerical data that this plateau extends to smaller frequencies when approaching the transition. This is in accordance with the discussion in Section 2.3.2: It has been observed in simulation that the DOS in amorphous solids becomes constant above a characteristic frequency scale ω_*, specifying the energy needed to resolve the disorder and hence heralding the failure of the continuous elastic medium approximation (Liu *et al.*, 2011; Mizuno and Ikeda, 2018; Wyart *et al.*, 2005). According to Equation (2.56) the characteristic frequency ω_* vanishes when approaching the critical point. Apparently, the ERM model and the theory both pick up on this salient feature. Moreover, the DOS becoming constant indicates that the reduced Density of States $D(\omega)/D_D(\omega)$ exhibits a maximum close to ω_*. This gives the Boson peak, which is extensively studied in the literature, *e.g.*(Parshin *et al.*, 2007; Schirmacher and Ruocco, 2022; Schober, 2011; Shintani and Tanaka, 2008). The ERM model's success in capturing the transition from a continuous elastic medium to a disorder-dominating system underlines that the ERM model can serve as a simplified model to qualitatively and even quantitatively investigate amorphous solids. Furthermore, the theory's quantitative predictive power is also remarkable. After discussing sound propagation, attenuation, and the DOS in the jammed state, we will turn to the unjammed phase in the next section.

5.4 The unjammed phase

Stability ceases below the jamming transition as stresses and restoring forces decay with time, implying $\lim_{s\to 0} s\hat{\mathrm{G}}_q(s) = 0$. Figure 5.7 displays an example of $\mathrm{K}_q(t)$ for different wavenumbers. Contrary to Figure 5.1, no oscillations are visible as the autocorrelation function decays to a q-dependent plateau. This plateau is a direct consequence of the vanishing stresses.

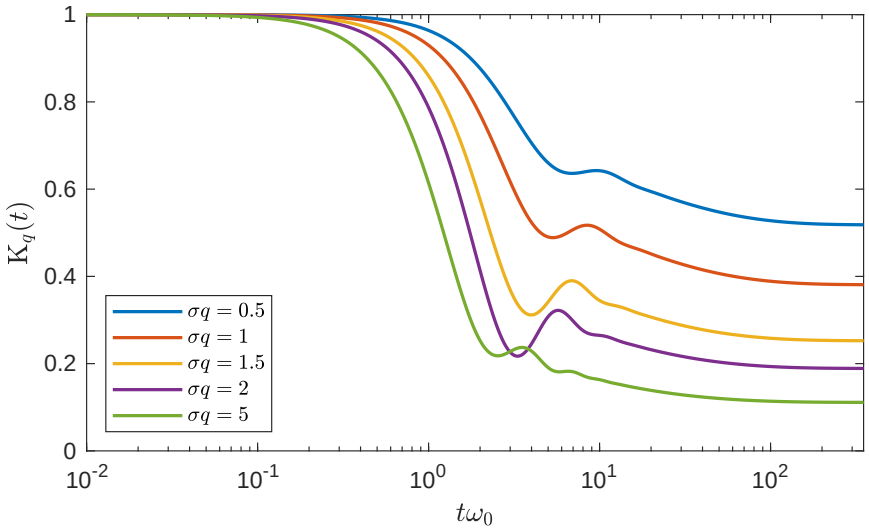

Figure 5.7: Example of the correlator $\mathrm{K}_q(t)$ in the unjammed state. The figure depicts the numerical Solution of Equation (5.80) for five different wavenumbers with the Theta springfunction $\mathcal{K}^{\Theta}(r) = m\omega_0^2\Theta(1 - r/\sigma)$. The spatial dimension is $d = 3$ and the number density has been set to $n^* = \frac{N\sigma^3}{V} = 0.75$, which is well below the jamming transition at $n^*_{c,T} = 0.830(1)$.

It becomes apparent from the set of self-consistent Equations displayed in (5.66) that the vanishing of the generalized viscosity implies that the quantity

$$\kappa_q^{\perp} = \lim_{s\to 0}(s + \xi)\hat{\mathrm{K}}_q^{\perp}(s) \tag{5.134}$$

obtaines a finite value in the unjammed case. This is a direct consequence of the presence of floppy modes as described in Section 2.3. The floppy modes or null-modes are modes with zero restoring forces. In the harmonic approximation, they correspond to eigenvectors of the Hessian with eigenvalue zero. It follows from the discussion in Section 4.4 that the overlap of the initial conditions with the null model of the Hessian precisely gives

$$\kappa_q^{\perp} = \frac{1}{N}\sum_{k\in\{\lambda^k=0\}} \langle |\boldsymbol{e}^k \cdot \boldsymbol{v}^{\perp}(\boldsymbol{q}, 0)|^2 \rangle \ . \tag{5.135}$$

Here, λ^k is the k^{th} eigenvalue of the Hessian, and $\boldsymbol{e}^k$ is the associated eigenvector. Thus, the physical picture behind the finite long time value

$\lim_{s\to 0}(s+\xi)\hat{\mathrm{K}}_q^{\perp}(s)$ reads as follows: Even an arbitrarily small perturbation can lead to a plastic response if the imposed displacement field has finite overlap with a null mode. As $\kappa_q^{\perp}$ is constituted by modes without restoring forces, $\kappa_q^{\perp}$ represents the *quasi-stationary* current response. As discussed in Section 5.2.1, our equations predict a laminar flow field that decays exponentially for long times due to the Langevin function ξ and even remains constant in the Newtonian case. Hence, the stationary current $\kappa_q^{\perp}$ can be considered a *nonergodicity parameter* for $\xi = 0$. Figure 5.8 displays an illustration of $\kappa^{\perp}$. The depicted 2d configuration of the blue spheres allows exactly one direction for a displacment without restoring forces, represented by the red arrow. The contribution to the stationary current $\kappa_q^{\perp}$ is given by the overlap of the black arrow with the floppy mode $\boldsymbol{f}$. The finite long time value of the current $\kappa_q^{\perp} > 0$ implies that $(s+\xi)\hat{\mathrm{W}}_q^{\perp}(s) \equiv \hat{\mathcal{W}}_q(s)$ and $(s+\xi)\underline{\hat{\boldsymbol{\mathcal{V}}}}_{\boldsymbol{k},\boldsymbol{q}}(s) \equiv \underline{\hat{\boldsymbol{\Upsilon}}}_{\boldsymbol{k},\boldsymbol{q}}(s)$ also acquire finite contributions for $s \to 0$. Once more, this can be seen directly from the constituting Equations (5.66). In order to keep the notation concise, we define $\underline{\hat{\boldsymbol{\mathcal{M}}}}_k(s) = (s+\xi)\hat{\mathrm{M}}_k^{\perp}(s)(\mathbb{1} - \hat{\boldsymbol{k}}\hat{\boldsymbol{k}})$ and $(s+\xi)\hat{\mathrm{K}}_q^{\perp}(s) = \overline{\mathrm{K}}_q(s)$. After multiplying Equation (5.67) with $(s+\xi)$, the equation for the new renormalised vertex $\underline{\hat{\boldsymbol{\Upsilon}}}_{\boldsymbol{k},\boldsymbol{q}}(s)$ reads

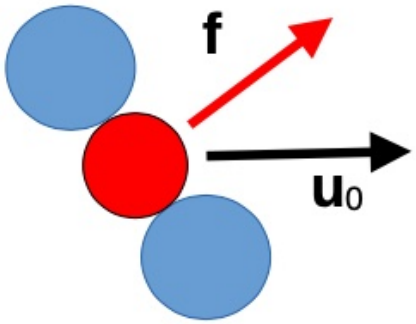

Figure 5.8: Illustration of $\kappa^{\perp}$. The stationary current results from the overlap of the initial displacement or initial momentum, depicted by the black arrow, with the floppy mode $\boldsymbol{f}$, depicted by the red arrow.

$$
\begin{aligned}
&\Big[s(s+\xi) + k^2(c_k^{\perp})^2 + (c_k^{\perp})^2\underline{\hat{\boldsymbol{\mathcal{M}}}}_k(s)\Big]\cdot\underline{\hat{\boldsymbol{\Upsilon}}}_{\boldsymbol{k},\boldsymbol{q}}(s) \\
&\qquad + \frac{(c_k^{\perp})^2}{N}\sum_{\boldsymbol{p}}\underline{\tilde{\boldsymbol{V}}}(\boldsymbol{q},\boldsymbol{k},\boldsymbol{p})\cdot\underline{\hat{\boldsymbol{\Upsilon}}}_{\boldsymbol{p},\boldsymbol{q}}(s)\,\overline{\mathrm{K}}_{|\boldsymbol{q}-\boldsymbol{k}-\boldsymbol{p}|}(s) \\
&= \Big[s(s+\xi) + (c_k^{\perp})^2\underline{\hat{\boldsymbol{\mathcal{M}}}}_k(s)\Big]\cdot\underline{\boldsymbol{V}}^{\dagger}_{\boldsymbol{k},\boldsymbol{q}}S_{|\boldsymbol{q}-\boldsymbol{k}|} \\
&\qquad + \frac{(c_k^{\perp})^2}{N}\sum_{\boldsymbol{p}}\underline{\tilde{\boldsymbol{V}}}(\boldsymbol{q},\boldsymbol{k},\boldsymbol{p})\cdot\underline{\boldsymbol{V}}^{\dagger}_{\boldsymbol{p},\boldsymbol{q}}\overline{\mathrm{K}}_{|\boldsymbol{q}-\boldsymbol{k}-\boldsymbol{p}|}(s)S_{|\boldsymbol{q}-\boldsymbol{p}|}\,\cdot
\end{aligned}
\tag{5.136}
$$

In contrast to the jammed case, Equation (5.136) does not simplify much in the small frequency limit $s \to 0$:

$$\begin{aligned}&\sum_{\boldsymbol{p}} \left\{ \left[k^2 + \underline{\hat{\boldsymbol{\mathcal{M}}}}_k(0)\right] \delta_{\boldsymbol{k},\boldsymbol{p}} + \frac{1}{N}\underline{\tilde{\boldsymbol{V}}}(\boldsymbol{q},\boldsymbol{k},\boldsymbol{p})\kappa^{\perp}_{|\boldsymbol{q}-\boldsymbol{k}-\boldsymbol{p}|} \right\} \cdot \underline{\hat{\boldsymbol{\Upsilon}}}_{\boldsymbol{p},\boldsymbol{q}}(0) \\ =&\sum_{\boldsymbol{p}} \left\{ \underline{\hat{\boldsymbol{\mathcal{M}}}}_p(0)\delta_{\boldsymbol{k},\boldsymbol{p}} + \frac{1}{N}\underline{\tilde{\boldsymbol{V}}}(\boldsymbol{q},\boldsymbol{k},\boldsymbol{p})\ \kappa^{\perp}_{|\boldsymbol{q}-\boldsymbol{k}-\boldsymbol{p}|} \right\} \cdot \underline{\boldsymbol{V}}^{\dagger}_{\boldsymbol{p},\boldsymbol{q}} S_{|\boldsymbol{q}-\boldsymbol{p}|}\ .\end{aligned} \tag{5.137}$$

Notably, this Equation is also independent of the Langevin damping ξ, reflecting that the null-modes directly result from the geometric configuration and are hence independent of the dynamical details. The non-linear nature of Equation (5.137) for the zero frequency limit of the renormalized vertex $\underline{\hat{\boldsymbol{\Upsilon}}}_{\boldsymbol{p},\boldsymbol{q}}(0)$ makes it numerically difficult to calculate the quasi-stationary $\hat{\mathcal{W}}_q(s \to 0)$ via the rescaled version of Equation (5.40). However, $\hat{\mathcal{W}}_q(0)$ is intimately connected to the quasi-stationary current $\kappa^{\perp}_q$:

$$\frac{\kappa^{\perp}_q}{1-\kappa^{\perp}_q} = \frac{\hat{\mathcal{W}}_q(s=0)}{q^2}\ . \tag{5.138}$$

Thus, we aim for a simpler expression for $\underline{\hat{\boldsymbol{\Upsilon}}}_{\boldsymbol{p},\boldsymbol{q}}(0)$ to calculate the quasi-stationary current response $\kappa^{\perp}_q$: The number of null-modes decreases when approaching the jamming transition from below. Thus, $\kappa^{\perp}_q = \lim_{s\to 0}(s+\xi)\hat{\mathrm{K}}^{\perp}_q(s)$ supposedly becomes small sufficiently close to the transition. This motivates extending the $F1$-approximation introduced in Equation (5.90) to the unjammed state. Consequentially, we approximate $\underline{\hat{\boldsymbol{\Upsilon}}}_{\boldsymbol{k},\boldsymbol{q}}(s)$ by the two-loop self-consistent theory:

$$k^2\underline{\hat{\boldsymbol{\Upsilon}}}_{\boldsymbol{k},\boldsymbol{q}}(0) \approx \underline{\hat{\boldsymbol{\mathcal{M}}}}_k(s=0)\cdot\underline{\boldsymbol{V}}^{\dagger}_{\boldsymbol{k},\boldsymbol{q}}\ S_{|\boldsymbol{q}-\boldsymbol{k}|} + \frac{1}{N}\sum_{\boldsymbol{p}}\underline{\tilde{\boldsymbol{V}}}(\boldsymbol{q},\boldsymbol{k},\boldsymbol{p})\cdot\underline{\boldsymbol{V}}^{\dagger}_{\boldsymbol{p},\boldsymbol{q}}\ \kappa^{\perp}_{|\boldsymbol{q}-\boldsymbol{k}-\boldsymbol{p}|}\ \cdot \tag{5.139}$$

Within this approximation, the stability matrix again determines the $s=0$ limit:

$$\hat{\mathcal{W}}_q(s=0) \approx \sum_p p^{d-1} C_{q,p}\kappa^{\perp}_p\ . \tag{5.140}$$

Notably, the Born term does not appear. The accuracy of this approximation improves closer to the transition. Figure 5.9 displays the numerical solution of Equation (5.138) within the scalar ERM-approximation specified in Equation (5.79). Furthermore, the long time limit of the solutions in the time domain $\mathrm{K}_q(t\to\infty)$ are additionally dis-

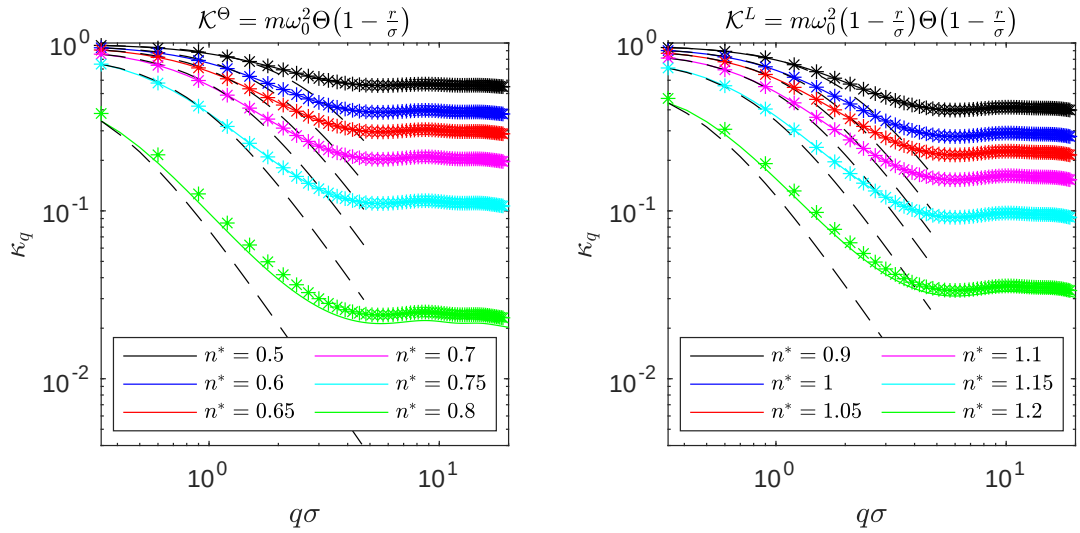

(a) Theta Spring function

(b) Linear Spring function

Figure 5.9: Display of the nonergodicity parameter κ_q for different number density n^*: Panel 5.9a depicts the data for the Theta-spring function $\mathcal{K}^{\Theta}$ and Panel 5.9b shows the results for the linear spring function $\mathcal{K}^{L}$, both for a uniform distribution of the particles. The solid lines represent the data obtained from Equation (5.138). The symbols depict the long time limit of the solution of the self-consistent model in the time domain. The methods are specified in Chapter C. The dashed black lines display the small wavenumber-fit of the Lorentzian from Equation (5.143), with the adjusted value for $\kappa_q \to 0$. Again, note that the perpendicular sign was omitted as the data was obtained from the scalar ERM model.

played. Both data sets agree. Furthermore, there is also no qualitative difference between the two displayed spring functions $\mathcal{K}^{\Theta}$ and $\mathcal{K}^{L}$. The nonergodicity parameter exhibits a plateau for high wavenumbers for all densities. Equation (5.135) suggests that this plateau is due to small clusters or even single particles, which can be moved without restoring forces. For $q \to 0$, Equation (5.66a) implies that $\kappa^{\perp}_{q\to 0} = 1$ must hold. This reflects global translational invariance. A uniform shift of the whole system is always a nullmode. The numerical solution of our final equations does not reflect this fact. It might be because it was impossible to include wavenumbers with $q\sigma \leq 0.3$ in the numerical calculations. More details on the numerical difficulties arising from small wavenumbers are presented in Appendix C.

As already anticipated in Equation (5.17), the zero frequency limit defines the generalized shear viscosity

$$\eta_q^\perp = \frac{nm}{\mu_q^\perp}\xi \ . \tag{5.141}$$

Here, $\mu_q^\perp = \mathcal{W}_q(s=0)$ is the stationary fluidity. Notably, the viscosity is zero in the Newtonian case ($\xi = 0$). This is in accordance with the discussion of athermal soft sphere systems in Chapter 2. No spheres overlap in the unjammed system. Here, injected momentum leads to ballistic motion. With the stationary fluidity $\mu_q^\perp$, we can express the quasi-stationary response as

$$\kappa_q^\perp = \frac{1}{1+\frac{q^2}{\mu_q^\perp}} \ . \tag{5.142}$$

Since $p^{d-1}C_{0,p} > 0$ is finite, $\kappa_q^\perp$ is predicted to have a *Lorentzian shape* in the hydrodynamic limit:

$$\kappa_{q\to 0}^\perp = \frac{1}{1+q^2(\lambda_-^\perp)^2} \ . \tag{5.143}$$

Here, $\lambda_-^\perp = \frac{1}{\sqrt{\mu_0^\perp}}$ is a characteristic length scale in the unjammed state. On the one hand, $\lambda_-^\perp$ specifies the distance over which injected momentum stays correlated in the Newtonian case for $\xi = 0$. On the other hand, for $\xi > 0$, the length scale $\lambda_-^\perp$ describes the average distance over which injected momentum dissipates. When approaching the critical density, the system becomes increasingly connected, which leads to a divergence of $\lambda_-^\perp$. This immediately follows from identifying the quasi-stationary current response $\kappa_q^\perp$ as the overlap of the initial condition with the null-modes of the system. In the jammed state, the only floppy modes arise from single weakly connected particles, *i.e.* rattlers, which do not affect the system's stability. Thus, the non-ergodicity parameter $\kappa_q^\perp$ is supposed to be small in the stable phase, which implies that the length scale $\lambda_-^\perp$ diverges when approaching the transition. This becomes especially illustrative in the ERM model, where $\lambda_-^\perp$ describes the averaged spatial extent of the disconnected clusters. We will further discuss this in Chapter 6, where we also argue that the jamming transition in the scalar ERM model reveals itself as a percolation transition. The Lorentzian from Equation (5.143) is represented in Figure 5.9 by dashed black lines. The different plots agree for small wavenumbers. We will

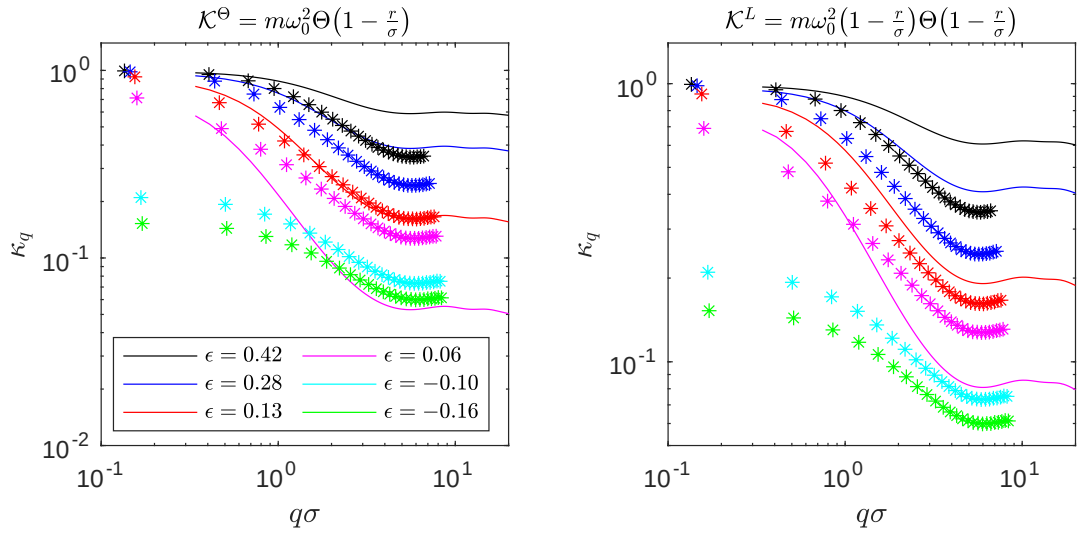

(a) Theta Spring function

(b) Linear Spring function

Figure 5.10: Comparison of the theoretical and numerical results for the nonergodicity parameter: Panel 5.10a displays the data for the Theta spring function $\mathcal{K}^{\Theta}$ and Panel 5.10b shows the results for the Linear spring function $\mathcal{K}^{L}$. The full lines display the theoretical predictions and are calculated from Equation (5.138) and Equation (5.140) for different distances to the critical point $\epsilon = \frac{n_c^* - n_*}{n_c^*}$ where n_c^* marks the jamming transition. The symbols represent the data obtained from numerical diagonalization by Philipp Baumgärtel. The methods are specified in (Vogel *et al.*, 2025). As Section 5.3.1 mentions, the theory and the numerical investigation predict different values for the critical density n_c^*. See Chapter 6 for details. To compare the two datasets, it was thus essential to look at nonergodicity parameters with the same relative distance to the critical point. The legend applies to both panels. The data for the Theta spring function for positive ϵ has been published in (Vogel *et al.*, 2025).

further discuss the density dependency of $\lambda_{\perp}^{\perp}$ in Section 5.5, where we consider the critical dynamics and the observable's scaling when approaching the (un-) jamming transition.

Figure 5.10b compares the theory's prediction with the results obtained from the numerical investigation of the ERM model. Both Panel 5.10a and Panel 5.10b display quantitative differences between the two data sets. Most probable, the differences arise mainly from the *F1*-approximation performed in Equation (5.140). A qualitative difference arises as the theory predicts $\kappa_q = 0$ in the jammed state while the numerical in-

vestigation picks up the non-vanishing contribution of disconnected single particles, *i.e.* rattlers. Apparently, the theory only describes the largest cluster in the jammed state and disregards rattlers entirely. Notably, the numerical investigation by Philipp Baumgärtel do not detect any differences between the solutions for the different spring functions. This observation, paired with Equation (5.135), suggests that the floppy modes are independent of the interaction details and fully determined by the system's geometry and structure. This observation agrees with the discussion in Section 2.3. In the next section, we will discuss the scaling of the observables when approaching the critical point.

5.5 Critical dynamics

As we discussed in Section 5.2.4, the transition between the jammed or stable phase and the unjammed phase is characterized by a change in the long-time limit of the generalized shear modulus $\lim_{s\to 0} s\hat{\mathrm{G}}_q^{\perp}(s)$. As outlined in Section 5.3.1 and Section 5.4, this causes the inverse compliance $(qv_q^{\perp})^2$ and the non-ergodicity parameter $\kappa_q^{\perp}$ to vanish at the critical density n_c^*. Based on these observations, we define the auxiliary quantity

$$s\hat{\varphi}_q(s) = \frac{s(s+\xi)}{(c_q^{\perp})^2} + (s+\xi)\hat{\mathrm{W}}_q^{\perp}(s) \;, \tag{5.144}$$

which becomes small for $s \to 0$ and when approaching the transition from either side. Following Götze, this section discusses a non-linear stability analysis, *e.g.* performed in (Götze, 2009; Schnyder, 2014; Schnyder *et al.*, 2011). Using Fredholm's solvability criterion we can express $s\hat{\varphi}_q(s)$ via the leading eigenvector h_p of the stability matrix $p^{d-1}C_{q,p}$ and two scaling functions $g(s/\omega_*)$ and $\tilde{g}(s/\omega_*)$. Here, ω_* is a characteristic frequency which vanishes at the transition. Our analysis will relate ω_* to the onset of the plateau discussed in the context of Figure 5.6. Moreover, with $g(s/\omega_*)$, we can also express the scaling of main observables like $v_q^{\perp}$ and $\kappa_q^{\perp}$ in terms of ω_*. As it turns out, the predicted scaling relations are comparable to the ones predicted in (DeGiuli *et al.*, 2015) and observed in (Mizuno and Ikeda, 2018).

This section is structured as follows. First, Section 5.5.1 derives the scaling equation for $g(s/\omega_*)$. As it turns out, it will be crucial that the left leading eigenvector $\hat{h}_q$ of the stability matrix $p^{d-1}C_{q,p}$ vanishes with q^{d-1} for $q \to 0$. Section 5.5.2 traces this vanish-

ing of $\hat{h}_q$ back to Rayleigh damping and to the inclusion of the non-planar terms. Next, in Section 5.5.3, we discuss the scaling of the static observables like $v_q^\perp$ and $\kappa_q^\perp$ before turning to the divergence of the sound attenuation and the Density of States in Section 5.5.4. Here, the analysis needs special care, as investigating frequency-dependent quantities requires the second scaling function $\tilde{g}(s/\omega_*)$. Lastly, Section 5.5.5 discusses the relation to the Allen-Feldman Theory as ω_* turns out to mark the onset of the diffusive regime discussed in the Sections 2.3.3 and 2.4.

5.5.1 Götze's stability analysis

First, we aim for a constituting equation for $s\hat{\varphi}_q(s)$ defined in Equation (5.144). Noticeable, the generalized shear modulus reads in terms of this auxiliary quantity $\hat{\mathrm{G}}_q^\perp(s) = \frac{s+\xi}{s\hat{\varphi}_q(s)}$. Thus, key observables in the unjammed and jammed phase can be expressed as follows

$$\lim_{s,q\to 0} s\hat{\varphi}_q(s) = \frac{1}{(\lambda_-^\perp)^2}\,, \quad \lim_{s\to 0} s\hat{\varphi}_q(s) = \frac{s(s+\xi)}{(v_q^\perp)^2}\,. \tag{5.145}$$

The first equation for the length scale $\lambda_-^\perp$ holds in the unjammed state, and the second one for the inverse compliance $(qv_q^\perp)^2$ is valid in the jammed phase. Both equations suggest that $s\hat{\varphi}_q(s)$ vanishes at the critical point if s goes sufficiently fast to zero. Furthermore, Equation (5.145) implies that the solution for $s\hat{\varphi}_q(s)$ degenerates at the critical point, where the system becomes unstable to small density changes. Based on the idea that $s\hat{\varphi}_q(s)$ becomes small at the transition, we will linearize the soon-to-be-derived constituting equation of $s\hat{\varphi}_q(s)$ and look for the vanishing of the associated matrix' determinant. As already anticipated in the context of Equation (5.89), degeneracy takes place when the eigenvalue of the stability matrix $p^{d-3}C_{p,q}$ becomes unity. As the final equations are linear, the following analysis utilizes standard linear algebra and Fredholm's theorem. Furthermore, the ensuing discussion is based on the assumption that the largest eigenvalue is simple. This section discusses the single steps of the stability equation's derivation.

The general equation for $s\hat{\varphi}_q(s)$: The derivation starts by noticing that $s\hat{\varphi}_q(s)$ agrees with the quasi stationary fluidity $\hat{\mathcal{W}}_q(s \to 0) = \lim_{s\to 0}(s+\xi)\hat{\mathrm{W}}_{\mathrm{q}}^{\perp}(\mathrm{s})$ in the unjammed state and in the limit $s \to 0$. Hence, we begin by recalling Equation (5.136) for the vertex $\underline{\hat{\boldsymbol{\Upsilon}}}_{\boldsymbol{k},\boldsymbol{q}}(s)$:

$$\begin{aligned}
&\left[s(s+\xi) + k^2(c_k^{\perp})^2 + (c_k^{\perp})^2 \underline{\hat{\boldsymbol{\mathcal{M}}}}_k(s)\right] \cdot \underline{\hat{\boldsymbol{\Upsilon}}}_{\boldsymbol{k},\boldsymbol{q}}(s) \\
&\qquad + \frac{(c_k^{\perp})^2}{N} \sum_{\boldsymbol{p}} \underline{\tilde{\boldsymbol{V}}}(\boldsymbol{q},\boldsymbol{k},\boldsymbol{p}) \cdot \underline{\hat{\boldsymbol{\Upsilon}}}_{\boldsymbol{p},\boldsymbol{q}}(s)\, \overline{\mathrm{K}}_{|\boldsymbol{q}-\boldsymbol{k}-\boldsymbol{p}|}(s) \\
&= \left[s(s+\xi) + (c_k^{\perp})^2 \underline{\hat{\boldsymbol{\mathcal{M}}}}_k(s)\right] \cdot \underline{\boldsymbol{V}}_{\boldsymbol{k},\boldsymbol{q}}^{\dagger} S_{|\boldsymbol{q}-\boldsymbol{k}|} \\
&\qquad + \frac{(c_k^{\perp})^2}{N} \sum_{\boldsymbol{p}} \underline{\tilde{\boldsymbol{V}}}(\boldsymbol{q},\boldsymbol{k},\boldsymbol{p}) \cdot \underline{\boldsymbol{V}}_{\boldsymbol{p},\boldsymbol{q}}^{\dagger} \overline{\mathrm{K}}_{|\boldsymbol{q}-\boldsymbol{k}-\boldsymbol{p}|}(s) S_{|\boldsymbol{q}-\boldsymbol{p}|} \ .
\end{aligned} \tag{5.146}$$

Same as in Section 5.4, we again used the abbreviations $\underline{\hat{\boldsymbol{\mathcal{M}}}}_k(s) = (s+\xi)\hat{\mathrm{M}}_k^{\perp}(s)(\mathbb{1}-\hat{\boldsymbol{k}}\hat{\boldsymbol{k}})$ and $(s+\xi)\hat{\mathrm{K}}_q^{\perp}(s) = \overline{\mathrm{K}}_q(s)$ to keep the notation concise. Furthermore, we notice that we can write

$$\overline{\mathrm{K}}_q(s) = \frac{s\hat{\varphi}_q(s)}{s\hat{\varphi}_q(s)+q^2} = \frac{s\hat{\varphi}_q(s)}{q^2} - \frac{(s\hat{\varphi}_q(s))^2}{s\hat{\varphi}_q(s)+q^2}\frac{1}{q^2} \ . \tag{5.147}$$

As the difference between the stable and the unstable phase transpires in differences of the long-time value of the generalized shear modulus $\mathrm{G}_q^{\perp}(t)$, the main attention is dedicated to the small frequency limit. Section 5.3.2 discussed, that the non-linear contributions of $\hat{\mathrm{K}}_q^{\perp}(s)$ to $\underline{\hat{\boldsymbol{\Upsilon}}}_{\boldsymbol{k},\boldsymbol{q}}(s)$ can be safely neglected for $s \to 0$. This suggests expanding the renormalized vertex in the non-linear terms of Equation (5.146). Stopping after the leading term in s leads to:

$$\underline{\hat{\boldsymbol{\Upsilon}}}_{\boldsymbol{p},\boldsymbol{q}}(s) = \frac{s(s+\xi)}{s(s+\xi)+(pc_p^{\perp})^2} S_{|\boldsymbol{q}-\boldsymbol{p}|} \underline{\boldsymbol{V}}_{\boldsymbol{p},\boldsymbol{q}}^{\dagger} + \mathcal{O}(s^2(s+\xi)\hat{\varphi}_q(s)) \ . \tag{5.148}$$

Inserting this expansion in Equation (5.40) gives according to Equation (5.144):

$$
\begin{aligned}
s\hat{\varphi}_q(s) - \frac{s(s+\xi)}{(c_q^\perp)^2} &= \frac{1}{N}\sum_{\boldsymbol{k}} \underline{\boldsymbol{V}}_{\boldsymbol{q},\boldsymbol{k}} : \underline{\hat{\boldsymbol{\Upsilon}}}_{\boldsymbol{k},\boldsymbol{q}}(s) \\
&= -\frac{s(s+\xi)}{N^2}\sum_{\boldsymbol{k},\boldsymbol{p}} \underline{\boldsymbol{V}}_{\boldsymbol{q},\boldsymbol{k}} : \underline{\boldsymbol{V}}^\dagger_{\boldsymbol{k},\boldsymbol{q}} \overline{\mathrm{K}}_p(s) \frac{(c_k^\perp)^2 S_{|\boldsymbol{q}-\boldsymbol{k}|}}{[s(s+\xi)+k^2(c_k^\perp)^2]^2} \underline{\boldsymbol{V}}_{\boldsymbol{k},\boldsymbol{p}} : \underline{\boldsymbol{V}}^\dagger_{\boldsymbol{p},\boldsymbol{k}} S_{|\boldsymbol{k}-\boldsymbol{p}|} \\
&\quad - \frac{s(s+\xi)}{N^2}\sum_{\boldsymbol{k},\boldsymbol{p}} \overline{\mathrm{K}}_b(s) \frac{\hat{\chi}_k^{(0)}(s)(c_k^\perp)^2 S_{|\boldsymbol{q}-\boldsymbol{p}|}}{s(s+\xi)+p^2(c_p^\perp)^2} \underline{\boldsymbol{V}}_{\boldsymbol{q},\boldsymbol{k}} : (\underline{\tilde{\boldsymbol{V}}}(\boldsymbol{q},\boldsymbol{k},\boldsymbol{p}) \cdot \underline{\boldsymbol{V}}^\dagger_{\boldsymbol{p},\boldsymbol{q}}) \\
&\quad + \frac{1}{N}\sum_{\boldsymbol{k}} \hat{\chi}_k^{(0)}(s) \underline{\boldsymbol{V}}_{\boldsymbol{q},\boldsymbol{k}} : \Big\{ \Big[s(s+\xi) + (c_k^\perp)^2 \underline{\boldsymbol{\mathcal{M}}}_k(s) \Big] \cdot \underline{\boldsymbol{V}}^\dagger_{\boldsymbol{k},\boldsymbol{q}} S_{|\boldsymbol{q}-\boldsymbol{k}|} \\
&\quad + \frac{(c_k^\perp)^2}{N}\sum_{\boldsymbol{p}} \underline{\tilde{\boldsymbol{V}}}(\boldsymbol{q},\boldsymbol{k},\boldsymbol{p}) \cdot \underline{\boldsymbol{V}}^\dagger_{\boldsymbol{p},\boldsymbol{q}}\, \overline{\mathrm{K}}_b(s) S_{|\boldsymbol{q}-\boldsymbol{p}|} \Big\} + \mathcal{O}(s^2(s+\xi)\varphi_q(s))
\end{aligned}
\tag{5.149}
$$

Here, we wrote $\boldsymbol{b} = \boldsymbol{q} - \boldsymbol{k} - \boldsymbol{p}$ to keep the notation concise. After inserting Equation (5.147) in this first expression of $s\hat{\varphi}_q(s)$, it becomes apparent that the second and the third line can be neglected for small frequencies $s \to 0$. However, the term in third line $\propto s(s+\xi)\chi_k^{(0)}(s)$ has to be kept even for $s \to 0$. The associated contribution represents the one-loop correction or Born term and renormalizes the bare constants $(c_q^\perp)$. Similarly to Equation (5.89) and Equation (5.87), we write the first order renormalized dispersion relation as

$$
\frac{1}{(\tilde{c}_q^\perp(s))^2} = \frac{1}{(c_q^\perp)^2} + \frac{1}{N}\sum_{\boldsymbol{k}} \underline{\boldsymbol{V}}_{\boldsymbol{q},\boldsymbol{k}} : \underline{\boldsymbol{V}}^\dagger_{\boldsymbol{k},\boldsymbol{q}} \frac{S_{|\boldsymbol{q}-\boldsymbol{k}|}}{s^2 + (kc_k^\perp)^2} \,. \tag{5.150}
$$

According to Equation (5.106), the attenuation arising from the Born term plays no role close to the unjamming transition whereas $v_0^\perp \to 0$ holds. This suggest $(\tilde{c}_q^\perp(s))^2 = (\tilde{c}_q^\perp(s=0))^2 \equiv (\tilde{c}_q^\perp)^2$. Generally, the non-analyticity in $\chi_k^{(0)}(s)$ plays a subdominant role. Thus, inserting Equation (5.147) in the fourth and fifth line of Equation (5.149) recovers the F1-Model for sufficiently small frequencies

$$
\begin{aligned}
s\hat{\varphi}_q(s) - \frac{s(s+\xi)}{(\tilde{c}_q^\perp)^2} - \sum_p p^{d-3} C_{q,p}\, s\hat{\varphi}_p(s) = &- \sum_p p^{d-3} C_{q,p} \frac{(s\hat{\varphi}_p(s))^2}{s\hat{\varphi}_p(s) + p^2} \\
&+ \mathcal{O}(s^2(s+\xi)\hat{\varphi}_q(s)) \,.
\end{aligned}
\tag{5.151}
$$

Again, $p^{d-3}C_{q,p}$ denotes the stability matrix defined in Equation (5.88). To investigate Equation (5.151) and to probe its solutions close to the degeneracy signaling the transition, we interpret $p^{d-3}C_{q,p} \longrightarrow \underline{\tilde{\boldsymbol{C}}} \in \mathbb{R}^{m\times m}$ as a square matrix, where $m \to \infty$ is the number of considered Fourier modes. The associated Jordanform of $\underline{\tilde{\boldsymbol{C}}}$ reads $\underline{\tilde{\boldsymbol{C}}} = \underline{\boldsymbol{E}}^{-1} \cdot \underline{\boldsymbol{J}} \cdot \underline{\boldsymbol{E}}$, where $\underline{\boldsymbol{J}}$ is the Jordan block-matrix and the transformation matrix $\underline{\boldsymbol{E}}$ is constituted by the generalised eigenvectors of $\underline{\tilde{\boldsymbol{C}}}$. Generally, if $(\boldsymbol{v}^{(i)})^T$ is a left eigenvector to the eigenvalue λ_i and $\boldsymbol{u}^{(j)}$ is a right generalised eigenvector to a different associated eigenvalue $\lambda_j \neq \lambda_i$ then $\boldsymbol{v}^{(i)} \cdot \boldsymbol{u}^{(j)} = 0$ holds. Hereinafter, we assume, without proof, that the largest eigenvalue λ_{max} of $\underline{\tilde{\boldsymbol{C}}}$ is simple, *i.e.* its geometric multiplicity is 1. As already discussed in the context of Equation (5.89), the transition occurs at $\lambda_{max} = 1$. We denote the eigenvector associated with the largest eigenvalue at the transition as $\boldsymbol{h}$. We call the associated left eigenvector $\hat{\boldsymbol{h}}$. Furhtermore,we adopt the two normalisations $\hat{\boldsymbol{h}}^T \cdot \boldsymbol{h} = 1$ and $\sum_p \hat{h}_p \frac{h_p^2}{p^2} = 1$. Directly at the critical point, the Jordan decomposition gives

$$\tilde{C}^c_{q,p} = h_q \hat{h}_p + C^{\#}_{q,p} \, . \tag{5.152}$$

Here, the index c indicates the stability matrix is evaluated directly at the critical point. The assumption of the largest eigenvalue being simple dictates that $\hat{\boldsymbol{h}}$ and $\boldsymbol{h}$ are orthogonal to all other generalized (left) eigenvectors:

$$\sum_p C^{\#}_{q,p} h_p = \sum_q \hat{h}_q C^{\#}_{q,p} = 0 \tag{5.153}$$

Slightly away from the transition, we can write the stability matrix as

$$\tilde{C}_{q,p} = \tilde{C}^c_{q,p} + \Delta\tilde{C}_{q,p} = h_q \hat{h}_p + C^{\#}_{q,p} + \Delta\tilde{C}_{q,p} \, . \tag{5.154}$$

The matrix $\Delta\tilde{C}_{q,p}$ accounts for all the differences in the spectrum and eigenspaces of the stability matrix in comparison with $\tilde{C}^c_{q,p}$. However, we assume that the auxiliary quantity $s\hat{\varphi}_q(s)$ can be written with the eigenvectors of $\tilde{C}^c_{q,p}$. This suggest that $s\hat{\varphi}_q(s)$ is mainly determined by the critical eigenvector $\boldsymbol{h}$ (Götze, 2009, Chapter 4.3). Thus, we adopt the ansatz

$$s\hat{\varphi}_q(s) = \varsigma\big(s_* g(s_*) + \varsigma^{\alpha} s_* \tilde{g}(s_*)\big) h_q + \varsigma^{1+\beta} s_* X^{\#}_q(s_*) \, , \tag{5.155}$$

with $\alpha, \beta > 0$ and $\hat{\boldsymbol{h}} \cdot \boldsymbol{X}^{\#} = 0$ due to the orthogonality of the eigenvectors. Furthermore, we introduced the dimensionless frequency $s_* = st_*$. The dynamic slows down at the transition, which generally causes the scale t_* to diverge when the distance ς to the transition vanishes[12]. However, ς and t_* are yet unspecified. Later, we will express both quantities with the distance matrix $\Delta\underline{\tilde{\boldsymbol{C}}}$. The time scale t_* also defines a characteristic frequency $\omega_* = 1/t_*$.

Inserting the Ansatz (5.155) into Equation (5.151) gives

$$\begin{aligned}
&\frac{1}{\varsigma}\Big[s_* g(s_*) + s_* \varsigma^{\alpha} \tilde{g}(s_*)\Big] h_q - \frac{\lambda}{\varsigma} \sum_p h_q \hat{h}_p \Big[s_* g(s_*) + s_* \varsigma^{\alpha} \tilde{g}(s_*)\Big] h_p \\
&\quad = \varsigma^{\beta-1}\Big[s_* X_q^{\#}(s_*) - \sum_p C_{q,p}^{\#} s_* X_p^{\#}(s_*)\Big] + \frac{1}{\varsigma}\Big[s_* g(s_*) + \varsigma^{\alpha} \tilde{g}(s_*)\Big] \sum_p \Delta \tilde{C}_{q,p} h_p \\
&\quad + \frac{s(s+\xi)}{(\varsigma \tilde{c}_q^{\perp})^2} - \frac{1}{\varsigma^2} \sum_p \tilde{C}_{q,p} \frac{(s\hat{\varphi}_p(s))^2}{s\hat{\varphi}_p(s) + p^2} \,. \qquad (5.156)
\end{aligned}$$

with $\lambda = 1$. Of course, the left-hand side of the previous equation evaluates to zero. However, Equation (5.156) resembles an inhomogeneous Fredholm integral equation, where the right-hand side gives the inhomogeneity. The solvability criterion is given by the following theorem (Zemyan, 2012, Theorem 1.3.3):

Theorem 2 (Fredholm's Third Theorem)**.** *Let λ be a complex parameter, $f(x)$ be a complex-valued continuous function defined on the interval $[a, b]$, and $K(x, t)$ be a complex-valued continuous kernel defined on the square $Q(a, b)$. If λ is an eigenvalue of the kernel $K(x, t)$, then the inhomogeneous Fredholm integral equation*

$$\phi(x) = f(x) + \lambda \int_a^b K(x, t)\phi(t)dt \qquad (5.157)$$

[12] Matthias Fuchs came up with the Ansatz (5.155). The author of this monograph only considered the first term in the round bracket. Neglecting the term proportional to ς^{α} leads to the correct scaling of the inverse compliance $(qv_q^{\perp})^2$ and of $\kappa_q^{\perp}$ with the parameter ϵ. However, it gives erroneous results for the frequency-dependent sound attenuation. The original calculation of Florian Vogel is published in (Vogel *et al.*, 2025). The main novelties resulting from the new Ansatz (5.155) are discussed in Section 5.5.1. There, Matthias Fuchs's contributions are carefully distinguished from the contributions of the present author.

has solutions if and only if the inhomogeneous part $f(x)$ is orthogonal to all the eigenfunctions of the homogeneous adjoint equation

$$\psi(x) = \overline{\lambda} \int_a^b \overline{K(t,x)}\psi(t)dt \; . \tag{5.158}$$

The following paragraph exploits this theorem, and discusses the solution for the first scaling equation $g(s/\omega_*)$. This will enable us to determine the scaling of the static observables $v_q^\perp$ and $\kappa_q^\perp$ close to the transition.

Scaling equation for the static observables: This paragraph discusses the solution of $s\hat{\varphi}_q(s)$ for $s_* \to 0$ and subsequentially $\varsigma \to 0$. It will become apparent that this limit is governed by the scaling function $g(s_*)$. To see this, we expand Equation (5.156) for small ς:

$$\begin{aligned}\varsigma^{\beta-1}\Big[s_* X_q^{\#}(s_*) - \sum_p C_{q,p}^{\#} s_* X_p^{\#}(s_*)\Big] &= \frac{1}{\varsigma}\Big[s_* g(s_*) + s_* + \varsigma^\alpha \tilde{g}(s_*)\Big] \sum_p \Delta\tilde{C}_{q,p} h_p \\ + \frac{s(s+\xi)}{(\varsigma\tilde{c}_q^\perp)^2} - \sum_p p^{d-3} C_{q,p} \Bigg\{ &\frac{h_p^2}{p^2}(s_* g(s_*))^2 \Big[1 - \frac{\varsigma s_* g(s_*) h_p}{p^2 + s\hat{\varphi}_p(s)}\Big] \\ &+ \frac{h_p^2}{p^2} 2\varsigma^\alpha s_*^2 g(s_*)\tilde{g}(s_*) + 2\varsigma^\beta s_*^2 g(s_*) X_p^{\#}(s_*)\frac{h_p}{p^2} + \mathcal{O}(s_*^2 \varsigma^{2\min\{\alpha,\beta\}})\Bigg\} \; .\end{aligned} \tag{5.159}$$

Taking the limit $s_* \to 0$, Equation (5.159) simplifies to

$$\begin{aligned}\varsigma^{\beta-1}\Big[s_* X_q^{\#,(0)}(s_*) - s_* \sum_p C_{q,p}^{\#} X_p^{\#,(0)}(s_*)\Big] \\ = \frac{1}{\varsigma} s_* g(s_*) \sum_p \Delta\tilde{C}_{q,p} h_p + \frac{s(s+\xi)}{(\varsigma^2\tilde{c}_q^\perp)^2} - \sum_p \tilde{C}_{q,p}\, \frac{h_p^2}{p^2}(s_* g(s_*))^2 \; ,\end{aligned} \tag{5.160}$$

with the main contribution of the correction term $s_* X_q^{\#,(0)}(s_*) = \lim_{s_*\to 0} s_* X_q^{\#}(s_*)$. As anticipated, the limit $s_* \to 0$ for small but finite ς is determined by the first scaling function $g(s_*)$. According to Theorem 2, Fredholm's solubility criterion for Equation (5.156) is obtained by multiplying through with $\hat{h}_q$ from the left and summing over the wavenumber q. Together with the adopted normalization $\sum_p \hat{h}_p \frac{h_p^2}{p^2} = 1$, this provides

us with an Equation for $g(s_*)$:

$$\frac{t_0^2 s(s+\xi)}{\varsigma^2} + \frac{\epsilon}{\varsigma} s_* g(s_*) = (s_* g(s_*))^2 \ . \tag{5.161}$$

When deriving this result, we have neglected the contribution

$$\sum_{q,p} \hat{h}_q \Delta\tilde{C}_{q,p} \frac{h_p^2}{p^2} (s_* g(s_*))^2 \approx \mathcal{O}(\varsigma) \tag{5.162}$$

as it plays a subdominant role at the transition. The time-scale parameter t_0 results from $t_0^2 = \sum_q \frac{\hat{h}_q}{(\tilde{c}_q^\perp)^2}$. Furthermore, we have introduced the second distance paramater

$$\epsilon \equiv \sum_{p,q} \hat{h}_q \Delta\tilde{C}_{q,p} h_p \ . \tag{5.163}$$

Sufficiently close to the transition, ϵ measures the distances of the largest eigenvalue to unity which can be visualized with the informal and imprecise idea:

$$\Delta\tilde{C}_{q,p} \approx \epsilon h_q \hat{h}_p. \tag{5.164}$$

However, this is supposed to be only an illustration. Equation (5.163) makes this concept precise and concrete. Equation (5.160) and Equation (5.161) can only have finite solutions when approaching the transition, if all the quantities have a finite limit for $\varsigma \to 0$. Thus, we identify $\varsigma = |\epsilon|$, which immediately leads to the identification $\beta = 1$. All in all, Equation (5.161) can be written as

$$t_0^2 \frac{s(s+\xi)}{\varsigma^2} + \mathrm{sgn}(\epsilon) s_* g(s_*) = (s_* g(s_*))^2 \ , \tag{5.165}$$

with $\mathrm{sgn}(\epsilon) = \epsilon/|\epsilon|$. Noticeably, there exists no unique positive solution for the inverse compliance $(q v_q^\perp)^2$ for eigenvalues larger than unity (compare with Equation (5.89)). Hence, eigenvalues larger than unity or $\epsilon > 0$ respectively occur in the unjammed phase. We denote the different solutions of Equations (5.161) with $g_\pm(s_*)$, where the index is dictated by the sign of ϵ. In Section 5.5.3, we use $g_\pm(s_*)$ to investigate the scaling of the static quantities like the stationary current $\kappa_q^\perp$ and the inverse compliance $(q v_q^\perp)^2$ in the unjammed and the jammed phase respectively. Limiting the discussion to the static quantities originates in considering the limit $s_* \to 0$ before taking $\varsigma \to 0$. As Equa-

tion (5.159) anticipates, we must consider additional correction terms when we want to investigate the influence of small but finite frequencies s_*. Notably, these corrections quantify the scaling of the sound attenuation close to the critical point. Section 5.5.4 covers the scaling of the frequency-dependent quantities. However, before proceeding to the scaling of the observables, we first have to elaborate on a subtle detail: When setting the square bracket in the second line of Equation (5.159) to unity, one discards an additional term resulting from a non-analiticity. To be more concrete, it was already mentioned that $s\hat{\varphi}_q(s) \underset{s\to 0}{\longrightarrow} \frac{s^2}{(v_q^\perp)^2}$ holds in the Newtonian case for $\epsilon < 0$. Setting $s = -i\omega + 0^+$ in Equation (5.159) leads to a divergence at the sound pole $p = \omega/v_0^\perp$. Generally, the resulting term has to be added to Equation (5.161) and potentially even dominates for $\omega, \varsigma \to 0$. An example is discussed in (Schnyder *et al.*, 2011). However, we argue in the next section that the pole in Equation (5.159) can be safely ignored even in lower dimension with $d < 4$ as the critical left eigenvector vanishes for $p \to 0$ according to $\hat{h}_p \propto p^{d-1}$.

5.5.2 The critical left eigenvector

As explained in the previous section, it is crucial in lower dimensions that the left critical eigenvector $\hat{h}_p$ vanishes for $p \to 0$. This section clarifies that $\hat{h}_{p\to 0} \propto p^{d-1}$ indeed holds, as any other scaling would contradict the proven Rayleigh-Sound attenuation. Additionally, we provide numerical confirmation of this claim in $d = 3$.

We consider the case $d = 3$ and temporarily assume $\hat{h}_{q\to 0} = const.$ However, it will become apparent that we could have investigated the more general ansatz $\hat{h}_{q\to 0} = q^\gamma$. The result would be the same: Only $\gamma = d-1$ is in accordance with Rayleigh-damping. However, we deliberately choose γ to exemplify an *reductio ad absurdum* argument. In the following, we set the Lagenvin damping rate to zero, $\xi = 0$, and consider the jammed case $\epsilon < 0$, where $\lim_{s\to 0} s\hat{\varphi}_q(s) = \frac{s^2}{(v_q^\perp)^2}$ holds. The Sokhotski–Plemelj Theorem (Equation (5.91)) gives for $s \to 0$:

$$\sum_{q,p} \hat{h}_q \tilde{C}_{q,p} \frac{\big(\varsigma h_p s_* g(s_*)\big)^2}{p^2 + h_p s_* g(s_*)\varsigma} = \frac{\pi}{2}\sqrt{\varsigma s_* g(s_*)}^3 \sum_q \hat{h}_q \tilde{C}_{q,0}\sqrt{h_0}^3 + \mathcal{O}(s_*^2 g(s_*)^2)\ . \tag{5.166}$$

As the reference to the higher order terms suggests, the leading term vanishes slower than the right-hand side of Equation (5.165). This makes it inappropriate to neglect the term $s\hat{\varphi}_q(s)$ in the denominator of Equation (5.159). Rather, we have to follow Schnyder *et al.* and replace the right-hand side of Equation (5.165) with the right-hand side of Equation (5.166) (Schnyder *et al.*, 2011). Furthermore, the previous equation suggests that we should not rely on the normalisation $\sum_p \hat{h}_p \frac{h_p^2}{p^2} = 1$ but should use instead $1 = \frac{\pi}{2}\sum_q \hat{h}_q C_{q,0} h_0^{3/2}$. All in all, the new scaling function reads for $\xi = 0$ and $\epsilon < 0$:

$$\frac{t_0^2 s^2}{\varsigma^{3/2}} + \frac{\epsilon}{\sqrt{\varsigma}} s_* g(s_*) = (s_* g(s_*))^{3/2} \,. \tag{5.167}$$

We also have to update the identifications of the parameter ς: In this alternative scenario the separation parameter is given by $\epsilon^2 = \varsigma$, and we find for the characteristic frequency $\omega_* = \frac{\varsigma^{3/4}}{t_0}$. The solution in the jammed state for $|s_*| \ll 1$ reads $g_-\,(|s_*| \ll 1) \to s_* - s_*^2$. The relation $\hat{\mathrm{G}}_q^{\perp}(s) = \frac{s+\xi}{s\hat{\varphi}_q(s)}$ gives for alternative susceptibility:

$$\hat{\chi}_q^{\mathrm{A}}(s \to 0) = \frac{1}{s^2 + \frac{q^2}{h_q}\frac{\omega_*^2}{\varsigma}\frac{1}{1+s_*}} \tag{5.168}$$

Notably, $v_0^{\perp} > 0$ implies that the right eigenvector h_q must stay finite for $q \to 0$. Thus, the sound attenuation is given by $\tilde{\Gamma}^A(\omega) \propto \omega q^2$ in contradiction to the result

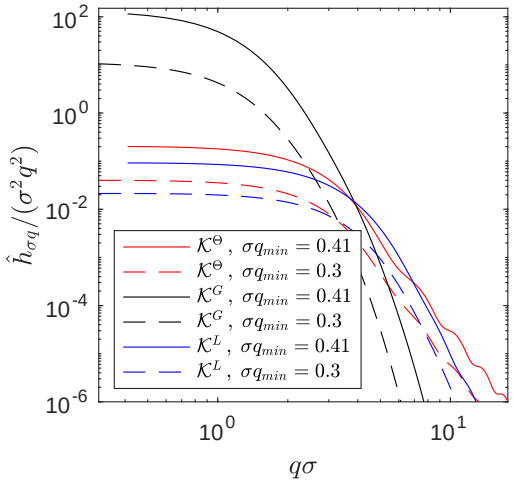

Figure 5.11: The figure displays critical left eigenvector divided by q^2 for three different spring functions $\mathcal{K}^{\Theta}$, $\mathcal{K}^{G}$ and $\mathcal{K}^{L}$. Two different distributions of the wavenumbers are shown for each spring function. The dotted lines display a logarithmic distribution with $\sigma q_{min} = 0.3$, and the solid lines show the data for a uniform distribution of $q\sigma$ with $\sigma q_{min} = 0.41$. The smallest considered wavenumber was neglected, leading to the change $\sigma q_{min} = 0.34 \to \sigma q_{min} = 0.41$ when considering the uniform spacing. The data for the springfunctions $\mathcal{K}^{\Theta}$ and $\mathcal{K}^{L}$ has been published in (Vogel *et al.*, 2025) .

obtained in Section 5.3.2. Hence, the left eigenvector[13] must vanish with $\hat{h}_p \propto p^2$ in $d = 3$. From the consideration of the sound pole, it becomes evident that $\hat{h}_{p\to 0} \propto p^{d-1}$ is dictated by the already proven Rayleigh attenuation. This crucial scaling is also confirmed numerically. Figure 5.11 depicts the critical left eigenvector divided by q^2 for the three spring functions considered. We clearly see, that $\hat{h}_{p\to 0} \propto p^2$ holds. Furthermore, data for a linear and a logarithmic distribution of the wavenumbers are plotted with only quantitative differences stemming from the different normalizations. However, we have confirmed that the distribution of the Fourier modes does not affect the shown results for observables like $v_q^\perp$. The scaling $\hat{h}_p \propto p^{d-1}$ implies that the term arising from the divergence is indeed negligible for $s \to$ in any dimension $d \geq 2$. After having confirmed that Equation (5.165) holds, we can discuss the solutions of the scaling equation $g_\pm(s_*)$ in the next section. Ultimately, this enables us to investigate how $v_q^\perp$ and $1/\lambda_-$ vanish with ω_*. Expressing the scaling in terms of ω_* also allows comparing with simulations (Mizuno and Ikeda, 2018).

5.5.3 Scaling of the static observables

This section discusses the solution of the long-time limit of observables. Here, we consider the case $s_* \to 0$. As discussed in the context of Equation (5.160), this case is controlled by the scaling function $g(s_*)$. The general solution of Equation (5.161) reads

$$g(s_*) = \frac{\mathrm{sgn}(\epsilon) \pm \sqrt{1 + 4st_0^2(s+\xi)/\varsigma^2}}{2s_*} \,. \tag{5.169}$$

As stated in Equation (3.18), the spectrum of a correlation function must be positive. Thus, one must *choose* the positive sign in the previous equation. The subsequent two paragraphs discuss the solutions $g_\pm(s_*)$ in the Newtonian case for $\xi = 0$ and in the Langevin case $\xi \neq 0$.

[13] Notably, the divergence is also present if the critical left eigenvector scales as p^2. However, here, the resulting residual contribution vanishes with $\sqrt{s_* g(s_*)}^5$ and hence faster than the right-hand side of Equation (5.165).

Newtonian case: As the right hand side of Equation (5.169) depends only on the rescaled frequency s_*. It follows that the frequency scale reads $\omega_* = |\epsilon|/t_0$ for $\xi = 0$. The general solution for the scaling function $g(s_*)$ is given by

$$g(s_*) = \frac{\mathrm{sgn}(\epsilon) \pm \sqrt{1 + 4s_*^2}}{2s_*} \tag{5.170}$$

Notably, $g(s_*)$ is an uneven function in s_*. According to the Ansatz (5.155), the leading order of $s\hat{\varphi}_q$ for $s_* \to 0$, therefore, becomes an even function in s_*. Hence, the imaginary part of the generalized shear modulus is zero. This can be immediately be inferred from the expression

$$\lim_{s\to 0} s\hat{\mathrm{G}}_q^{\perp}(s) = \lim_{s\to 0} \frac{s^2}{s_* g(s_*) h_q} \,. \tag{5.171}$$

Thus, any attenuation is neglected, and Equation (5.169) considers the *fate of elasticity* (Vogel *et al.*, 2025). We obtain the following relation for g_- in the jammed and for g_+ in the unjammed phase:

$$\begin{aligned} g_\pm(|s| \gg \omega_*) &\to 1 \\ g_-(|s| \ll \omega_*) &\to s_* - s_*^3 \\ g_+(|s| \ll \omega_*) &\to \frac{1}{s_*} + s_* \end{aligned} \tag{5.172}$$

In the unjammed phase ($\epsilon > 0$) holds $\lim_{s\to 0} s\hat{\varphi}_q(s) = \hat{\mathcal{W}}_q(s \to 0)$. Thus

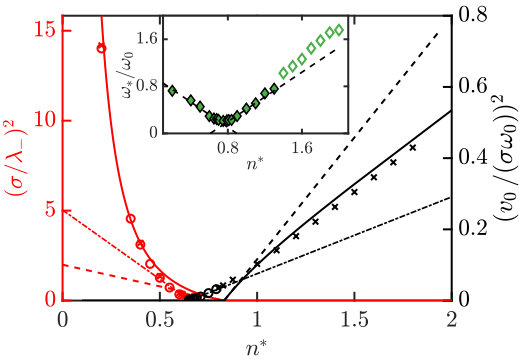

Figure 5.12: The figure displays the length scale λ_- and the speed of sound v_0 in the scalar ERM model for the Theta spring function $\mathcal{K}^\Theta$ for a uniform particle distribution. The solid lines display the solutions of the Equations (5.89) and (5.138). The symbols denote the results of the numerical diagonalization of the scalar ERM model performed by Philipp Baumgärtel, who also created this Figure. The numerical details are specified in (Vogel *et al.*, 2025). The dashed lines show the linear nature of the theory curves close to the critical point. The dashed-dotted lines depict linear fits of the numerical data. The inset shows the scaling of ω_* obtained from the numerical diagonalization. The filled symbols were used for the associated linear fit. Reprinted from *Self-Consistent Current Response Theory of Unjamming and Vibrational Modes in Low-Temperature Amorphous Solids.*, by F. Vogel, P. Baumgärtel. M. Fuchs, Phys. Rev. X. 2025, vol. 68, page 011030. Reprinted with permission Doi:10.1103/PhysRevX.15.011030.

Equation (5.155) and Equation (5.172) give for the long time limit of the fluidity

$$\mu_q = \lim_{s\to 0} \hat{\mathcal{W}}_q(s) = \epsilon h_q \ . \tag{5.173}$$

Considering the limit $q \to 0$, we find that the characteristic length scale diverges at the transition: $\lambda_-^\perp = 1/\sqrt{h_0\epsilon}$. Remarkably, the absence of the Born term in Equation (5.140) is reflected in the absence of the time-scale parameter t_0 in the equation for μ_q. For $\epsilon < 0$, Equation (5.172) gives for the inverse compliance

$$\begin{aligned}\lim_{s\to 0} s\hat{\mathrm{G}}_q^\perp(s) &= \lim_{s\to 0} s\frac{s^2}{\varsigma s_* g(s_*) h_q} \\ &= \frac{-\epsilon}{t_0^2 h_q} = \frac{\omega_*}{t_0 h_q}.\end{aligned} \tag{5.174}$$

The scaling $\propto \omega_*^{-1}$ is in accordance with the results for soft spheres with an harmonic interaction, discussed in Section 2.3.3. However, the derived scaling law is independent of the pair interaction and therefore contradicts the results summarized in Section 2.3.3 and discussed in (Ellenbroek *et al.*, 2009a; Liu *et al.*, 2011; Makse *et al.*, 1999; Mizuno *et al.*, 2016b; O'Hern *et al.*, 2003; van Hecke, 2009). This discrepancy to simulations might be caused by neglecting longitudinal modes and structural changes altogether. As noted in Section 2.3.3, non-affine displacements are thought to be of qualitative importance close to the transition. To describe non-affine motion, one needs the longitudinal modes. The continuity equation $\dot{\rho}(\boldsymbol{q}, t) = iqv^\parallel(\boldsymbol{q}, t)$ suggests that density fluctuations $\delta\rho(\boldsymbol{q}, t)$ must be considered as well. Albeit, here, we would have to consider a concrete perturbation and can not rely on thermal motion in the limit $T \to 0$ as suggested by the response formulas in Chapter 4. This generalization is left for future work. Nevertheless, the predicted scaling of the speed of sound $v_0^\perp$ is in qualitative and quantitative accordance with the scaling observed in the scalar ERM model with uncorrelated disorder. Here, one has $\epsilon = \frac{n_c - n}{n_c}$. Figure 5.12 shows the associated length-scale λ_- and the speed of sound v_0 for the $\mathcal{K}^\Theta$ spring function. The Figure compares the data from numerical diagonalization of the Hessian with the theory's prediction. The predicted values of v_0 and λ_- lie close to the numerical solution of the ERM model. This agreement is somewhat surprising in the unjammed phase since we used Equation (5.140) and the $F1$-model instead of the full equations. However, this agreement is in accordance with the data shown in Figure 5.10. There, the agreement between theory and numerical diagonalization was also good for small q. The deviations for higher wavenumbers most

likely stem from rattlers. Furthermore, Figure 5.12 displays linear fits of the data close to the transition. First of all, these fits confirm the theory's predictions $(\lambda_-)^{-2}, v_0^2 \propto \epsilon$. Furthermore, they can be used to determine the critical density. The lines depicting the linear fits of the theoretical prediction coincide at $n_c^* = 0.830(1)$. The linear fits of ω_*, v_0, and λ_- for the numerical data cross zero at different points. Using all available fit parameters[14] leads to the conjecture: $n_c^* = 0.69(8)$. Chapter 6 comments further on the transition in the ERM model and interprets it as a percolation transition.

Langevin case: The Langevin case is defined by $\xi \neq 0$. For $s \to 0$ holds

$$t_0^2 \frac{s(s+\xi)}{\varsigma^2} \underset{s\to 0}{\longrightarrow} \frac{s}{\omega_*} = s_* \, . \tag{5.175}$$

The characteristic frequency in the Langevin case is given by $\omega_* = \frac{\varsigma^2}{t_0^2 \xi}$. Thus, Equation (5.169) becomes

$$g(s_*) = \frac{\text{sign}(\epsilon) \pm \sqrt{1+4s_*}}{2s_*} \tag{5.176}$$

which has the following limits

$$g_\pm(|s| \gg \omega_*) \to \sqrt{s_*}^{-1}, \quad g_-(|s| \ll \omega_*) \to 1 - s_* \, , \quad g_+(|s| \ll \omega_*) \to \frac{1}{s_*} + 1 - s_* \, . \tag{5.177}$$

Notably, this again leads to $\lambda_- = 1/\sqrt{\epsilon h_0}$ and $(v_q^\perp)^2 = \frac{|\epsilon|}{t_0^2 h_q}$. Importantly, the length scale λ_- and $v_q^\perp$ are therefore independent of ξ, which once more emphasizes that the stability transition is independent of the dynamics and the friction. The discussion of the static observables is restricted to investigating the time-independent compliance $\hat{\chi}_q^\perp(0)$ and the quasi-static current $\kappa_q^\perp$. Frequency-dependent quantities are discussed in the next section.

[14] The quantitative analysis of the scalar ERM model has been done by Philipp Baumgärtel.

5.5.4 Scaling of frequency dependent quantities

This section investigates the behavior of frequency-dependent quantities such as the vibrational Density of States (vDOS) and the sound attenuation close to the transition. It becomes apparent from Equation (5.159) that the discussion in the previous section only holds for $\left|\frac{\varsigma^\alpha \tilde{g}(s_*)}{s_*}\right| \ll 1$. Thus, the validity of section 5.5.3 depends on the order of the limits $\varsigma \to 0$ and $s_* \to 0$. In the previous section, we considered $s_* \to 0$ for small but finite ς. This section considers the second case and assumes s_* to be small but finite. Hence, frequency-dependent quantities enter Equation (5.160). The first part of this section is dedicated to deriving the second scaling function $\tilde{g}(s_*)$. Subsequently, we turn to the sound attenuation and discuss the vibrational Density of States $D(\omega)$. As the vDOS can only be defined for $\xi = 0$, the following consideration is restricted to the Newtonian case in $d = 3$. Furthermore, as the main interest lies in the scaling of the sound attenuation, we also focus on the jammed case $\epsilon < 0$.

The second scaling function $\tilde{g}(s_*)$: Denoting the first order correction term as $s_* X_q^{\#,(1)}(s_*) = s_* X_q^{\#}(s_*) - s_* X_q^{\#,(0)}(s_*)$, the difference between the two Equations (5.159) and (5.160) gives the following constituting Equation:

$$\begin{aligned}\Big[s_* X_q^{\#,(1)}(s_*) - s_* \sum_p C_{q,p}^{\#} X_p^{\#,(1)}(s_*)\Big] &= \varsigma^{\alpha-1} s_* \varsigma \tilde{g}_-(s_*) \sum_p \Delta \tilde{C}_{q,p} h_p \\ &+ \sum_p \tilde{C}_{q,p} \left\{ \frac{h_p^2}{p^2} (s_* g_-(s_*))^2 \Big[\frac{s_* \varsigma g_-(s_*) h_p}{p^2 + s\hat{\varphi}_p(s)}\Big] \right. \\ &\left. - \frac{h_p^2}{p^2} 2\varsigma^\alpha s_*^2 g_-(s_*) \tilde{g}_-(s_*) - 2\varsigma s_*^2 g_-(s_*) X_p^{\#,(0)}(s_*) \frac{h_p}{p^2} + \mathcal{O}(\varsigma^{2\min\{\alpha,\beta\}}) \right\}\end{aligned} \tag{5.178}$$

Notably, the two scaling functions $g(s_*)$ and $\tilde{g}(s_*)$ both bear a minus sign to indicate that both of them refer to the solution in the jammed phase. The result of Section 5.5.3 for $g(s_*)$ suggests, that the right hand side of Equation (5.160) vanishes with s_*^2 for $\epsilon < 0$ and $\xi = 0$. We conjecture that $X_q^{\#,(0)}(s_* \to 0) \propto s_*$ holds in the Newtonian jammed phase. Hence, we neglect the last term on the right-hand side of Equation (5.178). Contracting Equation (5.178) with $\hat{h}_q$ from the left gives

$$s_* \tilde{g}_-(s_*) \varsigma^\alpha \Big(2 s_* g_-(s_*) - \mathrm{sgn}(\epsilon)\Big) = \varsigma (s_* g_-(s_*))^3 \sum_p \frac{\hat{h}_p h_p^3}{p^2} \frac{1}{p^2 + s\hat{\varphi}_q(s)} \,. \tag{5.179}$$

Here, we aditionally neglected the term

$$\sum_{q,p} \hat{h}_q \Delta\tilde{C}_{q,p} \, \frac{h_p^3}{p^2} (s_* g_-(s_*))^3 \frac{s_* \varsigma}{p^2 + s\hat{\varphi}_p(s)} \approx \mathcal{O}(\varsigma^{1.5} s_*^4) \tag{5.180}$$

as it plays no role sufficiently close to the transition. However, the whole term $\propto \tilde{g}(s_*)h_q$ indeed matters for $\varsigma \to 0$ due to an infrared divergency on the right side of Equation (5.179). Nevertheless, this divergency only plays a role in the jamed phase for $s \to 0$. Thus, we set $\epsilon < 0$ in the following and write $s\hat{\varphi}_q(s) = \frac{s^2}{(v_q^\perp)^2}$. As discussed in Section 5.5.2 the critical left eigenvector vanishes for $p \to 0$ with $\hat{h}_{p\to 0} \propto p^{d-1}$. Thus, the Sokhotski–Plemelj theorem from Equation (5.91) gives in $d = 3$ and for $s = -i\omega + 0^+$

$$s_* \tilde{g}_-(s_*) \varsigma^\alpha \Big(2 s_* g_-(s_*) + 1 \Big) = \frac{\pi \varsigma}{2} \frac{\left[s_* g_-(s_*) \right]^3}{s / v_0^\perp} \lim_{p\to 0} \frac{\hat{h}_p}{p^2} h_0^3 + \mathcal{O}(s_*^3). \tag{5.181}$$

As $v_0^\perp = \frac{\sqrt{\varsigma}}{t_0 \sqrt{h_0}}$ holds, we conclude $\alpha = \frac{1}{2}$ and find for $s_* \to 0$

$$\tilde{g}_-(s_*) = \mathcal{A} s_*^4 , \qquad \mathcal{A} = \lim_{p\to 0} \frac{\pi}{2} \frac{\hat{h}_p}{p^2} h_0^{\frac{5}{2}}. \tag{5.182}$$

Here, we used $\omega_* = \varsigma / t_0$ and inserted $g_-(s_* \to 0) = s_*$, Importantly, the whole calculation above only applies in the jammed phase. In the unjammed phase holds $\lim_{s\to 0} s\varphi_q(s) = \mu_q^\perp$. Thus, the right-hand side of Equation (5.179) does not feature a pole for $\epsilon > 0$, which alters the whole calculation. Furthermore, the calculation only holds for lower dimensions with $d < 4$. The reminder on the right-hand side of Equation (5.181) dominates in higher dimensions $d \geq 4$. After having obtained the second scaling function $\tilde{g}(s_*)$, we can investigate frequency-dependent quantities in the limit $s, \varsigma \to 0$.

The critical sound attenuation The considerations in Section 5.3.2 and Equation (5.106) in particular, suggest that the attenuation vanishes at the transition $\propto v_0^\perp$. However, the deduction in Section 5.3.2 relied on considering the limit $s \to 0$. But, we saw in the previous paragraphs that the order of the two limits $s \to 0$, $\varsigma \to 0$ can not be interchanged. Indeed, taking the limit $s \to 0$ first and calculating the attenuation based

on Equation (5.161) just reproduces

$$\Gamma_q^\perp \approx \left.\frac{\tilde{\Gamma}_q(\omega)}{\omega}\right|_{\omega=v_0^\perp q} \to (qv_0^\perp)^4 \frac{\pi}{2k_D^3}\frac{\beta_0^{(2)}}{(v_0^\perp)^3} \; . \tag{5.183}$$

This becomes equivalent to Equation (5.106) close to the transition. The second term in Equation (5.106) becomes negligible for $\varsigma \to 0$. However, in the previous paragraph, we saw that a second contribution to the sound attenuation arises if the limit $\varsigma \to 0$ is considered first for finite but small s_*. This term dominates close to the transition. To calculate the critical sound attenuation, we start from Equation (5.155) and take the limit $\varsigma \to 0$:

$$s\hat{\varphi}_q(s) = \varsigma\big(s_* g_-(s_*) + s_*\sqrt{\varsigma}\tilde{g}_-(s_*)\big)h_q \underset{s_*\to 0}{\longrightarrow} \frac{s^2}{(v_q^\perp)^2}\Big(1 + \sqrt{\varsigma}\mathcal{A}s_*^3\Big) \; . \tag{5.184}$$

Inserting this expression in the equation for the susceptibility gives for $s = -i\omega + 0^+$

$$\hat{\chi}_q^\perp(-i\omega + 0^+) = \left.\frac{1}{s^2 + \frac{q^2 s^2}{s\hat{\varphi}_q(s)}}\right|_{s=-i\omega} \underset{s_*\to 0}{\longrightarrow} \frac{1}{-\omega^2 + (qv_q^\perp)^2\big(1 - i\mathcal{A}\frac{\omega^3}{\sqrt{\omega_*}^5}\sqrt{t_0}\big)} \; . \tag{5.185}$$

Thus, the sound attenuation[15] is given by

$$\Gamma_q^\perp \equiv -\frac{\mathrm{Im}(\hat{\chi}_q(\omega))^{-1}}{\omega}\Big|_{\omega=qv_q^\perp} = (qv_q^\perp)^4 \frac{\mathcal{A}\sqrt{t_0}}{\sqrt{\omega_*}^5} \; . \tag{5.186}$$

This contribution to the attenuation dominates over the term in (5.183). Notably, Wyart's effective medium theory predicts the same scaling of the attenuation (DeGiuli *et al.*, 2014). Equation (5.186) suggests that the transverse scattering length $l_q^\perp = 2v_0^\perp/\Gamma_q^\perp$ (Mizuno and Ikeda, 2018) diverges when approaching the transition. We look at the propagating wave regime, where $\omega < \omega_*$ holds where q is sufficiently small that the linear dispersion relation holds. The last point , which implies $v_q^\perp \approx v_0^\perp$. The result

[15] Matthias Fuchs came up with the Ansatz (5.155). Additionally, Professor Fuchs presented the first calculations on the divergence of the sound attenuation close to the transition. The present author is responsible for the flawed calculation of the critical sound attenuation published in (Vogel *et al.*, 2025). Furthermore, the author of this monograph slightly improved Matthias Fuchs' considerations by specifying the dependence on the spatial dimension. However, the discussion of the critical sound damping is Mathias Fuchs' intellectual property.

$v_0 \propto \sqrt{\omega_*}$ from Equation (5.174) gives

$$l_q^\perp \propto \frac{w_*^3}{(q v_0^\perp)^4} \,. \tag{5.187}$$

The scattering length does not diverge when approaching the transition or respectively for $\omega_* \to 0$ since $q v_0^\perp = \omega < \omega_*$ holds by assumption. However, simulations found an even stronger divergence $\propto 1/\omega_*^3$ of the sound attenuation (Mizuno and Ikeda, 2018), which results in a weaker dependency of $l_q^\perp$ on ω_*. Philipp Baumgärtel's numerical investigations of the ERM model do not yet allow for a conclusive statement about the attenuation in the ERM model. Thus, resolving the discrepancy between the theory's predicted scaling and the observed attenuation is left for future work. After considering the imaginary part of the inverse susceptibility, *i.e.* the attenuation, we now turn to the Density of States.

Density of States: According to Section 5.3.3, the vibrational Density of States $D(\omega)$ is given by the integral over the imaginary part of $\hat{\chi}_q(-i\omega)$:

$$D(\omega) \approx \frac{2\omega(d-1)}{dn\pi} \int_{|\boldsymbol{q}|<k_D} \frac{d^d\boldsymbol{q}}{(2\pi)^d} \operatorname{Im}\left\{\hat{\chi}_q^\perp(s=-i\omega+0^+)\right\} \,, \tag{5.188}$$

where we have again neglected the longitudinal modes. The transverse susceptibility reads

$$\hat{\chi}_q^\perp(s) = \frac{\hat{\mathrm{K}}_q^\perp(s)}{s} = \frac{1}{s^2}\frac{s\hat{\varphi}_q(s)}{s\hat{\varphi}_q(s)+q^2} = \frac{1}{s^2+\frac{q^2 s^2}{s\hat{\varphi}_q(s)}} \,. \tag{5.189}$$

As it is only possible to define *states* in an arrested system, the ensuing consideration is again restricted to $\epsilon < 0$. Here, the previous two sections have led to the expression:

$$s\hat{\varphi}_q(s) = \varsigma\big(s_* g_-(s_*) + s_*\sqrt{\varsigma}\tilde{g}_-(s_*)\big)h_q \,, \tag{5.190}$$

with $g_-(s_*)$ given in Equation (5.176) and $\tilde{g}_-(s_*)$ specified in Equation (5.182). As we have only obtained an expression for $\tilde{g}_-(s_*)$ for $|s| \ll \omega_*$, we will restrict ourselves to the limiting cases and subsequentially derive expressions for the vDOS for $\omega \ll \omega_*$ and $\omega \gg \omega_*$ with $s = -i\omega + 0^+$. As we saw, $\tilde{g}_-(s_*)$ depends non-trivially on the dimension d. Thus, we will restrict ourselves to $d = 3$ hereinafter.

1) $\underline{\omega \ll \omega_*}$: Equation (5.185) suggests that the system is populated by damped waves for frequencies smaller than ω_*. Here, the system can be regarded as an elastic medium, and the susceptibility reads

$$\hat{\chi}_q^{\perp}(-i\omega + 0^+) = \frac{1}{-\omega^2 + (qv_q^{\perp})^2\left(1 - i\mathcal{A}\frac{\omega^3}{\sqrt{\omega_*^5}}\sqrt{t_0}\right)} \,. \tag{5.191}$$

The equation for the vDOS decomposes in two independent contributions

$$D(\omega \to 0) = D_D(\omega) + \frac{d-1}{d}\frac{\omega^4}{\sqrt{\omega_*^5}}\frac{\mathcal{A}}{n\pi^3}\int_0^{k_D}\frac{dq}{(v_q^{\perp})^2} \,, \tag{5.192a}$$

$$\begin{aligned} D_D(\omega) &= \frac{d-1}{d}\frac{2\omega}{n\pi}\int_{|\boldsymbol{q}|<k_D}\frac{d^d\boldsymbol{q}}{(2\pi)^3}\,\mathrm{Im}\left\{\frac{1}{-\omega^2 - i0^+ + q^2(v_q^{\perp})^2}\right\} \\ &= \frac{d-1}{d}\frac{\omega^2}{(k_D v_0^{\perp})^3} \,. \end{aligned} \tag{5.192b}$$

where the Debye-wavenumber in $d = 3$ reads $k_D = \sqrt[3]{2\pi^2 n}$. We again relied on Equation (5.91) when writing down the solution for the Debye DOS $D_D(\omega)$. Notably, the Debye contribution dominates as $\omega \ll \omega_*$ holds by assumption and as $v_0^{\perp} \propto \sqrt{\varsigma}$ has been found in Section 5.5.3. Furthermore, it is important to emphasize that the excess vDOS $D(\omega) - D_D(\omega)$ stems from Rayleigh-damping as its exponent varies with the dimension as $d + 1$. Thus, this excess term can not be related to Quasi-Localised Modes, introduced in Section 2.3.3. Their contribution to the vDOS is supposed to be independent of the dimension (Lerner and Bouchbinder, 2021).

2) $\underline{\omega \gg \omega_*}$: It becomes apparent from Equation (5.159), that the terms $\propto \varsigma^{\alpha} = \sqrt{\varsigma}$ do not contribute for $\varsigma \to 0$ as s_* remains finite for $\omega > \omega_*$. Thus, it suffices to consider the scaling function $g_-(s_*)$ from Equation (5.176). Consequentially, for $\omega \gg \omega_*$ holds

$$s\hat{\varphi}_q(s) = \varsigma s_* h_q = -i\varsigma\frac{\omega}{\omega_*}h_q \,. \tag{5.193}$$

This gives the vDOS

$$D(\omega \gg \omega_*) = \frac{2}{dn\pi} \int_{|\boldsymbol{q}|<k_D} \frac{d^d\boldsymbol{q}}{(2\pi)^3} \operatorname{Im}\left\{ \frac{i\varsigma}{\omega_*} \frac{h_q}{q^2 - \underbrace{i\frac{\omega\varsigma}{\omega_*}}_{\approx 0} h_q} \right\} \approx \frac{t_0}{dn\pi^3} \int_0^{k_D} dq h_q \ . \tag{5.194}$$

Thus, the theory predicts a constant vDOS for $\omega_* \ll \omega \ll \omega'_{BR}$, where ω'_{BR} denotes an upper-frequency limit where the discussed analysis breaks down. Importantly, the value of the plateau is also independent of the distance to the critical point as $\frac{1}{n_*^c - \epsilon} \approx \frac{1}{n_*^c}$ holds for $\epsilon \to 0$. The prediction of a plateau is in accordance with the discussion presented in the context of Equation (2.52). Furthermore, the constant vDOS is also observed in the ERM model. The prediction of Equation (5.194) is included in Figure 5.6 as horizontal black dashed lines. The theory lines have decent quantitative agreement with the data obtained from numerical diagonalization. Interpreting ω_* as the onset of the plateau in the vDOS allows the conjecture that the reduced Density of States $D(\omega)/D(\omega)$ exhibits a peak close to ω_*. This suggests that the characteristic frequency ω_* is close to the frequency of the Boson peak ω_{BP} as has been found in simulations (Mizuno and Ikeda, 2018; Shintani and Tanaka, 2008). Philipp Baumgärtel's yet unpublished investigations of the scalar ERM model also confirm that ω_* and ω_{BP} are close to each other.

The differences in the vDOS for $\omega \ll \omega_*$ and $\omega \gg \omega_*$ connects back to a narrative discussed in Section 2.3.2: The characteristic frequency ω_* is supposed to separate two vibrational regimes. While the system can be regarded as an elastic medium for $\omega \ll \omega_*$, disorder dominates for $\omega \gg \omega_*$. Here, a mode supposedly has sufficient energy to resolve the disorder, suggesting a diffusive instead of a propagating nature of the modes (Allen *et al.*, 1999; Beltukov *et al.*, 2013; Liu *et al.*, 2011). We will substantiate this line of thought in the next section.

5.5.5 Disorder induced modes

This section discusses the nature of the modes with frequencies above ω_*. Again, we focus on the Newtonian case $\xi = 0$ and restrict ourselves to three spatial dimensions, $d = 3$. It has been established by Equation (5.185) that the system is populated by weakly damped sound waves for $\omega \ll \omega_*$. Here, the system can be treated as a continuous medium where the disordered nature of the system is only reflected in the attenuation. However, Equation (5.193) implies that the susceptibility for $\omega \gg \omega_*$ can be written as

$$\hat{\chi}_q^\perp(-i\omega) \approx \frac{1}{-\omega^2 - i\omega\frac{q^2\omega_*}{\varsigma h_q}} = \frac{1}{-\omega^2 - \frac{i\omega}{\omega_*}(qv_q^\perp)^2} \; . \tag{5.195}$$

As we will see in the first part of this section, Equation (5.195) is the susceptibility associated with diffusive motion. Again, this connects back to the Allen-Feldmann theory, stating that ω_* marks the transition between the propagating and diffusive regime. However, we will discuss in the second part of this section that it is not straightforward to relate ω_* to the Ioffe-Regel limit as the divergence of the Rayleigh sound attenuation discussed in Section 5.5.4 is too weak.

The critical law: At the critical point, $\varsigma = \omega_* = 0$, the validity of Equation (5.195) extends down to $\omega = 0$. Thus, the expression

$$\hat{\chi}_q^\perp(s) = \frac{1}{s^2 + \frac{q^2 s^2}{s_* \varsigma g(s_*) h_q}} \underset{\omega_* \to 0}{\longrightarrow} \frac{1}{s} \frac{1}{s + \frac{q^2}{t_0 h_q}} \tag{5.196}$$

is valid for all s, and we can perform the inverse Laplace transformation to look at the susceptibility in the time domain. The general properties of the Laplace transformation imply the following relation

$$\int_0^\infty dt e^{-st} \frac{d}{dt} \chi_q^\perp(t) = s\hat{\chi}_q^\perp(s) + \chi_q^\perp(t=0) \; , \tag{5.197}$$

with the inital condition $\chi_q^\perp(t=0) = \lim_{s\to\infty} s\hat{\mathrm{K}}_q^\perp(s) = 0$. Thus, we get the result

$$\frac{d}{dt}\chi_q^\perp(t) = e^{-\frac{q^2}{t_0 h_q}t} \tag{5.198a}$$

$$\implies \chi_q^\perp(t) = \frac{t_0 h_q}{q^2}\left(1 - e^{-\frac{q^2}{t_0 h_q}t}\right) . \tag{5.198b}$$

Equation (5.198a) represents the diffusion law for $\boldsymbol{q} \to 0$. Thus, any perturbation spreads diffusively through the system at the critical point. The diffusion coefficient is given by $D_q = \frac{1}{h_q t_0}$, independent of the distance to the critical point. Generalizing this finding to small but finite ς suggests that the propagator $\tilde{\chi}_q^\perp(\omega \gg \omega_*)$ in Equation (5.195) also describes diffusive modes. Hence, the modes above for $\omega \gg \omega_*$ can be identified with the *Diffusons* from the Allen-Feldmann Theory (Allen *et al.*, 1999) outlined in Section 2.3.3. Again, this suggests that the characteristic frequency ω_* marks the transition between two vibrational regimes. The last missing piece in the narrative is the connection between ω_* and the transverse Ioffe-Regel limit, which is the topic of the following paragraph.

The Ioffe-Regel limit The crossover from a propagating to a diffusive regime transpires in a change in the imaginary part of the complex dispersion relation $\mathrm{Im}\{\hat{v}_q^\perp(-i\omega))^2\} = \mathrm{Im}\{\big(\hat{\chi}_q^\perp(-i\omega)\big)^{-1}\}$. Below ω_* the imaginary part of $(\tilde{v}_q^\perp(\omega))^2$ corresponds to Rayleigh-damping characterised by $\omega\Gamma_q^\perp(\omega) \propto \omega q^{d+1}$. On the other hand, Equation (5.195) gives $\mathrm{Im}\{(\tilde{v}_q^\perp(\omega))^2\} = \frac{\omega}{\omega_*}(q v_q^\perp)^2$ for $\omega \gg \omega_*$. Here, the imaginary part is independent of the dimension and the distance to the critical point. As discussed in Section 2.3.3, this crossover has been observed in experiments and simulations alike and has been the subject of theoretical investigations, see *e.g.* (Mizuno and Ikeda, 2018; Monaco and Giordano, 2009; Schirmacher *et al.*, 2007). In general, this change in the nature of the modes and the imaginary part is connected to the Ioffe-Regel limit as a mode can not propagate when its wavelength $\lambda = \frac{2\pi}{q}$ becomes equal to the mean free path length–defined in Equation (2.60). The Ioffe-Regel for the transverse modes criterion reads (Mizuno and Ikeda, 2018):

$$\frac{\Gamma^\perp(\Omega_{\mathrm{IR}}^\perp)}{\Omega_{\mathrm{IR}}^\perp} = 1 .$$

Here, $\Omega^\perp = qv_q^\perp$ denotes the propagating transverse frequency. The index IR specifies the transverse Ioffe-Regel frequency[16]. As a reminder

$$\Gamma_q^\perp = \left.\frac{-\operatorname{Im}\{\left(\hat{\chi}_q^\perp(s=-i\omega)\right)^{-1}\}}{\omega}\right|_{\omega=\Omega^\perp} \tag{5.199}$$

denotes the negative imaginary part of the complex dispersion relation. The discussed shift in $\omega\Gamma_q^\perp$ from $\propto \omega\Omega^4$ valid for $\omega \ll \omega_*$ to $\propto \omega\Omega^2$ for $\omega \gg \omega_*$ suggest, that $\Omega_{\mathrm{IR}}^\perp$ scales linearly with ω_*. This has also been found in simulations (Mizuno and Ikeda, 2018). There, it was additionally reported that ω_* and $\Omega_{\mathrm{IR}}^\perp$ do not coincide but lie close to each other. The authors found $\Omega_{\mathrm{IR}}^\perp < \omega_*$. Moreover, the scaling $\Omega_{\mathrm{IR}}^\perp \propto \omega_*$ implies that $\Gamma^\perp(\Omega^\perp)$ is continuous at $\Omega_{\mathrm{IR}}^\perp$ at least up to logarithmic correction if the sound attenuation diverges as $\Gamma^\perp(\Omega^\perp) \propto \frac{(\Omega^\perp)^4}{\omega_*^3}$ for $\Omega^\perp < \omega_*$. Again, this scaling was indeed observed in (Mizuno and Ikeda, 2018). However, the discussion in the Section 5.5.4 contradicts this conjecture: If one interpolates the validity of Equation (5.195) down to $qv_0^\perp = \Omega_{\mathrm{IR}}^\perp$, the theory's predicted scaling of the sound attenuation $\Gamma^\perp(\Omega^\perp) \propto \frac{(\Omega^\perp)^4}{\omega_*^{5/2}}$ implies a discontinuity of $\Gamma^\perp(\Omega^\perp)$ at $\Omega_{\mathrm{IR}}^\perp$ or points to an extended crossover interval. The reason for this discrepancy or incommensurability is that the Self-Consistent Current Response Theory misses the strong divergence of the attenuation for $\omega \ll \omega_*$ reported in (Mizuno and Ikeda, 2018). No pertinent and conclusive results for the ERM model are available yet. So, the relation of ω_* and $\Omega_{\mathrm{IR}}^\perp$ remains an open question.

The investigation of the critical dynamics concludes the discussion of the transverse current response theory. Chapter 5 has outlined the construction of the theory and explained the predicted results for the jammed and the unjammed phases and the associated transition. It has become apparent from the content of Section 5.2.5 and from comparing the numerical solutions with the scalar ERM model that a deep connection exists between the self-consistent current response theory and the ERM model. This connection is further strengthened by the considerations in Chapter 4 and Appendix A. The next chapter takes a closer look at the transition in the scalar ERM model.

[16]Notably, there is also a longituidnal Ioffe-Regel. However, this chapter exclusively focuses on the transverse modes.

6 | The transition in the scalar ERM model

We have discussed in Chapter 2 how the vibrational properties of amorphous solids differ from the ones of crystals. Ultimately, the characteristic properties all originate from the underlying topological disorder. Prominent examples are Rayleigh damping, the Boson peak, and the change from the propagating to the diffusive regime of the modes. Extensive experiments and simulations have provided detailed and deep insight into the underlying physics (Baldi *et al.*, 2010, 2014, 2013; Caponi *et al.*, 2009; Mizuno and Ikeda, 2018; Wang *et al.*, 2019b; Wuttke *et al.*, 1995). Several theories have been proposed to rationalize the emergent phenomena. Wyart's effective medium theory (DeGiuli *et al.*, 2015), Schirmacher's Heterogeneous-Elasticity Theory (Schirmacher and Ruocco, 2022) and Mean-Field theories in infinite dimensions (Charbonneau *et al.*, 2017; Parisi *et al.*, 2020) stand out. However, all of them have their shortcomings: Theories valid for $d \to \infty$ have little predictive power in $d = 3$, Wyart's effective medium theory also misses the strong divergence of the attenuation found in (Mizuno and Ikeda, 2018). Additionally, similar to the Heterogeneous-Elasticity Theory, their effective medium theory predicts negative eigenvalues of the Hessian below the critical point. Moreover, the preparation protocol matters as the jammed state is generally out of equilibrium (Szamel and Flenner, 2022; Wang *et al.*, 2019a,b). The Self-Consistent Current Response Theory developed in Chapter 5 strived to rationalize which phenomena are purely disorder-induced in contrast to features that might be distinct to some metastable state. However, despite some shortcomings like the weak divergence of the sound attenuation at the critical point, the theory has turned out to be quite evolved and costly to solve numerically. All of this calls for an idealized model where parts of the phenomena can be isolated and studied in detail. The ERM model introduced in Chapter 4 promises to be such a model. As the model can be solved for scalar and vector excitations and the influence of initial stresses can be neglected at will, the ERM model allows studying the influence of different sources of complexity. Furthermore, different

distributions of the particles $\Psi_Q(\{\boldsymbol{R}\}_{i=1}^N)$ can easily be studied. In Appendix A, we derive a theory for the ERM model following the steps of (Szamel, 2025). In Chapter 5, we looked at different aspects of the theory and remarked on the good quantitative agreement with the exact numerical diagonalization of the scalar ERM model performed by Philipp Baumgärtel. This chapter looks at the transition occurring in the scalar ERM model. As we will see, the rigidity transition is related to the largest cluster percolating the system. The chapter is structured as follows: First, in Section 6.1, the Covariance Theorem of the Mode-Coupling Theory is utilized to propose a second correlation function that allows further insight into the nature of the vibrational modes in the unjammed state. We will conclude that no sound-like excitations exist below the critical density $n < n_c$. Section 6.2 provides evidence for the Percolation transition. Hereinafter, we exclusively work in the scalar ERM model and consequentially set $\xi = 0$. Notably, we only assume a uniform distribution of the particles when we discuss numerical data. The presented analytical results are independent of the distribution.

6.1 The Covariance Theorem and the phonon gap

Injecting momentum in the unstable structure below jamming leads to the quasi-stationary current κ_q. As discussed in Section 5.4, κ_q is given by the overlap between injected momentum and modes with zero restoring forces. However, the overlap with modes still feeling restoring forces again causes vibrational modes even in the unjammed state. To study these *precursors of stability*, we define the new correlation function

$$\hat{\phi}_q^{\mathrm{SERM}}(s) = \frac{\hat{\mathrm{K}}_q^{\mathrm{SERM}}(s) - \frac{\kappa_q}{s}}{1-\kappa_q} \,, \tag{6.1}$$

where the correlator of the scalar ERM model is given by

$$\hat{\mathrm{K}}_q^{\mathrm{SERM}}(s) = s\hat{\chi}_q^{\mathrm{SERM}}(s) = \frac{s}{N}\overline{\sum_{i,j=1}^{N} e^{-i\boldsymbol{q}\cdot(\boldsymbol{R}_i-\boldsymbol{R}_j)}\left[s^2 + \underline{\boldsymbol{\mathcal{H}}}^{\mathrm{SERM}}\right]_{ij}^{-1}} \tag{6.2}$$

$$= \frac{s}{s^2 + \frac{q^2(c_q^{\mathrm{SERM}})^2}{1+\frac{\hat{\Sigma}_q^{\mathrm{SERM}}(s)}{(qc_q^{\mathrm{SERM}})^2}}} \,. \tag{6.3}$$

The explicit expression for the self-energy $\hat{\Sigma}_q^{\mathrm{SERM}}(s)$ is given in Equation (A.70) and $\kappa_q \equiv \lim_{s\to 0} s\hat{\mathrm{K}}_q^{\mathrm{SERM}}(s)$ holds by definition. All these quantities supposedly model the objects defined and discussed in Section 5. The new correlator $\hat{\phi}_q(s)$ describes the vibrations on the system's stable structures relative to the quasi-stationary momentum field κ_q. Notably, $\phi_q^{\mathrm{SERM}}(t=0) = \lim_{s\to\infty} s\hat{\phi}_q^{\mathrm{SERM}}(s) = 1$ holds and $\hat{\phi}_q^{\mathrm{SERM}}(s)$ generally shares all the properties of a correlation function as defined in Chapter 3. This is the Covariance Theorem elaborated on in (Götze, 2009, Chapter 4.2). Notably,

$$\lim_{s\to 0} s\hat{\phi}_q^{\mathrm{SERM}}(s) = 0 \ , \tag{6.4}$$

holds in the stable as well as in the unstable phase. Thus, we can always define a second susceptibility via

$$\hat{\mathrm{X}}_q^{\mathrm{SERM}}(s) = \frac{\hat{\phi}_q^{\mathrm{SERM}}(s)}{s} \ . \tag{6.5}$$

Later in this section, we employ $\hat{\mathrm{X}}_q^{\mathrm{SERM}}(s)$ to analyze the modes in the unstable state and to investigate the changes at the transition. The following paragraph provides an expression for $\hat{\mathrm{X}}_q^{\mathrm{SERM}}(s)$ suitable for further investigations.

The susceptibility on the stable substructures $\hat{\mathrm{X}}_q^{\mathrm{SERM}}(s)$: This paragraph is dedicated to deriving an expression for $\hat{\mathrm{X}}_q^{\mathrm{SERM}}(s)$ which does not need direct references to κ_q and which can be further analyzed in the subsequent paragraphs. To keep the notation concise, we restrict ourselves to the $F1$ approximation introduced in Section 5.2.5. As visible in the Figures 5.2 and 5.10, it has been proven a good approximation for small s and close to the transition. We start the deduction by defining two auxiliary quantities. The first one is the rescaled long time limit of the self-energy:

$$A_q = \lim_{s\to 0} \frac{s^2}{(qc_q^{\mathrm{SERM}})^2} \hat{\Sigma}_q^{\mathrm{SERM}}(s) = \frac{\kappa_q}{1-\kappa_q} (qc_q^{\mathrm{SERM}})^2 \tag{6.6}$$

The second auxiliary quantity can only be defined in the $F1$ approximation:

$$\hat{B}_q(s) = \frac{1}{N(qc_q^{\mathrm{SERM}})^2} \sum_p p^{d-1} \tilde{C}_{q,p}^{\mathrm{SERM}} \hat{\phi}_p(s) \tag{6.7}$$

Here, $\tilde{C}^{\mathrm{SERM}}_{q,p} = C^{\mathrm{SERM}}_{q,p}(1-\kappa_p)$ denotes the rescaled stability matrix of the scalar ERM model. Originally, the stability matrix $C_{q,p}$ was introduced in Equation (5.88). The corresponding expression in the scalar ERM model reads

$$\begin{aligned} C^{\mathrm{SERM}}_{q,p} =& \frac{1}{N^2}\int d^{d-1}\hat{p}\sum_{\boldsymbol{k}}\frac{1}{(kc^{\mathrm{SERM}}_k)^2}V^{\mathrm{SERM}}_{\boldsymbol{q},\boldsymbol{k}}\cdot V^{\mathrm{SERM}}_{\boldsymbol{k},\boldsymbol{p}}S_{|\boldsymbol{q}-\boldsymbol{k}|}\cdot\ldots \\ &\cdot\left[\frac{1}{(kc^{\mathrm{SERM}}_k)^2}V^{\mathrm{SERM}}_{\boldsymbol{k},\boldsymbol{p}}\cdot S_{|\boldsymbol{k}-\boldsymbol{p}|}V^{\mathrm{SERM}}_{\boldsymbol{q},\boldsymbol{k}}+\frac{1}{(bc^{\mathrm{SERM}}_b)^2}V^{\mathrm{SERM}}_{\boldsymbol{p},\boldsymbol{q}+\boldsymbol{p}-\boldsymbol{k}}\cdot S_{|\boldsymbol{k}-\boldsymbol{p}|}V^{\mathrm{SERM}}_{\boldsymbol{q},\boldsymbol{p}+\boldsymbol{q}-\boldsymbol{k}}\right]. \end{aligned} \tag{6.8}$$

Here, we wrote $\boldsymbol{b} = \boldsymbol{q}+\boldsymbol{p}-\boldsymbol{k}$ to keep the notation concise. The expression for the vertex is given in Equation (A.38). Importantly, we used $\left(V^{\mathrm{SERM}}_{\boldsymbol{k},\boldsymbol{q}}\right)^\dagger = V^{\mathrm{SERM}}_{\boldsymbol{q},\boldsymbol{k}}$ to shorten the expression. Notably, the ensuing derivation is, in principle, not restricted to the $F1$ approximation. One can look up in (Götze, 2009, Equation 4.22) how the coupling coefficients in the full theory need to be updated when expressing the self-energy with $\hat{\phi}^{\mathrm{SERM}}_q(s)$. Lastly, we include the Born term in a renormalized frequency

$$\tilde{s} = s\left(1+\frac{1}{N(qc^{\mathrm{SERM}}_q)^2}\sum_{\boldsymbol{p}}\left(V^{\mathrm{SERM}}_{\boldsymbol{q},\boldsymbol{p}}\right)^2\frac{S_{|\boldsymbol{q}-\boldsymbol{p}|}}{s^2+(pc^{\mathrm{SERM}}_p)^2}\right) = s+s\hat{\Delta}^{\mathrm{SERM}}_q(s)\,. \tag{6.9}$$

The Born term $\hat{\Delta}^{\mathrm{SERM}}_q(s)$ is the scalar ERM equivalent to Equation (5.87) and similarly arises from the one-loop correction. All of these abbreviations simplify the notation. Basic manipulations lead to the following expression of the new correlator $\hat{\phi}^{\mathrm{SERM}}_q(s)$:

$$\begin{aligned} \hat{\phi}^{\mathrm{SERM}}_q(s) = \hat{\mathrm{K}}^{\mathrm{SERM}}_q(s) - \frac{\kappa_q}{s} &= \left[s+\frac{(qc^{\mathrm{SERM}}_q)^2}{\tilde{s}+\frac{A_q}{s}+\hat{B}_q(s)}\right]^{-1} - \left[s+\frac{(qc^{\mathrm{SERM}}_q)^2}{\frac{A_q}{s}}\right]^{-1} \\ &= \frac{\tilde{s}+\frac{A_q}{s}+\hat{B}_q(s)}{s\tilde{s}+A_q+s\hat{B}_q(s)+(qc^{\mathrm{SERM}}_q)^2} - \frac{\frac{A_q}{s}}{A_q+(qc^{\mathrm{SERM}}_q)^2} \\ &= \frac{\tilde{s}(qc^{\mathrm{SERM}}_q)^2+\hat{B}_q(s)(qc^{\mathrm{SERM}}_q)^2}{(A_q+(qc^{\mathrm{SERM}}_q)^2)^2+(A_q+(qc^{\mathrm{SERM}}_q)^2)(s\tilde{s}+s\hat{B}_q(s))} \\ &= \frac{(qc^{\mathrm{SERM}}_q)^2}{(A_q+(qc^{\mathrm{SERM}}_q)^2)}\frac{\tilde{s}+\hat{B}_q(s)}{(A_q+(qc^{\mathrm{SERM}}_q)^2)+(s\tilde{s}+s\hat{B}_q(s))} \\ &= \frac{(qc^{\mathrm{SERM}}_q)^2}{(A_q+(qc^{\mathrm{SERM}}_q)^2)}\frac{1}{s+\frac{(A_q+(qc^{\mathrm{SERM}}_q)^2)}{\tilde{s}+\hat{B}_q(s))}} \end{aligned} \tag{6.10}$$

Using Equation (6.6), the first fraction in the last line can be identified with $(1-\kappa_q)$. All in all, this gives the new susceptibility

$$\hat{\mathrm{X}}_q^{\mathrm{SERM}}(s) = \frac{\hat{\phi}_q(s)}{s} = \frac{1}{s^2 + \frac{(qc_q^{\mathrm{SERM}})^2 + A_q}{1+\hat{\Delta}_q^{\mathrm{SERM}}(s) + \frac{\overline{\Sigma}_q(s)}{(qc_q^{\mathrm{SERM}})^2}}} \,. \tag{6.11}$$

Where the new self-energy reads $\overline{\Sigma}_q(s) = \frac{(qc_q^{\mathrm{SERM}})^2}{s}\hat{B}_q(s)$. The susceptibility $\hat{\mathrm{X}}_q^{\mathrm{SERM}}(s)$ describes the evolution of vibrational modes in the stable structures of the system. In the following paragraphs, we will derive several conclusions about the changes in the nature of the modes at the critical point.

Phonon gap: We have discussed in Section 5.5.4 and in particular in the context of Equation (5.185) that the system in the jammed phase is populated by damped sound modes for sufficiently small frequencies $\omega < \omega_*$. Equation (6.11) and the new susceptibility $\hat{X}^{\mathrm{SERM}}(s)$ allow studying the small energy modes in the unjammed state. This section will show that no sound modes are present in the unjammed case, even for $\omega \to 0$. As discussed in Section 5.5.4, the Debye Density of States, quantifying the density of sound modes, originates from the sound pole in the susceptibility. For example, this has been discussed in the context of Equation (5.192). Hence, we aim for an expression that allows us to study the relation of ω and q for small frequencies. We focus on small separation parameters ς as the $F1$ approximation generally improves closer to the critical point and as we need the frequency scale ω_* to separate the propagating and the diffusive regime. Only interested in the static quantities, we consider $s_* \to 0$. Using the results of Section 5.5.3 and Equation (5.172), we find for the new self energy:

$$\begin{aligned} 1 + \hat{\Delta}_q^{\mathrm{SERM}}(s) + \frac{\overline{\Sigma}_q^{\mathrm{SERM}}(s)}{(qc_q^{\mathrm{SERM}})^2} &= \frac{1}{s^2}\Big(s^2 + s^2\frac{\hat{\Sigma}_q^{\mathrm{SERM}}(s)}{(qc_q^{\mathrm{SERM}})^2} - A_q\Big) \\ &= \frac{1}{s^2}\Big((qc_q^{\mathrm{SERM}})^2 s\hat{\varphi}_q(s) - A_q\Big) \\ &= \frac{1}{s^2}\Big((qc_q^{\mathrm{SERM}})^2 \varsigma h_q\left[s_*^2 + \frac{1+\epsilon}{2}\right] - A_q\Big) \,. \end{aligned} \tag{6.12}$$

Writting $A_q = \frac{1+\text{sign}(\epsilon)}{2}(qc_q^{\text{SERM}})^2 \varsigma h_q$ leads to

$$1 + \Delta_q(s) + \frac{\overline{\Sigma}_q^{\text{SERM}}(s)}{(qc_q^{\text{SERM}})^2} = (qc_q^{\text{SERM}})^2 \frac{\varsigma h_q}{\omega_*^2} \ . \tag{6.13}$$

Importantly, this expression is valid in both phases. Inserting all of this in Equation (6.11) gives an expression for the new susceptibility close to the transition and in the limit $s_* \to 0$:

$$\hat{\text{X}}_q^{\text{SERM}}(s) = \frac{1}{s^2 + q^2 v_q^2 + \frac{1+\text{sign}(\epsilon)}{2}\omega_*^2} \ . \tag{6.14}$$

Here, we wrote $v_q^2 = \frac{\omega_*^2}{\varsigma h_q}$. Again, Equation (6.14) is valid on both sides of the transition and for $\frac{s}{\omega_*} \to 0$.

Using the $\hat{\text{X}}_q^{\text{SERM}}(s)$ and Equation (5.123) to calculate the vibrational Density of States D^ϕ on the stable structures but below jamming[1] ($\epsilon > 0$) gives for $\omega \geq \omega_*$:

$$D_D^\phi(\omega) = \frac{2\omega}{n\pi} \int_{|\boldsymbol{q}|<k_D} \frac{d^d\boldsymbol{q}}{(2\pi)^d} \, \text{Im}\left\{\hat{\text{X}}_q^{\text{SERM}}(s = -i\omega + 0^+)\right\} = 0 \ . \tag{6.15}$$

The Debye density of states is zero in the unjammed state for $\omega \leq \omega_*$ as a phonon gap has opened in the spectrum[2]. The same result has been found in (Beltukov and Parshin, 2011; Düring *et al.*, 2013). As the scalar ERM model considers scalar excitations, long-wavelength modes generally exist if the largest cluster percolates the system. This is the first hint that the scalar ERM model disintegrates into disconnected clusters at the unjamming transition, which hence becomes a percolation transition in this specific model. The next paragraph discusses the dispersion relation below jamming arbitrarily far from the transition.

The dispersion relation in the unjammed state: The previous paragraph concluded that no sound modes exist below the critical point. Investigating the eigenspace of the random matrix $\underline{\boldsymbol{\mathcal{H}}}^{\text{SERM}}$, this section studies the relation between the frequency ω and the

[1] Notably, there is no contribution from the second scaling function $\tilde{g}(s_*)$ below jamming as Equation (5.179) features no divergence for $\epsilon > 0$.

[2] Notably, the analysis of the phonon gap is not restricted to the scalar ERM model. The same considerations hold in the Self-Consistent Current Theory. Hence, the theory discussed in Chapter 5 also predicts the phonon gap below jamming.

Fourier mode q at the dominating pole in the susceptibility $\hat{\mathrm{X}}_q^{\mathrm{SERM}}(s)$. We will derive that the general dispersion relation reads

$$\mathrm{Re}\left\{\left(\hat{\mathrm{X}}_q(-i\omega+0^+)^{\mathrm{SERM}}\right)^{-1}\right\} = -\omega^2 + (qv_q)^2 + b\,. \tag{6.16}$$

Where the linear shift b is only nonzero in the unstable phase.

Within the ERM approximation, we look at the correlation function

$$\hat{\mathrm{K}}_q^{\mathrm{SERM}}(s) = \frac{s}{N}\overline{\sum_{i,j=1}^{N} e^{-i\boldsymbol{q}\cdot(\boldsymbol{R}_i-\boldsymbol{R}_j)}\left[s^2+\underline{\boldsymbol{\mathcal{H}}}^{\mathrm{SERM}}\right]^{-1}_{ij}}\,. \tag{6.17}$$

As in Section 4.4, the vector $|\boldsymbol{u}(t=0)\rangle = |\boldsymbol{u}_0\rangle = \frac{1}{\sqrt{N}}(e^{i\boldsymbol{q}\cdot\boldsymbol{R}_1},...,e^{i\boldsymbol{q}\cdot\boldsymbol{R}_N})^T$ denotes the initial condition or the particles' displacement at $t=0$. Since the Hessian is real and symmetric, we can use the eigenvectors of $\underline{\boldsymbol{\mathcal{H}}}^{\mathrm{SERM}}$ to define an orthonormal basis. To recall the definitions of Chapter 4, we call the k-th eigenvalue ω_k^2 and the associated eigenvector $|\boldsymbol{e}^k\rangle$. Thus, we find

$$\hat{\mathrm{K}}_q^{\mathrm{SERM}}(s) = s\overline{\langle\boldsymbol{u}_0|\left[s^2+\underline{\boldsymbol{\mathcal{H}}}\right]^{-1}|\boldsymbol{u}_0\rangle} = s\overline{\sum_k Q_k\frac{1}{s^2+\omega_k^2}}\,, \tag{6.18}$$

where we have used the orthogonality of the eigenvectors. The overlap with initial elongation reads: $Q_k = |\,\langle\boldsymbol{u}_0|\boldsymbol{e}^k\rangle\,|^2$. Section 5.4 discussed that the nonergodicity parameter is given by the eigenmodes with eigenvalue zero:

$$\kappa_q(s) = \lim_{s\to 0} s^2\overline{\sum_k Q_k\frac{1}{s^2+\omega_k^2}} = \overline{\sum_{k\in\{\omega_k=0\}} Q_k}\,. \tag{6.19}$$

However, it is not possible to similarly define the compliance as the zero frequency limit of the susceptibility $\hat{\chi}_q^{\mathrm{SERM}}(s)$. The same definition as in Section 5.3 can not applied when investigating the ERM model on the level of the eigenvalues and eigenvectors. The reason is the increasing amount of soft modes when approaching the transition from above the jamming threshold. More concretely, one finds for the small frequency

limit of the susceptibility:

$$\hat{\chi}_q^{\mathrm{SERM}}(s \to 0) = \lim_{s\to 0} \overline{\sum_k Q_k \frac{1}{s^2+\omega_k^2}} = \overline{\sum_{k,\omega_k>0} Q_k \frac{1}{\omega_k^2}} + \lim_{s\to 0} \overline{\sum_{k,\omega_k=0} Q_k \frac{1}{s^2}} \,. \tag{6.20}$$

As confirmed in Figure 5.10, there are rattlers and unstable structures even in the jammed state, which generally lead to a divergence of the right-hand side of Equation (6.20) [3].

To define a reasonable expression for the compliance and hence for the dispersion relation for small frequencies, it is advisable to look at the correlator $\hat{\phi}_q^{\mathrm{SERM}}(s)$:

$$\hat{\phi}_q^{\mathrm{SERM}}(s) = \frac{\hat{\mathrm{K}}_q^{\mathrm{SERM}}(s) - \frac{\kappa_q}{s}}{1-\frac{\kappa_q}{s}} = s \frac{\overline{\sum_k Q_k \frac{1}{s^2+\omega_k^2}} - \overline{\sum_{k,\omega_k=0} Q_k \frac{1}{s^2}}}{\overline{\sum_k Q_k} - \overline{\sum_{k,\omega_k=0} Q_k}} \tag{6.21}$$

Here, we used the completeness relation for the eigenvectors of $\underline{\boldsymbol{\mathcal{H}}}^{\mathrm{SERM}}$ and that the initial conditions are normalized:

$$\sum_k Q_k = \frac{1}{N} \sum_{i=1}^{N} e^{i\boldsymbol{q}\cdot\boldsymbol{R}_i} e^{-i\boldsymbol{q}\cdot\boldsymbol{R}_i} = 1 \tag{6.22}$$

Since the average over the disorder is a linear functional, we find for the susceptibility on the stable structures $\hat{\mathrm{X}}_q^{\mathrm{SERM}}(s)$:

$$\hat{\mathrm{X}}_q^{\mathrm{SERM}}(s) = \frac{\overline{\sum_{k,\omega_k\neq 0} Q_k \frac{1}{s^2+\omega_k^2}}}{\overline{\sum_{k,\omega_k\neq 0} Q_k}} = \frac{1}{N} \frac{\overline{\sum_{k,\omega_k\neq 0} Q_k \frac{1}{s^2+\omega_k^2}}}{1-\kappa_q} \,, \tag{6.23a}$$

$$\hat{\mathrm{X}}_q^{\mathrm{SERM}}(0) = \frac{1}{N} \frac{\overline{\sum_{k,\omega_k\neq 0} Q_k \frac{1}{\omega_k^2}}}{1-\kappa_q} \tag{6.23b}$$

The susceptibility $\hat{\mathrm{X}}_q^{\mathrm{SERM}}(s)$ only takes the modes with finite eigenvalues and, therefore, with finite restoring forces into account. The dispersion relation qv_q can now be

[3] Notably, the Self-Consistent Current Response Theory developed in Chapter 5 and the equivalent theory for the ERM model in Appendix A both neglect the presence of unstable structures in the jammed phase. Here, the zero frequency limit of the resolvents $\lim_{s\to 0} \hat{\chi}_q^{\perp}(s)$ and $\lim_{s\to 0} \hat{\chi}_q^{\mathrm{ERM}}(s)$ are well defined.

unambiguously defined by the zero frequency limit:

$$\frac{1}{(qv_q)^2} \equiv \hat{\mathrm{X}}_q^{\mathrm{SERM}}(s=0) \; . \tag{6.24}$$

In fact, this is how Philipp Baumgärtel calculated the data displayed in Figure 5.2. Additional information on the numerical investigations is provided in (Vogel *et al.*, 2025).

Importantly, $\hat{\mathrm{X}}_q^{\mathrm{SERM}}(s)$ has a well-defined zero frequency limit in the jammed and the unjammed phase. Hereinafter, we investigate $\hat{\mathrm{X}}_q^{\mathrm{SERM}}(s=0)$ in the unjammed state to establish a dispersion relation for the remaining stable structures below the critical density n_c. The nonergodicity parameter has a Lorenzian shape for small q and for $\epsilon > 0$. Thus, we find

$$1 - \kappa_q^{\mathrm{SERM}} = \frac{q^2\lambda_-^2}{1+q^2\lambda_-^2} \underset{q\to 0}{\longrightarrow} q^2\lambda_-^2 \; . \tag{6.25}$$

Since all the eigenvalues of the Hessian are real and since $Q_k \geq 0$ holds as well, this result implies

$$\overline{\sum_{k,\omega_k\neq 0} Q_k} = 1 - \kappa_q^{\mathrm{SERM}} \propto q^2 \; . \tag{6.26}$$

Hence, we can conclude that $Q_k \propto q^\alpha$ with $\alpha \geq 2$ has to hold on average for nonzero overlaps: The average overlap of the finite eigenvalue eigenvectors $|\boldsymbol{e}^k\rangle$ with the initial displacement $|\boldsymbol{u}(0)\rangle$ vanish with the Fourier mode of the imposed wave. This is a direct consequence of the global translational invariance. As the denominator of Equation (6.23b) also vanishes $\propto q^2$, we hence find $\hat{\mathrm{X}}_q^{\mathrm{SERM}}(s=0) \propto q^0$ for $q \to 0$. As a consequence, global translational invariance gives for small but finite q

$$\hat{\mathrm{X}}_q^{\mathrm{SERM}}(s=0) \approx \frac{1}{q^2 a + b} \tag{6.27}$$

with $a, b \in \mathbb{R}$. This is in full accordance with Equation (6.14), which furthermore suggests that $b = \frac{1+\mathrm{sgn}(\epsilon)}{2}\omega_*$ holds. Notably, the derivation is built on $1-\kappa_q \propto q^2$, which is only valid in the unjammed state. No extensive structures can be moved without restoring forces for $\epsilon < 0$. Thus, one expects $1-\kappa_q \propto q^0$ in the jammed state, which

is confirmed by Philipp Baumgärtels findings of the nonzero nonegrodicity parameter for $\epsilon < 0$ displayed in Figure 5.10. Hence, in the jammed phase, one has $Q_k \propto q^0$ for some nonzero Q_k. Thus, the eigenvectors of $\underline{\boldsymbol{\mathcal{H}}}^{\mathrm{SERM}}$ undergo a significant change at the transition. All of this makes the quantity $\hat{\mathrm{X}}_q^{\mathrm{SERM}}(s=0)$ an ideal object for studying the transition numerically. Preliminary results by Philipp Baumgärtel look promising and will be published soon. In Section 6.2, we will relate these changes to the system falling apart at the critical density n_c^* and conjecture that the system decomposes into disconnected clusters in the unjammed phase. However, we first look at the changes in the eigenvalues ω_k.

Changes in the eigenvalues at the critical point In the last paragraph, we looked at changes in the eigenspace of $\underline{\boldsymbol{\mathcal{H}}}^{\mathrm{SERM}}$ at the transition. We found that the averaged overlap $\overline{Q_k} = \overline{|\langle \boldsymbol{u}_0 | \boldsymbol{e}^k \rangle|^2}$ undergoes significant changes at the transition. In this section, we investigate the changes of the eigenvalues ω_k^2 at n_c^*. We ask if the eigenvalues of the modes with nonzero projection coefficient have a finite value or if they vanish linearly with the wavenumber of the plane wave excitation $\omega_k \propto q$.

We start our consideration by recalling the explicit form of the scalar Euclidean Random Matrix:

$$\mathcal{H}_{ij}^{\mathrm{SERM}} = -\frac{1}{m}\mathcal{K}(|\boldsymbol{R}_i - \boldsymbol{R}_j|) + \frac{\delta_{ij}}{m}\sum_k \mathcal{K}(|\boldsymbol{R}_i - \boldsymbol{R}_k|)\ . \tag{6.28}$$

Here $\mathcal{K}(r)$ is a finite ranged springfunction vanishing for $r > \sigma$, where σ can be interpreted as the particle diameter. The set $\{\boldsymbol{R}_i\}_{i=1}^N$ denotes the position of the particles in the quenched disorder. Again, using that the eigenvectors of $\underline{\boldsymbol{\mathcal{H}}}^{\mathrm{SERM}}$ form a basis of the considered vector space, leads to

$$\begin{aligned} m\,\langle \boldsymbol{u}_0 |\, \underline{\boldsymbol{\mathcal{H}}}^{\mathrm{SERM}}\, | \boldsymbol{u}_0 \rangle &= m\sum_k Q_k \omega_k^2 \\ &= -\sum_{ij} \mathcal{K}(|\boldsymbol{R}_i - \boldsymbol{R}_j|) e^{-i\boldsymbol{q}\cdot(\boldsymbol{R}_i - \boldsymbol{R}_j)} + \sum_{ij}\mathcal{K}(|\boldsymbol{R}_i - \boldsymbol{R}_j|)\ . \end{aligned} \tag{6.29}$$

As $\mathcal{K}(r > \sigma) = 0$ holds, we can expand the exponential for $\sigma q \ll 1$:

$$e^{-i\boldsymbol{q}\cdot(\boldsymbol{R}_i - \boldsymbol{R}_j)} \approx 1 - i\boldsymbol{q}\cdot(\boldsymbol{R}_i - \boldsymbol{R}_j) - \frac{1}{2}\Big[\boldsymbol{q}\cdot(\boldsymbol{R}_i - \boldsymbol{R}_j)\Big]^2 \tag{6.30}$$

Inserting this expansion in Equation (6.29) gives

$$\sum_k Q_k \omega_k^2 \approx \frac{1}{2} \sum_{\langle ij \rangle} \mathcal{K}(R_{ij}) (\boldsymbol{q} \cdot \boldsymbol{R}_{ij})^2 \propto q^2 \sigma^2 \ . \tag{6.31}$$

Here, the notation $\langle ij \rangle$ denotes the sum over all *contacts*, meaning particles with distances $R_{ij} \leq \sigma$. Notably, the first order term $\propto i\boldsymbol{q} \cdot \boldsymbol{R}_{ij}$ has to vanish as all the eigenvalues are real. On the right-hand side, this results from $\mathcal{K}(R_{ij})$ only depending on the absolute value of the particles' distance.

Notably, Equation (6.31) is valid independent of the phase. Taking the averaged over the quenched disorder on both sides of Equation (6.31) allows discussing the average relation of ω_k and q: On the one hand side, the previous paragraph has established that $Q_k \propto q^\alpha$ holds in the unjammed phase for $\omega_k, Q_k \neq 0$. Equation (6.26) dictates that $\alpha \geq 2$ must hold. Thus, the vibrational excitations of the system caused by an initially imposed plane wave $u_i(0) = \exp[-i\boldsymbol{q} \cdot \boldsymbol{R}_i]$ decompose in eigenmodes with finite eigenvalues. This is in accordance with the Equations (6.14) and (6.27). The fact that ω_k can not be proportional to q can informally be written as $\omega_k \not\propto q$. On the other hand, in the jammed state is the projection of order one for some eigenmodes: $Q_k \propto q^0$. Thus, the perturbation leads mainly to the excitation of eigenmodes with vanishing frequencies $\omega_k \propto q$. In opposition to the unstable phase, modes with linear dispersion relation exist in the jammed state. Here, the vibrational modes for $\omega \to 0$ can be identified with sound modes. All of the results in this subsection suggest that the rigidity transition in the scalar ERM model is, in fact, a percolation transition. The following section provides further evidence for this interpretation.

6.2 The percolation transition

This section establishes that the transition in the scalar ERM model is, in fact, a percolation transition. It has already been discussed in the context of Figure 5.2, Figure 5.10, and mainly Figure 5.12 that the transition in the scalar ERM model has to be of geometric nature as it is sensitive only to the interaction range and not to its details. As a consequence and in contrast to the theory, the numerical solution of the ERM model predicts the same critical density for the linear springfunction $\mathcal{K}^L$ and the Theta springfunction $\mathcal{K}^\Theta$.

Interpolating from Figure 5.12 where the nonergodicity parameter κ_q, the dispersion relation v_q and the characteristic frequency ω_* vanish, gives $n_c^* = 0.69(8)$ as the critical density. Furthermore, Figure 6.1 displays the number of clusters relative to the total number of particles N and the ratio of particles belonging to the largest cluster. Here, we say that two particles belong to the same cluster if a connecting path exists via bonded particles. A bond between two particles exists if the distance of their center of mass fulfills the requirement $|\boldsymbol{R}_i - \boldsymbol{R}_j| \leq \sigma$. The data has been recorded in $d = 3$. Figure 6.1 shows a distinct increase in the largest cluster size at $n^* = 0.65$. Strong finite-size effects are visible for smaller densities. The depicted results are independent of the concrete form of the springfunction $\mathcal{K}$. The independence of the interaction details and the connection of n_c^* with a distinct increase of the largest cluster size indicate a percolation transition[4]: Moreover, the critical density $n_c^* = 0.69(8)$ is in agreement with studies of three dimensional overlapping spheres (Elam *et al.*, 1984; Rintoul, 2000). There, the authors have established $\tilde{n}_p^* = 0.652\ 960$ as the critical number density for the percolation problem in the thermodynamic limit[5]. Notably, the data shown in Figure 6.1 and the number-based discussion above refer to a uniform distribution of the particles. However, the result that stability in the scalar ERM

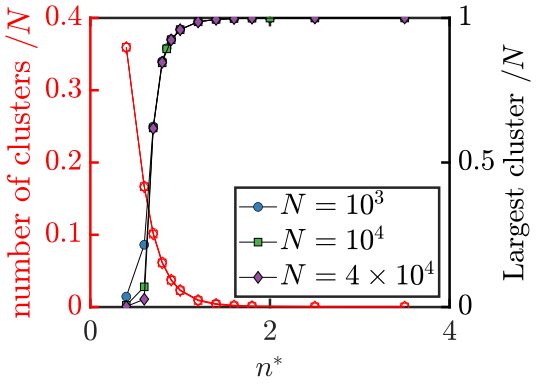

Figure 6.1: The red symbols (left axis) display the number of clusters, while the colored symbols with black lines (right axis) show the ratio of particles. The data has been recorded for the scalar ERM model for $\mathcal{K}^\Theta(r) = \Theta(1 - r/\sigma)$ and for a uniform particle distribution. Different system sizes are displayed. The figure was created by Philipp Baumgärtel. Reprinted from *Self-Consistent Current Response Theory of Unjamming and Vibrational Modes in Low-Temperature Amorphous Solids.*, by F. Vogel, P. Baumgärtel. M. Fuchs, Phys. Rev. X. 2025, vol. 68, page 011030. Reprinted with permission Doi:10.1103/PhysRevX.15.011030.

[4]The discussion of the geometric nature of the transition and the conjecture that the critical density $n_c^* = 0.69(8)$ indicates a percolation transition is build on Philipp Baumgärtels insight and his numerical investigations of the scalar ERM model. Furthermore, this discussion has been published in (Vogel *et al.*, 2025).

[5]Percolation in the ERM model was also discussed in (Amir *et al.*, 2013). The authors considered a Gaussian spring function $\mathcal{K}^G$ with infinite support there. Here, the transition occurs at $n_c^G = 0$.

model corresponds to a percolating largest cluster holds independent of the underlying distribution function $\Psi_Q(\{\boldsymbol{R}_i\}_{i=1}^N)$.

The system disintegrates into disconnected clusters below n_c^*. On average, none of them percolates the system. This concept fits nicely with the results of Section 6.1: Equation (6.26) has established that the average overlap of the initial condition with the eigenmodes associated with finite eigenvalues vanishes with the imposed wavenumber $\overline{Q_k} = \overline{|\langle \boldsymbol{u}_0 | \boldsymbol{e}^k \rangle|^2} \propto q^2$. This can be rationalized as vibrational eigenmodes can only exist on clusters of finite extent in the unjammed case. This also connects nicely with the result of Equation (6.31). There, it was stated that the eigenfrequencies ω_k do not scale with q for $q \to 0$. Again, this stems from the fact that disconnected clusters are independent. Thus, eigenmodes must have a finite spatial extent. In the scalar ERM model, sound modes can only be supported if a cluster of particles percolates the system. Importantly, this result is not at odds with the consensus in the literature that the jamming transition is accurately described by the Maxwell criterion stated in Equation (2.41) and discussed in Section 2.3.1. The apparent contradiction can be resolved by noticing that additional constraints are needed to ensure rigidity and the presence of restoring forces if vector displacements are considered. In Appendix A, we develop a theory for the vector ERM model. However, an analytical investigation as in Section 6.1 and a numerical study as summarized in Figure 6.1 are still lacking. Both are needed for concluding statements on the vector ERM model's transition point. However, Wyart's discussion of the Maxwell criterion also starts from a harmonic energy expansion and should thus apply to the vector ERM model (Wyart, 2005, 2010). Nevertheless, it is an open question whether the ERM model helps studying the jamming transition. The solution of the vector ERM Model in Appendix A.2 suggests no qualitative difference between the longitudinal and the transverse modes. This is summarized in Equation (A.79). However, this is at odds with the discussion in Section 2.3.2. Simulations predict that the shear modulus vanishes faster than the Bulk modulus when approaching the unjamming transition (Mizuno *et al.*, 2016b; O'Hern *et al.*, 2003). The results for the vector ERM model in Appendix A.2 might suggest that it is necessary to go beyond a harmonic expansion of the energy to describe all the salient features of the unjamming transition.

7 | Conclusion

In this monograph, we have looked at disordered solids at zero temperature. We have investigated the vibrational properties of the stable or jammed phase and the properties of the unstable or unjammed state. Furthermore, we have studied the transition between the two phases. Using the language of correlation functions and the Zwanzig-Mori projection operator formalism, we constructed and discussed the Self-Consistent Transverse Current Response Theory. Starting from the concept of stability as the ability to support transverse sound modes and to sustain shear stress, we inquired about the vibrational response properties of a disordered athermal system. The Self-Consistent Current Response Theory is able to adequately describe salient features of the stable jammed state, such as a transition from a propagating to a diffusive regime of the modes. This transition occurs when a mode's energy suffices to resolve the local disorder. This is not only a first-principles substantiation of the Allen-Feldmann Theory, but also suggests that our theory can describe parts of the thermal transport properties of low-temperature disordered solids outlined in Section 2.4 (Allen *et al.*, 1999) . Furthermore, the Self-Consistent Current Response Theory predicts no viscous flow below the jamming transition as the Density of States remains non-negative for all frequencies. However, a phonon gap opens in the spectrum below the jamming transition. On the contrary, injected momentum stays correlated over a length scale $\lambda_{-}^{\perp}$, which diverges at the transition. Thus, our theory is well attuned to be generalized to finite temperatures and to describe the stable unjammed glass state discussed in (Ikeda *et al.*, 2013) and reported in Figure 1.1.

The unjamming transition is marked by the system's failure to host transverse sound modes. Thus, the vanishing of the shear modulus heralds the instability. Below the transition, an extensive number of modes without restoring forces implies that the system yields to long-wavelength shear perturbation. Mathematically, we found that the maximal eigenvalue of the stability matrix controls the system's stability. Hence, the energy landscape and the system's structure directly govern the stability. Consequently,

we found that stability is independent of a microscopic damping rate and the dynamical details. This agrees with network analyses and computer simulations (Alexander, 1998; Mizuno and Ikeda, 2018; O'Hern *et al.*, 2003; Yan *et al.*, 2016). Moreover, the derivation of an equivalent theory for the vector ERM model in Appendix A points to a general universality of the unjamming transition as the critical correlation functions are the same in different stochastic settings, *i.e.* Langevin noise and quenched disorder. A stability analysis close to the transition revealed that the scaling of the static observables as the dispersion relation is independent of the dimension. However, this changes when frequency-dependent quantities are considered as the dominating contribution to the imaginary part of the self-energy $\mathrm{Im}\{\tilde{\Sigma}_q(\omega)\}$ scales with the frequency ω and the wavenumber q as $q^2\omega^{d-1}$, where d denotes the spatial dimension. Our theory predicts the same scaling of the associated Rayleigh damping coefficient as Wyart's effective medium theory (DeGiuli *et al.*, 2015). Nevertheless, the found divergence is still too weak as a stronger one has been reported in simulations (Mizuno and Ikeda, 2018). Moreover, our theory points to an unphysical discontinuity of the self-energy's imaginary part at the transition from the propagating to the diffusive regime, *i.e.* the Ioffe-Regel limit. Furthermore, our theory predicts no dimension-independent contribution to the low-frequency part of the vibrational Density of States. Consequently, the Self-Consistent Current Response Theory does not account for Quasi-localized Modes as their contribution to the low-frequency Density of States is supposedly independent of the spatial dimension (Lerner and Bouchbinder, 2021; Schirmacher *et al.*, 2024). This could be related to the theory being derived under the assumption of perfect annealing and the absence of internal stresses (Flenner and Szamel, 2025; Wang *et al.*, 2019b). As internal stresses also amplify the sound attenuation, it becomes an interesting research question if the weak divergence of the Rayleigh sound attenuation close to the transition can also be explained with the theory being derived at the bottom of the potential energy landscape. In general, the influence of internal stresses can be studied by analyzing the prestressed version of the vector Euclidean Random Matrix model proposed in Appendix A.

We have discussed in Section 5.3.2 that the prediction of Rayleigh damping required a non-trivial generalization of the Mode-Coupling Theory. Rayleigh sound attenuation depends on the inclusion of non-planar contributions. We have discussed that these non-planar terms correspond to a permutation of the scattering sequence first

discussed in the context of the Lorentz-gas (Höfling *et al.*, 2006; Leutheusser, 1983). We used the term *Leutheusser symmetry* to account for the necessity of taking the additional non-planar terms into account (Vogel *et al.*, 2025). The problem of resuming all the terms and constructing a self-consistent theory was resolved by introducing the renormalized retarded vertex $\underline{\boldsymbol{\mathcal{V}}}$, which encodes the topological information on the local scattering events. Importantly, including the non-planar terms also solved a known small wavenumber divergence close to the critical point, potentially spoiling the stability analysis (Schnyder *et al.*, 2011). On the downside, the non-planar contributions potentially violate the positivity of the elastic constants and could lead to a negative spectrum of the correlation function $\mathrm{Im}\{\tilde{\mathrm{K}}_q^{\perp}(\omega)\}$. In fact, the numerical solutions of the model show that positivity is only ensured if we exclude very small wave numbers $q\sigma$. Investigating whether this stems from numerical errors or has a more systematic reason in the non-planar terms is also left for future work.

The theory needs to be updated to include longitudinal modes as well for several reasons: We have discussed in Section 2.3.2 that the bulk modulus also vanishes at the unjamming transition at zero temperature. Furthermore, non-affine displacements, *i.e.* the coupling of longitudinal and transverse velocities, have been found to be of qualitative importance close to unjamming (Flenner and Szamel, 2025; van Hecke, 2009). Lastly, the bulk and shear modulus scaling differs when approaching the critical density. This is shown in the Figures 2.7a and 2.7b. However, the vector generalization of the ERM model in Appendix A suggests no differences between the shear and the bulk modulus. Thus, time-dependent structural rearrangements must be considered to correctly describe the system falling apart at the unjamming transition. As the time derivative of a density fluctuation is related to the longitudinal current, considering a time-dependent dynamic structure factor breaks the symmetry between longitudinal and transverse modes. However, the Euclidean Random Matrix (ERM) model cannot describe time-dependent structural changes, as it requires a stable reference frame. Ultimately, our considerations of the vector ERM model suggest that we have to go beyond the harmonic approximation of the energy discussed in Section 2.2.2 and Section 2.3. Nevertheless, a clear path exists to include a time-dependent structure in the Self-Consistent Current Response Theory, making it a good candidate to fully rationalize stability in disordered solids.

To summarize, we have developed and discussed a first-principles theory of stability in amorphous solids. As the pair-interaction potential and the structure are the only input variables, the theory offers qualitative insight and predictive power, awaiting comparison to experiments and to molecular dynamic simulations. The remaining open challenges and shortcomings of the theory can be systematically addressed. In conclusion, the theory contributes to the long-term goal of rationalizing amorphous solids and to one day explain the phase diagram in Figure 1.1.

8 | Publications of the author

Before the time as a PhD student:

1) F. Vogel, A. Zippelius and M. Fuchs;. *Emergence of Goldstone excitations in stress correlations of glass-forming colloidal dispersions*. Europhys. Lett., vol. 125, 2019.

2) F. Vogel and M. Fuchs. *Stress correlation function and linear response of brownian particles*. Eur. Phys. J. E, vol. 43(11), 2020.

During the time as a PhD student:

3) Florian Vogel and Matthias Fuchs. *Vibrational Phenomena in Glasses at Low Temperatures Captured by Field Theory of Disordered Harmonic Oscillators*. Phys. Rev. Lett., vol. 130:236101, 2023.

4) Philipp Baumgärtel, Florian Vogel and Matthias Fuchs. *Properties of stable ensembles of Euclidean random matrices*. Phys. Rev. E, vol. 109:014120, 2024.

5) Florian Vogel, Philipp Baumgärtel and Matthias Fuchs. *Self-consistent current response theory of unjamming and vibrational modes in low-temperature amorphous Solids*. Phys. Rev. X, vol. 15: 011030, 2025.

6) Valentin Wilhelm, Matthias Krüger, Matthias Fuchs and Florian Vogel. *Evaluation of the probability current in the stochastic path integral formalism*, J. Phys. A: Math. Theor. 58: 335001, 2025

Appendices

A | Generalisation of the Euclidean Random Matrix model

This chapter looks closely at the Euclidean Random Matrix (ERM) model defined in Chapter 4. Usually, scalar excitations and a uniform particle distribution are studied. However, it is straightforward to generalize the ERM model to arbitrary distributions and vector displacements, as we will show in this chapter. Ultimately, the ERM model becomes a reasonable model for disordered athermal system, where the Hessian $\underline{\boldsymbol{\mathcal{H}}}$ fully determines the system. As discussed in Chapter 2, the observed universality of jammed systems suggests that the full vector ERM model can even be used for quantitative predictions and be compared to experiments. This chapter is organized as follows: First, in Section A.1, we generalize Szamel's treatment of the scalar ERM model to arbitrary distributions of the particles (Szamel, 2025). After this, in Section A.2, we generalize the results to include vector displacements, eventually giving us a theory of athermal disorder systems, which could compared to simulations and experiment. Remarkably, we will recover equivalent expression for the instantaneous modulus $(c_q^{\perp})^2$ and the bare vertex $\underline{\boldsymbol{V}}_{\boldsymbol{q},\boldsymbol{k}}$ of the Self-Consistent Current Response Theory discussed in Chapter 5. Lastly, Section (A.3) demonstrates how initial stresses can be included.

A.1 ERM model for arbitrary particle distributions

In this section, we analyze the scalar Euclidean Radom Matrix (SERM) model, defined in Section 4.2. We adopt the projection-operator-based approach to Euclidean Random Matrices introduced in (Szamel, 2025). However, there, the author only discussed a uniform distribution of the particles:

$$\Psi_Q(\{\boldsymbol{R}_i\}_{i=1}^N) = \Psi(\boldsymbol{R}_1) \cdot ... \cdot \Psi(\boldsymbol{R}_N) = \frac{1}{V^N} \, . \tag{A.1}$$

Note that the ERM model assumes a frozen-in structure, where $\{\boldsymbol{R}_i\}_{i=1}^N$ denotes the set of positions defining the reference frame. As in the main text, we again use capital letters to refer to the positions in the reference frame. The overwhelming part of the literature on the ERM model assumes a uniform distribution of the particles. For example, see (Ciliberti *et al.*, 2003; Ganter and Schirmacher, 2010, 2011; Grigera *et al.*, 2011, 2001; Martin-Mayor *et al.*, 2001). However, as discussed in Section 2.3, a uniform distribution of the particles oversimplifies the theory as unjamming is supposed to be a geometrical transition featuring major structural hallmarks like the pair distribution function's divergence or the coordination number's jump. To make the ERM model more realistic, we therefore want to avoide approaches, which set all distribution functions and the static structure factor to unity $g^{(n)} = S_q = 1$. Furthermore, we mentioned in Section 4.5 that the Self-Consistent Current Response Theory developed in Section 5 becomes equivalent to the (vector) ERM model sufficiently deep in the jammed state, where the harmonic expansion of the elastic energy holds. Thus, considering non-trivial distribution Ψ_Q functions allows us to quantify the approximation-induced errors of the Self-Consistent Current Response Theory discussed in Chapter 5. The dependence on the distribution function Ψ_Q enters the final version of the Self-Consistent Current Response Theory only via the pair- and triplet correlation function $g(r)$ and $g^{(3)}(\boldsymbol{r}, \boldsymbol{r}')$. As they can be defined in any quenched disorder, the final versions of the two theories should be equivalent. Thus, we leave the concrete form $\Psi_Q(\{\boldsymbol{R}_i\}_{i=1}^N)$ unspecified in the following and define the disorder average as

$$\overline{\cdots} = \int \prod_{m=1}^{N} d^d\boldsymbol{R}_m (\cdots) \Psi_Q(\{\boldsymbol{R}_i\}_{i=1}^N) = \int d\Gamma' (\cdots) \Psi_Q(\{\boldsymbol{R}_i\}_{i=1}^N) \,, \tag{A.2}$$

Nevertheless, we assume that all the particles are statistically equivalent, which implies:

$$\overline{A_i(\boldsymbol{q})} = \frac{1}{N} \sum_{j=1}^{N} \overline{A_j(\boldsymbol{q})} \tag{A.3}$$

for any dynamical field variable $A_i(\boldsymbol{q})$ depending only on one particle position. Additionally, we assume that rotational and translational invariance are obeyed. Hence, the symmetry results stated in Section 3 are applicable. We define the averaged k-particle

distribution function as

$$\overline{g^{(k)}}(\boldsymbol{R}_1, \boldsymbol{R}_2, ..., \boldsymbol{R}_{k-1}) = \frac{1}{n^k N} \overline{\sum_{i_1 \neq ... \neq i_k = 1}^{N} \prod_{m=1}^{k-1} \delta(\boldsymbol{R}_m - (\boldsymbol{R}_{i_1} - \boldsymbol{R}_{i_{m+1}}))} \, , \tag{A.4}$$

where the sum is to be understood as a sum over all indices with non being equal to each other[1]. For notational brevity, we write $\overline{g^{(2)}}(\boldsymbol{r}) \equiv \overline{g}(\boldsymbol{r})$. Note that Definition (A.4) differs from the particle distribution function $g^{(k)}$ frequently used in Chapter 5. There, only an annealed disorder was considered. The quenched disorder average in Equation (A.4) additionally averages over the positions of the reference frame $\{\boldsymbol{R}_i\}_{i=1}^N$. We define the average static structure factor as

$$\overline{S}_q = \frac{1}{N} \overline{\sum_{i,j=1}^{N} e^{-i\boldsymbol{q}\cdot(\boldsymbol{R}_i - \boldsymbol{R}_j)}} - \delta_{\boldsymbol{q},0} \, . \tag{A.5}$$

Remarkably, the quenched disorder average of the density $\overline{\rho_{\boldsymbol{q}}}$ vanishes due to the assumed translational invariance and stays finite only for $q = 0$: $\overline{\rho(\boldsymbol{q})} = N\delta_{\boldsymbol{q},0}$. This is a clear difference to the thermal average considered in Chapter 5, where the annealed average value of the density $N \langle \rho_{\boldsymbol{q}} \rangle = \sum_{i=1}^{N} e^{-i\boldsymbol{q}\cdot\boldsymbol{R}_i}$ is determined by the reference frame. Generally, neither $\overline{S}_q$ and S_q nor $\overline{g}^{(k)}$ and $g^{(k)}$ coincide. However, we assume throughout this monograph that the system possesses the self-averaging property. This implies that the distributions of $g^{(k)}$ and S_q concentrate around their mean for sufficiently large samples. The assumption is, that one almost surely observes $g^{(k)} \approx \overline{g}^{(k)}$ and $S_q \approx \overline{S}_q$. Thus, we will drop the overline again in the following. This is supposed to emphasize that the averaged structure factor and the average distribution function equal the ones used in Chapter 5. In this Section, we aim to formulate a theory for the resolvent in the scalar ERM model:

$$\hat{\chi}_q^{\text{SERM}}(s) = \frac{1}{N} \overline{\sum_{i,j=1}^{N} e^{-i\boldsymbol{q}\cdot(\boldsymbol{R}_i - \boldsymbol{R}_j)} \left[s^2 + \underline{\boldsymbol{\mathcal{H}}}^{\text{SERM}} \right]^{-1}_{ij}} \, . \tag{A.6}$$

[1] From the definition of the k-particles distribution function in Equation (A.4), it is straightforward to show that the $\overline{g^{(k)}} = 1$ holds if one assumes a uniform distribution function Ψ_Q. One subsequentially has to integrate over $\boldsymbol{R}_1$, $\boldsymbol{R}_2$... From Equation (4.10) follows that $S_q = 1$ holds as well.

Here, the Hessian $\underline{\boldsymbol{\mathcal{H}}}^{\mathrm{SERM}}$ is constituted by spring function $\mathcal{K}(r) \equiv \frac{\partial^2 U(r)}{\partial r^2}$:

$$\mathcal{H}_{ij}^{\mathrm{SERM}} = \frac{1}{m}\delta_{ij}\sum_{k\neq j}\mathcal{K}(|\boldsymbol{R}_j - \boldsymbol{R}_k|) - \frac{1}{m}\mathcal{K}(|\boldsymbol{R}_j - \boldsymbol{R}_i|) \tag{A.7}$$

In Section A.2, we take the correct tensorial structure of the Hessian into account by setting

$$\mathcal{K}(r) \to \mathcal{K}_{\alpha\beta}(r) = \frac{\partial}{\partial r_\alpha}\frac{\partial}{\partial r_\beta}U(r)\ , \tag{A.8}$$

where $U(r)$ quantifies the pair-interaction potential. However, in this section, we stick with scalar excitations and analyze Equation (A.6). Here, the Hessian is a $\mathbb{R}^{N\times N}$ matrix. Notably, in Equation (A.7), we divided the spring constants by the mass m so that the Hessian has the units of frequency square. Similiarly to the Self-Consistend Current Response Theory in Chapter 5, the resulting equations will only require the particle distribution functions $g^{(k)}$ and the spring function $\mathcal{K}(r)$ as input.

The following derivation closely follows Szamel (Szamel, 2025). However, there are a few differences. We will highlight all of them: First of all, we stress the notational difference, that we adopt the convention $s^2 = -\omega^2 - i0^+$ instead of $s^2 = \omega^2 + i0^+$ used in (Szamel, 2025). Furthermore, our resolvent is defined with an additional overall minus sign. We start by expressing the resolvent via the self-energy $\hat{\Sigma}_q^{\mathrm{SERM}}(s)$ and a renormalized vertex $\hat{\mathcal{V}}_{\boldsymbol{k},\boldsymbol{q}}^{\mathrm{SERM}}(s)$. The forthcoming projection-operator formalism is in analogy to the Zwanzig-Mori formalism employed in Section 5.2.

A.1.1 The self-energy

In this Section, we first derive an expression for the self-energy of the scalar ERM model $\hat{\Sigma}_q^{\mathrm{SERM}}(s)$. Remarkably, the resulting formula will closely resemble the fluidity discussed in Section 5.2.2. Similar to the Self-Consistent Current approach in Chapter 5, we can define a bare vertex $V_{\boldsymbol{q},\boldsymbol{k}}^{\mathrm{SERM}}$ only depending on the averaged structure and the interaction details, which constitutes– together with a renormalized vertex $\hat{\mathcal{V}}_{\boldsymbol{k},\boldsymbol{q}}^{\mathrm{SERM}}$– the self-energy. We will look at the two vertices in the second half of this Section.

The first projection and the definition of the Self-Energy: Following (Szamel, 2025), we define the Fourier mode of the local density associated with particle i as

$$\rho_i(\boldsymbol{q}) = e^{-i\boldsymbol{q}\cdot\boldsymbol{R}_i}. \tag{A.9}$$

The associated projection operator reads

$$P_i f = \rho_i(-\boldsymbol{q})\overline{\rho_i(\boldsymbol{q})f} = \sum_{j=1}^{N} \frac{\rho_i(-\boldsymbol{q})\overline{\rho_j(\boldsymbol{q})f}}{N} \ , \tag{A.10}$$

where f denotes an arbitrary function of the reference frame $f = f(\{\boldsymbol{R}_i\}_{i=1}^N)$. The associated projector on the orthogonal complement reads

$$Q_i f = f - P_i f \ . \tag{A.11}$$

This notation is again adopted from (Szamel, 2025). Rewriting Equation (A.6) for the resolvent as

$$s^2\hat{\chi}_q^{\mathrm{SERM}}(s) - 1 = -\frac{1}{N}\overline{\sum_{i,j,k=1}^{N} e^{-i\boldsymbol{q}\cdot(\boldsymbol{R}_i-\boldsymbol{R}_j)}\mathcal{H}_{ik}^{\mathrm{SERM}}\left[s^2 + \underline{\boldsymbol{\mathcal{H}}}^{\mathrm{SERM}}\right]^{-1}_{kj}} \tag{A.12}$$

gives after inserting $P_k + Q_k = 1$

$$\begin{aligned} s^2\hat{\chi}_q^{\mathrm{SERM}}(s) - 1 = &-\overline{\frac{1}{N}\sum_{i,k=1}^{N}\rho_i(\boldsymbol{q})\mathcal{H}_{ik}^{\mathrm{SERM}}\rho_k(-\boldsymbol{q})}\ \overline{\frac{1}{N}\sum_{l,j=1}^{N}\rho_l(\boldsymbol{q})\left[s^2 + \underline{\boldsymbol{\mathcal{H}}}^{\mathrm{SERM}}\right]^{-1}_{lj}\rho_j(-\boldsymbol{q})} \\ &- \overline{\frac{1}{N}\sum_{i,j,k=1}^{N}\rho_i(\boldsymbol{q})\mathcal{H}_{ik}^{\mathrm{SERM}}Q_k\left[s^2 + \underline{\boldsymbol{\mathcal{H}}}^{\mathrm{SERM}}\right]^{-1}_{kj}\rho_j(-\boldsymbol{q})} \ . \end{aligned} \tag{A.13}$$

First, we note that the second factor on the right-hand side in the first line is again given by $\hat{\chi}_q^{\mathrm{SERM}}(s)$. The first factor defines the bare dispersion relation of the scalar ERM

model $(qc_q^{\mathrm{SERM}})^2$:

$$\begin{aligned}
&\overline{\frac{1}{N}\sum_{i,k=1}^{N} e^{-i\boldsymbol{q}\cdot\boldsymbol{R}_i}\mathcal{H}_{ik}^{\mathrm{SERM}}e^{i\boldsymbol{q}\cdot\boldsymbol{R}_k}} \\
&= \frac{1}{mN}\overline{\sum_{i,k=1}^{N} e^{-i\boldsymbol{q}\cdot\boldsymbol{R}_i}\left[\delta_{ik}\sum_{m\neq i}\mathcal{K}(\boldsymbol{R}_m-\boldsymbol{R}_i)-(1-\delta_{ik})\mathcal{K}(\boldsymbol{R}_i-\boldsymbol{R}_k)\right]e^{i\boldsymbol{q}\cdot\boldsymbol{R}_k}} \\
&= \int d^d\boldsymbol{r}\,\overline{\frac{1}{mN}\sum_{i,k\neq i}^{N}\delta(\boldsymbol{r}-(\boldsymbol{R}_i-\boldsymbol{R}_k))}\left[1-e^{-i\boldsymbol{q}\cdot\boldsymbol{r}}\right]\mathcal{K}(r) \\
&= (qc_q^{\mathrm{SERM}})^2\,.
\end{aligned} \tag{A.14}$$

Here, we inserted the following expression for the instantaneous modulus:

$$(c_q^{\mathrm{SERM}})^2 = n\int d^d\boldsymbol{r}\,g(r)\frac{1-e^{-i\boldsymbol{q}\cdot\boldsymbol{r}}}{mq^2}\mathcal{K}(r) = n\int d^d\boldsymbol{r}\,g(r)\frac{1-e^{-i\boldsymbol{q}\cdot\boldsymbol{r}}}{mq^2}\frac{\partial^2}{\partial r^2}U(r) \tag{A.15}$$

Importantly, the averaged pair distribution function $g(r)$ only depends on the Euclidean distance r due to the distribution function Ψ_Q possessing rotational and translational invariance. Comparing this result with Equation (5.25) it becomes apparent that the only difference to the bare dispersion relation in the Self-Consistent Transverse Current Theory $(qc_q^{\perp})^2$ arises form the missing spatial projection $\underline{\boldsymbol{P}}(\boldsymbol{q}) = [\underline{\mathbf{1}} - \hat{\boldsymbol{q}}\hat{\boldsymbol{q}}]$, which also causes the factor $\frac{1}{d-1}$ in (5.25). However, this suggests that the excitations in the scalar ERM model can neither be identified with the transverse nor the longitudinal modes. The ERM excitations are purely non-affine as they have, by construction, nothing to do with the incident wavevector $\boldsymbol{q}$. Apart from this obvious difference, the bare dispersion relation of the ERM closely resembles the bare dispersion relation occurring in the Self-Consistent Current approach. Notably, when the particles are uniformly distributed, one recovers the standard dispersion relation of the ERM model $(qc_q^{\mathrm{SERM}})^2 = \frac{n}{m}(\mathcal{K}(0)-\mathcal{K}(q))$ frequently used in the literature, *e.g.* (Ganter and Schirmacher, 2010; Martin-Mayor *et al.*, 2001; Szamel, 2025; Vogel and Fuchs, 2023).

After having obtained an expression for the instantaneous modulus $(qc_q^{\mathrm{SERM}})^2$, Equation (A.13) simplifies to

$$[s^2 + (qc_q^{\mathrm{SERM}})^2]\hat{\chi}_q^{\mathrm{SERM}}(s) - 1 = -\frac{1}{N}\overline{\sum_{i,j,k=1}^{N} \rho_i(\boldsymbol{q})\mathcal{H}_{ik}^{\mathrm{SERM}} Q_k \Big[s^2 + \underline{\boldsymbol{\mathcal{H}}}^{\mathrm{SERM}}\Big]_{kj}^{-1} \rho_j(-\boldsymbol{q})} \ . \tag{A.16}$$

Continuing following Szamel, we introduce an auxiliary dynamical variable to keep the notation concise (Szamel, 2025):

$$g_k(-\boldsymbol{q}, s) \equiv Q_k \sum_{j=1}^{N} \Big[s^2 + \underline{\boldsymbol{\mathcal{H}}}^{\mathrm{SERM}}\Big]_{kj}^{-1} \rho_j(-\boldsymbol{q}) \ . \tag{A.17}$$

The idea is to derive a constituting equation of $g_k(-\boldsymbol{q}, s)$ in terms of the full resolvent and then to insert it back into Equation (A.16). Looking at $s^2 g_k(-\boldsymbol{q}, s)$ one gets

$$\begin{aligned} s^2 g_k(-\boldsymbol{q}, s) =& \underbrace{Q_k \sum_{l,j=1}^{N} \Big[s^2 + \underline{\boldsymbol{\mathcal{H}}}^{\mathrm{SERM}}\Big]_{kl} \Big[s^2 + \underline{\boldsymbol{\mathcal{H}}}^{\mathrm{SERM}}\Big]_{lj}^{-1} \rho_j(-\boldsymbol{q})}_{=0} \\ & - Q_k \sum_{l,j=1}^{N} \mathcal{H}_{kl}^{\mathrm{SERM}} \Big[s^2 + \underline{\boldsymbol{\mathcal{H}}}^{\mathrm{SERM}}\Big]_{lj}^{-1} \rho_j(-\boldsymbol{q}) \\ =& - Q_k \sum_{l,j=1}^{N} \mathcal{H}_{kl}^{\mathrm{SERM}} (P_l + Q_l) \Big[s^2 + \underline{\boldsymbol{\mathcal{H}}}^{\mathrm{SERM}}\Big]_{lj}^{-1} \rho_j(-\boldsymbol{q}) \\ =& - \sum_{l=1}^{N} Q_k \mathcal{H}_{kl}^{\mathrm{SERM}} \rho_l(-\boldsymbol{q}) \hat{\chi}_q^{\mathrm{SERM}}(s) - \sum_{l=1}^{N} Q_k \mathcal{H}_{kl}^{\mathrm{SERM}} Q_l g_l(-\boldsymbol{q}, s) \ . \end{aligned} \tag{A.18}$$

In the last line, when identifying the full resolvent, we again used the equivalence of the particles.

Inserting the expression for the resolvent from Equation (A.13) finally yields

$$\begin{aligned} s^2 g_k(-\boldsymbol{q}, s) =& \frac{1}{(q c_q^{\mathrm{SERM}})^2} \sum_{l=1}^{N} Q_k \mathcal{H}_{kl}^{\mathrm{SERM}} \rho_l(-\boldsymbol{q}) [s^2 \hat{\chi}_q^{\mathrm{SERM}}(s) - 1] \\ & - \sum_{l=1}^{N} Q_k \mathcal{H}_{kl}^{\mathrm{SERM}} Q_l g_l(-\boldsymbol{q}, s) \\ & + \frac{1}{N(q c_q^{\mathrm{SERM}})^2} \overline{\sum_{i,j=1}^{N} \rho_i(\boldsymbol{q}) \mathcal{H}_{ij}^{\mathrm{SERM}} Q_j g_j(-\boldsymbol{q}, s)} \sum_{l=1}^{N} Q_k \mathcal{H}_{kl}^{\mathrm{SERM}} \rho_l(-\boldsymbol{q}) \ . \end{aligned} \tag{A.19}$$

Rearranging the terms eventually leads to an expression for $g_k(-\boldsymbol{q}, s)$ in terms on $\hat{\chi}_q^{\mathrm{SERM}}(s)$:

$$\begin{aligned} & \sum_{j=1}^{N} \Big(s^2 \delta_{jk} + Q_k \mathcal{H}_{kj}^{\mathrm{SERM}} Q_j - \sum_{i,l=1}^{N} \frac{Q_k \mathcal{H}_{kl}^{\mathrm{SERM}} \rho_l(-\boldsymbol{q})}{N(q c_q^{\mathrm{SERM}})^2} \mathcal{P} \rho_i(\boldsymbol{q}) \mathcal{H}_{ij}^{\mathrm{SERM}} Q_j \Big) g_j(-\boldsymbol{q}, z) \\ & \qquad = \frac{1}{(q c_q^{\mathrm{SERM}})^2} \sum_{l=1}^{N} Q_k \mathcal{H}_{kl}^{\mathrm{SERM}} \rho_l(-\boldsymbol{q}) [s^2 \hat{\chi}_q^{\mathrm{SERM}}(s) - 1] \ . \end{aligned} \tag{A.20}$$

Here, we defined the operator $\mathcal{P}$ via $\mathcal{P} f = \overline{f}$, valid for any funcion f of the reference frame $\{\boldsymbol{R}_i\}_{i=1}^{N}$. Equation (A.20) suggests defining the reduced Hessian as

$$\mathcal{H}_{kj}^{\Sigma} = Q_k \mathcal{H}_{kj}^{\mathrm{SERM}} Q_j - \frac{1}{N(q c_q^{\mathrm{SERM}})^2} \sum_{i,l=1}^{N} Q_k \mathcal{H}_{kl}^{\mathrm{SERM}} \rho_l(-\boldsymbol{q}) \mathcal{P} \rho_i(\boldsymbol{q}) \mathcal{H}_{ij}^{\mathrm{SERM}} Q_j \ , \tag{A.21}$$

which is reminiscent of the one-particle irreducible time-evolution operator discussed in (Cichocki and Hess, 1987). The formal solution of the auxiliary state hence reads

$$g_j(-\boldsymbol{q}, s) = \frac{1}{(q c_q^{\mathrm{SERM}})^2} \sum_{k,l} \Big[s^2 + \underline{\boldsymbol{\mathcal{H}}}^{\Sigma} \Big]_{jk}^{-1} Q_k \mathcal{H}_{kl}^{\mathrm{SERM}} \rho_l(-\boldsymbol{q}) [s^2 \hat{\chi}_q^{\mathrm{SERM}}(s) - 1] \tag{A.22}$$

Inserting the solution for $g_j(-\boldsymbol{q}, z)$, *i.e.* Equation (A.22), in Equation (A.16) gives

$$\begin{aligned} & \big[s^2 \hat{\chi}_q^{\mathrm{SERM}}(s) - 1 \big] \Big(1 + \frac{1}{(q c_q^{\mathrm{SERM}})^2} \hat{\Sigma}_q^{\mathrm{SERM}}(s) \Big) = -(q c_q^{\mathrm{SERM}})^2 \hat{\chi}_q^{\mathrm{SERM}}(s^2) \\ \Longleftrightarrow & \hat{\chi}_q^{\mathrm{SERM}}(s) = \frac{1}{s^2 + \frac{q^2 (c_q^{\mathrm{SERM}})^2}{1 + \frac{\hat{\Sigma}_q^{\mathrm{SERM}}(s)}{(q c_q^{\mathrm{SERM}})^2}}} \ . \end{aligned} \tag{A.23}$$

Here, we defined the self-energy of the ERM model

$$\hat{\Sigma}_q^{\mathrm{SERM}}(s) = \frac{1}{N}\overline{\sum_{i,j,k,l=1}^{N} \rho_i(\boldsymbol{q})\mathcal{H}_{ik}^{\mathrm{SERM}} Q_k \Big[s^2 + \underline{\boldsymbol{\mathcal{H}}}^{\Sigma}\Big]^{-1}_{kj} Q_j \mathcal{H}_{jl}^{\mathrm{SERM}} \rho_l(-\boldsymbol{q})} \ . \tag{A.24}$$

Equation (A.23) already has the same structure as Equation (5.74a) for the resolvent of the Self-Consistent Transverse Current Response Theory $\hat{\chi}_q^{\perp}(s)$ discussed in Chapter 5. The resemblance becomes even more striking after remembering that both theories feature the same bare dispersion relation up to the spatial projections. The similarity will even extend to the bare vertex as we will show next. In order to calculate the vertex $V_{\boldsymbol{q},\boldsymbol{k}}^{\mathrm{SERM}}$, we look at

$$\begin{aligned}
\sum_{l=1}^{N} Q_j \mathcal{H}_{jl}^{\mathrm{SERM}} \rho_l(-\boldsymbol{q}) &= \frac{1}{m} Q_j \sum_l \Big[\delta_{jl} \sum_{i\neq j} \mathcal{K}(\boldsymbol{R}_i - \boldsymbol{R}_j) - (1-\delta_{jl})\mathcal{K}(\boldsymbol{R}_j - \boldsymbol{R}_l)\Big] e^{i\boldsymbol{q}\cdot\boldsymbol{R}_l} \\
&= \frac{1}{m} Q_j \sum_{\boldsymbol{k}} \left(\sum_{i\neq l} \mathcal{K}(\boldsymbol{q}-\boldsymbol{k}) e^{-i(\boldsymbol{q}-\boldsymbol{k})\cdot(\boldsymbol{R}_j - \boldsymbol{R}_i)} e^{i\boldsymbol{q}\cdot\boldsymbol{R}_j} - \sum_{l\neq j} \mathcal{K}(\boldsymbol{k}) e^{i\boldsymbol{k}\cdot(\boldsymbol{R}_j - \boldsymbol{R}_l)} e^{i\boldsymbol{q}\cdot\boldsymbol{R}_l} \right) \\
&= \frac{1}{m} \sum_{\boldsymbol{k}} \Big(\mathcal{K}(\boldsymbol{q}-\boldsymbol{k}) - \mathcal{K}(\boldsymbol{k})\Big) Q_j \sum_{l\neq j} e^{-i(\boldsymbol{q}-\boldsymbol{k})\cdot(\boldsymbol{R}_j - \boldsymbol{R}_l)} e^{i\boldsymbol{q}\cdot\boldsymbol{R}_j} \\
&= \frac{1}{m} \sum_{\boldsymbol{k}} \Big(\mathcal{K}(\boldsymbol{q}-\boldsymbol{k}) - \mathcal{K}(\boldsymbol{k})\Big) Q_j \sum_{l=1}^{N} e^{-i(\boldsymbol{q}-\boldsymbol{k})\cdot(\boldsymbol{R}_j - \boldsymbol{R}_l)} e^{i\boldsymbol{q}\cdot\boldsymbol{R}_j} \ .
\end{aligned} \tag{A.25}$$

In the last line, we used that the summand $l = j$ vanishes due to the projection operator. Szamel continues to project on the product of the density fluctuation on side l and the collective density of all sides except l (Szamel, 2025):

$$\begin{aligned}
Q_j \sum_{l=1}^{N} e^{-i(\boldsymbol{q}-\boldsymbol{k})\cdot(\boldsymbol{R}_j - \boldsymbol{R}_l)} e^{i\boldsymbol{q}\cdot\boldsymbol{R}_j} =& Q_j e^{i\boldsymbol{k}\cdot\boldsymbol{R}_j} \sum_{l=1}^{N} e^{i(\boldsymbol{q}-\boldsymbol{k})\cdot\boldsymbol{R}_l} \\
=& e^{i\boldsymbol{k}\cdot\boldsymbol{R}_j} \sum_{l=1}^{N} e^{i(\boldsymbol{q}-\boldsymbol{k})\cdot\boldsymbol{R}_l} - e^{i\boldsymbol{q}\cdot\boldsymbol{R}_j} \overline{\frac{1}{N} \sum_{l,j=1}^{N} e^{i(\boldsymbol{q}-\boldsymbol{k})\cdot(\boldsymbol{R}_l - \boldsymbol{R}_j)}} \\
\equiv& n_{j,2}(-\boldsymbol{k}, \boldsymbol{k}-\boldsymbol{q})
\end{aligned} \tag{A.26}$$

This identity suggests the next projection operator:

$$\tilde{P}^{\boldsymbol{q}}_{j,2} = \sum_{\boldsymbol{k}} \frac{n_{j,2}(-\boldsymbol{k}, \boldsymbol{k}-\boldsymbol{q}) n_{j,2}(\boldsymbol{k}, \boldsymbol{q}-\boldsymbol{k})}{\overline{n_{j,2}(\boldsymbol{k}, \boldsymbol{q}-\boldsymbol{k}) n_{j,2}(-\boldsymbol{k}, \boldsymbol{k}-\boldsymbol{q})}} \, . \tag{A.27}$$

However, the normalization is not easy to calculate. Because of this and the principle idea that we want to be as close as possible to the derivation of the Self-Consistent Current Response Theory developed in chapter 5, we assume that

$$\overline{\frac{1}{N} \sum_{l,j=1}^{N} e^{i(\boldsymbol{q}-\boldsymbol{k})\cdot(\boldsymbol{R}_l - \boldsymbol{R}_j)}} = \frac{\overline{\rho(\boldsymbol{k}-\boldsymbol{q})}^2}{N} + S_{|\boldsymbol{k}-\boldsymbol{q}|} \approx \overline{\rho(\boldsymbol{k}-\boldsymbol{q})} \tag{A.28}$$

holds. At first glance, it seems like the approximation in (A.28) is justified due to the relation $\overline{\rho(\boldsymbol{k}-\boldsymbol{q})} = N\delta_{\boldsymbol{q},\boldsymbol{k}}$. As the static structure factor is of order $\mathcal{O}(1)$, it should be negligible compared to the average in the thermodynamic limit. However, Equation (A.28) is, in fact, an approximation even for $N \to \infty$ as the neglected density fluctuation contributes to the sum over the wavevectors as

$$\sum_{\boldsymbol{k}} \to \frac{V}{(2\pi)^d} \int d^d\boldsymbol{k} \tag{A.29}$$

is always true. Thus, the approximation in Equation (A.28) equals a high-density approximation. However, we rely on this simplification, as the same approximation was used in Equation (5.38) when deriving the Self-Consistent Current Response Theory and expressing the fluidity $\hat{\mathrm{W}}^{\perp}_{q}(s)$ in Equation (5.40) via the bare and the renormalized vertex. However, within the approximation of Equation (A.28), Equation (A.26) simplifies to

$$n_{j,2}(-\boldsymbol{k}, \boldsymbol{k}-\boldsymbol{q}) \approx e^{i\boldsymbol{k}\cdot\boldsymbol{R}_j} \Big[\sum_{l=1}^{N} e^{i(\boldsymbol{q}-\boldsymbol{k})\cdot\boldsymbol{R}_l} - \overline{\rho(\boldsymbol{k}-\boldsymbol{q})} \Big] = e^{i\boldsymbol{k}\cdot\boldsymbol{R}_j} \delta\rho(\boldsymbol{k}-\boldsymbol{q}) \, . \tag{A.30}$$

As said above, there is no real justification for this approximation, and it is in contrast to the derivation in (Szamel, 2025). The projection operator used hereinafter reads:

$$P_{j,2} f(\{\boldsymbol{R}_i\}_{i=1}^{N}) = \sum_{\boldsymbol{k}} \frac{e^{i\boldsymbol{k}\cdot\boldsymbol{R}_j} \delta\rho(\boldsymbol{q}-\boldsymbol{k})}{N S_{|\boldsymbol{q}-\boldsymbol{k}|}} \overline{e^{-i\boldsymbol{k}\cdot\boldsymbol{R}_j} \delta\rho(\boldsymbol{k}-\boldsymbol{q}) f(\{\boldsymbol{R}_i\}_{i=1}^{N})} \, , \tag{A.31}$$

again for an arbitrary function $f(\{\boldsymbol{R}_i\}_{i=1}^N)$ of the reference frame. Inserting this projection operator in Equation A.24 between the Hessian $\mathcal{H}_{ik}^{\mathrm{SERM}}$ and Q_k leads to an expression of the self-energy in terms of a bare and a renormalized vertex:

$$\hat{\Sigma}_q^{\mathrm{SERM}}(s) \approx \frac{1}{N}\sum_{\boldsymbol{k}} V_{\boldsymbol{q},\boldsymbol{k}}^{\mathrm{SERM}} \hat{\mathcal{V}}_{\boldsymbol{k},\boldsymbol{q}}^{\mathrm{SERM}}(s) \tag{A.32}$$

The two vertices read:

$$V_{\boldsymbol{q},\boldsymbol{k}}^{\mathrm{SERM}} = -\frac{\overline{\sum_{i,j}\rho_i(\boldsymbol{q})\mathcal{H}_{ij}^{\mathrm{SERM}}Q_j\rho_j(-\boldsymbol{k})\delta\rho(\boldsymbol{k}-\boldsymbol{q})}}{NS_{|\boldsymbol{q}-\boldsymbol{k}|}} \tag{A.33a}$$

$$\hat{\mathcal{V}}_{\boldsymbol{k},\boldsymbol{q}}^{\mathrm{SERM}}(s) = \sum_{\boldsymbol{p}}\sum_{j,l}\overline{\frac{e^{-i\boldsymbol{k}\cdot\boldsymbol{R}_j}}{N^2}\delta\rho(\boldsymbol{q}-\boldsymbol{k})Q_j\left[s^2+\underline{\boldsymbol{\mathcal{H}}}^{\Sigma}\right]_{jl}^{-1}Q_l e^{i\boldsymbol{p}\cdot\boldsymbol{R}_l}\delta\rho(\boldsymbol{p}-\boldsymbol{q})}\left(V^{\mathrm{SERM}}\right)_{\boldsymbol{p},\boldsymbol{q}}^{\dagger} \tag{A.33b}$$

Again, we relied on the statistical equivalence of the particles. Notably, there is now a difference to (Szamel, 2025). Using the projector defined in Equation (A.27) still gives an exact expression for the self-energy, and the vertex would read

$$\tilde{V}_{\boldsymbol{q},\boldsymbol{k}}^{\mathrm{SERM}} = \frac{n}{m}[\mathcal{K}(\boldsymbol{k}) - \mathcal{K}(\boldsymbol{q}-\boldsymbol{k})] \tag{A.34}$$

independent of the distribution function. However, this is not true for the projection operator defined in Equation (A.31). The next paragraph derives a formulae for the bare vertex $V_{\boldsymbol{q},\boldsymbol{k}}^{\mathrm{SERM}}$.

The bare vertex $V_{\boldsymbol{q},\boldsymbol{k}}^{\mathrm{SERM}}$ in the scalar ERM model: Hereinafter, we continue with the projection defined in Equation (A.31) and derive an expression for the bare vertex $V_{\boldsymbol{q},\boldsymbol{k}}^{\mathrm{SERM}}$. Due to the projection Q_j in Equation (A.33a) arise two contributions. In analogiy to Appendix D, we calculate them separately. On the one hand, one has

$$\begin{aligned}&\frac{1}{N}\overline{\sum_{i,j}\rho_i(\boldsymbol{q})\mathcal{H}_{ij}^{\mathrm{SERM}}P_j\rho_j(-\boldsymbol{k})\delta\rho(\boldsymbol{k}-\boldsymbol{q})}\\ &\quad= \frac{1}{N}\overline{\sum_{i,j}\rho_i(\boldsymbol{q})\mathcal{H}_{ij}^{\mathrm{SERM}}\rho_j(-\boldsymbol{q})}\frac{1}{N}\overline{\rho(\boldsymbol{q}-\boldsymbol{k})\delta\rho(\boldsymbol{k}-\boldsymbol{q})} = (qc_q^{\mathrm{SERM}})^2 S_{|\boldsymbol{q}-\boldsymbol{k}|}\ .\end{aligned} \tag{A.35}$$

Here, we inserted the expression for the bare dispersion relation $(qc_q^{\mathrm{SERM}})^2$ derived in Equation (A.14). On the other hand, the second term arises from

$$\begin{aligned} &-\frac{1}{N}\overline{\sum_{i,j}\rho_i(\boldsymbol{q})\mathcal{H}_{ij}^{\mathrm{SERM}}\rho_j(-\boldsymbol{k})\delta\rho(\boldsymbol{k}-\boldsymbol{q})} \\ &\qquad = -\frac{1}{N}\overline{\sum_{i,j=1}^{N}\rho_i(\boldsymbol{q})\mathcal{H}_{ij}^{\mathrm{SERM}}\rho_j(-\boldsymbol{k})\rho(\boldsymbol{k}-\boldsymbol{q})} + \overline{\rho(\boldsymbol{k}-\boldsymbol{q})}(qc_q^{\mathrm{SERM}})^2 \end{aligned} \tag{A.36}$$

Only the first term on the right-hand side is non-trivial and needs to be evaluated further.

$$\begin{aligned} &-\frac{1}{N}\overline{\sum_{i,j=1}^{N}\rho_i(\boldsymbol{q})\mathcal{H}_{ij}^{\mathrm{SERM}}\rho_j(-\boldsymbol{k})\rho(\boldsymbol{k}-\boldsymbol{q})} \\ &= -\frac{1}{mN}\overline{\sum_{i,j,l}e^{-i\boldsymbol{q}\cdot\boldsymbol{R}_i}\left[\delta_{ij}\sum_{h\neq i}\mathcal{K}(\boldsymbol{R}_h-\boldsymbol{R}_i)-(1-\delta_{ij})\mathcal{K}(\boldsymbol{R}_i-\boldsymbol{R}_j)\right]e^{i\boldsymbol{k}\cdot\boldsymbol{R}_j}e^{-i(\boldsymbol{k}-\boldsymbol{q})\cdot\boldsymbol{R}_l}} \\ &= -\frac{1}{mN}\overline{\sum_{l,j,i\neq j}\left[e^{-i(\boldsymbol{q}-\boldsymbol{k})\cdot(\boldsymbol{R}_j-\boldsymbol{R}_l)}-e^{-i\boldsymbol{q}\cdot(\boldsymbol{R}_i-\boldsymbol{R}_l)}e^{-i\boldsymbol{k}\cdot(\boldsymbol{R}_l-\boldsymbol{R}_j)}\right]\mathcal{K}(\boldsymbol{R}_i-\boldsymbol{R}_j)}\,. \end{aligned} \tag{A.37}$$

As one can see, the calculation proceeds in complete analogy to Equation (D.13). Thus, we can immediately jump to the result:

$$V_{\boldsymbol{q},\boldsymbol{k}}^{\mathrm{SERM}} = -\frac{\overline{\sum_{i,j}\rho_i(\boldsymbol{q})\mathcal{H}_{ij}Q_j\rho_j(-\boldsymbol{k})\delta\rho(\boldsymbol{k}-\boldsymbol{q})}}{NS_{|\boldsymbol{q}-\boldsymbol{k}|}} = (qc_q^{\mathrm{SERM}})^2 \tag{A.38}$$
$$-n\int d^d\boldsymbol{r}d^d\boldsymbol{r}'\frac{ng^{(3)}(\boldsymbol{r},\boldsymbol{r}')-ng(r)+g(r)\Big(\delta(\boldsymbol{r}')+\delta(\boldsymbol{r}-\boldsymbol{r}')\Big)}{mS_{|\boldsymbol{q}-\boldsymbol{k}|}}e^{i(\boldsymbol{k}-\boldsymbol{q})\cdot\boldsymbol{r}'}\Big[1-e^{i\boldsymbol{q}\cdot\boldsymbol{r}}\Big]\mathcal{K}(r)$$

This result closely resembles the vertex discussed in Appendix D. The only differences to Equation (D.16) arise from multiplying through with $q(c_q^{\mathrm{SERM}})^2$ and from the replacement $[\underline{\mathbf{1}}-\hat{\boldsymbol{q}}\hat{\boldsymbol{q}}]\cdot\nabla[\underline{\mathbf{1}}-\hat{\boldsymbol{k}}\hat{\boldsymbol{k}}]\cdot\nabla U(r)\longrightarrow\frac{\partial^2}{\partial r^2}U(r)=\mathcal{K}(r)$. Consequentially, the vertex of the scalar ERM model satisfies the same symmetry relations: $V_{\boldsymbol{q},\boldsymbol{k}}^{\mathrm{SERM}}=\left(V_{\boldsymbol{k},\boldsymbol{q}}^{\mathrm{SERM}}\right)^\dagger=V_{-\boldsymbol{q},-\boldsymbol{k}}^{\mathrm{SERM}}$. We will use them in the following to simplify our notations. The two vertices defined in Equation (A.34) and (A.38) coincide for uniform particle distribution Ψ_Q. However, this is not true for general distribution functions. After having obtained an expression for the bare vertex $V_{\boldsymbol{q},\boldsymbol{k}}^{\mathrm{SERM}}$, we now turn to the renormalised vertex $\mathcal{V}_{\boldsymbol{q},\boldsymbol{k}}^{\mathrm{SERM}}$.

The renormalised vertex in the scalar ERM model: We continue in the spirit of (Szamel, 2025). The derivation is in complete analogy to the preceding section and the derivation of $\hat{\Sigma}_q^{\mathrm{SERM}}(s)$. The guiding idea is again to establish an equation for $\hat{\mathcal{V}}^{\mathrm{SERM}}_{\boldsymbol{k},\boldsymbol{q}}(s) - \lim_{s\to\infty} s^2\hat{\mathcal{V}}^{\mathrm{SERM}}_{\boldsymbol{k},\boldsymbol{q}}(s)$ resembling equation (A.12) and then to define the associated self-energy. Projecting on the pair state of single-side density fluctuation and $\delta\rho$ gives for the high-frequency limit of the renormalized vertex:

$$\begin{aligned}\lim_{s\to\infty} s^2\hat{\mathcal{V}}^{\mathrm{SERM}}_{\boldsymbol{k},\boldsymbol{q}}(s) &= \lim_{s\to\infty}\frac{s^2}{N^2}\sum_{\boldsymbol{p}}\overline{\sum_{j,l} e^{-i\boldsymbol{k}\cdot\boldsymbol{R}_j}\delta\rho(\boldsymbol{q}-\boldsymbol{k})\left[s^2+\underline{\boldsymbol{\mathcal{H}}}^{\Sigma}\right]^{-1}_{jl} e^{i\boldsymbol{p}\cdot\boldsymbol{R}_l}\delta\rho(\boldsymbol{p}-\boldsymbol{q})}V^{\mathrm{SERM}}_{\boldsymbol{q},\boldsymbol{p}} \\ &= \frac{1}{N^2}\sum_{\boldsymbol{p}}\overline{\sum_{l} e^{-i(\boldsymbol{k}-\boldsymbol{p})\cdot\boldsymbol{R}_j}\delta\rho(\boldsymbol{q}-\boldsymbol{k})\delta\rho(\boldsymbol{p}-\boldsymbol{q})}V^{ERM}_{\boldsymbol{q},\boldsymbol{p}} \approx S_{|\boldsymbol{q}-\boldsymbol{k}|}V^{\mathrm{SERM}}_{\boldsymbol{q},\boldsymbol{k}}\end{aligned} \tag{A.39}$$

If we used the projection operator defined in Equation (A.27), the right-hand side was given by $\tilde{V}^{\mathrm{SERM}}_{\boldsymbol{q},\boldsymbol{k}}$. Notable, we have used $\left(V^{\mathrm{SERM}}\right)^{\dagger}_{\boldsymbol{k},\boldsymbol{q}} = V^{\mathrm{SERM}}_{\boldsymbol{q},\boldsymbol{k}}$ to shorten the notation. We will continue doing so hereinafter to simplify the equations. When proceeding to final result, we assumed that density fluctuations concentrate around $\rho(\boldsymbol{k}-\boldsymbol{p}) \approx N\delta_{\boldsymbol{k},\boldsymbol{p}}$. As in Equation (A.28), this simplification resemblances a high-density approximation and is not entirely justified. Thus, this derivation is not in complete analogy with the derivation of the Self-Consistent Current Response Theory presented in Chapter 5 as Equation (5.45) was still exact. However, we will continue with this simplification. Defining $Q_{j,2} = 1 - P_{j,2}$, the constituting equation for the renormalised vertex becomes

$$\begin{aligned}&s^2\hat{\mathcal{V}}^{\mathrm{SERM}}_{\boldsymbol{k},\boldsymbol{q}}(s) - S_{|\boldsymbol{q}-\boldsymbol{k}|}V^{\mathrm{SERM}}_{\boldsymbol{q},\boldsymbol{k}} \\ &= -\frac{1}{N^2}\sum_{\boldsymbol{p}}\overline{\sum_{j,l,m} e^{-i\boldsymbol{k}\cdot\boldsymbol{R}_j}\delta\rho(\boldsymbol{q}-\boldsymbol{k})\mathcal{H}^{\Sigma}_{jm}\left[s^2+\underline{\boldsymbol{\mathcal{H}}}^{\Sigma}\right]^{-1}_{ml} e^{i\boldsymbol{p}\cdot\boldsymbol{R}_l}\delta\rho(\boldsymbol{p}-\boldsymbol{q})}V^{\mathrm{SERM}}_{\boldsymbol{q},\boldsymbol{p}} \\ &= -\sum_{\boldsymbol{p}}\frac{\overline{\sum_{j,m} e^{-i\boldsymbol{k}\cdot\boldsymbol{R}_j}\delta\rho(\boldsymbol{q}-\boldsymbol{k})\mathcal{H}^{\Sigma}_{jm}e^{i\boldsymbol{p}\cdot\boldsymbol{R}_m}\delta\rho(\boldsymbol{p}-\boldsymbol{q})}}{N^2 S_{|\boldsymbol{q}-\boldsymbol{p}|}}\hat{\mathcal{V}}^{\mathrm{SERM}}_{\boldsymbol{p},\boldsymbol{q}}(s) \\ &\quad -\frac{1}{N^2}\sum_{\boldsymbol{p}}\overline{\sum_{j,l,m} e^{-i\boldsymbol{k}\cdot\boldsymbol{R}_j}\delta\rho(\boldsymbol{q}-\boldsymbol{k})\mathcal{H}^{\Sigma}_{jm}Q_{m,2}\left[s^2+\underline{\boldsymbol{\mathcal{H}}}^{\Sigma}\right]^{-1}_{ml} e^{i\boldsymbol{p}\cdot\boldsymbol{R}_l}\delta\rho(\boldsymbol{p}-\boldsymbol{q})}V^{\mathrm{SERM}}_{\boldsymbol{q},\boldsymbol{p}}\,.\end{aligned} \tag{A.40}$$

Here, we inserted $1 = P_{j,2} + Q_{j,2}$ after the second line. Calculating the prefactors of the renormalized vertex in the third line of the previous equation is rather tedious. However, finding an exact expression for the overlap is worth doing as it sheds light on

the approximation performed in Equation 5.51, where we assumed a simple expression for the Force-Density-Matrix element. The two expressions correspond to each other. Thus, the following section presents the detailed calculation.

A.1.2 Exact expression of the force-density matrix elements

This section is concerned with the calculion of the overlap

$$\mathcal{F}(\boldsymbol{q},\boldsymbol{k},\boldsymbol{p}) = \frac{\overline{\sum_{j,m} e^{-i\boldsymbol{k}\cdot\boldsymbol{R}_j}\delta\rho(\boldsymbol{q}-\boldsymbol{k})\mathcal{H}^{\Sigma}_{jm}e^{i\boldsymbol{p}\cdot\boldsymbol{R}_m}\delta\rho(\boldsymbol{p}-\boldsymbol{q})}}{N^2 S_{|\boldsymbol{q}-\boldsymbol{p}|}} \tag{A.41}$$

explicitly. There are two independent contributions arising from the definition of the reduced Hessian defined in Equation (A.21):

$$\begin{aligned}
&\frac{1}{N^2}\overline{\sum_{j,l=1}^{N} e^{-i\boldsymbol{k}\cdot\boldsymbol{R}_j}\delta\rho(\boldsymbol{q}-\boldsymbol{k})\mathcal{H}^{\Sigma}_{jl}e^{i\boldsymbol{p}\cdot\boldsymbol{R}_l}\delta\rho(\boldsymbol{p}-\boldsymbol{q})} \\
=&\frac{1}{N^2}\overline{\sum_{j,l=1}^{N} e^{-i\boldsymbol{k}\cdot\boldsymbol{R}_j}\delta\rho(\boldsymbol{q}-\boldsymbol{k})Q_j\mathcal{H}^{\mathrm{SERM}}_{jl}Q_l e^{i\boldsymbol{p}\cdot\boldsymbol{R}_l}\delta\rho(\boldsymbol{p}-\boldsymbol{q})} \\
&-\overline{\frac{\sum_{j,h=1}^{N} e^{-i\boldsymbol{k}\cdot\boldsymbol{R}_j}\delta\rho(\boldsymbol{q}-\boldsymbol{k})Q_j\mathcal{H}^{\mathrm{SERM}}_{jh}e^{i\boldsymbol{q}\cdot\boldsymbol{R}_h}}{N^3(qc^{\mathrm{SERM}}_q)^2}\sum_{i,l=1}^{N} e^{-i\boldsymbol{q}\cdot\boldsymbol{R}_i}\mathcal{H}^{\mathrm{SERM}}_{il}Q_l e^{i\boldsymbol{p}\cdot\boldsymbol{R}_l}\delta\rho(\boldsymbol{p}-\boldsymbol{q})}
\end{aligned} \tag{A.42}$$

We analyze them separately and start with the first one.

Term 1) $\frac{1}{N^2}\overline{\sum_{j,m} e^{-i\boldsymbol{k}\cdot\boldsymbol{R}_j}\delta\rho(\boldsymbol{q}-\boldsymbol{k})Q_j\mathcal{H}^{\mathrm{SERM}}_{jm}Q_m e^{i\boldsymbol{p}\cdot\boldsymbol{R}_m}\delta\rho(\boldsymbol{p}-\boldsymbol{q})}$:
First of all, we record the identity

$$\begin{aligned}
Q_j\mathcal{H}^{\mathrm{SERM}}_{jm}Q_m &= \mathcal{H}^{\mathrm{SERM}}_{jm} + P_j\mathcal{H}^{\mathrm{SERM}}_{jm}P_m - \mathcal{H}^{\mathrm{SERM}}_{jm}P_m - P_j\mathcal{H}^{\mathrm{SERM}}_{jm} \\
&= \mathcal{H}^{\mathrm{SERM}}_{jm}Q_m + Q_j\mathcal{H}^{\mathrm{SERM}}_{jm} - \mathcal{H}^{\mathrm{SERM}}_{jm} + P_j\mathcal{H}^{\mathrm{SERM}}_{jm}P_m \\
&= (P_j+Q_j)\mathcal{H}^{\mathrm{SERM}}_{jm}Q_m + Q_j\mathcal{H}^{\mathrm{SERM}}_{jm}(P_m+Q_m) - \mathcal{H}^{\mathrm{SERM}}_{jm} + P_j\mathcal{H}^{\mathrm{SERM}}_{jm}P_m \\
&\Longrightarrow Q_j\mathcal{H}^{\mathrm{SERM}}_{jm}Q_m = \mathcal{H}^{\mathrm{SERM}}_{jm} - P_j\mathcal{H}^{\mathrm{SERM}}_{jm}P_m - Q_j\mathcal{H}^{\mathrm{SERM}}_{jm}P_m - P_j\mathcal{H}^{\mathrm{SERM}}_{jm}Q_m\ .
\end{aligned} \tag{A.43}$$

This identity allows us to express the overlap with distribution functions $g^{(k)}$ alone. Hereinafter, we analyse the four terms one by one: The two last terms on the right-

hand side in the fourth line lead to the emergence of the bare vertex defined in Equation (A.33a):

$$\begin{aligned}
&\frac{1}{N^2}\overline{\sum_{j,m} e^{-i\boldsymbol{k}\cdot\boldsymbol{R}_j}\delta\rho(\boldsymbol{q}-\boldsymbol{k})P_j\mathcal{H}_{jm}^{\mathrm{SERM}}Q_m e^{i\boldsymbol{p}\cdot\boldsymbol{R}_m}\delta\rho(\boldsymbol{p}-\boldsymbol{q})} \\
=&\frac{S_{|\boldsymbol{q}-\boldsymbol{k}|}}{N}\frac{1}{N}\overline{\sum_{j,m} e^{-i\boldsymbol{q}\cdot\boldsymbol{R}_j}\mathcal{H}_{jm}^{\mathrm{SERM}}Q_m e^{i\boldsymbol{p}\cdot\boldsymbol{R}_m}\delta\rho(\boldsymbol{p}-\boldsymbol{q})} \\
=&\frac{S_{|\boldsymbol{q}-\boldsymbol{k}|}S_{|\boldsymbol{q}-\boldsymbol{p}|}}{N}V_{\boldsymbol{q},\boldsymbol{p}}^{\mathrm{SERM}}
\end{aligned} \tag{A.44}$$

Due to the symmetry of the bare vertex $\left(V^{\mathrm{SERM}}\right)^{\dagger}_{\boldsymbol{k},\boldsymbol{q}} = V^{\mathrm{SERM}}_{\boldsymbol{q},\boldsymbol{k}}$ arises an equivalent expression when calculating the overlap using the third matrix element $Q_j\mathcal{H}_{jm}P_m$ instead of $P_j\mathcal{H}_{jm}Q_m$. One only has to replace the two Fourier modes $\boldsymbol{k} \longleftrightarrow \boldsymbol{p}$. Even though it looks like both terms disappear for $N \to \infty$, one has to keep in mind that the sum over the wavevectors introduces a factor V as

$$\sum_{\boldsymbol{p}} \to \frac{V}{(2\pi)^d}\int d^d\boldsymbol{p} \tag{A.45}$$

holds in the thermodynamic limit. Thus, both terms do contribute but vanish in a high-density approximation $n \to \infty$. Next, we look at the overlap with the two P-projection operators. Using the expression for the bare dispersion relation, given in Equation (A.14), and the statistical equivalence of the particles, this term becomes

$$\frac{1}{N^2}\overline{\sum_{j,m} e^{-i\boldsymbol{k}\cdot\boldsymbol{R}_j}\delta\rho(\boldsymbol{q}-\boldsymbol{k})P_j\mathcal{H}_{jm}P_m e^{i\boldsymbol{p}\cdot\boldsymbol{R}_m}\delta\rho(\boldsymbol{p}-\boldsymbol{q})} = \frac{S_{|\boldsymbol{q}-\boldsymbol{k}|}S_{|\boldsymbol{q}-\boldsymbol{p}|}}{N}(qc_q^{\mathrm{SERM}})^2 \tag{A.46}$$

Lastly, we turn to the contribution arising from the full Hessian. Here, four different terms arise:

$$\begin{aligned}
&\frac{1}{N^2}\overline{\sum_{j,m} e^{-i\boldsymbol{k}\cdot\boldsymbol{R}_j}\delta\rho(\boldsymbol{q}-\boldsymbol{k})\mathcal{H}_{jm}^{\mathrm{SERM}}e^{i\boldsymbol{p}\cdot\boldsymbol{R}_m}\delta\rho(\boldsymbol{p}-\boldsymbol{q})} \\
&\quad= \frac{1}{N^2}\overline{\sum_{j,m} e^{-i\boldsymbol{k}\cdot\boldsymbol{R}_j}\rho(\boldsymbol{q}-\boldsymbol{k})\mathcal{H}_{jm}^{\mathrm{SERM}}e^{i\boldsymbol{p}\cdot\boldsymbol{R}_m}\rho(\boldsymbol{p}-\boldsymbol{q})} \\
&\quad+ \delta_{\boldsymbol{p},\boldsymbol{k}}\delta_{\boldsymbol{q},\boldsymbol{k}}\overline{\sum_{j,m} e^{-i\boldsymbol{k}\cdot\boldsymbol{R}_j}\mathcal{H}_{jm}^{\mathrm{SERM}}e^{i\boldsymbol{k}\cdot\boldsymbol{R}_m}} \\
&\quad- \frac{1}{N}\delta_{\boldsymbol{q},\boldsymbol{p}}\overline{\sum_{j,m} e^{-i\boldsymbol{k}\cdot\boldsymbol{R}_j}\rho(\boldsymbol{q}-\boldsymbol{k})\mathcal{H}_{jm}^{\mathrm{SERM}}e^{i\boldsymbol{q}\cdot\boldsymbol{R}_m}} \\
&\quad- \frac{1}{N}\delta_{\boldsymbol{q},\boldsymbol{k}}\overline{\sum_{j,m} e^{-i\boldsymbol{q}\cdot\boldsymbol{R}_j}\mathcal{H}_{jm}^{\mathrm{SERM}}e^{i\boldsymbol{p}\cdot\boldsymbol{R}_m}\rho(\boldsymbol{p}-\boldsymbol{q})}
\end{aligned} \tag{A.47}$$

All the terms can be expressed with the quadruplet, the triplet, and the pair distribution function, respectively. However, we again apply the high-density approximation discussed in Equation (A.28). With it, we can express the three last terms as

$$\begin{aligned}
&\delta_{\boldsymbol{p},\boldsymbol{k}}\delta_{\boldsymbol{q},\boldsymbol{k}}\overline{\sum_{j,m} e^{-i\boldsymbol{k}\cdot\boldsymbol{R}_j}\mathcal{H}_{jm}^{\mathrm{SERM}}e^{i\boldsymbol{k}\cdot\boldsymbol{R}_m}} \\
&- \frac{1}{N}\delta_{\boldsymbol{q},\boldsymbol{p}}\overline{\sum_{j,m} e^{-i\boldsymbol{k}\cdot\boldsymbol{R}_j}\rho(\boldsymbol{q}-\boldsymbol{k})\mathcal{H}_{jm}^{\mathrm{SERM}}e^{i\boldsymbol{q}\cdot\boldsymbol{R}_m}} \\
&- \frac{1}{N}\delta_{\boldsymbol{q},\boldsymbol{k}}\overline{\sum_{j,m} e^{-i\boldsymbol{q}\cdot\boldsymbol{R}_j}\mathcal{H}_{jm}^{\mathrm{SERM}}e^{i\boldsymbol{p}\cdot\boldsymbol{R}_m}\rho(\boldsymbol{p}-\boldsymbol{q})} \approx -N\delta_{\boldsymbol{p},\boldsymbol{k}}\delta_{\boldsymbol{q},\boldsymbol{k}}(qc_q^{\mathrm{SERM}})^2 \ .
\end{aligned} \tag{A.48}$$

Thus, the only term left to consider is the one in the second line of Equation (A.47). The quadruplet distribution function is defined in Equation (A.4):

$$g^{(4)}(\boldsymbol{r},\boldsymbol{r}',\boldsymbol{r}'') \equiv \frac{1}{n^3 N}\overline{\sum_{i\neq j\neq l\neq n}\delta(\boldsymbol{r}-(\boldsymbol{R}_i-\boldsymbol{R}_j))\delta(\boldsymbol{r}'-(\boldsymbol{R}_i-\boldsymbol{R}_l))\delta(\boldsymbol{r}''-(\boldsymbol{R}_i-\boldsymbol{R}_n))} \ . \tag{A.49}$$

One gets for the term in the second line of Equation (A.47):

$$
\begin{aligned}
&\overline{\sum_{i,j,l,m} e^{-i\boldsymbol{k}\cdot(\boldsymbol{R}_j-\boldsymbol{R}_l)} e^{-i\boldsymbol{q}\cdot(\boldsymbol{R}_l-\boldsymbol{R}_i)} e^{-i\boldsymbol{p}\cdot(\boldsymbol{R}_i-\boldsymbol{R}_m)} \Big[\delta_{jm} \sum_{r\neq m} \mathcal{K}(\boldsymbol{R}_m-\boldsymbol{R}_r) - (1-\delta_{jm})\mathcal{K}(\boldsymbol{R}_j-\boldsymbol{R}_m)\Big]} \\
&= \int d^d\boldsymbol{r} d^d\boldsymbol{r}' d^d\boldsymbol{r}'' \overline{\sum_{i,l,m,j\neq m} \delta(\boldsymbol{r}-(\boldsymbol{R}_j-\boldsymbol{R}_m))\delta(\boldsymbol{r}'-(\boldsymbol{R}_j-\boldsymbol{R}_l))\delta(\boldsymbol{r}''-(\boldsymbol{R}_j-\boldsymbol{R}_i))} \\
&\quad \times e^{-i\boldsymbol{k}\cdot\boldsymbol{r}'} e^{-i\boldsymbol{q}\cdot(\boldsymbol{r}''-\boldsymbol{r}')} \Big[e^{i\boldsymbol{p}\cdot\boldsymbol{r}''} - e^{-i\boldsymbol{p}\cdot(\boldsymbol{r}-\boldsymbol{r}'')}\Big] \mathcal{K}(r) \\
&= N \int d^d\boldsymbol{r} d^d\boldsymbol{r}' d^d\boldsymbol{r}'' \Big(n^3 g^{(4)}(\boldsymbol{r},\boldsymbol{r}',\boldsymbol{r}'') + n^2 g^{(3)}(\boldsymbol{r},\boldsymbol{r}')\delta(\boldsymbol{r}'') + n^2 g^{(3)}(\boldsymbol{r},\boldsymbol{r}'')\delta(\boldsymbol{r}') \\
&\quad + n^2 g^{(3)}(\boldsymbol{r},\boldsymbol{r}'')\delta(\boldsymbol{r}'-\boldsymbol{r}) + n^2 g^{(3)}(\boldsymbol{r},\boldsymbol{r}')\delta(\boldsymbol{r}''-\boldsymbol{r}) + n^2 g^{(3)}(\boldsymbol{r},\boldsymbol{r}')\delta(\boldsymbol{r}''-\boldsymbol{r}') \\
&\quad + n g(r) \Big[\delta(\boldsymbol{r}''-\boldsymbol{r})\delta(\boldsymbol{r}'-\boldsymbol{r}) + \delta(\boldsymbol{r}''-\boldsymbol{r})\delta(\boldsymbol{r}') + \delta(\boldsymbol{r}'-\boldsymbol{r})\delta(\boldsymbol{r}'')\Big] \\
&\quad \times e^{-i\boldsymbol{k}\cdot\boldsymbol{r}'} e^{-i\boldsymbol{q}\cdot(\boldsymbol{r}''-\boldsymbol{r}')} e^{i\boldsymbol{p}\cdot\boldsymbol{r}''} \Big[1 - e^{-i\boldsymbol{p}\cdot\boldsymbol{r}}\Big] \mathcal{K}(r) \ .
\end{aligned}
\tag{A.50}
$$

Again, all the terms discussed so far contribute to $N \to \infty$ due to the integral or sum over the Fourier mode $\boldsymbol{p}$.

Term 2) $\overline{\frac{\sum_{j,m} e^{-i\boldsymbol{k}\cdot\boldsymbol{R}_j}\delta\rho(\boldsymbol{q}-\boldsymbol{k})Q_j\mathcal{H}^{\mathrm{SERM}}_{jm}e^{i\boldsymbol{q}\cdot\boldsymbol{R}_m}}{N^3(qc_q^{\mathrm{SERM}})^2}} \overline{\sum_{i,l} e^{-i\boldsymbol{q}\cdot\boldsymbol{R}_i}\mathcal{H}^{\mathrm{SERM}}_{il}Q_l e^{i\boldsymbol{p}\cdot\boldsymbol{R}_l}\delta\rho(\boldsymbol{p}-\boldsymbol{q})}$:
This second term is much easier to calculate as the two overlaps are given by the bare vertex. Inserting the Equation (A.38) immediately leads to

$$
\begin{aligned}
&\frac{1}{N^3(qc_q^{\mathrm{SERM}})^2} \overline{\sum_{j,m} e^{-i\boldsymbol{k}\cdot\boldsymbol{R}_j}\delta\rho(\boldsymbol{q}-\boldsymbol{k})Q_j\mathcal{H}^{\mathrm{SERM}}_{jm}e^{i\boldsymbol{q}\cdot\boldsymbol{R}_m} \sum_{i,l} e^{-i\boldsymbol{q}\cdot\boldsymbol{R}_i}\mathcal{H}^{\mathrm{SERM}}_{il}Q_l e^{i\boldsymbol{p}\cdot\boldsymbol{R}_l}\delta\rho(\boldsymbol{p}-\boldsymbol{q})} \\
&\qquad = \frac{S_{|\boldsymbol{q}-\boldsymbol{k}|}S_{|\boldsymbol{q}-\boldsymbol{p}|}}{N(qc_q^{\mathrm{SERM}})^2} V_{\boldsymbol{q},\boldsymbol{k}}V_{\boldsymbol{q},\boldsymbol{p}} \ .
\end{aligned}
\tag{A.51}
$$

Summing all these contributions with the correct sign gives an exact formula for the right-hand side of Equation (A.42) and hence for the prefactor of the renormalized vertex in Equation (A.40). Szamel derived a much simpler expression for the overlap (Szamel, 2025). However, the author used the projector defined in Equation (A.27) instead of the one from Equation (A.31). As we saw, this leads to a different vertex $\tilde{V}^{\mathrm{SERM}}_{\boldsymbol{q},\boldsymbol{p}}$, which does not depend on the system's structure. Hence, in this sense, Szamel derives and discusses a different theory (Szamel, 2025). Because of this assessment, it is worth

adding that the statements made in (Szamel, 2025) about the approximation in Equation (5.51) are not applicable as, ultimately, different quantities are discussed in both theories. The analog approximation to Equation (5.51) in the ERM model reads

$$\begin{aligned}
&\frac{\overline{\sum_{j,m} e^{-i\boldsymbol{k}\cdot\boldsymbol{R}_j}\delta\rho(\boldsymbol{q}-\boldsymbol{k})\mathcal{H}^{\Sigma}_{jm}e^{i\boldsymbol{p}\cdot\boldsymbol{R}_m}\delta\rho(\boldsymbol{p}-\boldsymbol{q})}}{N^2 S_{|\boldsymbol{q}-\boldsymbol{p}|}} \\
&\approx \frac{\overline{\delta\rho(\boldsymbol{q}-\boldsymbol{k})\delta\rho(\boldsymbol{p}-\boldsymbol{q})}}{NS_{|\boldsymbol{q}-\boldsymbol{p}|}}\frac{1}{N}\overline{\sum_{j,m=1}^{N} e^{-i\boldsymbol{k}\cdot\boldsymbol{R}_j}\mathcal{H}^{\Sigma}_{jm}e^{i\boldsymbol{p}\cdot\boldsymbol{R}_m}} \\
&\approx \frac{\overline{\delta\rho(\boldsymbol{q}-\boldsymbol{k})\delta\rho(\boldsymbol{p}-\boldsymbol{q})}}{NS_{|\boldsymbol{q}-\boldsymbol{p}|}}\frac{1}{N}\overline{\sum_{j,m=1}^{N} e^{-i\boldsymbol{k}\cdot\boldsymbol{R}_j}\mathcal{H}^{\mathrm{SERM}}_{jm}e^{i\boldsymbol{p}\cdot\boldsymbol{R}_m}} = \delta_{\boldsymbol{k},\boldsymbol{p}}(kc_k^{\mathrm{SERM}})^2 \ .
\end{aligned} \tag{A.52}$$

As the calculations in this section suggest, such an approximation is not valid at all. Furthermore, the approximation also does not amount to simply neglecting off-diagonal elements, which was erroneously claimed in (Szamel, 2025). Equation (A.52) is purely motivated by convenience and a wish for simplification without mathematical justification. However, we adopt this exact approximation hereinafter. In the next section, we seek an approximation, which allows us to express the renormalized vertex as a function of the resolvent.

A.1.3 Closure and the factorisation approximation

In this section, we derive an expression for the renormalized vertex $\hat{\mathcal{V}}^{\mathrm{SERM}}_{\boldsymbol{k},\boldsymbol{q}}(s)$. Inserting the approximation (A.52) in Equation (A.40) leads to

$$\begin{aligned}
&s^2\hat{\mathcal{V}}^{\mathrm{SERM}}_{\boldsymbol{k},\boldsymbol{q}}(s) - S_{|\boldsymbol{q}-\boldsymbol{k}|}V^{\mathrm{SERM}}_{\boldsymbol{q},\boldsymbol{k}} = -(kc_k^{\mathrm{SERM}})^2\hat{\mathcal{V}}^{\mathrm{SERM}}_{\boldsymbol{k},\boldsymbol{q}}(s) \\
&- \frac{1}{N^2}\sum_{\boldsymbol{p}}\overline{\sum_{j,l,m} e^{-i\boldsymbol{k}\cdot\boldsymbol{R}_j}\delta\rho(\boldsymbol{q}-\boldsymbol{k})\mathcal{H}^{\Sigma}_{jm}Q_{m,2}\left[s^2+\underline{\boldsymbol{\mathcal{H}}}^{\Sigma}\right]^{-1}_{ml}e^{i\boldsymbol{p}\cdot\boldsymbol{R}_l}\delta\rho(\boldsymbol{p}-\boldsymbol{q})}V^{\mathrm{SERM}}_{\boldsymbol{q},\boldsymbol{p}} \ .
\end{aligned} \tag{A.53}$$

We go through the following derivation in detail, even though the calculation still proceeds in analogy to (Szamel, 2025). One reason is the sake of completeness. Secondly, there are still differences that ultimately arise from using a different projection operator. Nevertheless, those differences only matter when applying the factorization approximation similar to the one discussed in Section 5.2.3. Understanding this approximation better is the last reason for covering the discussion in detail.

The derivation of a closed equation for the renormalized vertex mimics the procedure discussed at the beginning of Section A.1.1. Again, we introduce an auxiliary function of the reference frame

$$v_m(-\boldsymbol{q},s) = \sum_{\boldsymbol{p}}\sum_{l=1}^{N} Q_{m,2}\left[s^2 + \underline{\boldsymbol{\mathcal{H}}}^{\Sigma}\right]^{-1}_{ml} e^{i\boldsymbol{p}\cdot\boldsymbol{R}_l}\delta\rho(\boldsymbol{p}-\boldsymbol{q})V^{\mathrm{SERM}}_{\boldsymbol{q},\boldsymbol{p}} \ . \tag{A.54}$$

In complete analogy to the investigation of $g_k(-\boldsymbol{k},s)$, the goal is now to express $v_m(-\boldsymbol{q},s)$ in terms of the renormalized vertex $\hat{\mathcal{V}}^{\mathrm{SERM}}_{\boldsymbol{k},\boldsymbol{q}}(s)$:

$$\begin{aligned}
s^2 v_m(-\boldsymbol{q},s) =& \underbrace{\sum_{\boldsymbol{p}} Q_{2,m}\sum_{l,j=1}^{N}\left[s^2+\underline{\boldsymbol{\mathcal{H}}}^{\Sigma}\right]_{mj}\left[s^2+\underline{\boldsymbol{\mathcal{H}}}^{\Sigma}\right]^{-1}_{jl} e^{i\boldsymbol{p}\cdot\boldsymbol{R}_l}\delta\rho(\boldsymbol{p}-\boldsymbol{q})V^{\mathrm{SERM}}_{\boldsymbol{q},\boldsymbol{p}}}_{=0} \\
&- \sum_{\boldsymbol{p}} Q_{2,m}\sum_{l,j=1}^{N}\mathcal{H}^{\Sigma}_{mj}\left[s^2+\underline{\boldsymbol{\mathcal{H}}}^{\Sigma}\right]^{-1}_{jl} e^{i\boldsymbol{p}\cdot\boldsymbol{R}_l}\delta\rho(\boldsymbol{p}-\boldsymbol{q})V^{\mathrm{SERM}}_{\boldsymbol{q},\boldsymbol{p}} \qquad (A.55)\\
=& -\sum_{\boldsymbol{p}} Q_{2,m}\sum_{l,j=1}^{N}\mathcal{H}^{\Sigma}_{mj}\Big(P_{2,j}+Q_{2,j}\Big)\left[s^2+\underline{\boldsymbol{\mathcal{H}}}^{\Sigma}\right]^{-1}_{jl} e^{i\boldsymbol{p}\cdot\boldsymbol{R}_l}\delta\rho(\boldsymbol{p}-\boldsymbol{q})V^{\mathrm{SERM}}_{\boldsymbol{q},\boldsymbol{p}} \\
=& -\sum_{\boldsymbol{p}}\sum_{j=1}^{N}\frac{Q_{2,m}\mathcal{H}^{\Sigma}_{mj}}{NS_{|\boldsymbol{q}-\boldsymbol{p}|}} e^{i\boldsymbol{p}\cdot\boldsymbol{R}_j}\delta\rho(\boldsymbol{p}-\boldsymbol{q})\hat{\mathcal{V}}^{\mathrm{SERM}}_{\boldsymbol{p},\boldsymbol{q}}(s) - \sum_{j=1}^{N} Q_{2,m}\mathcal{H}^{\Sigma}_{mj}v_j(-\boldsymbol{q},s)
\end{aligned}$$

Inserting Equation (A.53) for the renormalised vertex, leads to

$$\begin{aligned}
s^2 v_m(-\boldsymbol{q},s) =& \sum_{\boldsymbol{p}}\sum_{l=1}^{N}\frac{Q_{2,m}\mathcal{H}^{\Sigma}_{ml}e^{i\boldsymbol{p}\cdot\boldsymbol{R}_l}}{NS_{|\boldsymbol{q}-\boldsymbol{p}|}(pc_p^{\mathrm{SERM}})^2}\delta\rho(\boldsymbol{p}-\boldsymbol{q})\Big(s^2\hat{\mathcal{V}}^{\mathrm{SERM}}_{\boldsymbol{p},\boldsymbol{q}}(s) - S_{|\boldsymbol{q}-\boldsymbol{p}|}V^{\mathrm{SERM}}_{\boldsymbol{q},\boldsymbol{p}}\Big) \\
&- \sum_{j=1}^{N} Q_{2,m}\mathcal{H}^{\Sigma}_{mj}Q_{2,j}v_j(-\boldsymbol{q},s) + \sum_{\boldsymbol{p}}\overline{\sum_{j,i} e^{-i\boldsymbol{p}\cdot\boldsymbol{R}_j}\delta\rho(\boldsymbol{q}-\boldsymbol{p})\mathcal{H}^{\Sigma}_{ji}Q_{2,i}v_i(-\boldsymbol{q},s)} \\
&\times\sum_{j=1}^{N}\frac{Q_{2,m}\mathcal{H}^{\Sigma}_{mj}}{N^3S_{|\boldsymbol{q}-\boldsymbol{p}|}(pc_p^{\mathrm{SERM}})^2}e^{i\boldsymbol{p}\cdot\boldsymbol{R}_j}\delta\rho(\boldsymbol{p}-\boldsymbol{q}) \qquad (A.56)
\end{aligned}$$

This last equation has the solution

$$\sum_{j=1}^{N}\left(s^2+\underline{\boldsymbol{\mathcal{H}}}^{\mathcal{V}}\right)_{mj} v_j(-\boldsymbol{q},s) \tag{A.57}$$
$$=\sum_{\boldsymbol{p}}\sum_{l=1}^{N}\frac{Q_{2,m}\mathcal{H}^{\Sigma}_{mj}}{NS_{|\boldsymbol{q}-\boldsymbol{p}|}(pc_p^{\mathrm{SERM}})^2}e^{i\boldsymbol{p}\cdot\boldsymbol{R}_l}\delta\rho(\boldsymbol{p}-\boldsymbol{q})(s^2\hat{\mathcal{V}}^{\mathrm{SERM}}_{\boldsymbol{p},\boldsymbol{q}}(s)-S_{|\boldsymbol{q}-\boldsymbol{p}|}V^{\mathrm{SERM}}_{\boldsymbol{q},\boldsymbol{p}})\ .$$

Here, we have defined the second projected Hessian:

$$\mathcal{H}^{\mathcal{V}}_{mj}\equiv Q_{2,m}\mathcal{H}^{\Sigma}_{mj}Q_{2,j} \tag{A.58}$$
$$-\sum_{\boldsymbol{p}}\frac{\sum_{l=1}^{N}Q_{2,m}\mathcal{H}^{\Sigma}_{ml}e^{i\boldsymbol{p}\cdot\boldsymbol{R}_l}\delta\rho(\boldsymbol{p}-\boldsymbol{q})}{N^3S_{|\boldsymbol{q}-\boldsymbol{p}|}(pc_p^{\mathrm{SERM}})^2}\mathcal{P}\sum_{i=1}^{N}e^{-i\boldsymbol{p}\cdot\boldsymbol{R}_i}\delta\rho(\boldsymbol{q}-\boldsymbol{p})\mathcal{H}^{\Sigma}_{ij}Q_{2,j}\ .$$

Notably the second projected Hessian $\mathcal{H}^{\mathcal{V}}_{mj}$ is defined in complete analogy to first projected Hessian $\mathcal{H}^{\Sigma}_{mj}$ of Equation (A.22). The solution for $v_j(-\boldsymbol{q},s)$ reads

$$v_j(-\boldsymbol{q},s)= \tag{A.59}$$
$$=\sum_{\boldsymbol{p}}\sum_{m,l=1}^{N}\frac{\left[s^2+\underline{\boldsymbol{\mathcal{H}}}^{\mathcal{V}}\right]^{-1}_{jm}Q_{2,m}\mathcal{H}^{\Sigma}_{ml}}{NS_{|\boldsymbol{q}-\boldsymbol{p}|}(pc_p^{ERM})^2}e^{i\boldsymbol{p}\cdot\boldsymbol{R}_l}\delta\rho(\boldsymbol{p}-\boldsymbol{q})(s^2\mathcal{V}_{\boldsymbol{q},\boldsymbol{p}}(s)-S_{|\boldsymbol{q}-\boldsymbol{p}|}V^{\mathrm{SERM}}_{\boldsymbol{q},\boldsymbol{p}})\ .$$

Inserting the solution for $v_j(-\boldsymbol{q},s)$ in Equation (A.53) leads to the definition of a second self-energy

$$\hat{\Sigma}^{\mathcal{V}}(\boldsymbol{q},\boldsymbol{k},\boldsymbol{p},s)= \tag{A.60}$$
$$=\frac{1}{N^2S_{|\boldsymbol{q}-\boldsymbol{p}|}}\overline{\sum_{i,j,l,m}e^{-i\boldsymbol{k}\cdot\boldsymbol{R}_l}\delta\rho(\boldsymbol{q}-\boldsymbol{k})\mathcal{H}^{\Sigma}_{lj}Q_{j,2}\left[s^2+\underline{\boldsymbol{\mathcal{H}}}^{\mathcal{V}}\right]^{-1}_{jm}Q_{2,m}\mathcal{H}^{\Sigma}_{mi}e^{i\boldsymbol{p}\cdot\boldsymbol{R}_i}\delta\rho(\boldsymbol{p}-\boldsymbol{q})}$$

and Equation (A.53) for the renormalized vertex becomes

$$s^2\hat{\mathcal{V}}^{\mathrm{SERM}}_{\boldsymbol{k},\boldsymbol{q}}(s)-S_{|\boldsymbol{q}-\boldsymbol{k}|}V^{\mathrm{SERM}}_{\boldsymbol{q},\boldsymbol{k}} \tag{A.61}$$
$$=-(kc_k^{\mathrm{SERM}})^2\hat{\mathcal{V}}^{\mathrm{SERM}}_{\boldsymbol{k},\boldsymbol{q}}(s)-\sum_{\boldsymbol{p}}\frac{\hat{\Sigma}^{\mathcal{V}}(\boldsymbol{q},\boldsymbol{k},\boldsymbol{p},s)}{(pc_p^{\mathrm{SERM}})^2}\left(s^2\hat{\mathcal{V}}^{\mathrm{SERM}}_{\boldsymbol{p},\boldsymbol{q}}(s^2)-S_{|\boldsymbol{q}-\boldsymbol{p}|}V^{\mathrm{SERM}}_{\boldsymbol{q},\boldsymbol{p}}\right)\ . \tag{A.62}$$

Up to this point, each step was equivalent to the steps in (Szamel, 2025). However, the mathematical objects inside the averages differ. This changes now, as we again search for closure. Here, the concrete form of the pair states becomes important. We aim for an expression of the single matrix elements of the self-energy $\hat{\Sigma}^{\mathcal{V}}$. Thus, we look at the functions of the reference frame occurring in Equation (A.60):

$$\sum_{i=1}^{N} Q_{2,j}\mathcal{H}^{\Sigma}_{ji}e^{i\boldsymbol{p}\cdot\boldsymbol{R}_i}\delta\rho(\boldsymbol{p}-\boldsymbol{q}) = \sum_{i=1}^{N} Q_{2,j}Q_j\mathcal{H}^{\mathrm{SERM}}_{ji}Q_i e^{i\boldsymbol{p}\cdot\boldsymbol{R}_i}\delta\rho(\boldsymbol{p}-\boldsymbol{q}) - \frac{1}{N(qc_q^{\mathrm{SERM}})^2}\sum_{l,i,m=1}^{N} Q_{2,j}Q_j\mathcal{H}^{\mathrm{SERM}}_{jl}e^{i\boldsymbol{q}\cdot\boldsymbol{R}_l}\overline{e^{-i\boldsymbol{q}\cdot\boldsymbol{R}_m}\mathcal{H}^{\mathrm{SERM}}_{mi}Q_i e^{i\boldsymbol{p}\cdot\boldsymbol{R}_i}\rho(\boldsymbol{p}-\boldsymbol{q})} \tag{A.63}$$

Here, we inserted the expression for the first reduced Hessian $\underline{\boldsymbol{\mathcal{H}}}^{\Sigma}$ from Equation (A.21). Equation (A.33a) states that the averaged quantity in the second line is proportional to the bare vertex $V^{\mathrm{SERM}}_{\boldsymbol{q},\boldsymbol{p}}$. Only looking at the second line, we get

$$\begin{aligned}
&\frac{1}{N(qc_q^{\mathrm{SERM}})^2}\sum_{l,i,m=1}^{N} Q_{2,j}Q_j\mathcal{H}^{\mathrm{SERM}}_{jl}e^{i\boldsymbol{q}\cdot\boldsymbol{R}_l}\overline{e^{-i\boldsymbol{q}\cdot\boldsymbol{R}_m}\mathcal{H}^{\mathrm{SERM}}_{mi}Q_m e^{i\boldsymbol{p}\cdot\boldsymbol{R}_i}\rho(\boldsymbol{p}-\boldsymbol{q})} = \qquad \text{(A.64)}\\
&= \frac{1}{m}Q_{2,j}Q_j\sum_{l=1}^{N}\Big(\delta_{jl}\sum_{i\neq l}^{N}\mathcal{K}(\boldsymbol{R}_l-\boldsymbol{R}_i) - (1-\delta_{lj})\mathcal{K}(\boldsymbol{R}_j-\boldsymbol{R}_l)\Big)e^{i\boldsymbol{q}\cdot\boldsymbol{R}_l}\frac{V^{\mathrm{SERM}}_{\boldsymbol{q},\boldsymbol{p}}S_{|\boldsymbol{q}-\boldsymbol{p}|}}{(qc_q^{\mathrm{SERM}})^2}\\
&= \frac{1}{m}\sum_{\boldsymbol{b}}\Big(\mathcal{K}(\boldsymbol{q}-\boldsymbol{b})-\mathcal{K}(\boldsymbol{b})\Big)Q_{2,j}Q_j\sum_{j,l\neq j}^{N}e^{-i(\boldsymbol{q}-\boldsymbol{b})\cdot(\boldsymbol{R}_j-\boldsymbol{R}_l)}e^{i\boldsymbol{q}\cdot\boldsymbol{R}_j}\frac{V^{\mathrm{SERM}}_{\boldsymbol{q},\boldsymbol{p}}S_{|\boldsymbol{q}-\boldsymbol{p}|}}{(qc_q^{\mathrm{SERM}})^2}\ .
\end{aligned}$$

However, we have already discussed in the Equations (A.25), (A.26) and (A.27) that

$$Q_{2,m}Q_i\sum_{i=1}^{N}e^{-i(\boldsymbol{q}-\boldsymbol{k})\cdot(\boldsymbol{R}_m-\boldsymbol{R}_i)}e^{i\boldsymbol{q}\cdot\boldsymbol{R}_m} \approx 0 \tag{A.65}$$

approximately holds. Even though we have already seen that this approximation is ultimately not completely justified, we neglect the term in the last line of Equation (A.63). Thus, we find

$$\sum_{i=1}^{N}Q_{2,m}\mathcal{H}^{\Sigma}_{mi}e^{i\boldsymbol{p}\cdot\boldsymbol{R}_i}\delta\rho(\boldsymbol{p}-\boldsymbol{q}) \approx \sum_{i=1}^{N}Q_{2,m}Q_m\mathcal{H}^{\mathrm{SERM}}_{mi}Q_i e^{i\boldsymbol{p}\cdot\boldsymbol{R}_i}\delta\rho(\boldsymbol{p}-\boldsymbol{q}) \tag{A.66}$$

Now, we assume that the particle positions are independent. Strictly speaking, this only applies for a uniform distribution of the particles. However, it suggest that the projector Q_m does not act on the density fluctuation. This leads us to

$$\begin{aligned}\sum_{i=1}^{N} Q_{2,m} Q_m \mathcal{H}_{mi}^{\mathrm{SERM}} Q_i e^{i\boldsymbol{p}\cdot\boldsymbol{R}_i} \delta\rho(\boldsymbol{p}-\boldsymbol{q}) &\approx \sum_{i=1}^{N} Q_{2,m} \delta\rho(\boldsymbol{p}-\boldsymbol{q}) Q_m \mathcal{H}_{mi}^{\mathrm{SERM}} e^{i\boldsymbol{p}\cdot\boldsymbol{R}_i} \\ &= \sum_{i=1}^{N} Q_{2,m} \delta\rho(\boldsymbol{p}-\boldsymbol{q}) (P_{m,2} + Q_{m,2}) Q_m \mathcal{H}_{mi}^{\mathrm{SERM}} e^{i\boldsymbol{p}\cdot\boldsymbol{R}_i} \\ &\approx \sum_{\boldsymbol{b}} Q_{2,m} e^{i\boldsymbol{b}\cdot\boldsymbol{R}_m} \delta\rho(\boldsymbol{b}-\boldsymbol{p}) \delta\rho(\boldsymbol{p}-\boldsymbol{q}) V_{\boldsymbol{q},\boldsymbol{b}}^{\mathrm{SERM}} \,. \end{aligned} \tag{A.67}$$

In the third line, we relied on the result from Equation (A.26), which implies

$$Q_m \mathcal{H}_{mi} e^{i\boldsymbol{q}\cdot\boldsymbol{R}_i} \approx \sum_{\boldsymbol{b}} e^{i\boldsymbol{b}\cdot\boldsymbol{R}_m} \delta\rho(\boldsymbol{b}-\boldsymbol{q}) V_{\boldsymbol{q},\boldsymbol{b}}^{\mathrm{SERM}} \,. \tag{A.68}$$

The expression for the bare vertex $\underline{\boldsymbol{V}}_{\boldsymbol{q},\boldsymbol{b}}$ is given in Equation (A.33a). All in all, we found that the second free energy can be written as a six-point correlation function:

$$\begin{aligned}\hat{\Sigma}^{\mathcal{V}}(\boldsymbol{q},\boldsymbol{k},\boldsymbol{p},s) &\approx \frac{1}{N^2 S_{|\boldsymbol{q}-\boldsymbol{p}|}} \sum_{\boldsymbol{b},\boldsymbol{b}'} V_{\boldsymbol{q},\boldsymbol{b}}^{\mathrm{SERM}} \\ &\times \sum_{l,m} e^{-i\boldsymbol{b}\cdot\boldsymbol{R}_l} \delta\rho(\boldsymbol{k}-\boldsymbol{b}) \delta\rho(\boldsymbol{q}-\boldsymbol{k}) Q_{l,2} \left[s^2 + \underline{\boldsymbol{\mathcal{H}}}^{\mathcal{V}} \right]^{-1}_{lm} Q_{2,m} \delta\rho(\boldsymbol{b}'-\boldsymbol{p}) \delta\rho(\boldsymbol{p}-\boldsymbol{q}) e^{i\boldsymbol{b}'\cdot\boldsymbol{R}_m} V_{\boldsymbol{q},\boldsymbol{b}'}^{\mathrm{SERM}} \\ &\approx \frac{1}{N} \sum_{\boldsymbol{b}} V_{\boldsymbol{q},\boldsymbol{b}}^{\mathrm{SERM}} \hat{\chi}_b^{\mathrm{SERM}}(s) \Big(S_{|\boldsymbol{k}-\boldsymbol{b}|} \delta_{\boldsymbol{k},\boldsymbol{p}} + S_{|\boldsymbol{q}-\boldsymbol{k}|} \delta_{\boldsymbol{k}-\boldsymbol{b},\boldsymbol{q}-\boldsymbol{p}} \Big) V_{\boldsymbol{q},\boldsymbol{b}}^{\mathrm{SERM}} \end{aligned} \tag{A.69}$$

In the last line, we again performed the factorization and dressing approximation reminiscent of the MCT approximation and equivalent to the one performed at the end of Equation (5.58). As discussed in Section 5.3.2, it is crucial to keep both terms.

Equation (A.69) concludes our discussion of the scalar Euclidean Random matrix model. The obtained set of self-consistent equations reads

$$\hat{\chi}_q^{\mathrm{SERM}}(s) = \overline{\frac{1}{N}\sum_{i,j=1}^{N} e^{-i\boldsymbol{q}\cdot(\boldsymbol{R}_i-\boldsymbol{R}_j)}\left[s^2+\underline{\boldsymbol{\mathcal{H}}}^{\mathrm{SERM}}\right]^{-1}_{ij}} = \frac{1}{s^2+\frac{q^2(c_q^{\mathrm{SERM}})^2}{1+\frac{\hat{\Sigma}_q^{\mathrm{SERM}}(s)}{(qc_q^{\mathrm{SERM}})^2}}} \tag{A.70a}$$

$$\hat{\Sigma}_q^{\mathrm{SERM}}(s) = \frac{1}{N}\sum_{\boldsymbol{k}} V_{\boldsymbol{q},\boldsymbol{k}}^{\mathrm{SERM}}\hat{\mathcal{V}}_{\boldsymbol{k},\boldsymbol{q}}^{\mathrm{SERM}}(s) \tag{A.70b}$$

$$\sum_{\boldsymbol{p}}\left[[s^2+k^2(c_k^{\mathrm{SERM}})^2]\delta_{\boldsymbol{k},\boldsymbol{p}} + s^2\frac{\hat{\Sigma}^{\mathcal{V}}(\boldsymbol{q},\boldsymbol{k},\boldsymbol{p},s)}{(pc_p^{\mathrm{SERM}})^2}\right]\hat{\mathcal{V}}_{\boldsymbol{p},\boldsymbol{q}}^{\mathrm{SERM}}(s) \tag{A.70c}$$

$$= S_{|\boldsymbol{q}-\boldsymbol{k}|}V_{\boldsymbol{q},\boldsymbol{k}}^{\mathrm{SERM}} + \sum_{\boldsymbol{p}}\frac{\hat{\Sigma}^{\mathcal{V}}(\boldsymbol{q},\boldsymbol{k},\boldsymbol{p},s)}{(pc_p^{\mathrm{SERM}})^2}S_{|\boldsymbol{q}-\boldsymbol{p}|}V_{\boldsymbol{q},\boldsymbol{p}}$$

$$\hat{\Sigma}^{\mathcal{V}}(\boldsymbol{q},\boldsymbol{k},\boldsymbol{p},s) = \frac{1}{N}\sum_{\boldsymbol{b}} V_{\boldsymbol{k},\boldsymbol{b}}^{\mathrm{SERM}}\hat{\chi}_b^{\mathrm{SERM}}(s)\Big(S_{|\boldsymbol{k}-\boldsymbol{b}|}\delta_{\boldsymbol{k},\boldsymbol{p}} + S_{|\boldsymbol{q}-\boldsymbol{k}|}\delta_{\boldsymbol{k}-\boldsymbol{b},\boldsymbol{q}-\boldsymbol{p}}\Big)V_{\boldsymbol{p},\boldsymbol{b}}^{\mathrm{SERM}}\,. \tag{A.70d}$$

The structure of this set of self-consistent equations already equals the set stated in Equation (5.66). Nevertheless, we have discussed in this section that the bare dispersion relation $(qc_q^{\mathrm{SERM}})^2$ and the bare vertex $V_{\boldsymbol{q},\boldsymbol{k}}^{\mathrm{SERM}}$ still deviate from their counterparts $(qc_q^{\perp})^2$ and the bare vertex $\underline{\boldsymbol{V}}_{\boldsymbol{q},\boldsymbol{k}}$ defined in the Equations (5.25) and (D.16) respectively. We discussed that the differences stem from the missing spatial projections. In the next section, we discuss the vector ERM model. The resulting set of equations becomes equivalent to Equation (5.66) after neglecting the longitudinal contributions.

A.2 Vector generalisation of the ERM model

As discussed in Section 2.2.4, the equations of motions for compression and shear do not decouple due to the disorder and initial stresses. Among other consequences, this leads to qualitatively differences between the scaling laws for the Bulk modulus B and for the hydrodynamic limit of shear-modulus $G = \lim_{q,s\to 0} s\hat{G}_q^{\perp}(s)$. We have discussed this in Section 2.3.1. Furthermore, the coupling of the different degrees of freedom drastically enhances sound attenuation. Thus, the vector nature of the displacements does indeed matter and the simplistic scalar ERM model does not suffice to capture the salient vibrational features of amorphous solids. Ultimately, one is interested in

developing a theory for

$$\chi_{\alpha\beta}^{\mathrm{ERM}}(\boldsymbol{q},s) \equiv \frac{1}{N}\overline{\sum_{i,j=1} e^{-i\boldsymbol{q}\cdot\boldsymbol{R}_i}\Big[s^2+\underline{\boldsymbol{\mathcal{H}}}^{\mathrm{ERM}}\Big]^{-1}_{i\alpha,j\beta} e^{i\boldsymbol{q}\cdot\boldsymbol{R}_j}} \tag{A.71}$$

with the Hessian defined in Equation (2.38):

$$\begin{aligned}\mathcal{H}_{i\vartheta,j\varphi}^{\mathrm{ERM}} &= \delta_{ij}\sum_{k\neq i} M_{i\vartheta,k\varphi} - M_{i\vartheta,j\varphi}\ ,\\ M_{i\vartheta,j\varphi} &= \frac{1}{m}\hat{R}_{ij}^{\vartheta}\Big(\mathcal{K}_{ij}-\frac{\mathcal{T}_{ij}}{R_{ij}}\Big)\hat{R}_{ij}^{\varphi}+\frac{\mathcal{T}_{ij}}{mR_{ij}}\delta_{\vartheta\varphi}\end{aligned} \tag{A.72}$$

The bond tension and the spring function arise from derivatives of the pair potential $\mathcal{T}(r) = \frac{\partial}{\partial r}U(r)$ and $\mathcal{K}(r) = \frac{\partial^2}{\partial r^2}U(r)$. In this section, we discuss the unstressed vector ERM model. Neglecting initial stresses and assuming that the system is perfectly annealed amounts to setting the bond tension $\mathcal{T}$ to zero. The theory developed in Section A.1 can then straightforwardly be generalized to include vector displacements by updating the spring function to a tensorial quantity:

$$\mathcal{K}(R_{ij}) \longrightarrow \hat{R}_{ij}^{\vartheta}\mathcal{K}(R_{ij})\hat{R}_{ij}^{\varphi} = \frac{1}{\partial R_{ij}^{\vartheta}}\frac{1}{\partial R_{ij}^{\varphi}}E_{\mathrm{Pot}}(\{\boldsymbol{R}_l\}_{l=1}^{N}) \equiv \mathcal{K}_{\vartheta\varphi}(R_{ij}) \tag{A.73}$$

Assuming that the spring function continues to depend on the Euclidean distances between the particles alone, the rotational symmetry of the distribution function Ψ_Q suggests that the susceptibility can be written as the sum of a longitudinal and a transverse contribution:

$$\hat{\underline{\boldsymbol{\chi}}}^{\mathrm{ERM}}(\boldsymbol{q},s) = \hat{\boldsymbol{q}}\hat{\boldsymbol{q}}\hat{\chi}_q^{\mathrm{ERM},\parallel}(s) + \Big[\underline{\mathbf{1}}-\hat{\boldsymbol{q}}\hat{\boldsymbol{q}}\Big]\hat{\chi}_q^{\mathrm{ERM},\perp}(s) \tag{A.74}$$

It becomes easy to generalize Equation (A.70) by introducing sums over the two spatial degrees of freedom. First of all, we include the spatial projection operators as

$$\underline{\boldsymbol{P}}^{\parallel}(\boldsymbol{q}) \equiv \hat{\boldsymbol{q}}\hat{\boldsymbol{q}}\ , \qquad \underline{\boldsymbol{P}}^{\perp}(\boldsymbol{q}) \equiv \underline{\mathbf{1}}-\hat{\boldsymbol{q}}\hat{\boldsymbol{q}}\ . \tag{A.75}$$

Furthermore, we need a normalization factor which counts the transverse and the longitudinal modes, respectively

$$\mathcal{N}^{\parallel} = 1 \ , \quad \mathcal{N}^{\perp} = \frac{1}{d-1} \tag{A.76}$$

Having this, we find for $\alpha, \beta, \nu, \mu \in \{\parallel, \perp\}$:

$$\hat{\chi}_q^{\mathrm{ERM},\alpha}(s) = \frac{\mathcal{N}^{\alpha}}{N} \mathrm{Tr} \left\{ \overline{\sum_{i,j=1}^{N} e^{-i\boldsymbol{q}\cdot(\boldsymbol{R}_i - \boldsymbol{R}_j)} \underline{\boldsymbol{P}}^{\alpha}(\boldsymbol{q}) \cdot \left[s^2 + \underline{\boldsymbol{\mathcal{H}}}^{\mathrm{ERM}} \right]^{-1}_{ij} \cdot \underline{\boldsymbol{P}}^{\alpha}(\boldsymbol{q})} \right\} \tag{A.77a}$$

$$= \frac{1}{s^2 + \frac{q^2 (c_q^{\alpha})^2}{1 + \frac{\hat{\Sigma}_q^{\mathrm{ERM},\alpha}(s)}{(q c_q^{\alpha})^2}}}$$

$$\hat{\Sigma}_q^{\mathrm{ERM},\alpha}(s) = \frac{\mathcal{N}^{\alpha}}{N} \mathrm{Tr} \left\{ \sum_{\beta \in \{\parallel,\perp\}} \sum_{\boldsymbol{k}} \underline{\boldsymbol{V}}^{\alpha\beta}_{\boldsymbol{q},\boldsymbol{k}} \cdot \underline{\boldsymbol{\mathcal{V}}}^{\beta\alpha}_{\boldsymbol{k},\boldsymbol{q}}(s) \right\} \tag{A.77b}$$

$$\sum_{\nu \in \{\parallel,\perp\}} \sum_{\boldsymbol{p}} \left[[s^2 + k^2 (c_k^{\beta})^2] \delta_{\beta\nu} \delta_{\boldsymbol{k},\boldsymbol{p}} + s^2 \frac{\underline{\boldsymbol{\Xi}}^{\beta\nu}(\boldsymbol{q},\boldsymbol{k},\boldsymbol{p},s)}{(p c_p^{\beta})^2} \right] \cdot \underline{\boldsymbol{\mathcal{V}}}^{\nu\alpha}_{\boldsymbol{p},\boldsymbol{q}}(s) \tag{A.77c}$$

$$= \sum_{\nu \in \{\parallel,\perp\}} \sum_{\boldsymbol{p}} \left[\delta_{\beta\nu} \delta_{\boldsymbol{k},\boldsymbol{p}} + \frac{\underline{\boldsymbol{\Xi}}^{\beta\nu}(\boldsymbol{q},\boldsymbol{k},\boldsymbol{p},s)}{(p c_p^{\beta})^2} \right] \cdot \left(\underline{\boldsymbol{V}}^{\alpha\nu}_{\boldsymbol{q},\boldsymbol{p}} \right)^T$$

$$\underline{\boldsymbol{\Xi}}^{\beta\nu}(\boldsymbol{q},\boldsymbol{k},\boldsymbol{p},s) = \frac{1}{N} \sum_{\mu \in \{\parallel,\perp\}} \sum_{\boldsymbol{b}} \underline{\boldsymbol{V}}^{\beta\mu}_{\boldsymbol{k},\boldsymbol{b}} \hat{\chi}_b^{\mu}(s) \Big(S_{|\boldsymbol{k}-\boldsymbol{b}|} \delta_{\boldsymbol{k},\boldsymbol{p}} + S_{|\boldsymbol{q}-\boldsymbol{k}|} \delta_{\boldsymbol{k}-\boldsymbol{b},\boldsymbol{q}-\boldsymbol{p}} \Big) \left(\underline{\boldsymbol{V}}^{\nu\mu}_{\boldsymbol{p},\boldsymbol{b}} \right)^T \tag{A.77d}$$

The transverse and longitudinal bare dispersion relation read

$$(q c_q^{\perp})^2 = \frac{n}{m(d-1)} \int d^d\boldsymbol{r} g(r) \Big(1 - e^{i\boldsymbol{q}\cdot\boldsymbol{r}} \Big) \hat{\boldsymbol{r}} \cdot [\underline{\mathbf{1}} - \hat{\boldsymbol{q}}\hat{\boldsymbol{q}}] \cdot \hat{\boldsymbol{r}} \frac{\partial^2}{\partial r^2} U(r) \tag{A.78a}$$

$$(q c_q^{\parallel})^2 = \frac{n}{m} \int d^d\boldsymbol{r} g(r) \Big(1 - e^{i\boldsymbol{q}\cdot\boldsymbol{r}} \Big) \hat{\boldsymbol{r}} \cdot \hat{\boldsymbol{q}}\hat{\boldsymbol{q}} \cdot \hat{\boldsymbol{r}} \frac{\partial^2}{\partial r^2} U(r) \ . \tag{A.78b}$$

The other input quantity is the bare vertex:

$$\begin{aligned}\underline{\boldsymbol{V}}^{\alpha\beta}_{\boldsymbol{q},\boldsymbol{k}} =&(qc_q^\alpha)^2\underline{\boldsymbol{P}}^\alpha(\boldsymbol{q})\cdot\underline{\boldsymbol{P}}^\beta(\boldsymbol{k})\\ &-n\int d^d\boldsymbol{r}d^d\boldsymbol{r}'\frac{ng^{(3)}(\boldsymbol{r},\boldsymbol{r}')-ng(r)+g(r)\Big(\delta(\boldsymbol{r}')+\delta(\boldsymbol{r}-\boldsymbol{r}')\Big)}{mS_{|\boldsymbol{q}-\boldsymbol{k}|}}\\ &\times e^{i(\boldsymbol{k}-\boldsymbol{q})\cdot\boldsymbol{r}'}\Big[1-e^{i\boldsymbol{q}\cdot\boldsymbol{r}}\Big]\hat{\boldsymbol{r}}\cdot\underline{\boldsymbol{P}}^\alpha(\boldsymbol{q})\underline{\boldsymbol{P}}^\beta(\boldsymbol{k})\cdot\hat{\boldsymbol{r}}\frac{\partial^2}{\partial r^2}U(r)\end{aligned} \tag{A.79}$$

with the indices $\alpha,\beta\in\{\|,\perp\}$. The the transpose vertex just replaces the order of the spatial projection operators:

$$\begin{aligned}\left(\underline{\boldsymbol{V}}^{\alpha\beta}_{\boldsymbol{q},\boldsymbol{k}}\right)^T =&(qc_q^\alpha)^2\underline{\boldsymbol{P}}^\beta(\boldsymbol{k})\cdot\underline{\boldsymbol{P}}^\alpha(\boldsymbol{q})\\ &-n\int d^d\boldsymbol{r}d^d\boldsymbol{r}'\frac{ng^{(3)}(\boldsymbol{r},\boldsymbol{r}')-ng(r)+g(r)\Big(\delta(\boldsymbol{r}')+\delta(\boldsymbol{r}-\boldsymbol{r}')\Big)}{mS_{|\boldsymbol{q}-\boldsymbol{k}|}}\\ &\times e^{i(\boldsymbol{k}-\boldsymbol{q})\cdot\boldsymbol{r}'}\Big[1-e^{i\boldsymbol{q}\cdot\boldsymbol{r}}\Big]\hat{\boldsymbol{r}}\cdot\underline{\boldsymbol{P}}^\beta(\boldsymbol{k})\underline{\boldsymbol{P}}^\alpha(\boldsymbol{q})\cdot\hat{\boldsymbol{r}}\frac{\partial^2}{\partial r^2}U(r)\end{aligned} \tag{A.80}$$

It is noteworthy, that $\underline{\boldsymbol{V}}^{\alpha\beta}_{\boldsymbol{q},\boldsymbol{k}\to 0} = (qc_q^\alpha)^2\underline{\boldsymbol{P}}^\alpha(\boldsymbol{q})\cdot\underline{\boldsymbol{P}}^\beta(\boldsymbol{k})$ holds. The second summand on the right-hand side of Equation (A.79) vanishes for $\boldsymbol{k}=0$. For the first of the four terms, this follows from the symmetry $g^{(3)}(\boldsymbol{r},\boldsymbol{r}')=g^{(3)}(\boldsymbol{r},\boldsymbol{r}-\boldsymbol{r}')$. The other three terms vanish immediately after integrating over $\boldsymbol{r}'$. Remarkably, the equation for the transverse dispersion relation $(c_q^\perp)^2$ and the equation for $V^{\perp,\perp}_{\boldsymbol{q},\boldsymbol{k}}$ agree with the corresponding quantities derived within the Self-Consistent Transverse Current Theory. The associated Equations are given in Equation (5.25) and Equation (D.16). This correspondence is why we have used the same symbols for the bare dispersion relation. Furthermore, the equivalence suggests that the equilibrium approach with a Boltzmann distribution is well enough tuned to describe the non-equilibrium phenomena of glassy and jammed states. The structure enters via the distribution functions $g^{(n)}$, and as we saw in Section A.1, the set of equations is independent of the concrete form of the particle distribution function Ψ_Q.

In 2003, Ciliberti and coworkers also proposed a self-consistent theory for the vector ERM model (Ciliberti *et al.*, 2003). The authors relied on a planar resumation scheme to construct their self-consistent model from a high-density perturbation theory. Thus, their theory fails to capture Rayleigh damping. Furthermore, the authors of (Ciliberti

et al., 2003) assumed a uniform distribution of the particles $S_q = g(r) = g^{(3)}(\boldsymbol{r}, \boldsymbol{r}') = 1$. Also adopting these simplifications, we recover the same vertex as in (Ciliberti *et al.*, 2003):

$$\underline{\boldsymbol{V}}^{\alpha\beta}_{\boldsymbol{q},\boldsymbol{k}} = \frac{n}{m} \int d^d\boldsymbol{r} \Big[e^{i\boldsymbol{q}\cdot\boldsymbol{r}} - e^{i(\boldsymbol{k}-\boldsymbol{q})\cdot\boldsymbol{r}} \Big] \hat{\boldsymbol{r}} \cdot \underline{\boldsymbol{P}}^{\alpha}(\boldsymbol{q}) \underline{\boldsymbol{P}}^{\beta}(\boldsymbol{k}) \cdot \hat{\boldsymbol{r}}\, \mathcal{K}(r) \tag{A.81}$$

Hence, the model outlined in Equation (A.77) becomes equivalent to the vector ERM model of Ciliberti and coworkers in a high density and low frequency approximation after additionally neglecting the non-planar contributions. This limiting case can be obtained as outlined in (Vogel *et al.*, 2025). However, and significantly, the planar model proposed in (Ciliberti *et al.*, 2003) predicts negative eigenvalues of the Hessian below an instability, which is an artefact of the approximations. In the next section, we argue that the Equation (A.77) does not predict negative eigenvalues by analysing the longitudinal and transverse modulus.

A.2.1 The Elastic Moduli

This section investigates the scaling of the longitudinal modulus B and the shear modulus G at the transition. We saw in Chapter 2 that the two elastic moduli scale differently with the distance to the transition in athermal soft particle systems. In the following, we investigate if the ERM model in general and our vector model displayed in Equation (A.77) in particular capture this subtle fact. Hereinafter, we restrict ourselves to three spatial dimensions $d = 3$. The moduli read

$$G = (v_0^{\mathrm{ERM},\perp})^2 = \lim_{q\to 0} \frac{(c_q^{\perp})^2}{1 + \frac{\hat{\Sigma}_q^{\mathrm{ERM},\perp}(0)}{(qc_q^{\perp})^2}} \,, \tag{A.82a}$$

$$B = (v_0^{\mathrm{ERM},\parallel})^2 = \lim_{q\to 0} \frac{(c_q^{\parallel})^2}{1 + \frac{\hat{\Sigma}_q^{\mathrm{ERM},\parallel}(0)}{(qc_q^{\parallel})^2}} \,. \tag{A.82b}$$

We start our investigations by writing for $\alpha \in \{\parallel, \perp\}$.

$$(qv_0^{\mathrm{ERM},\alpha})^2 = \lim_{q\to 0} \frac{(qc_q^{\alpha})^2}{1 + \frac{\hat{\Sigma_q^{\mathrm{ERM},\alpha}}(0)}{(qc_q^{\alpha})^2}} = (qc_q^{\alpha})^2 - \frac{\hat{\Sigma}_q^{\mathrm{ERM},\alpha}(0)}{1 + \frac{\hat{\Sigma}_q^{\mathrm{ERM},\alpha}(0)}{(qc_q^{\alpha})^2}} \,. \tag{A.83}$$

Next, we use an identity for the irreducible resolvent $\left[s^2 + \underline{\boldsymbol{\mathcal{H}}}^{\mathrm{ERM}}\right]^{-1}$ used in Equation (A.24), where the reduced Hessian is the tensor generalization of Equation (A.21). The following identity is valid for arbitrary operators A and B and complex numbers s^2 as long as the relevant inverses exist (Chichocki and W.Hess, 1987; Vogel and Fuchs, 2020):

$$[s^2 + A]^{-1} = [s^2 + A - B]^{-1}\Big(1 - B[s^2 + A]^{-1}\Big) \ . \tag{A.84}$$

We identify

$$A_{i\vartheta,j\varphi} = Q_i \mathcal{H}^{\mathrm{ERM}}_{i\vartheta,j\varphi} Q_j \ , \tag{A.85a}$$

$$B_{i\vartheta,j\varphi} = \frac{1}{N^2}\left[\sum_{k,r} \overline{e^{-i\boldsymbol{q}\cdot(\boldsymbol{R}_k - \boldsymbol{R}_r)} \underline{\boldsymbol{\mathcal{H}}}^{\mathrm{ERM}}_{kr}}\right]^{-1}_{\vartheta\beta} \sum_{p,l=1}^{N} Q_i \mathcal{H}^{\mathrm{ERM}}_{i\beta,l\tau} \rho_l(-\boldsymbol{q}) \mathcal{P} \rho_p(\boldsymbol{q}) \mathcal{H}^{\mathrm{ERM}}_{p\tau,j\varphi} Q_j \ . \tag{A.85b}$$

Here, we used the sum convention again for the spatial Greek indices. As in Chapter 1, we emphasize the notational inconsistency that $\underline{\boldsymbol{\mathcal{H}}}^{\mathrm{ERM}}_{ij}$ denotes a $d \times d$ matrix while $\underline{\boldsymbol{\mathcal{H}}}^{\mathrm{ERM}}$ represents a $N \times d \times N \times d$ tensor of order four or a $Nd \times Nd$ block matrix. The identity in Equation (A.84) implies that the susceptibility of the vector ERM model can be written as

$$\underline{\boldsymbol{\chi}}^{\mathrm{ERM}}(\boldsymbol{q}, s) = \Bigg[s^2 + \frac{1}{N} \overline{\sum_{i,j} e^{-i\boldsymbol{q}\cdot(\boldsymbol{R}_i - \boldsymbol{R}_j)} \underline{\boldsymbol{\mathcal{H}}}^{\mathrm{ERM}}_{ij}} \tag{A.86}$$

$$- \frac{1}{N} \overline{\sum_{ijkl} e^{-i\boldsymbol{q}\cdot\boldsymbol{R}_i} \underline{\boldsymbol{\mathcal{H}}}^{\mathrm{ERM}}_{ik} Q_k \cdot \left[s^2 + \boldsymbol{Q}\underline{\boldsymbol{\mathcal{H}}}^{\mathrm{ERM}}\boldsymbol{Q}\right]^{-1}_{kl} \cdot Q_l \underline{\boldsymbol{\mathcal{H}}}^{\mathrm{ERM}}_{lj} e^{i\boldsymbol{q}\cdot\boldsymbol{R}_j}} \Bigg]^{-1} \ .$$

Here, we wrote $(\boldsymbol{Q}\underline{\boldsymbol{\mathcal{H}}}\boldsymbol{Q})_{kl} = Q_k \underline{\boldsymbol{\mathcal{H}}}_{kl} Q_l$. This expression resembles the expression studied in (Szamel and Flenner, 2022). The term renormalizing the bare moduli has been labelled the non-affine contribution (Mizuno *et al.*, 2016a; Szamel and Flenner, 2022). The reason is that the stresses built up due to a deformation couple the longitudinal and the transverse degrees of freedom. On the other hand, the bare elastic constants were labelled the affine contributions to B and G. The elastic constants B and G can be

obtained from the limit $\boldsymbol{q}, s \to 0$. Here, the susceptibility reads:

$$\left(\underline{\boldsymbol{\chi}}^{\mathrm{ERM}}(\boldsymbol{q} \to 0, 0)\right)^{-1} = -\frac{1}{2N}\overline{\sum_{i,j}(\boldsymbol{q}\cdot\boldsymbol{R}_{ij})^2\underline{\boldsymbol{\mathcal{H}}}^{\mathrm{ERM}}_{ij}} \tag{A.87}$$
$$-\frac{1}{N}\overline{\sum_{ijkl} e^{-i\boldsymbol{q}\cdot\boldsymbol{R}_i}\underline{\boldsymbol{\mathcal{H}}}^{\mathrm{ERM}}_{ik}Q_k\cdot\left[\boldsymbol{Q}\underline{\boldsymbol{\mathcal{H}}}^{\mathrm{ERM}}\boldsymbol{Q}\right]^{-1}_{kl}\cdot Q_l\underline{\boldsymbol{\mathcal{H}}}^{\mathrm{ERM}}_{lj}e^{i\boldsymbol{q}\cdot\boldsymbol{R}_j}} \ .$$

From this, we can obtain the bare or affine elastic constants B_A and G_A. Choosing $\boldsymbol{q} = q\hat{\boldsymbol{e}}_z$, we find

$$G_A = (c_0^{\perp})^2 = \frac{2\pi}{15}\frac{n}{m}\int_0^\infty drg(r)r^4\frac{\partial^2 U(r)}{\partial r^2} \ , \tag{A.88a}$$
$$B_A = (c_0^{\parallel})^2 = \frac{2\pi}{5}\frac{n}{m}\int_0^\infty drg(r)r^4\frac{\partial^2 U(r)}{\partial r^2} \tag{A.88b}$$

The two bare moduli are equivalent to the expressions in (Zwanzig and Mountain, 1965). Following (Mizuno *et al.*, 2016a). We can also write the elastic constants as averages over the contributions of single contacts $B_A = \frac{1}{N}\sum_{ij}\langle B_A^{ij}\rangle$ and $G_A = \frac{1}{N}\sum_{ij}\langle G_A^{ij}\rangle$ with

$$B_A^{ij} = \frac{1}{2m}R_{ij}^2\cos(\theta_{ij})^4\mathcal{K}(R_{ij}) \ , \tag{A.89a}$$
$$G_A^{ij} = \frac{1}{4m}R_{ij}^2\cos(\theta_{ij})^2\sin(\theta_{ij})^2\mathcal{K}(R_{ij}) \ . \tag{A.89b}$$

Here, we used the spherical basis $(x, y, z) = r(\sin(\theta)\cos(\phi), \sin(\theta)\sin(\phi), \cos(\theta))$. In this spherical basis θ_{ij} defines the polar angle of the vector $\boldsymbol{R}_{ij} = \boldsymbol{R}_i - \boldsymbol{R}_j$ and ϕ_{ij} the associated azimuthal angle. Noticeable, this result slightly deviates from the convention used in (Mizuno *et al.*, 2016a) where the authors define the elastic constants via a uniform compression of each single bond and only looked at a single component of the stress tensor to quantify the shear modulus.

Secondly, we look at the non-affine contribution for $\boldsymbol{q} \to 0$. We start with rewriting the involved states as

$$\lim_{\boldsymbol{q}\to 0} \sum_i e^{-i\boldsymbol{q}\cdot\boldsymbol{R}_i} \underline{\boldsymbol{\mathcal{H}}}^{\mathrm{ERM}}_{ij} Q_j = \lim_{\boldsymbol{q}\to 0} \frac{e^{-i\boldsymbol{q}\cdot\boldsymbol{R}_j}}{m} \sum_l \left(1 - e^{-i\boldsymbol{q}\cdot\boldsymbol{R}_{lj}}\right) \hat{\boldsymbol{R}}_{lj} \mathcal{K}(R_{lj}) \hat{\boldsymbol{R}}_{lj} Q_j$$
$$= \frac{1}{m} \sum_l i(\boldsymbol{q}\cdot\boldsymbol{R}_{lj}) \hat{\boldsymbol{R}}_{lj} \mathcal{K}(R_{lj}) \hat{\boldsymbol{R}}_{lj} + \mathcal{O}(q^2) \ . \tag{A.90}$$

Noticeable, the projection Q_j disappears as it only affects higher orders in $\mathcal{O}(\boldsymbol{q})$ Next, we introduce the normalized $3N$ eigenvectors $\boldsymbol{e}^r$ of the Hessian $\underline{\boldsymbol{\mathcal{H}}}^{\mathrm{ERM}}$ with $r \in \{1, ...3N\}$ via the eigenvalue equation

$$(\omega^r)^2 \boldsymbol{e}^r = \underline{\boldsymbol{\mathcal{H}}}^{\mathrm{ERM}} \cdot \boldsymbol{e}^r \ . \tag{A.91}$$

Here, we have interpreted $\underline{\boldsymbol{\mathcal{H}}}$ as a real symmetric $3N \times 3N$ matrix. Its eigenspace forms a basis of $\mathbb{R}^{3N}$. The eigenvalues of the Hessian are given as

$$(\omega^r)^2 = \boldsymbol{e}^r \cdot \underline{\boldsymbol{\mathcal{H}}} \cdot \boldsymbol{e}^r = \frac{1}{2} \sum_{ij} \mathcal{K}(R_{ij}) (e^r_{ij})^2 \ , \tag{A.92}$$

where we have introduced the notation $e^r_{ij} = \hat{\boldsymbol{R}}_{ij} \cdot (\boldsymbol{e}^r_i - \boldsymbol{e}^r_j)$. The vector $\boldsymbol{e}^r_i$ is the 3-dimensional polarisation of the i^{th} particle in the eigemode $\boldsymbol{e}^r$, a $3N$-dimensional vector. As a subsequential step, we realize that the orthogonal projection Q_i takes out the uniform displacements of all particles for $\boldsymbol{q} \to 0$:

$$Q_i \underset{\boldsymbol{q}\to 0}{\longrightarrow} 1 - \mathcal{P}. \tag{A.93}$$

Here, $\mathcal{P}$ denotes the average over the disorder. Ignoring rattlers, the three uniform displacements are the only null modes of the Hessian in the jammed state. Thus, we can write above the transition

$$\lim_{\boldsymbol{q}\to 0} Q_i \underline{\boldsymbol{\mathcal{H}}}^{\mathrm{ERM}}_{il} Q_l = \sum_{r:\{\omega^r>0\}} \boldsymbol{e}^r_i (\omega^r)^2 \boldsymbol{e}^r_l \tag{A.94}$$

The sum runs from $r = 1$ to $r = 3N - 3$, the number of eigenmodes with non-zero frequencies. Using the fact that,

$$i(\boldsymbol{q} \cdot \boldsymbol{R}_{lj})\hat{\boldsymbol{R}}_{lj}\mathcal{K}(R_{lj})\hat{\boldsymbol{R}}_{lj} = -i(\boldsymbol{q} \cdot \boldsymbol{R}_{jl})\hat{\boldsymbol{R}}_{jl}\mathcal{K}(R_{jl})\hat{\boldsymbol{R}}_{jl} \tag{A.95}$$

holds and relying on the idea that the eigenvectors of a symmetric real matrix $\underline{\boldsymbol{\mathcal{H}}}^{\mathrm{ERM}}$ span the whole space, we arrive at a concise expression for the non-affine contributions in the limit $\boldsymbol{q} \to 0$

$$\begin{aligned} &\frac{1}{N}\overline{\sum_{ijkl} e^{-i\boldsymbol{q}\cdot\boldsymbol{R}_i}\underline{\boldsymbol{\mathcal{H}}}^{\mathrm{ERM}}_{ij} Q_j \cdot \left[\boldsymbol{Q}\underline{\boldsymbol{\mathcal{H}}}^{\mathrm{ERM}}\boldsymbol{Q}\right]^{-1}_{jk} \cdot Q_k \underline{\boldsymbol{\mathcal{H}}}^{\mathrm{ERM}}_{kl} e^{i\boldsymbol{q}\cdot\boldsymbol{R}_l}} \\ &\quad \xrightarrow[\boldsymbol{q}\to 0]{} \frac{1}{N}\sum_{kl,ij}\overline{\sum_{r:\{\omega^r>0\}} \Xi^r_{ij}\frac{1}{(\omega^r)^2}\Xi^r_{kl}}. \end{aligned} \tag{A.96}$$

Here, we have defined

$$\Xi^r_{ij} \equiv \frac{1}{2m}(\boldsymbol{q} \cdot \boldsymbol{R}_{ij})\mathcal{K}(R_{ij})\hat{\boldsymbol{R}}_{ij}e^r_{ij} \ , \tag{A.97}$$

which is connected to the vector field of forces resulting from affine displacements (Maloney, 2006; Maloney and Lemaître, 2004, 2006; Mizuno *et al.*, 2016a). The crucial point in the derivation of Equation (A.96) is the identity

$$\sum_{ij}(\boldsymbol{q} \cdot \boldsymbol{R}_{ij})\hat{\boldsymbol{R}}_{ij}\mathcal{K}(R_{ij})\hat{\boldsymbol{R}}_{ij} \cdot \boldsymbol{e}^r_j = \frac{1}{2}\sum_{ij}(\boldsymbol{q} \cdot \boldsymbol{R}_{ij})\hat{\boldsymbol{R}}_{ij}\mathcal{K}(R_{ij})\hat{\boldsymbol{R}}_{ij} \cdot (\boldsymbol{e}^r_j - \boldsymbol{e}^r_i) \ . \tag{A.98}$$

So far, the results are in complete analogy to the considerations in (Mizuno *et al.*, 2016a). Using Equation (A.96), we can write down the non-affine contributions to the

longitudinal modulus B_N and the shear modulus G_N in $d = 3$:

$$B_N = \frac{1}{q^4 N} \sum_{ijkl} \sum_{r:\{\omega^r>0\}} \langle \boldsymbol{q} \cdot \boldsymbol{\Xi}^r_{ij} \frac{1}{(\omega^r)^2} \boldsymbol{\Xi}^r_{kl} \cdot \boldsymbol{q} \rangle \tag{A.99a}$$

$$= \frac{1}{4m^2 N} \sum_{ijkl} \sum_{r:\{\omega^r>0\}} \Big\langle \cos(\theta_{ij})^2 \mathcal{K}(R_{ij}) R_{ij} \frac{e^r_{ij} e^r_{kl}}{(\omega^r)^2} \cos(\theta_{kl})^2 \mathcal{K}(R_{kl}) R_{kl} \Big\rangle$$

$$G_N = \frac{1}{2q^2 N} \mathrm{Tr} \Big\{ \sum_{ijkl} \sum_{r:\{\omega^r>0\}} \langle (\underline{\mathbf{1}} - \hat{\boldsymbol{q}}\hat{\boldsymbol{q}}) \cdot \boldsymbol{\Xi}^r_{ij} \frac{1}{(\omega^r)^2} \boldsymbol{\Xi}^r_{kl} \cdot (\underline{\mathbf{1}} - \hat{\boldsymbol{q}}\hat{\boldsymbol{q}}) \rangle \} \tag{A.99b}$$

$$= \frac{1}{8m^2 N} \sum_{ijkl} \sum_{r:\{\omega^r>0\}} \Big\langle \cos(\theta_{ij}) \sin(\theta_{ij}) (\cos(\phi_{ij}) + \sin(\phi_{ij})) \mathcal{K}(R_{ij}) R_{ij} \tag{A.99c}$$

$$\times \frac{e^r_{ij} e^r_{kl}}{(\omega^r)^2} \cos(\theta_{kl}) \sin(\theta_{kl}) (\cos(\phi_{kl}) + \sin(\phi_{kl})) \mathcal{K}(R_{kl}) R_{kl} \Big\rangle$$

Remarkably, no approximations have been made, and these results are exact. Before investigating whether our self-consistent model reproduces these equations, we first look at the unjamming transition in the soft particle systems with harmonic interactions.

A.2.2 Example: Soft particles with harmonic interactions

We have already discussed the phenomenology of the soft particle system in Section 2.3. Looking at an interaction potential $U(r) \propto (r/\sigma - 1)^\alpha \Theta(1 - r/\sigma)$, we saw that the longitudinal modulus scales as $B \propto \Delta\phi^{\alpha-2}$ and the shear modulus scales as $B \propto \Delta\phi^{\alpha-3/2}$. Here $\Delta\phi = \phi - \phi_c$ is the excess volume fraction and ϕ_c is the volume fraction at the transition. The parameter α specifies the soft sphere potential. Importantly, it has been observed in simulations that the bulk modulus jumps at the transition for a harmonic interaction ($\alpha = 2$) (O'Hern *et al.*, 2003). Following (Mizuno *et al.*, 2016a), we will show that B stays finite at the point of isostaticity criterion for $\alpha = 2$.

As outlined in Section 2.3, the unjamming transition occurs at $z = 2d = 6$. In soft sphere systems, the particles lose contact at the transition. Thus, one has for harmonic i($\alpha = 2$) nteractions: $R_{ij}/\sigma = 1 = \frac{\mathcal{K}(R_{ij})}{m\omega_0^2}$ for all the $N_c = \frac{zN}{2}$ contacts (i, j). Hence, the critical affine longitudinal modulus B_{Ac} and shear modulus G_{Ac} read for harmonic

interactions:

$$B_{Ac}^{\alpha=2} = \frac{\omega_0^2}{2N} \sum_{(i,j)\in N_c} \langle \cos(\theta_{ij})^4 \rangle \ , \tag{A.100a}$$

$$G_{Ac}^{\alpha=2} = \frac{\omega_0^2}{4N} \sum_{(i,j)\in N_c} \langle \cos(\theta_{ij})^2 \sin(\theta_{ij})^2 \rangle \ . \tag{A.100b}$$

Here, we used Equation (A.89). The notation $\sum_{(i,j)\in N_c} = \sum_{i,j=1}^{N} \Theta(1 - R_{ij}/\sigma)$ refers to a sum over particles in contact. It has been numerically confirmed in (Mizuno *et al.*, 2016a) that the joint distribution $\Psi_\theta(\phi_{ij}, \theta_{ij})$ of the ϕ_{ij} and θ_{ij} can be written as

$$\Psi_\theta(\phi_{ij}, \theta_{ij}) \approx \frac{1}{2\pi} \sin(\theta_{ij}) \tag{A.101}$$

with $\theta_{ij} \in [0, \pi]$ and $\phi_{ij} \in [0, 2\pi]$. Thus, we find

$$B_{Ac}^{\alpha=2} = \frac{6\omega_0^2}{5} \tag{A.102a}$$

$$G_{Ac}^{\alpha=2} = \frac{6\omega_0^2}{15} = \frac{2\omega_0^2}{5} \ . \tag{A.102b}$$

To determine the non-affine contributions to the moduli at the transition, we split up the sum over the particles as $\sum_{ijkl} \to \sum_{(i,j)\in N_c} \sum_{(k,l)\in N_c}$. To make further analytically progress, we assume that the projections of the distance difference arising from affine motion $\hat{\boldsymbol{R}}_{ij} \cdot (\boldsymbol{e}_i^r - \boldsymbol{e}_j^r)$ are independent of the angle θ_{ij}. Furthermore, we assume that θ_{ij} and θ_{kl} are uncorrelated for $(i, j) \neq (k, l)$. These two assumptions appear reasonable for disordered systems and have been confirmed numerically (Mizuno *et al.*, 2016a). Next, we isolate the sum over the same contacts to obtain the bulk modulus at the unjamming transition:

$$B_{Nc}^{\alpha=2} = B_{Ac}^{\alpha=2} + \frac{1}{2m^2N} \Big\langle \sum_{r\in\{\omega^r>0\}} \sum_{(i,j)} \sum_{(k,l)\neq(i,j)} \cos(\theta_{ij})^2 \frac{e_{ij}^r e_{kl}^r}{(\omega^r)^2} \cos(\theta_{kl})^2 \Big\rangle \tag{A.103}$$

Here, we used Equation (A.92) to identify the affine term:

$$B_{Ac}^{\alpha=2} = \frac{1}{4m^2N} \Big\langle \sum_{(i,j)\in N_c} \sum_{r\in\{\omega^r>0\}} \cos(\theta_{ij})^4 \frac{(e_{ij}^r)^2}{(\omega^r)^2} \Big\rangle \ . \tag{A.104}$$

The point is that the eigenvalue equation reads at the transition

$$(\omega^r)^2 = \boldsymbol{e}^r \cdot \underline{\boldsymbol{\mathcal{H}}} \cdot \boldsymbol{e}^r = \frac{1}{2} \sum_{(i,j)\in N_c} (e_{ij}^r)^2 \ . \tag{A.105}$$

All in all, we find for the longitudinal modulus

$$B_c^{\alpha=2} = B_{Ac}^{\alpha=2} - B_{Nc}^{\alpha=2} = -\omega_0^2 \frac{2(3N-1)}{3} \Big\langle \sum_{r:\omega^r>0} \frac{e_{ij}^r e_{kl}^r}{(\omega^r)^2} \Big\rangle_{(i,j)\neq(k,l)} \ . \tag{A.106}$$

It has been show for small systems that the average in the last line is negative but finite at the transition (Mizuno *et al.*, 2016a). Thus, the longitudinal modulus $B^{\alpha=2}$ jumps at $z = 6$ from a finite value to zero. On the other hand, the shear modulus supposedly vanishes continuously at the transition. Here, we have

$$\begin{aligned} G_{Nc}^{\alpha=2} &= G_{Ac}^{\alpha=2} + \frac{1}{8m^2} \Big\langle \sum_{r:\omega^r>0} \sum_{(i,j)} \sum_{(k,l)\neq(i,j)} \cos(\theta_{ij}) \sin(\theta_{ij}) (\cos(\phi_{ij}) + \sin(\phi_{ij})) \\ &\qquad \times \frac{e_{ij}^r e_{kl}^r}{(\omega^r)^2} \cos(\theta_{kl}) \sin(\theta_{kl}) (\cos(\phi_{kl}) + \sin(\phi_{kl})) \Big\rangle \\ &= G_{Ac}^{\alpha=2} \ . \end{aligned} \tag{A.107}$$

Again, when writing down this result, we relied on our assumption that the angles θ_{ij} and θ_{kl} are statistically independent for $(i,j) \neq (k,l)$ and that e_{ij}^r also is not correlated with θ_{ij}. Hence, the affine and non-affine contributions of the shear modulus cancel each other exactly at the transition. The transverse modes are more susceptible to non-affine displacements.

A.2.3 The non-affine contribution for arbitrary structures

In this section, we ask if general differences exist between the longitudinal modulus B and the shear modulus G at the transition. Are the differences discussed in Section A.2.2 due to the particles losing contact, or are there general qualitative differences? Let us agree on the following assumptions for any disordered structure and any density:

1) The distribution of the angles ϕ_{ij} and θ_{ij} is given by

$$\Psi_\theta(\phi_{ij}, \theta_{ij}) \approx \frac{1}{2\pi} \sin(\theta_{ij}) \tag{A.108}$$

with $\theta_{ij} \in [0, \pi]$ and $\phi_{ij} \in [0, 2\pi]$

2) The projections of the distance difference arising from affine motion $\hat{\boldsymbol{R}}_{ij} \cdot (\boldsymbol{e}_i^r - \boldsymbol{e}_j^r)$ are statistically independent of the angle θ_{ij}. Here, $\boldsymbol{e}_i^r$ denotes the polarisation of the i^{th} particle in the eigenmode $\boldsymbol{e}^r$.

3) The angles θ_{ij} and θ_{kl} are uncorrelated for $(i, j) \neq (k, l)$.

These assumptions have been verified numerically in a soft sphere system with harmonic interactions (Mizuno *et al.*, 2016a). Furthermore, the results appear reasonable for uniform particle distributions. We define the form factor

$$\mathcal{F}_{ij,kl} = \frac{1}{4m^2 N} \Big\langle \sum_{r:\{\omega^r>0\}} \mathcal{K}(R_{ij}) R_{ij} \frac{e_{ij}^r e_{kl}^r}{(\omega^r)^2} \mathcal{K}(R_{kl}) R_{kl} \Big\rangle_{\{\boldsymbol{e}\}} \tag{A.109}$$

Here, the index $\{\boldsymbol{e}\}$ indicates that the average is taken with respect to the distribution of the eigenmodes $(\boldsymbol{e})$ and the eigenvalues $(\omega^r)^2$ of $\underline{\boldsymbol{\mathcal{H}}}^{\text{ERM}}$. Noticable, $\mathcal{F}_{ij,kl}$ is not expected to be zero for $(i, j) \neq (k, l)$. For example, it has been calculated in (Mizuno *et al.*, 2016a) that $\mathcal{F}_{ij,kl}$ is non-zero for different bonds at the soft sphere transition $z = 2d = 6$. However, we can also construct an argument independent of the structure. For simplification, we look at the high density limit $n \to \infty$, where the system can be regarded as an elastic medium. The eigenmodes can safely be approximated as plane waves for high densities and in the low eigenvalue limit. We look at a longitudinal sound mode characterized by the wavevector $\boldsymbol{k}$. In the high density limit $n \to \infty$, the associated eigenvalue reads $\omega^r \approx k c_0^{\parallel}$ for sufficiently small k. The polarisation of the i^{th} particle associated with this eigenmode can be written as

$$\boldsymbol{e}_i \approx \frac{a}{\sqrt{N}} \hat{\boldsymbol{e}}_z \sin(\boldsymbol{k} \cdot \boldsymbol{R}_i) \ . \tag{A.110}$$

Here, $a = \mathcal{O}(1)$ is an normalisation constant of order 1, *i.e.* independent of N. Furthermore, we have set $\boldsymbol{k} = k\hat{\boldsymbol{e}}_z$, where $\hat{\boldsymbol{e}}_z = (0, 0, 1)$ is the uni-vector in $\hat{z}$-direction. For simplicity, we again look at an harmonic interaction $\alpha = 2$ with $\mathcal{K}(r) = m\omega_0^2 \Theta(r/\sigma - 1)$, with the particle diameter σ. For $k \gg \frac{2\pi}{\sigma}$ we find for two particles in contact $R_{ij} < \sigma$:

$$\begin{aligned} e_{ij}^{kc_0^{\parallel}} = \hat{\boldsymbol{R}}_{ij} \cdot (\boldsymbol{e}_i^r - \boldsymbol{e}_j^r) &= \frac{a}{\sqrt{N}} \cos(\theta_{ij}) \big(\sin(\boldsymbol{k} \cdot \boldsymbol{R}_i) - \sin(\boldsymbol{k} \cdot \boldsymbol{R}_i - \boldsymbol{k} \cdot \boldsymbol{R}_{ij}) \big) \\ &\underset{R_{ij} \leq \sigma \ll k^{-1}}{\approx} k \cos(\theta_{ij})^2 R_{ij} \cos(\boldsymbol{k} \cdot \boldsymbol{R}_i) \end{aligned} \tag{A.111}$$

Thus, we find for $l \neq k$ for this particular eigenmode

$$\mathcal{F}^{kc_0^{\parallel}}_{ik,il} \approx \frac{a^2\omega_0^4}{4N^2(c_0^{\parallel})^2}\langle\cos(\theta_{ik})^2\cos(\theta_{il})^2 R_{il}^2 R_{ik}^2\cos(\boldsymbol{k}\cdot\boldsymbol{R}_i)^2\Theta\left(\frac{R_{ik}}{\sigma}-1\right)\Theta\left(\frac{R_{il}}{\sigma}-1\right)\rangle \tag{A.112}$$

$$> 0\ .$$

Summing over the connected neighbours k, l with $k \neq l$ gives a factor $z(z-1)$ where z is the average contact number. Thus $z(z-1) = \mathcal{O}(1)$ is of order unity. The sum over the index i gives a factor N. For $n \to \infty$, there are of order $\mathcal{O}(N)$ longitudinal sound modes. Thus, we expect $\mathcal{F}_{ij,kl}$ to be finite for $(i,j) \neq (k,l)$ even for $N \to \infty$. After having established that the Formfactor $\mathcal{F}$ is generally non-zero, we can write down the general non-affine contributions to the longitudinal modulus and the shear modulus:

$$\begin{aligned} B_N &= \sum_{ij}\langle\cos(\theta_{ij})^4\rangle_\theta\,\mathcal{F}_{ij,ij} + \sum_{(i,j)}\sum_{(k,l)\neq(i,j)}\langle\cos(\theta_{ij})^2\rangle_\theta\langle\cos(\theta_{kl})^2\rangle_\theta\,\mathcal{F}_{ij,kl} \qquad \text{(A.113a)}\\ &= \frac{2}{5}\sum_{ij}\mathcal{F}_{ij,ij} + \frac{4}{9}\sum_{(i,j)}\sum_{(k,l)\neq(i,j)}\mathcal{F}_{ij,kl} \\ G_N &= \frac{1}{2}\sum_{ij}\langle\cos(\theta_{ij})^2\sin(\theta_{ij})^2\rangle_\theta\,\mathcal{F}_{ij,ij} \qquad \text{(A.113b)}\\ &\quad + \frac{1}{2}\sum_{(i,j)}\sum_{(k,l)\neq(i,j)}\langle\cos(\theta_{ij})\sin(\theta_{ij})(\cos(\phi_{ij})+\sin(\phi_{ij}))\rangle_\theta \\ &\qquad\qquad \times\langle\cos(\theta_{kl})\sin(\theta_{kl})(\cos(\phi_{kl})+\sin(\phi_{kl}))\rangle_\theta\,\mathcal{F}_{ij,kl} \\ &= \frac{2}{15}\sum_{ij}\mathcal{F}_{ij,ij} \end{aligned}$$

Here, the index θ indicates the average over the angles θ_{ij} and ϕ_{ij}. We identify the transition as the point where $v_0^{\perp} = 0$ holds. Here, the affine and non-affine contributions to the shear modulus become equal. From Equation (A.89) follows at the transition

$$G_{Ac} = G_{N_c} \Longrightarrow \sum_{ij}\mathcal{F}_{ij,ij} = \frac{1}{2m}\langle\sum_{ij}R_{ij}^2\mathcal{K}(R_{ij})\rangle \tag{A.114}$$

This is valid for any structure and interaction in an unstressed system with only repulsive interactions. Thus, we find for the longitudinal modulus

$$B_{Ac} - B_{Nc} = -\frac{4}{9} \sum_{(i,j)} \sum_{(k,l)\neq(i,j)} F_{ij,kl} \geq 0 \ . \tag{A.115}$$

Hence, we expect the longitudinal modulus B to behave qualitatively differently at the transition than the shear modulus. In Chapter 2, and Equation (2.44), we have introduced the mean overlap $\langle\delta\rangle$ between the particles. Let us assume a soft particle interaction

$$U(r_{ij}) = \begin{cases} \epsilon\delta_{ij}^{\alpha} & \text{for } \delta_{ij} \geq 0 \\ 0 & \text{else} \end{cases} \tag{A.116}$$

with $\delta_{ij} = 1 - \frac{r_{ij}}{\sigma}$. From Equation (A.115) follows, that

$$B \propto \langle\delta\rangle^{\alpha-2} \tag{A.117}$$

holds close to the transition. Notably, this implies that the longitudinal modulus stays finite at the transition when one assumes a uniform distribution of the particles. For the athermal soft particle systems studied numerically and discussed in Chapter 2, the bulk modulus becomes zero at the unjamming transition, and Equation (A.117) confirms the results of *e.g.* (O'Hern *et al.*, 2003). The next section discusses whether our self-consistent model can reproduce this non-trivial result.

A.2.4 The self-consistent model's prediction for the elastic moduli

In this section, we answer the question whether the self-consistent model proposed in Equation (A.77) captures the non-trivial scaling of the elastic constants. We start our considerations by writing down the bare moduli. The bare transverse dispersion relation in $d = 3$ reads:

$$\begin{aligned}(qc_q^{\perp})^2 &= \frac{n}{2m}\int_0^{\infty} drg(r)r^2\frac{\partial^2 U(r)}{\partial r^2}\int_0^{\pi}\sin(\theta)\big(1-\cos(\theta)^2\big)\Big[1-e^{-iqr\cos(\theta)}\Big] \\ &= 4\pi\frac{n}{m}\int_0^{\infty} drg(r)r^2\frac{\partial^2 U(r)}{\partial r^2}\left(\frac{1}{3}+\frac{(qr)\cos(qr)-\sin(qr)}{(qr)^3}\right) \\ &\underset{q\to 0}{\longrightarrow} q^2\frac{2\pi}{15}\frac{n}{m}\int_0^{\infty} drg(r)r^4\frac{\partial^2 U(r)}{\partial r^2}\ ,\end{aligned} \tag{A.118}$$

The bare longitudinal dispersion relation in $d = 3$ reads

$$\begin{aligned}(qc_q^{\parallel})^2 &= \frac{n}{m}\int_0^{\infty} drg(r)r^2\frac{\partial^2 U(r)}{\partial r^2}\int_0^{\pi}\sin(\theta)\cos(\theta)^2\Big[1-e^{-iqr\cos(\theta)}\Big] \\ &= 4\pi\frac{n}{m}\int_0^{\infty} drg(r)r^2\frac{\partial^2 U(r)}{\partial r^2}\left(\frac{1}{3}-\frac{\sin(qr)}{qr}-2\frac{(qr)\cos(qr)-\sin(qr)}{(qr)^3}\right) \\ &\underset{q\to 0}{\longrightarrow} q^2\frac{2\pi}{5}\frac{n}{m}\int_0^{\infty} drg(r)r^4\frac{\partial^2 U(r)}{\partial r^2}\end{aligned} \tag{A.119}$$

From the zero frequency limit ($s = 0$) of the self-energy follows a concise expression for the elastic moduli. Equation (A.83) leads to the linear Equation

$$\sum_p\begin{pmatrix}\delta_{q,p}-C_{q,p}^{\parallel,\parallel} & -C_{q,p}^{\parallel,\perp}\\ -C_{q,p}^{\perp,\parallel} & \delta_{q,p}-C_{q,p}^{\perp,\perp}\end{pmatrix}\cdot\begin{pmatrix}\frac{1}{(v_p^{\parallel})^2}\\ \frac{1}{(v_p^{\perp})^2}\end{pmatrix}=\begin{pmatrix}\frac{1}{(\tilde{c}_q^{\parallel})^2}\\ \frac{1}{(\tilde{c}_q^{\perp})^2}\end{pmatrix}\ . \tag{A.120}$$

This is the generalisation of Equation (5.89). The inverse Born renormalised compliances read

$$\frac{1}{(\tilde{c}_q^{\parallel})^2}=\frac{1}{(c_q^{\parallel})^2}+\frac{1}{Nq^2(c_q^{\parallel})^4}\mathrm{Tr}\left\{\sum_{\beta\in\{\parallel\perp\}}\sum_{\boldsymbol{k}}\frac{1}{k^2(c_k^{\beta})^2}\underline{\boldsymbol{V}}_{\boldsymbol{q},\boldsymbol{k}}^{\parallel,\beta}\cdot\left(\underline{\boldsymbol{V}}_{\boldsymbol{q},\boldsymbol{k}}^{\parallel,\beta}\right)^T\right\} \tag{A.121a}$$

$$\frac{1}{(\tilde{c}_q^{\perp})^2}=\frac{1}{(c_q^{\perp})^2}+\frac{1}{Nq^2(c_q^{\perp})^4}\mathrm{Tr}\left\{\sum_{\beta\in\{\parallel\perp\}}\sum_{\boldsymbol{k}}\frac{S_{|\boldsymbol{q}-\boldsymbol{k}|}}{k^2(c_k^{\beta})^2}\underline{\boldsymbol{V}}_{\boldsymbol{q},\boldsymbol{k}}^{\perp,\beta}\cdot\left(\underline{\boldsymbol{V}}_{\boldsymbol{q},\boldsymbol{k}}^{\perp,\beta}\right)^T\right\} \tag{A.121b}$$

The coupling coefficients are defined in complete analogy to Equation (5.88). They read for $\alpha, \beta \in \{\|, \perp\}$:

$$C_{q,p}^{\alpha,\beta} = \frac{1}{q^2 (c_q^\alpha)^2} \frac{\mathcal{N}^\alpha}{N^2} \int d^2\hat{p} \mathrm{Tr} \Bigg\{ \sum_{\boldsymbol{k}} \sum_{\gamma,\tau \in \{\|,\perp\}} \underline{\boldsymbol{V}}_{\boldsymbol{q},\boldsymbol{k}}^{\alpha,\gamma} \cdot \underline{\boldsymbol{V}}_{\boldsymbol{k},\boldsymbol{p}}^{\gamma,\beta} \frac{S_{|\boldsymbol{q}-\boldsymbol{k}|}}{k^2 (c_k^\gamma)^2} \cdot ... \tag{A.122}$$
$$\cdot \Big[\Big(\underline{\boldsymbol{V}}_{\boldsymbol{k},\boldsymbol{p}}^{\tau,\beta} \Big)^T \cdot \Big(\underline{\boldsymbol{V}}_{\boldsymbol{q},\boldsymbol{k}}^{\alpha,\tau} \Big)^T \frac{S_{|\boldsymbol{k}-\boldsymbol{p}|}}{k^2 (c_k^\tau)^2} + \Big(\underline{\boldsymbol{V}}_{\boldsymbol{b},\boldsymbol{p}}^{\tau,\beta} \Big)^T \cdot \frac{S_{|\boldsymbol{k}-\boldsymbol{p}|}}{b^2 (c_b^\tau)^2} \Big(\underline{\boldsymbol{V}}_{\boldsymbol{q},\boldsymbol{b}}^{\alpha,\tau} \Big)^T \Big]_{\boldsymbol{b}=\boldsymbol{q}+\boldsymbol{p}-\boldsymbol{k}} \Bigg\} ,$$

with

$$\mathcal{N}^\| = 1 \, , \quad \mathcal{N}^\perp = \frac{1}{d-1} \tag{A.123}$$

From the strucure of Equation (A.120) follows, that $v_q^\|$ and $v_q^\perp$ scale similarly when approaching the transition unless $C^{\|,\perp} = 0$ or $C^{\perp,\|} = 0$ holds. To test this, we assume a uniform distribution of the particles resulting in $S_q = g(r) = g^{(3)}(\boldsymbol{r}, \boldsymbol{r}') = 1$. Furthermore, we notice the purely geometric result

$$\int d^d\boldsymbol{r} \frac{n}{m} \Big[1 - e^{i\boldsymbol{q}\cdot\boldsymbol{r}} \Big] \hat{\boldsymbol{r}} \cdot \underline{\boldsymbol{P}}^\alpha(\boldsymbol{q}) \underline{\boldsymbol{P}}^\beta(\boldsymbol{k}) \cdot \hat{\boldsymbol{r}} \, \mathcal{K}(r) \tag{A.124}$$
$$= \int d^d\boldsymbol{r} \frac{n\mathcal{N}^\alpha}{m} \Big[1 - e^{i\boldsymbol{q}\cdot\boldsymbol{r}} \Big] \hat{\boldsymbol{r}} \cdot \underline{\boldsymbol{P}}^\alpha(\boldsymbol{q}) \cdot \hat{\boldsymbol{r}} \, \mathcal{K}(r) \underline{\boldsymbol{P}}^\alpha(\boldsymbol{q}) \cdot \underline{\boldsymbol{P}}^\beta(\boldsymbol{k}) = (q c_q^\alpha)^2 \underline{\boldsymbol{P}}^\alpha(\boldsymbol{q}) \cdot \underline{\boldsymbol{P}}^\beta(\boldsymbol{k}) \, .$$

Having this in mind, the bare vertex reads for a uniform distribution reads ($\alpha, \beta \in \{\|$ $, \perp\}$):

$$\underline{\boldsymbol{V}}_{\boldsymbol{q},\boldsymbol{k}}^{\alpha\beta} = (q c_q^\alpha)^2 \underline{\boldsymbol{P}}^\alpha(\boldsymbol{q}) \cdot \underline{\boldsymbol{P}}^\alpha(\boldsymbol{k}) \tag{A.125}$$
$$- n \int d^d\boldsymbol{r} d^d\boldsymbol{r}' \frac{\delta(\boldsymbol{r}') + \delta(\boldsymbol{r} - \boldsymbol{r}')}{m} e^{i(\boldsymbol{k}-\boldsymbol{q})\cdot\boldsymbol{r}'} \Big[1 - e^{i\boldsymbol{q}\cdot\boldsymbol{r}} \Big] \hat{\boldsymbol{r}} \cdot \underline{\boldsymbol{P}}^\alpha(\boldsymbol{q}) \underline{\boldsymbol{P}}^\beta(\boldsymbol{k}) \cdot \hat{\boldsymbol{r}} \, \mathcal{K}(r)$$
$$= \frac{n\mathcal{N}^\alpha}{m} \int d^d\boldsymbol{r} \Big[e^{i\boldsymbol{k}\cdot\boldsymbol{r}} - e^{i(\boldsymbol{k}-\boldsymbol{q})\cdot\boldsymbol{r}} \Big] \hat{\boldsymbol{r}} \cdot \underline{\boldsymbol{P}}^\alpha(\boldsymbol{q}) \underline{\boldsymbol{P}}^\beta(\boldsymbol{k}) \cdot \hat{\boldsymbol{r}} \, \mathcal{K}(r)$$

All in all, we find for the stability matrix $C_{q,p}^{\parallel,\perp}$:

$$C_{q,p}^{\parallel,\perp} = \frac{1}{q^2(c_q^{\parallel})^2 N^2} \int d^2\hat{p} \sum_{\boldsymbol{k}} \sum_{\gamma,\tau\in\{\parallel,\perp\}} ... \tag{A.126}$$

$$\left[\mathrm{Tr}\left\{ \frac{\underline{\boldsymbol{V}}_{\boldsymbol{q},\boldsymbol{k}}^{\parallel,\gamma} \cdot \underline{\boldsymbol{V}}_{\boldsymbol{k},\boldsymbol{p}}^{\gamma,\perp}}{k^2(c_k^{\gamma})^2} \cdot \frac{\left(\underline{\boldsymbol{V}}_{\boldsymbol{k},\boldsymbol{p}}^{\tau,\perp}\right)^T \cdot \left(\underline{\boldsymbol{V}}_{\boldsymbol{q},\boldsymbol{k}}^{\parallel,\tau}\right)^T}{k^2(c_k^{\tau})^2} \right\} + \mathrm{Tr}\left\{ \frac{\underline{\boldsymbol{V}}_{\boldsymbol{q},\boldsymbol{k}}^{\parallel,\gamma} \cdot \underline{\boldsymbol{V}}_{\boldsymbol{k},\boldsymbol{p}}^{\gamma,\perp}}{k^2(c_k^{\gamma})^2} \cdot \frac{\left(\underline{\boldsymbol{V}}_{\boldsymbol{b},\boldsymbol{p}}^{\tau,\perp}\right)^T \cdot \left(\underline{\boldsymbol{V}}_{\boldsymbol{q},\boldsymbol{b}}^{\tau,\parallel}\right)^T}{b^2(c_b^{\tau})^2} \right\} \right]$$

with $\boldsymbol{b} = \boldsymbol{q} + \boldsymbol{p} - \boldsymbol{k}$ This expression does not vanish due to the different projections alone. Hence, we conclude that $C_{q,p}^{\parallel,\perp} \neq 0$ holds, which implies the same scaling of the bulk and shear modulus at the transition. We also confirm this numerically. Figure A.1a shows the longitudinal and transverse inverse compliance for different number densities computed in $d = 2$. It becomes apparent that the inverse longitudinal compliance is larger than the transverse one for small wavenumbers. However, the two quantities have the same long q limit. Both vanish at a critical density $n_c^* = 3.32(1)$. Importantly, the inverse compliance is non-negative $(qv_q^{\alpha})^2 \geq 0$, which we take as a sign that our theory does not predict negative eigenvalues in opposition to the vector model analysed in (Ciliberti *et al.*, 2003). However, our model predicts the same scaling for both elastic moduli for $n^* \to n_c^*$ as displayed in Figure A.1b. As the insert shows, both moduli vanish linearly with the excess density. A full theoretical investigation, as in Section 5.5, is still missing and will be part of future work.

Nevertheless, our theory for the Vector ERM model predicts the same scaling of the longitudinal and transverse modulus. This is at odds with the discoveries discussed in Section 2.3.2. Thus, the derivation of the vector ERM model must include a systematic error, as the initial equation indeed predicts a qualitative difference between the longitudinal and shear modulus, which the resulting model does not capture. This qualitative error awaits correction in future works. Importantly, the ERM model is generally sensitive to this difference between the two moduli as discussed in Section A.2.3. It was shown in (Mizuno *et al.*, 2016a) that the additional term for the longitudinal modulus in Equation (A.113) stays finite at the unjamming transition in soft sphere systems where the particles lose contact, as in (Mizuno *et al.*, 2016a). However, it remains to be seen if this is also true in uncorrelated disorder, as in a uniform distribution of the particles. A first comparison with the numeric data from Philipp Baumgärtel looks promising. The data is shown in Figure A.2. Extrapolating the existing data from numerical di-

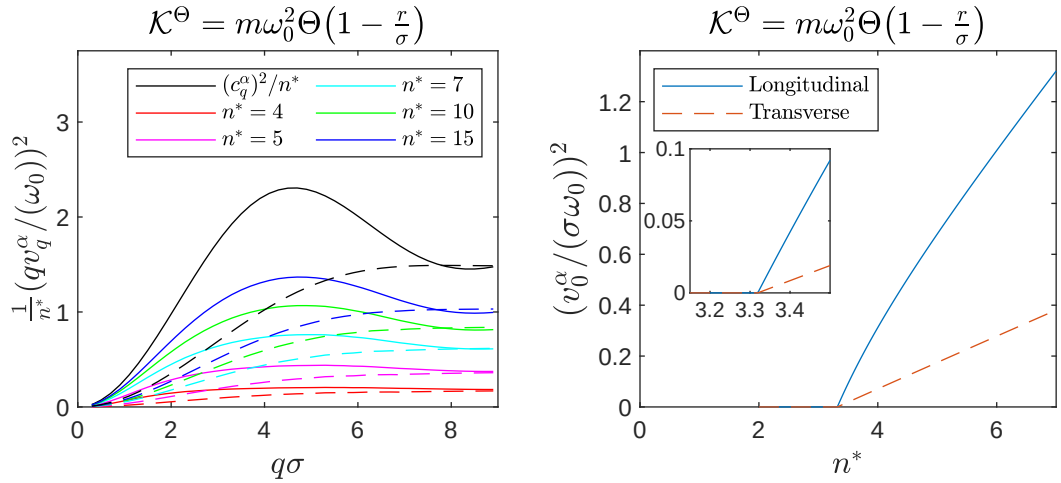

(a) Inverse compliance in $d = 2$

(b) Elastic Moduli

Figure A.1: Solution of Equation (A.77) for the Theta-Springfunction $\mathcal{K}^\Theta(r)$ for $s = 0$ and for the vertex of an uncorrelated disorder spelled out in Equation (A.81). We solved the equations as described in Section C.1 in two spatial dimensions ($d = 2$) to keep the numerical solution feasible. The left Panel A.1a shows the inverse longitudinal (solid lines) and transverse (dashed lines) compliance $(qv_q^\alpha)^2$. The different colours depict the solutions for different number densities n^* and black curves show the results for the bare elastic constants $(qc_q^\alpha)^2$. The right Panel A.1b depicts the longitudinal and transverse moduli scaling with the dumber density n^*. The insert shows the same data but focuses on the interval of the number density n^* where $B = (v_0^\parallel)^2$ and $G = (v_0^\perp)^2$ approach zero.

agonalisation, the longitudinal and transverse modulus apparently vanish at the same critical number density and even exhibit the same scaling relations. This confirms the results for random networks reported in (Ellenbroek *et al.*, 2009b; van Hecke, 2009). Furthermore, the same scaling points at the hypothesis that the different scaling of bulk and shear modulus reported in Chapter 2 is caused by the highly correlated disorder at the unjamming transition in soft sphere systems. However, it is too early for conclusive statements. Lastly, the theory's predictions only show semi-quantitative agreement with the exact numerical data. This is mainly a consequence of missing the critical number density n_c^*. The theory's predicted value $n_c^* = 3.32(1)$ is above the true value $n_c^* \in [2, 2.5]$. As one can see, the quantitative differences between numerical calculation

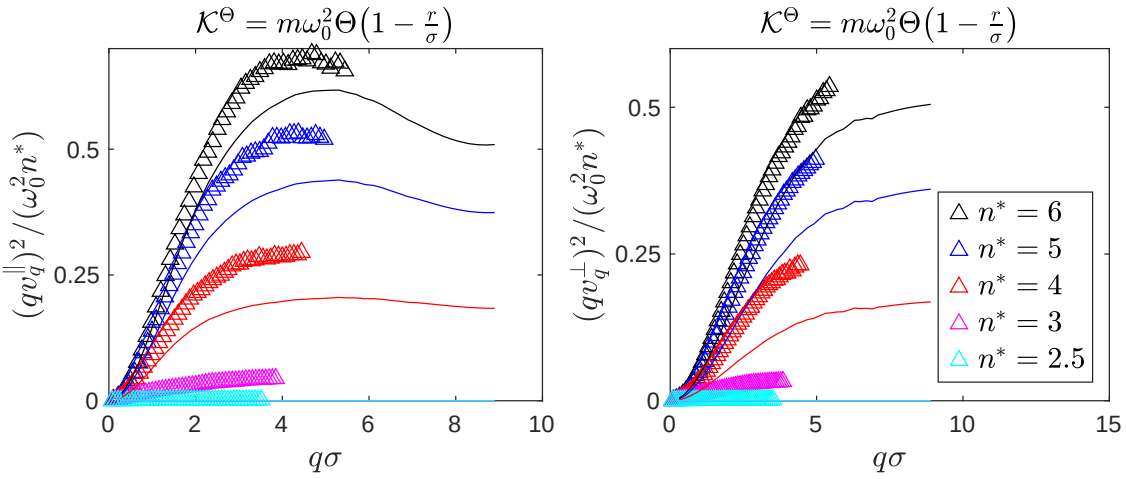

(a) Longitudinal inverse compliance **(b)** Transverse inverse compliance

Figure A.2: Comparisons of the zero frequency limit of the $2d$ inverse compliance with preliminary results from Philipp Baumgärtel. The symbols display the data obtained by exact numerical diagonalisation of the Hessian, done by Philipp Baumgärtel. The solid lines represent the theory's prediction. Figure A.2a displays the data for the inverse longitudinal compliance, and Figure A.2b shows the results for the inverse transverse compliance. Different number densities n^* are shown. The colour coding is the same for both panels. Philipp used 20.000 particles for his calculations.

and theoretical prediction diminish for higher densities. We have shown in this section how the vector character of displacements can be incorporated into the theory. However, the self-consistent equations enlisted in Equation (A.77) are still not fully general, as the initial stresses have been set to zero. Unsurprisingly, the Boltzmann approach in Chapter 5 also neglects the residual stresses as it is a genuine equilibrium approach and assumes perfect annealing. In the next section, we discuss how initial stresses can be taken into account when defining the Hessian.

A.3 The ERM model with initial stresses

As discussed in Section 2.3.1, the harmonic expansion of the energy in terms of the atomic displacements can still be written via a Hessian even in the presence of initial stresses. A linear term shifts the entries of the dynamical matrix. The explicit expression

was already given in Equation (2.38). It reads

$$\begin{aligned}\mathcal{H}_{i\vartheta,j\varphi} &= \delta_{ij}\sum_k M_{i\vartheta,k\varphi} - M_{i\vartheta,j\varphi}\ ,\\ M_{i\vartheta,j\varphi} &= \frac{1}{m}\hat{R}^{\vartheta}_{ij}\Big(\mathcal{K}_{ij} - \frac{\mathcal{T}_{ij}}{R_{ij}}\Big)\hat{R}^{\varphi}_{ij} + \frac{\mathcal{T}_{ij}}{mR_{ij}}\delta_{\vartheta\varphi}\end{aligned} \tag{A.127}$$

with

$$\mathcal{K}_{ij} \equiv \frac{\partial^2}{\partial r^2}U(r)\Big|_{r=R_{ij}}\ , \qquad \mathcal{T}_{ij} \equiv \frac{\partial}{\partial r}U(r)\Big|_{r=R_{ij}} \tag{A.128}$$

To simplify the ensuing consideration, we denote the result of the unstressed system as $(q\tilde{c}^{\vartheta\varphi}(\boldsymbol{q}))^2$ and use the abbreviation

$$\begin{aligned}h^{\vartheta\varphi}(\boldsymbol{R}_i - \boldsymbol{R}_j) &= -\hat{R}^{\vartheta}_{ij}\frac{\mathcal{T}_{ij}}{R_{ij}}\hat{R}^{\varphi}_{ij} + \frac{\mathcal{T}_{ij}}{R_{ij}}\delta_{\vartheta\varphi} = \frac{\mathcal{T}_{ij}}{R_{ij}}\big(\delta_{\vartheta\varphi} - \hat{R}^{\vartheta}_{ij}\hat{R}^{\varphi}_{ij}\big)\\ \underline{\boldsymbol{h}}(\boldsymbol{R}_{ij}) &= \int d^d\boldsymbol{r}\frac{1}{r}\frac{\partial U}{\partial r}(\underline{\mathbf{1}} - \hat{\boldsymbol{r}}\hat{\boldsymbol{r}})\delta(\boldsymbol{r} - \boldsymbol{R}_{ij})\ .\end{aligned} \tag{A.129}$$

Thus, we get from the definition of the bare dispersion relation in Equation (A.14):

$$\begin{aligned}(qc^{\vartheta\varphi}(\boldsymbol{q}))^2 &= \overline{\frac{1}{N}\sum_{i,k=1}^{N} e^{-i\boldsymbol{q}\cdot\boldsymbol{R}_i}\mathcal{H}^{\mathrm{ERM}}_{i\vartheta,l\varphi}e^{i\boldsymbol{q}\cdot\boldsymbol{R}_k}} = (q\tilde{c}^{\vartheta\varphi}(\boldsymbol{q}))^2\\ &+ \overline{\frac{1}{Nm}\sum_{i,k=1}^{N} e^{-i\boldsymbol{q}\cdot\boldsymbol{R}_i}\left[\delta_{ik}\sum_{l\neq i}h^{\vartheta\varphi}(\boldsymbol{R}_l - \boldsymbol{R}_i) + (1-\delta_{ik})h^{\vartheta\varphi}(\boldsymbol{R}_i - \boldsymbol{R}_k)\right]e^{i\boldsymbol{q}\cdot\boldsymbol{R}_k}}\\ &= (q\tilde{c}^{\vartheta\varphi}(\boldsymbol{q}))^2 - \int d^d\boldsymbol{r}\,\overline{\frac{1}{Nm}\sum_{i\neq k}^{N}\delta(\boldsymbol{r} - (\boldsymbol{R}_i - \boldsymbol{R}_k))}\Big[1 - e^{-i\boldsymbol{q}\cdot\boldsymbol{r}}\Big]h^{\vartheta\varphi}(\boldsymbol{r})\,.\end{aligned} \tag{A.130}$$

Here, the Greek indices denote spatial directions. The longitudinal component can be found by multiplying through with $\hat{q}^{\vartheta}$ and $\hat{q}^{\varphi}$ and summing over the Greek spatial indices. After all, we find for the longitudinal:

$$\begin{aligned}(qc^{\parallel}_q)^2 =& (q\tilde{c}^{\parallel}_q)^2 + \frac{n}{m}\int d^d\boldsymbol{r}\,g(r)\Big[1 - e^{-i\boldsymbol{q}\cdot\boldsymbol{r}}\Big]\frac{1}{r}\frac{\partial U}{\partial r}\Big\{\big(\underline{\mathbf{1}} - \hat{\boldsymbol{r}}\hat{\boldsymbol{r}}\big) : \hat{\boldsymbol{q}}\hat{\boldsymbol{q}}\Big\}\\ =& (q\tilde{c}^{\parallel}_q)^2 + \frac{n}{m}\int_0^{\infty} dr\,g(r)r^{d-2}\frac{\partial U}{\partial r}\int d^d\hat{\boldsymbol{r}}\Big[1 - e^{-iqr\cos(\theta)}\Big](1 - \cos(\theta)^2)\end{aligned} \tag{A.131}$$

Here, we have chosen $\boldsymbol{q} = q\hat{\boldsymbol{e}}_z$. To investigate three spatial dimensions, we set $d = 3$. The contribution from the unstressed system $(q\tilde{c}_q^{\parallel})^2$ is given in Equation (A.119). We find for the bare dispersion relation in a system with initial stresses:

$$(qc_q^{\parallel})^2 = (q\tilde{c}_q^{\parallel})^2 + 8\pi\frac{n}{m}\int_0^\infty dr g(r) r^{d-2}\frac{\partial U}{\partial r}\Big(\frac{1}{3} + \frac{qr\cos(qr) - (qr)^2\sin(qr)}{(qr)^3}\Big) \tag{A.132}$$

$$\underset{q\to 0}{\longrightarrow} (q\tilde{c}_0^{\parallel})^2 + \frac{4}{15}\pi\frac{n}{m}\int_0^\infty dr g(r) r^3\frac{\partial U}{\partial r}\ .$$

On the other hand, we find for the transverse component

$$(qc_q^{\perp})^2 = (q\tilde{c}_q^{\perp})^2 + \frac{n}{m(d-1)}\int d^d\boldsymbol{r} g(r)\Big[1 - e^{-i\boldsymbol{q}\cdot\boldsymbol{r}}\Big]\frac{1}{r}\frac{\partial U}{\partial r}\Big\{\big(\underline{\mathbf{1}} - \hat{\boldsymbol{r}}\hat{\boldsymbol{r}}\big) : \big(\underline{\mathbf{1}} - \hat{\boldsymbol{q}}\hat{\boldsymbol{q}}\big)\Big\} \tag{A.133}$$

$$= (q\tilde{c}_q^{\perp})^2 + \frac{n}{m(d-1)}\int_0^\infty dr g(r) r^{d-2}\frac{\partial U}{\partial r}\int d^d\hat{\boldsymbol{r}}\Big[1 - e^{-iq\cos(\theta)}\Big](d - 2 + \cos(\theta)^2)$$

Again, specifying $d = 3$ leads to

$$(qc_q^{\perp})^2 = (q\tilde{c}_q^{\perp})^2 + 4\pi\frac{n}{m}\int_0^\infty dr g(r) r\frac{\partial U}{\partial r}\left(\frac{2}{3} - \frac{\sin(qr)}{(qr)} - \frac{(qr)\cos(qr) - \sin(qr)}{(qr)^3}\right) \tag{A.134}$$

$$\underset{q\to 0}{\longrightarrow} (q\tilde{c}_0^{\perp})^2 + q^2\frac{8\pi}{15}\frac{n}{m}\int_0^\infty dr g(r) r^3\frac{\partial U}{\partial r}$$

The contribution from the unstressed system $(q\tilde{c}_q^{\perp})^2$ is given in Equation (A.118). The bare vertex can be calculated in an analog fashion. For $\alpha, \beta \in \{\parallel, \perp\}$ again denoting the longitudinal and the transverse direction, the result reads:

$$\underline{\boldsymbol{V}}_{\boldsymbol{q},\boldsymbol{k}}^{\alpha\beta} = (qc_q^{\alpha})^2\underline{\boldsymbol{P}}^{\alpha}(\boldsymbol{q})\cdot\underline{\boldsymbol{P}}^{\alpha}(\boldsymbol{k})\delta_{\alpha\beta} \tag{A.135}$$
$$- n\int d^d\boldsymbol{r}d^d\boldsymbol{r}'\frac{ng^{(3)}(\boldsymbol{r},\boldsymbol{r}') - ng(r) + g(r)\Big(\delta(\boldsymbol{r}') + \delta(\boldsymbol{r} - \boldsymbol{r}')\Big)}{mS_{|\boldsymbol{q}-\boldsymbol{k}|}}$$
$$\times e^{i(\boldsymbol{k}-\boldsymbol{q})\cdot\boldsymbol{r}'}\Big[1 - e^{i\boldsymbol{q}\cdot\boldsymbol{r}}\Big]\left\{\Big(\frac{\partial}{\partial\boldsymbol{r}} - \frac{\boldsymbol{r}}{r^2}\Big)\cdot\underline{\boldsymbol{P}}^{\alpha}(\boldsymbol{q})\underline{\boldsymbol{P}}^{\beta}(\boldsymbol{k})\cdot\frac{\partial}{\partial\boldsymbol{r}} + \underline{\boldsymbol{P}}^{\alpha}(\boldsymbol{q})\cdot\underline{\boldsymbol{P}}^{\beta}(\boldsymbol{k})\frac{1}{r}\frac{\partial}{\partial r}\right\}U(r)$$

Due to the inclusion of initial stresses, new terms enter the equations for the bare dispersion relation and the equation for the vertex. However, the adjustment is relatively

modest. The structure of the self-consistent set of Equations of the vector-ERM model, given in Equation (A.77), remains unchanged. Importantly, and as expected from the discussion of Section A.2.3, our equations still do not predict a qualitative difference between the longitudinal and the transverse susceptibility. Again, this suggests that the longitudinal modulus B and the shear modulus G exhibit the same scaling relations close to unjamming. This is expected to also hold for the Self-Consistent Current Theory discussed in Chapter 5. Thus, the MCT approximation scheme requires further correction. One should go back to the field theoretical considerations in (Grigera *et al.*, 2011; Vogel and Fuchs, 2023) to investigate which additional diagrams could become important and why longitudinal modes are less affected by the non-affine coupling. This is left for future work.

B | The Current Response Theory in real space

We have discussed in Section 5.3.2 that Rayleigh damping is only predicted if non-planar contributions are taken into account. Furthermore, the critical dynamic of Chapter 5.5 also only applies if the theory goes beyond the standard self-consistent Born approximation. We have mentioned in Section 5.3.2 that the necessity of considering non-planar contributions results from an underlying symmetry in the sequence of local events. We have called the requirement *Leutheusser symmetry* (Vogel *et al.*, 2025). In this chapter, we derive the Self-Consistent Current Response Theory in real space to make the origin of the Leutheusser symmetry apparent.

B.1 The velocity autocorrelation in real space

In analogy to Chapter 5, the main object of interest is the velocity autocorrelation function defined in Equation (5.2):

$$\underline{\hat{\mathbf{K}}}(\boldsymbol{r}_1 - \boldsymbol{r}_2, s) = \frac{\int d\Gamma\, \boldsymbol{v}(\boldsymbol{r}_1)\hat{R}(s)\boldsymbol{v}(\boldsymbol{r}_2)^*\, \Psi(\Gamma)}{N\frac{k_B T}{m}} \tag{B.1}$$

Here

$$\boldsymbol{v}(\boldsymbol{r}_1) = \sum_{i=1}^{N} \boldsymbol{v}_i \delta(\boldsymbol{r}_1 - \boldsymbol{r}_i) \tag{B.2}$$

denotes the local current field. Notably, the positions with an Arabic number index, *e.g.* $\boldsymbol{r}_1$ refer to position in the system while letter indices, *e.g.* $\boldsymbol{r}_i$, refer to the position of the i^{th} particle. As defined in Chapter 3, $\Gamma = (\{\boldsymbol{p}\}_{i=1}^N, \{\boldsymbol{r}\}_{i=1}^N, t)$ denotes the $2dN$ dimensional phasespace and $\Psi(\Gamma, t) = \Psi(\{\boldsymbol{p}\}_{i=1}^N, \{\boldsymbol{r}\}_{i=1}^N, t)$ is the distribution function. As before, we assume, that Ψ is given by the Boltzmann-distributiojn $\Psi_{\mathrm{eq}} \propto e^{-\beta H}$. As

in Chapter 5, we mainly work in the Laplace domain. Again, the Laplace transformation of the time evolution operator gives the resolvent $\hat{R}(s) = [s+\Omega]^{-1}$, where Ω denotes the Klein-Kramers operator from Equation (3.3). Notably, translational invariance implies that Equation (B.1) only depends on the spatial distance $\boldsymbol{r}_1 - \boldsymbol{r}_2$. The same applies to all correlation functions of two field variables $A(\boldsymbol{r}_1)$ and $B(\boldsymbol{r}_2)$. Furthermore, rotational invariance implies that the spatial Fourier transformation of $\underline{\hat{\mathbf{K}}}(\boldsymbol{r}_1 - \boldsymbol{r}_2, s)$ decomposes into a longitudinal part parallel to $\boldsymbol{q}$ and a transverse part orthogonal to $\boldsymbol{q}$:

$$\underline{\hat{\mathbf{K}}}(\boldsymbol{q}, s) = \hat{\mathrm{K}}_q^{\parallel}(s)\hat{\boldsymbol{q}}\hat{\boldsymbol{q}} + \hat{\mathrm{K}}_q^{\perp}(s)\big(\underline{\mathbf{1}} - \hat{\boldsymbol{q}}\hat{\boldsymbol{q}}\big) \ . \tag{B.3}$$

However, such a decomposition is not available to us as we analyse the correlation function in real space. Thus, we have to work with the full matrix-valued quantity[1] $\underline{\hat{\mathbf{K}}}(\boldsymbol{r}_1 - \boldsymbol{r}_2, s)$.

Hereinafter, we derive an expression for $\underline{\hat{\mathbf{K}}}(\boldsymbol{r}_1 - \boldsymbol{r}_2, s)$ in the small temperature limit $T \to 0$. We will exploit the projection operator formalism in analogy to Chapter 5. The ensuing calculation provides additional insight for the derivation in Section 5.2. To simplify the notation from the start, we set $1 \equiv \boldsymbol{r}_1$. To shorten the notation further, we will abbreviate the integral over the position by an overline over the associated number. For example, the integral over $A(\boldsymbol{r}_1)$ reads

$$\int d^d\boldsymbol{r}_1 A(\boldsymbol{r}_1) \longrightarrow A(\overline{1}) \ . \tag{B.5}$$

Furthermore, we write $\boldsymbol{r}_1 - \boldsymbol{r}_2 = 12$, to indicate that a quantity only depends on the spatial distance, *e.g.* $\underline{\hat{\mathbf{K}}}(12, s)$.

The projection operator on the velocity fields reads

$$P_1 = \frac{m}{k_B T N} \left|\boldsymbol{v}(\overline{1})\right\rangle \left\langle\boldsymbol{v}(\overline{1})\right| \ . \tag{B.6}$$

[1] Notable, we inconsistently assume that the structure is again time independent as in Chapter 5. This contradicts the continuity equation

$$\rho(1,t) = -\nabla \cdot \boldsymbol{v}(1,t) \ . \tag{B.4}$$

However, it is the primary purpose of this Appendix to substantiate the notion *Leutheuser-symmetry*, and a time-independent structure simplifies the consideration. Furthermore, density fluctuations can systematically be included.

By multiplying the operator identity in Equation (3.30) from the left with $\frac{m}{Nk_BT}\langle \boldsymbol{v}(1)|$ and from the right with $|\boldsymbol{v}(3)\rangle$, we obtain the real space Zwanzig-Mori equation of motions for the velocity-autocorrelation:

$$\left[(s+\xi)\underline{\boldsymbol{\delta}}(1\overline{2}) + \hat{\underline{\boldsymbol{\mathcal{G}}}}(1\overline{2}, s)\right] \cdot \hat{\underline{\mathbf{K}}}(\overline{2}3, s) = \underline{\boldsymbol{\delta}}(13) \ . \tag{B.7}$$

Here, we wrote $\underline{\boldsymbol{\delta}}(12) = \underline{\mathbf{1}}\delta(12)$ to shorten the notation and $\xi = \frac{\zeta_0}{m}$ is the Langevin damping rate. Furthermore, we can identify the inverse of the bare propagator of the fluid phase: $\hat{\underline{\mathbf{K}}}^{(0)}(12, s) \equiv \frac{\underline{\boldsymbol{\delta}}(12)}{s+\xi}$. It corresponds to an incompressible fluid with no memory effects and zero viscosity. The first memory kernel $\hat{\underline{\boldsymbol{\mathcal{G}}}}(12, s)$ reads

$$\hat{\underline{\boldsymbol{\mathcal{G}}}}(12, s) = -\frac{\langle \boldsymbol{v}(1)\Omega\hat{R}_1(s)\Omega\boldsymbol{v}(2)\rangle}{N\frac{k_BT}{m}} = \frac{\langle \boldsymbol{F}(1)\hat{R}_1(s)\boldsymbol{F}(2)\rangle}{Nmk_BT} \ . \tag{B.8}$$

Same as in Chapter 5, the reduced resolvent, $\hat{R}_1(s) = Q_1[s - \Omega_1]^{-1}Q_1$ is defined by the reduced Klein-Kramers Operator $Q_1\Omega Q_1 \equiv \Omega_1$ with $Q_1 = 1 - P_1$. The minus in the middle of Equation (B.8) originates from the operator identity in Equation (3.30). It disappears on the right-hand side due to the anti-hermitian property of the part of Ω which alters the time-inversion parity. The fluctuating force field in real space reads

$$\boldsymbol{F}(1) = m\sum_i \boldsymbol{v}_i\boldsymbol{v}_i \cdot \frac{\partial}{\partial \boldsymbol{r}_i}\delta(\boldsymbol{r}_1 - \boldsymbol{r}_i) + \sum_{i=1} \boldsymbol{F}_i\delta(\boldsymbol{r}_1 - \boldsymbol{r}_i) \ . \tag{B.9}$$

The following section discusses the Zwanzig-Mori equation of motion for the force correlator $\hat{\underline{\boldsymbol{\mathcal{G}}}}(12, s)$.

B.2 The self-energy in real space

We have to point out a crucial difference to the derivation in Chapter 5: The memory function $\hat{\underline{\boldsymbol{\mathcal{G}}}}(12, s)$ is defined as an autocorrelation of the forces. This is in opposition to the definition of the generalized shear modulus in Equation (5.16) via the stresses. Thus, $\hat{\underline{\boldsymbol{\mathcal{G}}}}(12, s)$ can not be expressed with the elastic moduli G, B introduced in Section 2.2. Conversely, $s\hat{\underline{\boldsymbol{\mathcal{G}}}}(12, s)$ equals the dispersion relation tensor in real space. In fact, the derivation in this chapter is equivalent to the consideration of the ERM model in Appendix A and only in analogy to the derivation presented in Chapter 5. However, we have discussed in Section 5.2.5 how the two approaches are related. Ultimately,

there is no qualitative difference. Hereinafter, we first derive an expression of the force correlator in terms of the self-energy $\hat{\underline{\Sigma}}$. Secondly, we derive and discuss the self-consistent Born approximation of the associated Zwanzig-Mori equation of motion.

The Zwanzig-Mori equation for the dispersion relation tensor: In analogy to Section (5.2.1), we define the second projector P_2 as

$$P_2 \equiv |\boldsymbol{F}(\overline{1}\rangle \cdot \big(\langle \boldsymbol{F}(\overline{1})\boldsymbol{F}(\overline{2})\rangle \big)^{-1} \cdot \langle \boldsymbol{F}(\overline{2})| \ . \tag{B.10}$$

Here, the normalisation $\big(\langle \boldsymbol{F}(1)\boldsymbol{F}(2)\rangle \big)^{-1}$ is formally defined as the inverse of the overlap

$$\big(\langle \boldsymbol{F}(1)\boldsymbol{F}(\overline{2})\rangle \big)^{-1} \cdot \langle \boldsymbol{F}(\overline{2})\boldsymbol{F}(3)\rangle = \langle \boldsymbol{F}(1)\boldsymbol{F}(\overline{2})\rangle \cdot \big(\langle \boldsymbol{F}(\overline{2})\boldsymbol{F}(3)\rangle \big)^{-1} = \delta(13) \ . \tag{B.11}$$

This ensures that $(P_2)^2 = P_2$ holds. We use the identity $\int d\Gamma \boldsymbol{F}_j A \Psi_{\mathrm{eq}} = -k_B T \int d\Gamma \Psi_{\mathrm{eq}} \nabla_j A$ and neglect higher orders in T. This approximation leads us to an expression for the instantaneous dispersion relation $\underline{\boldsymbol{\mathcal{G}}}(12, t=0)$:

$$\begin{aligned} \frac{\langle \boldsymbol{F}(1)\boldsymbol{F}(2)\rangle}{N n k_B T} &= \underline{\boldsymbol{\mathcal{G}}}(12, t=0) + \mathcal{O}(T^2) \\ &= n \int d\boldsymbol{r} g(\boldsymbol{r}+\boldsymbol{r}_1, \boldsymbol{r}_1) \Big(\delta(12) - \delta(\boldsymbol{r} - (\boldsymbol{r}_1 - \boldsymbol{r}_2)) \Big) \nabla\nabla U(r) + \mathcal{O}(T^2) \end{aligned} \tag{B.12}$$

Here, the function $g(\boldsymbol{r}+\boldsymbol{r}_1, \boldsymbol{r}_1) = \frac{1}{nN} \langle \sum_{i,j\neq i} \delta(\boldsymbol{r}+\boldsymbol{r}_1-\boldsymbol{r}_j)) \delta(\boldsymbol{r}_1 - \boldsymbol{r}_i) \rangle$ denotes the pair distribution function without the assumption of homogeneity and isotropy (Hansen and McDonald, 2009, Equation 2.5.14). The terms of order $\mathcal{O}(T^2)$ arise from the kinetic contributions to the stresses and from terms proportional to the first derivative of the potential energy. The later terms vanish as the system must be force and stress free in the athermal limit under the assumption of a Boltzmann distribution $\Psi_{\mathrm{eq}} \propto e^{-\beta H}$. Notably, the Fourier transformation of $\underline{\boldsymbol{\mathcal{G}}}(12, t=0)$ gives the bare dispersion relations of the vector ERM model written down in Equation (A.78). To derive the Zwanzig Mori equation for $\hat{\underline{\boldsymbol{\mathcal{G}}}}(12, s)$, we look at the following version of the identity in Equation (3.30):

$$\Big[s - P_2 \Omega_1 P_2 - P_2 \Omega_1 \hat{R}_2(s) \Omega_1 P_2 \Big] P_2 \hat{R}_1(s) P_2 = P_2 \ . \tag{B.13}$$

The second reduced resolvent is defined as $\hat{R}_2(s) = Q_2\big[s-\Omega_2\big]^{-1}Q_2$ and the associated operators are $\Omega_2 = Q_2\,\Omega\,Q_2$ and $Q_2 = 1 - P_1 - P_2$. Multiplying with $\frac{1}{Nmk_BT}\,\langle \boldsymbol{F}(1)|$ from the left and $|\boldsymbol{F}(4)\rangle$ from the right gives the Zwanzig-Mori equation of motion for the dispersion relation tensor:

$$\Big[s\underline{\boldsymbol{\delta}}(1\overline{3}) + s\hat{\underline{\boldsymbol{\Sigma}}}(1\overline{2},s)\cdot\big(\underline{\boldsymbol{\mathcal{G}}}(\overline{2}\,\overline{3},t=0)\big)^{-1}\Big]\cdot\hat{\underline{\boldsymbol{\mathcal{G}}}}(\overline{3}4,s) = \underline{\boldsymbol{\mathcal{G}}}(14,t=0)\ : \tag{B.14}$$

Here, we neglected an instantaneous damping term $\propto \xi k_BT$, as it vanishes with the temperature. This attenuation rate is a generalisation of Equation (5.32). The self-energy $\hat{\underline{\boldsymbol{\Sigma}}}(12,s)$ is a tensor generalisation of Equation (A.24). The constituting Equation reads

$$\hat{\underline{\boldsymbol{\Sigma}}}(12,s) = -\frac{1}{s}\frac{\langle \boldsymbol{F}(1)\Omega_1\hat{R}_2(s)\Omega_1\boldsymbol{F}(2)\rangle}{Nmk_BT}\ . \tag{B.15}$$

Notably, we have included the additional factor $\frac{1}{s}$ in the definition of $\hat{\underline{\boldsymbol{\Sigma}}}(12,s)$, ensuring that $\hat{\underline{\boldsymbol{\Sigma}}}(12,s\to 0)$ has a finite limit in the jammed state. Furthermore, the factor $\frac{1}{s}$ is necessary to ensure notational consistency with Equation (A.24).

Remembering the discussion of Section 5.2.2 and Equation (5.35), we recall that the time derivative of the potential part of the stresses can be expressed by a pair state of velocity field and density field $|\boldsymbol{v}(2)\delta\rho(1)\rangle$ with:

$$\rho(1) = \sum_{i=1}^{N}\delta(1i)\ , \qquad \delta\rho(1) = \rho(1) - \langle\rho(1)\rangle\ . \tag{B.16}$$

These considerations lead to the next projection operator P_3:

$$P_3 \equiv \frac{1}{N^2\frac{k_BT}{m}}\,|\boldsymbol{v}(\overline{1})\delta\rho(\overline{2})\rangle\cdot\big(S(\overline{23})\big)^{-1}\,\langle\boldsymbol{v}(\overline{1})\delta\rho(\overline{3})|\ . \tag{B.17}$$

Here, we defined the static structure factor in real space $S(12)\equiv\frac{1}{N}\,\langle\delta\rho(1)\delta\rho(2)\rangle$ and its inverse $\big(S(12)\big)^{-1}$ via $\big(S(1\overline{2})\big)^{-1}S(\overline{2}3) = \delta(13)$. The normalisation in Equation (B.17)

follows from

$$\langle \delta\rho(1)\boldsymbol{v}(2)\delta\rho(3)\boldsymbol{v}(4))\rangle = \frac{k_BT}{m}\underline{\mathbf{1}}\delta_{2,4}\langle\rho(2)\delta\rho(1)\delta\rho(3)\rangle \underset{N\to\infty}{\longrightarrow} N^2\frac{k_BT}{m}\underline{\mathbf{1}}\delta_{2,4}S(13)\ . \tag{B.18}$$

Noteably, we used the global translational invariance of the system. Inserting the projection P_3 operator to the left and to the right of $\hat{R}_3(s)$ in Equation (B.15) expresses the self-energy with a renormalized vertex

$$s\hat{\underline{\boldsymbol{\Sigma}}}(12,s) \approx \frac{1}{N}\tilde{\underline{\boldsymbol{V}}}(1,\overline{3},\overline{4})\cdot\tilde{\underline{\boldsymbol{\mathcal{V}}}}(\overline{3},\overline{4},2,s) \tag{B.19}$$

Here, we have neglected the kinetic contributions to the forces. The definitions of the bare vertex $\tilde{\underline{\boldsymbol{V}}}(1,3,4)$ and the renormalised vertex $\tilde{\underline{\boldsymbol{\mathcal{V}}}}(3,4,2,s)$ follow from Equation (B.15) and Equation (B.17):

$$\tilde{\underline{\boldsymbol{V}}}(1,3,4) \equiv -\frac{\langle \boldsymbol{F}(1)\Omega Q_1\boldsymbol{v}(3)\delta\rho(\overline{5})\rangle}{Nk_BT}\big(S(\overline{5}4)\big)^{-1}\ , \tag{B.20a}$$

$$\tilde{\underline{\boldsymbol{\mathcal{V}}}}(3,4,2,s) = m\frac{\langle \boldsymbol{v}(3)\delta\rho(4)\hat{R}_2(s)\boldsymbol{v}(\overline{5})\delta\rho(\overline{6})\rangle}{N^2k_BT}\cdot\tilde{\underline{\boldsymbol{V}}}^{\dagger}(\overline{5},\overline{6},2)\ . \tag{B.20b}$$

The vertex $\tilde{\underline{\boldsymbol{V}}}(1,3,4)$ can be calculated with an analogous calculation as in Appendix D. Alternatively, it is also possible to consider the inverse Fourier transformation of Equation (A.79) . The result reads

$$\begin{aligned}\tilde{\underline{\boldsymbol{V}}}(1,3,4) = &-\underline{\boldsymbol{\mathcal{G}}}(13,t=0)\delta(34) + \frac{n}{m}\int d^d\boldsymbol{r}d^d\boldsymbol{r}'\Big(ng^{(3)}(\boldsymbol{r}+\boldsymbol{r}_3,\boldsymbol{r}'+\boldsymbol{r}_3,\boldsymbol{r}_3)\\ &+ g(\boldsymbol{r}+\boldsymbol{r}_3,\boldsymbol{r}_3)[\delta(\boldsymbol{r}-\boldsymbol{r}')+\delta(\boldsymbol{r}')-\langle\rho(\boldsymbol{r}'+\boldsymbol{r}_3)\rangle]\Big)\delta(\boldsymbol{r}'+3\overline{5})\\ &\times\Big[\delta(13)-\delta(\boldsymbol{r}-13)\Big]\big(S(\overline{5}4)\big)^{-1}\nabla\nabla U(r)\end{aligned} \tag{B.21}$$

As in Chapter 5, both vertices[2] are independent of T and stay finite for $N\to\infty$. Noticeable, the four-point correlation function in Equation (B.20b) vanishes linearly with the temperature. Putting all together, the self-energy $\hat{\underline{\boldsymbol{\Sigma}}}_q(s)$ has a finite limit for $T\to 0$

[2] As in Appendix D, it is convenient to look at the three different contributions to $\tilde{\underline{\boldsymbol{V}}}(1,3,4)$ separately. The first one reads:

$$-\frac{\langle \boldsymbol{F}(1)\boldsymbol{F}(\overline{6})\rangle\cdot\langle\boldsymbol{v}(\overline{6})\boldsymbol{v}(3)\delta\rho(\overline{5})\rangle}{(Nk_BT)^2}\big(S(\overline{5}4)\big)^{-1} = -\underline{\boldsymbol{\mathcal{G}}}(13,t=0)\delta(34)$$

and $N \to \infty$. As in Section 5.2.2, we now search for closure. We will show in the next section that the self-consistent Born approximation violates a symmetry constraint.

B.3 The self-consistent Born approximation

The standard MCT-approximation consists of diagonalising, factorising, and dressing the four-point correlation function occurring in Equation (B.20b) for the renormalised vertex $\underline{\tilde{\boldsymbol{\mathcal{V}}}}(3,4,2,s)$ (Götze, 2009; Pihlajamaa *et al.*, 2023). Assuming that the dynmic structure factor $S(12,t)$ is time independent gives

$$m\frac{\langle \boldsymbol{v}(1)\delta\rho(2)\hat{R}_2(s)\boldsymbol{v}(3)\delta\rho(4)\rangle}{N^2 k_B T} \approx S(24)\underline{\hat{\mathbf{K}}}(13,s)\ . \tag{B.22}$$

However, we have already discussed in Section 5.3.2 that this approximation does not give the correct sound damping in the jammed phase. Instead of Rayleigh-like attenuation, Equation (B.22) leads to a sound attenuation $\underline{\boldsymbol{\Gamma}} \propto q^2\omega$ after a spatial Fourier transformation and with $s = -i\omega + 0^+$. We also discussed in Section 5.3.2 that this erroneous damping results from neglecting non-planar contributions to the self-energy. This suggests that the standard MCT-approximation is related to a self-consistent Born-approximation (Leutheusser, 1983). To confirm this anticipation, we look at the Zwanzig-Mori equation of motion for the four-point correlation function

$$\underline{\hat{\boldsymbol{C}}}^{(4)}(1,2,3,4,s) = m\frac{\langle \boldsymbol{v}(1)\delta\rho(2)\hat{R}_2(s)\boldsymbol{v}(3)\delta\rho(4)\rangle}{N^2 k_B T}\ . \tag{B.23}$$

The second contribution reads

$$\begin{aligned}\frac{\langle \boldsymbol{F}(1)\boldsymbol{F}(3)\rho(\bar{5})\rangle}{Nmk_BT}\big(S(\bar{5}\bar{4})\big)^{-1} =& \frac{1}{mN}\int d^d\boldsymbol{r}d^d\boldsymbol{r}'\,\langle \sum_{j,l,i\neq j}\delta(\boldsymbol{r}+3i)\delta(\boldsymbol{r}'+3l)\delta(3j)\rangle \\ &\times \delta(\boldsymbol{r}'+3\bar{5})\Big[\delta(13)-\delta(\boldsymbol{r}-13)\Big]\big(S(\bar{5}\bar{4})\big)^{-1}\nabla\nabla U(r) \\ =& \int d^d\boldsymbol{r}d^d\boldsymbol{r}'\Big(ng^{(3)}(\boldsymbol{r}+\boldsymbol{r}_3,\boldsymbol{r}'+\boldsymbol{r}_3,\boldsymbol{r}_3)+g(\boldsymbol{r}+\boldsymbol{r}_3,\boldsymbol{r}_3)[\delta(\boldsymbol{r}-\boldsymbol{r}')+\delta(\boldsymbol{r}')]\Big) \\ &\times \frac{n}{m}\delta(\boldsymbol{r}'+3\bar{5})\Big[\delta(13)-\delta(\boldsymbol{r}-13)\Big]\big(S(\bar{5}\bar{4})\big)^{-1}\nabla\nabla U(r)\ .\end{aligned}$$

Here, the average in the first line leads to the distribution functions $g^{(3)}(\boldsymbol{r},\boldsymbol{r}',\boldsymbol{r}'')$ in the third line (Hansen and McDonald, 2009, Section 2.5). The last term can be written as $\langle\rho(5)\rangle = \int d^d\boldsymbol{r}'\,\langle\rho(\boldsymbol{r}'+\boldsymbol{r}_3\rangle)\delta(\boldsymbol{r}'+35)$. Adding all three terms leads to Equation (B.21).

The projection operator P_3 defined in Equation (B.17) gives rise to the following operator identity

$$\Big[s - P_3\Omega_2 P_3 - P_3\Omega_2\hat{R}_3(s)\Omega_2 P_3\Big] P_3\hat{R}_2(s)P_3 = P_3 \; . \tag{B.24}$$

Here $\hat{R}_3(s) = Q_3[s+\Omega_3]^{-1}Q_3$ denotes the third reduced dynamics with $Q_3 = 1 - P_3$ and $\Omega_3 = Q_3\Omega_2 Q_3$. Multiplying with $\frac{m}{k_B T}\langle \boldsymbol{v}(1)\delta\rho(2)|$ from the left and $|\boldsymbol{v}(5)\delta\rho(6)\rangle$ from the right gives

$$\Big[\underbrace{(s+\xi)\underline{\boldsymbol{\delta}}(1\overline{3})}_{=\left(\hat{\underline{\mathbf{K}}}^{(0)}(1\overline{3},s)\right)^{-1}} \delta(2\overline{4}) + \hat{\underline{\mathbf{\Pi}}}(1,2,\overline{3},\overline{4},s)\Big] \cdot \hat{\underline{\boldsymbol{C}}}^{(4)}(\overline{3},\overline{4},5,6,s) = S(26)\underline{\boldsymbol{\delta}}(15) \; . \tag{B.25}$$

This result is the real space analogue for Equation (5.45). The new memory kernel is defined as

$$\hat{\underline{\mathbf{\Pi}}}(1,2,3,4,s) = -\frac{m}{N^2 k_B T}\langle \boldsymbol{v}(1)\delta\rho(2)\Omega_2\hat{R}_3(s)\Omega_2\boldsymbol{v}(3)\delta\rho(\overline{5})\rangle \cdot \big(S(\overline{5}4)\big)^{-1} \; . \tag{B.26}$$

The Born approximation equals setting the memory term to zero $\hat{\underline{\mathbf{\Pi}}}(1,2,3,4,s) = 0$. This leads to the concise expression for the four-point correlation function:

$$\hat{\underline{\boldsymbol{C}}}^{(4)}(1,2,3,4,s) \approx S(24)\hat{\underline{\mathbf{K}}}^{(0)}(13,s) \tag{B.27}$$

Seemingly, this approximation only improves if the bare propagator $\hat{\underline{\mathbf{K}}}^{(0)}(13,s)$ is replaced with the full propagator $\hat{\underline{\mathbf{K}}}(13,s)$. Because of this and as anticipated, the approximation for the four-point correlation function $\hat{\underline{\boldsymbol{C}}}^{(4)}$ in Equation (B.22) indeed corresponds to a self-consistent Born-approximation. Here, the memory term $\hat{\underline{\mathbf{\Pi}}}$ is given by the dispersion relation tensor $\hat{\underline{\boldsymbol{\mathcal{G}}}}$:

$$\hat{\underline{\mathbf{\Pi}}}(1,2,3,4,s) \approx \hat{\underline{\boldsymbol{\mathcal{G}}}}(13,s)\delta(24) \; . \tag{B.28}$$

We have already exhaustively discussed in Section 5.3.2 and in Section 5.5 that the self-consistent Born approximation leads to qualitative wrong predictions. However, hereinafter, we will point out, that Equation (B.28) violates a symmetry constrain. To

see this, we start our considerations by writing

$$\begin{aligned}\underline{\hat{\mathbf{\Pi}}}(1,2,3,4,s) &= -\frac{m}{N^2 k_B T}\left\langle \boldsymbol{v}(1)\delta\rho(2)\Omega_2\hat{R}_3(s)\Omega_2\boldsymbol{v}(3)\delta\rho(\bar{5})\right\rangle\cdot\left(S(4\bar{5})\right)^{-1} \\ &\approx \frac{1}{N^2 k_B T m}\left\langle \boldsymbol{F}(1)\delta\rho(2)\hat{R}_3(s)\boldsymbol{F}(3)\delta\rho(\bar{5})\right\rangle\cdot\left(S(4\bar{5})\right)^{-1}.\end{aligned} \tag{B.29}$$

In the second line, we assumed that the structure is time-independent. Furthermore, we neglected the additional projector Q_2 as the third reduced dynamics $\hat{R}_3(s)$ approximates the fluctuating forces as constant anyhow. This is the same approximation as in Equation (5.49). Now, we rely on the interparticle forces arising from a potential $U(r)$. This suggests writing

$$\begin{aligned}|\boldsymbol{F}(1)\delta\rho(2))\rangle &\approx \sum_{i,j}|\boldsymbol{F}_i\delta(\boldsymbol{r}_1-\boldsymbol{r}_i)\delta(\boldsymbol{r}_2-\boldsymbol{r}_j)\rangle - |\boldsymbol{F}(1)\rangle\langle\rho(2)\rangle \\ &= -\sum_{i,j,m\neq i}\int d^d\boldsymbol{r}_3\,|\delta(\boldsymbol{r}_3-(\boldsymbol{r}_i-\boldsymbol{r}_m))\delta(\boldsymbol{r}_1-\boldsymbol{r}_i)\delta(\boldsymbol{r}_2-\boldsymbol{r}_j)\rangle\,\frac{\partial U(\boldsymbol{r}_3)}{\partial\boldsymbol{r}_3} \\ &\quad - |\boldsymbol{F}(1)\rangle\langle\rho(2)\rangle \\ &= -\sum_{i,m\neq i}\int d^d\boldsymbol{r}_3\,|\delta(\boldsymbol{r}_3-(\boldsymbol{r}_i-\boldsymbol{r}_m))\delta(\boldsymbol{r}_1-\boldsymbol{r}_i)\delta\rho(2\rangle\,\frac{\partial U(\boldsymbol{r}_3)}{\partial\boldsymbol{r}_3}\,.\end{aligned} \tag{B.30}$$

Here, we neglected the kinetic contributions to the fluctuating force $\boldsymbol{F}$. With the result of Equation (B.30), we can take a closer look at the self-consistent Born approximation for the memory kernel $\underline{\hat{\mathbf{\Pi}}}$ in Equation (B.28). We again neglect the kinetic contributions. Furthermore, we write $\delta(\boldsymbol{r}_3-(\boldsymbol{r}_i-\boldsymbol{r}_m))\equiv\delta(3-im)$ and $\frac{\partial U(\boldsymbol{r}_3)}{\partial\boldsymbol{r}_3}\equiv\nabla_3 U(3)$ to shorten the notation. The self-consistent Born approximation in Equation (B.28) equals the following simplification:

$$\begin{aligned}&N^2 k_B T m\underline{\hat{\mathbf{\Pi}}}(1,2,3,\bar{5},s)S(\bar{5}4) = \left\langle \boldsymbol{F}(1)\delta\rho(2)\hat{R}_3(s)\boldsymbol{F}(3)\delta\rho(4)\right\rangle \\ &= \sum_{i,j,m\neq i}\sum_{l,k,n\neq l}\left\langle\delta(\bar{5}-im)\delta(1i)\big[\delta(2j)-\langle\delta(2j)\rangle\big]\hat{R}_3(s)\delta(\bar{6}-ln)\delta(3l)\big[\delta(4k)-\langle\delta(4k)\rangle\big]\right\rangle \\ &\qquad\qquad\times[\nabla_{\bar{5}}U(\bar{5})][\nabla_{\bar{6}}U(\bar{6})] \\ &\overset{\text{Eq.}C.27}{\approx} N\sum_{i,j,m\neq i}\sum_{l,k,n\neq l}\left\langle\delta(\bar{5}-im)\delta(1i)\hat{R}_3(s)\delta(\bar{6}-ln)\delta(3l)\right\rangle[\nabla_{\bar{5}}U(\bar{5})][\nabla_{\bar{6}}U(\bar{5})]S(24)\end{aligned} \tag{B.31}$$

Thus, the self-consistent Born approximation in Equation (B.28) does not treat the positions $\boldsymbol{r}_1,\boldsymbol{r}_2,\boldsymbol{r}_3$ and $\boldsymbol{r}_4$ on equal footing. However, this is dictated by the assumed statis-

tical equivalence of the particles. This requirement implies that the right-hand side must be invariant under the permutation $2 \leftrightarrow 1$ and $3 \leftrightarrow 4$. Thus, the self-consistent Born approximation violates a symmetry constrain. This violation gives rise to the qualitative wrong prediction discussed in Chapter 5. The next section shows how this symmetry constraint can be adequately incorporated.

B.4 The symmetrised equation for the self-energy

The Mode-Coupling approximation consists of breaking a multiple-point correlator and expressing it via a function of two-point correlators. We saw in the last section that symmetry constraints arise as the final expression has to be invariant under a permutation of the positions. The self-consistent Born approximation of Equation (B.28) explicitly violates this symmetry request. In this section, we derive a symmetrised equation for the renormalized vertex $\underline{\tilde{\boldsymbol{\mathcal{V}}}}$. We start by multiplying Equation (B.25) by $\underline{\tilde{\boldsymbol{V}}}^{\dagger}(6,5,7)$ and integrating over the positions 5 and 6. Remembering the definition of the renormalized vertex $\underline{\tilde{\boldsymbol{\mathcal{V}}}}$ in Equation (B.20b) leads to

$$\Big[(s+\xi)\underline{\boldsymbol{\delta}}(1\overline{3})\delta(2\overline{4}) + \underline{\hat{\boldsymbol{\Pi}}}(1,2,\overline{3},\overline{4},s)\Big] \cdot \underline{\tilde{\boldsymbol{\mathcal{V}}}}(\overline{3},\overline{4},7,s) = S(2\overline{6})\underline{\tilde{\boldsymbol{V}}}^{\dagger}(1,\overline{6},7) \; . \tag{B.32}$$

As discussed in Section 5.2.3, we need one more projection to recover the current as our main time-dependent quantity. Furthermore, correctly symmetrizing Equation (B.31) remains elusive. In analogy to Equation (5.50), the fourth projection operator reads

$$P_4 = \frac{1}{N^2 m k_B T} \left|\boldsymbol{F}(\overline{1})\delta\rho(\overline{2})\right\rangle \cdot \big(\underline{\boldsymbol{\mathcal{G}}}(\overline{1}\,\overline{3}, t=0)\big)^{-1}\big(S(\overline{2}\,\overline{4})\big)^{-1} \left\langle \boldsymbol{F}(\overline{3})\delta\rho(\overline{4})\right| \; . \tag{B.33}$$

Here, we have approximated the overlap by its diagonal contribution

$$\langle \boldsymbol{F}(1)\delta\rho(2)\boldsymbol{F}(3)\delta\rho(4))\rangle \approx N^2 k_B T m \, \underline{\boldsymbol{\mathcal{G}}}(13, t=0)S(24) \; . \tag{B.34}$$

As in Section 5.2.3, the new projection operator P_4 defines the fourth reduced resolvent $\hat{R}_4(s) = Q_4[s+\Omega_4]^{-1}Q_4$ via $Q_4 = 1 - P_4$ and $\Omega_4 = Q_4\Omega_3 Q_4$. The new operator identity reads

$$\Big[s - P_4\Omega_3 P_4 - P_4\Omega_3 Q_4 \hat{R}_4(s) Q_4 \Omega_3 P_4\Big] P_4 \hat{R}_3(s) P_4 = P_4 \; . \tag{B.35}$$

Multiplying with $\frac{1}{N^2 k_B T m} \langle \boldsymbol{F}(1)\delta\rho(2)|$ from the left and $|\boldsymbol{F}(5)\delta\rho(\overline{7})\rangle) \cdot \big(S(\overline{7}6)\big)^{-1}$ from the right, leads to

$$\Big[s\underline{\boldsymbol{\delta}}(1\overline{3})\delta(2\overline{4}) + \hat{\underline{\Xi}}(1,2,\overline{3},\overline{4},s)\Big] \cdot \hat{\underline{\mathbf{\Pi}}}(\overline{3},\overline{4},5,6,s) = \underline{\boldsymbol{\mathcal{G}}}(15,t=0)\delta(26)\ . \tag{B.36}$$

Here, we have neglected an instantaneous damping matrix $\propto \xi k_B T$, which is the generalization of Equation (5.56). The last memory kernel reads:

$$\hat{\underline{\Xi}}(1,2,3,4,s) = -\frac{\langle \boldsymbol{F}(1)\delta\rho(2)\Omega_3 \hat{R}_4(s)\Omega_3\delta\rho(\overline{5})\boldsymbol{F}(\overline{6})\rangle}{N^2 k_B T m} \cdot \big(\underline{\boldsymbol{\mathcal{G}}}(\overline{64})\big)^{-1}\big(S(\overline{5}3)\big)^{-1}\ . \tag{B.37}$$

Again, this is in complete analogy to Equation (5.53). With the same motivations as in Section 5.2.3, we approximate

$$Q_3 Q_2 \Omega Q_2 \,|\delta\rho(3)\boldsymbol{F}(4)\rangle \approx Q_3\,|\delta\rho(3)(\Omega\boldsymbol{F}(4))\rangle\ . \tag{B.38}$$

The idea for this approximation is that the structure is supposedly time independent and that the time derivative of the forces $|\boldsymbol{F}\rangle$ can be written via a pair state of density and velocity field $|\boldsymbol{v}\rho\rangle$ as written down in Equation (5.35).

Now, we again assume Gaussian fluctuations and that we can write the pair state $|\delta\rho(3)\boldsymbol{F}(4)\rangle$ as a product state $|\delta\rho(3)\rangle \otimes |\boldsymbol{F}(4)\rangle$. Based on this assumption, we can perform the same calculation as in Equation (5.58):

$$\begin{aligned}
&-\frac{\langle \boldsymbol{F}(1)\delta\rho(2)\Omega_3 \hat{R}_4(s)\Omega_3\delta\rho(3)\boldsymbol{F}(4)\rangle}{N^2 k_B T m} \\
&\quad\approx -\frac{\big(\,\langle\delta\rho(2)|\otimes\langle(\Omega^\dagger\boldsymbol{F}(1))|\,[P_3+Q_3]\big)Q_3\hat{R}_4(s)Q_3\big([P_3+Q_3]\,|\boldsymbol{F}(4)\rangle\otimes|\delta\rho(3)\rangle\,\big)}{N^2 k_B T m} \\
&\quad= \underline{\tilde{\boldsymbol{V}}}(1,\overline{5},\overline{6})\cdot\frac{\langle \boldsymbol{v}(\overline{5})\delta\rho(\overline{6})\delta\rho(2)Q_3\hat{R}_4(s)\boldsymbol{v}(\overline{7})\delta\rho(\overline{8})\delta\rho(3)\rangle}{N^2\frac{k_B T}{m}}\cdot\underline{\tilde{\boldsymbol{V}}}^\dagger(\overline{7},\overline{8},4) \\
&\quad\approx \frac{1}{N}\underline{\tilde{\boldsymbol{V}}}(1,\overline{5},\overline{6})\cdot\hat{\underline{\mathbf{K}}}(\overline{5}\,\overline{7},s)\cdot\underline{\tilde{\boldsymbol{V}}}^\dagger(\overline{7},\overline{8},4)\Big[S(\overline{6}\,\overline{8})S(23)+S(\overline{6}3)S(2\overline{8})\Big]
\end{aligned} \tag{B.39}$$

In the last line, we performed the factorisation and subsequential dressing approximation of the Mode-Coupling Theory. The same approximation was performed at the end

of Equation (5.58). Notably, we made sure that the square bracket is invariant under permutations $2 \leftrightarrow 8$ and $6 \leftrightarrow 3$. Thus, the requirement of statistical equivalence of the positions is obeyed. Inserting this result in Equation (B.37) leads to

$$\begin{aligned}\hat{\underline{\Xi}}(1,2,3,4,s) \approx & \frac{1}{N}\tilde{\underline{V}}(1,\overline{5},\overline{6}) \cdot \hat{\underline{\mathbf{K}}}(\overline{5}\,\overline{7},s) \cdot \tilde{\underline{V}}^{\dagger}(\overline{7},\overline{8},\overline{9}) \cdot \left(\underline{\boldsymbol{\mathcal{G}}}(\overline{9}4)\right)^{-1} \\ & \times \left[S(\overline{6}\,\overline{8})\delta(23) + \delta(\overline{6}3)S(2\overline{8})\right] .\end{aligned} \tag{B.40}$$

This result is in complete analogy to Equation (5.64). The only differences arise from not projecting on the transverse modes and a redefinition of the bare vertex $\tilde{\underline{V}}(1,2,3)$. To obtain the constituting equation for the renormalised vertex $\tilde{\underline{\boldsymbol{\mathcal{V}}}}$, we multiply Equation (B.36) with $\tilde{\underline{\boldsymbol{\mathcal{V}}}}(5,6,7,s)$ from the right and integrate over the positions 5 and 6. Furthermore, we insert a rearranged version of Equation (B.32):

$$\hat{\underline{\mathbf{\Pi}}}(1,2,\overline{3},\overline{4},s) \cdot \tilde{\underline{\boldsymbol{\mathcal{V}}}}(\overline{3},\overline{4},7,s) = S(2\overline{6})\tilde{\underline{V}}^{\dagger}(1,\overline{6},7) - (s+\xi)\tilde{\underline{\boldsymbol{\mathcal{V}}}}(1,2,7,s) \, . \tag{B.41}$$

This leads to the final expression for the renormalized vertex in real space:

$$\begin{aligned}\Big[\big(s(s+\xi)\underline{\boldsymbol{\delta}}(1\overline{3}) + \underline{\boldsymbol{\mathcal{G}}}(1\overline{3},t=0)\big)\delta(2\overline{4}) + (s+\xi)\hat{\underline{\Xi}}(1,2,\overline{4},\overline{3},s)\Big] \cdot \tilde{\underline{\boldsymbol{\mathcal{V}}}}(\overline{3},\overline{4},5,s) \\ = \Big[s\underline{\boldsymbol{\delta}}(1\overline{3})\delta(2\overline{4}) + \hat{\underline{\Xi}}(1,2,\overline{4},\overline{3},s)\Big] \cdot S(\overline{4}\,\overline{6})\underline{\boldsymbol{V}}^{\dagger}(\overline{3},\overline{6},5)\end{aligned} \tag{B.42}$$

Here, $\big(s(s+\xi)\underline{\boldsymbol{\delta}}(12) + \underline{\boldsymbol{\mathcal{G}}}(12,t=0)\big) = \big(\chi(12)^{(0)}\big)^{-1}$ is the inverse bare propagator of the jammed phase. Again, this final expression for the renormalized vertex $\tilde{\underline{\boldsymbol{\mathcal{V}}}}$ is in complete analogy to Equation (5.67).

In Section 5.2.5, we have established that $\hat{\underline{\boldsymbol{\chi}}}(12,s) = \frac{1}{s}\hat{\underline{\mathbf{K}}}(12,s)$ can be understood as describing an excitation travelling from $\boldsymbol{r}_1$ to $\boldsymbol{r}_2$ On its path, the excitation interacts with the disorder. We call these interactions *scattering events*. Equation (B.42) for the renormalised vertex $\tilde{\underline{\boldsymbol{\mathcal{V}}}}$ provides insights into the topology of scattering events that have to be considered.

B.5 The topology of inelastic scattering events

We have discussed that the self-consistent Born approximation in Equation (B.28) violates a symmetry constrain: Different positions are not treated as statistically equivalent. By continuing the sequence of the Zwanzig-Mori steps further, we have derived an equation for the renormalised vertex $\underline{\tilde{\boldsymbol{\mathcal{V}}}}$, which explicitly obeys the statistical equivalence of the positions. Equation (B.42) allows us to specify the implications on the considered scattering events. Hereinafter, we consider the high density limit $n \to \infty$ and look at the susceptibility $\underline{\hat{\boldsymbol{\chi}}}(12, s) = \frac{1}{s}\underline{\hat{\mathbf{K}}}(12, s)$. Here, the system is close to a continuous elastic medium and the dispersion relation tensor $s\underline{\hat{\boldsymbol{\mathcal{G}}}}(12, s)$ stays close to its instantaneous value $\underline{\boldsymbol{\mathcal{G}}}(12, t = 0)$. The Zwanzig-Mori equation of motion reads

$$\Big[s(s+\xi)\underline{\boldsymbol{\delta}}(1\overline{2}) + s\underline{\hat{\boldsymbol{\mathcal{G}}}}(1\overline{2}, s)\Big] \cdot \underline{\hat{\boldsymbol{\chi}}}(\overline{2}3, s) = \underline{\boldsymbol{\delta}}(13) \tag{B.43a}$$

$$\Big[\underline{\boldsymbol{\delta}}(1\overline{3}) + \underline{\hat{\boldsymbol{\Sigma}}}(1\overline{2}, s) \cdot \big(\underline{\boldsymbol{\mathcal{G}}}(\overline{2}\,\overline{3}, t = 0)\big)^{-1}\Big] \cdot s\underline{\hat{\boldsymbol{\mathcal{G}}}}(\overline{3}4, s) = \underline{\boldsymbol{\mathcal{G}}}(14, t = 0) \tag{B.43b}$$

The self-energy $\underline{\hat{\boldsymbol{\Sigma}}}$ varies as n^0 for $n \to 0$ but the instantaneous bare dispersion relation tensor $\underline{\boldsymbol{\mathcal{G}}}$ increases linearly with n. Thus, the high-density approximation gives for the dispersion relation tensor

$$s\underline{\hat{\boldsymbol{\mathcal{G}}}}(14, s) \approx \underline{\boldsymbol{\mathcal{G}}}(14, t = 0) - \underline{\hat{\boldsymbol{\Sigma}}}(14, s)\ . \tag{B.44}$$

Hence, we find the Dyson equation for the susceptibility in the high-density approximation

$$\underline{\hat{\boldsymbol{\chi}}}(12, s) \approx \underline{\hat{\boldsymbol{\chi}}}^{(0)}(12, s) + \underline{\hat{\boldsymbol{\chi}}}^{(0)}(1\overline{3}, s) \cdot \underline{\hat{\boldsymbol{\Sigma}}}(\overline{3}\,\overline{4}, s) \cdot \underline{\hat{\boldsymbol{\chi}}}(\overline{4}2, s)\ . \tag{B.45}$$

Here, the bare propagator is given by

$$\underline{\hat{\boldsymbol{\chi}}}^{(0)}(12, s) = \big[s(s+\xi)\underline{\boldsymbol{\delta}}(12) + \underline{\boldsymbol{\mathcal{G}}}(12, t = 0)\big]^{-1}\ . \tag{B.46}$$

Equation (B.42) for the renormalized vertex $\underline{\tilde{\boldsymbol{\mathcal{V}}}}$ simplifies for $n \to \infty$: As $\underline{\hat{\boldsymbol{\Xi}}}$ also varies with n^0 for $n \to \infty$, the square bracket on the left side of Equation (B.42) becomes equal to the inverse bare propagator $\big(\underline{\hat{\boldsymbol{\chi}}}^{(0)}(12, s)\big)^{-1}$. This is similar to the $F1$ approximation in (5.79). Solving the simplified Equation for $\underline{\tilde{\boldsymbol{\mathcal{V}}}}$ and inserting the result back in Equation

(B.19) leads to three contributions to the self-energy $\underline{\hat{\Sigma}}$:

$$\begin{aligned}\underline{\hat{\Sigma}}(12,s) =& \frac{1}{N}\underline{\tilde{V}}(1,\overline{3},\overline{4})\cdot\underline{\hat{\chi}}^{(0)}(\overline{3}\,\overline{5},s)S(\overline{4}\,\overline{6})\cdot\underline{\tilde{V}}^{\dagger}(\overline{5},\overline{6},2) \\ &+\frac{1}{N^2}\underline{\tilde{V}}(1,\overline{3},\overline{4})\cdot\underline{\hat{\chi}}^{(0)}(\overline{3}\,\overline{5},s)\cdot\underline{\tilde{V}}(\overline{5},\overline{6},\overline{7})\cdot\underline{\hat{\chi}}(\overline{6}\,\overline{8},s)\cdot\underline{\tilde{V}}^{\dagger}(\overline{8},\overline{9},\overline{10})\cdot ... \\ &\cdot\left(\underline{\mathcal{G}}\right)^{-1}(\overline{10}\,\overline{11},t=0)\cdot\underline{\tilde{V}}^{\dagger}(\overline{11},\overline{12},2)S(\overline{4}\,\overline{12})S(\overline{7}\,\overline{9}) \\ &+\frac{1}{N^2}\underline{\tilde{V}}(1,\overline{3},\overline{4})\cdot\underline{\hat{\chi}}^{(0)}(\overline{3}\,\overline{5},s)\cdot\underline{\tilde{V}}(\overline{5},\overline{6},\overline{7})\cdot\underline{\hat{\chi}}(\overline{6}\,\overline{8},s)\cdot\underline{\tilde{V}}^{\dagger}(\overline{8},\overline{9},\overline{10})\cdot ... \\ &\cdot\left(\underline{\mathcal{G}}\right)^{-1}(\overline{10}\,\overline{11},t=0)\cdot\underline{\tilde{V}}^{\dagger}(\overline{11},\overline{12},2)S(\overline{4}\,\overline{9})S(\overline{7}\,\overline{12})\end{aligned} \tag{B.47}$$

As this expression is not really illustrative, we rely on a diagrammatic representation as in Section 5.2.5. The Feynman rules read:

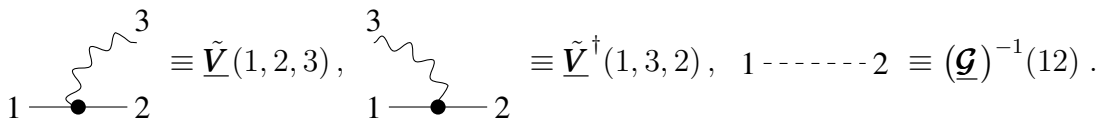

(B.48)

Thus, we find the following graphical representation of the Dyson series in Equation (B.45) valid for high densities:

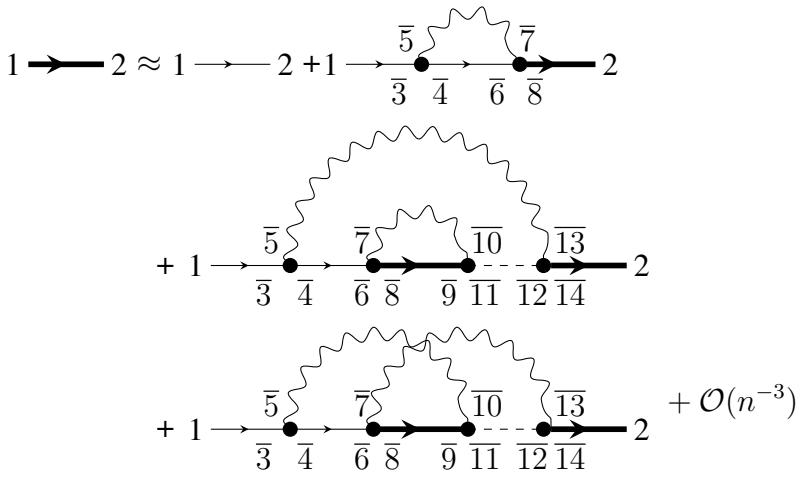

(B.49)

Equation (B.47) and Equation (B.48) suggests the following narrative: An excitation travels through the medium and eventually scatters inelastically with the disorder, creat-

ing a density fluctuation. Both excitations eventually recombine at a different location. However, when two or more density fluctuations are present, the statistical equivalence of the positions dictates that the self-energy $\hat{\underline{\Sigma}}$ is invariant under a permutation of the scatter sides. This gives rise to the non-planar diagrams in Equation (B.48). The imperative of taking the non-planar terms into account originates from the statistical equivalence of the particles and thus from a symmetry of disordered systems.

C | Numerical solution

This chapter discusses the numerical implementation of the scalar ERM model. The relevant formulas are given in Equations (5.80) and (A.70). For simplicity, we assume that $\hat{\chi}_q^{\mathrm{SERM}}(s)$ is a reasonable approximation for $\hat{\chi}_q^{\perp}(s)$. This approximation neglects the tensor structure of the Equations (5.66) and (5.74), which makes the numerical solutions of the vector models impracticable. This chapter discusses numerical solution methods in the time and the Laplace domains. Each comes with advantages and disadvantages, and hence needs different approximations to make the numerical solution feasible. Writing down the equations in the Laplace domain gives a concise expression as convolutions of two functions in the time domain become mere products. However, as discussed in Section 5.3.2 about Rayleigh-damping, both the propagator $\hat{\chi}_q^{\mathrm{SERM}}(s)$ and the bare propagator $\hat{\chi}_q^{(0)}(s)$ feature a divergence, which gives rise to the attenuation. In the continuum's limit, this pole leads to a Dirac-delta $\delta(\omega^2 - q^2(c_q^{\mathrm{SERM}})^2)$. Thus, to make the numerical solution of the full problem stable, one needs a large number of Fourier modes. However, $2d$ integrals must be solved when calculating the self-consistent contribution to the self-energy, where d denotes the spatial dimension. This high number makes it unfeasible to solve the full frequency-dependent problem in the Laplace domain. However, the long-time limit is easily accessible due to the relation $\lim_{t\to\infty} f(t) = \lim_{t\to\infty} s\hat{f}(s)$, as any pole disappears in the limit $s \to 0$ or rather does not alter the result. It is just the other way around in the time domain. Here, no poles or non-analyticities are present, as the divergences in the Laplace domain lead to an exponential attenuation in the time domain. Consequently, the full-time-dependent solution is much more easily accessible than the frequency-dependent solution. However, this comes at the price of having to calculate the convolution of the self-energy and the time derivative of the velocity autocorrelation $\int_0^t dt' \Sigma_q^{\mathrm{SERM}}(t-t')\dot{\mathrm{K}}_q^{\mathrm{SERM}}(t')$ which becomes very costly for large times. Hereinafter, we describe how the self-consistent model was solved in both domains, starting with the Laplace domain. We assume that the particles are uniformly distributed to simplify the numerical task further. We restrict ourselves

to $d = 3$ in this chapter. Furthermore, we only consider a uniform distribution of the particles and set $g^{(n)} = S_q = 1$.

C.1 Numerical solution for the long-time limit

As stated above, it is numerically not feasible to solve the self-consistent equations in the frequency domain for all $\omega = is - i0^+$. To circumvent the divergences from the sound pole, we focus on the $s = 0$ limit and aim to determine the value of the non-ergodicity parameter κ_q and the inverse transverse compliance $(qv_q)^2$. To solve the self-consistent model for $s = 0$, we first use the Equations (5.88) and (5.87) to calculate the stability matrix $\underline{\boldsymbol{C}}$ and the zero-frequency limit of the Born term to the self-energy $\hat{\Sigma}_q^{(0)}(0)$. These quantities were defined in Equation (5.88) and Equation (5.87). Consecutively, we calculate these quantities for all considered spring functions and store the results. A linear convergence algorithm suffices to solve the linear integral Equations (5.89) and (5.138). When evaluating the compliance, we employ the inverse bare dispersion $(qc_q)^{-2}$ as a reasonable starting value for the algorithm. When calculating the non-ergodicity parameter, we start from $\kappa_q = 1$. In both cases, the algorithm runs until the Euclidean distance between two iterations, *i.e.* $||\boldsymbol{\kappa}(j+1) - \boldsymbol{\kappa}(j)||$ becomes smaller than 10^{-12}. Here, $\boldsymbol{\kappa} = (\kappa_1, \kappa_2, ...\kappa_m)$ is the array of the non-ergodicity parameters. The integer number j in $\boldsymbol{\kappa}(j)$ specifies the number of performed iterations.

In $d = 3$, six integrals have to be calculated. One of them, an angular integral, can be performed analytically. Due to the high dimensionality, a numerical error is at least possible. Looking at the entries of the stability matrix, we observe that the diagonal elements of the coupling matrix become negative for $q\sigma < 0.2$. It is open to whether this nonphysical feature stems from a numerical error or has a systematic reason caused by taking non-diagonal contributions into account. If the latter is true, higher loop corrections in the theory must be taken into account to resolve this issue. Investigating this artifact is left for future work. Here, we circumvent the problem by taking 600 wavenumbers $q\sigma = [q_{\min}\sigma, 60]$ into account to calculate the stability matrix, where we ensured the diagonal elements were all positive. We then discarded the smallest two wavenumbers as a discontinuous jump in their values was observed, independent of their actual value. We ensured that the results do not depend on the choice of wavenumbers. We chose different distributions– linear and logarithmic– and also altered the smallest

wavenumber considered. If the smallest wavenumber $\sigma q_{\min}$ was not too large, none of this affects the results qualitatively or quantitatively. As a means to calculate the critical eigenvectors h_q and $\hat{h}_p$ defined in Section 5.5.1, we relied on the standard Matlab routine to obtain the eigenvectors of the stability matrix $p^2 C_{\boldsymbol{q},\boldsymbol{p}}$ and its associated eigenvalues. We also relied on the concrete form h and $\hat{h}$ to calculate the plateau value appearing in the Density of States when approaching the transition and displayed in Figure 5.6. The methods used to solve the self-consistent model for $s = 0$ have also been explained in (Vogel *et al.*, 2025). There, the numerical investigation of the ERM model was also elaborated on. This is not repeated here, as this has been done by Philipp Baumgärtel. The stored results for the stability matrix $p^2 C_{\boldsymbol{q},\boldsymbol{p}}$ are also used for the solution in the time domain, which we will discuss next.

C.2 Time dependent solution

We first have to discuss the transformation from the Laplace domain back to the time domain. To keep the discussion on general grounds, we start with Equation (5.66) for the Transverse Current Response Theory and only perform the scalar ERM approximation at the end of our considerations. All the occurring quantities have been introduced in Chapter 5. We have:

$$\begin{aligned}
\hat{\mathrm{K}}_q^{\perp}(s) &= \frac{1}{s + \xi + \frac{q^2 (c_q^{\perp})^2}{s + (c_q^{\perp})^2 \hat{\mathrm{W}}_q^{\perp}(s)}} \\
&= \frac{s + (c_q^{\perp})^2 \hat{\mathrm{W}}_q^{\perp}(s)}{s(s+\xi) + (s+\xi)(c_q^{\perp})^2 \hat{\mathrm{W}}_q^{\perp}(s) + q^2 (c_q^{\perp})^2} \\
\iff [s(s+\xi) + q^2 (c_q^{\perp})^2] \hat{\mathrm{K}}_q^{\perp}(s) - s &= -[(s+\xi)\hat{\mathrm{K}}_q^{\perp}(s) - 1](c_q^{\perp})^2 \hat{\mathrm{W}}_q^{\perp}(s) \, .
\end{aligned} \tag{C.1}$$

In order to apply Equation (G.5b), we need the initial conditions for the transverse current autocorrelation $\mathrm{K}_q^{\perp}(t)$. They follow immediately from the definition of velocity autocorrelation in $d = 3$ dimensions:

$$\mathrm{K}_q^{\perp}(t=0) = \frac{1}{2} \frac{\mathrm{Tr}\{\langle \boldsymbol{v}^{\perp}(\boldsymbol{q}) \boldsymbol{v}^{\perp}(-\boldsymbol{q}) \rangle\}}{\frac{1}{2} \langle |\boldsymbol{v}^{\perp}(\boldsymbol{q})|^2 \rangle} = 1 \tag{C.2a}$$

$$\dot{\mathrm{K}}_q^{\perp}(t=0) = \frac{1}{2} \frac{\mathrm{Tr}\{\langle \Omega^{\dagger} \boldsymbol{v}^{\perp}(\boldsymbol{q}) \boldsymbol{v}^{\perp}(-\boldsymbol{q}) \rangle\}}{\frac{1}{2} \langle |\boldsymbol{v}^{\perp}(\boldsymbol{q})|^2 \rangle} = -\xi \tag{C.2b}$$

Together with the properties of the Laplace transformation enlisted in Appendix G, this leads to the integro-differential equation:

$$\ddot{\mathrm{K}}_q^{\perp}(t) = -q^2(c_q^{\perp})^2\mathrm{K}_q^{\perp}(t) - \xi\dot{\mathrm{K}}_q^{\perp}(t) - (c_q^{\perp})^2\int_0^t dt'\mathrm{W}_q^{\perp}(t-t')\Big(\frac{d}{dt'}+\xi\Big)\mathrm{K}_q^{\perp}(t') \; . \tag{C.3}$$

The fluidity in the time domain reads $\mathrm{W}_q^{\perp}(t) = \frac{1}{N}\sum_{\boldsymbol{k}} \underline{\boldsymbol{V}}_{\boldsymbol{q},\boldsymbol{k}} : \underline{\boldsymbol{\nu}}_{\boldsymbol{q},\boldsymbol{k}}(t)$, where the time-dependent renormalized vertex $\underline{\boldsymbol{\nu}}_{\boldsymbol{q},\boldsymbol{k}}(t)$ is the solution of the inverse Laplace-transformation of Equation (5.67). However, this self-consistent matrix equation with multiple convolutions is too challenging to solve numerically. Thus, we restrict ourselves to investigating a modification of the well-known $F1$ model where only the linear term in the velocity autocorrelation and the Born term are kept. This approximation was introduced in Equation (5.79), and the time domain version of the fluidity reads:

$$\mathrm{W}_q^{\perp}(t) \approx \frac{1}{N}\sum_{\boldsymbol{k}} \underline{\boldsymbol{V}}_{\boldsymbol{q},\boldsymbol{k}} : \underline{\boldsymbol{V}}^{\dagger}_{\boldsymbol{k},\boldsymbol{q}} e^{-\frac{\xi}{2}t}\Big(\cos(tk\bar{c}_k^{\perp}) - \frac{\xi}{2k\bar{c}_k^{\perp}}\sin(tk\bar{c}_k^{\perp})\Big) + \sum_p p^2 C_{q,p}\mathrm{K}_p^{\perp}(t) \tag{C.4}$$

The argument of the cosine- and the sine function reads $k\bar{c}_k^{\perp} = \sqrt{(kc_k^{\perp})^2 + \frac{\xi^2}{4}}$. Here, $C_{q,p}$ is again the stability matrix defined in Equation (5.88). As discussed in Section 5.5, neglecting the non-linear terms becomes reasonable for long times and close to the transition where the non-ergodicity parameter becomes small.

As already mentioned in Section C.1, very small wavenumbers σq can not be considered as the diagonal elements of the stability matrix $q^2C_{q,q}$ become negative. However, these very small wavenumbers lead to the sound attenuation for long times as they are involved in the non-analycity of $[-\omega^2 - i0^+ + k^2(c_k^{\perp})^2]^{-1}$. Thus, ignoring small wavenumber contributions implies crudely missevaluating the attenuation. Consequently, the solution algorithm becomes unstable, and the long time limit $\mathrm{K}_q^{\perp}(t\to\infty)$ diverges.

To stabilize the solution algorithm and to take the attenuation due to the Born term correctly into account, we replace the first-order term of the fluidity by its $s \to 0$ limit. For $s = -i\omega + 0^+$, the real and imaginary part read

$$\begin{aligned}\hat{\Delta}(s = -i\omega + 0^+) = \frac{1}{N}\sum_{\boldsymbol{k}} \underline{\boldsymbol{V}}_{\boldsymbol{q},\boldsymbol{k}} : \underline{\boldsymbol{V}}^{\dagger}_{\boldsymbol{k},\boldsymbol{q}} \frac{S_{|\boldsymbol{q}-\boldsymbol{k}|}}{-\omega^2 - i0^+ + k^2 (c_k^{\perp})^2} \\ \underbrace{\xrightarrow[\omega\to 0 \to 0]{} \frac{1}{N}\sum_{\boldsymbol{k}} \frac{\underline{\boldsymbol{V}}_{\boldsymbol{q},\boldsymbol{k}} : \underline{\boldsymbol{V}}^{\dagger}_{\boldsymbol{k},\boldsymbol{q}}}{k^2 (c_k^{\perp})^2} S_{|\boldsymbol{q}-\boldsymbol{k}|}}_{=\hat{\Delta}_q(0)} + i\frac{iS_q}{4\pi}\frac{\omega}{(c_0^{\perp})^3} q^2 \ .\end{aligned} \tag{C.5}$$

Here, when calculating the imaginary part, we used the Sokhotski–Plemelj formula, $\mathrm{Im}\,\frac{1}{x \pm i0^+} = \mp\pi\delta(x)$. Furhtermore, we inserted $\underline{\boldsymbol{V}}_{\boldsymbol{q},\boldsymbol{k}\to 0} = -q[\underline{\mathbf{1}} - \hat{\boldsymbol{q}}\hat{\boldsymbol{q}}] \cdot [\underline{\mathbf{1}} - \hat{\boldsymbol{k}}\hat{\boldsymbol{k}}]$. This relation was derived in Equation (D.18). Defining

$$\begin{aligned} s\tilde{\xi}_q &= \frac{1}{4\pi n}\frac{q^4 (c_q^{\perp})^4}{(c_0^{\perp})^3}\frac{1}{(1+\hat{\Delta}_q(0))^2} \ , \\ (\tilde{c}_q^{\perp})^2 &= \frac{(c_q^{\perp})^2}{1 + (c_q^{\perp})^2 \hat{\Delta}_q(0)} \end{aligned} \tag{C.6}$$

for abbreviation purposes leads to a second integro-differential Equation:

$$\begin{aligned} \hat{\mathrm{K}}_q^{\perp}(s) &= \frac{1}{s + \frac{q^2 (c_q^{\perp})^2}{s + (c_q^{\perp})^2 \hat{\mathrm{W}}_q^{\perp}(s)}} \\ &= \frac{1}{s + \frac{q^2 (c_q^{\perp})^2}{1 + (c_q^{\perp})^2 \hat{\Delta}_q(s)} \frac{1}{s + \frac{(c_q^{\perp})^2}{1 + (c_q^{\perp})^2 \hat{\Delta}_q(s)} \sum_p p^2 C_{q,p} \hat{\mathrm{K}}_p^{\perp}(s)}} \\ &\approx \frac{1}{s + \frac{q^2 (\tilde{c}_q^{\perp})^2 + s\tilde{\xi}_q}{s + (\tilde{c}_q^{\perp})^2 \sum_p p^2 C_{q,p} \hat{\mathrm{K}}_p^{\perp}(s)}} \\ \Longleftrightarrow \ddot{\mathrm{K}}_q^{\perp}(t) &= -q^2 (\tilde{c}_q^{\perp})^2 \mathrm{K}_q^{\perp}(t) - \tilde{\xi}_q \dot{\mathrm{K}}_q^{\perp}(t) - (\tilde{c}_q^{\perp})^2 \sum_p p^2 C_{q,p} \int_0^t \mathrm{K}_p^{\perp}(t-t') \dot{\mathrm{K}}_q^{\perp}(t') dt' \end{aligned} \tag{C.7}$$

When transiting from the second to the third line, the Born term has been replaced by its small frequency limit $s \to 0$. Importantly, this leads to different initial conditions:

$$\mathrm{K}_q^{\perp}(t=0) = 1 \ , \quad \dot{\mathrm{K}}_q^{\perp}(t=0) = -\tilde{\xi}_q \ . \tag{C.8}$$

Anticipating that a damped oscillator solves this second-order integro-differential equation, we rely on a Velocity-Verlet algorithm to solve Equation (C.8) numerically. The Verlet integrator has the advantage of leaving the phase space volume unchanged when integrating Newtonian equations of motion. We used a uniform spacing of the discrete time steps $t_{i+1} - t_i = \Delta t$ and label $t_j = j \cdot \Delta t$. The updated rules read:

$$\underline{\text{Step 1)}}\ \dot{\mathrm{K}}_q^{\perp}(t_i + \tfrac{1}{2}\Delta t) = \dot{\mathrm{K}}_q^{\perp}(t_i)\big(1 - \tilde{\xi}_q \tfrac{1}{2}\Delta t\big) - q^2(\tilde{c}_q^{\perp})^2 \mathrm{K}_q^{\perp}(t_i)\tfrac{\Delta t_i}{2} - \tfrac{\Delta t_i}{2} F_q(t_i)$$

$$\underline{\text{Step 2)}}\ \mathrm{K}_q^{\perp}(t_i + \Delta t) = \mathrm{K}_q^{\perp}(t_i) + \Delta t \dot{\mathrm{K}}_q^{\perp}(t_i + \tfrac{1}{2}\Delta t)$$

$$\underline{\text{Step 3)}}\ \dot{\mathrm{K}}_q^{\perp}(t_i + \Delta t_i) = \tfrac{\dot{\mathrm{K}}_q^{\perp}(t_i + \frac{1}{2}\Delta t)}{1 + \tilde{\xi}_q \frac{\Delta t}{2}} - q^2(\tilde{c}_q^{\perp})^2 \mathrm{K}_q^{\perp}(t_i)\tfrac{\Delta t}{2 + \xi \Delta t} - \tfrac{\Delta t}{2 + \xi \Delta t} F_q(t_i + \Delta t)$$

The function $F_q(t_i)$ is given by the convolution of the memory term and $\dot{\mathrm{K}}_q(t)$. The discretized expression reads

$$\begin{aligned} F_q(t_i) &= (\tilde{c}_q^{\perp})^2 \sum_p p^2 C_{q,p} \int_0^{t_i} \mathrm{K}_p^{\perp}(t_i - t') \dot{\mathrm{K}}_q^{\perp}(t') dt' \\ &= (\tilde{c}_q^{\perp})^2 \sum_p p^2 C_{q,p} \sum_{j=1}^{N_{t_j}-1} \int_{t_j}^{t_j + \Delta t_j} \mathrm{K}_p^{\perp}(t_i - t') \dot{\mathrm{K}}_q^{\perp}(t') dt' \\ &\approx (\tilde{c}_q^{\perp})^2 \sum_p p^2 C_{q,p} \sum_{j=1}^{N_{t_i}-1} \frac{\mathrm{K}_p^{\perp}(t_i - t_{j+1}) + \mathrm{K}_p^{\perp}(t_i - t_j)}{2} \Big[\mathrm{K}_q^{\perp}(t_{j+1}) - \mathrm{K}_q^{\perp}(t_j)\Big] . \end{aligned} \tag{C.9}$$

Here, we set $t_{N_{t_i}} = t_i$ and $t_1 = 0$. Before discussing the time-dependent solution of the self-consistent model, we convince ourselves in the next paragraph that the algorithm works by discussing a toy model simple enough to allow explicit analytic results.

The standard $F1$ model: To test the numerics, we ignore all wavevector dependency so that the model depends on one parameter only, plus an additional noise term. The standard underdamped $F1$ model reads

$$\hat{\mathrm{K}}^{\mathrm{F1}}(s) = \frac{1}{s + \frac{a + s\xi}{s + \hat{\mathrm{K}}(s)}} \tag{C.10}$$

As this toy model is used solely to test the algorithm, all units are set to unity in this paragraph. According to the properties of the Laplace transform, the long-time limits

can be calculated explicitly:

$$\begin{aligned} \kappa &= \lim_{t\to\infty} \hat{\mathrm{K}}^{\mathrm{F1}}(t) = \lim_{s\to\infty} s\hat{\mathrm{K}}^{\mathrm{F1}}(s) = \frac{1}{1+\frac{a}{\kappa}} \\ \iff \kappa^2 &= \kappa(1-a) \end{aligned} \tag{C.11}$$

The maximum property of the Mode-Coupling Theory (Götze, 2009, Section 4.3.1) gives

$$\kappa = \begin{cases} 1-a & \text{for } a < 1 \\ 0 & \text{for } a \geq 1 \end{cases} \tag{C.12}$$

independent of the attenuation. Figure C.1 shows examples of the time-dependent $F1$-correlator. The insert displays the long-time limit depending on the single parameter a. The numerical results coincide with the analytical prediction. This is convincing evidence that the algorithm and its implementation work.

To make the numerical calculations feasible, we neglected our equations' tensorial structure, particularly the vertex $\underline{\underline{V}}_{\boldsymbol{q},\boldsymbol{k}}$. In this monograph, all numerical calculations were done in the scalar ERM approximation introduced and discussed in the Chapter 4 and Appendix A. : The tensor structure was neglected and the vertex was taken as $V^{\mathrm{SERM}}_{\boldsymbol{q},\boldsymbol{k}} = n\big(\mathcal{K}(\boldsymbol{k}) - \mathcal{K}(\boldsymbol{q}-\boldsymbol{k})\big)$. For all the numerical calculations, a uniform distribution of the particles was assumed, which translates into $g^{(n)} = S_q = 1$. Furthermore, we restricted ourselves to $d = 3$. The numerical solutions of the inverse compliance $(qv_q)^2$, the frequency-dependent dispersion relation $\big(q\hat{v}_q(s)\big)^2$ and the non-ergodicity parameter κ_q, discussed in the Sections 5.3 and 5.4, show good agreement with the associated results obtained from the zero frequency calculations in the Laplace domain. Furthermore, the results in the jammed state exhibit convincing agreement with the data obtained from numerical diagonalization, as visible in Figure 5.2. However, all of those quantities are related to the real part of the susceptibility $\mathrm{Re}\{\hat{\chi}^{\mathrm{SERM}}_q(-i\omega+0^+)\}$. In the following paragraph, we will argue that the approximation explained in Equation (C.7) erroneously alters the imaginary part. Because of this, it was not possible to infer the attenuation rate Γ^{SERM}_q and the Density of States $D^{\mathrm{SERM}}(\omega)$ from the numerical solution in the time domain. We will discuss this in the next paragraph.

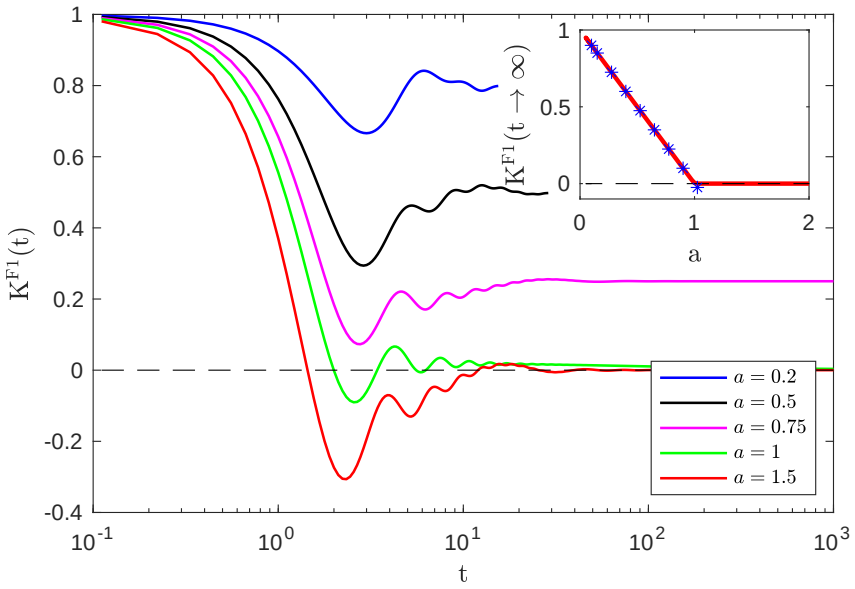

Figure C.1: The figure displays examples of the time dependent $F1$-correlator calculated from the inverse Laplace transform of Equation (C.10). The microscopic attenuation is set to $\xi = 0.1$. After initial damped oscillations, the correlator approaches its long-time limit, exhibiting features due to the anharmonic effects of the memory. The insert displays the long-time limit in dependence on the parameter a. Here, the red line shows the results calculated from the numerical solution, and the blue symbols indicate the theoretically predicted value, *i.e.* Equation (C.12).

Approximation induced error: The approximation performed in Equation (C.7) alters the small frequency properties of the imaginary part. This can be seen best by looking at the Density of States of the scalar ERM model in the $F1$-approximation of Equation (5.79). As stated in Section 5.3.3, the Density of States in the ERM model is given by the high momentum limit of susceptibility $D^{\mathrm{SERM}}(\omega) = 2\frac{\omega}{\pi}\,\mathrm{Im}\{\chi^{\mathrm{SERM}}_{q\to\infty}(-i\omega + 0^+)\}$. Using Equation (5.91) gives for the imaginary part $\mathrm{Im}\{\hat{\Sigma}^{\mathrm{SERM}}_{q\to\infty}(-i\omega + 0^+)\} \propto \omega$ for small frequencies $\omega \to 0$. The defining expression for the self-energy $\hat{\Sigma}_{q\to\infty}$ is given in Equation (5.74b). Thus, the scalar ERM model features the Debye vDOS for $\omega \to 0$:

$$D^{\mathrm{SERM}}(\omega \to 0) \propto \omega^2 \,. \tag{C.13}$$

However, the approximation of Equation (C.7) alters this small frequency result as the Equations predict

$$D^{\mathrm{SERM}}(\omega \to) \propto \omega \ , \tag{C.14}$$

independently of the spatial dimension. This eventually arises from changing the imaginary part of the complex-valued dispersion relation $(q\tilde{v}_q(-i\omega + 0^+))^2$. The erroneous Result (C.14) implies that the sound attenuation can also not be inferred from the numerical solution $\mathrm{K}_q(t)$ in the time domain. However, as this only affects the frequency-dependent quantities, the inverse compliance $(qv)^2$ and the non-ergodicity parameter κ_q are still correctly captured by the model introduced in Equation (C.7) and consequentially by its numerical solution. Taking smaller wavenumbers $q\sigma \to 0$ into account is essential to describe the frequency-dependent quantities correctly. Nevertheless, considering very small wavenumbers has led to problems as the diagonal elements of the stability matrix $q^2 C_{q,q}$ become negative. The solution to this problem is left for future work.

D | The bare vertex

This chapter contains an explicit analysis of the bare vertex

$$\underline{\boldsymbol{V}}_{\boldsymbol{q},\boldsymbol{k}} = -\frac{\langle \boldsymbol{F}^{\perp}(\boldsymbol{q})\Omega Q_1 \delta\rho(\boldsymbol{k}-\boldsymbol{q})\boldsymbol{v}^{\perp}(-\boldsymbol{k})\rangle}{N k_B T q (c_q^{\perp})^2 S_{|\boldsymbol{q}-\boldsymbol{k}|}} \,. \tag{D.1}$$

The goal is to establish an expression solely depending on the interaction potential and the structure, which are principally the only inputs required for the theory. In Section D.1, we derive an expression for the vertex, which only depends on the pair- and triplet correlation function:

$$g(r) \equiv \frac{1}{nN} \langle \sum_{i,m\neq i} \delta(\boldsymbol{r} - (\boldsymbol{r}_i - \boldsymbol{r}_m)) \rangle \tag{D.2a}$$

$$g^{(3)}(\boldsymbol{r},\boldsymbol{r}') \equiv \frac{1}{n^2 N} \langle \sum_{m\neq l\neq n} \delta(\boldsymbol{r} - (\boldsymbol{r}_l - \boldsymbol{r}_n))\delta(\boldsymbol{r}' - (\boldsymbol{r}_l - \boldsymbol{r}_m)) \rangle \tag{D.2b}$$

We continue in Section D.2 by discussing the properties of the vertex, namely its symmetry relations and the hydrodynamic limit $\boldsymbol{q}, \boldsymbol{k} \to 0$.

D.1 Vertex evaluation

This section aims to derive an expression for the vertex in terms of the pair- and triplet correlation function. The derivation starts from rewriting the equation for the bare vertex. One has:

$$\begin{aligned} -N k_B T q (c_q^{\perp})^2 S_{|\boldsymbol{q}-\boldsymbol{k}|} \underline{\boldsymbol{V}}_{\boldsymbol{q},\boldsymbol{k}} &= \langle \boldsymbol{F}^{\perp}(\boldsymbol{q})\Omega Q_1 \delta\rho(\boldsymbol{k}-\boldsymbol{q})\boldsymbol{v}^{\perp}(-\boldsymbol{k})\rangle \\ &= \langle \boldsymbol{F}^{\perp}(\boldsymbol{q})| \, \Omega \left[\underline{\mathbf{1}} - \frac{|\boldsymbol{v}^{\perp}(-\boldsymbol{q})\rangle \cdot \langle \boldsymbol{v}^{\perp}(\boldsymbol{q})|}{N \frac{k_B T}{m}} \right] |\delta\rho(\boldsymbol{k}-\boldsymbol{q})\boldsymbol{v}^{\perp}(-\boldsymbol{k})\rangle \end{aligned} \tag{D.3}$$

Here, we just inserted the definition of the projection operator $Q_1 = 1 - P_1$, where P_1 projects on the transverse current. We analyze the two terms in Equation (D.3)

independently and start with the second one. The following analysis is done using spatial indices to make the matrix multiplication more transparent:

Term 2: $\langle F_\alpha^\perp(\boldsymbol{q})\Omega v_\gamma^\perp(-\boldsymbol{q})\rangle \langle v_\gamma^\perp(\boldsymbol{q})\delta\rho(\boldsymbol{k}-\boldsymbol{q})v_\beta^\perp(-\boldsymbol{k})\rangle \frac{m}{Nk_BT}$.
Due to evaluating an equilibrium correlation function, time-reversal symmetry is obeyed. Thus, we only have to look at the part of $\Omega\,|\boldsymbol{v}^\perp(-\boldsymbol{q})\rangle$ with even time-inversion parity. Only considering the leading order in T, the first factor is proportional to the instantaneous modulus:

$$\begin{aligned} m\,\langle F_\alpha^\perp(\boldsymbol{q})\Omega v_\gamma^\perp(-\boldsymbol{q})\rangle + \mathcal{O}(T^2) &= -\,\langle F_\alpha^\perp(\boldsymbol{q})F_\gamma^\perp(-\boldsymbol{q})\rangle \\ &= -\Big(\delta_{\alpha\gamma}-\hat{q}_\alpha\hat{q}_\gamma\Big)q^2(c_q^\perp)^2Nk_BTm + \mathcal{O}(T^2) \end{aligned} \tag{D.4}$$

The second factor evaluates to

$$\begin{aligned} \langle v_\gamma^\perp(\boldsymbol{q})\delta\rho(\boldsymbol{k}-\boldsymbol{q})v_\beta^\perp(-\boldsymbol{k})\rangle &= \Big(\delta_{\gamma\mu}-\hat{q}_\gamma\hat{q}_\mu\Big)\langle v_\mu(\boldsymbol{q})\delta\rho(\boldsymbol{k}-\boldsymbol{q})v_\tau(-\boldsymbol{k})\rangle\Big(\delta_{\tau\beta}-\hat{k}_\tau\hat{k}_\beta\Big) \\ &= \Big(\delta_{\gamma\mu}-\hat{q}_\gamma\hat{q}_\mu\Big)N\frac{k_BT}{m}S_{|\boldsymbol{q}-\boldsymbol{k}|}\Big(\delta_{\mu\beta}-\hat{k}_\mu\hat{k}_\beta\Big)\,. \end{aligned} \tag{D.5}$$

Putting it all together, this leads to

$$\begin{aligned} &m\frac{\langle F_\alpha^\perp(\boldsymbol{q})\Omega v_\gamma^\perp(-\boldsymbol{q})\rangle \langle v_\gamma^\perp(\boldsymbol{q})\delta\rho(\boldsymbol{k}-\boldsymbol{q})v_\beta^\perp(-\boldsymbol{k})\rangle}{Nk_BT} \\ &\qquad = -\Big(\delta_{\alpha\gamma}-\hat{q}_\alpha\hat{q}_\gamma\Big)q^2(c_q^\perp)^2Nk_BTS_{|\boldsymbol{q}-\boldsymbol{k}|}\Big(\delta_{\gamma\beta}-\hat{k}_\gamma\hat{k}_\beta\Big) \end{aligned} \tag{D.6}$$

Term 1: $\langle \boldsymbol{F}^\perp(\boldsymbol{q})\Omega\delta\rho(\boldsymbol{k}-\boldsymbol{q})\boldsymbol{v}^\perp(-\boldsymbol{k})\rangle$.
We continue neglecting any kinetic contributions, since they become negligible for $T\to 0$. The lowest order in the temperature reads

$$\begin{aligned} m\,\langle \boldsymbol{F}^\perp(\boldsymbol{q})\Omega\delta\rho(\boldsymbol{k}-\boldsymbol{q})\boldsymbol{v}^\perp(-\boldsymbol{k})\rangle &= -\,\langle \boldsymbol{F}^\perp(\boldsymbol{q})\delta\rho(\boldsymbol{k}-\boldsymbol{q})\boldsymbol{F}^\perp(-\boldsymbol{k})\rangle + \mathcal{O}(T^2) \\ &= -\,\langle \boldsymbol{F}^\perp(\boldsymbol{q})\rho(\boldsymbol{k}-\boldsymbol{q})\boldsymbol{F}^\perp(-\boldsymbol{k})\rangle \\ &\quad + N^2\delta_{\boldsymbol{q},\boldsymbol{k}}k_BTm(qc_q^\perp)^2[\underline{\mathbf{1}}-\hat{\boldsymbol{q}}\hat{\boldsymbol{q}}] \\ &\quad + \mathcal{O}(T^2)\,. \end{aligned} \tag{D.7}$$

Taking the longitudinal current $\boldsymbol{v}^\parallel$ into account only affects higher orders in T. In the second line, we used $\delta\rho(\boldsymbol{q}-\boldsymbol{k}) = \rho(\boldsymbol{q}-\boldsymbol{k}) - \langle\rho(\boldsymbol{k}-\boldsymbol{q})\rangle$ and $\langle\rho(0)\rangle = N$. To

evaluate the term in the second line of Equation (D.7), we continue using vector notation. It keeps the notations easier as fewer indices appear. Also, the following calculation is reminiscent of the evaluation of the instantaneous modulus $(c_q^{\perp})^2$ in Equation (5.21). The vector notation makes the similarities more transparent. Again relying on $\int d\Gamma \boldsymbol{F}_j A \Psi_{eq} = -k_B T \int d\Gamma \Psi_{eq} \nabla_j A$, we get

$$
\begin{aligned}
&\frac{1}{k_B T} \langle \sum_{j,m,l} \boldsymbol{F}_j e^{-i\boldsymbol{q}\cdot\boldsymbol{r}_j} \cdot [\underline{\mathbf{1}} - \hat{\boldsymbol{q}}\hat{\boldsymbol{q}}] e^{-i(\boldsymbol{k}-\boldsymbol{q})\cdot\boldsymbol{r}_m} [\underline{\mathbf{1}} - \hat{\boldsymbol{k}}\hat{\boldsymbol{k}}] \cdot \boldsymbol{F}_l e^{i\boldsymbol{k}\cdot\boldsymbol{r}_l} \rangle \\
= &- \langle \sum_{j,m,l} \frac{\partial}{\partial \boldsymbol{r}_j} e^{-i\boldsymbol{q}\cdot\boldsymbol{r}_j} \cdot [\underline{\mathbf{1}} - \hat{\boldsymbol{q}}\hat{\boldsymbol{q}}] e^{-i(\boldsymbol{k}-\boldsymbol{q})\cdot\boldsymbol{r}_m} [\underline{\mathbf{1}} - \hat{\boldsymbol{k}}\hat{\boldsymbol{k}}] \cdot \boldsymbol{F}_l e^{i\boldsymbol{k}\cdot\boldsymbol{r}_l} \rangle \\
= &- \langle \sum_{m,l} (-i\boldsymbol{k}) \cdot \Big(e^{-i\boldsymbol{k}\cdot(\boldsymbol{r}_m - \boldsymbol{r}_l)} - e^{-i(\boldsymbol{q}-\boldsymbol{k})\cdot\boldsymbol{r}_l} e^{-i(\boldsymbol{k}-\boldsymbol{q})\cdot\boldsymbol{r}_m} \Big) \cdot [\underline{\mathbf{1}} - \hat{\boldsymbol{q}}\hat{\boldsymbol{q}}][\underline{\mathbf{1}} - \hat{\boldsymbol{k}}\hat{\boldsymbol{k}}] \cdot \boldsymbol{F}_l \rangle \\
&- \langle \sum_{j,m,l} e^{-i\boldsymbol{q}\cdot(\boldsymbol{r}_j - \boldsymbol{r}_m)} e^{-i\boldsymbol{k}\cdot(\boldsymbol{r}_m - \boldsymbol{r}_l)} \Big(\frac{\partial}{\partial \boldsymbol{r}_j} \cdot [\underline{\mathbf{1}} - \hat{\boldsymbol{q}}\hat{\boldsymbol{q}}][\underline{\mathbf{1}} - \hat{\boldsymbol{k}}\hat{\boldsymbol{k}}] \cdot \boldsymbol{F}_l \Big) \rangle = \ldots
\end{aligned}
\tag{D.8}
$$

Importantly, the first line after the last equality sign vanishes with the temperature. This can be seen by again applying $\int d\Gamma \boldsymbol{F}_j A \Psi_{eq} = -k_B T \int d\Gamma \Psi_{eq} \nabla_j A$. Hence, this vanishing is a consequence of considering an equilibrium distribution or rather due to assuming that the system is at the bottom of the potential energy landscape. Expressing the forces via the pair potential $U(r)$ gives

$$
\begin{aligned}
\ldots = &\langle \sum_{j,m,l,n\neq l} e^{-i\boldsymbol{q}\cdot(\boldsymbol{r}_j - \boldsymbol{r}_m)} e^{-i\boldsymbol{k}\cdot(\boldsymbol{r}_m - \boldsymbol{r}_l)} \Big(\frac{\partial}{\partial \boldsymbol{r}_j} \cdot [\underline{\mathbf{1}} - \hat{\boldsymbol{q}}\hat{\boldsymbol{q}}][\underline{\mathbf{1}} - \hat{\boldsymbol{k}}\hat{\boldsymbol{k}}] \cdot \frac{\partial}{\partial \boldsymbol{r}_l} U(\boldsymbol{r}_l - \boldsymbol{r}_n) \Big) \rangle \\
= &\langle \sum_{m,l,n\neq l} \Big(e^{-i(\boldsymbol{k}-\boldsymbol{q})\cdot(\boldsymbol{r}_m - \boldsymbol{r}_l)} - e^{-i\boldsymbol{q}\cdot(\boldsymbol{r}_n - \boldsymbol{r}_m)} e^{-i\boldsymbol{k}\cdot(\boldsymbol{r}_m - \boldsymbol{r}_l)} \Big) \\
&\times \frac{\partial}{\partial \boldsymbol{r}_l} \cdot [\underline{\mathbf{1}} - \hat{\boldsymbol{q}}\hat{\boldsymbol{q}}][\underline{\mathbf{1}} - \hat{\boldsymbol{k}}\hat{\boldsymbol{k}}] \cdot \frac{\partial U(\boldsymbol{r}_l - \boldsymbol{r}_n)}{\partial \boldsymbol{r}_l} \rangle = \ldots
\end{aligned}
\tag{D.9}
$$

Similarly to the derivation of the instantaneous modulus in Section 5.2.1, we can express the pair-potential via and integral over a delta-distribution

$$
U(|\boldsymbol{r}_l - \boldsymbol{r}_n|) = \int d^d \boldsymbol{r} U(r) \delta\big(\boldsymbol{r} - (\boldsymbol{r}_l - \boldsymbol{r}_n)\big) \, . \tag{D.10}
$$

This leads to

$$\begin{aligned} ... = \int d^d\boldsymbol{r} d^d\boldsymbol{r}' \langle \sum_{m,l\neq n} \delta(\boldsymbol{r} - (\boldsymbol{r}_l - \boldsymbol{r}_n))\delta(\boldsymbol{r}' - (\boldsymbol{r}_l - \boldsymbol{r}_m))\rangle \, e^{i(\boldsymbol{k}-\boldsymbol{q})\cdot\boldsymbol{r}'} \\ \times \left[1 - e^{i\boldsymbol{q}\cdot\boldsymbol{r}}\right] \nabla^{\perp,\boldsymbol{q}} \nabla^{\perp,\boldsymbol{k}} U(r) \; . \end{aligned} \tag{D.11}$$

Here, we introduced the transverse nabla operators:

$$\nabla^{\perp,\boldsymbol{q}} = \nabla \cdot [\underline{\mathbf{1}} - \hat{\boldsymbol{q}}\hat{\boldsymbol{q}}] \; . \tag{D.12}$$

The correlation function appearing in Equation (D.11) can be expressed with the pair and the triplet corrrelation functions $g(r)$ and $g^{(3)}(\boldsymbol{r}, \boldsymbol{r}')$. To see this, we split up the sums:

$$\begin{aligned} ... = \int d^d\boldsymbol{r} d^d\boldsymbol{r}' \Big\{ \langle \sum_{m\neq l\neq n} \delta(\boldsymbol{r} - (\boldsymbol{r}_l - \boldsymbol{r}_n))\delta(\boldsymbol{r}' - (\boldsymbol{r}_l - \boldsymbol{r}_m))\rangle \\ + \langle \sum_{l,n\neq l} \delta(\boldsymbol{r} - (\boldsymbol{r}_l - \boldsymbol{r}_n)\rangle \, \delta(\boldsymbol{r}') \\ + \langle \sum_{l,n\neq l} \delta(\boldsymbol{r} - (\boldsymbol{r}_l - \boldsymbol{r}_n)\rangle \, \delta(\boldsymbol{r}' - \boldsymbol{r}) \Big\} e^{i(\boldsymbol{k}-\boldsymbol{q})\cdot\boldsymbol{r}'} \left[1 - e^{i\boldsymbol{q}\cdot\boldsymbol{r}}\right] \nabla^{\perp,\boldsymbol{q}} \nabla^{\perp,\boldsymbol{k}} U(r) \end{aligned} \tag{D.13}$$

Here, the sum $\sum_{m\neq l\neq n}$ is understood as none of the three indices being equal to each other. Recognizing the definition of the pair- and the triplet correlation function $g(r)$ and $g^{(3)}(\boldsymbol{r}, \boldsymbol{r}')$ given in Equation (D.2) leads to a concise expression

$$\begin{aligned} ... = N \int d^d\boldsymbol{r} d^d\boldsymbol{r}' \Big(n^2 g^{(3)}(\boldsymbol{r}, \boldsymbol{r}') + n g(r)[\delta(\boldsymbol{r}') + \delta(\boldsymbol{r} - \boldsymbol{r}')] \Big) \\ \times e^{i(\boldsymbol{k}-\boldsymbol{q})\cdot\boldsymbol{r}'} \left[1 - e^{i\boldsymbol{q}\cdot\boldsymbol{r}}\right] \nabla^{\perp,\boldsymbol{q}} \nabla^{\perp,\boldsymbol{k}} U(r) \; . \end{aligned} \tag{D.14}$$

Lastly, we notice that the last term appearing in Equation (D.7) can be smoothly included since

$$n^2 \int d^d\boldsymbol{r} d^d\boldsymbol{r}' g(r) e^{i(\boldsymbol{k}-\boldsymbol{q})\cdot\boldsymbol{r}'} \left[1 - e^{i\boldsymbol{q}\cdot\boldsymbol{r}}\right] \nabla^{\perp,\boldsymbol{q}} \nabla^{\perp,\boldsymbol{k}} U(r) = N\delta_{\boldsymbol{k},\boldsymbol{q}} [\underline{\mathbf{1}} - \hat{\boldsymbol{q}}\hat{\boldsymbol{q}}] (c_q^{\perp})^2 m \tag{D.15}$$

holds. Here, we recognized Equation (5.25) for the instantaneous modulus $(c_q^{\perp})^2$.

Putting everything together, we get the following expression for the bare vertex:

$$\begin{aligned}\underline{\boldsymbol{V}}_{\boldsymbol{q},\boldsymbol{k}} =& -\frac{\langle \boldsymbol{F}^{\perp}(\boldsymbol{q})\Omega Q\delta\rho(\boldsymbol{k}-\boldsymbol{q})\boldsymbol{v}^{\perp}(-\boldsymbol{k})\rangle}{Nk_BTq(c_q^{\perp})^2S_{|\boldsymbol{q}-\boldsymbol{k}|}}\\ =& -q\Big(\underline{\mathbf{1}}-\hat{\boldsymbol{q}}\hat{\boldsymbol{q}}\Big)\cdot\Big(\underline{\mathbf{1}}-\hat{\boldsymbol{k}}\hat{\boldsymbol{k}}\Big)\\ &+\int d^d\boldsymbol{r}d^d\boldsymbol{r}'\frac{ng^{(3)}(\boldsymbol{r},\boldsymbol{r}')-ng(r)+g(r)\Big(\delta(\boldsymbol{r}')+\delta(\boldsymbol{r}-\boldsymbol{r}')\Big)}{q(c_q^{\perp})^2(m/n)S_{|\boldsymbol{q}-\boldsymbol{k}|}}\\ &\times e^{i(\boldsymbol{k}-\boldsymbol{q})\cdot\boldsymbol{r}'}\Big[1-e^{i\boldsymbol{q}\cdot\boldsymbol{r}}\Big]\nabla^{\perp,\boldsymbol{q}}\nabla^{\perp,\boldsymbol{k}}U(r)\end{aligned} \tag{D.16}$$

This formula is also the expression for the vertex given in (Vogel *et al.*, 2025). Notably, it is also possible to express the vertex $\underline{\boldsymbol{V}}_{\boldsymbol{q},\boldsymbol{k}}$ in terms of the static structure factor S_q. Similarly, we could express the instantaneous modulus $(c_q^{\perp})^2$ in terms of S_q in Section 5.2.1. However, as in the case of $(c_q^{\perp})^2$, the result for $\underline{\boldsymbol{V}}_{\boldsymbol{q},\boldsymbol{k}}$ depends on the phases as a reference frame exists in the jammed state and $\langle\rho(\boldsymbol{q})\rangle = N\delta_{\boldsymbol{q},0}$ does not hold anymore. When expressing $\underline{\boldsymbol{V}}_{\boldsymbol{q},\boldsymbol{k}}$ in terms of S_q, the resulting term reads differently for the two phases. Thus, we only use Equation (D.16) for the bare vertex. In the next section, we take a closer look at the properties of the vertex.

D.2 The vertex's properties

After obtaining an expression for the vertex, $\underline{\boldsymbol{V}}$, we can look at some of its characteristic properties. As correlation functions of scalar quantities only depend on the absolute modulus of the wavevector (see Section 3), a change of the integration variables and the symmetry of the triplet correlation function $g^{(3)}(\boldsymbol{r},\boldsymbol{r}') = g^{(3)}(-\boldsymbol{r},-\boldsymbol{r}') = g^{(3)}(\boldsymbol{r},\boldsymbol{r}-\boldsymbol{r}')$ lead to

$$\begin{aligned}&\underline{\boldsymbol{V}}^{\dagger}_{\boldsymbol{q},\boldsymbol{k}} = \left(\underline{\boldsymbol{V}}_{-\boldsymbol{k},-\boldsymbol{q}}\right)^T = \left(\underline{\boldsymbol{V}}_{\boldsymbol{k},\boldsymbol{q}}\right)^T\ ,\\ &\underline{\boldsymbol{V}}_{\boldsymbol{q},0} = \underline{\boldsymbol{V}}_{-\boldsymbol{q},0}\ , \qquad \underline{\boldsymbol{V}}_{0,\boldsymbol{k}} = -\underline{\boldsymbol{V}}_{0,-\boldsymbol{k}}\ .\end{aligned} \tag{D.17}$$

Again, $\left(\underline{\boldsymbol{V}}_{\boldsymbol{q},\boldsymbol{k}}\right)^T$ denotes the matrix transposed of the vertex interpreted as a $\mathbb{C}^{d\times d}$ matrix. The first expression in Equation (D.17) only holds for finite wavevectors $\boldsymbol{q},\boldsymbol{k}$. Furthermore, the symmetry of the triple correlation function also implies

$$\underline{\boldsymbol{V}}_{\boldsymbol{q},\boldsymbol{k}\to 0} \longrightarrow -q[\underline{\mathbf{1}}-\hat{\boldsymbol{q}}\hat{\boldsymbol{q}}]\cdot[\underline{\mathbf{1}}-\hat{\boldsymbol{k}}\hat{\boldsymbol{k}}]\ . \tag{D.18}$$

To evaluate the hydrodynamic limit of the vertex, it suffices to expand the exponential in Equation (D.16). Due to isotropy, the hydrodynamic limit reads:

$$\underline{\boldsymbol{V}}_{\boldsymbol{k}\to 0,\boldsymbol{q}\to 0} = \underline{\boldsymbol{V}}^{(1)} q + \underline{\boldsymbol{V}}^{(2)} \frac{\boldsymbol{k}\cdot\boldsymbol{q}}{q} \ , \tag{D.19}$$

where the two coefficients $\underline{\boldsymbol{V}}^{(1,2)}$ are independent of the absolute value Fouriermodes $|\boldsymbol{q}|, |\boldsymbol{k}|$ but only depend on their directions $\hat{\boldsymbol{q}}, \hat{\boldsymbol{k}}$. In the case of the ERM approximation discussed in Section 4.4, one has

$$\begin{aligned} \underline{\boldsymbol{V}}^{\perp,\perp}_{\boldsymbol{q},\boldsymbol{k}} &= -q(c^{\perp}_{q})^2 \underline{\boldsymbol{V}}_{\boldsymbol{q},\boldsymbol{k}} \\ \underline{\boldsymbol{V}}^{\perp,\perp}_{\boldsymbol{q}\to 0,\boldsymbol{k}\to 0} &= \underline{\tilde{\boldsymbol{V}}}^{(1)} q^2 + \underline{\tilde{\boldsymbol{V}}}(\boldsymbol{q}\cdot\boldsymbol{k}) \ . \end{aligned} \tag{D.20}$$

The ERM model is discussed exhaustively in Appendix A. The ERM vertex is derived in Section A.2.

E | The instantaneous damping $\underline{\tilde{\gamma}}$

In this chapter, we look at the non-zero frequency matrix

$$\underline{\tilde{\gamma}}(\boldsymbol{q},\boldsymbol{k},\boldsymbol{p}) = -\frac{\langle \boldsymbol{F}^{\perp}(\boldsymbol{k})\delta\rho(\boldsymbol{q}-\boldsymbol{k})\Omega_3\delta\rho(\boldsymbol{p}-\boldsymbol{q})\boldsymbol{F}^{\perp}(-\boldsymbol{p})\rangle}{N^2 m k_B T (k c_k^{\perp})^2 S_{|\boldsymbol{q}-\boldsymbol{k}|}} \,, \tag{E.1}$$

which is proportional to the Langevin damping rate ξ. However, hereinafter, we will show that $\underline{\tilde{\gamma}}$ vanishes linearly with the temperature. We start our analysis by noticing that $P_3\,|\boldsymbol{F}^{\perp}(\boldsymbol{k})\delta\rho(\boldsymbol{q}-\boldsymbol{k})\rangle = 0$ holds, due to the different time inversion parities of $|\boldsymbol{F}^{\perp}(\boldsymbol{k})\delta\rho(\boldsymbol{q}-\boldsymbol{k})\rangle$ and $|\boldsymbol{v}^{\perp}(\boldsymbol{k})\delta\rho(\boldsymbol{q}-\boldsymbol{k})\rangle$. Noticeable, we only have to consider the time derivative of the force $\Omega^{\dagger}\boldsymbol{F}^{\perp}(\boldsymbol{k})$, as $\Omega^{\dagger}\delta\rho \propto \boldsymbol{v}$ has odd time inversion parity. Furthermore, we notice that the only contribution with even time inversion parity arises from the kinetic part of fluctuating forces:

$$\langle \Omega^{\dagger}\boldsymbol{F}^{\perp}(\boldsymbol{k})| = 2\xi \left\langle \sum_{j=1}^{N} \frac{-i\boldsymbol{k}\cdot\boldsymbol{p}_j}{m}\boldsymbol{p}_j \cdot [\underline{\mathbf{1}} - \hat{\boldsymbol{k}}\hat{\boldsymbol{k}}]e^{-i\boldsymbol{k}\cdot\boldsymbol{r}_j}\right| + \Big[\cdots\Big] \tag{E.2}$$

Here, the square bracket contains all the terms with odd time inversion parity. With Equation (E.2) and relying on the identity $\int d\Gamma \boldsymbol{F}_j A\Psi_{\mathrm{eq}} = -k_B T \int d\Gamma \Psi_{\mathrm{eq}}\nabla_j\nabla_j A$, the four different contributions of $\underline{\tilde{\gamma}}$ arising from $[1-P_2]\Omega[1-P_2]$ can be calculated one by one:

(I) First, we look at

$$\begin{aligned} &-\frac{\langle \boldsymbol{F}^{\perp}(\boldsymbol{k})\delta\rho(\boldsymbol{q}-\boldsymbol{k})P_2\Omega P_2\delta\rho(\boldsymbol{p}-\boldsymbol{q})\boldsymbol{F}^{\perp}(-\boldsymbol{p})\rangle}{N^2 m k_B T (k c_k^{\perp})^2 S_{|\boldsymbol{q}-\boldsymbol{k}|}} \\ &\qquad = -\frac{\langle \underline{\boldsymbol{Y}}(\boldsymbol{k},-\boldsymbol{q})\rangle \cdot \langle (\Omega^{\dagger}\boldsymbol{F}^{\perp}(\boldsymbol{q}))\boldsymbol{F}^{\perp}(-\boldsymbol{q})\rangle \cdot \langle \underline{\boldsymbol{Y}}(-\boldsymbol{p},\boldsymbol{q})\rangle}{N^2 m k_B T (k c_k^{\perp})^2 S_{|\boldsymbol{q}-\boldsymbol{k}|}} \end{aligned} \tag{E.3}$$

with the abbreviation

$$\langle \underline{\boldsymbol{Y}}(\boldsymbol{k},-\boldsymbol{q})\rangle \equiv \cdot \frac{\langle \sum_j \nabla_j \cdot [\underline{\mathbf{1}} - \hat{\boldsymbol{k}}\hat{\boldsymbol{k}}]e^{-i\boldsymbol{k}\boldsymbol{r}_j}\delta\rho(\boldsymbol{q}-\boldsymbol{k})\boldsymbol{F}^{\perp}(-\boldsymbol{q})\rangle}{N m (q c_q^{\perp})^2} \,. \tag{E.4}$$

Here, the relation $\langle \boldsymbol{F}_j A\rangle = -k_B T \langle \nabla_j A\rangle$ was used. The calculation of $\langle \underline{\boldsymbol{Y}}(\boldsymbol{k},-\boldsymbol{q})\rangle$ resembles the evaluation of the vertex presented in Appendix D. The numerator equals the term analyzed from Equation (D.7) onwards up to a factor m. Ignoring the initial stresses gives us

$$\begin{aligned}\langle \underline{\boldsymbol{Y}}(\boldsymbol{k},-\boldsymbol{q})\rangle = \int d^d\boldsymbol{r} d^d\boldsymbol{r}' \frac{n^2 g^{(3)}(\boldsymbol{r},\boldsymbol{r}') - n g(r) + n g(r)[\delta(\boldsymbol{r}') + \delta(\boldsymbol{r}-\boldsymbol{r}')]}{m(q c_q^{\perp})^2} \\ \times e^{i(\boldsymbol{k}-\boldsymbol{q})\cdot\boldsymbol{r}'}\left[1 - e^{i\boldsymbol{q}\cdot\boldsymbol{r}}\right]\nabla^{\perp,\boldsymbol{k}}\nabla^{\perp,\boldsymbol{q}} U(r)\end{aligned} \tag{E.5}$$

with the abbreviations $\nabla\cdot[\underline{\mathbf{1}} - \hat{\boldsymbol{q}}\hat{\boldsymbol{q}}] \equiv \nabla^{\perp,\boldsymbol{q}}$ and $[\underline{\mathbf{1}} - \hat{\boldsymbol{k}}\hat{\boldsymbol{k}}]\cdot\nabla \equiv \nabla^{\perp,\boldsymbol{k}}$. Obviously, $\langle \underline{\boldsymbol{Y}}(\boldsymbol{k},-\boldsymbol{q})\rangle$ has a finite limit for $N\to\infty$. The remaining unknown term in Equation (E.3) is the frequency matrix element of the force fluctuation. Here, we use the index notation to make the matrix multiplication more transparent:

$$\begin{aligned}&-\langle \Omega^\dagger F_\alpha^{\perp}(\boldsymbol{q}) F_\beta^{\perp}(-\boldsymbol{q})\rangle \\ &\quad= 2\xi\frac{q_\nu q_\mu}{m^2}[\delta_{\tau\alpha} - q_\tau q_\alpha][\delta_{\eta\beta} - q_\eta q_\beta]\sum_{j,l=1}^{N}\langle p_{j,\nu} p_{j,\tau} p_{l,\mu} p_{l,\eta}\rangle \langle e^{-i\boldsymbol{q}\cdot(\boldsymbol{r}_j - \boldsymbol{r}_l)}\rangle \\ &\quad= 2\xi(k_B T)^2 q_\nu q_\mu[\delta_{\tau\alpha} - q_\tau q_\alpha][\delta_{\eta\beta} - q_\eta q_\beta] \\ &\qquad\times\sum_{j,l=1}^{N}\left(\delta_{\tau\nu}\delta_{\mu\eta} + \delta_{jl}\delta_{\mu\nu}\delta_{\tau\eta} + \delta_{jl}\delta_{\eta\nu}\delta_{\mu\tau}\right)\langle e^{-i\boldsymbol{q}\cdot(\boldsymbol{r}_j - \boldsymbol{r}_l)}\rangle \\ &\quad= 2N\xi(k_B T)^2 q^2[\delta_{\alpha\beta} - q_\alpha q_\beta]\end{aligned} \tag{E.6}$$

Only the second term in the bracket in line four contributes. The other two contributions vanish due to the spatial projections. The potential force $\sum_l \boldsymbol{F}_l e^{i\boldsymbol{p}\cdot\boldsymbol{r}_l}$ does not contribute due to the different time inversion parity. After putting everything together, it looks like the first term

$$-\frac{\langle \boldsymbol{F}^{\perp}(\boldsymbol{k})\delta\rho(\boldsymbol{q}-\boldsymbol{k}) P_2 \Omega P_2 \delta\rho(\boldsymbol{p}-\boldsymbol{q})\boldsymbol{F}^{\perp}(-\boldsymbol{p})\rangle}{N^2 m k_B T (k c_k^{\perp})^2 S_{|\boldsymbol{q}-\boldsymbol{k}|}} = \mathcal{O}(N^{-1}) \tag{E.7}$$

becomes negligible for $N\to\infty$. However, the sum over the wavenumbers $\boldsymbol{p}$ becomes an integral for $N,V\to\infty$. This leads to $\frac{1}{N}\sum_{\boldsymbol{p}} \to \frac{1}{n}\int\frac{d^d\boldsymbol{p}}{(2\pi)^d}$ and this term actually yields a finite contribution in the thermodynamic limit.

(II) The second term can be calculated analogously. Expressing it with $\langle \underline{\boldsymbol{Y}}(\boldsymbol{k}, -\boldsymbol{q})\rangle$ for abbreviating purposes, the formulae reads

$$- \langle \underline{\boldsymbol{Y}}(\boldsymbol{k}, -\boldsymbol{q})\rangle \cdot \frac{\langle (\Omega^\dagger \boldsymbol{F}^\perp(\boldsymbol{q}))\delta\rho(\boldsymbol{p}-\boldsymbol{q})\boldsymbol{F}^\perp(-\boldsymbol{p})\rangle}{N^2 m k_B T (k c_k^\perp)^2 S_{|\boldsymbol{q}-\boldsymbol{k}|}} = ... \tag{E.8}$$

To calculate the remaining unknown term, we utilize the index notation:

$$\begin{aligned}
&- \langle (\Omega^\dagger F_\alpha^\perp(\boldsymbol{q}))\delta\rho(\boldsymbol{p}-\boldsymbol{q})F_\beta^\perp(-\boldsymbol{p})\rangle = \\
&= 2\xi \frac{q_\nu p_\mu}{m^2}[\delta_{\tau\alpha} - q_\tau q_\alpha][\delta_{\eta\beta} - p_\eta p_\beta] \sum_{j,l=1}^{N} \langle p_{j,\nu} p_{j,\tau} p_{l,\mu} p_{l,\eta}\rangle \langle e^{-i\boldsymbol{q}\cdot\boldsymbol{r}_j}\delta\rho(\boldsymbol{p}-\boldsymbol{q})e^{i\boldsymbol{p}\cdot\boldsymbol{r}_l}\rangle \\
&= 2\xi (k_B T)^2 q_\nu p_\mu [\delta_{\tau\alpha} - q_\tau q_\alpha][\delta_{\eta\beta} - p_\eta p_\beta] \\
&\quad \times \sum_{j,l=1}^{N} \Big(\delta_{\tau\nu}\delta_{\mu\eta} + \delta_{jl}\delta_{\mu\nu}\delta_{\tau\eta} + \delta_{jl}\delta_{\eta\nu}\delta_{\mu\tau}\Big) \langle e^{-i\boldsymbol{q}\cdot\boldsymbol{r}_j}\delta\rho(\boldsymbol{p}-\boldsymbol{q})e^{i\boldsymbol{p}\cdot\boldsymbol{r}_l}\rangle \\
&= 2N\xi (k_B T)^2 S_{|\boldsymbol{q}-\boldsymbol{p}|} \\
&\quad \times \Big(q_\mu p_\mu [\delta_{\alpha\eta} - q_\alpha q_\eta][\delta_{\eta\beta} - p_\eta p_\beta] + p_\mu [\delta_{\alpha\mu} - q_\alpha q_\mu] q_\nu [\delta_{\nu\beta} - p_\nu p_\beta]\Big)
\end{aligned} \tag{E.9}$$

Again, this term can not rightfully be ignored even for $N \to \infty$ due to the sum over the wavevectors.

(III) After exchanging $\boldsymbol{q} \longleftrightarrow \boldsymbol{k}$ and $\boldsymbol{p} \longleftrightarrow \boldsymbol{q}$, the calculation of the third term mirrors the calculation of the second term. One hence has

$$\begin{aligned}
&- \frac{\langle (\Omega^\dagger F_\alpha^\perp(\boldsymbol{k}))\delta\rho(\boldsymbol{q}-\boldsymbol{k})F_\beta^\perp(-\boldsymbol{q})\rangle}{N^2 m k_B T (k c_k^\perp)^2 S_{|\boldsymbol{q}-\boldsymbol{k}|}} \langle Y_{\beta\zeta}(-\boldsymbol{p}, \boldsymbol{q})\rangle = \frac{2\xi k_B T}{N (k c_k^\perp)^2} \langle Y_{\beta\zeta}(-\boldsymbol{p}, \boldsymbol{q})\rangle \\
&\quad \times \Big(k_\mu q_\mu [\delta_{\alpha\eta} - k_\alpha k_\eta][\delta_{\eta\beta} - q_\eta q_\beta] + q_\mu [\delta_{\alpha\mu} - k_\alpha k_\mu] k_\nu [\delta_{\nu\beta} - q_\nu q_\beta]\Big)
\end{aligned} \tag{E.10}$$

(IV) No projection operators P_2 appear when evaluating the fourth and last term:

$$\begin{aligned}
&\langle(\Omega^\dagger F_\alpha^\perp(\boldsymbol{k}))\delta\rho(\boldsymbol{q}-\boldsymbol{k})\delta\rho(\boldsymbol{p}-\boldsymbol{q})F_\beta^\perp(-\boldsymbol{p})\rangle = \\
&= 2\xi\frac{k_\nu p_\mu}{m^2}[\delta_{\tau\alpha}-k_\tau k_\alpha][\delta_{\eta\beta}-p_\eta p_\beta] \\
&\quad\times\sum_{j,l=1}^{N}\langle p_{j,\nu}p_{j,\tau}p_{l,\mu}p_{l,\eta}\rangle\,\langle e^{-i\boldsymbol{k}\cdot\boldsymbol{r}_j}\delta\rho(\boldsymbol{q}-\boldsymbol{k})\delta\rho(\boldsymbol{p}-\boldsymbol{q})e^{i\boldsymbol{p}\cdot\boldsymbol{r}_l}\rangle \\
&= 2\xi(k_BT)^2k_\nu p_\mu[\delta_{\tau\alpha}-k_\tau k_\alpha][\delta_{\eta\beta}-p_\eta p_\beta] \\
&\quad\times\sum_{j,l=1}^{N}\Big(\delta_{\tau\nu}\delta_{\mu\eta}+\delta_{jl}\delta_{\mu\nu}\delta_{\tau\eta}+\delta_{jl}\delta_{\eta\nu}\delta_{\mu\tau}\Big)\,\langle e^{-i\boldsymbol{k}\cdot\boldsymbol{r}_j}\delta\rho(\boldsymbol{q}-\boldsymbol{k})\delta\rho(\boldsymbol{p}-\boldsymbol{q})e^{i\boldsymbol{p}\cdot\boldsymbol{r}_l}\rangle \\
&= 2N^2\xi(k_BT)^2S_{|\boldsymbol{q}-\boldsymbol{k}|}\delta_{\boldsymbol{k},\boldsymbol{p}}k^2[\delta_{\alpha\beta}-k_\alpha k_\beta]+\mathcal{O}(N)\ .
\end{aligned} \tag{E.11}$$

When proceeding to the sixth line, we used the homogeneity of the system, which implies $\langle\delta\rho(\boldsymbol{q}-k)\delta\rho(\boldsymbol{p}-\boldsymbol{q})\rangle = NS_{|\boldsymbol{q}-\boldsymbol{k}|}\delta_{\boldsymbol{p},\boldsymbol{q}}$.

As the sum of the four terms gives a rather lengthy expression, we keep only the diagonal term calculated last. This approximation is purely motivated by convenience. However, we will entirely neglect the damping term $\underline{\tilde{\gamma}}$ anyway, as it vanishes linearly with the temperature. Only keeping the diagonal term, we get

$$\underline{\tilde{\gamma}}(\boldsymbol{q},\boldsymbol{k},\boldsymbol{p}) \approx 2\frac{\xi k_BT}{m(c_k^\perp)^2}\delta_{\boldsymbol{k},\boldsymbol{p}}[\underline{\mathbf{1}}-\hat{\boldsymbol{k}}\hat{\boldsymbol{k}}]\ , \tag{E.12}$$

which does indeed not contribute to $T\to 0$. Note the analogy of this attenuation matrix with the instantaneous damping given in Equation (5.32).

F | The Fourier transformation

This chapter introduces and defines the Fourier transformation. Furthermore, some of its properties used in this monograph are also listed. A more detailed discussion of the Fourier transformation is given in (Götze, 2009, Appendix A.2), which is also the main source of the following introduction. In general, the Fourier transform expresses a time- or space-dependent function in terms of the temporal or spatial frequencies present in the original function. The transformation rules for spatial variables read

$$\mathrm{FT}[g(\boldsymbol{r})](\boldsymbol{q}) = \int_{\mathbb{R}^d} d^d\boldsymbol{r}\, g(\boldsymbol{r}) e^{-i\boldsymbol{q}\cdot\boldsymbol{r}} \;, \tag{F.1}$$

$$\mathrm{FT}^{-1}[g(\boldsymbol{q})](\boldsymbol{r}) = \int_{\mathbb{R}^d} \frac{d^d\boldsymbol{q}}{(2\pi)^d} g(\boldsymbol{q}) e^{i\boldsymbol{q}\cdot\boldsymbol{r}} \;. \tag{F.2}$$

Here, $\boldsymbol{r}$ and $\boldsymbol{q}$ are vectors in $\mathbb{R}^d$. The temporal transformation rule reads analogously but is defined in $\mathbb{R}$. The Fourier frequency is labelled ω. The Fourier transformation $\mathcal{F}[\cdot]$ is defined on the vector space W over the field $\mathbb{C}$ of absolute integrable functions $\{g\}$. Additionally, any $g \in W$ is required to be stepwise continuous. In this work the temporal Fourier transformation is indicated by a tilde: $\mathrm{FT}[g(t)](\omega) = \tilde{g}(\omega)$ while the spatial Fourier transformation indicated by the argument $\mathrm{FT}[g(\boldsymbol{r})](\boldsymbol{q}) = g(\boldsymbol{q})$ or with by an index $g_{\boldsymbol{q}}$. Some properties of the Fourier transformation are listed below:

I) The Fourier transformation is a linear integral transformation. For any two constants $a, b \in \mathbb{C}$ and for any two functions $f, g \in W$ holds

$$\mathrm{FT}[af + bg](\boldsymbol{q}) = a\mathrm{FT}[f](\boldsymbol{q}) + b\mathrm{FT}[g](\boldsymbol{q}) \;. \tag{F.3}$$

II) If the nth spatial derivative of $g \in W$ is stepwise continuous, one gets

$$\mathrm{FT}[\nabla^n g(\boldsymbol{r})](\boldsymbol{q}) = (-i\boldsymbol{q})^n \mathrm{FT}[g](\boldsymbol{q}) \;. \tag{F.4}$$

III) For $\boldsymbol{k}, \boldsymbol{d} \in \mathbb{C}^d$ and $g \in W$, a uniform shifts give rise to the following relations

$$\mathrm{FT}[e^{-i\boldsymbol{k}\cdot\boldsymbol{r}} g(\boldsymbol{r})](\boldsymbol{q}) = \mathrm{FT}[g(\boldsymbol{r})](\boldsymbol{q}+\boldsymbol{k}) \ , \tag{F.5a}$$

$$\mathrm{FT}[g(\boldsymbol{r}+\boldsymbol{d})](\boldsymbol{q}) = e^{-i\boldsymbol{d}\cdot\boldsymbol{q}} \mathrm{FT}[g(\boldsymbol{r})](\boldsymbol{q}) \ . \tag{F.5b}$$

IV) For two functions $f, g \in W$ hold the convolution theorems

$$\mathrm{FT}\left[\int_{\mathbb{R}^d} d^d\boldsymbol{r}' f(\boldsymbol{r}') g(\boldsymbol{r}-\boldsymbol{r}')\right](\boldsymbol{q}) = \mathrm{FT}[f(\boldsymbol{r})](\boldsymbol{q})\,\mathrm{FT}[g(\boldsymbol{r})](\boldsymbol{q}) \ , \tag{F.6a}$$

$$\mathrm{FT}^{-1}\left[\int_{\mathbb{R}^d} d^d\boldsymbol{k} f(\boldsymbol{k}) g(\boldsymbol{q}-\boldsymbol{k})\right](\boldsymbol{r}) = \mathrm{FT}^{-1}[f(\boldsymbol{q})](\boldsymbol{r})\,\mathrm{FT}^{-1}[g(\boldsymbol{q})](\boldsymbol{r}) \ . \tag{F.6b}$$

V) The Fourier transformation of the Delta-Distribution $\delta(\boldsymbol{r})$ reads

$$\mathrm{FT}[\delta(\boldsymbol{r})](\boldsymbol{q}) = 1 \ , \tag{F.7a}$$

$$\mathrm{FT}^{-1}[1](\boldsymbol{r}) = \frac{1}{(2\pi)^3}\delta(\boldsymbol{r}) \ . \tag{F.7b}$$

VI) The Riemann-Lebesgue Lemma holds (Grafakos, 2024, Proposition 2.2.3):

Theorem 3 (Riemann-Lebesgue Lemma)**.** *If $f \in L^1(\mathbb{R}^d)$ is an absolute integrable function $f : \mathbb{R}^d \to \mathbb{C}$, i.e. the integral over $|f|$ is finite, then is its Fourier transformed function $\tilde{f}$ a C_0-function, i.e. a continuous function, that vanishes at infinity.*

G | The Laplace transformation

The chapter specifies the convention of the Laplace transformation LT$[\cdot]$ and lists some of its properties frequently used in this work. A more substantial coverage of the Laplace transformation is given in (Götze, 2009, Appendix A.1), which is also the basis for this chapter. In general, the Laplace transformation is an integral transformation converting a complex-valued function $g(t)$ of a real variable $t > 0$ to a complex-valued function $\hat{g}(s)$ of a complex-valued parameter s via the transformation rule

$$\text{LT}[g(t)](s) = \int_0^\infty dt e^{-st} g(t) \equiv \hat{g}(s) \ , \quad \text{Re}\{s\} > 0 \ , \tag{G.1}$$

Throughout this monograph, the Laplace transformation is indicated by a hat $\text{LT}[g(t)](s) = \hat{g}(s)$.

The theory of the Laplace transformation starts with the definition of transformable functions: The integral transformation LT$[\cdot]$ of Equation (G.1) is defined on the vector space V of complex valued one-parameter functions $\{g(t)\}$ with $t \geq 0$. These functions obey the following requirements: They are continuous and bounded functions in t, and for this work, it is also needed that the functions $\{g(t)\}$ posses a first and second continuous derivative $\dot{g}(t)$ and $\ddot{g}(t)$. Furthermore, we requested that any function $g(t) \in V$ is absolute integrable in $[0, 1]$ and there is supposed to exist an integer $\alpha \in \mathbb{Z}$, such that $|g(t)|/t^\alpha$ is bounded for large t. These conditions ensure that the integral transformation in Equation (G.1) exists for $\text{Re}\, s > 0$. Moreover, $\hat{g}(s)$ defines a holomorphic function on the complex half-plane $\text{Re}\, s > 0$. In the following, we enlist some of the properties of the Laplace transformation used in this monograph:

I) Scaling in the time domain as xt with $x > 0$ gives the following scaling relation in the Laplace domain

$$g_x(t) = g(t/x) \Longrightarrow \hat{g}_x(s) = x\hat{g}(xs) \ . \tag{G.2}$$

II) We have defined the Laplace transformation for positive times. It is also possible to extend the validity of the Laplace transform to negative times t. Here, the real part of Laplace frequency must also be negative $\mathrm{Re}\{s\} < 0$. Under time inversion holds:

$$g(t) \to g(-t) \Longrightarrow \hat{g}(s) \to -\hat{g}(-s) \ . \tag{G.3}$$

IV) For complex conjugation holds

$$g(t) \to \hat{g}^*(t) \Longrightarrow \hat{g}(s) \to \hat{g}^*(s^*) \ . \tag{G.4}$$

V) The first and second derivative of $g(t) \in V$ become in the Laplace domain

$$\mathrm{LT}[\dot{g}(t)](s) = s\hat{g}(s) - g(t=0) \ . \tag{G.5a}$$
$$\mathrm{LT}[\ddot{g}(t)](s) = s^2\hat{g}(s) - sg(t=0) - \dot{g}(t=0) \ . \tag{G.5b}$$

VI) Complex analysis provides a connection between the Laplace transformed function $\hat{g}(s)$ and the Fourier transfomed function $\tilde{g}(\omega)$. More concretely, for an arbitrary holomorphic function $g \in V$ holds for $\mathrm{Re}\{s\} > 0$:

$$\begin{aligned} \hat{g}(s) &= \int_0^\infty dt g(t) e^{-st} = \frac{1}{2\pi} \int_{-\infty}^\infty d\omega \int_0^\infty dt \tilde{g}(\omega) e^{-t(-i\omega+s)} \\ &= \frac{1}{2\pi} \int_{-\infty}^\infty d\omega \frac{\tilde{g}(\omega)}{s - i\omega} = \tilde{g}(\omega = -is) \ . \end{aligned} \tag{G.6}$$

For the last equality, we completed the contour in the $\mathrm{Im}\{is\} > 0$ half-plane. Cauchy's integral formulae give the result.

H | Reuse permissions for external resources

Several graphics were included in this thesis, which were published before. Additionally, some of these publications were not co-authored by Florian Vogel. These figures are

1) Figure 1.1 taken from (Ikeda *et al.*, 2012)
2) Figure 2.1 taken from (O'Hern *et al.*, 2003)
3) Figure 2.5a taken from (O'Hern *et al.*, 2003)
4) Figure 2.5b taken from (Silbert *et al.*, 2006)
5) Figure 2.6 taken from (Silbert *et al.*, 2005)
6) Figure 2.7a taken from (O'Hern *et al.*, 2003)
7) Figure 2.7b taken from (O'Hern *et al.*, 2003)
8) Figure 2.8 taken from (Tanguy, 2023)
9) Figure 2.9 taken from (Zeller and Pohl, 1971)
10) Figure 5.5a reproduced from (Vogel and Fuchs, 2023)
11) Figure 5.5b taken from (Baumgärtel *et al.*, 2024)
12) Figure 5.12 taken from (Vogel *et al.*, 2025)
13) Figure 6.1 taken from (Vogel *et al.*, 2025)

The permission to show these figures was obtained from the authors. The exception is Figure 2.9 taken from (Zeller and Pohl, 1971), which was published in 1971. The *American Physical Society* granted permission to show this figure without contacting

the authors. Figure 2.8, Figure 5.12, and Figure 6.1 were published open-source. The explicit permission to show these figures was obtained from the authors. For the other figures,not published open source, the permissions from the authors and from the publisher, the *American Physical Society*, were obtained. The licences are attached below.

American Physical Society
Reuse and Permissions License

TERMS AND CONDITIONS

The American Physical Society (APS) is pleased to grant the Requestor of this license a non-exclusive, non-transferable permission, limited to Print and Electronic format, provided all criteria outlined below are followed.

1. You must also obtain permission from at least one of the lead authors for each separate work, if you haven't done so already. The author's name and affiliation can be found on the first page of the published Article.
2. For electronic format permissions, Requestor agrees to provide a hyperlink from the reprinted APS material using the source material's DOI on the web page where the work appears. The hyperlink should use the standard DOI resolution URL, http://dx.doi.org/{DOI}. The hyperlink may be embedded in the copyright credit line.
3. For print format permissions, Requestor agrees to print the required copyright credit line on the first page where the material appears: "Reprinted (abstract/excerpt/figure) with permission from [(FULL REFERENCE CITATION) as follows: Author's Names, APS Journal Title, Volume Number, Page Number and Year of Publication.] Copyright (YEAR) by the American Physical Society."
4. Permission granted in this license is for a one-time use and does not include permission for any future editions, updates, databases, formats or other matters. Permission must be sought for any additional use.
5. Use of the material does not and must not imply any endorsement by APS.
6. APS does not imply, purport or intend to grant permission to reuse materials to which it does not hold copyright. It is the requestor's sole responsibility to ensure the licensed material is original to APS and does not contain the copyright of another entity, and that the copyright notice of the figure, photograph, cover or table does not indicate it was reprinted by APS with permission from another source.
7. The permission granted herein is personal to the Requestor for the use specified and is not transferable or assignable without express written permission of APS. This license may not be amended except in writing by APS.
8. You may not alter, edit or modify the material in any manner.
9. You may translate the materials only when translation rights have been granted.
10. APS is not responsible for any errors or omissions due to translation.
11. You may not use the material for promotional, sales, advertising or marketing purposes.
12. The foregoing license shall not take effect unless and until APS or its agent, Aptara, receives payment in full in accordance with Aptara Billing and Payment Terms and Conditions, which are incorporated herein by reference.
13. Should the terms of this license be violated at any time, APS or Aptara may revoke the license with no refund to you and seek relief to the fullest extent of the laws of the USA. Official written notice will be made using the contact information provided with the permission request. Failure to receive such notice will not nullify revocation of the permission.
14. APS reserves all rights not specifically granted herein.
15. This document, including the Aptara Billing and Payment Terms and Conditions, shall be the entire agreement between the parties relating to the subject matter hereof.

8. Reuse permissions for external resources

American Physical Society
Reuse and Permissions License

05-May-2025

This license agreement between the American Physical Society ("APS") and Florian Vogel ("You") consists of your license details and the terms and conditions provided by the American Physical Society and SciPris.

Licensed Content Information

License Number:	**RNP/25/MAY/090794**
License date:	05-May-2025
DOI:	10.1103/PhysRevLett.109.018301
Title:	Unified study of glass and jamming rheology in soft particle systems
Author:	Atsushi Ikeda, Ludovic Berthier, and Peter Sollich
Publication:	Physical Review Letters
Publisher:	American Physical Society
Cost:	USD $ 0.00

Request Details

Does your reuse require significant modifications: No

Specify intended distribution locations:	Worldwide
Reuse Category:	Reuse in a thesis/dissertation
Requestor Type:	Student
Items for Reuse:	Figures/Tables
Number of Figure/Tables:	1
Figure/Tables Details:	Panel B) and C) of Figure 2
Format for Reuse:	Print and Electronic
Total number of print copies:	Up to 1000

Information about New Publication:

University/Publisher:	University of Konstanz
Title of dissertation/thesis:	A theory of Jamming and elastic instability in low temperature amorphous solids
Author(s):	Florian Vogel
Expected completion date:	May. 2025

License Requestor Information

Name:	Florian Vogel
Affiliation:	Individual
Email Id:	florian.vogel@uni-konstanz.de
Country:	Germany

8. Reuse permissions for external resources

American Physical Society
Reuse and Permissions License

15-Jan-2025

This license agreement between the American Physical Society ("APS") and Florian Vogel ("You") consists of your license details and the terms and conditions provided by the American Physical Society and SciPris.

Licensed Content Information

License Number:	**RNP/25/JAN/087251**
License date:	15-Jan-2025
DOI:	10.1103/PhysRevE.68.011306
Title:	Jamming at zero temperature and zero applied stress: The epitome of disorder
Author:	Corey S. O'Hern et al.
Publication:	Physical Review E
Publisher:	American Physical Society
Cost:	USD $ 0.00

Request Details

Does your reuse require significant modifications: No

Specify intended distribution locations:	Germany
Reuse Category:	Reuse in a thesis/dissertation
Requestor Type:	Student
Items for Reuse:	Figures/Tables
Number of Figure/Tables:	4
Figure/Tables Details:	Figure 3 Figure 5, Panel C from Figure 13 with the number C removed from the picture. Panel e and f from figure 14 with the letters (e) and (f) removed respectively
Format for Reuse:	Print and Electronic
Total number of print copies:	Up to 1000

Information about New Publication:

University/Publisher:	University of Konstanz
Title of dissertation/thesis:	A theory of jamming and elastic instability in low temperature amorphous solids
Author(s):	Florian Vogel
Expected completion date:	Mar. 2025

License Requestor Information

Name:	Florian Vogel
Affiliation:	Individual
Email Id:	florian.vogel@uni-konstanz.de
Country:	Germany

8. Reuse permissions for external resources

American Physical Society
Reuse and Permissions License

15-Jan-2025

This license agreement between the American Physical Society ("APS") and Florian Vogel ("You") consists of your license details and the terms and conditions provided by the American Physical Society and SciPris.

Licensed Content Information

License Number:	**RNP/25/JAN/087253**
License date:	15-Jan-2025
DOI:	10.1103/PhysRevLett.95.098301
Title:	Vibrations and Diverging Length Scales Near the Unjamming Transition
Author:	Leonardo E. Silbert, Andrea J. Liu, and Sidney R. Nagel
Publication:	Physical Review Letters
Publisher:	American Physical Society
Cost:	USD $ 0.00

Request Details

Does your reuse require significant modifications: No

Specify intended distribution locations:	Germany
Reuse Category:	Reuse in a thesis/dissertation
Requestor Type:	Student
Items for Reuse:	Figures/Tables
Number of Figure/Tables:	1
Figure/Tables Details:	Panel a) of Figure 1 with the (a) removed
Format for Reuse:	Print and Electronic
Total number of print copies:	Up to 1000

Information about New Publication:

University/Publisher:	Florian Vogel
Title of dissertation/thesis:	A theory of jamming and elastic instability in low temperature amorphous solids
Author(s):	Florian Vogel
Expected completion date:	Mar. 2025

License Requestor Information

Name:	Florian Vogel
Affiliation:	Individual
Email Id:	florian.vogel@uni-konstanz.de
Country:	Germany

8. Reuse permissions for external resources

American Physical Society
Reuse and Permissions License

05-May-2025

This license agreement between the American Physical Society ("APS") and Florian Vogel ("You") consists of your license details and the terms and conditions provided by the American Physical Society and SciPris.

Licensed Content Information

License Number:	**RNP/25/MAY/090793**
License date:	05-May-2025
DOI:	10.1103/PhysRevE.73.041304
Title:	Structural signatures of the unjamming transition at zero temperature
Author:	Leonardo E. Silbert, Andrea J. Liu, and Sidney R. Nagel
Publication:	Physical Review E
Publisher:	American Physical Society
Cost:	USD $ 0.00

Request Details

Does your reuse require significant modifications: No

Specify intended distribution locations:	Worldwide
Reuse Category:	Reuse in a thesis/dissertation
Requestor Type:	Student
Items for Reuse:	Figures/Tables
Number of Figure/Tables:	1
Figure/Tables Details:	Figure 1) The pair-correlation function
Format for Reuse:	Print and Electronic
Total number of print copies:	Up to 1000

Information about New Publication:

University/Publisher:	University of Konstanz
Title of dissertation/thesis:	A theory of Jamming and elastic instability in low temperature amorphous solids
Author(s):	Florian Vogel
Expected completion date:	May. 2025

License Requestor Information

Name:	Florian Vogel
Affiliation:	Individual
Email Id:	florian.vogel@uni-konstanz.de
Country:	Germany

American Physical Society
Reuse and Permissions License

05-May-2025

This license agreement between the American Physical Society ("APS") and Florian Vogel ("You") consists of your license details and the terms and conditions provided by the American Physical Society and SciPris.

Licensed Content Information

License Number:	**RNP/25/MAY/090792**
License date:	05-May-2025
DOI:	10.1103/PhysRevB.4.2029
Title:	Thermal Conductivity and Specific Heat of Noncrystalline Solids
Author:	R. C. Zeller and R. O. Pohl
Publication:	Physical Review B
Publisher:	American Physical Society
Cost:	USD $ 0.00

Request Details

Does your reuse require significant modifications: No

Specify intended distribution locations:	Worldwide
Reuse Category:	Reuse in a thesis/dissertation
Requestor Type:	Student
Items for Reuse:	Figures/Tables
Number of Figure/Tables:	1
Figure/Tables Details:	Figure 8) Thermal conductivity of amorphous solids
Format for Reuse:	Print and Electronic
Total number of print copies:	Up to 1000

Information about New Publication:

University/Publisher:	University of Konstanz
Title of dissertation/thesis:	A theory of Jamming and elastic instability in low temperature amorphous solids
Author(s):	Florian Vogel
Expected completion date:	May. 2025

License Requestor Information

Name:	Florian Vogel
Affiliation:	Individual
Email Id:	florian.vogel@uni-konstanz.de
Country:	Germany

8. Reuse permissions for external resources

American Physical Society
Reuse and Permissions License

05-May-2025

This license agreement between the American Physical Society ("APS") and Florian Vogel ("You") consists of your license details and the terms and conditions provided by the American Physical Society and SciPris.

Licensed Content Information

License Number:	**RNP/25/MAY/090791**
License date:	05-May-2025
DOI:	10.1103/PhysRevLett.130.236101
Title:	Vibrational Phenomena in Glasses at Low Temperatures Captured by Field Theory of Disordered Harmonic Oscillators
Author:	Florian Vogel and Matthias Fuchs
Publication:	Physical Review Letters
Publisher:	American Physical Society
Cost:	USD $ 0.00

Request Details

Does your reuse require significant modifications: No

Specify intended distribution locations:	Worldwide
Reuse Category:	Reuse in a thesis/dissertation
Requestor Type:	Author of requested content
Items for Reuse:	Figures/Tables
Number of Figure/Tables:	1
Figure/Tables Details:	Figure 2) Sound attenuation as function of wave vector p.
Format for Reuse:	Print and Electronic
Total number of print copies:	Up to 1000

Information about New Publication:

University/Publisher:	University of Konstanz
Title of dissertation/thesis:	A theory of Jamming and elastic instability in low temperature amorphous solids
Author(s):	Florian Vogel
Expected completion date:	May. 2025

License Requestor Information

Name:	Florian Vogel
Affiliation:	Individual
Email Id:	florian.vogel@uni-konstanz.de
Country:	Germany

8. Reuse permissions for external resources

American Physical Society
Reuse and Permissions License

02-Apr-2025

This license agreement between the American Physical Society ("APS") and Florian Vogel ("You") consists of your license details and the terms and conditions provided by the American Physical Society and SciPris.

Licensed Content Information

License Number:	**RNP/25/APR/089688**
License date:	02-Apr-2025
DOI:	10.1103/PhysRevE.109.014120
Title:	Properties of stable ensembles of Euclidean random matrices
Author:	Philipp Baumgärtel, Florian Vogel, and Matthias Fuchs
Publication:	Physical Review E
Publisher:	American Physical Society
Cost:	USD $ 0.00

Request Details

Does your reuse require significant modifications: No

Specify intended distribution locations:	Worldwide
Reuse Category:	Reuse in a thesis/dissertation
Requestor Type:	Publisher, not for profit
Items for Reuse:	Figures/Tables
Number of Figure/Tables:	1
Figure/Tables Details:	Figure 9: Comparison of the sound attenuation, obtained from numerical calculations with the theoretical prediction.
Format for Reuse:	Print and Electronic
Total number of print copies:	Up to 1000

Information about New Publication:

University/Publisher:	University of Konstanz
Title of dissertation/thesis:	A theory of Jamming and elastic instability in low temperature amorphous solids
Author(s):	Florian vogel
Expected completion date:	May. 2025

License Requestor Information

Name:	Florian Vogel
Affiliation:	Individual
Email Id:	florian.vogel@uni-konstanz.de
Country:	Germany

Bibliography

Alexander S. *Amorphous solids: their structure, lattice dynamics and elasticity*. Phys. Rep., vol. 296(2):65–236, 1998.

Allen P. B. and Feldman J. L. *Thermal conductivity of disordered harmonic solids*. Phys. Rev. B, vol. 48:12.581–12.588, 1993.

Allen P. B., Feldman J. L., Fabian J., and Wooten F. *Diffusons, locons and propagons: Character of atomic vibrations in amorphous si*. Philos. Mag. B, vol. 79(11–12):1715–1731, 1999.

Altland A. and Simons B. D. Condensed Matter Field Theory. Cambridge University Press, Cambridge, 2 ed., 2010.

Amir A., Krich J. J., Vitelli V., Oreg Y., and Imry Y. *Emergent percolation length and localization in random elastic networks*. Phys. Rev. X, vol. 3:021.017, 2013.

Amir A., Oreg Y., and Imry Y. *Mean-field model for electron-glass dynamics*. Phys. Rev. B, vol. 77(16), 2008.

Anderson P. W., Halperin B. I., and Varma C. M. *Anomalous low-temperature thermal properties of glasses and spin glasses*. Philos. Mag., vol. 25(1):1–9, 1972.

Ashcroft N. W. and Mermin N. D. Solid State Physics. Harcourt, Orlando, 1976.

Baiesi M., Maes C., and Wynants B. *Nonequilibrium linear response for markov dynamics, i: Jump processes and overdamped diffusions*. J. Stat. Phys., vol. 137(5):1094–1116, 2009.

Baldi G., Giordano V. M., Monaco G., and Ruta B. *Sound attenuation at terahertz frequencies and the boson peak of vitreous silica*. Phys. Rev. Lett., vol. 104:195.501, 2010.

Baldi G., Giordano V. M., Ruta B., Dal Maschio R., Fontana A., and Monaco G. *Anharmonic damping of terahertz acoustic waves in a network glass and its effect on the density of vibrational states*. Phys. Rev. Lett., vol. 112:125.502, 2014.

Baldi G., Zanatta M., Gilioli E., Milman V., Refson K., Wehinger B., Winkler B., Fontana A., and Monaco G. *Emergence of crystal-like atomic dynamics in glasses at the nanometer scale*. Phys. Rev. Lett., vol. 110:185.503, 2013.

Basu U., Krüger M., Lazarescu A., and Maes C. *Frenetic aspects of second order response*. Phys. Chem. Chem. Phys., vol. 17:6653–6666, 2015.

Baumgärtel P., Vogel F., and Fuchs M. *Properties of stable ensembles of euclidean random matrices*. Phys. Rev. E, vol. 109:014.120, 2024.

Beltukov Y. M., Kozub V. I., and Parshin D. A. *Ioffe-regel criterion and diffusion of vibrations in random lattices*. Phys. Rev. B, vol. 87:134.203, 2013.

Beltukov Y. and Parshin D. *Theory of sparse random matrices and vibrational spectra of amorphous solids*. Phys. Solid State, vol. 53:151–162, 2011.

Benassi P., Krisch M., Masciovecchio C., Mazzacurati V., Monaco G., Ruocco G., Sette F., and Verbeni R. *Evidence of high frequency propagating modes in vitreous silica*. Phys. Rev. Lett., vol. 77:3835–3838, 1996.

Benetti F. P. C., Parisi G., Pietracaprina F., and Sicuro G. *Mean-field model for the density of states of jammed soft spheres*. Phys. Rev. E, vol. 97:062.157, 2018.

Bosse J., Götze W., and Zippelius A. *Velocity-autocorrelation spectrum of simple classical liquids*. Phys. Rev. A, vol. 18:1214–1221, 1978.

Caponi S., Corezzi S., Fioretto D., Fontana A., Monaco G., and Rossi F. *Raman-scattering measurements of the vibrational density of states of a reactive mixture during polymerization: Effect on the boson peak*. Phys. Rev. Lett., vol. 102:027.402, 2009.

Caroli C. and Lemaître A. *Fluctuating elasticity fails to capture anomalous sound scattering in amorphous solids*. Phys. Rev. Lett., vol. 123:055.501, 2019.

Chaikin P. M. and Lubensky T. C. Principles of Condensed Matter Physics. Cambridge University Press, Cambridge, 1995.

Chapman S. *Boltzmann's h-theorem*. Nature, vol. 139(3526):931–931, 1937.

Charbonneau P., Kurchan J., Parisi G., Urbani P., and Zamponi F. *Glass and jamming transitions: From exact results to finite-dimensional descriptions*. Annu. Rev. Condens. Matter Phys., vol. 8(1):265–288, 2017.

Chichocki B. and W.Hess. *On the Memory function for the dynamic structure factor of interacting Brownian particels*. Physica A, vol. 141(2):475–488, 1987.

Cichocki B. and Hess W. *On the memory function for the dynamic structure factor of interacting brownian particles*. Physica A Stat. Mech. Appl., vol. 141(2):475–488, 1987.

Ciliberti S., Grigera T., Martin-Mayor V., Parisi G., and Verrocchio P. *Brillouin and boson peaks in glasses from vector euclidean random matrix theory*. J. Chem. Phys., vol. 119(16):8577–8591, 2003.

Coleman P. Introduction to Many-Body Physics. Cambridge Press, Cambrige, 2015.

Cugliandolo L. F. *Advanced statistical physics: Quenched random systems [lecture notes]*. 2022. Looked up at 09.05.2025 at `https://www.lpthe.jussieu.fr/~leticia/TEACHING/Master2022/disorder-2022.pdf`.

Debenedetti P. G. and Stillinger F. H. *Supercooled liquids and the glass transition*. Nature, vol. 410(6825):259–267, 2001.

DeGiuli E., Düring G., Lerner E., and Wyart M. *Unified theory of inertial granular flows and non-brownian suspensions*. Phys. Rev. E, vol. 91:062.206, 2015.

DeGiuli E., Laversanne-Finot A., Düring G., Lerner E., and Wyart M. *Effects of coordination and pressure on sound attenuation, boson peak and elasticity in amorphous solids*. Soft Matter, vol. 10:5628–5644, 2014.

Dotsenko V. Introduction to the Replica Theory of Disordered Statistical Systems. Collection Alea-Saclay: Monographs and Texts in Statistical Physics. Cambridge University Press, Cambridge, 2000.

Drenckhan W. and Hutzler S. *Structure and energy of liquid foams*. Adv. Colloid Interface Sci., vol. 224:1–16, 2015.

Düring G., Lerner E., and Wyart M. *Phonon gap and localization lengths in floppy materials*. Soft Matter, vol. 9:146–154, 2013.

Elam W. T., Kerstein A. R., and Rehr J. J. *Critical properties of the void percolation problem for spheres*. Phys. Rev. Lett., vol. 52:1516–1519, 1984.

Ellenbroek W. G., Somfai E., Hecke M., and Saarloos W. *Critical scaling in linear response of frictionless granular packings near jamming*. Phys. Rev. Lett., vol. 97:258.001, 2006.

Ellenbroek W. G., Hecke M., and Saarloos W. *Jammed frictionless disks: Connecting local and global response*. Phys. Rev. E, vol. 80(6), 2009a.

Ellenbroek W. G., Zeravcic Z., Saarloos W., and Hecke M. *Non-affine response: Jammed packings vs. spring networks*. Europhysics Letters, vol. 87(3):34.004, 2009b.

Eshelby J. D. and Peierls R. E. *The determination of the elastic field of an ellipsoidal inclusion, and related problems*. Proceedings of the Royal Society of London. Series A. Mathematical and Physical Sciences, vol. 241(1226):376–396, 1957.

Feng S., Thorpe M. F., and Garboczi E. *Effective-medium theory of percolation on central-force elastic networks*. Phys. Rev. B, vol. 31:276–280, 1985.

Flenner E. and Szamel G. *The origin of sound damping in amorphous solids: Defects and beyond*. Sci. Adv., vol. 11(15), 2025.

Flubacher P., Leadbetter A., Morrison J., and Stoicheff B. *The low-temperature heat capacity and the raman and brillouin spectra of vitreous silica*. J. Phys. Chem. Solids, vol. 12(1):53–65, 1959.

Folli V., Ruocco G., and Schirmacher W. *Moment-preserving theory of vibrational dynamics of topologically disordered systems*. Front. Phys., vol. 5:29, 2017.

Franosch T., Fuchs M., Götze W., Mayr M. R., and Singh A. P. *Asymptotic laws and preasymptotic correction formulas for the relaxation near glass-transition singularities*. Phys. Rev. E, vol. 55:7153–7176, 1997.

Franosch T. and Götze W. *A theory for a certain crossover in relaxation phenomena in glasses*. J. Phys. Condens. Mat., vol. 6(26):4807, 1994.

Franz S., Parisi G., Urbani P., and Zamponi F. *Universal spectrum of normal modes in low-temperature glasses*. Proc. Nat. Acad. Sci., vol. 112(47):14.539–14.544, 2015.

Ganter C. and Schirmacher W. *Rayleigh scattering, long-time tails, and the harmonic spectrum of topologically disordered systems*. Phys. Rev. B, vol. 82:094.205, 2010.

Ganter C. and Schirmacher W. *Euclidean random matrix theory: low-frequency non-analyticities and rayleigh scattering*. Phil. Mag., vol. 91(13-15):1894–1909, 2011.

Gelin S., Tanaka H., and Lematre A. *Anomalous phonon scattering and elastic correlations in amorphous solids*. Nat. Mater., vol. 15(11):1177–1181, 2016.

Giannini J. A., Lerner E., Zamponi F., and Manning M. L. *Scaling regimes and fluctuations of observables in computer glasses approaching the unjamming transition*. J. Chem. Phys., vol. 160(3):034.502, 2024.

Goetschy A. and Skipetrov S. E. *Euclidean random matrices and their applications in physics*. 2013. Looked up at 12.02.2025 at `https://arxiv.org/abs/1303.2880`.

Götze W. *The essentials of the mode-coupling theory for glassy dynamics*. Condens. Matter Phys., vol. 1:873, 1998.

Götze W. Complex Dynamics of Glass-Forming Liquid. Oxford University Press, New York, 2009.

Götze W. and Mayr M. R. *Evolution of vibrational excitations in glassy systems*. Phys. Rev. E, vol. 61:587–606, 2000.

Goyon J., Colin A., Ovarlez G., Ajdari A., and Bocquet L. *Spatial cooperativity in soft glassy flows*. Nature, vol. 454:84–7, 2008.

Grafakos L. Fundamentals of Fourier Analysis. Springer Cham, Cham, 2024.

Grigera T. S., Martin-Mayor V., Parisi G., Urbani P., and Verrocchio P. *On the high-density expansion for euclidean random matrices*. J. Stat. Mech.: Theory Exp., vol. 2011(02):P02.015, 2011.

Grigera T. S., Martín-Mayor V., Parisi G., and Verrocchio P. *Vibrational spectrum of topologically disordered systems*. Phys. Rev. Lett., vol. 87:085.502, 2001.

Gross R. and Marx A. Festkörperphysik. De Gruyter Oldenbourg, München, 2014.

Hansen J. and McDonald J. Theory of simple liquids, vol. 3. Elsevier Science B.V, London, 2009.

Hertz J. A., Roudi Y., and Sollich P. *Path integral methods for the dynamics of stochastic and disordered systems*. J. Phys. A Math. Theor., vol. 50(3):033.001, 2016.

Hess W. and Klein. R. *Generalized hydrodynamics of systems of Brownian particles*. Adv. Phys., vol. 32:173–283, 1983.

Höfling F., Franosch T., and Frey E. *Localization transition of the three-dimensional lorentz model and continuum percolation*. Phys. Rev. Lett., vol. 96:165.901, 2006.

Horbach J., Kob W., and Binder K. *High frequency sound and the boson peak in amorphous silica*. Eur. Phys. J. B, vol. 19:531–543, 2001.

Horn A. *Doubly stochastic matrices and the diagonal of a rotation matrix*. Am. J. Math., vol. 76(3):620–630, 1954.

Hu Y.-C. and Tanaka H. *Origin of the boson peak in amorphous solids*. Nat. Phys., vol. 18(6):669–677, 2022.

Ikeda A., Berthier L., and Sollich P. *Unified study of glass and jamming rheology in soft particle systems*. Phys. Rev. Lett., vol. 109:018.301, 2012.

Ikeda A., Berthier L., and Sollich P. *Disentangling glass and jamming physics in the rheology of soft materials*. Soft matter, vol. 9(32), 2013.

Ikeda A., Kawasaki T., Berthier L., Saitoh K., and Hatano T. *Universal relaxation dynamics of sphere packings below jamming*. Phys. Rev. Lett., vol. 124:058.001, 2020.

Ioffe A. F. and Regel A. R. *Non-crystalline, amorphous, and liquid electronic semiconductors*. Progress in Semiconductors, vol. 4:237–291, 1960.

Irving J. H. and Kirkwood J. G. *The statistical mechanical theory of transport processes. iv. the equations of hydrodynamics*. J. Chem. Phys., vol. 18(6):817–829, 1950.

Janssen L. M. C. *Mode-coupling theory of the glass transition: A primer*. Front. Phys., vol. 6, 2018.

Janssen L. M. C. and Reichman D. R. *Microscopic dynamics of supercooled liquids from first principles*. Phys. Rev. Lett., vol. 115:205.701, 2015.

Jop P., Mansard V., Chaudhuri P., Bocquet L., and Colin A. *Microscale rheology of a soft glassy material close to yielding*. Phys. Rev. Lett., vol. 108:148.301, 2012.

Kamenev A. Field Theory of Non-Equilibrium Systems. Cambridge University Press, Cambridge, 2011.

Kapteijns G., Richard D., Bouchbinder E., and Lerner E. *Elastic moduli fluctuations predict wave attenuation rates in glasses*. J. Chem. Phys., vol. 154(8):081.101, 2021.

Kaya D., Green N. L., Maloney C. E., and Islam M. F. *Normal modes and density of states of disordered colloidal solids*. Science, vol. 329(5992):656–658, 2010.

Krantz S. and Parks H. The Implicit Function Theorem: History, Theory, and Applications. Modern Birkhäuser classics. Birkhäuser, New York, 2002.

Kumar A., Procaccia I., and Singh M. *Density of quasi-localized modes in athermal glasses*. Europhys. Lett., vol. 135(6):66.001, 2021.

Landau L. D. and Lifshitz E. M. Statistical Physics, Part 1, vol. 5 of *Course of Theoretical Physics*. Butterworth-Heinemann, Oxford, 1980.

Landau L. and Lifshitz E. Fluid Mechanics, Second Edition: Volume 6 (Course of Theoretical Physics), vol. 6 of *Course of Theoretical Physics*. Butterworth-Heinemann, Oxford, 2 ed., 1987.

Landau L. D., Lifshitz E., Kosevichn A., and Pitaevskii L. P. Theory of Elasticity, vol. 7 of *Course of Theoretical Physics*. Pergamon Press, Oxford, 1970.

Leadbetter A. J. *Inelastic cold neutron scattering from different forms of silica*. J. Chem. Phys., vol. 51(2):779–786, 1969.

Lerner E. and Bouchbinder E. *Low-energy quasilocalized excitations in structural glasses*. J. Chem. Phys., vol. 155(20):200.901, 2021.

Lerner E. and Bouchbinder E. *Boson-peak vibrational modes in glasses feature hybridized phononic and quasilocalized excitations*. J. Chem. Phys., vol. 158(19), 2023.

Leutheusser E. *Self-consistent kinetic theory for the lorentz gas*. Phys. Rev. A, vol. 28:1762–1773, 1983.

Li B., Lou K., Kob W., and Granick S. *Anatomy of cage formation in a two-dimensional glass-forming liquid*. Nature, vol. 587(7833):225–229, 2020.

Lindemann F. *About the calculation of molecular own frequencies*. Physical Magazine, vol. 11:609–611, 1910.

Liu A. J., Nagel S. R., Saarloos W. v., and Wyart M. *2989 The jamming scenario—an introduction and outlook*. In: Dynamical Heterogeneities in Glasses, Colloids, and Granular Media. Oxford University Press, Oxford, 2011.

Maes C. *Response theory: A trajectory-based approach*. Front. Phys., vol. 8, 2020.

Maier M. Stress fluctuations in glass-forming liquids. Master's thesis, University of Konstanz, University of Konstanz, FB Physik, 2018.

Maier M., Zippelius A., and Fuchs M. *Stress auto-correlation tensor in glass-forming isothermal fluids: From viscous to elastic response*. J. Chem. Phys., 2018.

Makse H. A., Gland N., Johnson D. L., and Schwartz L. M. *Why effective medium theory fails in granular materials*. Phys. Rev. Lett, vol. 83(24):5070–5073, 1999.

Maloney C. E. *Correlations in the elastic response of dense random packings*. Phys. Rev. Lett., vol. 97:035.503, 2006.

Maloney C. and Lemaître A. *Universal breakdown of elasticity at the onset of material failure*. Phys. Rev. Lett., vol. 93:195.501, 2004.

Maloney C. E. and Lemaître A. *Amorphous systems in athermal, quasistatic shear*. Phys. Rev. E, vol. 74:016.118, 2006.

Marruzzo A., Köhler S., Fratalocchi A., Ruocco G., and Schirmacher W. *Vibrational anomalies and marginal stability of glasses*. Eur. Phys. J.: Spec., vol. 216(1), 2013a.

Marruzzo A., Schirmacher W., Fratalocchi A., and Ruocco G. *Heterogeneous shear elasticity of glasses: the origin of the boson peak*. Sci. Rep., vol. 3(1):1407, 2013b.

Martin-Mayor V., Mézard M., Parisi G., and Verrocchio P. *The dynamical structure factor in topologically disordered systems*. J. Chem. Phys., vol. 114(18):8068–8081, 2001.

Martín-Mayor V., Parisi G., and Verrocchio P. *Dynamical structure factor in disordered systems*. Phys. Rev. E, vol. 62:2373–2379, 2000.

Maxwell J. *On the dynamical theory of gases*. Philos. Trans. R. Soc. A, vol. 157:49, 1867.

Mehta M. L. Random Matrices. Pure and Applied Mathematics. Academic Press, New York, 3 ed., 2014.

Mezard M., Parisi G., and Virasoro M. Spin Glass Theory and Beyond. World scientific, Singapore, 1986.

Mizuno H. and Ikeda A. *Phonon transport and vibrational excitations in amorphous solids*. Phys. Rev. E, vol. 98:062.612, 2018.

Mizuno H., Saitoh K., and Silbert L. E. *Elastic moduli and vibrational modes in jammed particulate packings*. Phys. Rev. E, vol. 93:062.905, 2016a.

Mizuno H., Shiba H., and Ikeda A. *Continuum limit of the vibrational properties of amorphous solids*. Proc. Nat. Acad. Sci., vol. 114(46):E9767–E9774, 2017.

Mizuno H., Silbert L. E., and Sperl M. *Spatial distributions of local elastic moduli near the jamming transition*. Phys. Rev. Lett., vol. 116:068.302, 2016b.

Monaco G. and Giordano V. *Breakdown of the debye approximation for the acoustic modes with nanometric wavelengths in glasses*. Proc. Nat. Acad. Sci., vol. 106(10):3659–3663, 2009.

Monaco G., Masciovecchio C., Ruocco G., and Sette F. *Determination of the infinite frequency sound velocity in the glass former o-terphenyl*. Phys. Rev. Lett., vol. 80:2161–2164, 1998.

Monaco G. and Mossa S. *Anomalous properties of the acoustic excitations in glasses on the mesoscopic length scale*. Proc. Nat. Acad. Sci., vol. 106(40):16.907–16.912, 2009.

Moriel A., Kapteijns G., Rainone C., Zylberg J., Lerner E., and Bouchbinder E. *Wave attenuation in glasses: Rayleigh and generalized-rayleigh scattering scaling*. J. Chem. Phys., vol. 151(10):104.503, 2019.

Mossa S., Bryk T., Ruocco G., and Schirmacher W. *Heterogeneous-elasticity theory of instantaneous normal modes in liquids*. Sci. Rep., vol. 13:21.442, 2023.

Mézard M., Parisi G., and Zee A. *Spectra of euclidean random matrices*. Nucl. Phys. B., vol. 559(3):689–701, 1999.

O'Hern C. S., Silbert L. E., Liu A. J., and Nagel S. R. *Jamming at zero temperature and zero applied stress: The epitome of disorder*. Phys. Rev. E, vol. 68(1), 2003.

Parisi G., Urbani P., and Zamponi F. Theory of Simple Glasses: Exact Solutions in Infinite Dimensions. Cambridge University Press, Cambridge, 2020.

Parshin D. A., Schober H., and Gurevich Y. M. *Vibrational instability, two-level systems, and the boson peak in glasses*. Phys. Rev. B, vol. 76(6), 2007.

Phillips W. A. *Tunneling states in amorphous solids*. J. Low Temp. Phys., vol. 7(3):351–360, 1972.

Pihlajamaa I., Debets V., Laudicina C., and Janssen L. *Unveiling the anatomy of mode-coupling theory*. SciPost Phys., vol. 15, 2023.

Pitaevskii L. P. and Lifshitz E. M. Physical Kinetics, vol. 10 of *Course of Theoretical Physics*. Butterworth-Heinemann, Oxford, 1981.

Reichman D. and Charbonneau P. *Mode-coupling theory*. J. Stat. Mech.: Theory Exp., vol. 2005(05):P05.013, 2005.

Richard D., González-López K., Kapteijns G., Pater R., Vaknin T., Bouchbinder E., and Lerner E. *Universality of the nonphononic vibrational spectrum across different classes of computer glasses*. Phys. Rev. Lett., vol. 125:085.502, 2020.

Rintoul M. D. *Precise determination of the void percolation threshold for two distributions of overlapping spheres*. Phys. Rev. E, vol. 62:68–72, 2000.

Risken H. The Fokker-Planck Equation, vol. 2. Springer, Berlin, 1996.

Ruffle B., Ayrinhac S., Courtens E., Vacher R., Foret M., Wischnewski A., and Buchenau U. *Scaling the temperature-dependent boson peak of vitreous silica with the high-frequency bulk modulus derived from brillouin scattering data*. Phys. Rev. Lett., vol. 104(6):067.402, 2010.

Saitoh K., Hatano T., Ikeda A., and Tighe B. P. *Stress relaxation above and below the jamming transition*. Phys. Rev. Lett, vol. 124(11), 2020.

Sakurai J. and Napolitano J. Modern quantum mechanics. Addison-Wesley, San Francisco, 3 ed., 2011.

Schirmacher W. *Thermal conductivity of glassy materials and the "boson peak"*. Europhys. Lett., vol. 73(6):892, 2006.

Schirmacher W., Diezemann G., and Ganter C. *Harmonic vibrational excitations in disordered solids and the "boson peak"*. Phys. Rev. Lett., vol. 81:136–139, 1998.

Schirmacher W., Folli V., Ganter C., and Ruocco G. *Self-consistent euclidean-random-matrix theory*. J. Phys. A Math. Theor., vol. 52(46):464.002, 2019.

Schirmacher W., Paoluzzi M., Mocanu F. C., Khomenko D., Szamel G., Zamponi F., and Ruocco G. *The nature of non-phononic excitations in disordered systems*. Nat. Commun., vol. 15(1):3107, 2024.

Schirmacher W. and Ruocco G. *Heterogeneous elasticity: The tale of the boson peak*. In: Ramos M. (Editor) Low-Temperature Thermal and Vibrational Properties of Disordered Solids, chap. Chapter 9, pp. 331–373. World Scientific, 2022.

Schirmacher W., Ruocco G., and Scopigno T. *Acoustic attenuation in glasses and its relation with the boson peak*. Phys. Rev. Lett., vol. 98:025.501, 2007.

Schmid B. Mode-Coupling Theory: Generalizations, High Dimensions and Microscopic Dynamics. Phd thesis, University of Mainz, 2011. Available at `https://d-nb.info/1026802563/34`.

Schnyder S. Anomalous transport in heterogeneous media. Phd thesis, Heinrich-Heine-Universität Düsseldorf, 2014. Available at `https://docserv.uni-duesseldorf.de/servlets/DerivateServlet/Derivate-32053/dissertation_revised.pdf`.

Schnyder S., Höfling F., Franosch T., and Voigtmann T. *Long-wavelength anomalies in the asymptotic behavior of mode-coupling theory*. J. Phys. Condens. Mat., vol. 23(23):234.121, 2011.

Schober H. *Quasi-localized vibrations and phonon damping in glasses*. J. Non-Cryst. Solids, vol. 357(2):501–505, 2011.

Schober H. R. and Ruocco G. *Size effects and quasilocalized vibrations*. Phil. Mag., vol. 84(13-16):1361–1372, 2004.

Schofield P., Henderson J. R., and Rowlinson J. S. *Statistical mechanics of inhomogeneous fluids*. Proc. R. Soc. Lond. A. Math. Phys., vol. 379(1776):231–246, 1982.

Shi K., Smith E. R., Santiso E. E., and Gubbins K. E. *A perspective on the microscopic pressure (stress) tensor: History, current understanding, and future challenges*. J. Chem. Phys., vol. 158(4):040.901, 2023.

Shimada M., Mizuno H., and Ikeda A. *Anomalous vibrational properties in the continuum limit of glasses*. Phys. Rev. E, vol. 97(2):022.609, 2018.

Shintani H. and Tanaka H. *Universal link between the boson peak and transverse phonons in glass*. Nature Materials, vol. 7(11):870–877, 2008.

Silbert L. E., Ertaş D., Grest G. S., Halsey T. C., and Levine D. *Geometry of frictionless and frictional sphere packings*. Phys. Rev. E, vol. 65:031.304, 2002.

Silbert L. E., Liu A. J., and Nagel S. R. *Vibrations and diverging length scales near the unjamming transition*. Phys. Rev. Lett., vol. 95:098.301, 2005.

Silbert L. E., Liu A. J., and Nagel S. R. *Structural signatures of the unjamming transition at zero temperature*. Phys. Rev. E, vol. 73(4), 2006.

Simon S. H. The Oxford solid state basics. Oxford Univ. Press, Oxford, 2013.

Srednicki M. Quantum Field Theory. Cambridge Univ. Press, Cambridge, 2007.

Szamel G. *Colloidal glass transition: Beyond mode-coupling theory*. Phys. Rev. Lett., vol. 90:228.301, 2003.

Szamel G. *Self-consistent theory for sound propagation in a simple model of a disordered, harmonic solid*. Phys. Rev. E, vol. 111:024.137, 2025.

Szamel G. and Flenner E. *Microscopic analysis of sound attenuation in low-temperature amorphous solids reveals quantitative importance of non-affine effects*. J. Chem. Phys., vol. 156(14):144.502, 2022.

Tanguy A. *Vibrations and Heat Transfer in Glasses: The Role Played by Disorder*. C. R. Phys, vol. 24(S1):73–97, 2023.

Taraskin S. N. and Elliott S. R. *Ioffe-regel crossover for plane-wave vibrational excitations in vitreous silica*. Phys. Rev. B, vol. 61:12.031–12.037, 2000.

Tkachenko A. V. and Witten T. A. *Stress propagation through frictionless granular material*. Phys. Rev. E, vol. 60(1):687–696, 1999.

Hecke M. *Jamming of soft particles: geometry, mechanics, scaling and isostaticity*. J. Phys. Condens. Matter, vol. 22(3):033.101, 2009.

Kampen N. Stochastic Processes in Physics and Chemistry. Elsevier Science Publishers, Amsterdam, 1992.

Vogel F., Baumgärtel P., and Fuchs M. *Self-consistent current response theory of unjamming and vibrational modes in low-temperature amorphous solids*. Phys. Rev. X, vol. 15:011.030, 2025.

Vogel F. and Fuchs M. *Stress correlation function and linear response of brownian particles*. Eur. Phys. J. E, vol. 43(11), 2020.

Vogel F. and Fuchs M. *Vibrational phenomena in glasses at low temperatures captured by field theory of disordered harmonic oscillators*. Phys. Rev. Lett., vol. 130:236.101, 2023.

Vogel F., Zippelius A., and Fuchs; M. *Emergence of Goldstone excitations in stress correlations of glass-forming colloidal dispersions*. Europhys. Lett., vol. 125, 2019.

Voigtmann T. *Yield stresses and flow curves in metallic glass formers and granular systems*. Eur. Phys. J. E, vol. 34:1–12, 2011.

Wajnryb E., Altenberger A. R., and Dahler J. S. *Uniqueness of the microscopic stress tensor*. J. Chem. Phys., vol. 103:9782, 1995.

Wang L., Berthier L., Flenner E., Guan P., and Szamel G. *Sound attenuation in stable glasses*. Soft Matter, vol. 15:7018–7025, 2019a.

Wang L., Ninarello A., Guan P., Berthier L., Szamel G., and Flenner E. *Low-frequency vibrational modes of stable glasses*. Nat. Commun., vol. 10(1), 2019b.

Wilhelm V., Krüger M., Fuchs M., and Vogel F. *Evaluation of the probability current in the stochastic path integral formalism*. 2024. *preprint*, Available at `https://arxiv.org/abs/2411.14004`.

William Jones N. M. Theoretical Solid State Physics- Volume 1: Perfect Lattices in Quilibrium, vol. 1. John Wiley and Sons LtD., New York, 1973.

Wuttke J., Petry W., Coddens G., and Fujara F. *Fast dynamics of glass-forming glycerol*. Phys. Rev. E, vol. 52:4026–4034, 1995.

Wyart M. *On the rigidity of amorphous solids*. Annales de Physique, vol. 30(3):1–96, 2005.

Wyart M. *Scaling of phononic transport with connectivity in amorphous solids*. Europhys. Lett., vol. 89(6):64.001, 2010.

Wyart M., Silbert L. E., Nagel S. R., and Witten T. A. *Effects of compression on the vibrational modes of marginally jammed solids*. Phys. Rev. E, vol. 72:051.306, 2005.

Xiang X., Patinet S., Volz S., and Zhou Y. *Quasilocalized vibrational modes as efficient heat carriers in glasses*. Int. J. Heat Mass Transf., vol. 210:124.150, 2023.

Xu N., Wyart M., Liu A. J., and Nagel S. R. *Excess vibrational modes and the boson peak in model glasses*. Phys. Rev. Lett., vol. 98:175.502, 2007.

Yan L., DeGiuli E., and Wyart M. *On variational arguments for vibrational modes near jamming*. Europhys. Lett, vol. 114(2):26.003, 2016.

Yu C. C. and Carruzzo H. M. *Two-level systems and the tunneling model: A critical view*. In: Ramos M. (Editor) Low-Temperature Thermal and Vibrational Properties of Disordered Solids, chap. Chapter 4, pp. 113–139. World Scientific (Europe), London, 2022.

Zaccone A. and Scossa-Romano E. *Approximate analytical description of the nonaffine response of amorphous solids*. Phys. Rev. B, vol. 83:184.205, 2011.

Zeller R. C. and Pohl R. O. *Thermal conductivity and specific heat of noncrystalline solids*. Phys. Rev. B, vol. 4:2029–2041, 1971.

Zemyan S. The Classical Theory of Integral Equations- A Concise Treatment. Birkhaeuser, New York, 2012.

Zwanzig R. Nonequilibrium Statistical Mechanics. Oxford University Press, New York, 2001.

Zwanzig R. and Mountain R. D. *High-frequency elastic moduli of simple fluids*. J. Chem. Phys., vol. 43(12):4464–4471, 1965.

3. Fachbereich Physik

Eidesstattliche Versicherung gem. § 6 der Promotionsordnung der Universität Konstanz (Anlage 1 Promotionsordnung)

1. Bei der eingereichten Dissertation zu dem Thema

A theory of Jamming and elastic instability in low temperature amorphous solids

handelt es sich um meine eigenständig erbrachte Leistung.

2. ☒ Ich habe nur die angegebenen Quellen und Hilfsmittel benutzt und mich keiner unzulässigen Hilfe Dritter bedient. Insbesondere habe ich wörtlich oder sinngemäß aus anderen Werken übernommene Inhalte als solche kenntlich gemacht.

   ☒ Falls ich textgenerierende KI-Tools als Hilfsmittel verwendet habe, ist mir bewusst, dass ich allein für die inhaltliche Richtigkeit von KI generierten Textpassagen und die Kennzeichnung von Formulierungen und Ideen anderer Personen gemäß den Grundsätzen der guten wissenschaftlichen Praxis verantwortlich bin.

3. ☒ Die Arbeit oder Teile davon habe ich ~~wie folgt~~/bislang nicht[1] an einer Hochschule des In- oder Auslands als Bestandteil einer Prüfungs- oder Qualifikationsleistung vorgelegt.

Titel der Arbeit:

A theory of Jamming and elastic instability in low temperature amorphous solids

Hochschule und Jahr:

Universität Konstanz 2025

Art der Prüfungs- oder Qualifikationsleistung:

Promotion

4. ☒ Die Richtigkeit der vorstehenden Erklärungen bestätige ich.

5. ☒ Die Bedeutung der eidesstattlichen Versicherung und die strafrechtlichen Folgen einer unrichtigen oder unvollständigen eidesstattlichen Versicherung sind mir bekannt.

Ich versichere an Eides statt, dass ich nach bestem Wissen die reine Wahrheit erklärt und nichts verschwiegen habe.

Konstanz 03.05.2025 Aki Vall

Ort und Datum **(Unterschrift)**

[1] **Nicht Zutreffendes streichen. Bei Bejahung sind anzugeben: der Titel der andernorts vorgelegten Arbeit, die Hochschule, das Jahr der Vorlage und die Art der Prüfungs- oder Qualifikationsleistung**